Applied Condition Monitoring

Anna Timofiejczuk
Fakher Chaari
Radosław Zimroz
Walter Bartelmus
Mohamed Haddar *Editors*

Advances in Condition Monitoring of Machinery in Non-Stationary Operations

Proceedings of the 5th International Conference on Condition Monitoring of Machinery in Non-Stationary Operations, CMMNO'2016, 12–16 September 2016, Gliwice, Poland

Springer

Applied Condition Monitoring

Volume 9

About this Series

The book series Applied Condition Monitoring publishes the latest research and developments in the field of condition monitoring, with a special focus on industrial applications. It covers both theoretical and experimental approaches, as well as a range of monitoring conditioning techniques and new trends and challenges in the field. Topics of interest include, but are not limited to: vibration measurement and analysis; infrared thermography; oil analysis and tribology; acoustic emissions and ultrasonics; and motor current analysis. Books published in the series deal with root cause analysis, failure and degradation scenarios, proactive and predictive techniques, and many other aspects related to condition monitoring. Applications concern different industrial sectors: automotive engineering, power engineering, civil engineering, geoengineering, bioengineering, etc. The series publishes monographs, edited books, and selected conference proceedings, as well as textbooks for advanced students.

More information about this series at http://www.springer.com/series/13418

Anna Timofiejczuk · Fakher Chaari
Radosław Zimroz · Walter Bartelmus
Mohamed Haddar
Editors

Advances in Condition Monitoring of Machinery in Non-Stationary Operations

Proceedings of the 5th International Conference on Condition Monitoring of Machinery in Non-Stationary Operations, CMMNO'2016, 12–16 September 2016, Gliwice, Poland

Springer

Editors
Anna Timofiejczuk
Faculty of Mechanical Engineering
Silesian University of Technology
Gliwice
Poland

Walter Bartelmus
Institute of Mining Engineering
Wrocław University of Technology
Wrocław
Poland

Fakher Chaari
National School of Engineers of Sfax
Sfax
Tunisia

Mohamed Haddar
National School of Engineers of Sfax
Sfax
Tunisia

Radosław Zimroz
Institute of Mining Engineering
Wrocław University of Technology
Wrocław
Poland

ISSN 2363-698X ISSN 2363-6998 (electronic)
Applied Condition Monitoring
ISBN 978-3-319-61926-2 ISBN 978-3-319-61927-9 (eBook)
https://doi.org/10.1007/978-3-319-61927-9

Library of Congress Control Number: 2017944303

Printed on acid-free paper

This Springer imprint is published by Springer Nature
The registered company is Springer International Publishing AG
The registered company address is: Gewerbestrasse 11, 6330 Cham, Switzerland

Preface

The fifth edition of CMMNO conference was held together with the 6th International Congress on Technical Diagnostics in Gliwice, Poland, in September, 2016. This time, the event was organized by Silesian University of Technology in Gliwice, Faculty of Mechanical Engineering, and Polish Society of Technical Diagnostics. The conference have been interesting, convolving CMMNO with ICTD gave a chance to track new ideas in condition monitoring of machines under nonstationary operations for broader audience.

Mission of the conference is to be as close as possible to real problems in condition monitoring. It was a privilege and great honor to host as keynote speakers outstanding experts in field of diagnostics, both with academic and industrial background, namely:

- Prof. Fulei Chu, Department of Mechanical Engineering, Tsinghua University, Beijing, China
- Prof. Giorgio Dalpiaz, Department of Engineering, University of Ferrara, Italy
- Prof. Spilios D. Fassois, Stochastic Mechanical Systems & Automation (SMSA) Laboratory, Department of Mechanical and Aeronautical Engineering, University of Patras, Greece
- Dr. James Ottewill, ABB Corporate Research Center, Cracow, Poland
- Dr. Ibrahim A Sever, Rolls-Royce, UK

The conference (including ICDT that will be also summarized as separate volume in Applied Condition Monitoring series) consisted of 19 sessions, and it could be said that almost all from important areas of modern technical diagnostics have been presented.

All the chapters included in this book were rigorously reviewed by 2 referees, so we would like to express our gratitude to all reviewers. Based on reviewer's opinions, 34 papers have been selected to be published as CMMNO proceedings volume in Applied Condition Monitoring series.

Selected papers in most cases described novel diagnostic techniques that combine known signal processing methods or decision-making approaches. In a few cases, novel signal processing methods have been proposed, including adaptation of

known techniques to seriously nonstationary signals. Also several papers discussed technical aspects of condition monitoring systems (how to design it in the cheapest way, what techniques should be used to minimize energy consumption, especially in mobile, wireless systems, how to calibrate sensors, etc.). Two papers recalled model-based diagnostic approach, i.e., model of mechanical system or phenomena have been proposed and used to design diagnostic procedure.

It is worthy to mention that variety of objects have been investigated (gears, bearings, engines, pipes, blades… etc.), and researchers used various physical data to describe phenomena (vibration, acoustics, infrared thermography, temperature…).

It should be noted that majority of papers have highlighted nonstationarity of operating condition that proves that this conference should be continued, and we kindly invite researchers to Santander, Spain, in 2018 for sixth edition of CMMNO.

At the end, we would like to acknowledge to all authors, presenters, and participants of 5th edition of CMMNO, thanks to all of them; this conference is still important, has good reputation, and brings original contribution to engineering community.

Gliwice, Poland — Anna Timofiejczuk
Sfax, Tunisia — Fakher Chaari
Wrocław, Poland — Radosław Zimroz
Wrocław, Poland — Walter Bartelmus
Sfax, Tunisia — Mohamed Haddar
2017

Contents

Structural Health Monitoring of Aero-Engines in Non-stationary Operations 1
Mirosław Witos, Mariusz Zieja, Andrzej Szczepankowski and Janusz Szymczak

A New Approach to Tune the Vold-Kalman Estimator for Order Tracking 11
Amadou Assoumane, Julien Roussel, Edgard Sekko and Cécile Capdessus

Estimation of Cyclic Cumulants of Machinery Vibration Signals in Non-stationary Operation 21
J. Roussel, A. Assoumane, C. Capdessus and E. Sekko

Simplified Dynamic Model of a Wind Turbine Shaft Line Operating in Non-stationary Conditions Applied to the Analysis of IAS as a Machinery Surveillance Tool 33
Jose L. Gomez, Ilyes Khelf, Adeline Bourdon, Hugo André and Didier Rémond

Current Signal Analysis of an Induction Machine with a Defective Rolling Bearing 45
Aroua Fourati, Adeline Bourdon, Didier Rémond, Nabih Feki, Fakher Chaari and Mohamed Haddar

Fault Detection in Gears Using Stochastic Resonance 55
Clement Uchechukwu Mba, Stefano Marchesiello, Alessandro Fasana and Luigi Garibaldi

The Impact Estimation of Damping Foundations in Dynamics of the Rotor System in Non-stationary States 71
Andrzej Grządziela, Marcin Kluczyk and Paweł Chwin

Knife Diagnostics with Clustering Techniques and Support Vector Machines 81
Achraf Lahrache, Marco Cocconcelli and Riccardo Rubini

Stable Distributions and Fractal Diagnostic Models of Vibration Signals of Rotating Systems 91
Andrzej Puchalski and Iwona Komorska

Selection of Suitable Method for Speed Recovery from Vibration Signal 103
Adam Jabłoński, Kajetan Dziedziech and Ziemowit Dworakowski

How to Build a Vibration Monitoring System on Your Own? 111
Adam Jabłoński, Michał Żegleń, Wojciech Staszewski, Piotr Czop and Tomasz Barszcz

Optimization of Calculations for Wireless Condition Monitoring Systems 123
Kajetan Dziedziech, Adam Jabłoński and Tomasz Barszcz

Supervised Classification Methods in Condition Monitoring of Rolling Element Bearings 133
Paweł Różak, Jakub Zieliński, Piotr Czop, Adam Jabłoński, Tomasz Barszcz and Michał Mareczek

Empirical Signal Decomposition Methods as a Tool of Early Detection of Bearing Fault 147
Jacek Dybała and Jakub Komoda

Using Vibroacoustic Signals in Evaluation of Knocking Combustion in a Dual Fuel Engine 157
Krzysztof Szczurowski, Stanisław Radkowski, Łukasz Zieliński and Damian Walczak

Hybrid Scheme for Wind Turbine Condition Monitoring Based on Instantaneous Angular Speed and Pattern Recognition 167
Ilyes Khelf, Jose L. Gomez, Adeline Bourdon, Hugo Andre and Didier Remond

Fault Diagnostic of Machines Under Variable Speed Operating Conditions Using Order Tracking and Novelty Detection 179
O. Cardona-Morales and G. Castellanos-Dominguez

Bearing Fault Identification Based on Blind Extraction of Cyclostationary Signals Using Order Tracking 191
O. Cardona-Morales, E. F. Sierra-Alonso and G. Castellanos-Dominguez

Rotating Machinery Diagnostics Based on Fusion of Infrared and Vibration Measurements 203
Sebastian Budzan, Dariusz Buchczik, Marek Pawełczyk and Roman Wyżgolik

Calibration of Accelerometers Using Multisinusoidal Excitation 213
Dariusz Buchczik and Marek Pawełczyk

Operational Condition Monitoring of Wind Turbines Using Cointegration Method 223
Phong B. Dao, Wieslaw J. Staszewski and Tadeusz Uhl

Knocking Sounds in the Wind Turbine Gearbox During Slowing Down—Case Study 235
Tomasz Barszcz, Rafał Gawarkiewicz, Adam Jabłoński, Michał Sękal and Michał Wasilczuk

Multifractals in Technical Diagnostics General Concept 245
Damian Skupnik

Complementary View on Multivariate Data Structure Based on Kohonen's SOM, Parallel Coordinates and t-SNE Methods 255
Anna M. Bartkowiak and Radosław Zimroz

Engine Diagnosis Based on Vibration Analysis Using Different Fuel Blends 267
Jairo A. Grajales, Héctor F. Quintero, Carlos A. Romero and Edison Henao

Application of Cepstrum Prewhitening on Non-stationary Signals 275
L. Barbini, M. Eltabach and J. L. du Bois

Using of Entropy Method in Failure Diagnostics 285
Stanisław Radkowski, Marcin Jasiński, Robert Gumiński and Adam Gałęzia

Use of Bispectral Measures in Machines Faults Diagnostics—Examples 297
Marcin Jasiński

Hybrid Method for Researching Pulsating Flows in Pipes Exemplified with Orifice Application 309
Tomasz Pałczyński and Wojciech Rydlewicz

Dynamic Behavior of Spur Gearbox with an Elastic Coupling Under Acyclism Regime 319
Atef Hmida, Ahmed Hammami, Mohamed Taoufik Khabou, Fakher Chaari and Mohamed Haddar

Possibilities of Faults Detection of Rolling Bearings Using Energetic Descriptors of Vibrations Signals 329
Adam Gałęzia, Roman Barczewski and Bartosz Jakubek

Bearing Fault Feature Extraction Using Autoregressive Coefficients, Linear Discriminant Analysis and Support Vector Machine Under Variable Operating Conditions 339
Mourad Kedadouche, Zhaoheng Liu and Marc Thomas

Multidimensional Data Segmentation Based on Blind Source Separation and Statistical Analysis 353
Jacek Wodecki, Pawel Stefaniak, Pawel Śliwiński and Radosław Zimroz

Unsupervised Anomaly Detection for Conveyor Temperature SCADA Data 361
Jacek Wodecki, Paweł Stefaniak, Marta Polak and Radosław Zimroz

Index 371

Structural Health Monitoring of Aero-Engines in Non-stationary Operations

Mirosław Witos, Mariusz Zieja, Andrzej Szczepankowski and Janusz Szymczak

Abstract With the ultimate goal of rotating machinery diagnosis using Instantaneous Angular Speed (IAS) and Time of Arrival (TOA) signals, this paper provides the theoretical background of non-stationary processes existing in the aero-engines and their monitoring using atypical encoders (e.g. fans, compressors and turbine blades cooperating with the induction sensors, AC and DC generators). The model of TOA signal including aperiodic, periodic and stochastics components has been described. The classical and expert approach to monitoring of operational and structural health parameters (CM, NDT, SHM) of aircraft and its power transmission system has been also described. Finally, the experience of the Tip Timing method used in the Armed Forces of the Republic of Poland is presented. The possibility of structural health monitoring and active controlling of the material fatigue by the aero-engine user through interference in the fuel system adjustment quality has been confirmed. Phase portraits have been used to analyze TOA components in transient state of the engine. Diagnostic criteria and expert algorithms have been verified during active and passive experiments.

Keywords Transport · Fatigue of material · Condition monitoring · Structural health monitoring · Modal analysis · Time of arrival · Tip timing method · Encoder · Expertsystem · Safety

M. Witos (✉) · M. Zieja · A. Szczepankowski · J. Szymczak
Air Force Institute of Technology, Ks. Bolesława 6, 01-494 Warsaw, Poland
e-mail: witosm@itwl.pl

M. Zieja
e-mail: mariusz.zieja@itwl.pl

A. Szczepankowski
e-mail: andrzej.szczepankowski@itwl.pl

J. Szymczak
e-mail: janusz.szymczak@itwl.pl

A. Timofiejczuk et al. (eds.), *Advances in Condition Monitoring of Machinery in Non-Stationary Operations*, Applied Condition Monitoring 9,
https://doi.org/10.1007/978-3-319-61927-9_1

1 Introduction

Aircraft and helicopters are operated in nonstationary states. Even during:

- ground operation of an engine with constant average rotational speed, or
- an aircraft horizontal flight with constant forward speed,

exist random interferences (such as: wind, rain, thermal currents, bird ingestion, icing), which locally or globally create disturbances of stationary processes, generating reactions of different aircraft systems (i.e. an autopilot, a power-supply system, a hydraulic system). Factors creating disturbances of stationary processes are also pilot's actions regarding operation, navigation and providing aircraft stability. An issue of nonstationary processes concerns particularly a power transmission system and its subsystems.

Processes of:

- a flow round a rotating blade profile in a compressor or a turbine and their aerodynamic loads;
- fuel combustion with flow keying in the inlet and the outlet of the combustion chamber (through the compressor and the turbine, and modal properties of the combustion chamber);

are the main factors, that have an impact on the load spectrum, fatigue degradation processes of engine elements (problems of **L**ow **C**ycle **F**atigue, LCF, **H**igh **C**ycle **F**atigue, HCF, **V**ery **H**igh **C**ycle **F**atigue, VHCF and **T**hermo-**M**echanical **F**atigue, TMF) and the risk level of the aviation accident for technical reasons. Incomplete information on the spectrum of nonstationary processes in the engine is a challenge both for design and diagnostic engineers.

In the article many years' experience with active control of material fatigue in critical elements of the SO-3 jet engine. Experience is based on monitoring of engine's intermediate states, analyses of modal properties for critical elements and active interference in the spectrum of stationary and nonstationary processes [1].

2 Theoretical Basis

2.1 Stationary Versus Non-stationary Processes

Loosely speaking a stationary process is one whose *statistical properties* do not change over time. A strictly stationary stochastic process is one where given $t_1, \ldots, t_n$ the joint statistical distribution of $X_{t_1}, \ldots, X_{t_n}$ is the same as the joint statistical distribution of $X_{t_1+\tau}, \ldots, X_{t_n+\tau}$ for all n and τ. Since the definition of

strict stationarity is generally too strict for everyday life a weaker definition of second order or weak stationarity is usually used. *Weak stationarity* means that mean and the variance of a stochastic process do not depend on t and the auto covariance between X_t and $X_{t+\tau}$ only can depend on the lag τ (τ is an integer the quantities also need to be finite). Hence for stationary processes, $\{X_t\}$, the definition of autocovariance is

$$\gamma(\tau) = cov(X_t, X_{t+\tau}) = E[(X_t - E[X_t])(X_{t+\tau} - E[X_{t+\tau}])] \quad (1)$$

for integer τ. $E[X_t]$ is the expected value of X_t, also known as the mean of X_t. Stationary processes can be divided into deterministic and random [2].

Rotating machinery generally produces stationary vibration signals in order domain (f/f_r where f_f is frequency of the rotor), but no aero-engines with: (1) variable rotation speed, (2) low stiffness of the hull and the rotor, (3) nonlinearity of rotor supports, (4) broadband extortion (mass and aerodynamic), including the combustion process as the main source of extortion variables, and (5) interference vibration of compressor and turbine blades and the engine rotor with the control system. In aero-engines many processes are non-stationary, including processes of the material degradation.

A non-stationary process is one whose *statistical properties* change over time. Non-stationary behaviors can be trends, cycles (i.e. AM-FM-PM modulation of sine), random walks or combinations of the three [1, 2]. Before we get the point of transformation for the diagnostic of non-stationary time series data, we should distinguish between the different types of the non-stationary processes—Table 1. This will provide us with a better understanding of the processes and allow us to apply the correct transformation.

Table 1 Type of non-stationary processes existing in the aero-engines [1, 2]

Non-stationary process	Model
Non-stationarity in variance	$X_t = \mu_t + \varepsilon_t$
Non-stationarity in mean (trend)	$X_t = \mu_t = \sum_{i=1}^{d} c_i t^i$
Non-stationary sinusoid	$X_t = A_t e^{j(\varphi_t + \varphi_0)}$
Pure random walk	$X_t = X_{t-1} + \varepsilon_t$
Random walk with drift	$X_t = \alpha + X_{t-1} + \varepsilon_t$
Deterministic trend	$X_t = \alpha + \beta t + \varepsilon_t$
Random walk with drift and deterministic trend	$X_t = \alpha + X_{t-1} + \beta t + \varepsilon_t$

Where μ_t is a non-stochastic mean level, ε_t is random error component, A_t is amplitude of non-stationary sinusoid, φ_t is angle of non-stationary sinusoid, α is a drift, βt is regressed on a time trend.

2.2 Measurement Signals

Stationary and nonstationary processes $\{X_i(t)\}$ can be or have already been monitored with application of contemporary measuring techniques and methods of numerical analysis. A proper selection of:

- methods of process observation $H(t)$—an implicit transition function *processes* ⇒ *signals*, and
- a set of analogue signals $S(t)$—state observers,

should provide observability of monitored process on the level, which enables to make a diagnosis with minimum probability, POD. A stage of input data acquisition to monitor processes is described using the relationship (2). A matrix of analogue signals includes aperiodic $\mathbf{A}(t)$, periodic $\mathbf{P}(t)$ and stochastic components $\mathbf{I}(t)$.

$$\mathbf{S}(t) = \mathbf{H}(t) \cdot \{\mathbf{X}_i(t)\} = \mathbf{A}(t) + \mathbf{P}(t) + \mathbf{I}(t) \tag{2}$$

Contemporary systems to monitor operational and structural health parameters are based on the microprocessor technique and the digital discrete-time signal $\mathbf{S}(k)$. Digitalization of a continuous-time signal can be done with uniform and non-uniform steps of sampling [3, 4].

Results of measurements are always encumbered with noises and measurement interferences $\mathbf{I}_m(k)$, that can be different for particular measurement channels. As a result, diagnostician receives information about monitored processes in the form of noise time series:

$$\mathbf{S}_m(k) = \mathbf{S}(k) + \mathbf{I}_m(k) \tag{3}$$

in which can be found:

- duplicated spectrum (alias) of continuous-time signal $S(t)$,
- harmonics generated by nonlinearity of the function $H(t)$ and the measurement section,
- drift of the measurement section.

2.3 Signal Analysis

In order to reliably diagnose processes in the tested object, components $\mathbf{S}(k)$ and $\mathbf{I}_m(k)$ should be separated from measurement data $\mathbf{S}_m(k)$. The component $\mathbf{I}_m(k)$ enables the assessment of structural health of measurement section and reliability of measurement data. When measurement data are reliable, the signal matrix $\mathbf{S}(k)$ is analyzed in order to separate diagnostic symptoms and compare their values with reference criteria.

There are several books and papers on time series analysis without aliasing [5–10]. Most statistical books are concentrated on stationary time series and some texts provide complex coverage of "globally non-stationary" series. The problem of processing time series with aliases is overlooked in the literature, despite considerable benefits that can be achieved with the conscious use of aliasing in the diagnosis.

3 Condition Monitoring of Aircraft

Monitoring of operational and structural health parameters (CM, NDT, SHM) of aircraft and its power transmission system is done in order to decrease operational/maintenance costs and risk of aviation accidents. There are two different diagnostic approaches:

- classical,
- advisory and expert,

which are different taking the range and the purpose into consideration.

3.1 The Classical Approach

A classical approach is used to monitor how the aircraft operational/maintenance regulations are observed by flight crew and technical personnel, to assess operational parameters of functional systems, and to identify exceeding of operational limits. In order to monitor the power transmission system (a jet engine or a turboprop engine) there are used signals (Table 2) registered by:

- cockpit indicators (analogue and/or digital), that on-line inform flight crew about *average values* of operational parameters;
- accident data recorders, that inform flight crew and ground personnel about exceeding *instantaneous values* of operational parameters;
- flight data recorders, that inform ground personnel about *instantaneous values* of operational parameters during the flight (post factum analysis).

There are also used signals from periodical nondestructive testing and laboratory research of oil and fuel.

Diagnostic criteria are based on simple relations in the analysis of simple signals with complete disregard for relationships between registered signals (in fact, signals are mutually dependent by the thermodynamic cycle, the automatic control system and the thermal capacity of the engine and its systems). Criteria in the following form:

$$\textit{if}\,(\textit{value} \notin \textit{the scope of the rule points})\ \textit{then},\ \text{“1”}\ \textit{else}\ \ \text{“0”}, \tag{4}$$

Table 2 Typical signals applied in diagnostics of engine and power transmission system

Monitoring scheme	Advantages	Disadvantages
Rotation speed	Direct measurement of the range of aero-engine operation	The offset analogue gauges may be greater than the tolerance range of the engine
	Able to detect errors adjusting the fuel control system and its fault	
Torque	Direct measurement of the range of turboprop engine operation	High signal dynamics—a level exceeding the operational limitations may not be noticed by the crew (to transient conditions)
	Able to detect errors adjusting the pitch control unit and its fault and control errors by the crew	
Temperature at the inlet/outlet of the turbine	Detection TMF risk of turbine blade and adjust the fuel system errors or failures or errors automatic nozzle	High signal dynamics—a level exceeding the operational limitations may not be noticed by the crew (to transient conditions)
Temperature of oil	Detection of failure of the oil system, and operation errors	Do not detect overheating of the oil after the engine is stopped
Pressure of oil		
Setting the vanes of the compressor	Detection system failure of compressor mechanization	Information not available in the cabin
Vibration monitoring	Detection of unbalance and misalignment of the rotor	Low band signal—lack of information about the vibration of gears and rotating blades
	Reliable	

should detect exceeding of the acceptable operating range (state "1"). Among registered data there often are not signals of power unit control (power lever and collective pitch lever), which encumbers getting reliable diagnosis about causes for monitored exceeding even in stationary states. In classical monitoring systems detection of serious engine failures, which don't result in "visible" operational exceeding, is also encumbered—the example 1. The failures most often are not detected by classical monitoring systems!

Periodic nondestructive testing (e.g. visual inspections, ultrasonic inspections, eddy current inspections) and oil examination are aimed at detection of accelerated degradation of engine structure—results of unrecognized and unadjusted hazards, including adjustment errors for fuel and control systems [1, 13].

Example 1: The increase of temperature field non-uniformity before the turbine.

The temperature before/behind the turbine is registered by the system of thermocouples located circumferentially on the given draught (radius). The signal from thermocouples is subject to average before the arrival at the cockpit indicator and the flight data recorder. Growing circumferential non-uniformity of the temperature field, of the order of 30%, can be transformed by the thermocouple system into the temperature value decrease in regard to the expected value for the given engine operational mode. The situation takes place, when the majority of thermocouples is

located in minimums of the non-uniform temperature field. An operator finds out the existing hazard of TMF for turbine blades only during nondestructive testing of hot engine elements or after their break-off [1, 11].

The non-uniform temperature field before the turbine can modify also the aerodynamic and mass load spectrum for compressor blades (the influence of viscous flow on reverse propagation of the disturbance in the engine gas dynamical duct) and bearing. Also in the engine remoted areas, accelerated material degradation and failure conditions, resulting from the non-uniform temperature field before the turbine, can be present (RTO/NATO [1, 12]).

3.2 The Advisory and Expert Approach

Knowledge of classical approach disadvantages in power unit monitoring and financial cost incurred by operators are an inspiration to design and apply in aviation:

- developed monitoring systems of the power unit, i.e. CAMP Engine Health Monitoring application for Pratt and Whitney Canada engines, and Health and Usage Monitoring Systems (CAMP web, HUMS conference database), which include condition-based maintenance and operational data recording,
- new proactive methods of aircraft flight safety management (RTO/NATO [1, 12, 16, 17]).

Software of advisory and expert systems embodies multi-parametric criteria, covering the numerical model of the diagnosed object and processes, and relations existing between registered parameters. There are also available new broadband signals and results of trend analysis, which give signals to operators about increasing hazard of the lasting effect appearance in the engine and financial cost, i.e. the decrease of compressor/turbine efficiency as a result of erosion or excessive soil inside the engine (flights in dust-laden air). Multi-parametric monitoring systems have higher POD achieved at the expense of aircraft/helicopter equipping with additional measurement sections and increasing of processing time for measurement data.

3.3 Tip Timing Method

A distinctive approach to the expert and complex diagnosis of the aircraft engine has been implemented in the SNDŁ-1b/SPŁ-2b/CTM-PER monitoring system, which has been applied for operation/maintenance and overhauls of SO-3 engines for 20 years [18]. The SNDŁ-1b/SPŁ-2b/CTM-PER monitoring system uses only one signal—information on time of arrival TOA for rotating and vibrating compressor blades under a stationary sensor fixed in the fuselage (Tip Timing Method) [1, 19–22].

A system: a reluctance sensor—a rotating grid of blades and a rotor form a particular encoder. Blades with unknown but forecast modal characteristics (mechanical combo filter) are both the phase indicator of rotor turns and the observer of identified processes in the engine.

A sophisticated engine diagnosis by means of TTM method is practicable owing to the complex structure of TOA signal [1]. Measured TOA signal covering the measurement section noise $I_m(k)$ can be described using following relationship (5):

$$TOA(k) = \frac{1+\zeta_\varphi(k)}{1+\zeta_\omega(k)} TOA_t(k) + I_m(k) = A(k) + P(k) + I(k) \tag{5}$$

where: TOA_t is theoretical time of arrival of a blade from an ideal rotor without errors of scale, vibration and seating of the rotor in supports, resulting from the number of the phase marks (blades) N_B and the instantaneous average angular velocity of the rotor ω; ζ_φ is jitter of blades group components; ζ_ω is jitter of rotor group components.

All TOA signal components are used to diagnose the engine and the measurement section. On the basis of numerical decomposition of TOA components covering, i.e.:

- data on expected signal characteristics—Table 1,
- algorithms of the analysis of TOA signal components on the phase plane,
- models of dynamic effects, including engine rotation dynamics, verified on the basis of all year measurement data,

the engine operator complex and reliable information about:

- engine health (1st stage compressor rotor blades, fuel system, rotor bearing)—Figs. 1 and 2 [1, 13, 17],
- disadvantageous dynamic effects (stall, surge, flutter, resonance of blade or combustion chamber, foreign object in inlet, blade cracking).

Diagnostic rules are based on the multiple analysis of observed process dynamics, which can be described using following relationship:

$$\forall i \in (1, 2, \ldots, m) CV = \left[Par_i, \frac{dPar_i}{dt}, \frac{d^2 Par_i}{dt^2} \right] \in TS \rightarrow DUT \text{ is suitable}, \tag{6}$$

where CV is state vector, TS is technical specification.

Available simultaneous information on the rotor blade vibration spectrum and the quality of the fuel system enables operators and diagnosticians to interfere in engine dynamic processes [12]. The active control of fatigue processes of engines SO-3 is realized by means of individual optimization of engine operational conditions [1, 17, 18].

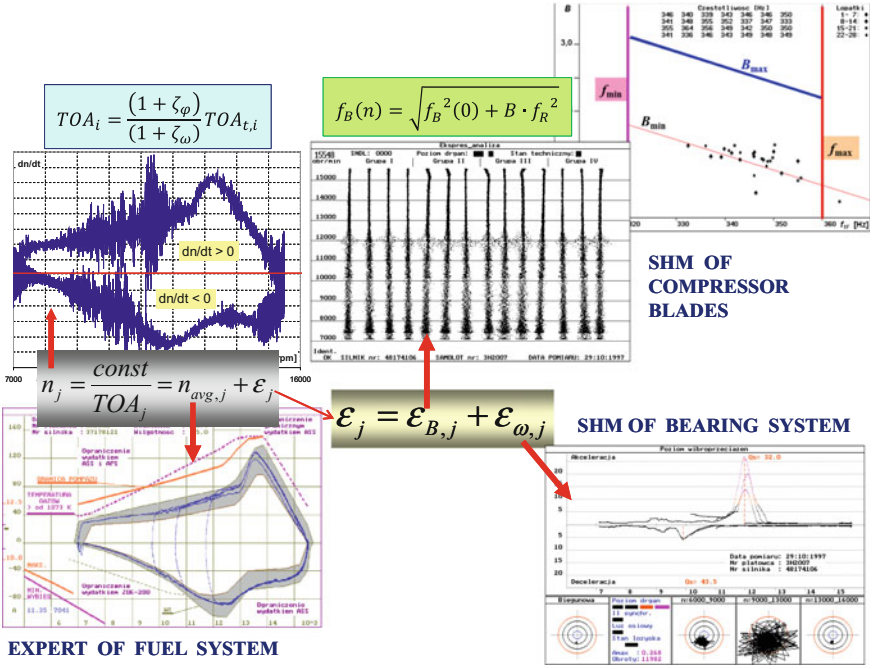

Fig. 1 Illustrated some capabilities of the expert diagnostic system SPŁ-2b/CTM-PER

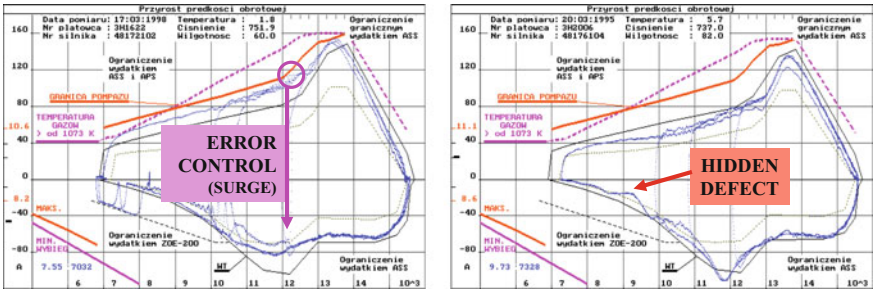

Fig. 2 Example problems with the engine power unit diagnosed by means of TTM method

4 Conclusions

The possibility of structural health monitoring and active controlling of the material fatigue by the aero-engine user through interference in the fuel system adjustment quality has been confirmed. Since 1991 any compressor blade crack in the SO-3 engine operation has not occurred—the statistical time between blade cracks has been prolonged for over **1500%**.

References

1. Witos, M. (2011). Increasing the Durability of Turbine Engine Components Through Active Diagnostics and Control. Research Works of AFIT, 29:324 p. (pol.). doi:10.13140/RG.2.1.4341.4560.
2. Nason, G. P. (2006). Stationary and non-stationary time series, In: H. M. Mader., Coles, S. G., Connor C. B., & Connor L. J. (Eds.), Statistics in Volcanology, Special Publication of IAVCEI, 1:129–142, Geological Society of London, London.
3. Sampath, S. (2005). *Sampling Theory and Methods* (2nd ed.). Alpha Science Int.
4. Bilinskis, I. (2007). *Digital Alias-free Signal Processing*. Wiley.
5. Reinsel, G. C. (2012). *Elements of Multivariate Time Series Analysis*. Berlin: Springer.
6. Douc, R. et al. (2014). *Nonlinear Time Series. Theory, Methods, and Application with R Examples*. London, New York: CRC Press.
7. Vinson, R. G. (2014). Rotating machine diagnosis using smart feature selection under non-stationary operating conditions. Thesis, University of Pretoria.
8. Ettefagh, M. M., & Sadeghi, M. H. (2011). Gear fault diagnosis via non-stationary adaptive MARTIN distance. *Scientia Iranica B, 18*(1), 59–65.
9. Muševič, S. (2013), Non-stationary sinusoidal analysis. Phd dissertation, Universitat Pompeu Fabra, Barcelona.
10. Bently, D. E., & Goldman, P. (2001). *Rolling Element Bearing Defect Detection and Diagnostics Using REBAM® Method* (pp. 12–25). Second Quarter: ORBIT Magazine.
11. Szczepankowski, A., & Szymczak, J. (2013). Identification of operational damages of air-turbine engines using visual diagnostics. *Solid State Phenomena, 199,* 33–42. doi:10.4028/3-908454-04-2.524.
12. Active control of engine dynamics. RTO EN-20/AVT-083, RTO/NATO 2002.
13. Szczepankowski, A. (1999). Diagnosing of technical condition of turbine engine using rotational speed phase-mapping method. Ph.D. dissertation, ITWL Warszawa (pol).
14. http://campsystem.com/PWCtransition.
15. http://humsconference.com.au/Papers.html.
16. Zieja, M., Smolinski, H., & Golda, P. (2015). Proactive methods—new quality in aircraft flight safety management. *Journal of KONBiN, 4*(36), 105–114.
17. Witoś, M. (2013). High Sensitive Methods for Health Monitoring of Compressor Blades and Fatigue Detection. *The Scientific World Journal, ID, 218460,* 31. doi:10.1155/2013/218460.
18. Witos, M., Wachlaczenko, M. (2015). Expert System to Support Operational Safety of the TS-11 "Iskra" Aircraft and Overhauls of the SO-3 Engines, 7th Int. Symposium on NDT in Aerospace, 16–18.11.2015 Bremen, Paper no Mo.4.A.7, The e-Journal of Nondestructive Testing, 2016-04 and 2016-05.
19. Duan, F. (2016). Method to improve the blade tip-timing accuracy of fiber bundle sensor under varying tip clearance. *Optical Engineering, 55*(1), 014106. doi:10.1117/1.OE.55.1.014106.
20. Vercoutter, A. et al. (2011). Tip Timing Spectral Estimation Method for Aeroelastic Vibration of Turbomachinery Blades. *International Forum on Aeroelasticity and Structural Dynamics, IFASD*-2011-82.
21. Ayes B. W. et al. (2005). Application of Generation 4 Non-contact Stress Measurement System on HCF Demonstrator Engines. In *Proceedings of 10th National Turbine Engine High Cycle Fatigue (HCF) Conference*. Dayton, USA.
22. Zielinski, M., Ziller, G. (2005). Noncontact blade vibration measurement system for aero engine application. In *17th International Symposium on Airbreathing Engines*, Munich, Paper No. ISABE-2005-1220.

A New Approach to Tune the Vold-Kalman Estimator for Order Tracking

Amadou Assoumane, Julien Roussel, Edgard Sekko and Cécile Capdessus

Abstract In the purpose to diagnose rotating machines using vibration signal, engineers use order tracking method to process non-stationary signals. We deal here with order tracking when the vibration signal is represented in a state space model. Such a methodology leads to the Kalman estimator that requires knowledge about the noise statistics affecting the state and the measurement equation. These noise statistics are usually unknown and need to be estimated from operating data for the use of the Kalman estimation algorithm. Several methods to tune these parameters have been developed for time-invariant model. In this paper, we introduce a technique to estimate the noise covariances for a linear time-variant system using the innovation process. The efficiency of this new approach is evaluated using a synthetic non-stationary vibration signal. The advantage of this approach is that it converges quickly and provides a small estimation error compared to those used for the linear time-invariant model.

Keywords Order tracking · Kalman estimator · Non-stationary signal · Covariance matrix estimation

1 Introduction

Nowadays, the tools dedicated to the condition monitoring deal more and more with non-stationary signal from mechanical systems. Non-stationary events occur during machine run-up or shut-down. The non-stationary phenomena can also be observed during the variation of wind speed in wind turbines or the variation of load in a crushing machine. Over the last two decades, several approaches have been proposed to extract information from non-stationary signals. All these approaches consist in tracking orders of a vibration signal under non-stationary conditions. The first category is based on the time-frequency representation. A well-known technique in this

A. Assoumane (✉) · J. Roussel · E. Sekko · C. Capdessus
Laboratoire PRISME, 21 Rue Loigny-La-Bataille, 28000 Chartres, France
e-mail: amadou.assoumane@etu.univ-orleans.fr

A. Timofiejczuk et al. (eds.), *Advances in Condition Monitoring of Machinery in Non-Stationary Operations*, Applied Condition Monitoring 9,
https://doi.org/10.1007/978-3-319-61927-9_2

category is the short time Fourier transform which supposes that the signal is stationary in a short time interval. And there is unanimity that the short time Fourier transform suffers from its time-frequency resolution limitation [1, 2]. The second one is the computed order tracking. This latter consists of re-sampling the non-stationary raw signal from time domain to angle domain in order to avoid the effects of speed variation. Computed order tracking is suitable for low speed variations [3]. For high speed variations, the computed order tracking method leads to a bad estimation of the envelope [4, 5]. It also has an impact on the re-sampled signal [6]. The last category uses adaptive estimators. The Kalman estimator is one of these kind of estimators which can be used for order tracking. This approach is based on the representation of the vibration signal in a state space model. For this purpose, Vold et al. proposed the Vold-Kalman estimator [7, 8]. This approach, from the first to the second generation of the Vold Kalman estimator, has known some important improvements.
However, the drawback of this tool is still the difficulty in correctly choosing the two parameters that influence the accuracy of the estimation. These parameters are: the covariance matrix of the measurement noise and the covariance matrix of the state noise. In the 1970, for the time invariant-model, Mehra [9] introduced a correlation method that produces unbiased and consistent estimates of these covariances. In [10], a new auto-covariance least-squares method is proposed which improves that of Mehra [9]. Few works have been devoted to the time variant-model. In this instance, Mohamed and Schwarz [11] have been one of the first authors to propose a tuning method. It is based on the innovation process and the residual error estimation. This method is modified by Almagbile et al. [12] for a problem related to the inertial navigation systems/global positioning systems. These approaches estimate the covariances of the disturbance signals using a sliding window. For application to the vibration signal, we remark that the positiveness of the covariance matrix of the state noise is not always guaranteed.
In the context above, we propose a new approach to tune the covariance matrix of the state noise. This one is based on the residual error estimation. The outline of the paper is as follows. The Sect. 2 presents the basics of the Vold-Kalman estimator. In the Sect. 3, we expose our new approach and the Sect. 4 presents simulations and comparative study with that of [12]. Conclusions are given in the Sect. 5.

2 The Vold-Kalman Estimator

The gearbox vibration signal can be modeled by the following equation

$$y(t) = \sum_{i=1}^{M} A_i(t) \cos(\theta_i(t) + \phi_i(t)) + v(t) \tag{1}$$

where A_i is the amplitude of the ith order, ϕ_i is the phase of the ith order, v is the measurement noise assumed to be centered, white and Gaussian and θ_i is the instantaneous angular displacement. It is calculated using the following equation

$$\theta_i(t) = 2\pi O_i \int_0^t f_r(u)du \tag{2}$$

where O_i is the value of the ith order, f_r is the instantaneous rotating frequency. Thus, the discrete form of the equation can be expressed as

$$\theta_i(k) = 2\pi O_i \sum_{j=1}^{k} \frac{f_r(j)}{f_s} \tag{3}$$

where f_s is the sampling frequency.
The Vold-Kalman estimator is a well known tool to process the vibration signal. And our goal is to evaluate the unknown amplitude and phase of some specific orders of interest using this tool. For this purpose, we construct the state equation and the measurement equation. These latter represent the basic equation of the Vold-Kalman estimator [8].

2.1 The Measurement Equation

The Eq. (1), in discrete domain, leads to

$$y(k) = \sum_{i=1}^{M} \left[\cos(\theta_i(k)) - \sin(\theta_i(k))\right] \begin{bmatrix} a_{i,c}(k) \\ a_{i,s}(k) \end{bmatrix} + v(k) \tag{4}$$

where $a_{i,c} = A_i \cos(\phi_i)$, $a_{i,s} = A_i \sin(\phi_i)$ and $v(k)$ is the discrete form of the measurement noise. Its covariance matrix is R_k.
Let put $a_i(k) = \begin{bmatrix} a_{i,c} \\ a_{i,s} \end{bmatrix}$ and $B_i(k) = \left[\cos(\theta_i(k)) - \sin(\theta_i(k))\right]$. Therefore, the Eq. (4) can be rewritten as

$$y(k) = \begin{bmatrix} \overbrace{0 \cdots 0}^{M-times} & B_1(k) \cdots B_M(k) \end{bmatrix} \begin{bmatrix} a_1(k-1) \\ \vdots \\ a_M(k-1) \\ a_1(k) \\ \vdots \\ a_M(k) \end{bmatrix} + v(k) \tag{5}$$

and symbolized by

$$y_k = H_k x_k + v_k \tag{6}$$

where $H_k = \begin{bmatrix} \overbrace{0 \cdots 0}^{M-times} & B_1(k) \cdots B_M(k) \end{bmatrix}$ is the measurement matrix and

$x_k = \begin{bmatrix} a_1(k-1) \\ \vdots \\ a_M(k-1) \\ a_1(k) \\ \vdots \\ a_M(k) \end{bmatrix}$ is the state variable.

The Eq. (6) represents the measurement equation of the Vold-Kalman estimator.

2.2 The State Equation

To estimate the components of the vector x_k, we use a Vold-Kalman constraint. It consists to model each component of the state variable by a smooth polynomial [7]. In general, this polynomial is of degree two and $2 - times$ differentiable. This approximation in time domain is

$$\frac{d^2 a_i(t)}{dt^2} = w_i(t) \tag{7}$$

where w_i is the ith state noise. In discrete time domain, the last equation becomes

$$a_i(k+1) - 2a_i(k) + a_i(k-1) = w_i(k) \tag{8}$$

The matrix form of the Eq. (8) yields to

$$\begin{bmatrix} a_i(k) \\ a_i(k+1) \end{bmatrix} = \begin{bmatrix} 0 & 0 \\ -1 & 2 \end{bmatrix} \begin{bmatrix} a_i(k-1) \\ a_i(k) \end{bmatrix} + \begin{bmatrix} 0 \\ w_i(k) \end{bmatrix} \tag{9}$$

To track all the M orders components, we generalize the previous equation and we obtain this one

$$\begin{bmatrix} a_1(k) \\ \vdots \\ a_M(k) \\ a_1(k+1) \\ \vdots \\ a_M(k+1) \end{bmatrix} = \begin{bmatrix} 0 & \cdots & 0 & 1 & \cdots & 0 \\ \vdots & \ddots & \vdots & \vdots & \ddots & \vdots \\ 0 & \cdots & 0 & 0 & \cdots & 1 \\ -1 & \cdots & 0 & 2 & \cdots & 0 \\ \vdots & \ddots & \vdots & \vdots & \ddots & \vdots \\ 0 & \cdots & -1 & 0 & \cdots & 2 \end{bmatrix} \begin{bmatrix} a_1(k-1) \\ \vdots \\ a_M(k-1) \\ a_1(k) \\ \vdots \\ a_M(k) \end{bmatrix} + \begin{bmatrix} 0 \\ \vdots \\ 0 \\ w_1(k) \\ \vdots \\ w_M(k) \end{bmatrix} \tag{10}$$

The symbolic form of the state equation is

$$x_{k+1} = Fx_k + w_k \tag{11}$$

where w is the state noise with an unknown covariance matrix Q_k Having a priori knowledge of R_k and Q_k, the algorithm to estimate the state variable can be implemented as follows

$$P_{k+1|k} = FP_kF^T + Q_k \tag{12}$$
$$K_{k+1} = P_{k+1|k}H_{k+1}^T[H_{k+1}P_{k+1|k}H_{k+1}^T + R_k]^{-1} \tag{13}$$
$$\hat{x}_{k+1} = F\hat{x}_k + K_{k+1}[y_{k+1} - H_{k+1}F\hat{x}_k] \tag{14}$$
$$P_{k+1} = (I - K_{k+1}H_{k+1})P_{k+1|k} \tag{15}$$

where $\hat{x}_k$ is the estimatio of x_k, K_k is the Kalman gain, $P_k = E[(x_k - \hat{x}_k)(x_k - \hat{x}_k)^T]$ is the updated covariance matrix of estimation error and $P_{k+1|k}$ is the predicted covariance matrix of estimation error using only the information available at time k.
$[\bullet]^T$ stands for transpose symbol. To compute this algorithm we need also the initial value of the state estimation $\hat{x}_1$ and the initial updated covariance matrix of estimation error P_1.

3 The Tuning of the Vold-Kalman Estimator

The proper choice of covariance matrices R_k and Q_k highly determines the accuracy of the estimation. In general, these parameters are arbitrary fixed. The estimation of the parameter R_k is done using an usual adaptive approach presented in [11, 12]. The main practical issue is the setting of Q_k. The new adaptive approach to estimate Q_k is established below.
From the Eq. (15), we remark that we can estimate the state noise at instant k as followed

$$\hat{w}_k = K_k[y_k - H_kF\hat{x}_k] \tag{16}$$

We show that the covariance matrix for each sample can be written

$$\hat{Q}_k = K_kH_k\hat{P}_kH_k^TK_k^T + K_k\hat{R}_kK_k^T \tag{17}$$

where $\hat{P}_k = E[(\hat{x}_k - F\hat{x}_{k-1})(\hat{x}_k - F\hat{x}_{k-1})^T]$ and $\hat{R}_k = [\hat{v}_k\hat{v}_k^T]$ with $\hat{v}_k = y_k - H_k\hat{x}_k$. We assume that the residual $(\hat{x}_k - F\hat{x}_{k-1})$ is uncorrelated from the estimated of the measurement noise $\hat{v}_k$.
According to Mohamed and Schwarz [11] and Ali et al. [12], R_k can be estimated using innovation process

$$I_k = y_k - H_kF\hat{x}_k \tag{18}$$

and then $\hat{R}_k$ is computed as follows

$$\hat{R}_k = C_I + H_k P_{k|k-1} H_k^T \tag{19}$$

where C_I is the variance of innovation process. It is computed using a window of length L and equal to

$$C_I = \frac{1}{L} \sum_{i=1}^{L} I_{k-i} I_{k-i}^T \tag{20}$$

4 Numerical Example

To evaluate the accuracy of the new tuning approach for the Vold-Kalman estimator, we use the synthetic signal (see Fig. 1) described by the following equation

$$y(t) = \sum_{i=1}^{3} A_i(t) \cos(2\pi O_i \int_0^t f_r(u)du) + v(t) \tag{21}$$

where f_r is the instantaneous frequency linearly increasing from 0 to 50 Hz in 5 *secondes*, O_i contains the value of orders and v is a centered, white and Gaussian noise.
The signal is composed of three orders presented in the Table 1. Figure 2 displays the rpm-frequency spectrum using the conventional windowing Fourier transform that characterizes three orders.

The initialization of the parameters of the estimator is as follows:

- The initial modeling error is $Q = 10^{-6} I$.
- The initial covariance matrix of the measurement noise is $R = 1$.

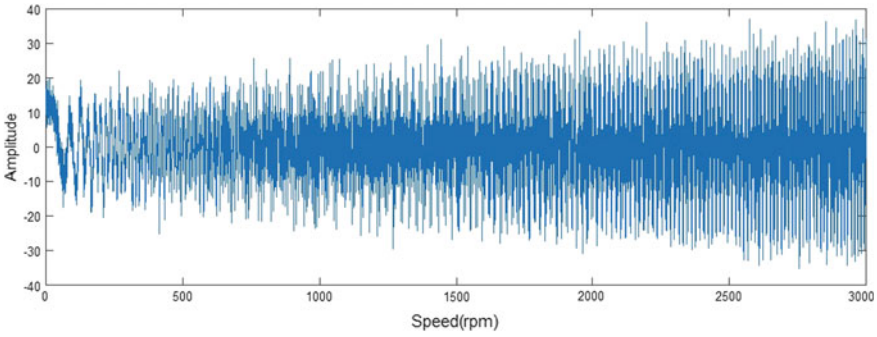

Fig. 1 Synthetic signal

Table 1 The synthetic signal's amplitude of orders

Order number	1	4	9
Amplitude	Linearly increasing from 0 to 10	Linearly increasing from 3 to 13	Fixed at 10

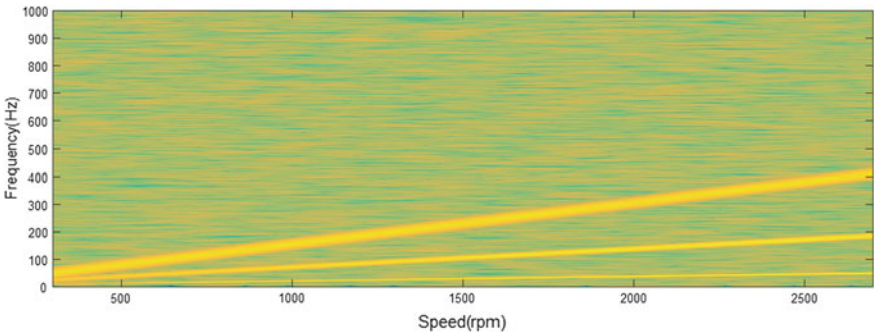

Fig. 2 Illustration of the rpm-frequency spectrum

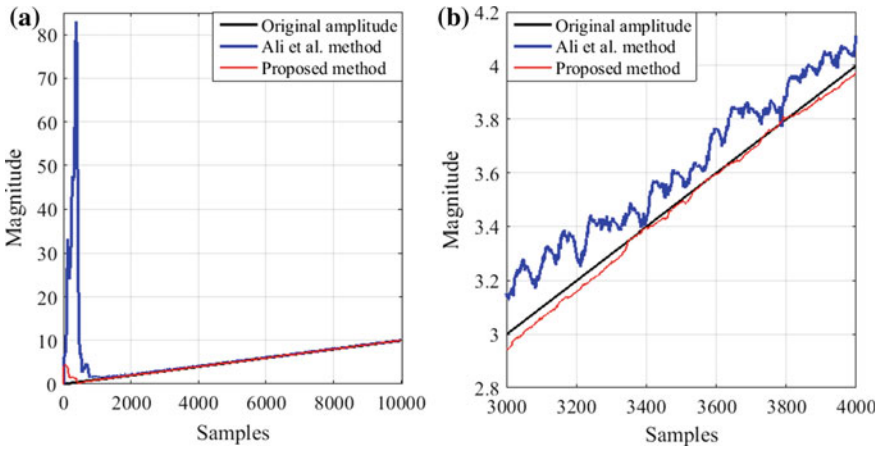

Fig. 3 **a** Estimation of the amplitude of the first order **b** Zoom on the estimation

- The initial value of the estimation is $\hat{x}_1 = [\underbrace{0, \ldots, 0}_{12-times}]$
- The initial covariance matrix of estimation error is $P_1 = 10^{-3}I$.

Here, the amplitudes of three orders are estimated by using the adaptive tuning approach of [12] and the one presented in this paper. On the Figs. 3, 4 and 5, we remark that we can quickly track the true amplitude of orders. The amplitude in red line (proposed method) is closer to the original amplitude than the amplitude in blue

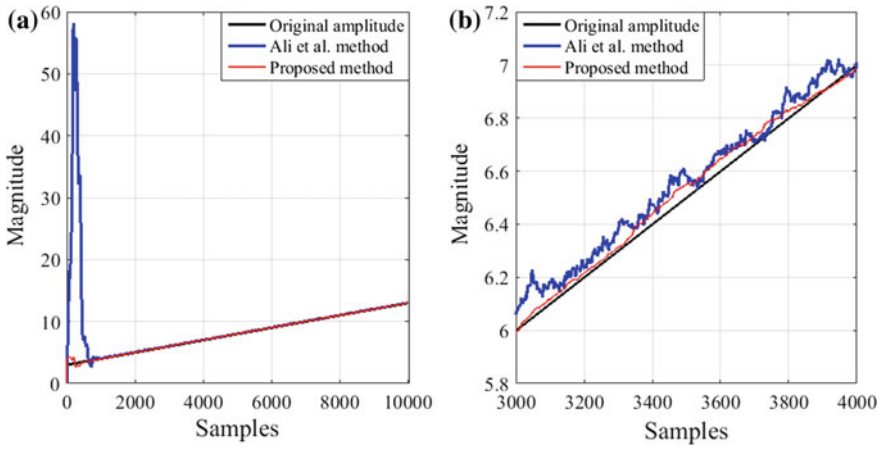

Fig. 4 **a** Estimation of the amplitude of the second order **b** Zoom on the estimation

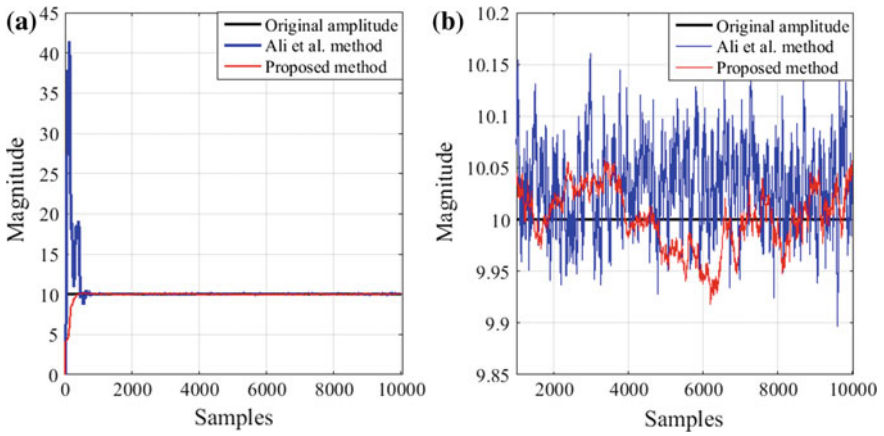

Fig. 5 **a** Estimation of the amplitude of the third order **b** Zoom on the estimation

line (Ali et al. method). For the constant amplitude, the estimation provides by the method of Ali et al. is very noisy and biaised. It confirms the effectiveness of the proposed method when dealing with a non-stationary signal.

To accurately evaluate the performance of each method, we use the criterion based on the output signal to noise ratio given by

$$SNR_{out} = 10log_{10}\frac{\sum_{k=1}^{N}(H_k x_k)^2}{\sum_{k=1}^{N}[H_k(x_k - \hat{x}_k)]^2} \tag{22}$$

where N is the number of samples. In the Table 2, we observe that the estimation is improved at least by 5 dB when the input $SNR = 5$ dB and by 11.71 dB when the input $SNR = 15$ dB using the proposed method.

Table 2 Performance comparison of Ali et al. and the proposed method

$SNR_{in}(dB)$	SNR_{out}	
	Ali et al. method	Proposed method
15	28.8776	40.4928
10	22.2278	33.4668
5	19.2005	24.8501

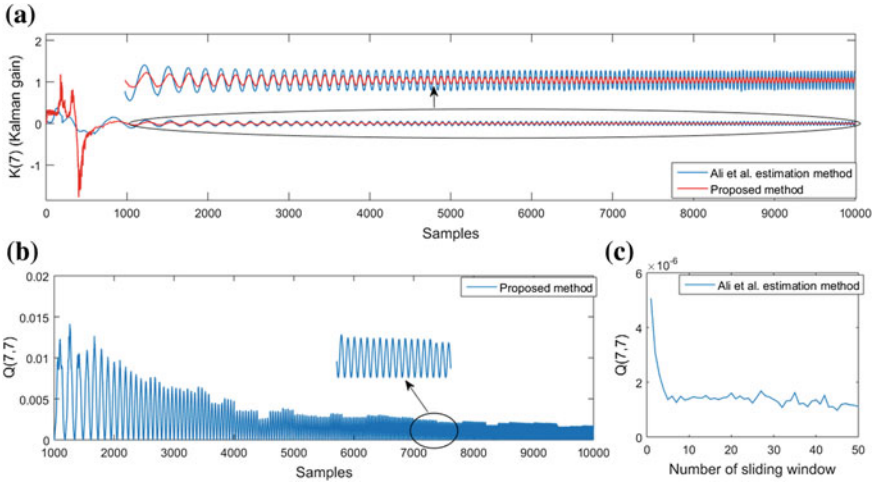

Fig. 6 **a** Kalman gain using the two methods of estimation, **b** Estimation of $Q(7,7)$ using the proposed method and **c** Estimation of $Q(7,7)$ using Ali et al. method [12]

The Fig. 6c represents the estimation of $Q_k(7,7)$ using the method in [12]. We remark that the estimation is almost constant. In the other side, on the Fig. 6b, the $Q_k(7,7)$ values decrease and change with the same frequency as that of the vibration signal. We observe the same behavior in the Kalman gain estimation (Fig. 6a). The Kalman gain has a constant amplitude by using the method of [12] (blue line) whereas it is amplitude is more small and converging toward zero (red line). This allows to the estimator to adapt it self and to provide a smallest estimation error.

5 Conclusion

In this paper, a new method has been introduced to estimate recursively the covariance matrices for the Vold-Kalman estimator. It is based on the residual estimation error. A new formula to calculate the covariance matrix of the state noise has been established. This approach allows to the estimator to adapt itself to the signal variations. It also ensures the positiveness of the covariance matrices. And finally, a numerical implementation has been made to prove the effectiveness of the method over the previous method reported here.

References

1. Bandhopadhyay, D. K., & Grifths, D. (1995). Methods for analyzing order spectra, SAE paper, No. 951273.
2. Pan, M. C., & Chen, J. X. (2003). Transmission noise identification using two-dimensional dynamic signal analysis. *Journal of Sound and Vibration*, *262*(1), 117140.
3. Bonnardot, F. (2004). Comparaison entre les analyses angulaire et temporelle des signaux vibratoires de machines tournantes. Etude du concept de cyclostationnarit floue (Doctoral dissertation, Institut National Polytechnique de Grenoble-INPG), 25–56.
4. Cheng, W., Gao, R. X., Wang, J., Wang, T., Wen, W., & Li, J. (2014). Envelope deformation in computed order tracking and error in order analysis. *Mechanical Systems and Signal Processing*, *48*(1), 92–102.
5. Fyfe, K. R., & Munck, E. D. S. (1997). Analysis of computed order tracking. *Mechanical Systems and Signal Processing*, *11*(2), 187–205.
6. El Badaoui, M., & Bonnardot, F. (2014). Impact of the non-uniform angular sampling on mechanical signals. *Mechanical Systems and Signal Processing*, *44*(1), 199–210.
7. Vold, H., Mains, M., & Blough, J. (1997). Theoretical foundations for high performance order tracking with the Vold-Kalman tracking filter. SAE Technical Paper, No. 972007.
8. Vold, H., & Leuridan, J. (1993). High resolution order tracking at extreme slew rates, using Kalman tracking lter, SAE paper, No. 931288.
9. Mehra, R. (1970). On the identification of variances and adaptive Kalman filtering. *IEEE Transactions on Automatic Control*, *15*(2), 175–184.
10. Odelson, B. J., Rajamani, M. R., & Rawlings, J. B. (2006). A new autocovariance least-squares method for estimating noise covariances. *Automatica*, *42*(2), 303–308.
11. Mohamed, A. H., & Schwarz, K. P. (1999). Adaptive Kalman filtering for INS/GPS. *Journal of Geodesy*, *73*(4), 193–203.
12. Almagbile, A., Wang, J., & Ding, W. (2010). Evaluating the performances of adaptive Kalman filter methods in GPS/INS integration. *Journal of Global Positioning Systems*, *9*(1), 33–40.

Estimation of Cyclic Cumulants of Machinery Vibration Signals in Non-stationary Operation

J. Roussel, A. Assoumane, C. Capdessus and E. Sekko

Abstract Cyclic statistics have been proved to be a powerful tool for the study of rotating machinery vibration signals. Indeed, such signals usually exhibit cyclostationary features related to the shaft speed and to the geometry of the components. Cyclostationarity can be studied at order one (periodic deterministic components) or order 2 and more. Cyclic statistics at order N comprise a pure Nth order cyclostationary part and a contribution from orders 1 to N − 1. It may be interesting to study pure cyclostationarity at order N, i.e. to remove the influence of smaller orders. This can be done by computing cyclic cumulants instead of cyclic moments. In order to compute 2nd order cumulants of the vibration signal, one must remove from the signal the 1st order cyclostationary components, that is to say the deterministic periodic components. Some classical approaches have been proposed, based on synchronized averaging or Fourier transform. But some limitations appear when the vibration signal comprises components tied to different rotation frequencies (for instance in the case of gears) or under variable speed. The method that we propose in order to extract these periodic components is based on a biquad filter bank. Biquad filters have been extensively used in audio processing and allow building band-pass or notch filter banks at low computational cost. We show how such filters can be used to remove the 1st order cyclic components from the signal. An extension to variable speed operation is proposed by having the filters central frequency follow the variations of the rotation frequency. The technique is applied to simulated signals as well as real life signals.

Keywords Second order statistics · Pure cyclostationarity · Cumulants · Non stationary operation · Biquad filters

J. Roussel (✉) · A. Assoumane · C. Capdessus · E. Sekko
PRISME Laboratory, University of Orléans, 21 Rue Loigny-La-Bataille,
28000 Chartres, France
e-mail: julien.roussel1@gmail.com

A. Timofiejczuk et al. (eds.), *Advances in Condition Monitoring of Machinery in Non-Stationary Operations*, Applied Condition Monitoring 9,
https://doi.org/10.1007/978-3-319-61927-9_3

1 Introduction

The vibrations of rotating machinery usually exhibit periodicities tied to the rotation speed. Depending on the machinery there can be either periodic deterministic components or repetitive ones, that are not strictly periodic but whose statistics are periodic. These two kinds of signals can be classified within the frame of cyclostationarity. Deterministic periodic components are described as first order cyclostationary signals, whereas random repetitive ones correspond to second or higher order cyclostationarity. So far this classification has served as a base for many analysis, processing and diagnosis methods. One point of interest is that of signals which comprise both a deterministic component and a random one at the same cyclostationary frequency. This mixture is described as impure cyclostationarity [1, 4, 5]. Separating these two contributions can lead to a refined diagnosis, either by allowing the separation of vibrations produced by two different parts of the system or by giving some more accurate information about the vibrations produced by one specific part of the system. Several techniques have been proposed in order to estimate and extract the deterministic periodic components, the best known being synchronized averaging [6]. This was shown by [2] to be a filtering technique and extended to a wider variety of filters. But these cannot be applied without prior synchronized sampling.

Here we propose a new technique based on the use of a biquadratic filter banks. Biquadratic filters (usually called biquad filters) are commonly used in the audio processing framework [8], mainly to build equalizers that allow enhancing or reducing some frequency bands or removing some periodic components. Our proposal is to use this last property to extract the periodic components from a cyclostationary signal, in order to keep only its random part, i.e. the so called higher order pure cyclostationary component. A notch filter bank can be built in order to remove all periodic components without prior synchronized resampling. In case the machinery comprises several shafts rotating at different frequencies, the filter bank can be designed so that all periodic components are removed whatever rotation speed they are related to. Furthermore, provided an encoder signal is available, the filters can be made to follow the speed variations by adapting the filters coefficients.

In Sect. 2 the concept of pure cyclostationarity will be introduced as well as some analysis tool that allows characterizing it. In Sect. 3 biquadratic filters will be presented and the proposed method for the extraction of first order cyclostationary components will be described. In the same section some simulations will be made to evaluate the performances of the proposed technique. In Sect. 4 the proposed method will be applied to real life toothed gearing vibrations. In Sect. 5 we will draw a conclusion and some perspectives.

2 Problem Formulation

In this section, the main properties of cyclostationary signals will be recalled. Pure and impure second order cyclosationary signals will be defined. Spectral coherence will be introduced as an efficient tool for measuring the signal cyclostationarity. Some simulations will be presented in order to illustrate these notions.

2.1 Cyclostationarity

A signal $s(t)$ is said to be cyclostationary at frequency α_0 if its temporal statistical moments are periodic over time at frequency α_0. The signal is first order cyclostationary at frequency α_0 if its statistic mean is periodic at frequency α_0, that is to say:

$$M(t) = E\{s(t)\} = E\{s(t + nT_0)\} \tag{1}$$

where $E\{\}$ stands for the statistical averaging, $T_0 = 1/\alpha_0$ and n can be any integer value.

The signal is second order cyclostationary at frequency α_0 if its autocorrelation function is periodic over time at frequency α_0, that is to say:

$$R_s(t, \tau) = E\left\{ s\left(t + \frac{\tau}{2}\right) s\left(t - \frac{\tau}{2}\right) \right\} = R_s(t + nT_0, \tau) \tag{2}$$

where τ stands for the time lag and the other parameters are defined as for Eq. (1).

2.2 Pure Versus Impure Second Order Cyclostationarity

The nth order moment of a signal comprises both a pure nth order contribution and contributions from all moments from order 1 to n − 1 [7]. It may be interesting to exclude these inferior orders contributions and to calculate the pure nth order contribution which is called the nth order cumulant of the signal. In what follows we will limit our study to second order moments and cumulants. A signal is said to be purely second order cyclosationary if its second order temporal moment, that is to say the autocorrelation function, is periodic over time and does not comprise any contribution from the first order moment, that is to say the mean. This condition is fulfilled whenever the signal is zero mean. A typical example of an impure second order cyclostationary signal is a signal described by Eq. (3) with $a(t)$ a random centered stationary process and $\bar{a}$ a constant non zero value:

$$s(t) = (\bar{a} + a(t))\cos(2\pi f_0 t) \tag{3}$$

The autocorrelation function of this signal is given by:

$$R_s(t,\tau) = \left(R_a(\tau) + \bar{a}^2\right)\frac{1}{2}(\cos(2\pi 2 f_0 t) + \cos(2\pi f_0 \tau)) \tag{4}$$

With $R_a(\tau)$ the autocorrelation function of the random process $a(t)$. It clearly comprises a part that comes from the non zero first order moment, i.e. $E\{s(t)\} = \bar{a}\cos(2\pi f_0 t)$.

In order to estimate the autocorrelation of the pure cyclostationary component of the signal, that is to say its second order cumulant $C_s(t,\tau)$, one must first remove from the signal its periodic mean, and thus compute:

$$C_s(t,\tau) = E\left\{\left(s\left(t+\frac{\tau}{2}\right) - E\left\{s\left(t+\frac{\tau}{2}\right)\right\}\right)\left(s\left(t-\frac{\tau}{2}\right) - E\left\{s\left(t-\frac{\tau}{2}\right)\right\}\right)\right\} \tag{5}$$

The second order cumulant of the signal described by Eq. (3) is:

$$C_s(t,\tau) = \frac{R_a(\tau)}{2}(\cos(2\pi 2 f_0 t) + \cos(2\pi f_0 \tau)) \tag{6}$$

In order to characterize second order cyclostationarity we propose to compute spectral correlation, which provides a normalized measure of cyclostationarity.

2.3 Spectral Coherence

Applying Fourier transform to the autocorrelation function of $s(t)$ both over t and τ results in the so called spectral correlation function, denoted here by $SC_s(\alpha,f) = E\left\{S\left(f+\frac{\alpha}{2}\right)S^*\left(f-\frac{\alpha}{2}\right)\right\}$, with S(f) the Fourier transform of s(t). $SC_s(\alpha,f)$ is the frequential 2nd order moment of the signal. It depends on the spectral frequency f obtained from the time lag τ, and the cyclic frequency α obtained from the time t. Spectral correlation exhibits spectral lines over α at frequency α_0 if the signal comprises a component that is cyclostationary at this frequency. Spectral coherence is a normalized version of spectral correlation, given by:

$$SCoh_s(\alpha,f) = \frac{E\left\{S\left(f+\frac{\alpha}{2}\right)S^*\left(f-\frac{\alpha}{2}\right)\right\}}{\sqrt{E\left\{S\left(f+\frac{\alpha}{2}\right)S^*\left(f+\frac{\alpha}{2}\right)\right\}E\left\{S\left(f-\frac{\alpha}{2}\right)S^*\left(f-\frac{\alpha}{2}\right)\right\}}} \tag{7}$$

This parameter is comprised between 0 and 1. Theoretically, it reaches zero for completely uncorrelated components $S\left(f+\frac{\alpha}{2}\right)$ and $S\left(f-\frac{\alpha}{2}\right)$ and reaches one for completely correlated ones. A high spectral correlation value at frequency α_0

reveals cyclostationary components at this frequency. As an example spectral coherence is applied to the test signal described by Eq. (8).

$$s(t) = (\bar{a}_1 + a_1(t))e^{2\pi j f_1 t} + (\bar{a}_2 + a_2(t))e^{2\pi j f_2 t} \tag{8}$$

with j the square root of -1, $\bar{a}_1$ and $\bar{a}_2$ real constant values and $a_1(t)$ and $a_2(t)$ random centered Gaussian processes. Reduced frequencies $f_1 = 0.0789$ and $f_2 = 0.2023$. The spectral coherence is computed for the only cyclic frequency $\alpha_0 = f_2 - f_1$. In case the two components are correlated, and the signal is thus cyclostationary at the cyclic frequency α_0 the spectral coherence should reach 1 at the spectral frequency $\frac{(f_1+f_2)}{2} = 0.1406$.

Three cases are examined (see Fig. 1):

- Case 1: $\bar{a}_1 = \bar{a}_2 = 0$ and $a_1(t)$ and $a_2(t)$ are not correlated ($s(t)$ stationary).
- Case 2: $\bar{a}_1 = \bar{a}_2 = 0$ and $a_1(t) = a_2(t)$ ($s(t)$ purely 2nd order cyclostationary at frequency $\alpha_0 = f_2 - f_1$).
- Case 3: $\bar{a}_1 = \bar{a}_2 = 1$ and $a_1(t)$ and $a_2(t)$ not correlated (impure cyclostationarity at frequency $\alpha_0 = f_2 - f_1$).

In case 1, the signal is stationary and the spectral coherence is approximately zero. In case 2, the signal is purely second order stationary at frequency $\alpha_0 = f_2 - f_1$ and the spectral coherence reaches 1 at spectral frequency $\frac{(f_1+f_2)}{2}$. In case 3, though there is no pure cyclostationarity at order 2, the spectral coherence almost reaches 1 due to the first order contribution.

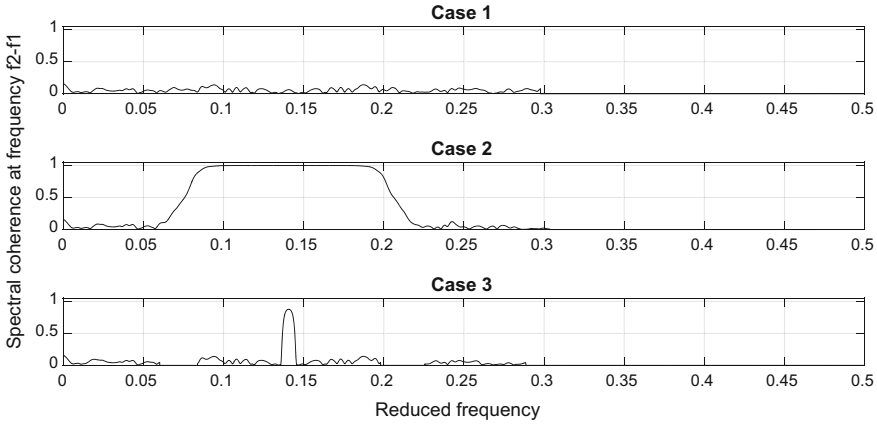

Fig. 1 Spectral coherence of the signal given by Eq. (7) computed at $\alpha_0 = f_2 - f_1$ for cases 1, 2 and 3

3 Proposed Method

In order to separate the first order and pure second order contributions to the cyclic moments, we propose to apply a filter bank to the signal prior to the 2nd order moment computation. This comes to computing the 2nd order cumulant of the signal. In order for the filters to follow the speed variations, they must be efficient while requiring few coefficients and their stability must be ensured whatever their central frequencies variations. We chose to apply biquad notch filters, which fulfill these requirements. Indeed, only five coefficients are required, and the poles are ensured to be inside the unit circle provided that the bandwidth of the filter is small relatively to its central frequency, which is the case in our application.

3.1 Biquad Filters

Biquad filters are recursive linear digital filters with 2 poles and 2 zeros. Their z transfer function can be expressed as:

$$H(z) = \frac{b_0 + b_1 z^{-1} + b_2 z^{-2}}{a_0 + a_1 z^{-1} + a_2 z^{-2}} \tag{9}$$

with $[\, b_0 \quad b_1 \quad b_2 \,]$ and $[\, a_0 \quad a_1 \quad a_2 \,]$ respectively the non-recursive and recursive coefficients of the filter [3].

These filters are commonly used in audio processing in order to enhance or remove periodic components or frequency bands. Their implementation is easy and any filter bank can be built from such second order cells. Since our goal is to remove from the signal deterministic periodic components, the filter bank will be built from cancelling second order cells, i.e. notch filters.

Given the central frequency of the filter f_0, its bandwidth BW (in octaves) and the sampling frequency f_s, the coefficients of the notch filter are given by:

$$\begin{cases} b_0 = 1 & b_1 = -2cos(\omega_0) & b_2 = 1 \\ a_0 = 1 + \alpha & a_1 = -2cos(\omega_0) & a_2 = 1 - \alpha \end{cases} \tag{10}$$

with:

$$\begin{cases} \omega_0 = 2\pi f_0 / f_s \\ \alpha = sin(\omega_0)/(2Q) \\ Q = \dfrac{1}{2 \cdot sinh\left(log(2) \cdot BW \cdot \frac{\omega_0}{2 \cdot sin(\omega_0)} \right)} \end{cases} \tag{11}$$

If the bandwidth Δf is given in Hz, the equivalent in octaves is calculated through:

$$BW = \frac{log\left(1 + \frac{2\Delta f}{2f_0 - \Delta f}\right)}{log(2)} \tag{12}$$

In all that follows, the bandwith of the filters will be fixed from the duration T of the signal: $\Delta f = 2/T$.

3.2 Extraction of the First Order Cyclostationary Component

Here the filtering is applied to a signal defined according Eq. (8) case 3, i.e. $\bar{a}_1 = \bar{a}_2 = 1$ and $a_1(t)$ and $a_2(t)$ uncorrelated Gaussian random processes with $f_1 = 0.0789$ and $f_2 = 0.2023$ in reduced frequency and the signal is generated over 65536 samples. Such a signal exhibits only impure cyclostationarity at frequency $\alpha_0 = f_2 - f_1$. Two notch filters with bandwidth $\Delta f = 2/T$ are successively applied to that signal at frequencies f_1 and f_2 in order to remove the first order cyclostationary contribution $\bar{a}_1 e^{2\pi j f_1 t} + \bar{a}_2 e^{2\pi j f_2 t}$.

Spectral coherence is computed on the raw signal (case 1), on the filtered signal (case 2) and on the residual part, i.e. the original signal minus the filtered one (case 3). The spectral coherence of case 2 thus comes to a normalized 2nd order frequential cumulant of the signal and since this signal comprises no 2nd order pure cyclostationarity, that cumulant is approximately zero. Whereas the spectral coherence of the residual part, i.e. the deterministic part of the signal, reaches 1 due to the first order contribution. All the following computations are performed on the second half of the signal not to take into account the transient response of the filters (Fig. 2).

In order to check that the first order component has properly been removed from the signal, the mean square error normalized by the signal power is computed first between the filtered signal and the random part of the original signal (i.e. the pure cyclostationary one $a_1(t)e^{2\pi j f_1 t} + a_2(t)e^{2\pi j f_2 t}$) and second between the residual and the deterministic part of the signal $\bar{a}_1 e^{2\pi j f_1 t} + \bar{a}_2 e^{2\pi j f_2 t}$. These two errors are respectively $MSE_{random} = -30.75$ dB and $MSE_{deterministic} = -30.79$ dB. These very good estimation results confirm our hypothesis that the deterministic component is to be eradicated with a filter whose bandwidth corresponds to one FFT channel. The part of the random component falling in that very channel probably explains for the estimation error of both components.

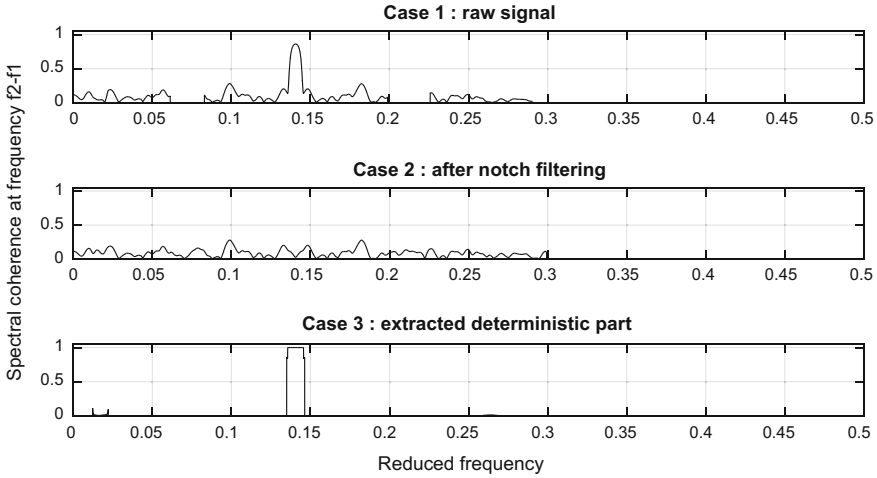

Fig. 2 Spectral coherence of the signal given by Eq. (7) computed at $\alpha_0 = f_2 - f_1$ for cases 1 (before filtering), 2 (after filtering) and 3 (residual)

3.3 Extension to Variable Speed Operation

The technique is now applied to the same synthetic signal as in Sect. 3.2 but both the frequencies f_1 and f_2 and the amplitudes of the corresponding components are varying with time: $f_1 = 0.789 \cdot f_v$ and $f_2 = 2.023 \cdot f_v$ with $f_v = 0.1 + 0.02 \cdot t$ and the amplitudes of the two components are multiplied by a factor ranging from 1 to 1.2 through the whole duration of the signal. The two notch filters are adapted so that their central frequencies follow respectively the variations of f_1 and f_2 while their bandwidth stays equal to $\Delta f = 4/T$. This bandwidth was chosen from a set of experiments. The theoretical study of the behavior of the filters is still ongoing. The same two errors as in Sect. 3.2 are computed and they are respectively equal to $MSE_{random} = -22.49\,\text{dB}$ and $MSE_{deterministic} = -25.62\,\text{dB}$. Unlike the constant speed case, the estimation error is probably due not only to the part of the random component falling in the filter bandwidth but also to a degraded deterministic component estimate, which can explain for the difference observed between MSE_{random} and $MSE_{deterministic}$.

4 Application to Real Life Signals

The technique was applied to real life signals recorded on the GOTIX test bench of the GIPSA-LAB (available at http://www.gipsa-lab.grenoble-inp.fr/projet/gotix/presentation.html). The device comprises 2 motors shafts linked by a gear train enclosed in a gear box. The gear train is a 57/15 multiplier, with parallel straight

teeth. The acquisition is performed on 20 synchronous channels, at 25 kHz sampling frequency. Two encoder signals are available, for the two different shafts. These encoder signals are sampled at 100 kHz. Several recordings were performed with different operating conditions. The signal that was chosen for our application was recorded under a 172 Nm loading torque from an accelerometer located on the bearing number 1, on the leading shaft, that corresponds to the 57 toothed wheel. The file name is "14-5 s-172.e02".

The rotation frequencies of the two shafts were estimated from the encoder signals. The leading shaft rotates at approximately 12.32 rotations per second. The variations around this mean value do not exceed 1.54×10^{-2} rotations per second. The other shaft rotates at approximately 46.8 rotations per second. The variations around this mean value do not exceed 0.11 rotations per second. Though these variations are small relatively to the shaft speed, they produce a non-negligible modulation of the highest harmonics of the rotation frequencies on the spectrum. For that reason, the filter banks were built to follow the frequency variations.

Two notch filter banks were successively applied to the accelerometer signal with bandwidth $\Delta f = 8/T$ where T = 2.048 s is the duration of the processed signal. The spectra of the original signal and of the filtered one are shown on Fig. 3. They were computed over the second half of the signals, not to take into account the transient part of the filters response. It can be observed that most of the spectral lines have been reduced. In order to check whether the two harmonic sets tied to the two rotation frequencies have been suppressed some markers were added at all harmonic positions (Fig. 4). Blue diamonds indicate harmonics of the leading shaft rotation frequency on the raw signal while red diamonds indicate the same harmonics on the filtered signal. In the same way black diamonds and green ones indicate harmonics of the other shaft rotation frequency respectively on the raw and filtered signals.

Two zooms are presented on Fig. 4. One on a medium frequency band and the other one on a high frequency band. As can be observed, all the harmonics of the

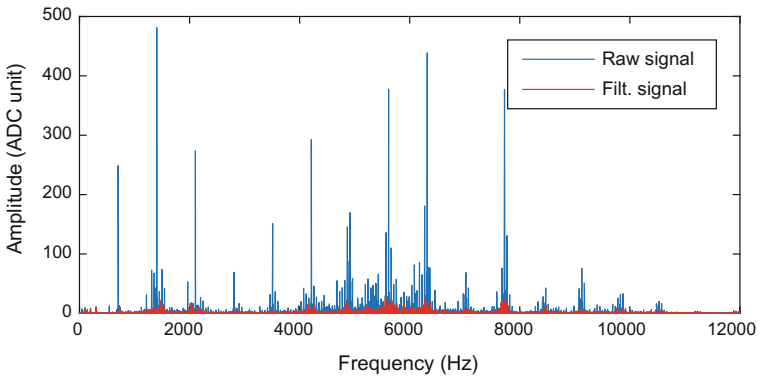

Fig. 3 Spectrum of the accelerometer signal before and after filtering

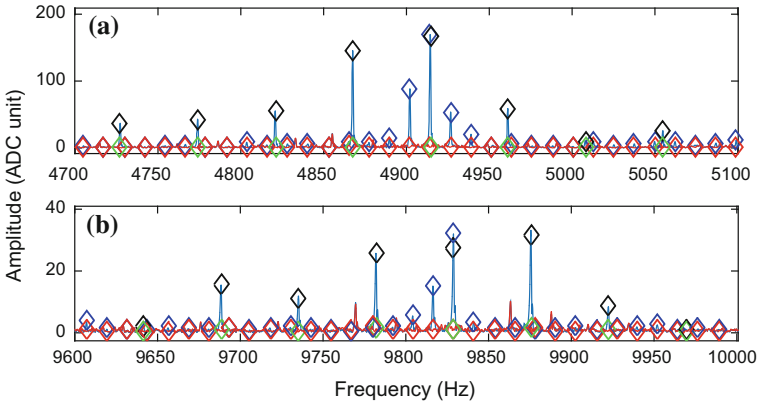

Fig. 4 Spectrum of the accelerometer signal before and after filtering. Zooms on medium frequencies (**a**) and on high frequencies (**b**)

rotation frequencies have been removed, even at very high frequencies, thanks to the fact that the filters were following the rotation frequencies variations. Interestingly some spectral lines remain on the spectrum, that do not belong to any of the two harmonic sets.

Since the proposed technique does not require prior angular resampling, the two harmonic sets could be removed by two filter banks following the rotation frequencies applied directly to the original signal.

5 Conclusion

In this paper we proposed a new technique for the extraction of the periodic deterministic components from a vibration signal. This technique is based on simple order two filters and does not require prior angular resampling, contrary to classical techniques such as synchronized averaging or comb filter. It can be applied on the same signal in order to extract different sets of harmonics linked to different rotation frequencies. We showed that this technique allows extracting the first order cyclostationary components from a signal in order to compute its second order cumulants. It was shown on simulated signals that the extraction is efficient as well in stationary operation as in non-stationary operation (variable speed and amplitude). The technique was eventually applied to a real life gear signal. Two filter banks following the two rotation frequencies allowed extract all the harmonics tied to these rotation frequencies up to the highest part of the spectrum. Further investigations are been done to explore the possibilities of this technique for early diagnosis or defect characterization.

Acknowledgements The authors gratefully acknowledge the GIPSA-LAB for sharing the gear vibration signals recorded on the GOTIX test bench.

References

1. Antoni, J., et al. (2004). Cyclostationary modelling of rotating machine vibration signals. *Mechanical Systems and Signal Processing, 18,* 1285–1314.
2. Braun, S. (2010). The synchronous (time domain) average revisited. *Mechanical Systems and Signal Processing, 25,* 1087–1102.
3. Bristow-Johnson, R. (2016). Cookbook formulae for audio EQ biquad filter coefficients. Retrieved July 2016 http://www.musicdsp.org/files/Audio-EQ-Cookbook.txt.
4. Capdessus, C. et al. (1994). Cyclostationarity: A New Signal Processing Tool for Vibration Analysis and Diagnostics. In *Proceedings of 1994 International Gearing Conference, Newcastle-upon-Tyne* (pp. 142–148).
5. Capdessus, C., et al. (2000). Cyclostationary processes: Application in gear faults early diagnosis. *Mechanical Systems and Signal Processing, 14*(3), 371–385.
6. Mark, W. D. (2015). Time-synchronous-averaging of gear-meshing-vibration transducer responses for elimination of harmonic contributions from the mating gear and the gear pair. *Mechanical Systems and Signal Processing, 62–63,* 21–29.
7. Mendel, J. M. (1991). Tutorial on higher-order statistics (Spectra) in signal processing and system theory: Theoretical results and some applications. *Proceedings of the IEEE, 79*(3), 278–305.
8. Smith J. O. (2007). *Introduction to Digital Filters: with Audio Applications*. W3 K Publishing.

Simplified Dynamic Model of a Wind Turbine Shaft Line Operating in Non-stationary Conditions Applied to the Analysis of IAS as a Machinery Surveillance Tool

Jose L. Gomez, Ilyes Khelf, Adeline Bourdon, Hugo André and Didier Rémond

Abstract Instantaneous Angular Speed (IAS) has been shown to be an alternative signal to detect bearing faults in geared systems. Detection of the presence of bearing faults in rotating systems requires understanding of the transfer way between the defect and its manifestation in the measured signal. This step is mainly performed by the development of numerical models describing the couplings between the defects and the rest of the device. To the authors' knowledge, the majority of the models in the literature are lump parameter models, with no regard between the dynamic of the bearing and the rotational degree of freedom of the shaft. The influence that the dynamics of a faulted bearing has over the rotating shaft leading to IAS variations has been presented in a previous work. This influence has been introduced by means of a roller bearing model which dynamics, modified by the defect, introduces torque perturbations to the shaft. The aim of this paper is to couple the faulted bearing model to a multiple gear stage simplified wind turbine transmission. The model is built with a classic finite element approach and is suitable for the test of non-stationary simulations. First results show bearing faults are detectable in different locations of the geared system by the measurement

J.L. Gomez · I. Khelf · A. Bourdon · D. Rémond (✉)
INSA-Lyon, LaMCoS, Université de Lyon, CNRS, UMR5259, 69621 Lyon, France
e-mail: didier.remond@insa-lyon.fr

J.L. Gomez
e-mail: jose-luis.gomez-chirinos@insa-lyon.fr; jlgomez@maiaeolis.fr

I. Khelf
e-mail: ilyes.khelf@insa-lyon.fr; ikhelf-externe@maiaeolis.fr

A. Bourdon
e-mail: adeline.bourdon@insa-lyon.fr

J.L. Gomez · I. Khelf · H. André
Maia-Eolis, Tour de Lille, Boulevard de Turin, 59000 Lille, France
e-mail: handre@maiaeolis.fr

A. Timofiejczuk et al. (eds.), *Advances in Condition Monitoring of Machinery in Non-Stationary Operations*, Applied Condition Monitoring 9,
https://doi.org/10.1007/978-3-319-61927-9_4

of IAS. Even if experimental validation have not been yet performed, numerical results appear very promising to deepen the understanding of the IAS variation phenomena.

Keywords Bearing default modelling · Gear modelling · Non-stationary machines · Instantaneous angular speed

1 Introduction

Condition monitoring has become a common practice when reliability and availability of machines are critical. Techniques for processing and analysis of signals measuring the vibratory behavior of the machine are in constant development, with the objective of detecting defects in rotating parts as early as possible. Wind turbines are a good example of machines needing for surveillance technology improvement. The total gear ratio of these machines are often more than 1:100. This consideration added to non-stationary operation, leads to high level of complexity when using radial vibration techniques.

Instantaneous Angular Speed (IAS) has been shown to be an alternative signal to detect bearing faults in mechanical systems [5]. Different work has been focus on the development and test of the IAS signal as a condition monitoring tool [1]. Being modelling of physical phenomena a fundamental feature allowing the comprehension, design and prediction of the behavior of mechanical systems, some work have been also dedicated to the analysis of dynamics leading to small speed variation in rotational systems [2]. Expression of the equations in the angle domain becomes natural to simulate non-stationary conditions by managing simulation steps through angular sampling and by taking into account the rotating degrees of freedom of the device of interest. In a recent work [3], a roller bearing model describing how the dynamics of a bearing leads to IAS variations have been presented. The presence of a defect affects the bearing races and rolling elements interaction, changing the IAS' response signature.

The aim of this paper is to present a simplified model of a wind turbine shaft line with a multi stage gear transmission. Different bearings have been modeled with two different approaches. The main bearing (MB), which support the rotor weight, has been simplified by being modeled as a deep groove ball bearing [3], while the rest of the bearings have been represented by means of the nonlinear Palgrem's formulation [4]. The Gear stages are modeled with a classic approach based on their geometrical matrices leading to stiffness and damping teeth interaction matrices. A brief description of the model approach and construction follows.

2 General Modelling Elements

2.1 General Approach

The model is built with a classic Finite Element Method approach. Let $\{X\}$ be the generalized displacement vector; $[M]$, $[C]$ and $[K]$ the real matrices of mass, stiffness and damping and $\{F_{ext}(t)\}$ the vector representing the external forces.

The shafts are discretized in beam elements considering three displacements and three rotations. The supports are modeled by punctual lumped elements connected by localized dampers and springs. The objective is then, solving the generalized system of dynamic equations to obtain the IAS variations of the nodes representing the shaft.

2.2 The Roller Bearing Model

Roller bearings are modeled by connecting forces linking the flexible supports with the shafts (See Fig. 1). Two approaches for the estimation of theses connecting forces are used. The former is considered as an extension of the one developed by Sawalhi and Randal [6] and it is completely described in [3], where consideration of the rolling resistance phenomena as well as the rotational DOF of the inner race (IR), permits the coupling of radial and tangential forces leading to IAS perturbations as it's described in Fig. 2. The second approach is the one described by Palgrem's formulation [4] where a global average nonlinear stiffness is considered meaning that the effect of loading distribution over the roller bearings is not included.

The forces are then translated onto the inner and outer races as two resultant forces, and a torque (if the former approach is used), that introduce the IAS variations (See Fig. 2).

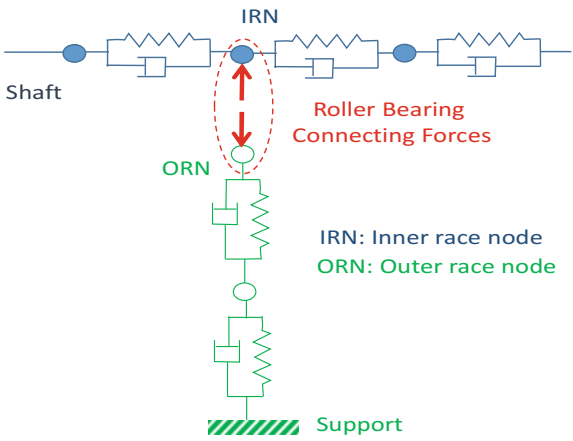

Fig. 1 Bearing connecting forces [3]

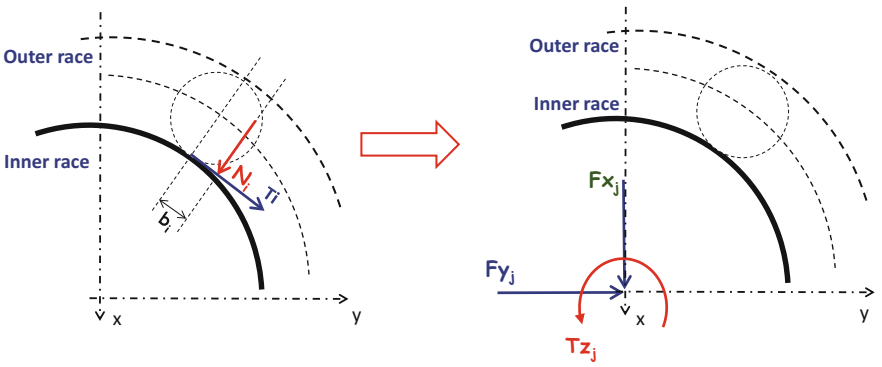

Fig. 2 Rolling element forces translated into the IR [3]

2.3 *Modelling the Gear Coupling*

A similar approach involving connecting forces is used for the modeling of the gears. Forces are obtained along the line of action by the following equation:

$$\{F_{gea}\} = [K_{gea}] \cdot \{X_{gea}\} \tag{1}$$

where vectors $\{F_{gea}\}$ and $\{X_{gea}\}$ are the gears connecting forces and the generalized displacements of the nodes representing the interacting gears. Matrix $[K_{gea}]$ represents the gear stiffness and is estimated as:

$$[K_{gea}] = K_o \cdot [G] \tag{2}$$

The constant K_o represents the average stiffness of the teeth in contact and is estimated using the ISO 6336 standard. The gear geometric matrix $[G]$ is a combination of gear characteristics (base diameters, helix angle, and gear pressure angle) and the displacements of the contact point of the teeth referenced to the FE nodes where the gears are attached. These displacements are equivalent to the squeezing of the teeth in contact. This approach has been widely used. Interested readers will find the entire formulation developed by [7]. Figure 3 shows a scheme of the approach. Once the geometrical matrix is obtained, gear forces can be calculated by means of Eq. 2.

An interesting fact is that, at the authors' knowledge, the chosen approach to describe the gears coupling has never been used including the system's rotational rigid modes, meaning that the shafts and therefore the gears, have free rotational movement (along Z axis on Fig. 3).

Notice that for this work, gears are considered perfect, meaning that no error transmission has been introduced. However, modelling the gear coupling as external forces allows, if desired, an easy introduction of nonlinear stiffness and

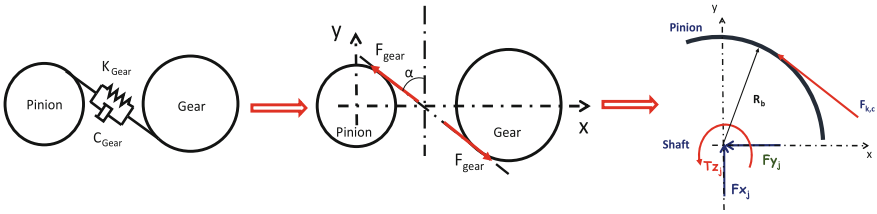

Fig. 3 Gears connecting forces

reduce computer time by avoiding the calculation of the entire system's stiffness matrix at each iteration step of the resolution. Only K_o has to be replaced by the chosen nonlinear law.

2.4 Model Assembly and Resolution

The mechanical system is then assembled into the following differential system of equations:

$$[M].\{\ddot{X}\} + [C].\{\dot{X}\} + [K]\{X\} = \{F_{ext}(t)\} + \{F_{bea}(t)\} + \{F_{gea}(t)\} \tag{3}$$

where $\{F_{bea}\}$ is the vector containing the resultant forces of each bearing on the system, $\{F_{gea}\}$ represents the vector containing the forces modelling the set of gears and $\{F_{ext}(t)\}$ is the vector containing the external forces and moments. Each component of the force vectors has to be located following the finite element connectivity arrangement.

Resolution of equations is performed with Matlab's nonlinear ODE solver. To achieve this, the system of n differential equations of order 2 is rearranged as a system of 2n differential equations of order 1. Then, the system is transformed into the angular domain which means that time is expressed as a function of the angular DOF θ. The system of equations becomes an angular one:

$$\begin{cases} \frac{d\tilde{Q}(\theta)}{d\theta} = \frac{1}{\tilde{\omega}(\theta)} \cdot [S]^{-1} \cdot \left([A] \cdot \tilde{Q}(\theta) + [B] \cdot \{U\}\right) \\ \frac{dt}{d\theta} = \frac{1}{\tilde{\omega}(\theta)} \end{cases} \tag{4}$$

where:

$$\{\tilde{Q}(\theta)\}_{2n} = \begin{Bmatrix} \{\tilde{x}\}_n \\ \{\dot{\tilde{x}}\}_n \end{Bmatrix} \tag{5}$$

And:

$$\{U\}_{2n} = \begin{Bmatrix} \{0\}_n \\ \{F_{ext}\}_n + \{F_{gear}\}_n + \{F_{beaN}\}_n \end{Bmatrix} \tag{6}$$

The symbol "∼" stands for angular variable. Matrix [S] contains the inertial part of the bearing forces (taking into account rolling elements inertia and acceleration) while the vector $\{F_{beaN}\}$ contains the non-inertial forces from bearings. Matrices $[A]$ and $[B]$ contain an arrangement of the matrices of mass, stiffness and damping of the system. The complete development of the equations can be found in [3].

3 Simplified Wind Turbine Model Description

The simplified wind turbine model is inspired on a 2 MW Senvion MM82 equipped with a Renk's gearbox. The nominal speed of the generator for 2 MW is 1800 RPM. The gearbox ratio is 1:105.5. A kinematic scheme of the shaft line is shown in Fig. 4.

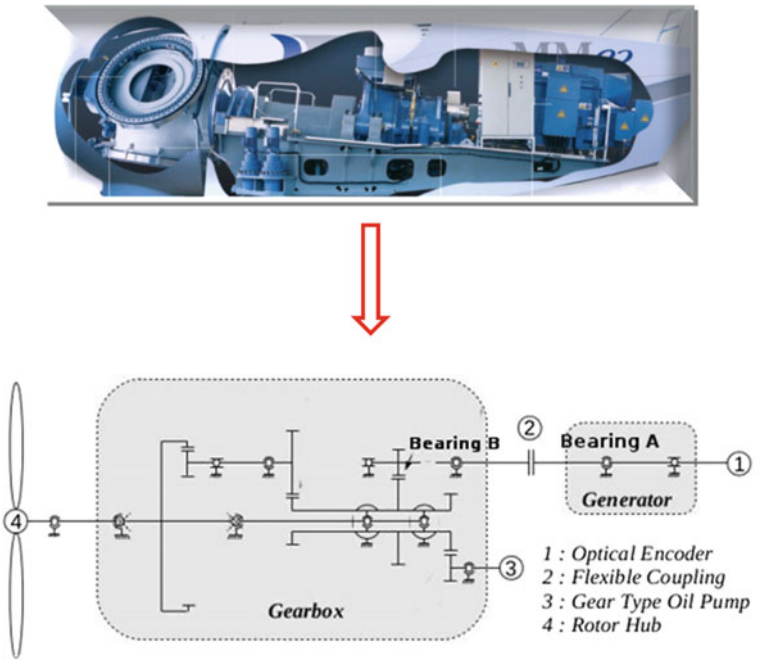

Fig. 4 Wind turbine scheme

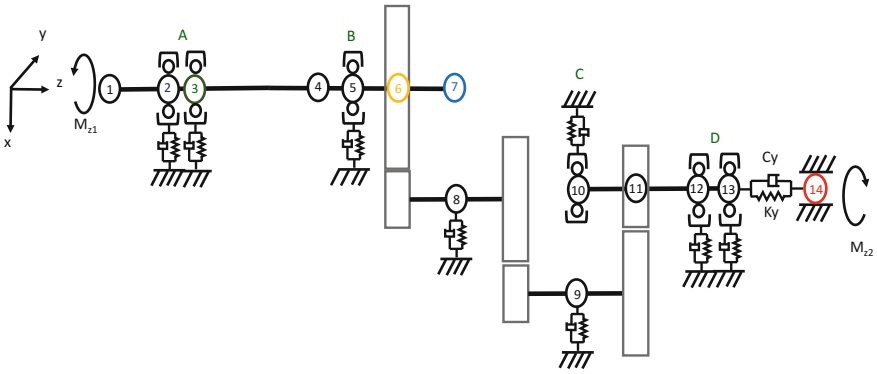

Fig. 5 Simplified wind turbine shaft line scheme

The gearbox has three stages. The first stage is a planetary transmission with fixed satellites. Due to the complexity of the machine kinematics several choices were made to simplify the system but keeping it as close as possible to the real parameters. Figure 5 shows a scheme of the simplified model.

Between the simplifications we stand out the following: the planetary transmission is modeled by an equivalent simple gear stage. Each one of the three transmission ratios are equal to the real ones. The Bearing A or main bearing (MB) is an skf 240/630 double row spherical roller bearing with an angle Ball Pass Frequency on the Outer race (BPFO) of 12.75 event per revolution (ev/rev). It was modelled with the approach of [3] as a deep groove ball bearing, meaning that no axial effects are taken into account. The bearings B, C and D, are the same as in the real wind turbine and were modeled with the Palgrem's formulation, meaning that the dynamics of load distribution over the rolling elements under the load zone is not taken into account, therefore, the only bearing adding perturbations related to the BPFO is the MB. The housing of the MB was reduced from its finite element model performed on ANSYS to a 4 DOF accounting for X and Y displacements.

The real gearbox is supported on by vibration pads. We supposed the housing rigid and resting over two DOF flexible supports accounting for X and Y displacements. The load and inertia of the rotor is lumped onto the node 1. Only the complete low speed shaft (LSS) and the high speed shaft (HSS) of the gearbox were discretized on FE. The intermediate shafts and gears were lumped onto nodes 8 and 9 respectively. These nodes are supported by the same flexible elements of the transmission bearings. Node 14 stands for the lumped generator shaft which is linked to the gearbox through a flexible coupling.

Finally, M_{z1} is the torque introduced by the wind through the rotor and M_{z2} is the electromagnetic torque induced by the generator.

4 Test of the Model and Results

The wind torque over the rotor, the electromagnetic torque from the generator and the mechanical loses permitting to reach the steady state were set up for the model to respond within the linear range of the real wind turbine which is between 1100 and 1800 RPM of the HSS, which is equivalent to 125–750 kW of power generation.

Stationary and nonstationary runs were made. Here, we show only the nonstationary one which was performed by means of a linear external torque variation, to obtain a HSS speed varying from 1500–1800 RPM within 50 revolutions of the LSS. These simulations were performed for healthy bearings and in presence of a bearing defect located in the outer race of the MB in the gearbox sided row and aligned with the rotor's weight. The defect has 150 microns of depth and its length is 10% of the angular distance between two rolling elements.

Figure 6 shows the non-stationary angular speed response of the nodes 7 and 14 for the healthy bearing simulation. Theses nodes represent usual points of encoder installation for IAS measurement.

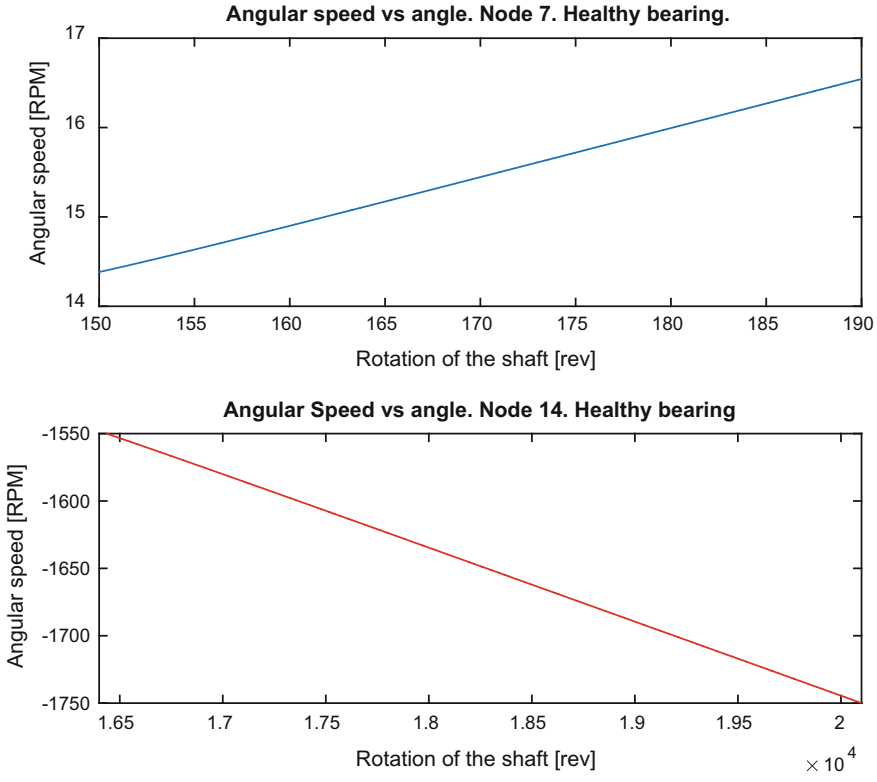

Fig. 6 Nonstationary angular speed response. Nodes 7 and 14. Healthy MB

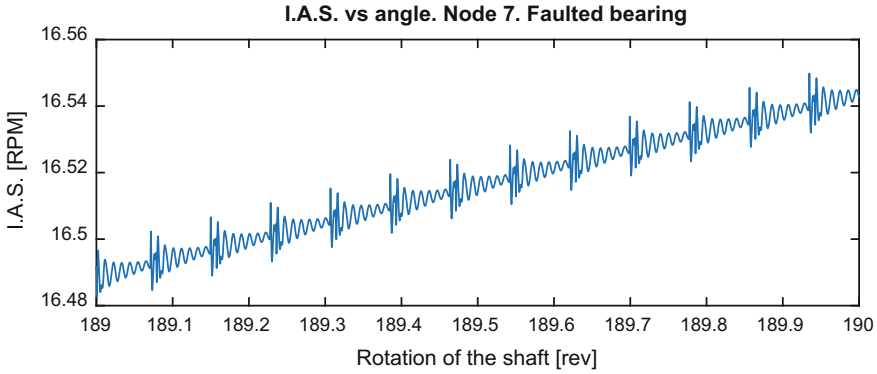

Fig. 7 Zoom of the nonstationary angular speed response. Nodes 7. Faulted MB

Figure 7 shows that IAS variations may be observed on the angular speed response in presence of the bearing defect when observing only around one shaft revolution.

Figure 8 shows Fast Fourier Transforms (FFT) of the IAS responses for nodes 7 and 14 for healthy and faulted bearing. For the healthy bearing we managed to see only the response of the node 14 which is much greater in amplitude along the spectral span. The fundamental frequency of the BPFO is predominant over the harmonics. Readers should know that this kind of response is rarely observed from experimental measurements on healthy bearings due to the low level of energy and the usual noise within this kind of signal.

We observed also that for the mechanical parameters chosen the IAS phenomena is amplified by the gears coupling.

In the case of the faulted bearing, the FFT treatment shows that the energy of the simulated IAS is amplified making it around ten times greater. The nature of a bearing defect introduces impulsive perturbations increasing the level of the BPFO harmonics. Specifically, for the node 7, the 5th and 6th harmonics have more than a hundred times more amplitude than the fundamental frequency.

Authors had verified that the response is strongly affected by the modal response of the shafts, the supports and the bearings. This means that directly tuning the simplified model with experimental measurements is not possible. However, the built phenomenological model allows to analyze the impact on the system response of the different mechanical parameters, the nonstationary loads and different fault levels, in different roller bearings. This applies not only for IAS observation but also for radial acceleration analysis.

Another interested fact that is not shown in this paper for sake of saving space is that the gears interaction, which is along the tangential pressure line (see Fig. 3) is a second source of coupling of tangential forces with the radial ones. This means that even neglecting the rolling resistance phenomena, the gear interaction introduces IAS perturbations by coupling the bearing forces with the tangential gear forces, which is translated in torque variations.

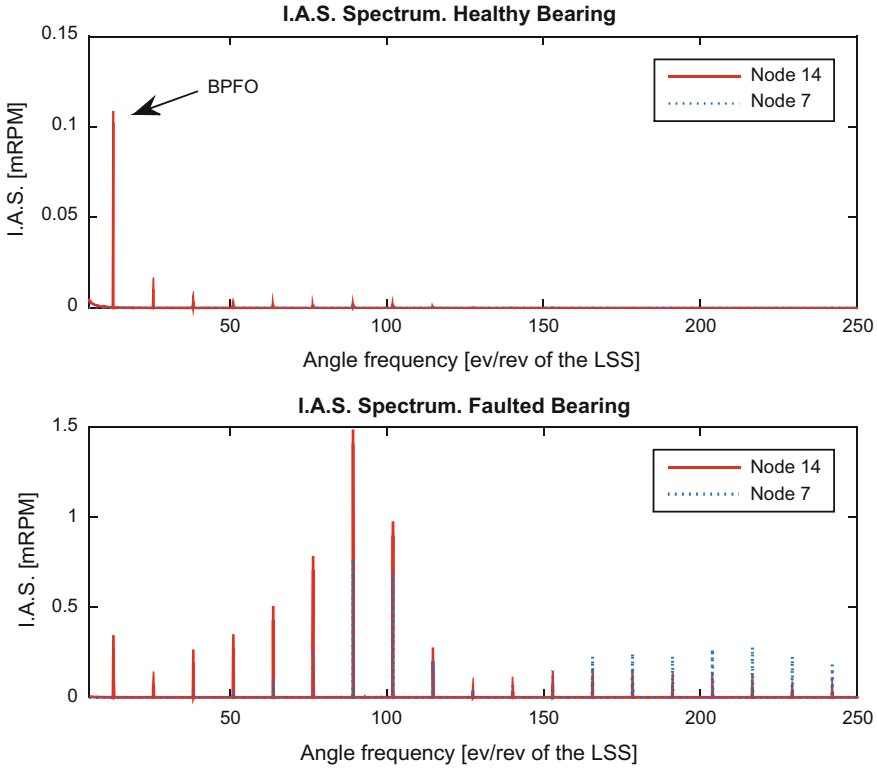

Fig. 8 Fast Fourier Transforms of the IAS responses for nodes 7 and 14 for healthy and faulted bearings

5 Conclusion

A simplified wind turbine shaft model was built, able to simulate the IAS phenomena introduced by the dynamics of the roller bearings in presence of defects and nonstationary operating conditions. The IAS phenomena was observed along all the modeled shafts. A MB localized OR defect was introduced. The presence of the defect increases substantially the energy of the IAS phenomena.

Further work will be performed using the current model to test a classification method based in Artificial Intelligence to test IAS fault indicators.

Acknowledgements Authors would like to thank Maia Eolis, LaMCoS, and France national research and technology association (ANRT) for funding this research.

References

1. André, H., Bourdon, A., & Rémond, D. (2012). Shaft line monitoring based on the instantaneous angular speed observation. In *11th German Wind Energy Conference*, DEWEK, Bremen.
2. Bourdon, A., André, H., & Rémond, D. (2014). Introducing angularly periodic disturbances in dynamic models of rotating systems under non-stationary conditions. *Journal Mechanical Systems and Signal Processing, 44,* 60–71.
3. Gomez, J. L., Bourdon, A., André, H., & Rémond, D. (2016). Modelling deep groove ball bearing localized defects inducing instantaneous angular speed variations. *Journal Tribology International, 98,* 270–281.
4. Palgrem, A. (1967). *Les roulements: Description, théorie et applications* (2ème ed.). Paris: S.K.F.
5. Renaudin, L., Bonnardot, F., Musy, O., Doray, J. B., & Rémond, D. (2010). Natural roller bearing fault detection by angular measurement of true instantaneous angular speed. *Journal Mechanical Systems and Signal Processing, 24,* 1998–2011.
6. Sawalhi, N., & Randall, R. (2008). Simulating gear and bearing interactions in the presence of faults Part. 1. The combined gear bearing dynamic models and the simulation of localized bearing faults. *Journal Mechanical Systems and Signal Processing, 22,* 1924–1951.
7. Velex, P. (1988). *Contribution à l'analyse du comportement dynamique de reducteur à engrenages à axes paralleles*. INSA de Lyon, France: Thèse de doctorat.

Current Signal Analysis of an Induction Machine with a Defective Rolling Bearing

Aroua Fourati, Adeline Bourdon, Didier Rémond, Nabih Feki, Fakher Chaari and Mohamed Haddar

Abstract With the ultimate goal of rotating machinery diagnosis using Motor Current Signal Analysis (MCSA), this paper provides a coupled electro-magnetic-mechanical model of a rotating shaft supported by rolling bearings and driven by a three-phase squirreled cage motor. The modeling is based on the hypothesis that a bearing defect causes torque and then Instantaneous Angular Speed (IAS) variations associated to air-gap eccentricity of the induction machine rotor. Dynamic analysis of the multiphysic system highlights the sub-systems interactions, especially, angular periodicities and frequency modulations. The global model can be characterized by a unique set of non-linear state equations which are solved iteratively by an angle-step scheme while considering the angle-time relation. The major interest of presenting this model is that it allows to decrypt the transfer path from a small localized bearing defect until its manifestation on electrical signals. Analysis of bearing defects were performed by applying Fourier Transform on current per-phase signals.

Keywords Machinery in non-stationary operations · Rotating machinery diagnosis · Angular approach · Bearing defect

A. Fourati (✉) · A. Bourdon · D. Rémond
University of Lyon, LaMCoS, INSA-Lyon, CNRS UMR5259, 69621 Lyon, France
e-mail: aroua.fourati@insa-lyon.fr; arwafourati@gmail.com

A. Bourdon
e-mail: adeline.bourdon@insa-lyon.fr

D. Rémond
e-mail: didier.remond@insa-lyon.fr

A. Fourati · N. Feki · F. Chaari · M. Haddar
LA2MP, National School of Engineers of Sfax–BP, 1173-3038 Sfax, Tunisia
e-mail: fekinabih@gmail.com

F. Chaari
e-mail: fakher.chaari@gmail.com

M. Haddar
e-mail: mohamed.haddar@enis.rnu.tn

A. Timofiejczuk et al. (eds.), *Advances in Condition Monitoring of Machinery in Non-Stationary Operations*, Applied Condition Monitoring 9,
https://doi.org/10.1007/978-3-319-61927-9_5

1 Introduction

MCSA method has been widely used in the domain of diagnosis of industrial equipments. Many investigations proved its efficiency to detect defects in mechanical devices linked to the corresponding motor especially in the case of rotating components such as gears and bearings [1]. Most of those investigations have used signal processing tools in order to prove the capacity of the methods to extract the presence of the localized defect from required signals [2]. However, in order to evaluate the efficiency of proposed method, it is required to understand the information path from the defect geometry to modification in electrical signal. By answering this question, the performance about the reliability of the method to the information about the presence and the size of the defect can be established. This is the main motivation for a model that represents precisely the multiphysic interactions between the different sub-systems involved in the transfer path. Starting by representing electro-magnetic behavior of an induction machine, several models were proposed [3]. However those investigations remain away from representing precisely small perturbations caused by the defect.

In [4], an electro-mechanical model of an induction machine coupled to a geared system was presented. This model was based on Permeance Network Model. Even if this model provides a good representation of the electro-magnetic-mechanical interactions, it is still not sufficient enough for exhibiting the effect of the periodicity of the rotating machinery geometry added to its inability to represent non-stationary operating conditions. In order to overcome these limitations, this model was coupled to angular approach in [5].

On the other hand, an intrusive model that represents the dynamic behavior a rolling bearing was well described in [6]. This model has proved, by estimating the efforts applied in each rolling element of the bearing, that the dynamic behavior of the bearing presents IAS fluctuations. In the presence of defect, the latter induces some additional IAS perturbations which are related to the geometry of the bearing, the geometry of the defect and its localization.

In this research work, we will investigate a model of an electro-magnetic-mechanical model of an induction machine coupled to a rotating shaft supported by rolling bearings. The electro-magnetic model of the induction machine is well adapted to adequate speed fluctuations that can be caused by the bearing dynamics and possibly the presence of a localized defect. This adaptation is insured by adopting an angular description of the motor and considering the angular periodicities of the motor geometry. This model has then been coupled to rolling bearing model and the methodology of electro-magnetic-mechanical coupling is well detailed. To validate the capacity of the global model, a realistic geometry of the defect is introduced and investigations are conducted by using Fourier Transform on the simulated stator per-phase current. Time and angular periodicities induced by the system interactions are particularly highlighted.

2 Electro-Magnetic-Mechanical Modeling

The proposed multiphysic model represents a system of a rotating shaft supported by rolling bearings and driven by a squirreled cage induction motor as shown in Fig. 1. The corresponding dynamic system is numerically simulated by combining: (i) a mechanical dynamic model of a rotating shaft and rolling bearings that takes into account variations of the IAS and (ii) an electro-magnetic model of an induction machine represented by a Permeances Network Model in order to consider small magnetic flux variations in the air-gap.

In the modelling, we consider a flexible model of the shaft discretized on four finite elements and five nodes. Six degrees of freedom are considered for each node (three displacements and three rotations). Displacements of the shaft nodes are used to compute the eccentricity at nodes where the bearing are located. Those values will be considered in the computing of the bearing efforts.

The rotating movement of the shaft is ensured by the electro-magnetic torque T_{em} produced by the induction machine. Radial forces F_r and resistive torque T_r are applied at different nodes of the shaft. Radial forces and resistive torque are produced by external sources of excitation to the proposed system.

During the shaft movement, we consider that rolling bearings are applying external forces F_{rlt}. These forces are calculated between each stator node and shaft node representative of each bearing. We represent the bearings inner races by two nodes located on the shaft and we consider that the outer race of the bearings as fixed on the stator of the induction machine.

Two types of models are used to represent the dynamic behavior of the rolling bearings. The first rolling bearing model is based on the model developed in [6]. This model is very well adapted to the proposed multiphysic system as it is represented using angular description in order to calculate forces applied in each rolling element. In the same time it takes into consideration small IAS variations produced by the presence of the defect as described in the reference. This first model is adapted for introducing mechanical perturbations induced by the defect. The second rolling bearing is modelled using a simple Palmgren model. This choice has been made in order to simplify the investigation of the results since efforts resulting from the bearing are considered as constant during the system motion.

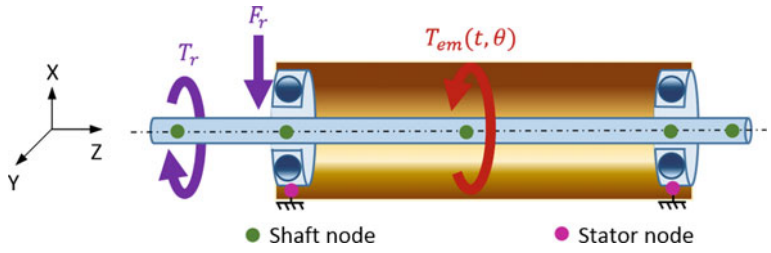

Fig. 1 View of the induction motor and shaft supported by rolling bearings: the multiphysic interactions

This system can be represented by a set of differential equations as shown in Eq. (1): The first equation represents the electro-magnetic behavior of the induction machine, the second equation corresponds to the mechanical model of the shaft and supports, where the efforts from the rolling bearings, possibly with defects, are introduced as additional forces. The third equation is the angle-time relation that allows switching from time to angle domains.

$$\begin{cases} (L+G(\theta))\cdot\omega(\theta)\cdot\frac{dI(t(\theta))}{d\theta}+(R+\omega(\theta)\cdot\frac{dG(\theta)}{d\theta})\cdot I(t(\theta))=V(t(\theta)) \\ \omega(\theta)\cdot\frac{dQ(t(\theta))}{d\theta}+\begin{pmatrix}0 & -\mathrm{I_d}\\ \mathrm{M^{-1}K} & \mathrm{M^{-1}C}\end{pmatrix}\cdot Q(t(\theta))=\begin{pmatrix}0\\ \mathrm{M^{-1}}\end{pmatrix}\cdot(\mathrm{F_r(t)}+\mathrm{T_r(t)}+\mathrm{F_{rlt}}(\theta)+\mathrm{T_{em}(t,\theta)}) \\ \frac{dt}{d\theta}=\frac{1}{\omega(\theta)} \end{cases} \tag{1}$$

In this equation, I is the generalized vector of stator-phases and rotor currents, V is the stator and rotor voltage vector. L and R are respectively real, constant matrices of inductances and resistances. G is the transformation matrix that describes links of fluxes in the stator and rotor to currents in the stator and rotor. ω is the IAS of the rotor. θ and t are respectively angular displacement and time variables.

$Q=\begin{pmatrix}\chi\\ \dot{\chi}\end{pmatrix}$ is the mechanical state vector

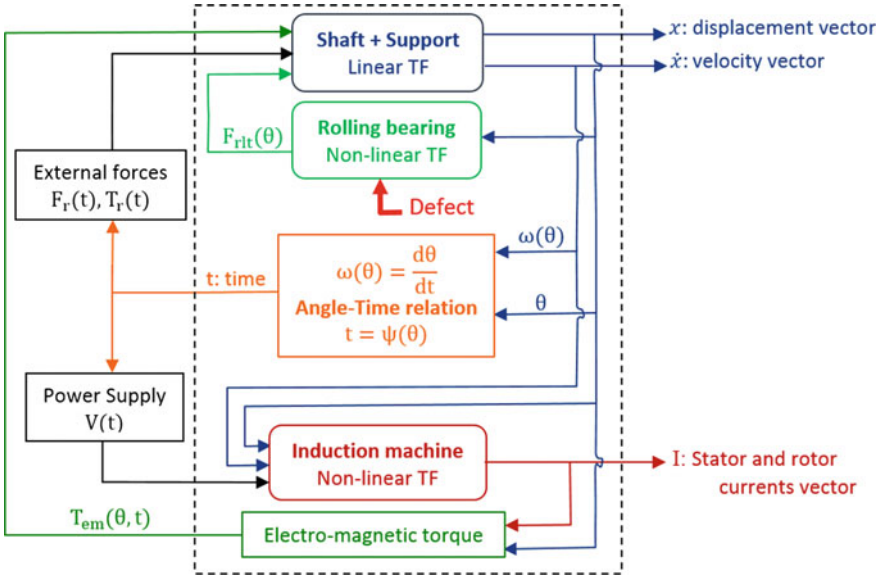

Fig. 2 The coupling methodology

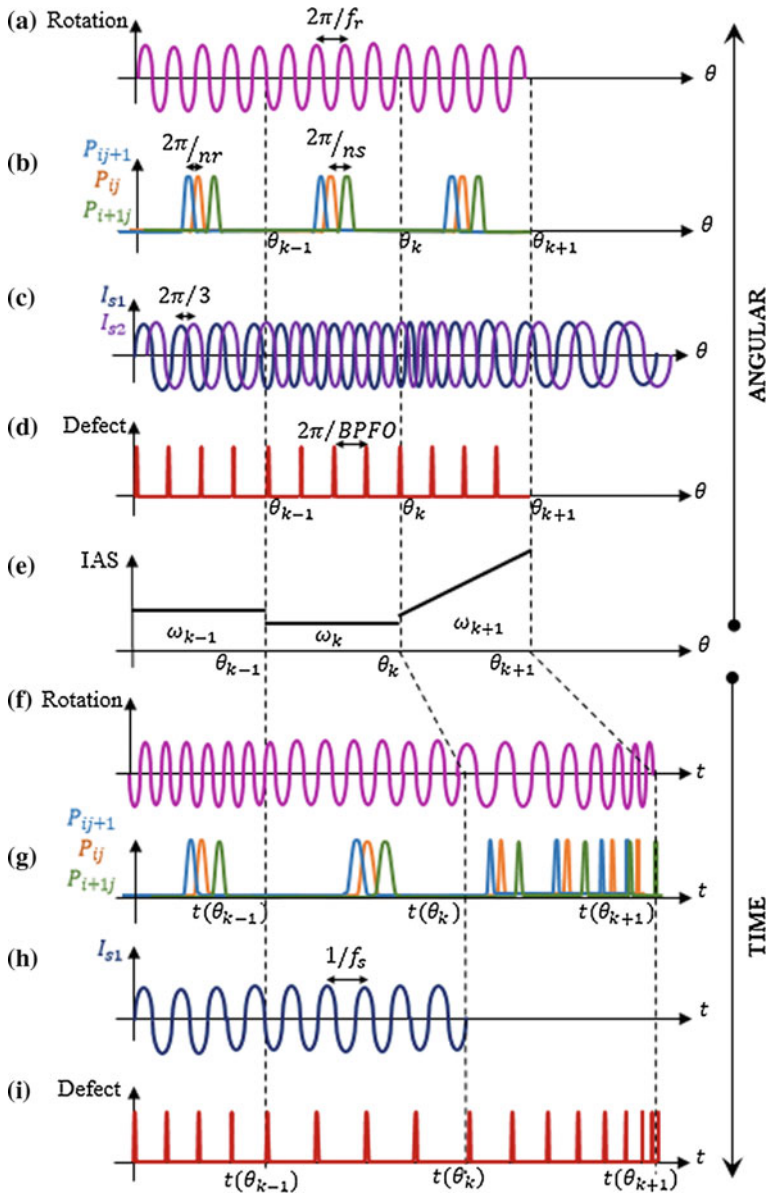

Fig. 3 Time and angular characteristic frequencies of the multiphysic system for three different operating conditions defined in **e**, **a** and **f**: rotation in time domain and angular domain, respectively **b** and **g**: air-gap permeances, **c** and **h**: stator-phase currents, **d** and **i**: Defect perturbation

where χ is the generalized displacement vector. M, C and K are respectively constant matrices of mass, stiffness and damping. I_d is the identity matrix.

Being associated to the angular approach, the proposed model is suitable for investigations with constant and varying conditions. In this paper, we are focalizing only on investigations with constant operating conditions.

The global model of electro-magnetic-mechanical coupling is schematized in the Fig. 2.

Figure 3 presents the angular and time variations of the multiphysic parameters which are involved in the electro-magnetic and the mechanical sub-systems interactions. Various operating conditions are shown as illustrated by three IAS levels.

Where *ns* and *nr* are respectively the number of stator teeth and the number of rotor teeth. P_{ij} is the air-gap permeance of the magnetic branch relating the 'i'th stator tooth to the 'j'th rotor tooth.

One can notice the presence of different characteristic frequencies corresponding to dynamics of the global system. The first frequency is related to the fact that we are dealing with a rotating machinery. It is equal to one event per revolution. A second type of characteristic frequencies is related to the induction machine geometry, in particular, to the stator and rotor slotting as a result of angularly varying air-gap permeances as shown in the angular representation of adjacent stator and rotor teeth air-gap permeances. Those values conserve their periodicity for the different operating conditions when represented in the angular description. However, this characteristic is hidden when described in time representation under non-stationary conditions. A third source of angularly periodic frequency is produced by the rolling bearing, possibly including defects, as represented by the Ball Pass Frequency on Outer Ring (BPFO) frequency. This frequency represents the same angular characteristic in an angular representation as the permeance variations. The fourth source of periodicity is related to the fundamental frequency of the per-phase stator current and it is produced by the electrical power supply of the induction machine. This frequency is constant in time description, whereas, it loses its periodic characteristics in an angular representation for non-stationary conditions.

In this research work, we are interested in this diversity of characteristic frequencies. The objective is to decrypt the interactions between those values representative of the multiphysic sub-systems.

3 Results and Discussion

The model presented in the previous section was used to simulation a three-phase squirreled induction machine representing 24 stator teeth and 30 rotor bars. The motor is fed by a 50 Hz power supply. The mechanical model is represented by a rotating shaft supported by a master rolling bearing characterized by a BPFO = 4.076 event/revolution. In addition, a defect on the outer race was introduced in the bearing model. It is parametrically defined to represent a realistic outer ring

Table 1 Multiphysic characteristic frequencies

Domain	Frequency	Description	Value [Hz]	Value [evt/rev]
Electric	f_{ph}	Stator phases	48.23	3
	f_s	Power supply	50	3.11
Magnetic	f_{st}	Stator teeth	385.85	24
	f_{sh}	Rotor bars	482.31	30
Mechanic	f_r	Rotation	16.07	1
	f_d = BPFO	Bearing defect	65.53	4.076

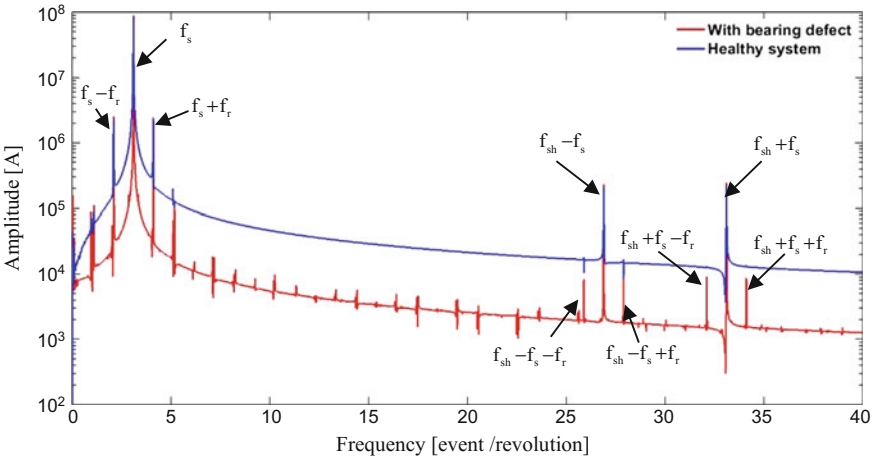

Fig. 4 Angular FT of the first-phase stator current for a healthy system and a system with a defective rolling bearing

localized defect. In (Table 1), the different characteristic frequencies of the global system are presented.

Simulations were performed to investigate the influence of a localized outer race defect on the current signal using Fourier Transform. Simulations were performed for stationary operating conditions for 100 revolutions of the rotor. The macroscopic rotation speed of the shaft is $\omega = 101$ rad/s. The FFT are estimated without windowing and presented in logarithmic scale to emphasize on small contributions as those produced by the defect. As shown in the Fig. 2, stator current and IAS are model outputs. In addition, in each iteration, the information about time and rotation angle were conserved. Accordingly, current and speed FFT were performed in time and angular domains.

What is important to show in those representations are the frequency modulations induced by the multiphysic interactions and the time and angular depending frequencies while ensuring the capacity of the proposed model to detect realistic defects.

In Fig. 4, the Fourier Transform of the first-phase stator current in the angular domain scaled in event per revolution. The spectrum are performed for a healthy

system and for a system with an outer race localized defect. They show the modulation of characteristic frequencies related to the induction machine. (Those frequencies are: 33.11, 26.89, 25.89, 27.89, 32.11 and 34.11 evt/rev, they correspond to: $f_{sh} \pm f_s \pm k.f_r$ evt/rev where k = 0, 1. Other characteristic frequencies related to the power supply are: 2.11, 3.11 and 4.11 evt/rev. These frequencies correspond to $f_s \pm k.f_r$ where k = 0, 1. As the model chosen to represent the bearing dynamic takes into consideration the presence the load sharing between rolling elements, the presence of the BPFO in the spectra is normal. However, when a defect exists on the bearing outer race, the contribution of this frequency is much more intense. By zooming the spectrum of the stator current with defect as shown in Fig. 5, we can explicit the frequencies related to the defect such as: 5.189, 7.189, 9.267, 11.33 evt/rev…. Those values correspond to: $f_s + k_1 .f_d \pm k_2 .f_r$ where k_1 is an integer number and $k_2 = 0, 1$.

Figure 6 shows the FT of the first-phase stator current in the time domain, and in Fig. 7, a zoom view of the FT is exhibited in order to explicit the contribution of the frequencies relative to the defect. The purpose from such investigation is to highlight angular and time modulations produced by the electrical-magnetic-mechanical interactions in order to emphasize the complementarity of the time and angular representations for diagnosis and phenomena comprehension. Either in the time or in angle representations, characteristic frequencies related to the induction machine and to the bearing defect are exhibited. However, the value of time-dependent frequency; mainly the current frequency, remains constant only in the time representation. We remark also that values of angular-dependent frequencies; mainly slots harmonic frequency, rotation frequency and bearing defect frequency, remain constant only when represented versus the angular representation.

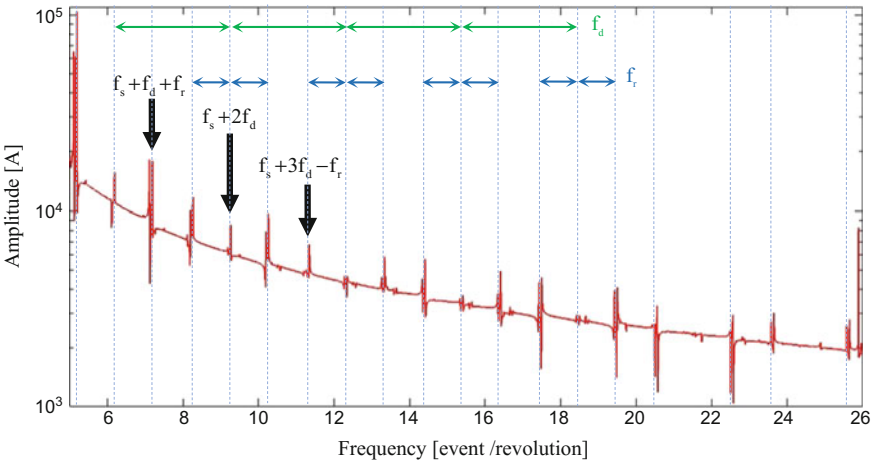

Fig. 5 Zoom view of the angular FT of the first-phase stator current for a system with a defective rolling bearing

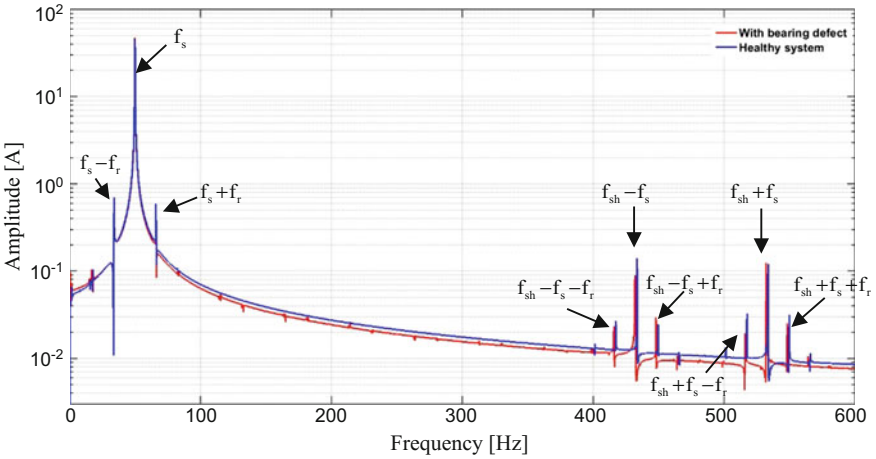

Fig. 6 Time FT of the first-phase stator current for a healthy system and a system with a defective rolling bearing

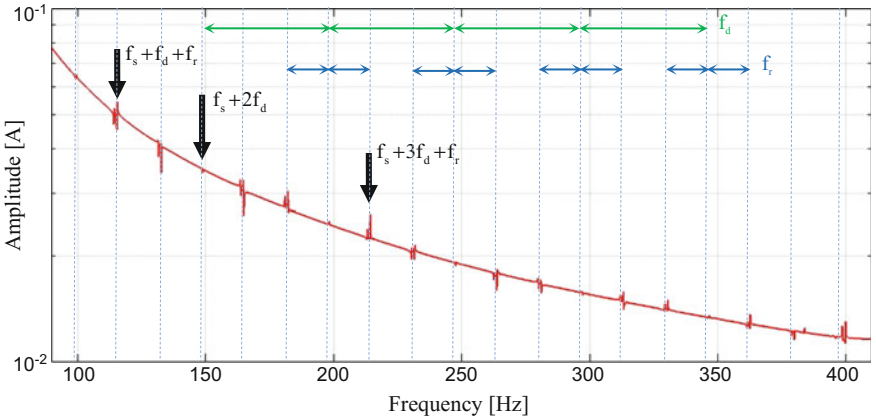

Fig. 7 Zoom view of the time FT of the first-phase stator current for a system with a defective rolling bearing: defect resulting frequencies

To conclude, in the case of a system representing simultaneously angular and time periodicities, inducing angular and time frequency modulations, instigations of the angular and the time spectrum are simultaneously needed.

4 Conclusion

In this paper, an electro-magnetic-mechanical model of a rotating shaft supported by rolling bearing and driven by a squirreled cage induction motor was presented. The model was described using an angular description in order to emphasize the angularly periodic character of the rotating system. Such a representation has allowed us to dissociate periodicities related to time from those related to angle. This consideration highlighted angular and time frequency modulations produced by the interactions of the multiphysic sub-systems. In this model, it was introduced a rolling bearing model that takes into account variations of efforts generated by the rolling elements passing specially in the case of a defective bearing. Simulated results have demonstrated the capacity of the model to detect defects using stator current signal and highlighted frequency modulations produced by the presence of the faulty rotating component. Further development can be realized in the case of non-stationary operating conditions, and by introducing further sources of time or/and angular periodicities to the model.

Acknowledgements Authors gratefully acknowledge Rhone-Alpes Council support via mobility grant "Accueil Doc" 13722.

References

1. Benbouzid, M. E. H. (2000). A review of induction motors signature analysis as a medium for faults detection. *IEEE Transactions on Industrial Electronics*, *47*(5).
2. Benbouzid, M. E. H., & Kliman, G. B. (2003). What stator current processing-based technique to use for induction motor rotor faults diagnosis? *IEEE Transactions on Energy Conversion*, *18* (2).
3. Luos, X., et al. (1993). Multiple coupled circuit modeling of induction machines. IEEE, 0-7803-1 462-x/93.
4. Feki, N., Clerc, G., & Velex, Ph. (2013). Gear and motor fault modeling and detection based on motor current analysis. *Electric Power Systems Research, 95,* 28–37.
5. Fourati, A., et al. (2014). Electrical modeling for faults detection based on motor current signal analysis and angular approach. In *Proceedings of the Fourth International Conference on Condition Monitoring of Machinery in Non-Stationary Operations*, CMMNO'2014, Lyon.
6. Gomez, J. L., Bourdon, A., André, H., & Rémond, D. (2016). Modelling deep groove ball bearing localized defects inducing instantaneous angular speed variations. *Tribology International, 98,* 270–281.

Fault Detection in Gears Using Stochastic Resonance

Clement Uchechukwu Mba, Stefano Marchesiello, Alessandro Fasana and Luigi Garibaldi

Abstract Investigations carried out so far on the application of Stochastic Resonance (SR) to mechanical system faults indicate that SR shows great promise as an advanced vibration-based condition-monitoring tool. However, majority of these studies only focus on faulty systems and thus, fail to adequately treat healthy systems. It is a well-known fact that some methodologies for fault detection give off false alarms when applied to a healthy system. With a view to addressing this problem, efforts are continuously made to either modify these methodologies or develop other methodologies that are more advanced. In addition to experimentally validating the use of SR as a vibration based condition-monitoring procedure, this paper attempts to address the issue of false alarms associated with SR and experimental data complexity by applying SR to pre-processed signals and raw signals, and comparing their results. The pre-processed signal could be either a residual signal, which is obtained by removing selected frequencies from the Time Synchronous Average (TSA) signal, or filtered signal, which is acquired by passing the raw signal through a high-pass filter with proper cut-off frequency. Furthermore, it is shown that kurtosis and other statistical features can be used as fault indicators when SR is applied to a signal.

Keywords Stochastic resonance · False alarms · Residual signals · Filtered signals

C.U. Mba (✉) · S. Marchesiello · A. Fasana · L. Garibaldi
DIRG – Politecnico Di Torino, Corso Duca Degli Abruzzi, 24-10129 Torino, Italy
e-mail: clement.mba@polito.it

S. Marchesiello
e-mail: stefano.marchesiello@polito.it

A. Fasana
e-mail: alessandro.fasana@polito.it

L. Garibaldi
e-mail: luigi.garibaldi@polito.it

A. Timofiejczuk et al. (eds.), *Advances in Condition Monitoring of Machinery in Non-Stationary Operations*, Applied Condition Monitoring 9,
https://doi.org/10.1007/978-3-319-61927-9_6

1 Introduction

Maintenance is periodically performed on machineries as part of cost saving and safety measures. There is no doubt that vibration based condition monitoring plays a key part in maintenance which is why numerous techniques for performing vibration based condition monitoring exist, some of which are quite new.

Stochastic Resonance (SR) has only been used recently for fault detection in mechanical systems. Its uniqueness lies in its ability to capitalize on the noise that is inherent in a system [1]. Moreover it has a simple equation that is quite easy to apply. But the downside to SR is that there is no clear theory for the selection of SR parameters although there are different methods currently in use. Additionally, SR computing time takes a while especially for large samples of vibration signal. Nevertheless, researches that have been conducted so far on the application of SR to mechanical systems have shown promising results [2–5] and thus, the application of SR remains an area of significant interest. Marchesiello et al. [2] used SR to enhance fault detection in bearings and also presented a method for the selection of SR parameters. By using numerical simulations, Mba et al. [3] showed that SR can be used for fault detection in spur gears. Leng et al. [4] used SR for the diagnosis of electromotor faults and metal cutting process. Lei et al. [5] applied SR to fault identification in a planetary gearbox by using an ant colony algorithm to optimize the parameters of SR. While all the researches mentioned present interesting results, there is still limited research on how well SR works when applied to healthy mechanical systems. Majority of available studies only focus on faulty systems.

The main aim of using SR in this paper on a real life gearbox is to validate the numerical simulation results in [3] as this would help to establish the suitability of SR as a diagnostic tool. Additionally, adequate attention is given to the application of SR on vibration signals from a healthy gearbox. Also, a short assessment of the most common diagnostic tools for gearbox condition monitoring is done with their results compared. The idea is to show that SR has the potential to act as an amplifier not only for kurtosis, but also for some of the other gearbox diagnostic tools. Furthermore, the effect of SR is shown in both time and frequency domain for numerical simulations and experimental data.

2 Brief Description and Application of Stochastic Resonance

SR is a non-linear time domain method whose dynamical behaviour is described by the Brownian motion equation of particles:

$$\frac{dx}{dt} = -\frac{dU(x)}{dx} + s(t) + n(t) \tag{1}$$

where $U(x)$ is the potential function, $s(t)$ is the input signal and $n(t) = \sqrt{2D}\varepsilon$ is the input noise with D being the noise intensity and ε the Gaussian noise. $U(x)$ is given as

$$U(x) = -\frac{1}{2}ax^2 + \frac{1}{4}bx^4 \tag{2}$$

Accordingly, Eq. (2) can be rewritten as

$$\frac{dx}{dt} = ax - bx^3 + s(t) + n(t) \tag{3}$$

a and b are the non-linear system parameters that are responsible for SR occurrence and they can be adjusted in such a way that the full effect of SR is obtained. Hence whether SR occurs depends on a and b. The height of the potential barrier ΔU, shows the following relationship between the non-linear system parameters a and b.

$$\Delta U = \frac{a^2}{4b} \tag{4}$$

Equation 3 is quite suitable for small parameter systems, i.e. amplitude and frequency of the input signal $\ll 1$ and noise intensity D $\ll$ 1. But realistic systems are usually large parameter systems, i.e. amplitude and frequency of the input signal $\gg 1$ and noise intensity D $\gg 1$. Because of this, large parameter systems are subjected to pre-processing techniques like scale normalization, modulation, re-scaling frequency, etc. [5] in order to make them meet the requirements of small parameter systems. Like the previous work, re-scaling frequency is used in this paper to ensure that the gearbox system meets the requirements needed for the functionality of SR. Furthermore, the input signal of the SR system is normalized with a standard deviation of 0.07. This helps to ensure that a and b can be tuned within a defined range to obtain the best results. These ranges are $a \in [0.1, 1]$ and $b \in [1, 11]$.

With a view to showing the effect of SR as a possible amplifier, Fig. 1 shows the changes that statistical features for gearbox condition undergo for both SR and non-SR signals as the fault severity progresses from 1 to 4 on the x axis with 1 being the healthy case, 2 being a small fault case, 3 being a medium fault case and 4 being a large fault case. Figure 1a shows the changes that occur when the statistical indicators are applied directly to either the raw signal, its TSA, residual or difference signal and Fig. 1b shows the changes that occur when the statistical indicators are applied to the output of the SR system after the raw signal is passed through the SR system. As can be seen with some of the indicators, SR tends to amplify the absolute changes that occur in all or some stages of fault growth. This is particularly true for the kurtosis, crest factor, FM0, FM4, M6A, NB4, M8A, ENA4 and energy

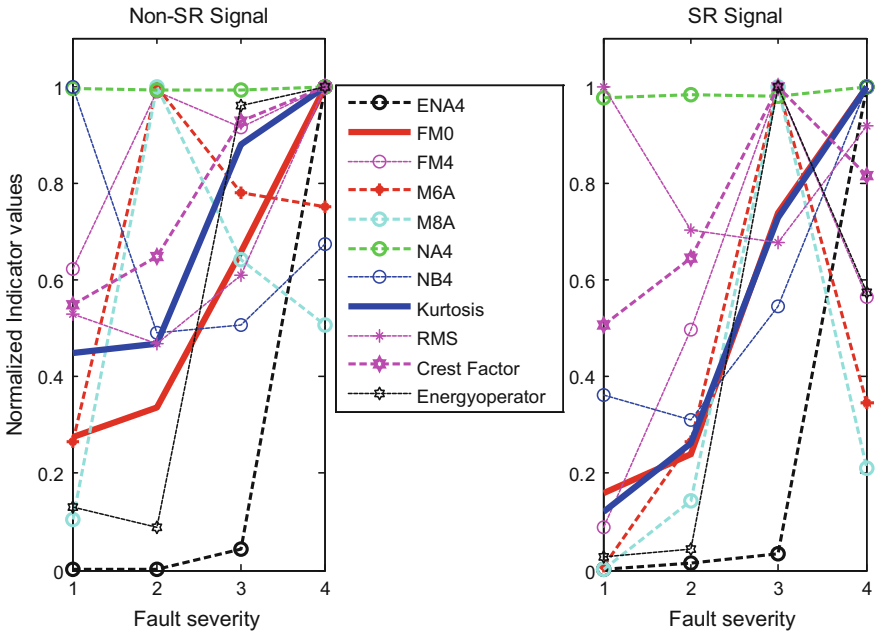

Fig. 1 Comparison of the changes in the most common gearbox fault diagnosis statistical features. On the x axis, 1 = healthy case, 2 = small fault case, 3 = medium fault case and 4 = large fault case **a** non-SR Signal **b** SR Signal

operator [6–8]. In general, the kurtosis and FM0 provide the clearest indication of these changes; however, the overall amplification is greater in the kurtosis than in any of the other indicators. This seems to imply that kurtosis might be the most fitting indicator for SR in the time domain.

2.1 Numerical Simulations and Analyses

The dynamic response of a single stage reduction gearbox with varying fault severities is evaluated as described in [3] with the addition of a pulse generator. The transmission path, which is simulated as the time response of an SDOF dynamic system to an arbitrary input, is taken into consideration. In addition, a Gaussian noise is added to the acceleration signal obtained from the transmission path to make the obtained acceleration signal as realistic as possible. The addition of Gaussian noise to the acceleration signal leads to different realizations of a "modified acceleration signal." In this paper, the same realization of modified acceleration signal is used for all analyses conducted.

Figure 2 shows the obtained results when the frequency spectra is computed for the time domain results with and without SR with a driving shaft speed of 1248

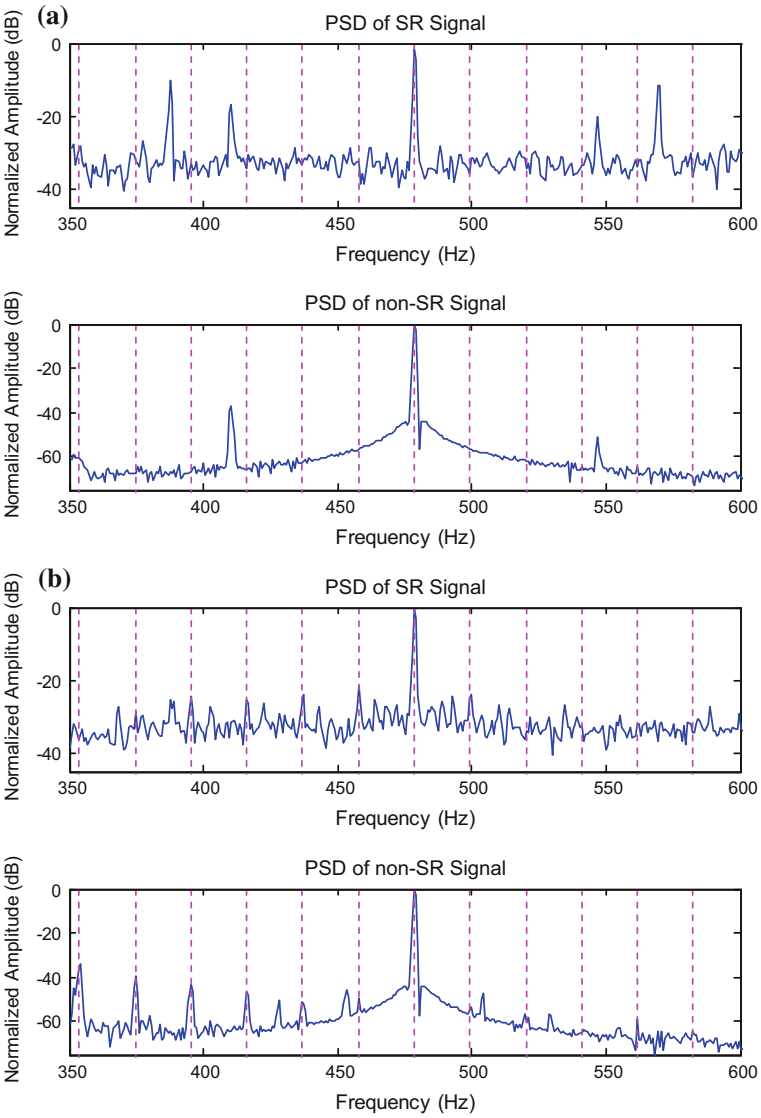

Fig. 2 Vibration spectrum of a single stage reduction 1248 rpm gearbox **a** healthy case **b** fault reduced by 90% **c** fault reduced by 50% **d** reference fault

revolutions per minute (rpm), and tooth meshing frequency of 478 Hz. The magenta lines in the figures show where the sidebands are supposed to be theoretically. As expected, the sideband amplitudes of the non-SR signal reduce as the fault severity reduces.

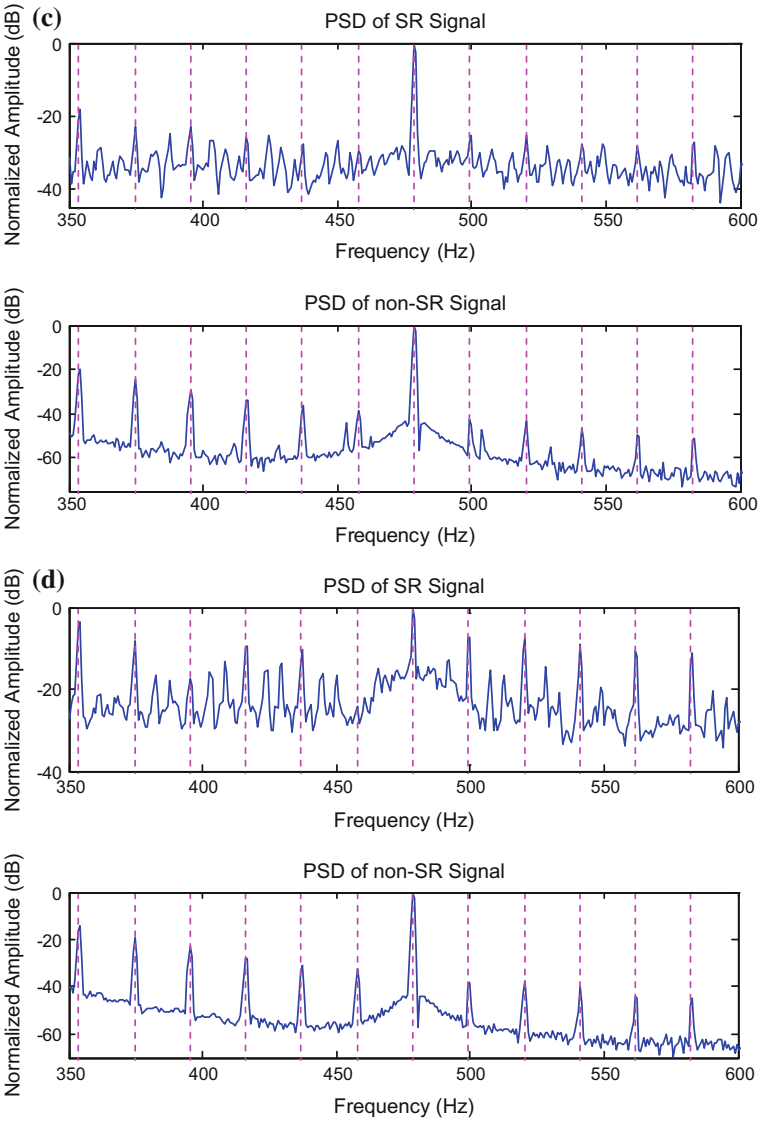

Fig. 2 (continued)

In the healthy case of Fig. 2a, there is no amplification of sidebands in the SR signal. However, a few more spikes can be seen in the SR signal when compared to the non-SR signal. In Fig. 2b and c, the effect of SR on the modified acceleration signal is not very obvious in the frequency domain unlike the time domain results in [3]. The effect of SR is quite evident in Fig. 2d as there are clear indications of amplification of the sidebands in the SR signal especially after the meshing

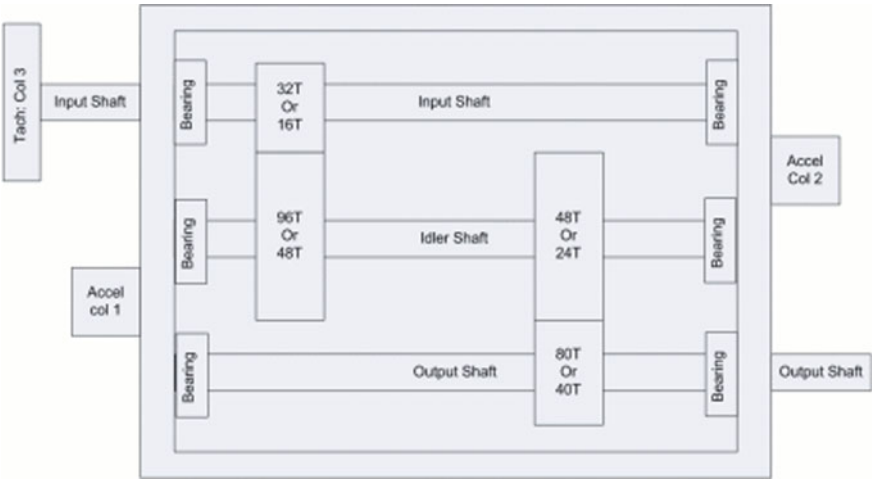

Fig. 3 Schematic diagram of a double stage reduction gearbox [9]

frequency. The sideband amplitudes are more distinct in the non-SR signals than the SR signals, which appear noisy at best. In the figures, it seems easier to differentiate the healthy gear from the faulty gear by looking at the non-SR signal which could bring one to the conclusion that the effect of SR on gear data is not very pronounced in the frequency domain (Fig. 3).

2.2 Experimental Results and Analyses

The experimental data used for validating the numerical results is obtained from PHM dataset 2009 [9] where a double stage reduction gearbox with different fault severities is run at different speeds with both high and low loads. The schematic of the gearbox is shown in Fig. 2. There is a completely healthy case, another case where there is a chipped gear tooth and another case where there is a broken gear tooth. In addition, the runs are repeated twice for each load and speed. Here, our analysis focuses on the first-run data with an input shaft speed of 30 Hz and high load as well as data from channel 2 and the spur gear setup. Furthermore, SR is applied to the healthy case, chipped tooth case and the broken tooth case with the results given below.

Figures 4, 5 and 6 show the vibration spectra obtained for the spur gearbox with its corresponding SR on the right hand side of the plot and non-SR signals on the left hand side of the plot. Each figure has an upper section corresponding to the spectrum for the lower meshing frequency range and a lower section corresponding to the spectrum for the upper meshing frequency range. The red and magenta lines represent the theoretical position of the sidebands around their corresponding fundamental frequencies.

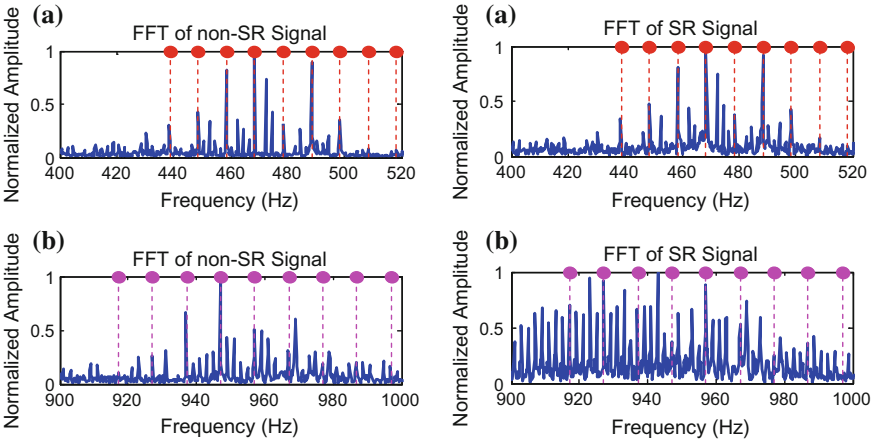

Fig. 4 Non-SR and SR vibration spectrum of a 1800 rpm double stage reduction spur gearbox—healthy tooth case **a** lower meshing frequency range **b** upper meshing frequency range

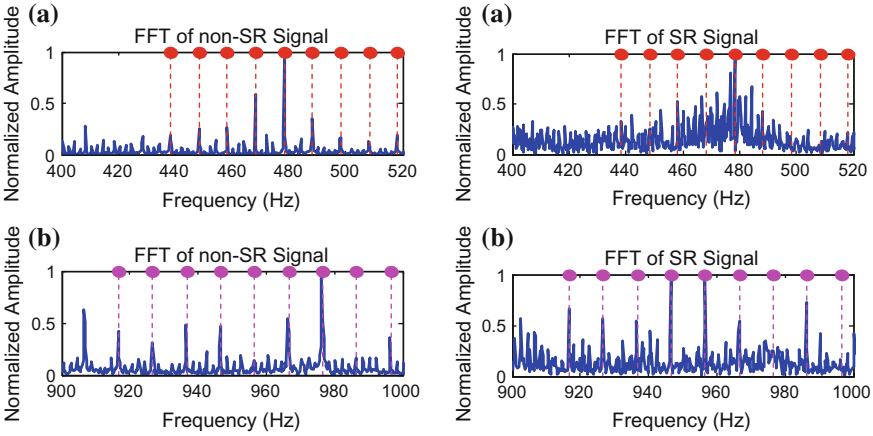

Fig. 5 Non-SR and SR vibration spectrum of a 1800 rpm double stage reduction spur gearbox—chipped tooth case **a** lower meshing frequency range **b** upper meshing frequency range

In the healthy case of Fig. 4, there is not a lot of difference between the non-SR and SR signal in the lower meshing frequency range, nevertheless, there is a huge amplification of sidebands in the higher meshing frequency range. In Fig. 5, the SR signal appears noisy in the lower meshing frequency range while there is an amplification of eccentric gear sidebands in the higher meshing frequency range. Comparing the non-SR signal and SR signal of Fig. 6, there is no obvious difference between them, however, the sidebands due to the broken gear appear to be somewhat more observable in the higher meshing frequency range of the SR signal.

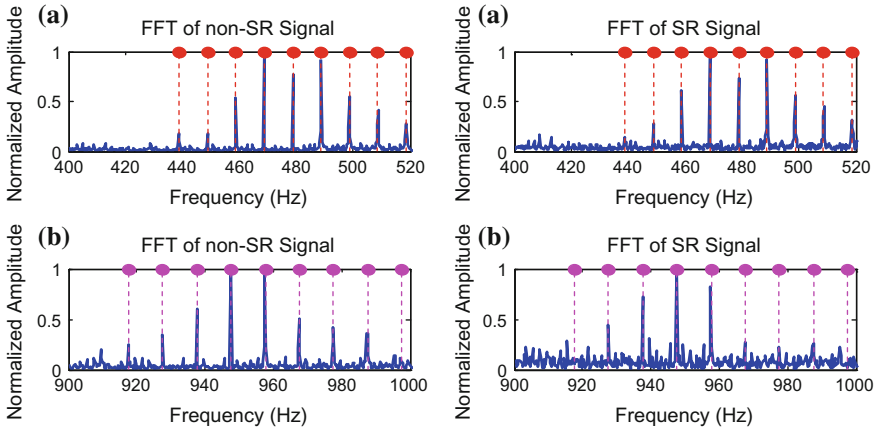

Fig. 6 Non-SR and SR vibration spectrum of a 1800 rpm double stage reduction spur gearbox—broken tooth case **a** lower meshing frequency range **b** upper meshing frequency range

In an overall sense, there always seems to be amplification in the SR signals with the amplifications in the higher meshing frequency range looking more noticeable and noisy. This also applies to the healthy signals, which could be because of all the frequencies contained in the raw signal. The amplification of sidebands in the healthy signals appears to be more apparent in the experimental case than the numerical case. It is a well-known fact that experimental data have more noise, vibration and complexity and as a result, they could be more difficult to analyse properly. Thus, it might be imperative to always pre-process experimental data signals before applying SR in order to obtain the best results.

3 Applying Stochastic Resonance to Residual Signals

The residual signal is determined by removing the meshing frequencies and the shaft frequencies along with their harmonics from the original time synchronous averaged signal [6–8].

$$r = x(t) - x_r(t) \tag{5}$$

where r is the residual signal, $x(t)$ is the original TSA and $x_r(t)$ is the signal containing the meshing frequencies, shaft frequencies and their harmonics. When the first order sidebands are removed from the residual signal, a difference signal is formed.

$$d = r - (f_m \pm \omega_i),\ i = 1 \tag{6}$$

where d is the difference signal, f_m is the signal meshing frequency and ω is the shaft frequency. Both the residual and difference signal were proposed in order to better observe the changes that occur in a vibration signal [6].

In our computation, the frequencies mentioned are removed from the exact realization of non-SR modified acceleration signals that are shown in Fig. 2 to obtain the non-SR signals shown in Fig. 7. Clearly, the sidebands are more evident in the signals and it is easier to understand them.

All the amplitudes in Fig. 7 are displayed in dB scale for more clarity. The SR and non-SR signals of Fig. 7a are almost the same, which means that false alarms

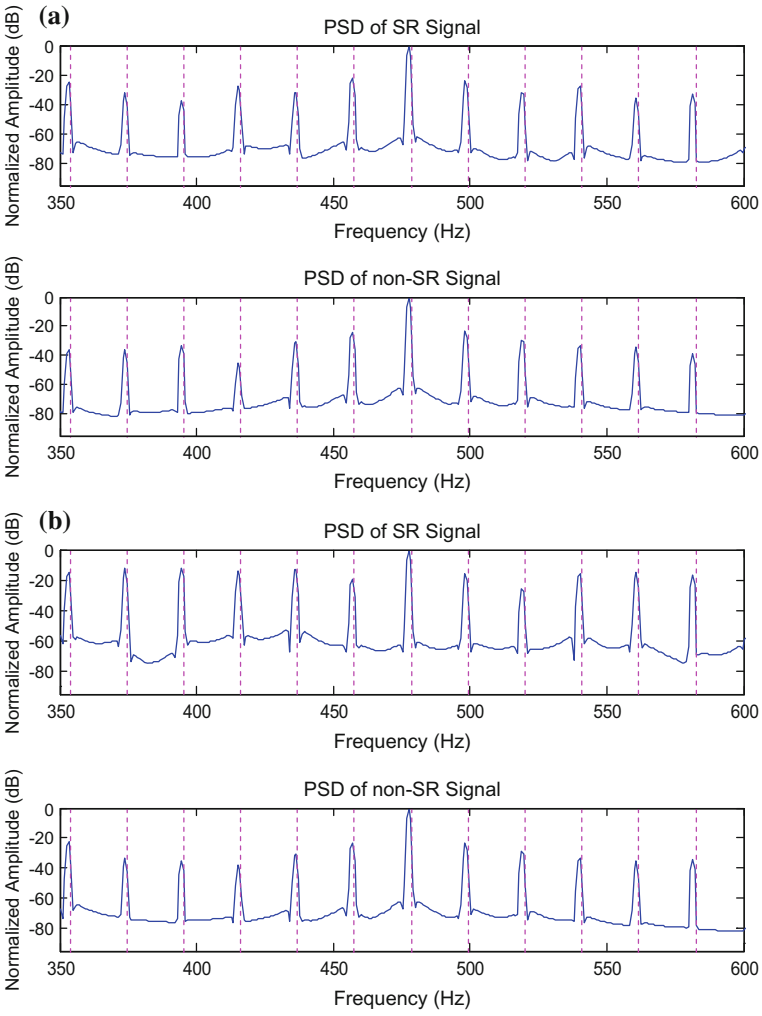

Fig. 7 Residual signal vibration spectrum of a single stage reduction 1248 rpm gearbox **a** healthy case **b** fault reduced by 90% **c** fault reduced by 50% **d** reference fault

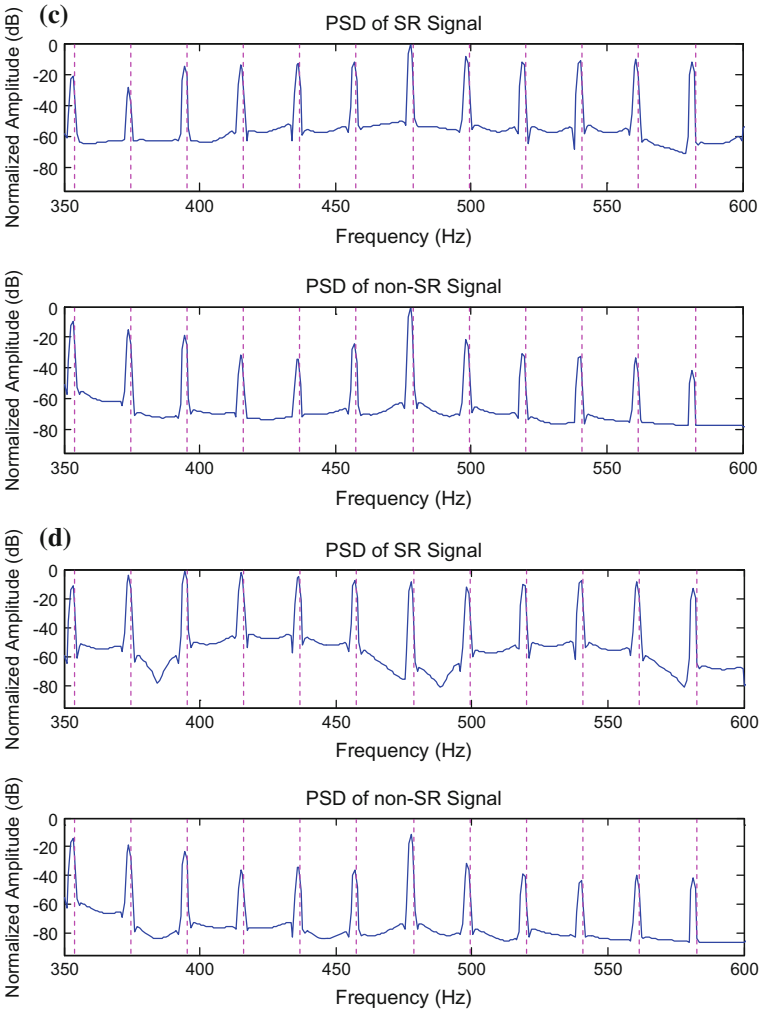

Fig. 7 (continued)

are almost non-existent in this scenario. In Fig. 7b, the sidebands in the SR signal are amplified randomly while in Fig. 7c, the amplification is done after 400 Hz. In Fig. 7d, the amplitude of the sidebands relative to that of the fundamental frequency is higher in the SR signal than in the non-SR signal.

When the same procedure is applied to the experimental data of the spur gear setup, the results obtained agree well with the numerical results as seen in Figs. 8, 9 and 10. In the healthy case, both the SR and non-SR signals are similar just like the numerical simulation result.

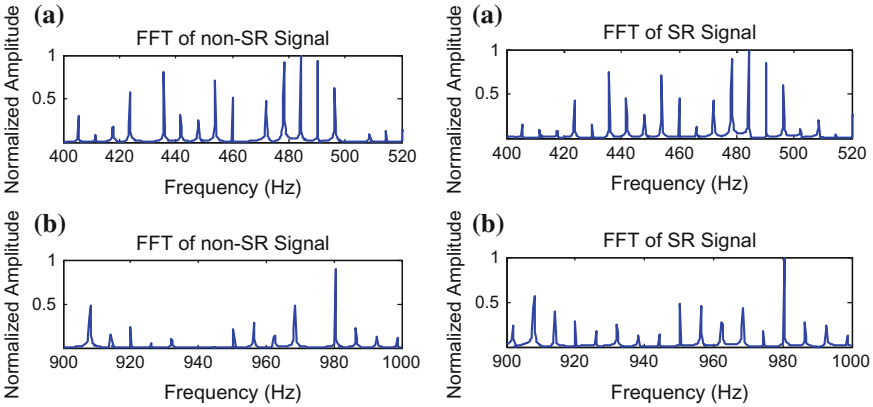

Fig. 8 Non-SR and SR residual signal vibration spectrum of a 1800 rpm double stage reduction spur gearbox—healthy tooth case **a** lower meshing frequency range **b** upper meshing frequency range

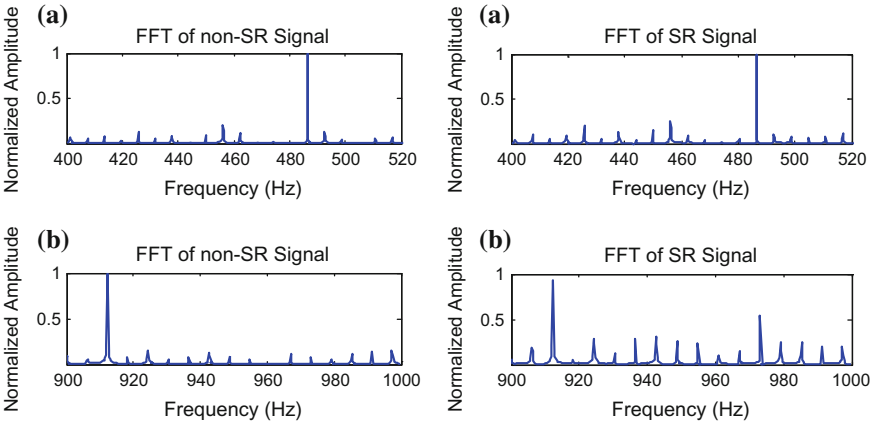

Fig. 9 Non-SR and SR residual signal vibration spectrum of a 1800 rpm double stage reduction spur gearbox—chipped tooth case **a** lower meshing frequency range **b** upper meshing frequency range

The frequency spikes are evident in the SR signal of Fig. 9 especially in the higher meshing frequency range. The spikes that are present in the lower meshing frequency range are most likely due to the eccentric gear which are not as conspicuous as the spikes in the higher meshing frequency range which are most likely due to the chipped gear. In Fig. 10 where there is an eccentric gear and a gear with broken tooth, the frequency spikes are very evident in both the lower and upper meshing frequency range. The frequency spikes in the lower meshing frequency range are due to the eccentric and broken tooth gears while the spikes in the upper

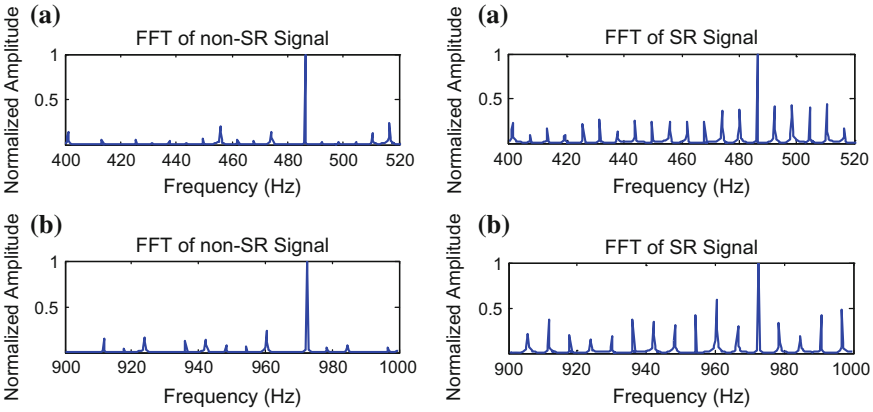

Fig. 10 Non-SR and SR residual signal vibration spectrum of a 1800 rpm double stage reduction spur gearbox—broken tooth case **a** lower meshing frequency range **b** upper meshing frequency range

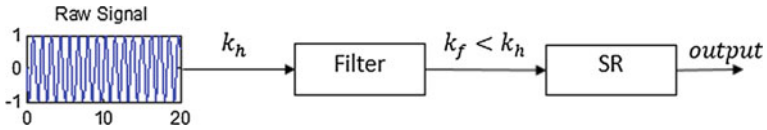

Fig. 11 Schematic diagram showing a possible way of choosing the high-pass filter cut-off frequency

meshing frequency range are most likely as a result of the harmonics of the spikes in the lower meshing frequency range. It should be noted that the frequency spacing of the non-SR signal is not regular while that of the SR signals is regular and spaced at 6 Hz corresponding to the speed of the output shaft.

4 Applying Stochastic Resonance to High-Pass Filtered Signals

In the time domain, the SR output of the experimental data of the healthy gears gives a high kurtosis. This is not the case for the numerical simulations, which gives a low kurtosis when SR is applied to the healthy gear signal. As indicated earlier, the most reasonable explanation for this phenomenon is that experimental data has more vibration, noise and complexity that make it difficult to properly examine them. In this section, a high-pass Butterworth filter with a proper cut-off frequency is used to make the data to be analysed "less complex." The cut-off frequency of the filter is selected in such a way that the kurtosis of the filtered signal is slightly less than the kurtosis of the original signal using the healthy case as reference. This is depicted schematically in Fig. 11.

The raw signal in Fig. 11 is a healthy signal, which was used as a reference because SR tends to always amplify the numerical value of the kurtosis and we are trying to keep the initial kurtosis as low as possible. k_h is the kurtosis of the healthy signal and k_f is the kurtosis of the filtered signal. The value of the cut-off frequency of the filter that coincides with k_f about 90% of k_h is selected in this case. It should be noted that the primary goal here is to contain false alarms in the time domain.

Using this procedure, 0.216 is selected as the normalized cut-off frequency of the high-pass Butterworth filter. The first column of Fig. 12 displays the raw signals, the second column displays the SR output without filtering and the third column displays the SR output after filtering. The green line in the second and third columns correspond to the negative well of the symmetric double well potential of the SR dynamic system, which is defined as $-\sqrt{\frac{a}{b}}$ while the red line in both columns correspond to the positive well of the symmetric double well potential of the SR dynamic system and is defined as $\sqrt{\frac{a}{b}}$. In Fig. 12a, the kurtosis of the SR output in the third column is much lower than the kurtosis of the SR output in the second

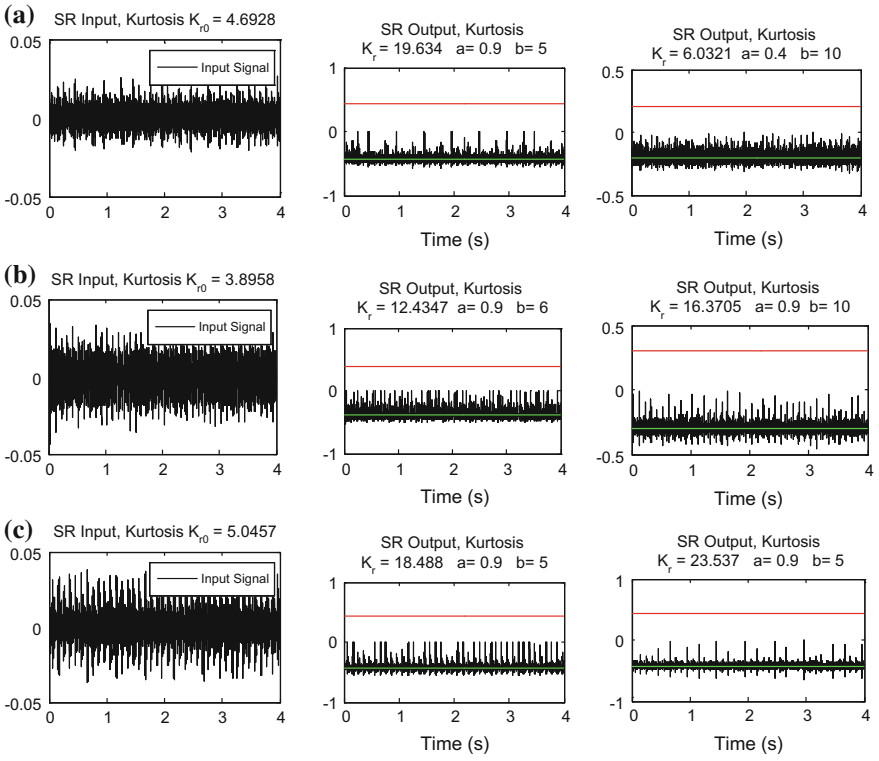

Fig. 12 Time histories of the non-linear dynamic system—experimental results for the spur gear setup (*1st column*) raw signal (*2nd column*) SR signal (*3rd column*) filtered SR signal. (*1st row*) healthy case (*2nd row*) chipped tooth case (*3rd row*) broken tooth case

column. In the third column of Fig. 12b and c, the kurtosis of the SR output is more amplified when compared with the second column of the same figures. These results demonstrate that false alarms in the time domain can be contained in SR output when the raw signal is filtered before passing it through the SR dynamic system.

5 Conclusions

There are many vibration-based condition-monitoring techniques amongst which, SR stands out in the sense that it can exploit system noise positively. In addition to amplifying the kurtosis for faulty gears in the time domain, it can also act as an amplifier for other fault detecting statistical features. Although few researches have been done on applying SR to mechanical problems, much of the already done research focuses on faulty cases. In this paper, more attention is given to the effect of SR on data from healthy gearboxes. Analyses conducted in the frequency domain tend to imply that the effect of SR on gearbox acceleration signals is neither clear nor well pronounced. In the time domain on the other hand, while there are no problems when SR is applied directly to data from numerical simulations, misleading results can be obtained when SR is applied directly to experimental data. Based on the complexity of realistic data, which seems to affect SR results, a plausible solution would be to pre-treat data in order to reduce its complexity before applying SR. Two strategies are taken to solve this problem in this work. The first tactic involves computation of the residual signal by removing some defined frequencies from the TSA. The second approach involves applying a high-pass filter with a proper cut-off frequency to the original signal. The results obtained when SR is applied to the residual signal and filtered signal, rather than the raw signal looks promising as can be seen in the latter part of this paper.

References

1. Yan, R., Zhao, R., & Gao, R. X. (2012). Noise-assisted data processing in measurement science: Part one part 40 in a series of tutorials on instrumentation and measurement. *Instrumentation & Measurement Magazine, IEEE, 15*(5), 41–44.
2. Marchesiello, S., Fasana, A., & Garibaldi, L. (2015). Best parameter choice of stochastic resonance to enhance fault signature in bearings. In *International Conference on Structural Engineering Dynamics*, pp. 1–7.
3. Mba, C.U., et al. (2015). Vibration based condition monitoring of spur gears in mesh using stochastic resonance. In *Surveillance 8 International Conference*, pp. 1–15.
4. Leng, Y. G., et al. (2006). Numerical analysis and engineering application of large parameter stochastic resonance. *Journal of Sound and Vibration, 292*(3), 788–801.
5. Lei, Y., et al. (2013). Planetary gearbox fault diagnosis using an adaptive stochastic resonance method. *Mechanical Systems and Signal Processing, 38*(1), 113–124.

6. Samuel, P. D., & Pines, D. J. (2005). A review of vibration-based techniques for helicopter transmission diagnostics. *Journal of Sound and Vibration, 282*(1), 475–508.
7. Lebold, M., et al. (2000). Review of vibration analysis methods for gearbox diagnostics and prognostics. In *Proceedings of the 54th Meeting of the Society for Machinery Failure Prevention Technology*.
8. Večeř, P., Kreidl, M., & Šmíd, R. (2005). Condition indicators for gearbox condition monitoring systems. *Acta Polytechnica 45*(6).
9. http://www.phmsociety.org/references/datasets. (2009). PHM Challenge Competition Data Set. 2009.

The Impact Estimation of Damping Foundations in Dynamics of the Rotor System in Non-stationary States

Andrzej Grządziela, Marcin Kluczyk and Paweł Chwin

Abstract The paper presents results of researches conducted on test bed of rotor system. The aim of research was to show how resonant frequency and amplitude might be changed by damping washers. Article presents an example of approach to the problem conducted in laboratory conditions, the results of which can be easily transferred on board of a ship or vessel.

Keywords Rotor system · Deceleration · Resonance · Damping

1 Introduction

High angular speed of unbalanced rotating masses causes forces transferred through the bearing to the foundation of machine. The amplitudes of vibrations connected with that forces become higher as far as the damping factor of foundation is getting worst. The paper contains the description of the active-passive experiment. The research stand consists of a foundation, spring washers, dampers, rotor system with two bearings and two masses and an electric motor with a speed controller.

Due to utilization of power inverter a smooth adjustment of acceleration and deceleration of rotor system (within 0–1480 rpm) was possible. The main aim of this work was to create characteristics of non-stationary state enable the selection and evaluation of damping elements. On the basis of the results of measurements set of resonant frequencies in the spectra of vibration amplitudes was determined. Another objective of the research was the methodology of selection of damping

A. Grządziela · M. Kluczyk (✉) · P. Chwin
Polish Naval Academy, Gdynia, Poland
e-mail: m.kluczyk@amw.gdynia.pl

A. Grządziela
e-mail: a.grzadziela@amw.gdynia.pl

P. Chwin
e-mail: p.chwin@wp.pl

A. Timofiejczuk et al. (eds.), *Advances in Condition Monitoring of Machinery in Non-Stationary Operations*, Applied Condition Monitoring 9,
https://doi.org/10.1007/978-3-319-61927-9_7

pads for the object of research, which has not been known all the data to determine the dynamic characteristics. Such situation often occurs during the repairs and maintenance process of rotating parts in the shipbuilding industry. The study was performed using the procedure of order tracking. The adopted methodology allows recognition of resonance frequencies in the process of acceleration and deceleration of the machine. It is essential for the proper calculation and selection of damping pads for rotating machines.

Rotating machines produce repetitive vibrations and acoustic signals connected with rotational speed. These relationships are not always obvious with standard dynamic signal analysis (for example FFT) and especially in this cases the order analysis is very useful. Order analysis becoming a commonly used technique for analysis of vibrations generated in machines, where many vibrations are related to machine RPMs.

The FFT process transforms time domain data to the frequency domain, creating a spectrum. Periodic signals in the time domain appear as peaks in the frequency domain. In order analysis the FFT transforms the revolution domain data into an order spectrum. Signals that are periodic in the revolution domain appear as peaks in the order domain. For example, in rotor with 10 blades without any unbalance and misalignment the peaks connected with blade passing frequency will appear as 10 order in the order spectrum.

In order analysis normally a signal from tachometer probe is used as a tracking reference. It allows a measurement to be related to the revolutions of a rotating element in the machinery. In the order analysis spectral elements that are constant with frequency, for example resonance peaks are well visualized, this is the reason why order analysis is often first step in a trouble-shooting scheme, in order to investigate whether a vibration problem is resonances or other reasons [6].

2 Object and Methodology of Researches

Researches was conducted on Schenck rotor system laboratory stand. It is combined of electrical motor coupled with set of two discs mounted on a solid shaft placed on two bearings—Fig. 1. Entire construction is attached to steel frame.

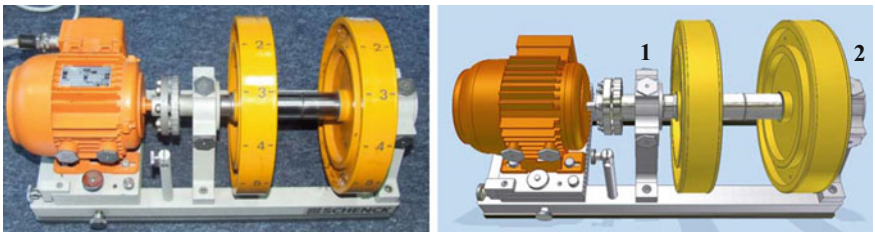

Fig. 1 Laboratory station Schenck, *left* figure—the photography and the *right*—spatial model with number of bearings

Metal discs have premade holes to be able to install additional masses to implement unbalance to the system.

Schenck rotor system is propelled with asynchronous three-phase motor AEG AM 56KY4. The power inlet was based on block of assembled capacitive-inductive reactance creating 3-phase electrical connection from 1-phase electrical line (230 V/50 Hz) by allowing phase shift for two additional phases (120° and 240°). After proper consideration of AEG motor it was replaced by existing power supply with ABB power inverter type ACS150-01E-02A4-2 (0.37 kW). The power feed was based on block of assembled capacitors creating 3-phase electrical connection from 1-phase electrical line (230 V/50 Hz) by allowing phase shift for two additional phases (120° and 240°). The negative outcome of such array was lack of possibility of any adjustments nor control.

The study used the process of deceleration of the rotor system, which in both variants of the experiment (with/without dampers) allowed unforced (free) vibration analysis. The adopted model of research has provided no interactions unexpected, external forces and torques, the effects of which could affect the results of the experiment. This approach to research, along with the possibility of variable speed has allowed to define the experiment as passive—active type.

3 Diagnostics Methodology

The aim of passive-active experiment is to observe the input signals with simultaneous measurement of the quality of state without the possibility of interference in their values (Fig. 2). It is possible to conduct the passive-active experiment during normal operation of machine [9].

The identification of dynamic parameters in mechanical systems is important for improving model-based control as well as for performing realistic dynamic simulations. Generally, when identification techniques are applied only a subset of so-called base parameters can be identified. In order to evaluate the forward dynamics response, an approach for obtaining the forward dynamics in terms of the relevant parameters is also proposed. To assess the impact on unbalance and

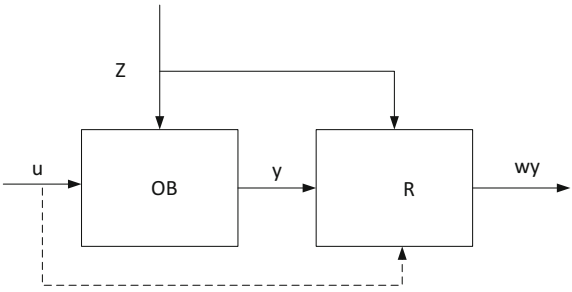

Fig. 2 Passive-active experiment S—control, u—forced control inputs OB—object of researches, ZE—external inputs, y—outputs, R—processing, wy—the result of the experiment [9]

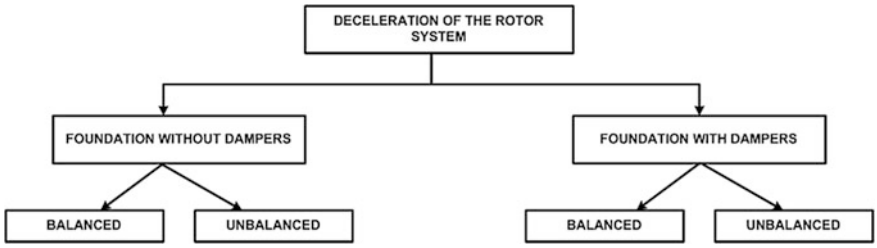

Fig. 3 The algorithm of the researches

damping value of measured vibrations, a series of measurements was performed, containing measurements:

- without any additional mass on cylinders and without any additional damping,
- without additional mass and with damping unit,
- with additional mass (causing unbalance), and without any additional damping,
- with additional mass (causing unbalance) and with damping unit.

The algorithm of the researches is presented on the Fig. 3.

Measurements was conducted during the run down of rotor system. Such approach allows to measure only the resonance of the rotor system without influence of current frequency and impact of power torque.

Exceeding acceptable unbalanced on rotors increases vibration energy. The consequence may be the excitation of resonant vibration and dynamic load growth. During operation rotors are subject to the occurrence of vibration in planes of bent, torsional and longitudinal. Working rotor should therefore be considered as a system of vibrating twist-bend-split.

In practice, most industrial and laboratory measured values are change in size over time. This variation is the base of criterion for the distribution of measurements: for static and dynamic measurements. In static measurements value do not change with time or variation of the measured value accuracy, but it does not affect the result. Dynamic measurement is made when the aim of the measurement is quantitative illustration of the time variation of the measured value. The result of a dynamic measurement is representation of the time course of the measured value. The outcome may be a plot of the measured value as a function of time, the so-called drawn directly by an analog recorder or within pairs of numbers $\{[t, x \cdot (t)] \cdot i\}$, where i is the number of time point, t is time and $x \cdot (t)$ is the instantaneous value of the measurement.

During measurements on laboratory test bed there were used two accelerometers type B&K 4514 B, tacho probe type MM024 and measurement frontend type 3650-B-120. Sampling frequency of 8192 Hz has been used.

4 Results of Researches and Comments

As a result of measurements time signals of accelerations had been obtained. With use of Pulse software platform signals were analyzed in frequency and order domain. At first stage frequency spectrum of accelerations has been calculated and then the order spectrum with 30 orders. Sample of obtained results has been presented on Figs. 4, 5, 6, 7. All results were collected in Table 1. Location of bearing in rotor system was presented on Fig. 1. On presented pictures it is clearly visible that in frequency spectrum it is possible to find resonance but it is no so obvious as on order spectrum.

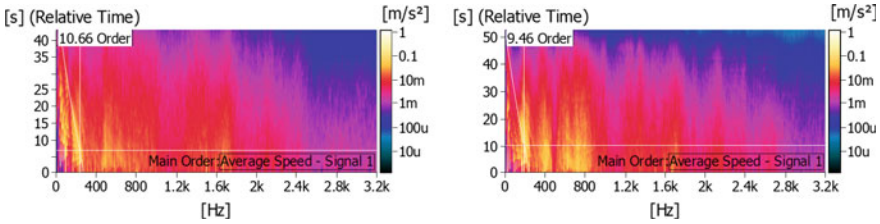

Fig. 4 Comparison of spectrogram of acceleration obtained on object without additional mass without dampers (*left* figure) and with dampers (*right* figure)

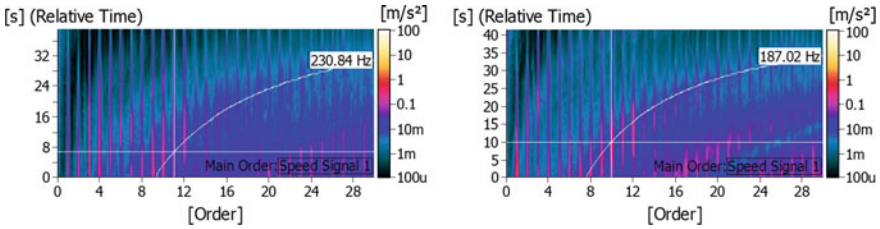

Fig. 5 Comparison of order spectrum of acceleration obtained on object without additional mass without dampers (*left* figure) and with dampers (*right* figure)—bearing no. 1

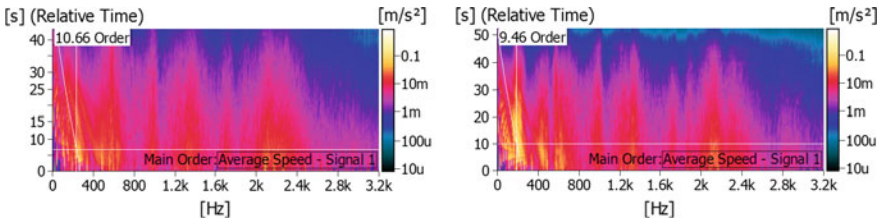

Fig. 6 Comparison of spectrogram of acceleration obtained on object without additional mass without dampers (*left* figure) and with dampers (*right* figure)—bearing no. 2

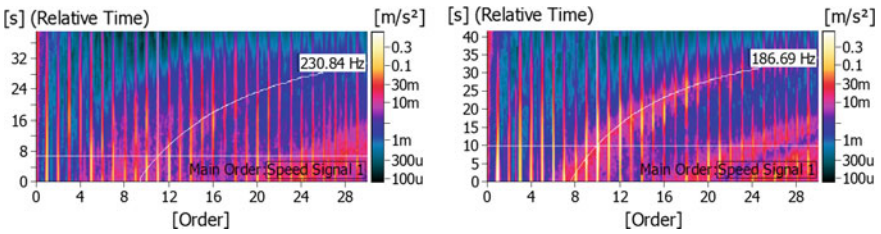

Fig. 7 Comparison of order spectrum of acceleration obtained on object without additional mass without dampers (*left* figure) and with dampers (*right* figure)—bearing no. 2

Calculated resonant frequency of a part of rotor system located between the bearings is 282 Hz. It was not possible to calculate the exactly resonant frequency of all rotor system due to the fact that authors has not exact technical data of electrical engine. On the other hand it was not necessary because it is clearly visible on vibration characteristic presented above. Estimated resonant frequency of rotor system without any additional mass and extra dampers as presented in Table 1 is 230 Hz. Analyzing the results of researches it is evident that use of damping washers change the vibration characteristic of rotor system. First resonant frequency of rotor system has decrease with frequency and amplitude. More over range of resonance had became more narrow. On the other hand at frequency around 400 Hz new resonance has occurred. It also visible that in domain of orders it is easier to find a resonance than in frequency domain.

Next step of researches was calculation of damping factor of damping elements used during measurements. To do this it was necessary to weight the rotor system and Vibrochoc unit.

$$\text{Rotor system weight:} \quad M_{RS} = 11.130\,kg$$

$$\text{Double Vibrochoc unit weight:} \quad M_{Vibro} = 1.288\,kg$$

Table 1 Results of vibration analysis

	Bearing 1		Bearing 2		Δf (Hz)
	Frequency (Hz)	Amplitude ($mm/s^{2)}$	Frequency (Hz)	Amplitude (mm/s^2)	
Without additional mass and without dampers	230	172	230	112	43
Without additional mass and with dampers	187	86	187	95	
With additional mass and without dampers	233	180	233	168	57
With additional mass and with dampers	196	67	196	77	

Table 2 Deflection of damping elements related to loaded mass

x (m)	m (kg)
0.00494	0
0.00488	1.344
0.00481	1.773
0.00470	2.467
0.00466	2.801
0.00462	3.137
0.00455	3.543
0.00444	4.001
0.00437	4.546
0.00423	5.14
0.00415	5.81
0.00408	6.741
0.00401	7.533
0.00400	8.842
0.00398	12.232

Next a series of various mass was placed on double Vibrochoc unit and its displacement was measured. Table 2 presents measurements on Vibrochoc unit.

Further results calculated from the measured values using formulas for:

$$\bullet \text{ displacement} \quad \Delta x_i = |x_i - x_{i+1}| \tag{1}$$

where index is number of next measurements $i = 1, 2, 3 \ldots 12$, number of conducted measurements was 13.

$$\bullet \text{ static force:} \quad F_i = m_i \cdot g, \tag{2}$$

where g is gravitational acceleration equal: $g = 9,81 \frac{m}{s^2}$

$$\bullet \text{ spring constant:} \quad k_i = \frac{F_i}{\Delta x_i} \tag{3}$$

Finally with calculated values it was possible to create spring characteristic chart—Fig. 8.

To calculate damping factor of Vibrochoc which is combination of spring and damping elements it is necessary to conduct some equation transformation. The resonant frequency of rotor system without damping is described by the Eq. (4):

$$f_k = \frac{\sqrt{\frac{k}{m}}}{2\pi} \tag{4}$$

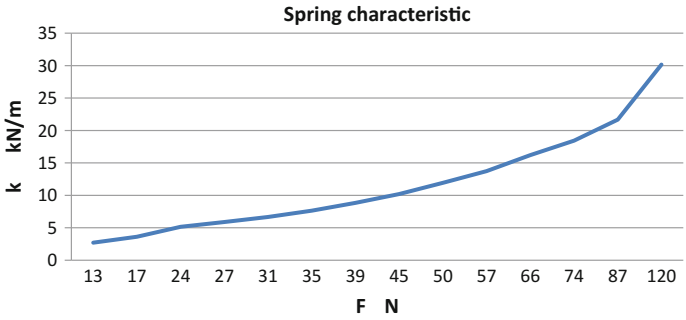

Fig. 8 Vibrochoc damping module characteristic

where: f_k—the resonant frequency of the stiffness, without damping, k—stiffness, m—mass.

If the resonant frequency of system with stiffness and damping f_{kc} is (5)

$$f_{kc} = \frac{\omega_n \sqrt{1 - \frac{c^2}{4m^2\omega_n^2}}}{2\pi} \tag{5}$$

where: $\omega_n = 2\pi f_k$—natural frequency (without damping), c—damping factor then it could be written:

$$\Delta f = f_k - f_{kc} = \frac{\sqrt{\frac{k}{m}}}{2\pi} - \frac{\omega_n \sqrt{1 - \frac{c^2}{4m^2\omega_n^2}}}{2\pi} = \sqrt{\frac{k}{m}} - \omega_n \sqrt{1 - \frac{c^2}{4m^2\omega_n^2}} = \sqrt{\frac{k}{m}} - \sqrt{\omega_n^2 - \frac{c^2}{4m^2}} \tag{6}$$

where: Δf—the frequency difference

Comparing the equation parties were obtained:

$$\omega_n^2 - \frac{c^2}{4m^2} > 0 \Leftrightarrow 4m^2\omega_n^2 - c^2 > 0 \tag{7}$$

$$\sqrt{\omega_n^2 - \frac{c^2}{4m^2}} = \sqrt{\frac{k}{m}} - \Delta f \Leftrightarrow \omega_n^2 - \frac{c^2}{4m^2} = \frac{k}{m} - 2\sqrt{\frac{k}{m}}\Delta f - (\Delta f)^2 \tag{8}$$

Thus:

$$c^2 = 4m^2\omega_n^2 - 4mk + 8\Delta f\sqrt{k} - 4m^2(\Delta f)^2 \tag{9}$$

$$c = \sqrt{4m^2 2\pi f_k^2 - 4mk + 8\Delta f\sqrt{k} + 4m^2(\Delta f)^2} \tag{10}$$

After substitution of data into Eq. (10) a results of damping in case of rotor without additional unbalance was calculated $c = 704.4$ kg/s, and in case when on rotor had been attached with additional mass $m = 0.013$ kg. When rotor system was unbalanced calculated value of damping factor is $c = 502.4$ kg/s.

5 Conclusion

The presented results of researches show a significant influence of damping to the resonance of rotor system. That influence is connected both with frequency of resonance as well as the maximum amplitude. It should be emphasized that this is the changing of the parameters of resonance of the entire system by introducing additional damping. The resonant frequency of the rotor remains unchanged, however, recorded resonance throughout whole system differs considerably. It is also proven the usefulness of tracking orders in determining the resonance frequencies. The presented algorithm calculations and measurements can be used in engine compartments of marine vessels. A significant number of adjacent rotating machines often causes local resonances in the ship's power plant. Applications up the proper damping pads may be one of the effective ways of detuning working devices in the engine compartment and solve the problem of resonance.

References

Journal Article

1. Randall, R. B., Coats, M. D., & Smith, W. A. (2016). Repressing the effects of variable speed harmonic orders in operational modal analysis. *Mechanical Systems and Signal Processing, 79,* 3–15. doi:10.1016/j.ymssp.2016.02.042.
2. Grządziela, A., Kluczyk, M. (2013). An application of order tracking procedure for diagnosis technical state of rotor system in shut-down process. *Journal of KONES Powertrain and Transport* 20(1).
3. Korbiel, T. (2007). Analiza rzędów w diagnostyce niestacjonarnych procesów wibroakustycznych. *Diagnostyka*, 3(43).
4. Grządziela, A. (1999). Vibroacoustic method of shafting coaxiality assessment of COGAG propulsion system of a vessel. *Polish Maritime Researches*, 3, 29–30.
5. Grządziela, A. (2004). Vibration analysis of unbalancing of marine gas turbines rotors. *Mechanika* 23(2), 187–194.
6. Pedersen, T. F., Gade, S., Harlufsen, H., Konstantin-Hansen, H. (2006). Order tracking in vibro-acoustic measurements: A novel approach eliminating the tacho probe. *Technical Review*, 1, 15–28, Brüel & Kjær.

Book

7. Randall, R. B. (2011). *Vibration-based condition monitoring*. A John Wiley and Sons Ltd: Publication.
8. Krzyworzeka, P., Adamczyk, J., Cioch, W., & Jamro, E. (2007). *Monitoring of nonstationary states informatation machinery*. Wydawnictwo ITeE: Biblioteka Problemów Eksploatacji.
9. Żółtowski, B. (1996). Podstawy diagnostyki maszyn, Bydgoszcz.

Knife Diagnostics with Clustering Techniques and Support Vector Machines

Achraf Lahrache, Marco Cocconcelli and Riccardo Rubini

Abstract This paper is about analysis of experimental data, verifying the applicability of signal analysis techniques for condition monitoring of a packaging machine. In particular, the activity focuses on the cutting process that divides a continuous flow of packaging paper into single packages. The cutting process is made by a steel knife driven by a hydraulic system. Actually the knives are frequently substituted, causing frequent stops of the machine and consequent lost production costs. The aim of this paper is developing a diagnostic procedure to assess the wear condition of the blades, reducing the stops for maintenance. The packaging machine was sensorized with pressure sensor that monitors the hydraulic system driving the blade. Processing of the pressure data comprises three main steps: the selection of scalar quantities that could be indicative of the health state of the knife. A clustering analysis to setup a threshold between healthy and faulted knives. Finally, a Support Vector Machine (SVM) model to classify the health state of knife during its lifetime.

Keywords Knife diagnostics · K-means · Features selection · Support vector machines

1 Introduction

Diagnostics is an important activity which is increasing its worth in industrial strategy planning. The supposed possibility of monitoring the health status of a complete although complex manufacturing line, would enable the reduction of manufacturing costs. In fact diagnostics allows to plan the replacement of specific machinery's components to avoid sudden and unexpected downtime. It can suggest replacement of the parts only if the component is really damaged, decreasing the maintenance costs [1, 2]. There are three main maintenance strategies in litera-

A. Lahrache · M. Cocconcelli (✉) · R. Rubini
Department of Sciences and Methods of Engineering, University of Modena and Reggio Emilia, Modena, Italy
e-mail: marco.cocconcelli@unimore.it

A. Timofiejczuk et al. (eds.), *Advances in Condition Monitoring of Machinery in Non-Stationary Operations*, Applied Condition Monitoring 9,
https://doi.org/10.1007/978-3-319-61927-9_8

ture [3]: the run-to-break, the time-based preventive maintenance and the condition-based maintenance (CBM). In the first strategy the machines run until they broke down and it is suggested only when components are not critical and could be replaced easily and cheaply. The preventive maintenance is done at regular intervals which are shorter than the expected time between failures. Most industries use this strategy to avoid production downtime. The CBM is the most challenging, since it predicts the failure of the component through regular condition monitoring of specific parameters. Among the others, vibration analysis is probably the most used technique for obtaining information about internal conditions of the machine [3], as proved by the huge literature available [4]. Unfortunately the use of vibration signal is not always possible and the CBM must take into account other type of input sensors. The lack of a specific literature can be overcome by the use of more general methodologies [5], e.g. expert systems or clustering techniques. In this paper those methodologies are applied to the diagnostics of a specific component in a packaging machine. Among several functions, the focus of the paper is on the cutting process that divides a continuous flow of packaging paper into single packages. The cutting process is made by a steel blade driven by a hydraulic system, in particular two small cylinders pull the knife outside its frame, allowing the cut of the package. At the end of the cut the pressure is dropped and the knife goes back in its frame thanks to a spring placed on the bottom part of the knife. The cutting process is driven by a PLC without any kind of closed loop control. This working condition requires a sharp blade, otherwise it will cause a rip of the paper instead of clear cut. The packaging machine was sensorized with pressure sensor that monitors the hydraulic system driving the blade. The paper is structured as follows: Sect. 2 briefly describes the expected pressure signal in the working conditions. Section 3 details the scalar parameters describing the working conditions of the knives. Sections 4 and 5 describe and show results of the proposed methodology. Conclusions close the paper.

2 Experimental Setup

A pressure sensor has been chosen and inserted in the hydraulic system that drives the knife. The setup is free from moving cables and could be mounted on the machine without drawbacks on the working conditions. The data acquisition is done with a PCB pressure sensor. Preview tests have been done to assess the differences in the pressure signal with or without the presence of the paper material. Results are shown in Fig. 1, but without the y-axis values due to an NDA with the customer.

As shown in Fig. 1 we can divide the knife's cycle in four parts:

1. **No Pressure** [0–12 ms]: The valve is just opened and the pressure is near to 0 bar, because the oil from the pump has not reached any obstacle yet.
2. **Over-Pressure** [12–37 ms]: For both signals (with and without paper) the pressure starts to increase due to a resistance in the hydraulic circuit. Is important to

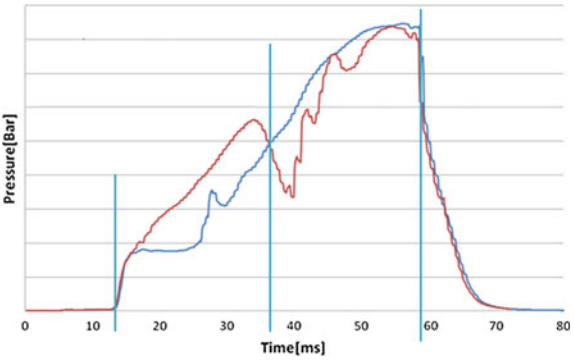

Fig. 1 Pressure signal difference: with paper (*red*) and without paper (*blue*)

see that in this step the two signals are different. In fact the presence of paper increases the pressure higher than the case without it.

3. **Under-Pressure** [37–60 ms]: The brake of paper seems to reduce the pressure signal to a lower value than the case without it. Probably there is a return of elastic energy due to the first deformation of the paper.
4. **Final pressure** [60–80 ms]: In this last step both signals are equal, because pressure values are only defined by the spring action that is the same for both cases.

The effect of paper is shown by the oscillation of pressure signal at the middle of the cycle, so the step 2 and 3 can be a good reference to monitoring the knives' damage.

Typical pressure signal is characterized by:

- sampling frequency ($Fs = 20$ kHz),
- acquisition time ($T = 0.13$ s),
- number of samples ($N = 2600$ points).

The acquisition system starts to acquire when the PLC sends an acknowledge to the valve and stops acquiring after a 0.13 s.

According to the maintenance policy the customer company has to keep an historical list of all the technical operations, like the substitution of a faulted knife. The list reports the code of the repaired machine, the date of substitution, the name of the customer, the number of knives replaced and the total running hours of the machine. The list allows identifying complete lives of the knives, and separating the corresponding data from the historical. It must be noted that an operator updates the list manually. It cannot be excluded that rarely some knives changes are not logged. Moreover the choice of the replacing time is based on the opinion of the single technician only, who looks at the production, by visual inspection, and decides that the knives are damaged and have to be replaced. Finally both knives are often replaced at the same time to avoid a second stop of the production to substitute the other knife. So a complete life of the knife does not means a complete useful life of the knife, which can be replaced even if it is still working well.

3 Data Analysis

Since no previous analysis was available, the choice of the physical parameters for data analysis is arbitrary, either in the type or in the number. In a preliminary stage several parameters could be suggested. Afterwards the number of these parameters will be reduced, according to some rules that will be defined later in the paper. The choice of preliminary dataset is done on two different domains: time domain and frequency domain.

3.1 Time Domain Parameters

The pressure signal in Fig. 1 has been originally described with 16 scalar parameters, such as the maxima, the kurtosis values, the main percentiles, etc. A preliminary analysis has been done by means of the Pearson product-moment correlation coefficients [6], as a measure of the degree of linear dependence between two variables. Parameters with high Pearson coefficient has been removed since the information carried was linearly dependent. Just two parameters have been considered at last:

1. The third quartile of all sampled points (***Q3***), whose trend over time is shown in Fig. 2.
2. The time interval between the start of acquisition and the maxima of the derivative of pressure signal when it is going to achieve the maximum (***It_der_max***). The trend is shown in Fig. 3.

Another data processing technique used is the Empirical Mode Decomposition (EMD). It is a procedure to decompose a signal into a series of components with specific characteristics. The mathematical background could be found in [7]. These components are called Intrinsic Mode Functions (IMFs). The sum of all these

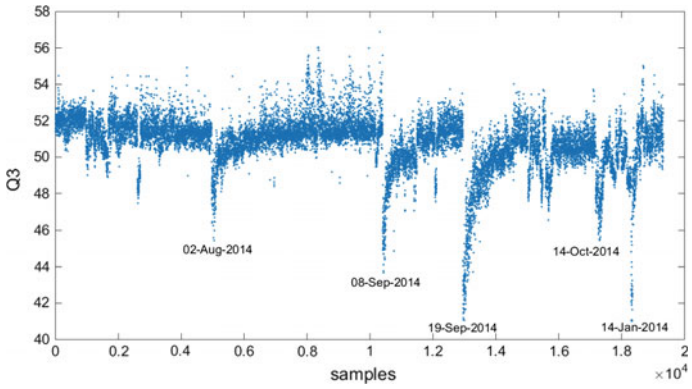

Fig. 2 Trend of the third quartile ($Q3$) over time

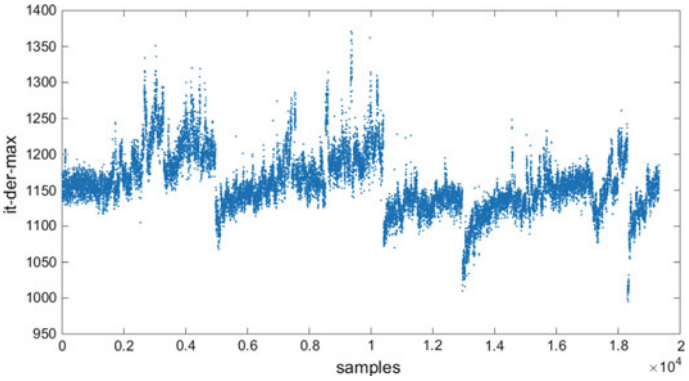

Fig. 3 Trend of the It_der_max parameter over time

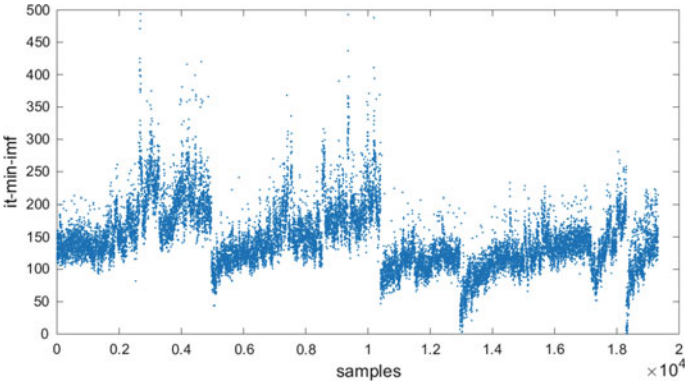

Fig. 4 Trend of the It_min_imf over time

components is equal to the original signal, i.e. it works in time-domain as a decomposition. It was developed to study non-stationary signals and the extracted components have a frequency content decreasing from the first one to the last [8]. Since we are interested into high frequency components rather than lower ones, the first two IMF are considered and added together. The main pro of the EMD is that resulting IMFs have a zero mean value that makes the identification of the local minima/maxima easier. In particular the phase of the second minima, labeled ***It_min_imf***, has been taken as third parameter in time domain. The trend of the It_min_imf over time is shown in Fig. 4.

3.2 *Frequency Domain Parameters*

Since the cutting process induces hammer's effects in the oil pressure, with visible harmonics, the choice of some physical parameters from the frequency domain seems promising. All the spectra of the available signals have been taken into account in the preliminary study. Subsequently the spectra components were reduced to the first 20 harmonics of cyclic frequency, i.e. the frequency of the cutting process. Finally the comparison of the trend of the amplitudes of these harmonics, with reference to different lives of the knife, leads to identify just 4 components:

1. ***A3***: amplitude of the 3rd spectrum component,
2. ***A4***: amplitude of the 4th spectrum component,
3. ***A5***: amplitude of the 5th spectrum component,
4. ***A6***: amplitude of the 6th spectrum component.

Fig. 5 shows the trend of the amplitude harmonics.

A list of dates of the knives' replacement was available. The trend of the physical parameters over time was compared with that list, in order to assess the sensitivity of the parameters. An example is given in Fig. 2, where the dates of knives' replacement overlay the signal. Figures 2, 3, 4 and 5 show the trend of the third quartile, the It_der_max parameter, the It_min_imf parameter, and the third to sixth harmonics respectively. The trend of these parameters clearly highlights discontinuity corresponding to a precise time instant (the replacement of the knife). The trend

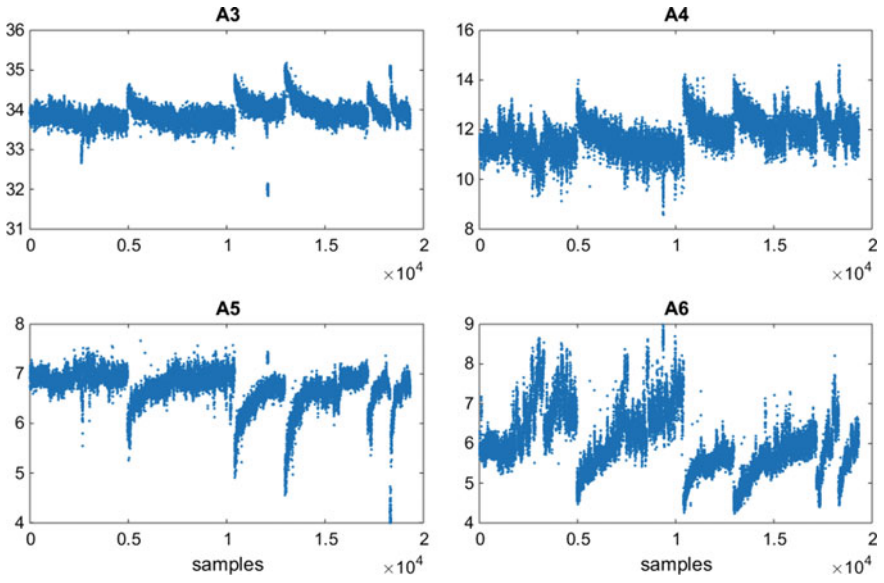

Fig. 5 Trend of the amplitude of the third to sixth harmonics

could be different, e.g. the $A3$ parameter has a higher value after the replacement that decreases during the lifetime of the knives, while the $A5$ parameter has an opposite behavior. It must be noticed that the behavior of the parameters is not relevant by itself, the key point is that the trend must have a discontinuity before and after the replacement, since it means the parameter is sensitive to the health state of the knife. Indeed the logarithmic behavior of all the data in Figs. 2, 3, 4 and 5 makes difficult to assess the deterioration of the knife over time, since the trend tends to be flat as the wear increases. An ideal behavior would be the exponential one, increasing the output value over time, but unfortunately none of the tested parameters exhibited that trend.

4 Clustering Analysis

Clustering analysis orders a set of data in terms of similarity among the elements of the dataset. A vector of seven components, the physical parameters identified in the previous section, substitutes each element of the dataset. Clustering analysis should highlight if the ensemble of the chosen parameters changes according to the life of the knife. The data available for this analysis has divided into four dataset, covering from July 2014 to February 2015. Each dataset refers to a specific knife available: two packaging machines mounting two knives each. The resulting complete lives collected are 16. A complete life is given by the data when the technical engineer substituted the knife in the ordinary maintenance.

The clustering analysis has been done by means of K-means algorithm. The K-means algorithm distributes the data in K clusters, minimizing the variance inside each cluster. This algorithm needs as input the number of clusters (N), the metrics to measure the similarity among data elements (*Distance*), the input matrix (X) each column lists the dataset for all the observations. The output of the cluster has two elements: the cluster's number for each observation (*Idx*), i.e. the labeling of data into a specific cluster; a vector giving an information (a number between -1 and +1) about the quality of the clustering for each data (*Silhouette*) [9].

The standard Euclidean distance is used as metrics and the number of clusters is chosen to be 10 ($N = 10$). Result for one of the chosen input parameters (*It_der_max*) is shown in Fig. 6. The ten colors gradually change one each other from the beginning of the life (left part of the figure) to the end (right part of the picture). The clustering could recognize the health status of the knife and could assign a proper label to it. In particular the clusters bounded with a new/good knife is in red color, while the cluster bounded to old knife is in green (cluster 1), yellow and violet (clusters 8–10). The x points are the centroids of each cluster. It seems that the progression of the wear of the knives is fast at the beginning and then decreases. This behavior is in accordance with the trends of physical parameters (logarithmic trend).

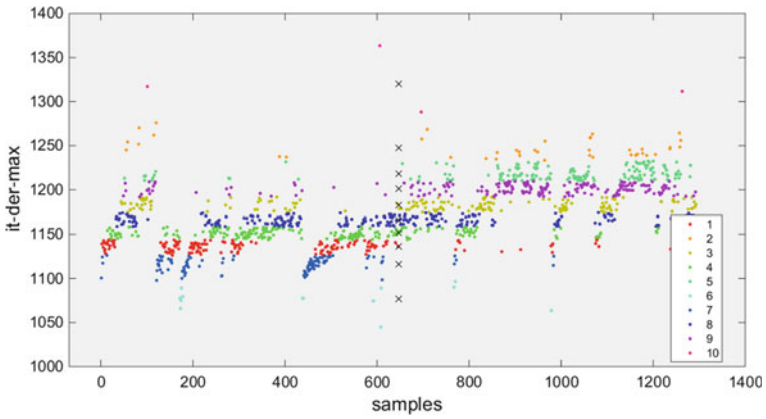

Fig. 6 K-means clustering of the *It_der_max* values with N = 10

5 Classification by SVM

The Support Vector Machines (SVM) belong to the algorithms of machine learning. In particular they are a class of supervised algorithms, which means it requires a training step where both healthy and faulty cases are needed. Supervised machine learning tools are very useful when a lot of historical data are available for training, and a physical and detailed model of the system is not necessary. In this paper the aim of SVM is to assess the faulted state of the knife. Among the 16 lives of knives available for the training and test, 11 lives are used in the training part, the remaining 5 lives in the test. Support vector machines try to define a separation plane (or hyper-plane) between two groups. The exact dimension of this plane depends on the dimension of the input array [10]. As described in the previous sections, the array used is made of 7 scalar values, i.e. the separation surface becomes a 7 dimension hyper-plane. Support vector machines are able to separate two groups at a time, while the clustering technique classified data into 10 different clusters in the previous section. As a consequence, data reduction is necessary before using the SVM, and could be done using the results of clustering algorithms.

In particular the ten clusters resulting from the previous step are divided into two classes only: the first 6 clusters are labeled as healthy, while the remaining 4 are labeled as faulted. The initial clustering into 10 clusters gives to the customer a degree of freedom more, that is the possibility to move the threshold according to experimental results. Figure 6 shows the classification of the data before this clustering reduction, while Fig. 7 shows the final classification into two classes only for one of the input parameter (*It_der_max*).

Finally Fig. 8 compares the classification of the SVM for test data with the classification provided by the K-means clustering. The percentage of success for the SVM is equal to 99.34%. It must be noted that test data are not taken into account during the training phase.

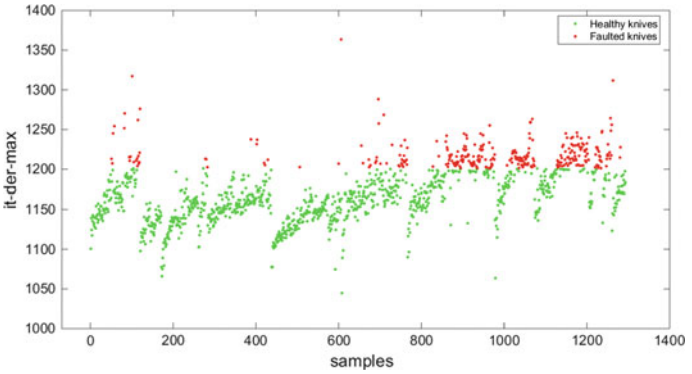

Fig. 7 Classification between health and faulted knives

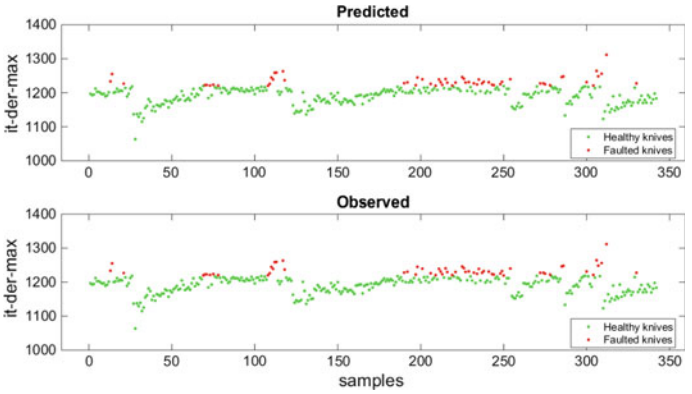

Fig. 8 Difference between predicted observation and pre-elaborated with k-means

6 Conclusions

This paper details a condition monitoring procedure to assess the health status of a cutting blade. The knife is driven by a hydraulic circuit whose pressure is measured by an acquisition system. The methodology involves the use of both clustering and Support Vector Machines. Pre-processing of the data is necessary to reduce the number of scalar quantities used to describe the status of the system. In particular the Pearson product-moment correlation coefficient is used to measure of the degree of linear dependence between two variables. The clustering of the remaining quantities allows to identify the most significant thresholds to recognize a class from another. Finally The availability of acquired data makes advisable to use supervised expert systems like SVM to classify the incoming signal. A rate of 99% of success in the testing makes the proposed methodology promising.

References

1. Jardine, A. K. S., Lin, D., & Banjevic, D. (2006). Review on machinery diagnostics and prognostics implementing condition-based maintenance. *Mechanical Systems and Signal Processing*, *20*(7), 1483–1510.
2. O'Connor, P. D. T., & Kleyner, A. (2012). *Practical reliability engineering*, Wiley.
3. Randall, R. B. (2011). *Vibration-based condition monitoring*, Wiley.
4. Lee, J., Wu, F., Zhao, W., Ghaffari, M., Liao, L., Siegel, D. (2014). Prognostics and health management design for rotary machinery systems—reviews, methodology and applications, *Mechanical Systems and Signal Processing*, *42*(1–2), 314–334.
5. Worden, K., Staszewski, W. J., & Hensman, J. J. (2011). Natural computing for mechanical systems research: A tutorial overview. *Mechanical Systems and Signal Processing*, *25*(1), 4–111.
6. Wilcox, R. R. (2005). *Introduction to robust estimation and hypothesis testing*. Academic Press.
7. Huang, N. E., Shen, Z., Long, S. R., Wu, M. L., Shih, H. H., Zheng, Q., et al. (1998). The empirical mode decomposition and Hilbert spectrum for nonlinear and non- stationary time series analysis. *In Proceedings of the Royal Society of London A*, (Vol. 454, pp. 903–995).
8. Rilling, G., Flandrin, P., & Gonçalves, P. (2003). On empirical mode decomposition and its algorithms. In *Proceedings of IEEE EURASIP Workshop on Nonlinear Signal and Image Processing, Jun 2003*. Grado, Italy.
9. Rousseeuw, P. J. (1987). Silhouettes: A graphical aid to the interpretation and validation of cluster analysis. *Computational and Applied Mathematics*, *20*, 53–65.
10. Cortes, C., & Vapnik, V. (1995). Support-vector networks. *Machine Learning*, *20*(3), 273–297.

Stable Distributions and Fractal Diagnostic Models of Vibration Signals of Rotating Systems

Andrzej Puchalski and Iwona Komorska

Abstract The main objective of the presented work is improving the knowledge of non-linear effects in vibrodiagnostics of rotating machinery components using multifractal analysis. The modeling is based on the data-driven approach, in which probabilistic models can be constructed to capture the structure of the time series. These models allow the identification of deviations from the training data during the monitoring of the system. The paper proposes the feature vector, being the data-driven empirical diagnostic model, of mechanical vibrations in the vehicle powertrain. Dynamic analysis of wearing and/or defects of complex rotating systems confirms the presence of non-linear, non-stationary and multiscale properties. The recorded time series exhibits the impulse-like nature and fluctuations. Probability distributions often deviate from the Gaussian distribution and exhibit heavy tails. Both broad density functions, typical for stable distributions, and long-term correlations are two important sources of multifractality. Analyses of fluctuations of the recorded vibration time series were carried out utilising the dependence between selected parameters of alpha-stable distributions and measures of singularity spectra.

Keywords Vibrodiagnostics · Multifractality · Stable distributions · Vehicle gearbox · Data-driven approach

1 Introduction

Linear stochastic models of Gaussian processes for decades were the dominant paradigm in the time series analysis, in particular for the model based vibrodiagnostics. Mostly conventional methods from the time-frequency domain such as the

A. Puchalski (✉) · I. Komorska
University of Technology and Humanities in Radom, Radom, Poland
e-mail: andrzej.puchalski@uthrad.pl

I. Komorska
e-mail: iwona.komorska@uthrad.pl

A. Timofiejczuk et al. (eds.), *Advances in Condition Monitoring of Machinery in Non-Stationary Operations*, Applied Condition Monitoring 9,
https://doi.org/10.1007/978-3-319-61927-9_9

short-term Fourier transform, Wigner–Ville distribution, wavelet transform, envelope analysis were applied in procedures of feature selection of signals, for which an assumption of stationary operating conditions cannot be made. The automatic control and diagnostics of more and more complex systems, consisting of many non-linearly interacting components which cannot be split into simpler ones without tampering with the dynamical properties, requires precise non-linear models [2, 3, 10, 13].

Data-driven approach is a useful method, in which a probabilistic model can be constructed to capture the structure of the time series. These models allow the identification of deviations from the training data during the monitoring of the system. Many methods based on statistical analysis were developed due to the classic statistical signal processing theory. However, there are several reasons for using alpha-stable distribution (ASD) to describe complex rotating systems. In the Generalized Central Limit Theorem (GCLT) the stable distributions are postulated as the only possible non-trivial limit of distributions of normalized sums of independent and identically distributed random variables [21]. The alpha–stable model was applied in the aerospace gas-turbine engine monitoring [26], bearing fault detection [28], heavy duty gearbox damage detection [29] and wind power forecast [5]. Analysis of the database signals of mechanical vibrations of complex rotating systems confirms the presence of not only non-linear and non-stationary properties but the scaling properties and long-term correlations. The time series fluctuations are often followed by a power law with a fractal dimension, at least asymptotically. Fractal and multifractal scaling behaviour was reported in many time series generated by complex systems. The self-affine time series or time series exhibiting self-affinity after the integration, describe multifractal dimensions D, corresponding to the Hurst exponents H [7]. Methods of the detrended fluctuation analyses (DFA) [22] and its multifractal version (MF-DFA) [9], can be used as means of estimating the Hurst exponent. The MF-DFA allowing investigations of the observed signals with regard to their multifractality, assures more stable approach to the multifractal formalism than the previously applied method of the wavelet transform of maximum module (WTMM) [1]. The ways of vibrodiagnostics of different rotating systems by means of the features vector formed of the vibrations signals fluctuation function were proposed and verified in study [18, 19]. Diagnostic features for modelling health conditions of gearboxes and bearings on the bases of parameters of the multifractal spectrum of vibrations signals were defined in papers [15, 16]. The multifractality of bearings vibration signals was also used in the diagnostic method encompassing a signal decomposition into several intrinsic scale components [17]. Health conditions of the vehicle valve system using statistical vibration measures were examined in [23–25].

Both, broad probability density functions (PDF) for the values of the time series and different long-term correlations of the small and large fluctuations, are two important sources of multifractality [8]. In the method for rolling bearings diagnosis based on feature fusion the advantages of MF-DFA and ASD were applied, to achieve an intelligent monitoring [27]. The problem of modulation recognition of signals in the ASD noise using multifractal spectrum was discussed in [30].

In this paper the authors present the results of time signals analysis of mechanical vibrations in the vehicle powertrain. Selected parameters of stable distributions and measures of singularity spectra in constructing diagnostic models are proposed and verified. In Sect. 2, the alpha-stable distribution and multifractal method theories in data modelling of impulse-like nature and long-term correlated signals and simulation studies are discussed. Section 3 covers the results of time signals investigations of mechanical vibrations in the vehicle powertrain. The conclusions are presented in Sect. 4.

2 Alpha-Stable Distribution and Multifractal Method in Data Modeling. Simulation Study

The recorded time series of complex rotating systems exhibit the impulse-like nature and fluctuations. Probability distributions often deviate from the Gaussian distribution and exhibit heavy tails. ASD family received interest due to its success in modelling data, which are too impulsive to accept the normal distribution. The lack of closed formulas for densities and distribution functions for all but a few stable distributions Gaussian, Cauchy and Levy were a major problem in using stable distributions in technical diagnostics. There are now reliable computer programs to compute stable densities, distribution functions and parameters [20]. With these programs, it is possible to apply stable models in a variety of practical problems. The alpha-stable distribution is described by its characteristic function:

$$\varphi(t) = exp\{j\delta t - \gamma|t|^{\alpha}[1 + j\beta sign(t)\omega(t,\alpha)]\} \tag{1}$$

where

$$\omega(t,\alpha) = \begin{cases} -tan\frac{\alpha\pi}{2} & if\ \alpha \neq 1 \\ \frac{2}{\pi}log|t| & if\ \alpha = 1 \end{cases} \tag{2}$$

Data modeling using stable distributions require four parameters to their full description. These parameters are as follows:

- stability index alpha $\alpha \in (0, 2]$;
- a skewness parameter $\beta \in [-1, 1]$;
- a scale parameter $\gamma > 0$;
- a location parameter $\delta \in R$

Index α describes impulsive character of distribution and thickness of distribution tail. For $\alpha = 2; 1$ and $0,5$ the Gaussian; Cauchy and Levy distributions can be modeled, respectively. For $\alpha < 2$ the decay distribution follows a power-laws. Skewness parameter $\beta = 0$ implies that the distribution is symmetric. Negative or positive β implies that the distribution is skewed to the left or to the right

respectively. The parameters γ and δ are similar to the variance and the mean of a normal distribution. Time series of simulated alpha-stable signals are shown in Fig. 1. Figure 2 shows effect of a stability index on stable distribution.

The relationship between the parameters of stable distributions and the multifractal spectra indicates the possibility of using both methods in modelling the diagnostic signals of complex rotating systems.

Due to a relatively simple way, suitable for the numerical implementation, the results presented in the paper are based on the box dimension [6, 14]. As the box fractal dimension D of the time series the curve dimension—being the diagram of the considered signal—was assumed. When L is a minimal number of sets coinciding with the given time series and s is the scale, then $L \approx 1/s^D$. The time series multifractal dimensions D, corresponds to the Hurst exponents H, according to the dependency: $D = 2 - H$. To determine the Hurst exponent of the recorded data the MF-DFA method was used. The procedure based on the elimination of the trend of the tested time series was performed, leading to the power-law relation of the fluctuation function $F_q(s)$:

$$F_q(s) = \left\{ \frac{1}{2N_s} \sum_{i=1}^{2N_s} \left[F^2(s,v) \right]^{\frac{q}{2}} \right\}^{\frac{1}{q}} \sim s^{H(q)} \tag{3}$$

where $H(q)$ is generalised Hurst exponent of the order equal to q.

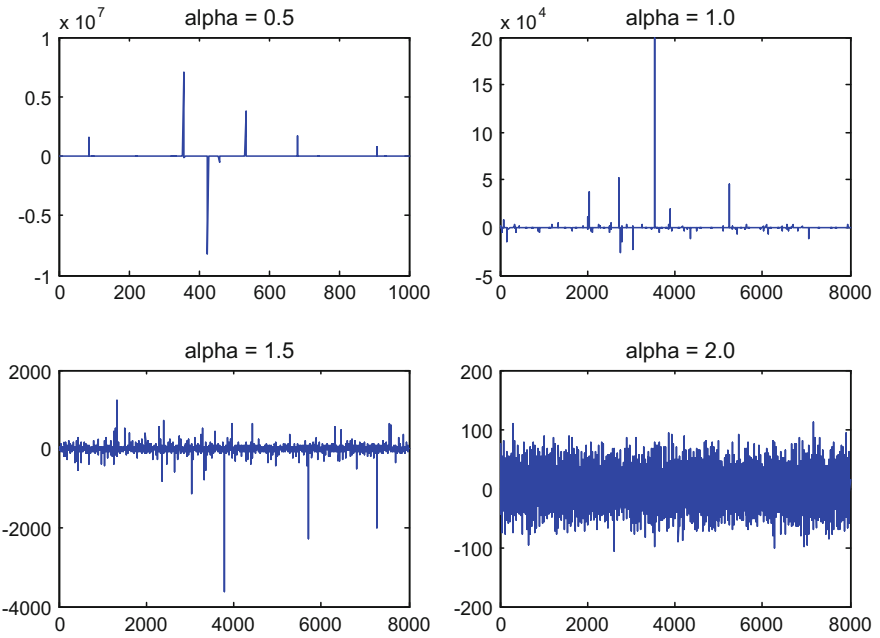

Fig. 1 Time series of simulated alpha-stable signals: alpha, beta = 0, gamma = 20, delta = 0

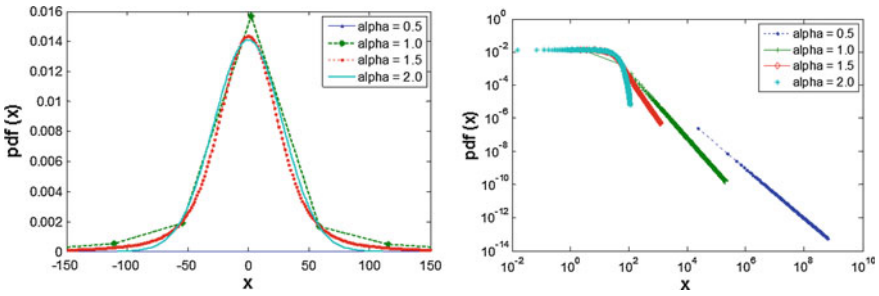

Fig. 2 PDF and *right* tail PDF of simulated alpha-stable signals

Fig. 3 Multifractal spectra of simulated alpha-stable signals

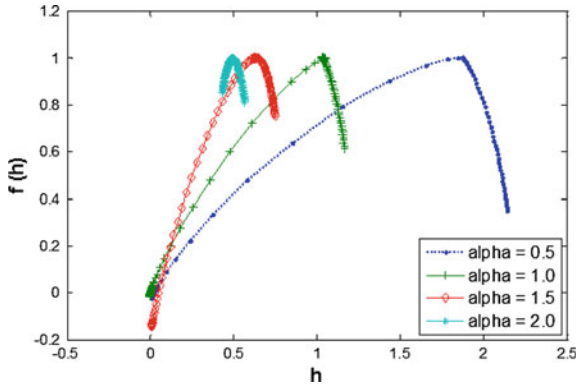

The exponent $H(q)$ is a decreasing function. For negative values of the q order, the generalised Hurst exponent describes scaling properties in segments of a low fluctuation level, while when the positive values of the q order are considered, segments of high variances are shaping the fluctuation function. Knowledge of the generalised Hurst exponent allows to determine the multiscaling exponent $\tau(q) = qH(q) - 1$ of local scaling, represented by the singularity (Hölder) exponent $h = \frac{d}{dq}\tau(q)$ and singularity spectra $f(h)$, related to the multiscaling exponent via the Legendre transform:

$$f(h) = qh - \tau(q) \tag{4}$$

Spectra of the simulated alpha-stable, symmetric time series shown in Fig. 3, can be treated as multifractal dimensions $f(h)$ related to singularities h representing local scaling in various places of the time series. The following values are used as parameters of the experimental diagnostic model:

- multifractality level, representing heterogeneity of the observed signal, $\Delta = h_{max} - h_{min}$, where h_{max} and h_{min} are singularities corresponding to the maximum and the minimum fluctuation of the observed signal, respectively;

- dimensions span of the singularities subsets $\Delta f = f(h_{max}) - f(h_{min})$;
- singularity of the maximum dimension, i.e. the most often met the time series singularity $\{h_0 : f(h_0) = \max f(h)\}$.

3 Case Study of Time Signals of Mechanical Vibrations in the Vehicle Powertrain

Signals of accelerations of mechanical vibrations originated from the monitoring of the vehicle powertrain were recorded during investigations [11, 12]. Successive measurements performed in equal time intervals, during road tests of the vehicle with S.I. engine 1.4 l represented values in the experimental data set. Experiments generated, after the angular resampling, time series consisting of 20 rotations of the crank shaft. Each time series of vibrations accelerations during 1 work cycle of the engine contained 3600 signal samples in the determined for the test work conditions. Apart from the signal of the acceleration of vertical vibrations of the main gearbox housing, voltage from the sensor of the crankshaft position and voltage from the sensor of the throttle position were also recorded. Accelerations of vibration signals of the powertrain were processed by means of the Bruel and Kjaer sensors type IEPE No. 4514. Signals were recorded by means of the portable data recording device, Bruel and Kjaer PULSE type 3560E with the sampling frequency of 65,536 Hz.

Tests were performed for no-fault and fault states of the gearbox. The analysis presented in the paper include several maintenance states: the gearbox in good condition—G1, the gearbox with a casual teeth wear—G2, the gearbox just before a failure—G3 and the gearbox after a repair—G4. Averaged empirical and theoretical probability density functions of gearbox vibration signals and their right tails in the tested maintenance states, are shown in Figs. 4 and 5, respectively.

During the goodness-of fit tests the conformity with the null hypothesis—assuming the normal distribution—was rejected. A divergence of empirical distributions with the normal distribution was increasing along with the fault degree of the gearbox. The verification of matching the alpha-stable model of empirical distributions was performed by means of the Anderson-Darling test at the significance level 0.05, after the preliminary graphical assessment. There are several methods and algorithms of estimating the index and parameters of alpha-stable distributions on the basis of experimental data [4]. The quantile method and the maximum likelihood method were applied in investigations. The results are presented in Table 1.

Successive diagnostic features were obtained due to the transformation of signals from the time domain to the singularity domain. Multifractal spectra in a similar fashion as probability distributions of the tested gearbox signals differ in placements and in shapes (Fig. 6). Defined spectrum parameters are presented in Table 2.

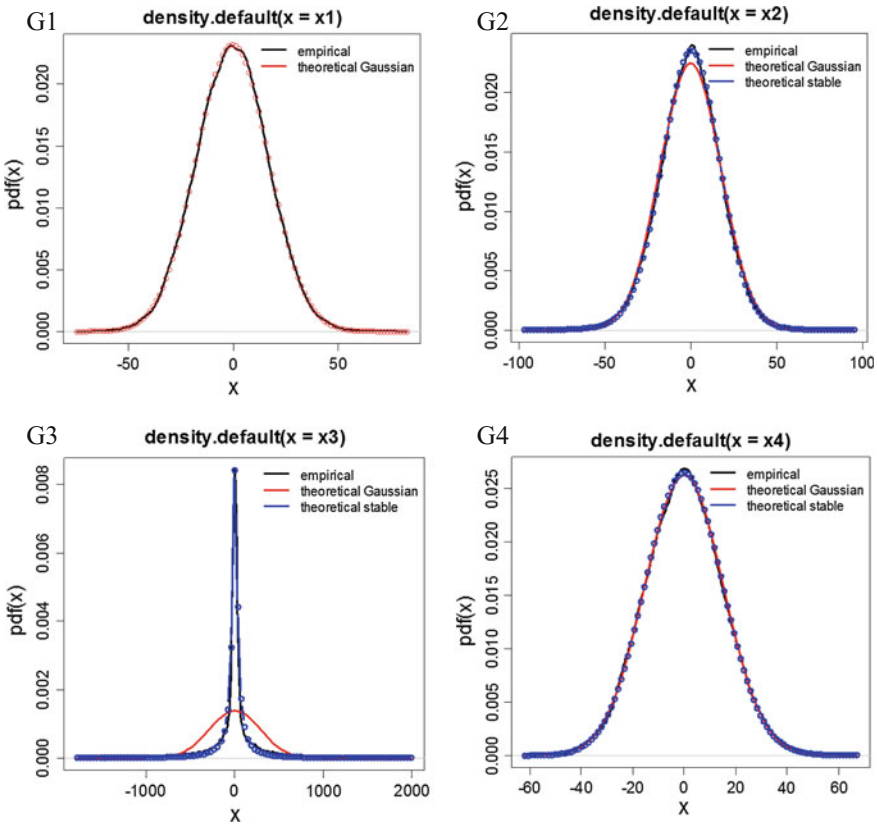

Fig. 4 PDF of gearbox vibration signals in tested maintenance states

Parameters of stable distributions and measures of singularity spectra were chosen as diagnostic features allowing to classify the simulated maintenance states of the tested powertrain.

The reduction of the feature vector dimension was performed by means of the principal components analysis. The classification was carried out by using 3-dimensional index of defects detection of coordinates corresponding to features: stability index—α, scale parameter—γ and multifractality level—Δ. In each maintenance state a series of 100 experiments was performed. Categorising of the tested state to the proper class as well as the classification quality analysis was done by means of the nearest neighbours method. The cross-validation technique was applied for the accuracy assessing. The classification accuracy was assessed on the ratio of the properly classified experimental results to their total number. All tested maintenance states were divided with 100% accuracy of the classification.

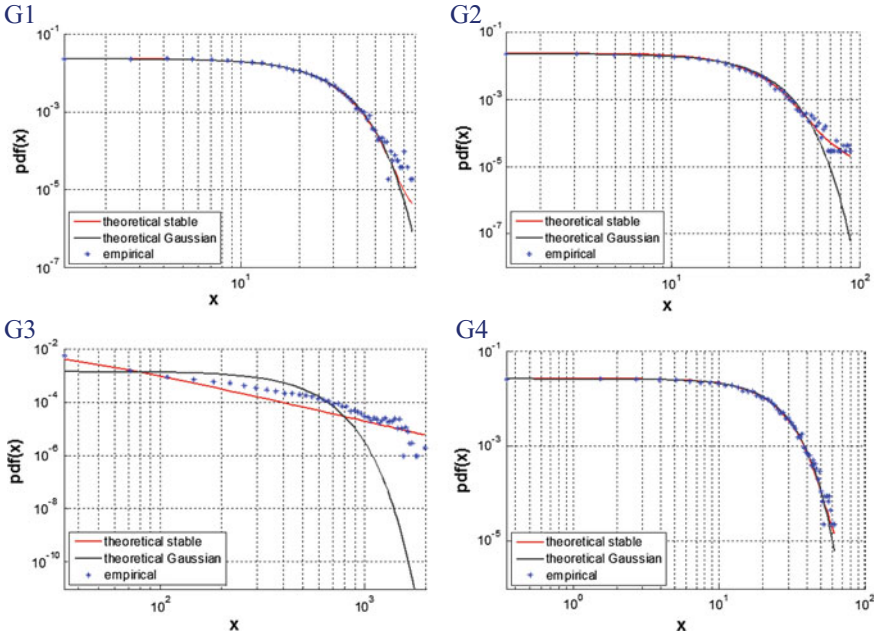

Fig. 5 *Right* tail PDF of gearbox vibration signal in tested maintenance states

Table 1 Averaged parameters of alpha-stable distributions of gearbox vibration signals in tested maintenance states

	Good	Initial wear	Before damage	After repair
α	**1.99129**	**1.90413**	**0.778433**	**1.988468**
β	−0.03625	−0.23442	−0.01019	0.141268
γ	**11.9267**	**11.83018**	**34.76653**	**10.51743**
δ	−0.46014	−0.05146	1.944857	0.041069

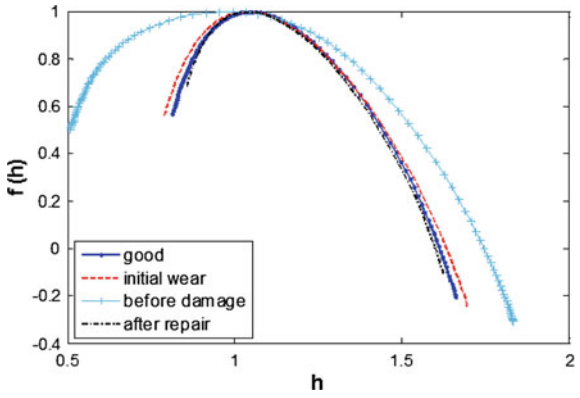

Fig. 6 Singularity spectra of gearbox vibration signals in tested maintenance states

Table 2 Averaged parameters of multifractal spectra of gearbox vibration signals in tested maintenance states

	Good	Initial wear	Before damage	After repair
h_{min}	0.8131	0.7883	0.5091	0.8567
h_{max}	1.66	1.696	1.833	1.625
Δ	**0.8469**	**0.9077**	**1.3239**	**0.7683**
$f(h_{max})$	0.5675	0.5531	0.5012	0.6854
$f(h_{min})$	−0.2023	−0.2431	−0.3078	−0.1079
Δf	0.7698	0.7962	0.809	0.7933
h_0	−0.1835	0.006	0.02005	0.005

4 Conclusion

The diagnostics method of wearing and/or defects of complex rotating systems, based on the stable distribution and fractal model of the signal of mechanical vibrations, is presented in the paper. The study of the vehicle gearbox confirmed non-Gaussian, heavy-tailed character of mechanical vibrations signals in the tested powertrain, during the defect increasing. Utilising the dependence between parameters of alpha-stable distributions and multifractal spectra signals the analysis of fluctuations of the recorded time series was also carried out. The feature vector, being the data-driven empirical diagnostic model, was separated and verified.

The proposed procedure of selection and classification can be realised within the vehicle on-board diagnostic system in the determined operating conditions. The currently continued research is focused on building experimental, non-linear diagnostic models and classification algorithms of the most often occurring mechanical defects in the vehicle powertrains.

References

1. Bashana, A., Bartsch, R., Kantelhardt, J. W., & Havlin, S. (2008). Comparison of detrending methods for fluctuation analysis. *Physica A, 387,* 5080–5090.
2. Batko, W., Dąbrowski, Z., & Kiciński, J. (2008). *Nonlinear effects in technical diagnostics*. Radom: Copyright ITE—PIB.
3. Batko, W., Dąbrowski, Z., Engel, Z., Kiciński, J., & Weyna, S. (2005). *Nowoczesne metody badania procesów wibroakustycznych I*. Radom: Wydawnictwo ITE—PIB.
4. Borak, S., Härdle, W., & Weron, R. (2005). *Stable distributions*. Humboldt-Universität zu Berlin. Retrieved April 29, 2016, from http://prac.im.pwr.edu.pl/~hugo/publ/SFB2005-008_Borak_Haerdle_Weron.pdf.
5. Bruninx, K., Delarue, E., & D'haeseleer, W. (2013). Statistical description of the error on wind power forecasts via a Lévy-stable distribution. *Energy and Environment,* Retrieved May, 2013, from http://www.mech.kuleuven.be/tme/research.
6. Butar, F. B., & Kale, M. (2011). Fractal analysis of time series and distribution properties of Hurst exponent. *Journal of Mathematics and Mathematical Sciences, 6*(1), 8–19.
7. Hurst, H. E. (1951). Long term storage capacity of reservoirs. *Transactions American Society of Civil Engineers, 116,* 770–799.

8. Kantelhardt, I. W. (2011). Fractal and multifractal time series. *Mathematics of Complexity and Dynamical Systems* 463–487.
9. Kantelhardt, J. W., Zschiegner, S. A., Koscielny-Bunde, E., Havlin, S., Bunde, A., & Stanley, H. E. (2002). Multifractal detrended fluctuation analysis of nonstationary time series. *Physica A, 316,* 87–114.
10. Kantz, H., & Schreiber, T. (2004). *Nonlinear time series analysis*. Cambridge: University Press.
11. Komorska, I., & Puchalski, A. (2013). On-board diagnostics of mechanical defects of the vehicle drive system based on the vibration signal reference model. *Journal of Vibroengineering, 15*(1), 450–458.
12. Komorska, I., & Puchalski, A. (2015). On-line diagnosis of mechanical defects of the combustion engine with principal components analysis. *Journal of Vibroengineering, 17*(8), 4279–4288.
13. Korbicz, J., Kościelny, J. M., Kowalczuk, Z., & Cholewa, W. (Eds.). (2004). *Fault diagnosis models, artificial intelligence, applications*. Berlin: Springer.
14. Li, J., Du, Q., & Sun, C. (2009). An improved box-counting method for image fractal dimension estimation. *Pattern Recognition, 42,* 2460–2469.
15. Lin, J., & Chen, Q. (2013). Fault diagnosis of rolling bearings based on multifractal detrended fluctuation analysis and Mahalanobis distance criterion. *Mechanical Systems and Signal Processing, 38,* 515–533.
16. Lin, J., & Chen, Q. (2014). A novel method for feature extraction using crossover characteristics of nonlinear data and its application to fault diagnosis of rotary machinery. *Mechanical Systems and Signal Processing, 48,* 174–187.
17. Liu, H., Wang, X., & Lu, C. (2015). Rolling bearing fault diagnosis based on LCD–TEO and multifractal detrended fluctuation analysis. *Mechanical Systems and Signal Processing, 60–61,* 273–288.
18. Moura, E. P., et al. (2016). Classification of imbalance levels in a scaled wind turbine through detrended fluctuation analysis of vibration signals. *Renewable Energy, 96,* 993–1002.
19. Moura, E. P., Souto, C. R., Silva, A. A., & Irmao, M. A. S. (2011). Evaluation of principal component analysis and neural network performance for bearing fault diagnosis from vibration signal processed by RS and DF analyses. *Mechanical Systems and Signal Processing, 25,* 1765–1772.
20. Nolan, J. P. (2008). Advances in nonlinear signal processing for heavy tailed noise. In *Proceedings of the International Workshop in Applied Probability*. Retrieved May 16, 2016, from http://fs2.american.edu/jpnolan/www/stable/NolanIWAP2008.pdf.
21. Nolan, J. P. (2015). *Stable distributions models for heavy tailed data*. Department of Mathematics and Statistics at American University. Retrieved June 1, 2016, from http://fs2.american.edu/jpnolan/www/stable/chap1.pdf.
22. Peng, C. K., Havlin, S., Stanley, H. E., & Goldberger, A. L. (1995). Quantification of scaling exponents and crossover phenomena in nonstationary heartbeat time series. *Chaos, 5,* 82–87.
23. Puchalski, A. (2015). A technique for the vibration signal analysis in vehicle diagnostics. *Mechanical Systems and Signal Processing, 56–57,* 173–180.
24. Puchalski, A. (2015). Multiscale analysis of vibration signals in engine valve system. *Journal of Vibroengineering, 17*(7), 3586–3593.
25. Puchalski, A., & Komorska, I. (2014). Looking for vibrational measure of vehicle powertrain using multifractal analysis. *Vibroengineering Procedia, 3,* 351–356.
26. Sundaram, S., & McDonald, K. (2010). Stable distributions for heavy-tailed data and their application in asset health monitoring. In *VII International Conference on Condition Monitoring and Machinery Failure Prevention Technologies*. Retrieved April 11, 2016, from http://www.robots.ox.ac.uk/~davidc/pubs/stable_dists.pdf.
27. Xiong, Q., Zhang, W., Lu, T., Mei, G., & Liang, S. (2016). *A fault diagnosis method for rolling bearings based on feature fusion of multifractal detrended fluctuation analysis and alpha stable distribution*. Hindawi Publishing Corporation Shock and Vibration. doi:10.1155/2016/1232893.

28. Yu, G., Li, C., & Zhang, J. (2013). A new statistical modeling and detection method for rolling element bearing faults based on alpha–stable distribution. *Mechanical Systems and Signal Processing, 41,* 155–175.
29. Żak, G., Wyłomańska, A., & Zimroz, R. (2016). Data-driven vibration signal filtering procedure based on the α-stable distribution. *Journal of Vibroengineering, 18*(2), 826–837.
30. Zhao, C., & Yang, W. (2013). Modulation recognition of MFSK signals based on multifractal spectrum. *Wireless Personal Communications, 72,* 1903–1914.

Selection of Suitable Method for Speed Recovery from Vibration Signal

Adam Jabłoński, Kajetan Dziedziech and Ziemowit Dworakowski

Abstract Typically, if order analysis of vibration signal is expected, a speed sensor (phase marker) or an encoder are installed on the shaft. However, in some practical scenarios, the speed information recorded in parallel to the vibration signal acquisition is not available; yet, it is still required. In this case, one is forced to use a raw vibration signal to extract the information about so-called instantaneous phase or instantaneous frequency of a selected component, and—if required—scale to a selected shaft. In recent years, few different techniques for speed recovery have been proposed, each one with different assumptions and each implementing more or less complexed mathematical apparatus. The current paper proposes a guidance how to select a suitable method on the basis of the visual deduction about signal characteristics with the implication on selection of the easiest and most automatized method sufficient for analysed case.

Keywords Condition monitoring · Speed recovery

1 Introduction

Vibration signals are nowadays broadly employed for the purpose of diagnostics of rotary machinery [1]. Most of the state-of-the-art methods (e.g. time-synchronous averaging, order analysis) require, however, either a constant speed during measurements [2–4] or precise speed reference [5]. Satisfying the former condition is challenging in many practical cases, as many machines operate under variable loads, which causes fluctuactions of the instantaneous speed. Latter case requires usage of tachometers, which in some cases are impossible to mount.

It is possible to overcome these issues by recovery of speed information from a vibrational signal itself. There are multiple approaches to perform this task. Early contributions to the area were summarized e.g. in a general review by Boshash

A. Jabłoński (✉) · K. Dziedziech · Z. Dworakowski
AGH University of Science and Technology, Kraków, Poland
e-mail: ajab@agh.edu.pl

A. Timofiejczuk et al. (eds.), *Advances in Condition Monitoring of Machinery in Non-Stationary Operations*, Applied Condition Monitoring 9,
https://doi.org/10.1007/978-3-319-61927-9_10

[6, 7]. Recently, numerous other approaches of speed tracking were proposed. Milloz et al. used for this purpose time-frequency distributions segmentation [8, 9]. Time-frequency approach was employed also by Zimroz et al. [10]. Several of speed-tracking algorihms were compared in papers by Coats et al. [11] and Urbanek et al. [12].

Recently, another approach was proposed by Urbanek et al. [13]. It is a two-step procedure that involves angular spectrogram-based resampling of a vibration signal and then frequency demodulation in one selected narrow band that contain selected component of the signal.

The aim of this paper is to present the range of application of method based on classical frequency spectrum and time-frequency spectrum. The organization of the paper is as follows: Sect. 2 provides scope of selected state-of-the-art literature-based solutions. Section 3 presents performance of the methods on example of numerical data. Section 4 presents performance of the methods on example of experimental data. Finally, the last chapter summarizes this paper.

2 Description of the Methods

Two methods have been selected for the comparison. First method, allows only low speed fluctuations [14] and is referred to as *Method A*, second method tracks the amplitude in time-frequency plane and enables large speed fluctuations [13] and is referred to as *Method B*.

Method A is the easiest in implementation, as it does not require advanced signal processing techniques. Time domain signal is transformed to frequency domain signal with use of the Fast Fourier Transform (FFT). After selection of appropriate Region of Interest (ROI), band-pass filtration is applied followed by the Inverse Fast Fourier Transform (IFFT) to obtain filtered time-domain signal. On the basis of filtered signal, Hilbert transform is calculated to obtain analytic signal from which instantaneous phase and frequency could be obtained. For the purpose of the clear presentation of results, obtained instantaneous frequency is smooth with moving average filter in this article.

Method B is currently state-of-the-art method for speed signal reconstruction. At first, modulus of Short-Time Fourier Transform (STFT) is calculated to obtain time-frequency distribution of the vibration signal. Semi-automatic ridge extraction algorithm is used for rough instantaneous frequency estimation. This algorithm requires selection of the starting point of the ridge. Once the rough instantaneous frequency is obtained, vibrations signal is resampled to angular domain, followed by Fourier transformation to order domain, where the band pass filtration in vicinity of the 1st order is calculated. With use of the inverse Fourier transform, signal is transformed back to angular domain, followed by resampling to time domain. On the basis of filtered signal, Hilbert transform is calculated to obtain analytic signal, from which instantaneous phase and frequency are obtained [13].

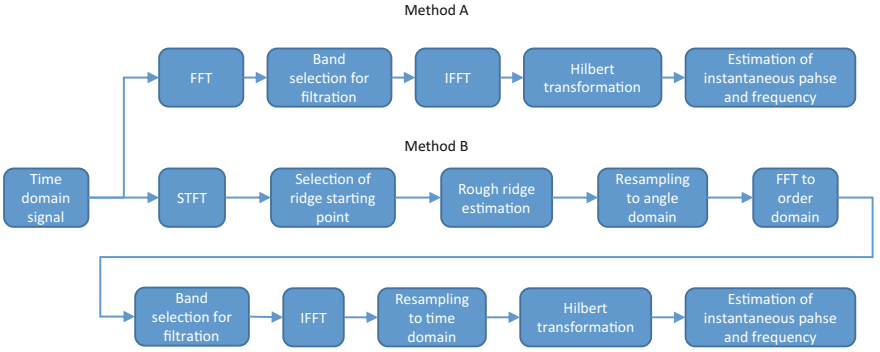

Fig. 1 Schematic workflow of method A and method B

Both methods are schematically presented in Fig. 1.

For the comparison purposes the percentage error functions are going to be calculated in following manner

$$PE = \frac{Extracted - Reference}{Reference} * 100 \tag{1}$$

where *Extracted* are the results of the above mentioned methods.

3 Numerical Example

For the purpose of the numerical comparison of the both methods, simple signal was created composed of fundamental signal with one harmonic (i.e. 2nd order) and two sub-harmonics signals (i.e. $^1/_2$ and $^1/_4$ orders), additionally white noise was added. Signal was sampled at frequency $F_s = 1000$ [Hz], and total time of the signal was $T = 20$ [s]. Rotational speed signal was created as a sine signal with period $T_p = 10$ [s], with mean speed $Speed_{mean} = 180$ [RPM] and peak-to-peak speed variation $Speed_{PP} = 40$ [RPM]. Created vibration signal (black curve) and rotational speed signal (green curve) are given in Fig. 2a, b respectively.

For the *Method A*, the modulus of the FFT presented in Fig. 3a reveals the frequency range in which energy of a single component oscillations are located in vicinity of the frequency $f = 180$ Hz. Selected band is presented in this figure as red curve overlaying the original black curve. Selected range was set to be $f = 150 \div 210$ Hz.

For the *Method B*, the modulus of the STFT presented in Fig. 3b reveals the direct relation between the vibration signal behaviour in time-frequency plane, with the speed evolution shown in Fig. 2b. The STFT have been calculated in limited frequency range of $f = 0 \div 500$ Hz, with the window length $w = 1$ s. Selected ridge is presented in Fig. 3b, as a set of blue dots selected by the semi-automatic ridge extraction algorithm.

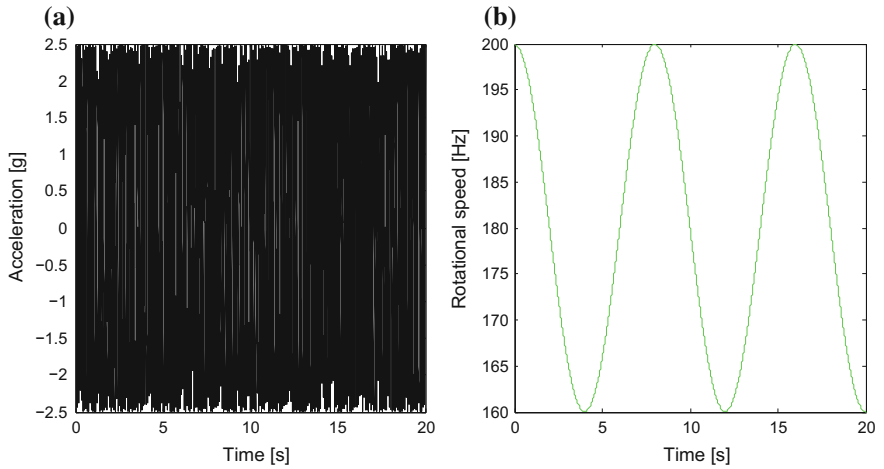

Fig. 2 **a** Created vibration signal; **b** rotational speed signal

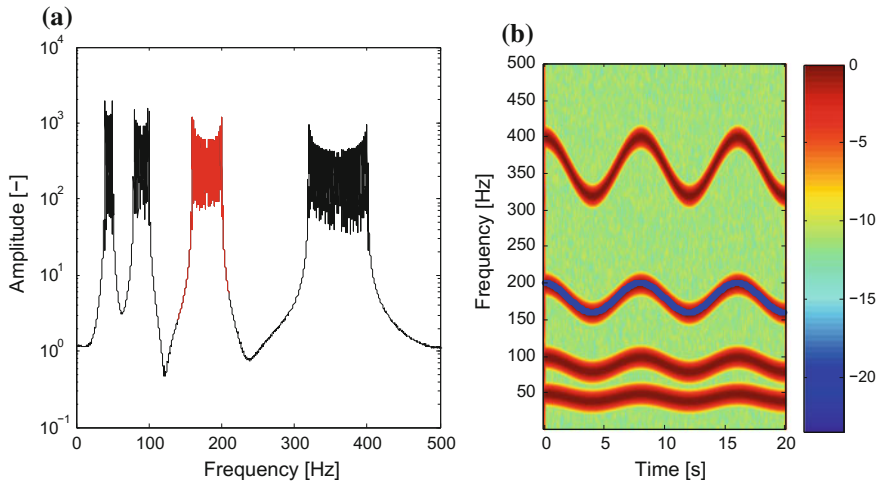

Fig. 3 **a** Amplitude-frequency spectrum of original signal (*black curve*) and selected part for *Method A* (*red curve*); **b** short-time fourier transform of acquired signal (*colour-map*) and selected ridge for *Method B* (*blue curve*)

On the basis of selected frequency band and rough ridge representing rough rotational velocity, the calculation procedures described in Sect. 2, finally lead to the rotational speeds as shown in Fig. 4a. For the quantitative comparison percentage error functions were calculated as shown in Fig. 4b. The quantitative analysis have shown that the mean percentage error in both cases is at the level of 0.1%.

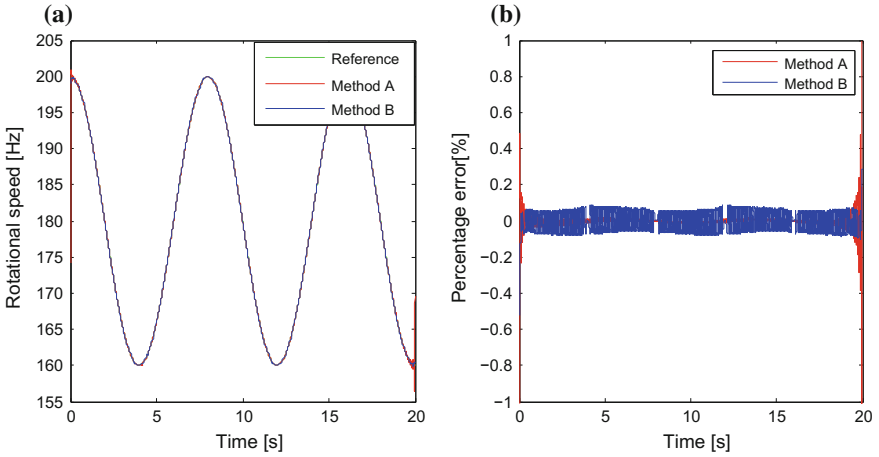

Fig. 4 **a** Rotational speed signals: reference signal (*green curve*), obtained with *Method A* (*red curve*) and obtained with *Method B* (*blue curve*); **b** percentage error of signals: obtained with *Method A* (*red curve*) and obtained with *Method B* (*blue curve*)

4 Experimental Example

Internal combustion engine was used for the experimental comparison of the both methods. Accelerometer was placed on the engine, whereas the speed sensor was located on the main shaft. Signal acquisition time was in total $T = 12.5$ s at sampling frequency $F_s = 25$ kHz. Acquired vibration signal is presented in Fig. 5a, whereas rotational speed signal is presented in Fig. 5b.

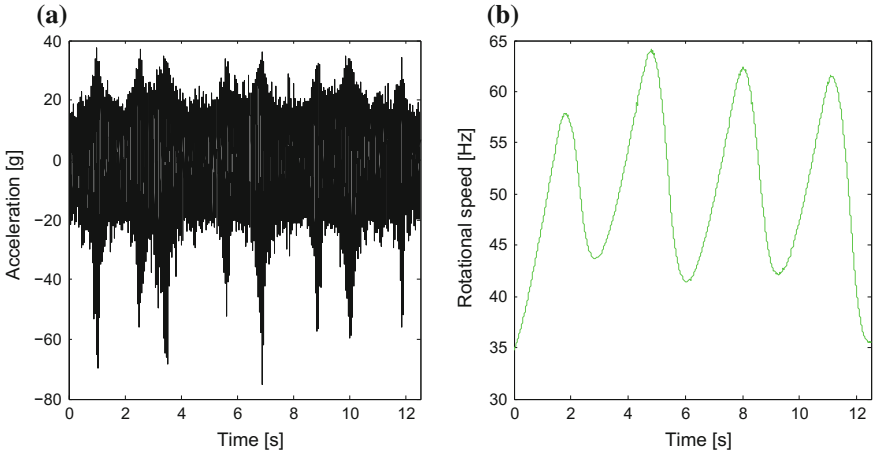

Fig. 5 **a** Acquired vibration signal; **b** rotational speed signal

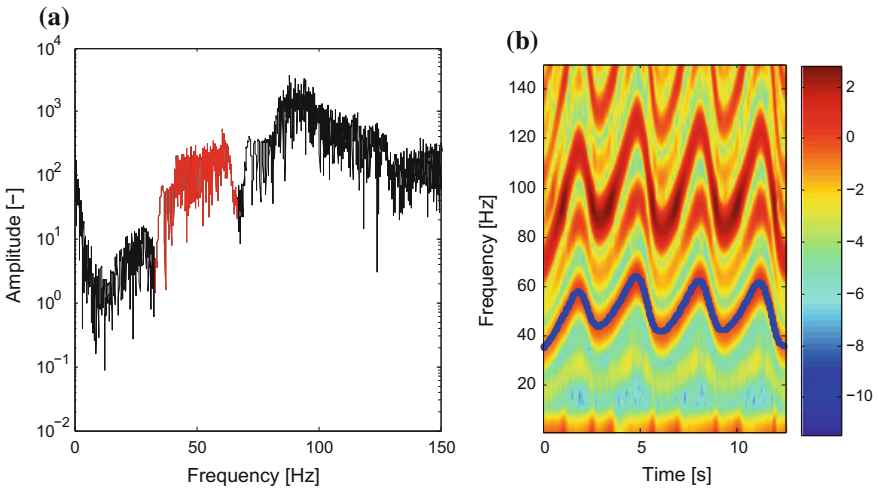

Fig. 6 **a** Amplitude-frequency spectrum of original signal (*black curve*) and selected part for *Method A* (*red curve*); **b** short-time fourier transform of acquired signal (*colour-map*) and selected ridge for *Method B* (*blue curve*)

For the *Method A*, the modulus of the FFT presented in Fig. 6a reveals the frequency range in which energy of a single component oscillations are located in vicinity of the frequency $f = 50$ Hz. Selected band is presented in this figure as red curve overlaying the original black curve. Selected range was set to be $f = 33 \div 67$ Hz.

For the *Method B*, the modulus of the STFT presented in Fig. 6b reveals the direct relation between the vibration signal behaviour in time-frequency plane, with the speed evolution shown in Fig. 5b. The STFT have been calculated in limited frequency range of $f = 0 \div 150$ Hz, with the window length $w = 0.5$ s. Selected ridge is presented in Fig. 6b, as a set of blue dots selected by the semi-automatic ridge extraction algorithm.

On the basis of selected frequency band and rough ridge representing rough rotational velocity, the calculation procedures described in Sect. 2, finally lead to the rotational speeds as shown in Fig. 7a. For the quantitative comparison percentage error functions were calculated as shown in Fig. 7b. The quantitative analysis have shown that percentage error in case of the *Method A* rising up to 13%, where as the percentage error for the *Method B* is oscillating in the range of mean value of $1 \div 1.5\%$. The reason for such a strange behaviour in case of the *Method A* is the fact that there is harmonic of order 1.5 that overlaps the same frequency region as the 1st order, and this is impossible to separate these frequency components in the frequency domain.

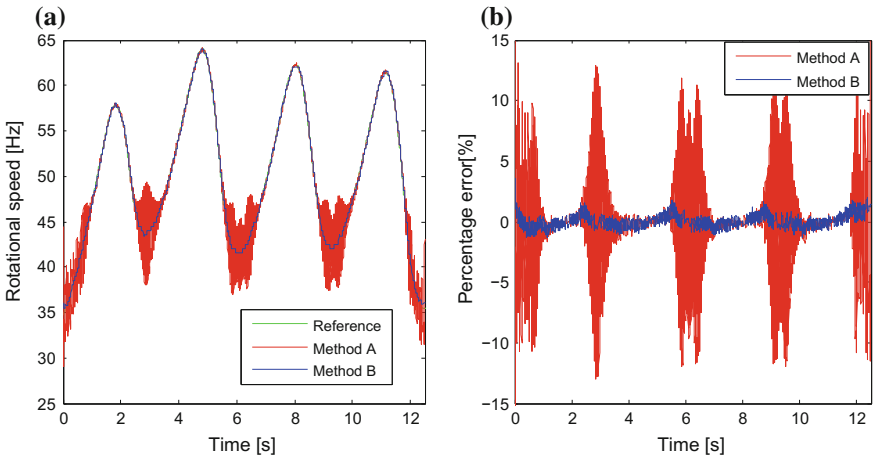

Fig. 7 **a** Rotational speed signals: reference signal (*green curve*), obtained with *Method A* (*red curve*) and obtained with *Method B* (*blue curve*); **b** percentage error of signals: obtained with *Method A* (*red curve*) and obtained with *Method B* (*blue curve*)

5 Conclusions

In the paper two state-of-the-art methods were presented and compared. For the case of the numerical example, both methods were able to correctly identify the rotational speed within the percentage error at level of 0.1%.

For the case of the experimental example, the signal was very similar to the one from the numerical case, and the procedure for selection of the frequency band was the same for the case of the *Method A* as presented in Fig. 6a, unfortunately due to the low amplitude frequency components shown in Fig. 6b, e.g. at time $t = 6\,\mathrm{s}$ and frequency $f = 60\,\mathrm{Hz}$, it is clearly visible that these components overlap with the components of the ridge that was actually being tracked with the semi-automatic algorithm.

It is authors conclusion that in all cases of the rotational speed recovery, modulus of the STFT should be calculated to check for the overlapping of the components, because it may not be visible at all in the modulus of the FFT.

Acknowledgements This work is partially supported by the National Centre for Research and Development in Poland under the research project no. PBS3/B6/21/2015. The authors also gratefully acknowledge the helpful comments and suggestions of the reviewers, which have improved the presentation.

References

1. Randall, R. B. (2011). *Vibration-based condition monitoring*.
2. Kurowski, W., & Miranowski, K. (2014). Cepstrum application in diagnostics of mechanical devices. *Diagnostyka*, *15*(4), 21–27.
3. Soleimani, A., & Khadem, S. E. (2015). Early fault detection of rotating machinery through chaotic vibration feature extraction of experimental data sets. *Chaos, Solitons & Fractals*, *78*, 61–75.
4. Liang, X., Zuo, M. J., & Hoseini, M. R. (2015). Vibration signal modeling of a planetary gear set for tooth crack detection. *Engineering Failure Analysis*, *48*, 185–200.
5. Groover, C. L., Trethewey, M. W., Maynard, K. P., & Lebold, M. S. (2005). Removal of order domain content in rotating equipment signals by double resampling. *Mechanical Systems and Signal Processing*, *19*, 483–500.
6. Boashash, B. (1992). Estimating and interpreting the instantaneous frequency of a signal—Part 1: Fundamentals. *Proceedings of the IEEE*, *80*(4), 520–538.
7. Boashash, B. (1992). Estimating and interpreting the instantaneous frequency of a signal—Part 2: Algorithms and applications. *Proceedings of the IEEE*, *80*(4), 540–568.
8. Millioz, F., & Martin, N. (2006). Time-frequency segmentation for engine speed monitoring. In *The Thirteenth International Congress on Sound and Vibration (ICSV13)*. Austria: Vienna.
9. Millioz, F., & Martin, N. (2007). Reassignment vector field for time-frequency segmentation. In *14th International Congress on Sound and Vibration (ICSV 14)*. Australia: Cairns.
10. Zimroz, R., & Bartkowiak, A. (2011). Investigation on spectral structure of gearbox vibration signals by principal component analysis for condition monitoring purposes. *Journal of Physics: Conference Series*, *305*, 012075.
11. Coats, M. D., Sawalhi, N., & Randall, R. B. (2009, November). Extraction of tach information from a vibration signal for improved synchronous averaging. In *Proceedings of Acoustics*.
12. Urbanek, J., Barszcz, T., Sawalhi, N., & Randall, R. B. (2011). Comparison of amplitude-based and phase-based methods for speed tracking in application to wind turbines. *Metrology and Measurement Systems, XVII*, *I*(2), 295–304.
13. Urbanek, J., Barszcz, T., & Antoni, J. (2013). A two-step procedure for estimation of instantaneous rotational speed with large fluctuations. *Mechanical Systems and Signal Processing*, *38*(1), 96–102.
14. Bonnardot, F., El Badaoui, M., Randall, R. B., Danière, J., & Guillet, F. (2005). Use of the acceleration signal of a gearbox in order to perform angular resampling (with limited speed fluctuation). *Mechanical Systems and Signal Processing*, *19*, 766–785.

How to Build a Vibration Monitoring System on Your Own?

Adam Jabłoński, Michał Żegleń, Wojciech Staszewski, Piotr Czop and Tomasz Barszcz

Abstract With the ultimate goal of cost reduction of condition monitoring, this paper illustrates how simple data acquisition and processing systems could be designed and realized taking advantage of latest cheap, yet powerful electronic elements. The discussed designs are based on recently popular STM32 and Raspberry Pi boards, and analog MEMS accelerometers. The final prototype design shown in the paper is developed on the F401re version of the STM family, which is working on ARM M4 Cortex processor, and the ADXL001-70 MEMS accelerometer from Analog Devices Ltd. The entire design has been develop using a standard notebook with Windows 10 operating system. The major interest of presenting this design is that in wide range of conditions, the self-made system developed from scratch with elements, price of which does not exceed 15 USD, is capable of generating a frequency spectrum equally significant to a spectrum generated by a full-scale, costly commercial condition monitoring system.

Keywords Condition monitoring system · Data acquisition · MEMS

1 Introduction

A vibration monitoring system may play a very important role in getting out the maximum potential of machinery by minimizing its downtime. It has been shown in the literature, for instance in [1–3] the maintenance that bases on condition monitoring systems (CMS) in compare to traditional, scheduled or corrective maintenance, more accurately fits in many aspects only with few disadvantages. The design and installation cost of condition monitoring system is unfortunately substantial in comparison to other maintenance approaches; therefore, usually it is only used for a

A. Jabłoński (✉) · M. Żegleń · W. Staszewski · P. Czop · T. Barszcz
Akademia Górniczo-Hutnicza im. Stanisława Staszica w Krakowie,
Wydział Inżynierii Mechanicznej i Robotyki, Katedra Robotyki i Mechatroniki,
Aleja Adama Mickiewicza 30, 30-059 Kraków, Poland
e-mail: ajab@agh.edu.pl

A. Timofiejczuk et al. (eds.), *Advances in Condition Monitoring of Machinery in Non-Stationary Operations*, Applied Condition Monitoring 9,
https://doi.org/10.1007/978-3-319-61927-9_11

huge machinery which downtime is extremely expensive. In that case, the longer the CMS is running, it provides benefits outshining the costs. In this paper, the authors try to make an attempt to evaluate the possibility of creation the CMS based on cheap electronic parts in order to provide some its benefits for much lower price. The entire purpose is to show some potential for more affordable option for constructing a simple data logger and viewer, which might be eventually turned into a basic CMS.

2 The Use of Vibrational Signals

Nowadays, in the age that is highly industrialized, the purpose of monitoring the conditions of an engineering systems has become an issue that requires great affection. Especially with the combination of well-known Internet communication methods and the expert knowledge of engineers. The on-site condition monitoring techniques that used to gather the measurement data have been investigated many times for several decades [4]. Usually when considering the process of maintenance, which could be right now defined as passive condition monitoring system. Along with the progress of this technology, three main philosophies have been established, i.e., breakdown, preventive (or scheduled), and predictive maintenance. The advantages that have been offered by the application of predictive maintenance techniques have in a past few years led to the increase in the development of a vast number of methods for condition monitoring/fault-diagnostic systems [5]. The modern diagnostic systems used for machinery monitoring consist of four main parts (see Fig. 1): (i) data acquisition, (ii) monitoring system, (iii) diagnostic system, (iv) safety system. The following subchapters describe them in details.

2.1 Data-Logger and Data Viewer

Establishing the vibration monitoring system may be a very expensive task, but what if such a system is only needed for just measurements of data? Development of entire automatic structure responsible for the monitoring and maintenance is therefore unnecessary. In such a case, there is a need for a device that may be attached to the machine permanently or just for a limited period of time and gather the measurement data. Nowadays, in order to achieve such a setup, it is necessary to buy an expensive measurement cards and sensors or portable vibration analyzers. The presented approach shows the possibility of creating small, cheap, socket or battery powered measurement system based on commonly existing electronic parts.

For the sake of troubleshooting there might be a need to visualize the state of technical condition of the machine at the moment of the measurement. In order to achieve that it is necessary to build the live data transmission system. The on-line

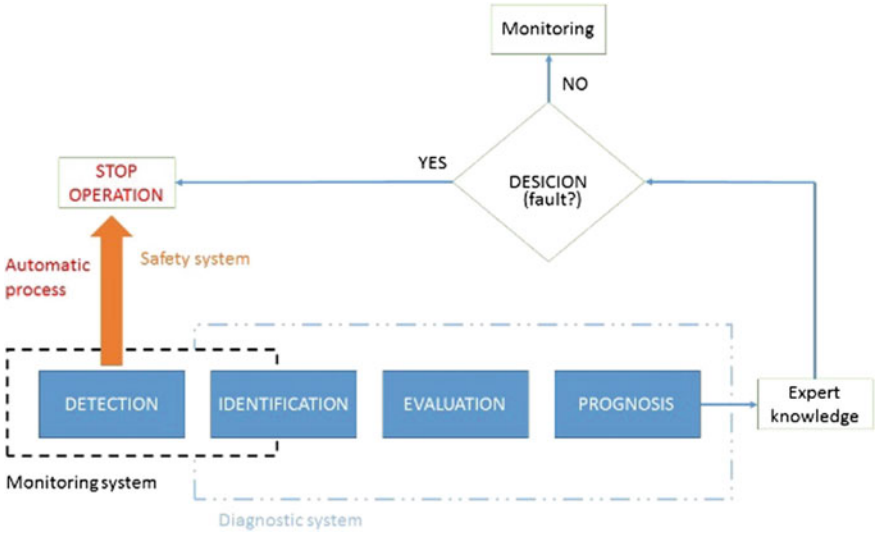

Fig. 1 Scheme of modern condition monitoring system

connection to the machine allows to visualize the actual condition, which is necessary in order to make a decision if the failure occurs. Moreover, display of a raw, live vibration data is not enough. There is a need to introduce a visualization software that will enable user the tools that are necessary for a full diagnosis, such as spectrum figures, order analysis and cursors.

2.2 Protection System and Monitoring System

The process of automatic supervision of machines state is realized mostly by limit checking (or threshold checking) of some variables that have been established as crucial, e.g. force, speed, pressure, liquid level, and temperature. Usually the alarms are raised when the limit value for a specific parameter is exceeded [3]. This process enables the introduction of automatic protection system, which in the moment of failure detection (exceeding the threshold value) will power down the machine in order to prevent from further damage.

For a number of machines, the systems that only realize the protection process are not enough. Some of the most precious information regarding the detection and development of a failure can be found at very early stage of this progress. Precise monitoring of such an evolution enables to plan maintenance accordingly, which may save a crucial downtime of machinery as well as protect other components from failure.

2.3 Diagnostic System

After detection of possible failure, mostly the diagnostic staff is responsible for taking further actions in order to verify the condition of the machinery. It may require further data acquisition in order to gather data that might be necessary in order to make appropriate decision regarding machines' condition. Nowadays, the new methods of modern systems theory show that use of the mathematical process and signal models, identification and estimation methods can provide better, more accurate and faster available information regarding machine condition. With use of these modern methods it is possible to establish new, advanced methods of fault detection and diagnosis in order to detect even small faults that occur quite early and to diagnose their origins in order to settle the primary cause [1]. This is also called condition monitoring. The goals of these methods are mainly: (i) increase of reliability and availability, (ii) improvement of safety, (iii) detection and diagnosis of faults, (iv) process condition-based maintenance and repair.

The Sects. 2.1–2.3 shortly describe the abilities and authorities of each part of a system. The authors want to show the possibilities of development of a project, which may lead into creation of a basic, but fully functional condition monitoring system. For different implementations, the actual configuration of systems may differ, enabling the end user to choose which system should be employed during the installation. It shows the modularity of considered solutions.

3 MEMS—The New Possibilities and Advantages

The Condition Monitoring Systems are usually setups for the high cost and huge size machines where the implementation and deployment of continuous monitoring may provide significantly lower service cost and drastically decrease maintenance time. Low cost MEMS-based accelerometer solutions such as presented in this paper, could be the solution for smaller machines. The Micro Electro-Mechanical System (MEMS) based Condition Monitoring Systems have reduced the installation cost per each node from $1000's to $100's [6]. The MEMS based sensors offer the capability to interconnect various interfaces used nowadays in the industrial applications, simplifying implementation for considered system and enabling its further development.

There are plenty of attributes of MEMS technology—such as size, weight, power, cost and high levels of functionality—are already compelling [7], but their presence on the market has been restricted by relatively low level of performance in terms of noise density and resonant frequencies. High frequency MEMS accelerometers have been available on the market since few years, offering resonant frequencies as high as 22 kHz and Full Scale Ranges up to ±500 g—unfortunately with the presence of high noise levels. Contrarily, available low noise MEMS sensors have low resonant frequency operation, used for some Condition

Monitoring Systems, where its application requires very low frequency operation, which of course limits the possibilities of diagnostic evaluation [8].

The investment and further development in MEMS process technology has advanced to the point where the improvements in performance obtained via technological development are enough to make MEMS a new available option for a wider range of CMS applications. MEMS sensors are nowadays also tolerant to the shock conditions, with stable sensitivity after subjecting to 1000's g of shock, or vibration to 10's of kHz. The accelerometers with embedded signal conditioning generally offer a full electro-static self- test of the moving element and signal conditioning circuits.

4 Low-Cost Own-Made Condition Monitoring System

For many years in order to achieve very accurate measurement of vibration signals of individual components of the machine in the industrial conditions, the maintenance engineers were obligated to use very expensive equipment. These appliances frequently exceed the budget for the maintenance process; therefore, only for a limited number cases such solutions are used. That is why the authors came to a conclusion that there is an enormous market to create low-cost architecture of data-acquisition device that could work in the industrial environment. The authors have been listening requirements and requests from companies and truly understood the need for this kind of cheap and accurate device. At the beginning, it was necessary to focus primarily on the selection of appropriate architecture of data-acquisition device. Microprocessor STM32 caught authors' attention during the long process of selection the main heart and brain of whole system. STM32 exceeds many different solutions and microcontrollers due to its powerful tools, embedded possibilities and obviously very low price. The research was based on STM32 version F401re which is working on ARM M4 Cortex and the maximum system core clock is 84 MHz which seems to be fine for own-made systems. The key features of ARM Cortex M4 are presented in Table 1.

One of the advantages of STM32 is presence of Direct Memory Access (DMA). DMA allows hardware to use Random-Access Memory (RAM) omitting Central Processing Unit (CPU). Moreover, DMA has the task of relieving processor from sending data. In considered case it allows for very accurate collection of samples from accelerometer without losing any data from entire measurement as well as

Table 1 ARM Cortex M4 features

Parameters
Up to 96 Kbyte of SRAM
1.7–3.6 V application supply and I/Os
Power consumption of run mode: 146 μA/MHz
1 × 12 bit, 2.4 MSPS A/D Converter
General-purpose DMA, up to 10 timers, RTC

sending data from buffers to SD Card. However, the selection of microcontroller was not the only problem which was faced. The accelerometers have analog outputs so it was necessary to choose a suitable Analog to Digital Converter (ADC). Fortunately, STM32 has embedded ADC converter which parameters seemed to fit the requirements of the proposed approach. A 12-bit analog-to-digital converter which shares up to 16 external channels can perform conversion in the single-shot or scan mode. The embedded ADC can be served by the DMA controller. To synchronize A/D conversion the ADC can be triggered by any timer.

For frequency of ADC = 30 MHz and sampling time of 3, the ADC cycles in single mode. It is possible to get even two millions of samples per second which is an amazing result. Furthermore, in triple mode it is possible get event six million of samples. Besides, while making research the authors used also the external A/D converter in order to verify the functionality of STM build-in ADC. For that purpose, the MCP 3202 ADC from Microchip company was chosen. It is dual channel 12-bit A/D converter with SPI Serial Interface.

It is worth mentioning that the MCP3202 A/D and embedded A/D in STM32 use successive approximation method. This method provides the accuracy that fits the needs as well as satisfying processing speed and has also low power consumption.

4.1 Possible Architectures

From the beginning of the project, the authors have been struggling in order to choose appropriate base for the own-made, low-cost condition monitoring system. Figure 2 shows two exemplary solutions: CMS based on STM32 (described in details in this paper) and CMS based on well-known platform called Raspberry Pi 2. Both of them differ from each other when it comes to parameters, data carriers, ADC converters and price.

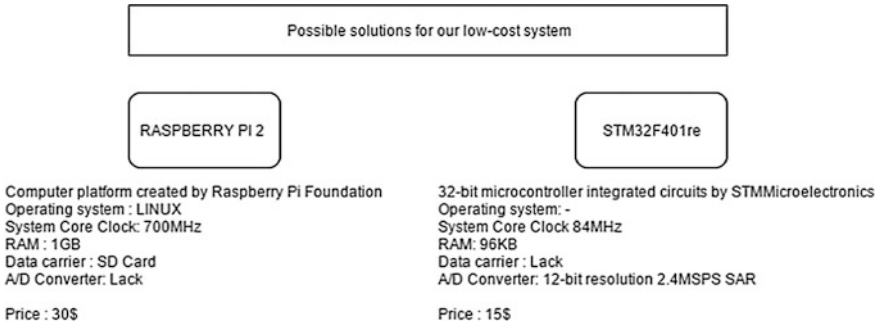

Fig. 2 Two exemplary solutions for the base of low-cost system

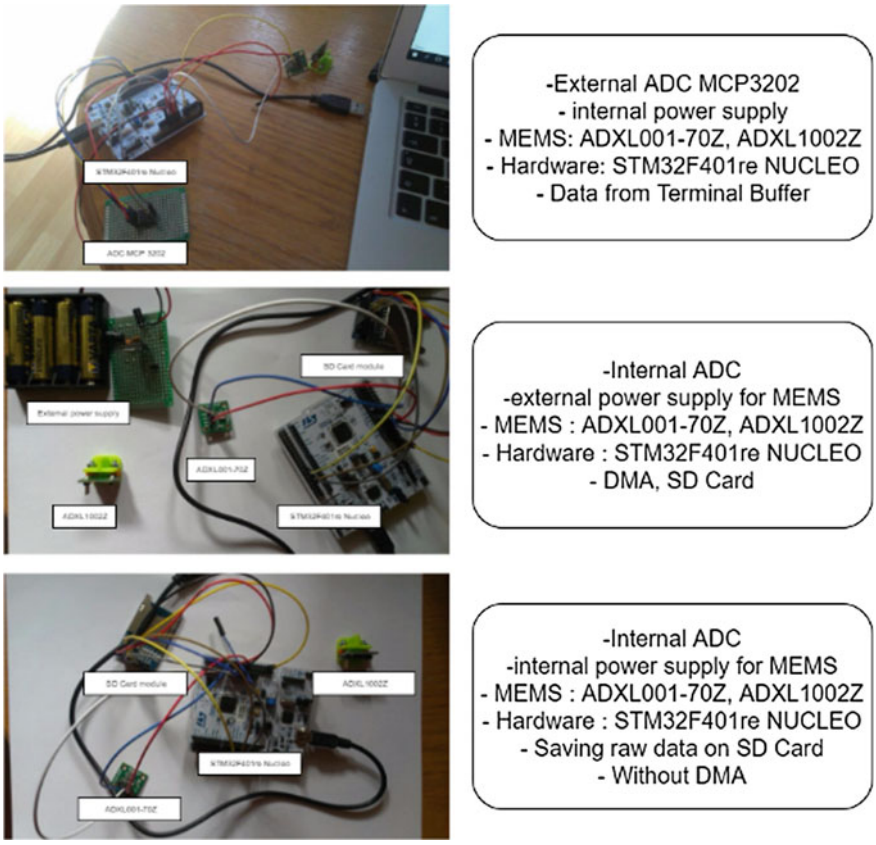

Fig. 3 Functionality of STM32 based solution

While considering the Raspberry Pi 2 as a base for the project, the authors had in mind functionality of that board that is available right out of the box. Such a system could be easily adapted for different purposes:

- Build-in SD card reader that supports up to 32GBs SD card enables to read and store lots of measurement samples without the need of exchanging the card or sending data to a computer,
- Build-in USB ports enable ease of development of wireless data transmission solution with use for instance a USB WIFI network extension card,
- Built-in Ethernet port allows to send measurement data directly to the host computer.

Similarly, a solution that is based on STM32 allows modularity, however each additional component requires further development. Figure 3 presents exemplary builds based on architecture using STM32. For both considered solutions, it is possible to power the system from an external power source (for instance phone

charger), from a computer (USB port is necessary) and from the battery—in the case of Raspberry Pi 2 it should be a power bank that supports 5 V 500 mA output and in case of STM32 four R6 (AA) batteries.

5 Experimental Verification of Data Acquisition

In order to verify the presented idea, a prototype board was created to check the operation of developed solution that is presented in the Fig. 3. An exemplary code was written on STM32F401re which was responsible for getting samples from MEMS accelerometer with the frequency of 10 kHz. Table 2 presents parameters of chosen accelerometer.

5.1 Noise Measurements

The first method utilizes the internal Analog-to-Digital Converter that is present on STM32 board. The ADC was triggered by an internal timer and data from ADC was managed by DMA in Double Buffer Mode. This was a precaution for the sake of making sure that not even one sample is lost during measurement and data saving process. The results are presented in the Fig. 4 (top left).

The second method utilizes the internal Analog-to-Digital Converter that is present on STM32 board and triggered by an internal timer. In this method DMA was omitted for the sake of making sure that its mechanism is not influencing the level on noise present in the measurement. The results are presented in the Fig. 4 (top right).

The third method utilizes the external Analog-to-Digital Converter that chosen in order to verify the results using two different converters. The ADC was triggered by an internal timer. In this method DMA was omitted for the sake of making sure that its mechanism is not influencing the level on noise present in the measurement. As well as verifying if ADCs are capable to manage 10 kHz measurement without software boost—DMA. The results are presented in the Fig. 4 (bottom).

Table 2 The parameters of chosen MEMS accelerometer

	ADXL001-70
Bandwidth (kHz)	22
Wideband range (g)	±70
Noise ($\mu g/\sqrt{Hz}$)	4000
Sensitivity (mV/g)	16
Power consumption (mA)	2.5

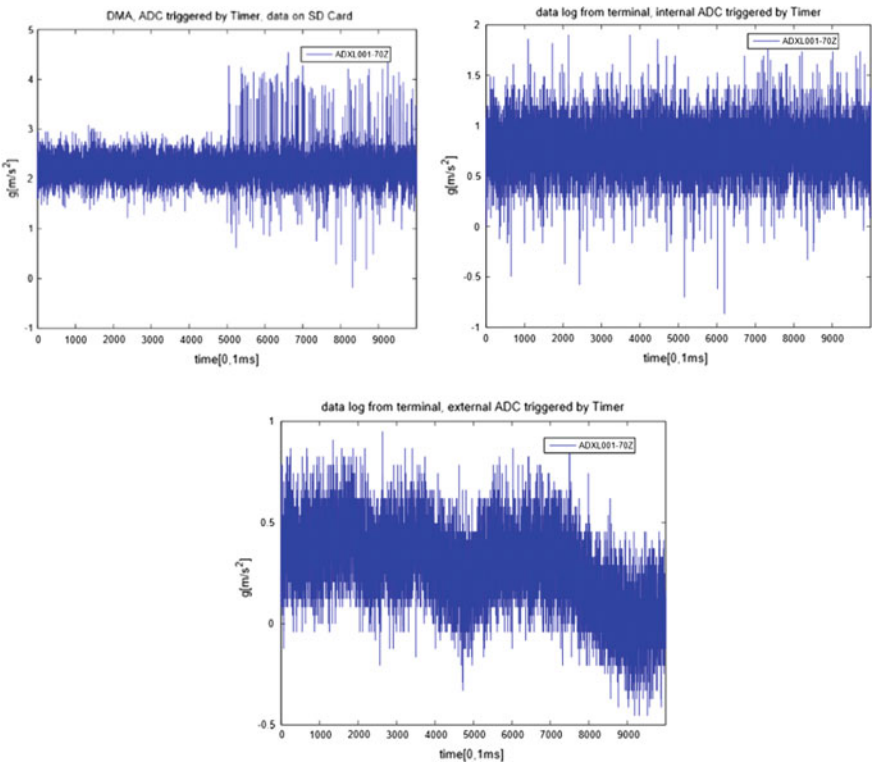

Fig. 4 Results obtained from MEMS accelerometer using all three methods

5.2 Results

In order to verify obtained results, the test case has been established based on a measurement of a simple domestic fan with an office clip attached to one of its blades serving as an imbalance. Two configurations have been used in order to gather measurement data: (i) the professional ACQ unit "Vibmonitor" equipped with 24bit ADC and industrial piezoelectric accelerometer IMI 61A02 (Fig. 5 top left), (ii) proposed system with 12bit ADC and ADXL001-70 MEMS accelerometer (Fig. 5 bottom left). To point out, the main imbalance component is well preserved in MEMS measurement (Fig. 5). However, the representation of higher components is worse than in case of piezoelectric accelerometer (used in a professional system —Fig. 5 right-blue), because of additional damping since the latest development of MEMS sensors is available only as a raw electronic board; therefore, in order to preserve high spectral bandwidth, it is necessary to develop a housing with relatively slow damping. This task is beyond the scope of this paper.

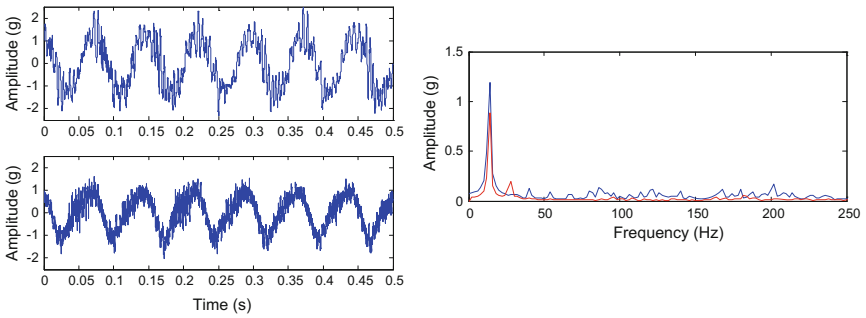

Fig. 5 Results obtained from the proposed solution and the professional system: *left-top* and *right blue*: IMI 61A02, *left-bottom* and *right-red*: ADXL001-70

6 Summary

The conducted study on the use of low cost MEMS-based accelerometer solutions for the purpose of building cheap condition monitoring system show different currently possible architectures of own-made condition monitoring system, suitable for different scenarios as well as a guidance for practical realizations. The presented exemplary realization could be the solution for smaller machines, for which the cost of CMS installation would exceed the budget for maintenance. The Micro Electro-Mechanical System based Condition Monitoring Systems would allow to reduce the installation cost per each monitoring node by the factor of 10. The authors have shown a concept in which the powerful tool of STM32 is used, including DMA and external ADC for better performance and results.

References

1. Blanke, M., Kinnaert, M., Lunze, J., & Staroswiecki, M. (2006). *Diagnosis and fault tolerant control* (2nd ed.). Berlin: Springer.
2. Hameed, Z., Ahn, S. H., & Cho, Y. M. (2010). Practical aspects of a condition monitoring system for a wind turbine with emphasis on its design, system architecture, testing and installation. *Renewable Energy, 5*(5), 879–894. doi:10.1016/.renene.2009.10.031.
3. Isermann, R. (2011). *Fault-diagnosis applications*. London: Blackwell.
4. Pan, M., Sas, P., & Van Brussel, H. (1996). Nonstationary time-frequency analysis for machine condition monitoring. doi:10.1109/TFSA.1996.550096.
5. Wang, W., Tse, P. W., & Lee, J. (2007). Remote machine maintenance system through Internet and mobile communication. *International Journal of Advanced Manufacturing Technology, 31,* 783–789. doi:10.1007/s00170-005-0236-1.
6. Albarbar, A., Badri, A., Jyoti, K., & Starr, S. (2008). Performance evaluation of MEMS accelerometers. *Measurement, 42,* 790–795. doi:10.1016/j.measurement.2008.12.002.

7. Nagel, D. J., & Zaghloul, M. E. (2001). MEMS: Micro technology, mega impact. *IEEE Circuits and Devices Magazine, 17*(2). doi:10.1109/101.920875.
8. Ratcliffe, C., Heider, D., Crane, R., Krauthauser, C., Yoon, M. K., & Gillespie, J. W. (2007). Investigation into the use of low cost MEMS accelerometers for vibration based damage detection. *Composite Structures, 82,* 61–70. doi:10.1016/j.compstruct.2006.11.012.

Optimization of Calculations for Wireless Condition Monitoring Systems

Kajetan Dziedziech, Adam Jabłoński and Tomasz Barszcz

Abstract Health Indicator for machine health monitoring are generally well-established. Regardless of the type of the Condition Monitoring System (stationary, remote, wireless) and the system's manufacturer, the most commonly applied Health Indicators include wideband estimators (peak-to-peak, Root Mean Square, kurtosis, crest factor, velocity Root Mean Square), narrowband estimators (speed harmonics, gear meshing frequencies, rolling-element bearing characteristic frequencies), and simple spectral bands corresponding to a group of machine elements, e.g. 100–2000 Hz for gearboxes. In order to improve the reliability of Health Indicators, stationary Condition Monitoring System implement averaging and advanced data acquisition logic. In order to detect faults in very early stage, Condition Monitoring System implement resampling, order analysis, Deterministic Random Separation, and for instance auxiliary visualization. However, in case of wireless Condition Monitoring System without a speed sensor, improvement might concern only three aspect, namely hardware realization, data transmission, and power savings, where the latter one might be decomposed into data transfer power consumption, data acquisition power consumption, and data analysis power consumption. The current paper illustrates few recent ideas on how to minimize the power consumptions for data analysis. As it will be shown, it is possible to reduce the computational cycles by more than 60% comparing to stationary Condition Monitoring System while losing acceptable level of the quality of calculated Health Indicators.

Keywords Wireless condition monitoring · Signal processing optimization

K. Dziedziech · A. Jabłoński (✉) · T. Barszcz
AGH University of Science and Technology, Kraków, Poland
e-mail: ajab@agh.edu.pl

A. Timofiejczuk et al. (eds.), *Advances in Condition Monitoring of Machinery in Non-Stationary Operations*, Applied Condition Monitoring 9,
https://doi.org/10.1007/978-3-319-61927-9_12

1 Introduction

As a consequence of non-perfect conversion of electrical or chemical (fuel) energy to desired work, any rotary machinery emits sound and vibration, and as a consequence due to the heat energy dissipation increases temperature. All of these physical phenomena can be quantitatively measured and converted into meaningful, physical quantities. The temperature is the easiest indicator to interpret, because it is a simple scalar value. Since typically, permissible operating temperatures of some mechanical elements are given by a manufacturer, it is a convenient "overall" diagnostic indicator. From a definition, vibrations refer to oscillatory movement, so the primary vibrations are displacement values. However, due to some scientific versus economical trade-off, typical vibrations are measured as "acceleration of motion", and are given as a fraction of [g] units. Still, the most widely used indicator, namely the "velocity RMS" is given as the "velocity of vibrations". The last signal, the sound, is an acoustic wave, which is this part of vibrations, which is not counterbalanced by machine foundations. Although sound bandwidth is theoretically unlimited (just like in case of any other value), it is accepted that the sound is constrained to a human hearing sense, which is about 20 Hz–15 kHz (numbers might vary).

In the current paper, the widely used vibrations signals are taken into account as a source of information of machine technical condition. The Health Indicators (HI), also called "signatures", "features", or diagnostic estimators are scalar results [1] of some processing of signal, e.g. statistical, filter-based or various customized [2].

From practical point of view, processing of vibration signals is like playing hide-and-seek. Regardless the used processing technique, the idea is always the same, i.e. to define such HI that would:

- detect a fault with a highest rate of reliability,
- detect a fault the earliest,
- identify the faulty component most accurately,
- approximate the Remaining Useful Life (RUL) most accurately.

From signal processing point-of-view, the requirement No. 1 calls for baseband signal analysis, where all signal components are present, i.e. no part is filtered out. On the other hand, requirements No. 2 and No. 3 aim in tracking narrowband, phase-locked frequency components or narrowband envelope characteristic components. In case of wireless hardware, which typically does not support phase markers, the scope of offered HIs includes broadband time domain estimators, narrowband frequency estimators, envelope estimators, and velocity-based estimators. The paper proposes some novel methods of reduction of number of calculations in the process of calculation of these HIs [3], which is irrelative for power-supplied data acquisition units, but is a true added value for wireless equipment, where power consumption is of upmost importance [4, 5]. In case of the wireless condition monitoring which are battery powered it is crucial to have the shortest calculations possible for the extension of the battery life-time.

Chapter 2 covers the classical way of calculating of the selected HIs. Chapter 3 discusses fast calculations algorithms that could be implemented into the wireless Condition Monitoring System (CMS) in terms of energy optimisation. Finally, the last chapter summarizes this paper.

2 Health Indicators

This section describes the most commonly used HIs in wireless condition monitoring.

2.1 Peak-to-Peak

The peak-to-peak value x_{peak} of the time sequence is simply a difference between the maximum and minimum values encountered in the given signal [6].

$$x_{max} = \max x \tag{1}$$

$$x_{min} = \min x \tag{2}$$

$$x_{peak} = x_{max} - x_{min} \tag{3}$$

2.2 Root Mean Square Value

The Root Mean Square (RMS) value x_{RMS} stands for a "root mean square" value. The name of the indicator explain the process of its calculation (reading from left to right). For a discrete signal, RMS is given as [6]

$$x_{RMS} = \sqrt{\frac{1}{n}\sum_{i=1}^{n} x_i^2} \tag{4}$$

The basic idea of using the RMS value as a diagnostic criterion is the fact, that any sort of failure generates additional vibrations, which increase the total energy of the system. The RMS value is an indicator of the average energy of the signal; thus, it may be used as a failure detection indication.

2.3 Crest Factor

The crest factor is simply the ratio of the peak value of the signal to the RMS value given as [6]

$$C = \frac{x_{peak}}{x_{RMS}} \tag{5}$$

It gives the idea how much of impacting is occurring in the vibration signal. Impacting is associated with the roller bearing and gear tooth failures.

2.4 Kurtosis

The kurtosis of the signal is defined as the measure of the "tailedness" of the signal. It is calculated according to the following equation

$$K = \frac{1}{n}\frac{\mu_4}{\sigma^4} \tag{6}$$

where μ_4 is fourth moment about the mean and σ is the standard deviation.

2.5 Velocity Root Mean Square Value

The VRMS value x_{VRMS} stands for a "velocity root-mean-square". The name of the indicator explains the process of its calculation (read from right to left) of the velocity signal. Most commonly used sensor for condition monitoring is accelerometer. Therefore it is expected at first to integrate the signal from acceleration to velocity

$$x_{vel_0} = \frac{x_{acc_0}}{F_s} \tag{7}$$

$$x_{vel_n} = x_{vel_{n-1}} + \frac{x_{acc_n}}{F_s} \tag{8}$$

Following step is the band-pass filtration in range of $f = 10 \div 1000\,\text{Hz}$, as this is required by most of the vibrodiagnostic standards. This filtration is easily achieved by the Fast Fourier Transform (FFT) combined with the selection of frequency bins that corresponds to the given frequency range and Inverse Fast Fourier Transform (IFFT).

$$X(\omega) = \int_{-\infty}^{\infty} x(t) e^{-2\pi j \omega t} dt \tag{9}$$

where ω is the frequency variable, j is a complex value operator. For the filtration a new variable should be considered as

$$Y(\omega) = \begin{cases} 2X(\omega) & \text{, if } 10 \leq \omega \leq 1000 \\ 0 & \text{, otherwise} \end{cases} \tag{10}$$

where $Y(\omega)$ is filtered signal to range of $f = 10 \div 1000$ Hz given in frequency domain, multiplication by 2 is required to compensate for the negative frequencies. Following step considers the IFFT operation given as

$$y(t) = \int_{-\infty}^{\infty} Y(\omega) e^{2\pi j \omega t} d\omega \tag{11}$$

where $y(t)$ is filtered signal given in time domain. Last step considers the calculation of RMS of obtained signal as

$$V_{RMS} = \sqrt{\frac{1}{n} \sum_{i=1}^{n} y_i^2} \tag{12}$$

2.6 "Band Limited" Energy

Spectrum analysis is performed using a FFT. It is assumed that spectrum will be grouped into several "Band Limited" Energy (BLE), i.e. energy will be integrated over given frequency bands. Different frequency bands will be related to different phenomena's, i.e. low frequency bands are related to, e.g. misalignment and/or unbalance, medium frequency bands are related to higher orders of operation, e.g. x2, x3, x4 etc., high frequency bands are related to, e.g. gear meshing frequencies.

At first FFT is calculated in the same manner as in Eq. (9). Energy content is integrated over given frequency ranges, for BEC_1 it is given as

$$BEC_1 = \sum_{\omega=0}^{\omega=30} 2X(\omega) \tag{13}$$

2.7 Envelope Root Mean Square

Envelope RMS calculation requires at first computation of FFT given as

$$X(\omega) = \int_{-\infty}^{\infty} x(t) e^{-2\pi j \omega t} dt \tag{14}$$

Following, filtration of appropriate band of interest should be done as

$$Y(\omega) = \begin{cases} 2X(\omega) & \text{, if } 4000 \leq \omega \leq 10000 \\ 0 & \text{, otherwise} \end{cases} \tag{15}$$

Once the signal is filtrated, IFFT should be calculated following the formula given as

$$y(t) = \int_{-\infty}^{\infty} Y(\omega) e^{2\pi j \omega t} d\omega \tag{16}$$

For the resulting function envelope should be calculated as

$$y_{env}(t) = |y(t)| \tag{17}$$

Finally, envelope RMS can be calculated as

$$E_{RMS} = \sqrt{\frac{1}{n} \sum_{i=1}^{n} y_{env_i}^2} \tag{18}$$

3 Fast Calculation Algorithms

This section describes fast calculation algorithms that could be implemented in wireless condition monitoring for energy efficient calculations.

3.1 Multiplication Order Considerations

It is in common sense to recalculate the measured discretized values to the physical values at the beginning of the entire signal processing, to remain in the physical world units as

$$X_{PU} = (X_{DV} - X_{SO}) * A_{DtEC} * B_{EtPC} \tag{19}$$

where X_{PU} are the values of measured signal in Physical Units (PU), X_{DV} are the values of measured signal in Discretized Values (DV), X_{SO} is the Systems Offset (SO), that has to be subtracted to obtain measured signal with negative values, A_{DtEC} is the Digital to Electric Coefficient (DtEC), that has to be used to obtain values in electrical units, B_{EtPC} is the Electric to Physical Coefficient (EtPC), that have to be used to obtain values in physical units.

Apart of above mention recalculations, it is always a good practice to remove the DC constant from the signal for the purpose of the further signal processing, as time-domain based methods are sensitive to DC offsets

$$X_{mean} = \frac{1}{n} \sum_{i=1}^{n} X_{PU_i} \tag{20}$$

$$X_{PU0M} = X_{PU} - X_{mean} \tag{21}$$

where X_{PU0M} is the finally obtained measured signal in Physical Units with 0 Mean (PU0M), which should be used in further calculations.

All of the abovementioned calculations are very simple and fast, but they do consume power. In order to obtained the finally measured signal PU0M, a list of operations that have to be conducted for every measured sample (we assume the n samples).

- Subtract the System Offset (n subtraction operations)
- Multiply by the Digital to Electric Coefficient (n multiplication operations)
- Multiply by the Electric to Physical Coefficient (n multiplication operations)
- Calculate the mean value (n addition operations)
- Subtract the mean value (n subtraction operations)

In total $5n$ operations have to be conducted, before actual signal processing. The proposition is to conduct signal processing on values with minimal preprocessing, and apply the appropriate coefficients after the signal processing. The proposed minimal preprocessing is as follows

$$X_{mean} = \frac{1}{n} \sum_{i=1}^{n} X_{DV_i} \tag{22}$$

$$X_{DV0M} = X_{DV} - X_{mean} \tag{23}$$

where X_{DV0M} is the measured signal in Discretized Values with 0 Mean (DV0M). The list of operations that have to be conducted for every measured sample (we assume the n samples)

- Calculate the mean value (n addition operations)
- Subtract the mean value (n subtraction operations)

In total $2n$ operations. After the signal processing correction coefficients have to be applied to a trend value, so in fact to a single sample. So it could be assumed that this results in reduction from $5n$ operations to $2n$ operations in preprocessing stage—reduction of 60% of operations.

After careful analysis it has been found that the application of the scaling coefficients should be done for the following trends:

- Peak-to-peak,
- RMS,
- Velocity RMS,
- BEC.

There is no need to apply the scaling coefficients for the following trends:

- Kurtosis,
- Crest factor.

3.2 *Application of Parseval's Theorem for Envelope RMS Calculation*

Classical calculation of envelope RMS assumes one FFT and one IFFT as shown in Sect. 2.7, which are very time consuming. Alternative way of calculation of envelope RMS could be achieved by application of Parseval's theorem given as

$$\sum_{i=1}^{n} |x_i|^2 = \frac{1}{n} \sum_{k=1}^{n} |X_k|^2 \tag{24}$$

where x_i is envelope signal given in discrete time domain, X_k is FFT of a envelope signal. Considering the equation for the RMS as

$$x_{RMS} = \sqrt{\frac{1}{n} \sum_{i=1}^{n} x_i^2} \tag{25}$$

Having this assumption made, RMS can be calculated directly from the frequency domain as

$$x_{RMS} = \sqrt{\frac{1}{n^2} \sum_{i=1}^{n} |X_k|^2} \tag{26}$$

In this manner calculation of envelope RMS could be done without a need to go back to the time domain via IFFT. Such a simplification can save almost 50% of calculation time of envelope RMS, as the FFT and IFFT are the most time consuming operations in this scheme.

3.3 Velocity RMS Calculation

Classical calculation of velocity RMS is done at first by numerical integration as shown in Sect. 2.5. This integration requires n operations. An alternative version assumes the integration in frequency domain as follows

$$X_{vel}(\omega) = \frac{X_{acc}(\omega)}{2\pi\omega} \tag{27}$$

In this manner a fraction of operations are needed to be done. Nowadays CMS analyse bandwidth of $B_w = 10\,\text{kHz}$, this means that the sampling frequency is at least $F_s = 20\,\text{kHz}$. Since there is a need for the analysis of the frequency range $10 \div 1000\,\text{Hz}$, this means a rough reduction of required operations for the numerical integration of 20 times.

4 Conclusions

In this article fast calculation algorithms for calculation of classical Health Indicators have been presented. It has been shown that such operations could save more than 50% of calculation time of certain operations, without any impact on the obtained results by performing calculations in different domains and applying constant coefficients on estimated indicators rather than on to raw data.

Acknowledgements This work is partially supported by the KIC InnoEnergy under the research project no. 32_2014_IP110_XSENSOR. The authors also gratefully acknowledge the helpful comments and suggestions of the reviewers, which have improved the presentation.

References

1. Igba, J., et al. (2016). Analysing RMS and peak values of vibration signals for condition monitoring of wind turbine gearboxes. *Renewable Energy*, *91*, 90–106.
2. Lebold, M., et al. (2000). Review of vibration analysis methods for gearbox diagnostics and prognostics. In *Proceedings of the 54th Meeting of the Society for Machinery Failure Prevention Technology* (Vol. 634).
3. Press, W. H., et al. (1996). *Numerical recipes in C* (Vol. 2). Cambridge: Cambridge University Press.
4. Aygün, B., & Gungor, V. C. (2011). Wireless sensor networks for structure health monitoring: Recent advances and future research directions. *Sensor Review*, *31*(3), 261–276.
5. Huang, Q., Tang, B., & Deng, L. (2015). Development of high synchronous acquisition accuracy wireless sensor network for machine vibration monitoring. *Measurement*, *66*, 35–44.
6. Večeř, P., Kreidl, M., & Šmíd, R. (2005). Condition indicators for gearbox condition monitoring systems. *Acta Polytechnica, 45*(6).

Supervised Classification Methods in Condition Monitoring of Rolling Element Bearings

Paweł Różak, Jakub Zieliński, Piotr Czop, Adam Jabłoński, Tomasz Barszcz and Michał Mareczek

Abstract Operational vibrational diagnostics is crucial for providing the reliability of mid and large scale combustion engine applications (e.g. railway, automotive heavy vehicles or electric generators). This work reports study presenting application of supervised learning and classification methods based on pattern recognition using different classifiers (e.g. logistic regression, k-nearest neighbor or normal density) in order to detect early warning diagnostic symptoms of malfunctioned rolling element bearings (REBs) in the presence of background disturbances from combustion diesel engine. The REB's malfunction type classification is based on time domain (RMS, peak to peak, Crest factor) as well as frequency domain signal processing methods like envelope analysis or modulation intensity distribution (MID) which allows to neglect the influence of background noise representing by non-stationary operating conditions and possible structural modifications (e.g. maintenance activities or parts replacing). The proposed data classification methods are compared and validated by using experimental measurements conducted on a dedicated combustion engine test bench for wide range of rotational speed and different levels of REB's radial load.

P. Różak · J. Zieliński · P. Czop · A. Jabłoński (✉) · T. Barszcz
AGH University of Science and Technology, Kraków, Poland
e-mail: ajab@agh.edu.pl

P. Różak
e-mail: rozak.pawel@gmail.com

J. Zieliński
e-mail: jzielin@agh.edu.pl

P. Czop
e-mail: pczop@agh.edu.pl

T. Barszcz
e-mail: tbarszcz@agh.edu.pl

M. Mareczek
Institute of Automobiles and Internal Combustion Engines, Cracow University of Technology, Kraków, Poland
e-mail: michal.mareczek@mech.pk.edu.pl

A. Timofiejczuk et al. (eds.), *Advances in Condition Monitoring of Machinery in Non-Stationary Operations*, Applied Condition Monitoring 9,
https://doi.org/10.1007/978-3-319-61927-9_13

Keywords Data mining · Vibrational monitoring · Data classification · Rolling element bearing · Supervised classification

1 Introduction

Operational vibrational diagnostics is important for mid and large scale combustion engine applications, especially those ones coupled to mechanical load (railway and automotive heavy vehicles) or electrical load (electric generator) where gearboxes and rolling element bearings (REBs) play a vital role. REBs account for a relatively large percentage of all machinery breakdowns, typically the failure results in a costly repair and unplanned downtime. The aim of this paper is to develop supervised data classification method in order to detect early warning diagnostic symptoms of malfunctioned rolling element bearings (REBs). The method is intended for bearing analysis in the presence of background disturbing signals from other machine components such as combustion engine. The disturbing signals mostly have harmonic- and impulse-like disturbing mechanism with a period of a fraction of the engine rotational speed. Thus high-frequency demodulation techniques are required to provide robust diagnostic symptoms. REBs diagnostics in presence of background disturbances was widely reported by Randall and Antoni [1] who provides a comprehensive tutorial regarding rolling element bearing diagnostics in particular in the presence of strong masking signals from other machine components such as gears [2]. Sawalhi and Randall [3] described the combined gear bearing dynamic model to present bearing-gear interactions and study the extended bearing faults [4].

The paper has two parts. The first reviews and proposes diagnostic indicators to detect the bearing failure mode in advance [5, 6]. The second validates a few proposed supervised methods used to classify REB conditions based on proposed time and frequency domain diagnostic indicators. Time-domain indicators are straightforward (broadband) signal estimates such as Root-Mean-Square (RMS), Peak-To-Peak (PP) measures. Frequency-domain indicators are amplitude of frequency components determined based on geometrical parameters of analyzed REBs based on vibration signals, i.e. Ball-Pass Frequency of Outer race (BPFO), Ball-Pass Frequency of Inner race (BPFI), Ball Spin Frequency (BSF) and Fundamental Train Frequency (FTF) [7]. Narrowband Envelope Analysis (NEA), Modulation Intensity Distribution (MID), and Integrated Modulation Intensity Distribution (IMID) methods [8] can be used to demodulate frequency component in order to improve signal-noise-ratio in the presence of background disturbances and complex malfunction resulting in a single or multiple amplitude-frequency-phase modulation effect. This paper applies widely used supervised classification methods, i.e. nearest neighbor and nearest mean classifiers, logistic regression, linear and quadratic discriminant analyses and radial basis function neural network [9, 10]. These methods proved their effectiveness in various engineering and, in particular, condition monitoring applications, as pointed throughout the article.

Their advantages can be found in relatively simple application and low computation time, thus it can be assumed that they can be directly applied in state-of-the-art Condition Monitoring Systems (CMS).

2 Supervised Classification Methods

Supervised classification is performed based on the relationship between the input explanatory independent vector of features and the dependent class or cluster. Each explanatory observation should be labeled with the corresponding class. Such training set can be used for teaching of a selected method until the relation between inputs and category is established. The obtained pattern is then used for the unseen testing data. The labels are not known to classifier until the verification stage, when the obtained results are compared with the actual indications. One of the most commonly used supervised classifier is a k-nearest neighbor (k-NN) one [11, 12]. An interesting approach is normal density-based linear classifier, also called linear discriminant analysis (LDA). It can be used to describe a linear combination of explanatory data that are most suitable for distinguishing of two or more categories of objects [13]. Similar to LDA, for the quadratic discriminant analysis (QDA) it is assumed that the observation vector is normally distributed for each category. The difference between the two methods can be found for covariance, which are supposed to be different. For QDA the classification is made using the likelihood ratio that calculates probability that a given observation belongs to particular class [14]. An interesting approach is radial basis function neural network (NN). The network is similar as for classical neural network and the inputs are formed using explanatory variables. At the input of each neuron, the distance between the neuron and the input vector is obtained. The outputs are calculated as weighted sum of the hidden layers and the unity bias. Most commonly, the basis function is the Gaussian bell one [15]. The neural networks were used for bearings diagnostics in [16], while in [17] the authors compared radial basis functions-based NN with back-propagation networks, showing their superiority based on the fast training time.

3 Engine Test Bench

Universal engine test bench (Fig. 1) was used in order to conduct REBs vibration measurements under variable load conditions. It consists of three main components: diesel engine (2) which is started by starting motor (1), electromagnetic brake (6) providing load on engine output shaft supported by tested REB (5). The engine has the following parameters: 4 cylinder, 16 valves, 90 HP (66 kW) at 4000 RPM (rotations per minute) and 200 Nm at 1750 RPM. A hydraulic actuator (7) applies

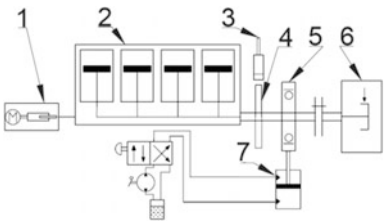

Fig. 1 Schematic representation of measurement setup

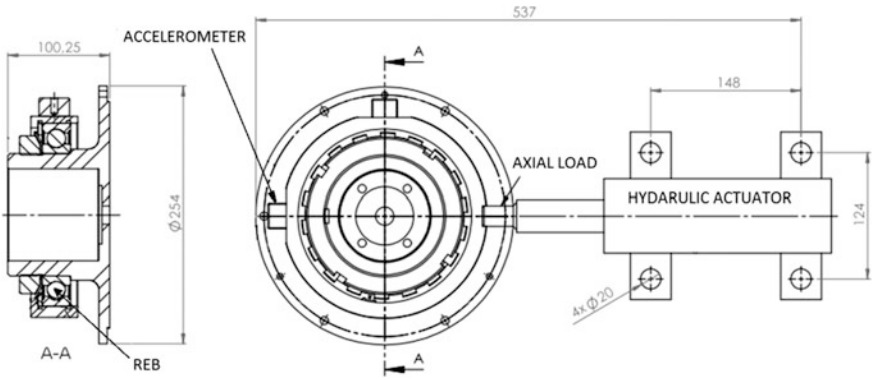

Fig. 2 Hydraulic system applying radial load

radial load (0–7.7 kN) to the REB housing that corresponds to 0–2 MPa hydraulic pressure supplying the actuator (Fig. 2). Rotational speed is measured by inductive sensor (3) which is activated once per shaft by marker attached to the engine flywheel (4).

The accelerometer (PCB 338B34; 10 mV/g; 10 kHz) is screwed (M6) to the bearing housing in vertical or horizontal direction as shown in Fig. 2.

A single row and deep groove ball bearing was used (FŁT 6024; $\Phi_{inn} = 120$ mm; $\Phi_{out} = 180$ mm). Vibrational data acquisition was conducted with a sampling rate of 25 kHz, while RPM was recorded with additional low-frequency data acquisition system. Figures 2 and 3 (left) shows bearing mounting and loading system. Vibrational measurements were conducted for 1.9, 3.8 and 7.7 kN load conditions with combination of the following rotational speeds: 2, 2.5, 3, 3.5, 4 and 5 kRPM. Engine torque was maintained at constant value of 50 Nm by electromagnetic brake. Load and speed combination measurements were recorded for further vibrational analysis. Two identical REBs (FŁT 6024) were installed and measured. The former was tested in poor lubrication conditions while the latter in proper lubrication conditions. Tested REBs were measured in reference and failure mode conditions. The failure was applied by slightly drilled inner race defect (a longitudinal scratch parallel to bearing axis) Fig. 3 (right).

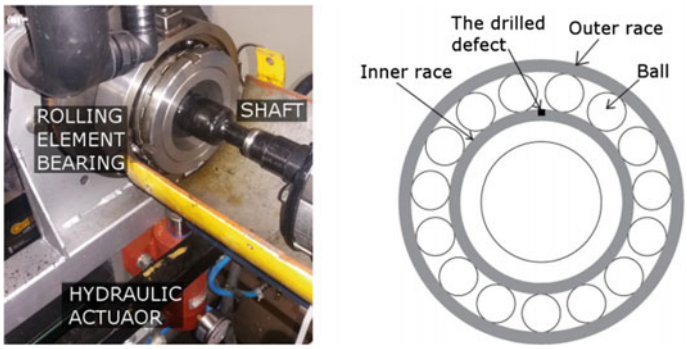

Fig. 3 Bearing loading system (*left*) and location of the bearing defect (*right*)

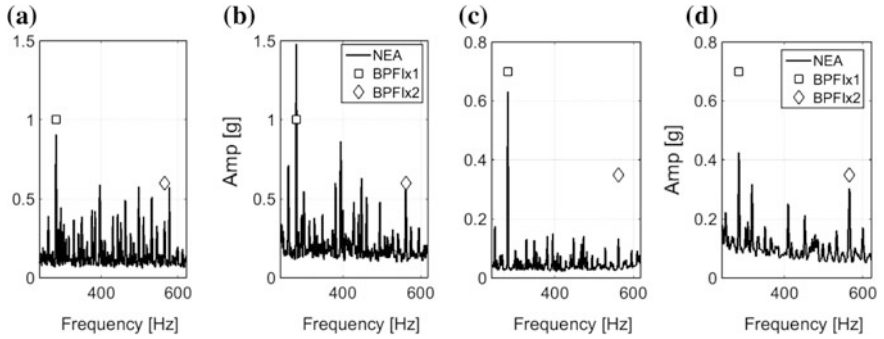

Fig. 4 Averaged NEA method results for REB proper lubrication **a** reference and **b** defected case (2000 RPM/1.9 kN load) and REB poor lubrication **c** reference and **d** defected case (2000 RPM/3.8 kN load)

4 Diagnostic Indicators

Amplitudes of REB frequency components BPFO, BPFI, BSF and FTF can be used as diagnostic indicators (i.e. symptoms of the failure). Early warning REB diagnostic symptoms can be obtained using time- and frequency domain analysis based on raw, filtered and demodulated signals [7]. NEA, MID and IMID methods [8] using demodulation techniques allow to reduce the influence of background disturbances, e.g. periodic impacts which are amplified by resonances of bearing, sensors, structure etc. Averaged NEA method was used to compare reference and malfunctioned bearing conditions. Figure 4 shows NEA plots averaged for 50 s of measurement and demodulation band from 8250 to 9750 Hz.

Averaged NEA method provides results which indicate REB malfunctions in both cases of poor and proper lubrication (growth of 1st and 2nd harmonic of BPFI). MID method is used in order to demodulate raw vibrational signal using spectral correlation method, however other approach can also be considered such as

spectral coherence, RMS, or kurtosis. MID method requires to assume the frequency component to be analyzed (e.g. BPFI) and the modulation band range. Mathematical notation of MID/IMID methods with use of Product of Spectral Correlation (PSC) and Spectral Correlation (SC) is as follows:

$$MID_{\Delta f}^{PSC}(f,\alpha) = SC_x^{\alpha}\left(f+\frac{\alpha}{2}\right) * SC_x^{\alpha}\left(f-\frac{\alpha}{2}\right) \tag{1}$$

$$SC_x^{\alpha}(f) = \lim_{\Delta f \to 0} \lim_{\Delta t \to \infty} \frac{1}{\Delta t} \int_{-\frac{\Delta t}{2}}^{\frac{\Delta t}{2}} \Delta f \cdot X_{\frac{1}{\Delta f}}\left(t, f+\frac{\alpha}{2}\right) \cdot X_{\frac{1}{\Delta f}}^{*}\left(t, f-\frac{\alpha}{2}\right) \tag{2}$$

$$X_{\frac{1}{\Delta f}}(t,f) \triangleq \int_{t-\frac{1}{2\Delta f}}^{t+\frac{1}{2\Delta f}} x(t) e^{-j2\Pi ft} dt \tag{3}$$

$$IMID_{f_1}^{f_2}(\alpha, \Delta f) = \int_{f_1}^{f_2} MID_{\Delta f}(f,\alpha) df \tag{4}$$

where:

t—time, *carrier frequency*, *α—cyclic frequency* (*e.g.* ± *BPFI*), $X_{\frac{1}{\Delta f}}$—*Envelope Complex Function of signal in range* $\langle f - \frac{\Delta f}{2}; f + \frac{\Delta f}{2} \rangle$.

The MID analysis shows significantly greater modulation intensity distribution of BPFI frequency component α in function of carrier frequency for the poorly and properly lubricated REB as shown in Figs. 5 and 6.

MID method can be extended to IMID method in order to facilitate vibration analysis by means of computing a sum of signal energy in frequency component domain for all or chosen carrier frequency range. The IMID graph in Fig. 7 confirms that a higher energy peak occurs around BPFI frequency component for defected REB in both cases of poor and proper lubrication. The BPFI frequency component exhibits frequency deviation (3.8 kN at 2000 RPM) resulting from RPM variation (i.e. error) during measurement.

IMID method has advantage compared to NEA method since it does not require to assume the demodulation frequency band which is unknown a priori and might be related to structural resonances. MID, IMID, NEA methods are used further in this paper to obtain the early warning diagnostic indicators which allow to apply supervised learning and classification methods in order to evaluate normal and deteriorated REBs operating conditions.

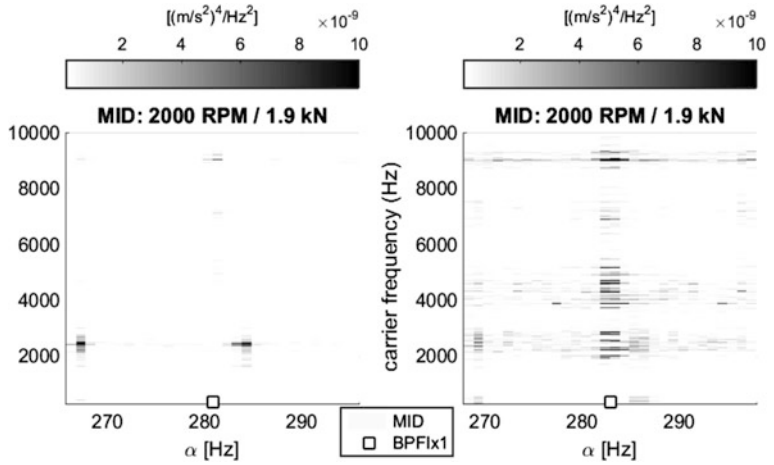

Fig. 5 MID map for REB proper lubrication in a reference (*left*) and defected (*right*) case

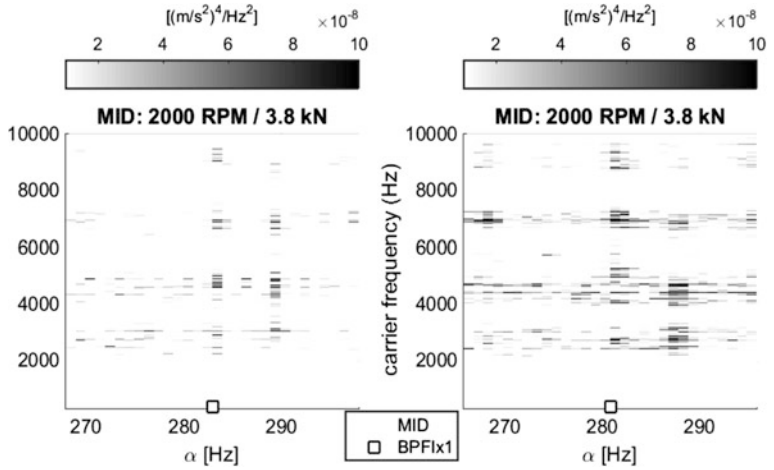

Fig. 6 MID map for REB poor lubrication in a reference (*left*) and defected (*right*) case

5 Supervised Learning and Classification Process

This section reports selective results obtained for REB subjected to radial load of 3.8 kN corresponding to 1 MPa hydraulic pressure in the actuator (Fig. 2). Engine rotating speed was set to 3000 RPM. The measured vibration data sets were divided into learning (60%) and testing part (40%) required by supervised learning and classification methods implemented based on Matlab Toolbox for Pattern Recognition [18]. Following data processing steps were applied: (i) defining and choosing

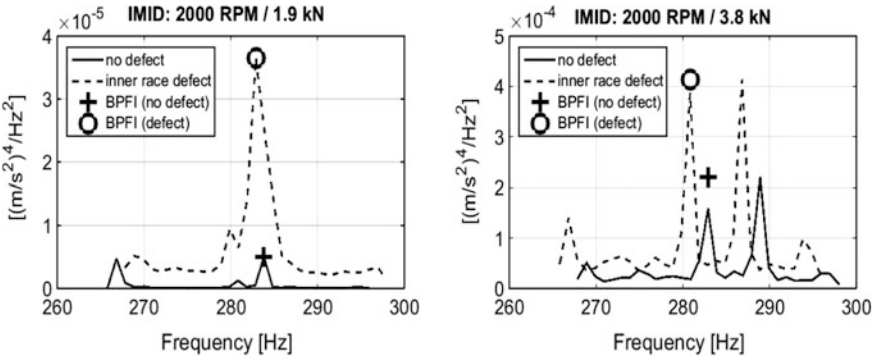

Fig. 7 IMID method results for properly (*left*) and poorly (*right*) lubricated REB

Table 1 Diagnostic strategies and their configuration parameters

Method	DS	DSEG (s)	MB (Hz)	DM (Hz)	Unit	Diagnostic strategy						
						1	2	3	4	5	6	7
Time domain	RMS	100	N/A	N/A	m/s^2	X						
	PTP	100	N/A	N/A	m/s^2	X						
	CF	100	N/A	N/A	–	X						
Direct frequency domain	BPFI	100	±5	N/A	m/s^2/Hz		X		X	X		
	BPFO	100	±5	N/A	m/s^2/Hz		X		X	X		
	FTF	100	±5	N/A	m/s^2/Hz		X		X	X		
Frequency domain NEA	BPFI	100	±5	8250–9750	m/s^2/Hz			X	X			X
	BPFO	100	±5	8250–9750	m/s^2/Hz			X	X			X
	FTF	100	±5	8250–9750	m/s^2/Hz			X	X			X
Frequency domain IMID	BPFI	100	N/A	BPFI*–1E4	$(m/s^2)^4$/Hz^4					X	X	X

Given frequency plus range of analysis 15 Hz (e.g. BPFI = BPFI + 15 Hz)

diagnostics indicators, (ii) determining learning and testing data sets, (iii) randomizing data sets, (iv) conducting learning process, (v) conducting validation process, and (vi) determining classification accuracy. Vibration data were a priori grouped into three REB condition categories (i.e. data clusters) namely: reference, poor lubricated and faulty (defected reference). Data processing parameters are presented in Table 1, while classification results in Table 2.

The parameter Diagnostic Symptom (DS) (Table 1) described the method to be used in order to determine the diagnostic indicator, i.e. RMS (Root Mean Square),

Table 2 Diagnostic strategies classification results (accuracy expressed in percentage scale)

Diagnostic strategy no.	Learning and classification method					
	Logistic regression classifier	k-nearest neighbour classifier	Normal densities based linear classifier	Normal densities based quadratic classifier	Normal densities based classifier	Neural network classifier
1	100.00	100.00	98.64	99.32	94.56	100.00
2	97.96	99.32	97.28	100.00	100.00	100.00
3	98.64	86.39	94.56	95.92	96.60	93.88
4	98.64	97.96	99.32	100.00	100.00	91.16
5	95.56	98.89	97.78	100.00	100.00	100.00
6	100.0	97.78	94.44	98.89	100.00	98.89
7	96.67	100.00	97.78	95.56	100.00	86.67

PTP (Peak To Peak), CF (Crest Factor) and BPFO, BPFI, BSF, FTF, briefly explained in Sect. 1. The first harmonic is only considered regarding all frequency components. The parameter Data Segment (DSEG) (Table 1) defines the length of an elementary vibration data segment represented in time-domain, which is used further to compute time and frequency based diagnostic indicators (i.e. symptoms). The parameter Mean Band (MB) defines a frequency tolerance range used to compute diagnostic indicators. This tolerance band is required to compensate inaccurate tracking of characteristic frequencies (i.e. BPFO, BPFI, BSF and FTF) due to engine rotating speed variations (i.e. speed measurements and control errors). The parameter Demodulation Band (DB) (Table 1) defines the frequency range used to demodulate the low-frequency vibration content. The category Diagnostic Strategy informs which diagnostic indicators were involved in particular strategies (Table 1).

Performed learning and classification process showed that time-domain analysis applying diagnostic strategy no. 1 (Table 1) with use of basic (naive) diagnostic indicators (e.g. RPM, PP) provided very good separation of tested REBs condition categories (Table 2; Fig. 8).

Similar results were achieved using direct frequency domain (Table 1) diagnostic indicators (e.g. BPFI, BPFO). Diagnostic indicators were significantly sensitive to varying operational conditions (poor-good lubrication) or change in the measurement setup (REB ass- and dissembling; test bench reconfiguration) instead of indicating a specific simulated failure mode (i.e. drilled scratch in the bearing inner race). Thus, time and direct frequency domain methods allow only to observe a drift of mean and bearing-to-bearing variance.

On the other hand, NEA, MID, and IMID methods allow to overcome the limitation resulted from masking the failure mode conditions, for example by operational conditions. NEA method provides very good separation (Fig. 9) using

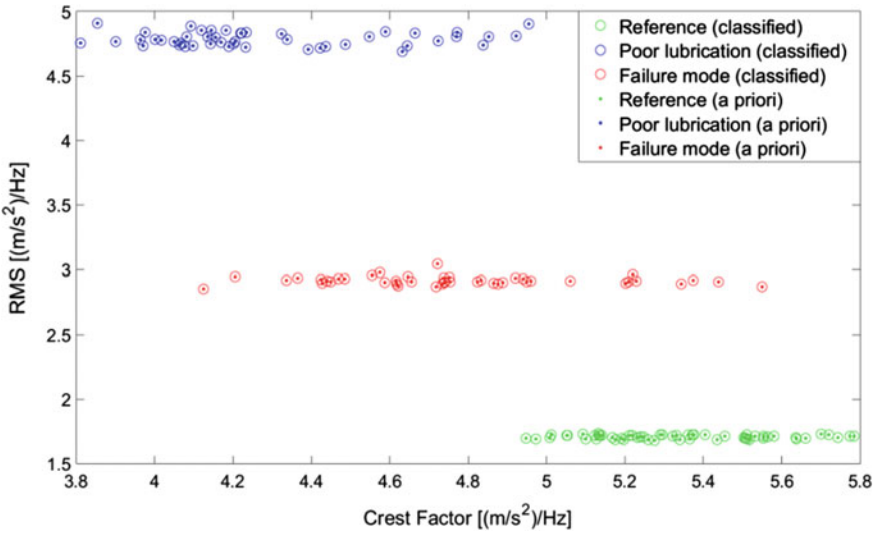

Fig. 8 Classification results (strategy no. 1, neural network classifier)

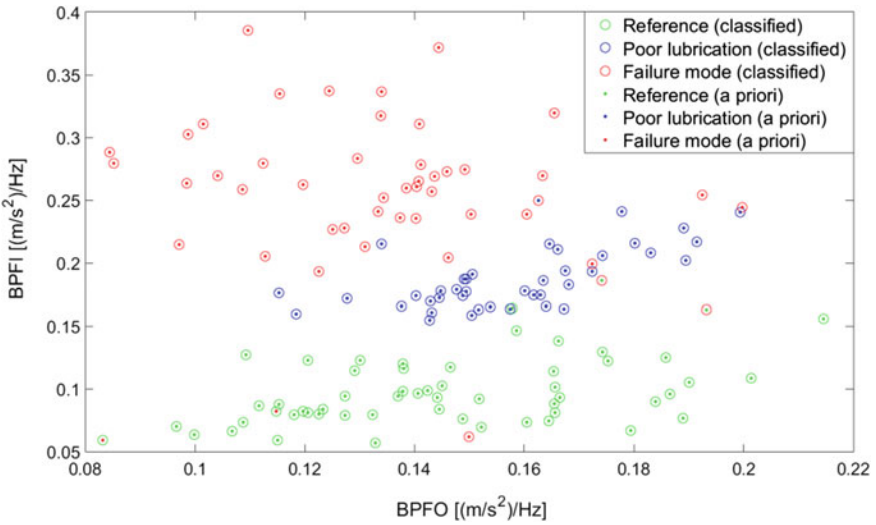

Fig. 9 Classification results (strategy no. 3, normal densities based quadratic classifier)

diagnostic strategy no. 3–4 (Table 2). NEA method distinguishes failure modes from reference conditions based on BPFI frequency component.

IMID method improves REB condition categories separation compared to NEA method (Figs. 10 and 11) using diagnostic strategy no. 7 (Table 2).

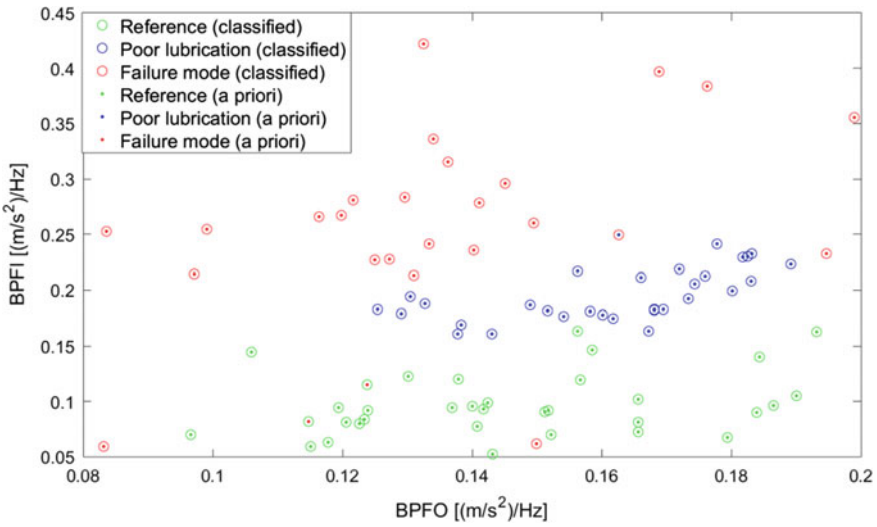

Fig. 10 Classification results (strategy no. 7, logistic regression classifier)

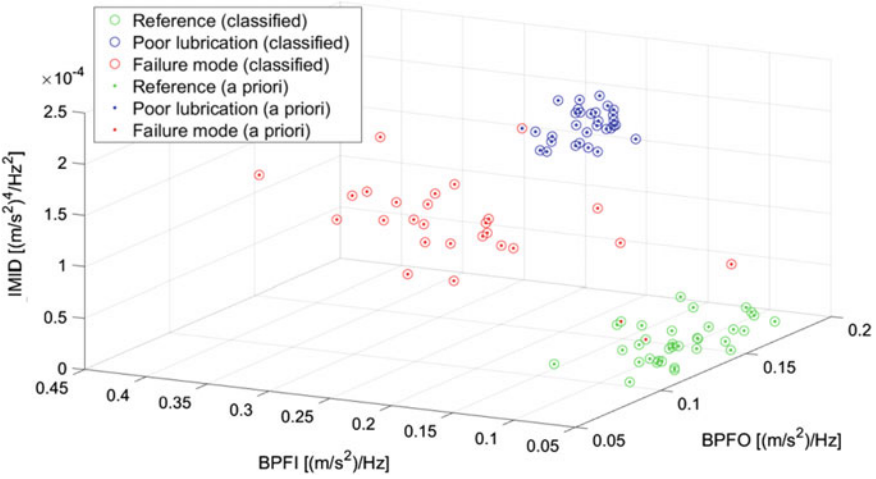

Fig. 11 Classification results in 3D plot (strategy no. 7, logistic regression classifier)

6 Conclusion

This paper reports only fragmented results to demonstrate the proposed data classification approach in order to diagnose REBs in the presence of background disturbing signals from other machine components such as combustion engine. The method is intended for automatized monitoring and diagnostics based on embedded

computers installed at vehicles (e.g. train, bus) or industrial installations (e.g. engine-generator tandem). The project scope covers statistical analysis including vibration data acquired for REB subjected to radial load in the range 1.9–7.7 kN (equivalent hydraulic load 0.5–2 MPa), stationary/non-stationary bearing operation at a few engine rotating speeds (2, 2.5, 3, 3.5, 4 and 5 kRPM), single/multiple bearing elements failures, different operating conditions (lubrication) and 10–20 REBs. Such comprehensive analysis allows to have more elaborated conclusions regarding repeatability and reproducibility of the proposed method.

Supervised learning and classification process feasibility study showed that using advance data processing methods (i.e. NEA, MID, IMID) important diagnostics information can be recovered using single-stage demodulation process and then use in robust data classification process. It was also shown that time and direct frequency methods allow to recognize correct REB condition categories. However these method do not allow to diagnose root cause of a failure mode since all the diagnostic indicators increases values. Automatized monitoring and diagnostics solutions should be more selective regarding particular diagnostic indicators and this is achievable using advance diagnostic indicators within NEA, MID, and IMID demodulation-based methods. Experimental tests showed clearly advantages of these methods and correct sensitivity to a priori applied bearing faults (e.g. inner race drilled scratch). This allows to neglect the influence of background noise representing by non-stationary operating conditions and possible structural modification (e.g. maintenance activates resulting in machine re-assembling or part replacing with new ones).

Future improvements concern higher accuracy of RPM measurements and application of unsupervised classification methods [19], while Design of Experiment (DOE) allows to conduct principal Component Analysis (PCA).

Acknowledgements The authors would like to thank to Institute of Automobiles and Internal Combustion Engines in Cracow University of Technology for making available engine tests and overall support in measurements and test-bench configuration.

References

1. Randall, R. B., & Antoni, J. (2011). Rolling element bearing diagnostics—A tutorial. *Mechanical Systems and Signal Processing, 25*(2), 485–520.
2. Popiolek K., & Pawlik P. (2016). Diagnosing the technical condition of planetary gearbox using the artificial neural network based on analysis of non-stationary signals. *Diagnostyka*, *17*(2), 57–64.
3. Sawalhi, N., & Randall, R. (2008). Simulating gear and bearing interactions in the presence of faults: Part II: Simulation of the vibrations produced by extended bearing faults. *Mechanical Systems and Signal Processing, 22*(8), 1952–1966.
4. Sawalhi, N., & Randall, R. (2008). Simulating gear and bearing interactions in the presence of faults: Part I. The combined gear bearing dynamic model and the simulation of localised bearing faults. *Mechanical Systems and Signal Processing, 22*(8), 1924–1951.

5. El-Thalji I., & Jantunen E. (2015). Fault analysis of the wear fault development in rolling bearings. *Engineering Failure Analysis*, *57*, 470–482
6. Ahmadi et al. (2015). A nonlinear dynamic vibration model of defective bearings–The importance of modelling the finite size of rolling elements. *Mechanical Systems and Signal Processing*, *52–53*, 309–326.
7. Randall, R. B. (2011). *Vibration-based condition monitoring: Industrial, aerospace and automotive applications*. New York: Wiley.
8. Urbanek, J., Antoni, J., & Barszcz, T. (2012). Detection of signal component modulations using modulation intensity distribution. *Mechanical Systems and Signal Processing, 28,* 399–413.
9. Strączkiewicz et al. (2016). Supervised and unsupervised learning process in damage classification of rolling element bearings. *Diagnostyka*, *17*(2),71–80.
10. Firla et al. (2015). Automatic method for spectral pattern association with characteristic frequencies. *Diagnostyka*, *16*(4), 77–84.
11. Mechefske, C., & Mathew, J. (1992). Fault detection and diagnosis in low speed rolling element bearings Part II: The use of nearest neighbour classification. *Mechanical Systems and Signal Processing, 6*(4), 309–316.
12. Moosavian, A., Ahmadi, H., Tabatabaeefar, A., & Khazaee, M. (2013). Comparison of two classifiers; K-nearest neighbor and artificial neural network, for fault diagnosis on a main engine journal-bearing. *Shock and Vibration, 20*(2), 263–272.
13. McLachlan, G. (2004). *Discriminant analysis and statistical pattern recognition* (Vol. 544). New York: Wiley.
14. Van Der Heijden, F., Duin, R., De Ridder, D., & M, D. (2005). *Tax, classification, parameter estimation and state estimation: An engineering approach using MATLAB*. New York: Wiley.
15. Er, M. J., Wu, S., Lu, J., & Toh, H. L. (2002). Face recognition with radial basis function (RBF) neural networks. *IEEE Transactions on Neural Networks, 13*(3), 697–710.
16. Paya, B., Esat, I., & Badi, M. (1997). Artificial neural network based fault diagnostics of rotating machinery using wavelet transforms as a preprocessor. *Mechanical Systems and Signal Processing, 11*(5), 751–765.
17. Baillie, D., & Mathew, J. (1996). A comparison of autoregressive modeling techniques for fault diagnosis of rolling element bearings. *Mechanical Systems and Signal Processing, 10*(1), 1–17.
18. Duin et al. (2000). A Matlab Toolbox for Pattern Recognition. *PRTools Version 3.0*, Delft University of Technolgy.
19. Strączkiewicz et al. (2015). Detection and classification of alarm threshold violations in condition monitoring systems working in highly varying operational conditions. *Journal of Physics: Conference Series*, *628*.

Empirical Signal Decomposition Methods as a Tool of Early Detection of Bearing Fault

Jacek Dybała and Jakub Komoda

Abstract In recent years proactive diagnostic strategies have gained more significance. Due to the need of reduction of production costs, machine downtime must be held at the lowest possible limits. This forces maintenance services to predict possible failures and plan repairs in advance. Rolling bearing faults are among the major reasons for breakdown of industrial machinery and bearing diagnosing is one of the most important topics in machine condition monitoring. Vibration signals offer great opportunity to provide reliable information about machine condition. However, in complex industrial environments the vibration signal of the rolling bearing may be covered or concealed by other vibration sources, such as gears. In case of masking the informative bearing signal by machine noise, extraction of useful diagnostic information from vibration signals becomes very difficult. The following paper presents two rolling bearing diagnosing approaches enabling early detection of rolling bearing faults at the low-energy stage of their development. By using empirical signal decomposition methods a raw vibration signal is divided into two parts: an informative bearing signal and a signal emitted from other machinery elements. For further bearing fault-related feature extraction from the informative bearing signal, the spectral analysis of the empirically determined local amplitude is applied. To test the operational effectiveness of the developed signal decomposition methods, raw vibration signals generated by complex mechanical systems employed in the industry are used. The test results show that the developed methods allow early identification of bearing fault in case of masking the informative bearing signal by signals derived from other sources.

J. Dybała (✉) · J. Komoda
Institute of Vehicles, Warsaw University of Technology,
Narbutta 84, 02-524 Warsaw, Poland
e-mail: jdybala@simr.pw.edu.pl

J. Komoda
e-mail: kuba.komoda@gmail.com

A. Timofiejczuk et al. (eds.), *Advances in Condition Monitoring of Machinery in Non-Stationary Operations*, Applied Condition Monitoring 9,
https://doi.org/10.1007/978-3-319-61927-9_14

Keywords Rolling-element bearings • Bearing diagnostics • Condition monitoring • Signal processing • Signal decomposition

1 Introduction

One of the key components of almost every technical application are rolling-element bearings, also known as rolling bearings. A catastrophic bearing damage often results in damage of a more expensive machine part (e.g. shaft, gear) and therefore the key issue of bearing diagnostics is the detection of their failure at the earliest possible point. Vibro-monitoring, due to bearing construction and characteristic of its work (interaction of rolling elements and raceways) allows recognizing a possible failure at an early stage when a bearing fault is a small pit or a spall [1–3]. Unfortunately, it often happens in industrial applications that the signals generated by different sources of vibration can disturb each other. Usually, a low-energy bearing vibration signal is recorded by an accelerometer installed on the bearing housing, which also records high-energy vibration signals generated by different machinery elements (e.g. by gears). Because many vibration diagnostic techniques are effective only at later stages of damage development, when the signal generated by the faulty component is an energy-significant part of analyzed vibration [4, 5], there is a need to use special methods of signal processing enabling separation of the vibration signal into parts generated by gears and by rolling bearings.

There is a number of techniques applied to separate bearing signals from background signals which mask it [3, 6–13]. In most cases, the effectiveness of some techniques depends, essentially, on adequate values of a given technique's parameters (e.g. convergence factor, filter order), which have to be determined in an empirical study. Moreover, some methods, such as e.g. Empirical Mode Decomposition, are quite complicated in use and time-consuming, which makes it problematic to conduct as a real-time or near-to-real time analysis [14–17]. For these reasons, such methods cannot present useful tools for industrial application and online monitoring.

The following paper presents two approaches for rolling bearing diagnostics. The authors propose two robust and fast empirical signal decomposition methods, which decompose a vibration signal into low-frequency (deterministic) and high-frequency (nondeterministic) parts. By using such methods a raw complex vibration signal of a machine is decomposed into parts generated by gears and by rolling bearings. For further bearing fault-related feature extraction from the isolated low-energy bearing vibration signal, the spectral analysis of the empirically determined local amplitude is used. The efficacy of the developed methods was verified on the basis of analysis of two real vibration signals generated by complex mechanical system employed in the industry, including vibration data of damaged and undamaged bearings.

2 Empirical Signal Decomposition Methods

This article presents two signal decomposition methods, which decompose any signal into low-frequency and high-frequency parts. According to this approach, each signal $x(t)$ can be represented as the sum of two signal parts: low-frequency $d(t)$ and high-frequency $n(t)$:

$$x(t) = d(t) + n(t) \tag{1}$$

The key issue in the presented approach is to determine the low-frequency component of the signal. Empirical Mean-based Signal Decomposition method (EMSD) determines this signal part using the technique introduced in Empirical Mode Decomposition method—the empirical determination of signal envelopes [18]. According to the devised EMSD method, the signal decomposition algorithm consists of the following steps:

Step 1: Identify all local extremes (maxima and minima) of the signal $x(t)$.
Step 2: Connect all local maxima (respectively minima) with a line known as the empirically determined upper envelope $E_{max}(t)$ (respectively the lower envelope $E_{min}(t)$). Local maxima (minima) are connected with a line by using piecewise cubic interpolation (Piecewise Cubic Hermite Interpolating Polynomials—PCHIP).
Step 3: Construct the mean of empirically determined upper and lower envelope (the low-frequency signal component) $d(t) = 0.5(E_{min}(t) + E_{max}(t))$.
Step 4: Define the high-frequency signal component as $n(t) = x(t) - d(t)$.

Median-based Signal Decomposition method (MSD) determines the low-frequency component of the signal using the technique called median filtering. Median filtering is a well-known method in the area of image processing [19–21]. The median filter is a nonlinear digital filtering technique, often used to remove noise from an image. The authors propose the use of the median filter to execute the diagnostic-oriented decomposition of a one-dimensional vibration signal to extract a diagnostically useful component of the signal. According to the MSD method, the signal decomposition algorithm consists of the following steps:

Step 1: Take as the low-frequency signal component $d(t)$ the result of median filtering of the one-dimensional signal $x(t)$.
Step 2: Define the high-frequency signal component as $n(t) = x(t) - d(t)$.

The key issue in median filtering is to determine a size of a filter window. The used value of the filter window size was determined empirically (selection criterion was to maximize the value of kurtosis of the high-frequency signal component).

Figure 1 presents the waveform of the simulated signal and the waveforms of the high-frequency and low-frequency signal components determined by the EMSD and MSD method.

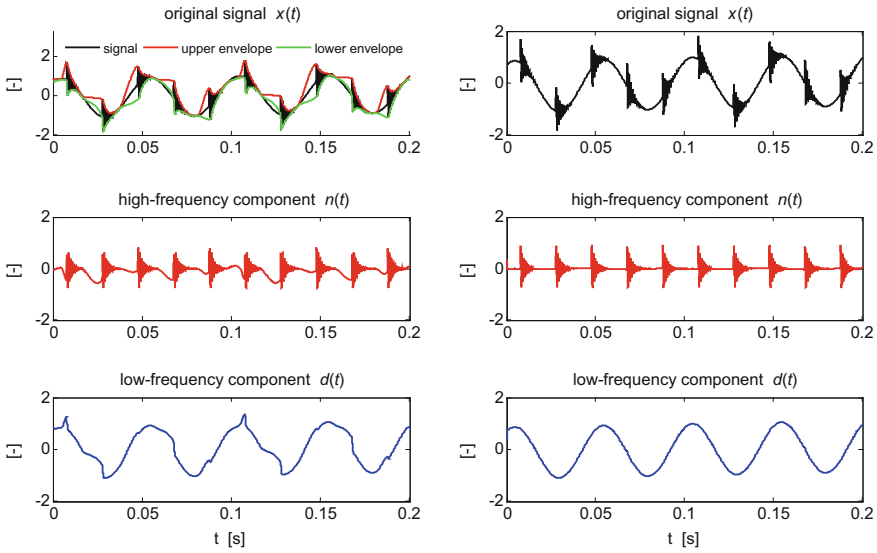

Fig. 1 Results of signal decomposition by the EMSD method (*left*) and by the MSD method (*right*)

3 Application of Proposed Diagnostic Approaches

3.1 Machine and Experiment Description

Mining machines represent a special class of machines—complex structure, high-power with time-varying load. The investigated object was a drive unit for a belt conveyor working in the mining company (Fig. 2). The drive unit consists of an electric motor, a coupling and a two-stage gearbox, that are connected with a pulley. The pulley consists of a shaft, two bearings and the coating covered by rubber (to increase friction between the pulley coating and the belt). Between the gearbox and the pulley a rigid coupling is used.

The aim of the diagnostic experiment was to evaluate the technical condition of the pulley bearing based on the analysis of acquired vibration signal. An accelerometer has been mounted using a screw on each pulley bearing housing. Two vibration signals generated by the drive unit, including vibration data of damaged and undamaged bearings, are used in this diagnostic experiment. For each measurement, the signal was acquired with the following parameters: sampling frequency $f_s = 19{,}200$ Hz, duration $T = 2.5$ s. Based on the bearing geometry and the shaft rotational speed, the characteristic defect frequencies of rolling bearings were calculated, namely: $f_{FTF} = 0.51$ Hz, $f_{BSF} = 4.45$ Hz, $f_{BFF} = 8.90$ Hz, $f_{BPFO} = 12.34$ Hz, $f_{BPFI} = 16.06$ Hz.

Unfortunately, due to rigid connection between gearbox and pulley, a serious participation of gearbox vibration in acquired vibration signal has been noticed.

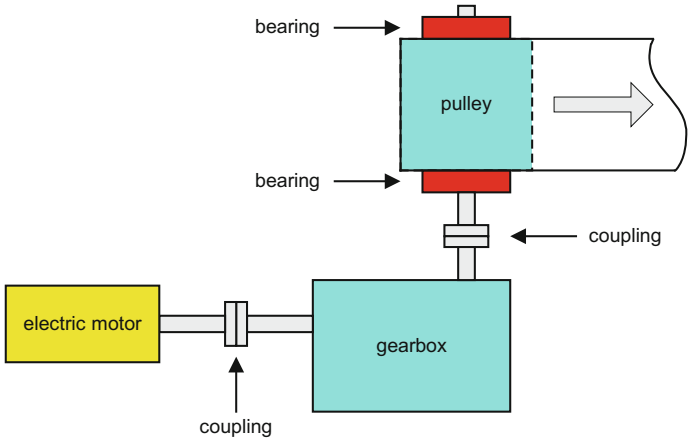

Fig. 2 Scheme of the drive unit for the belt conveyor

High-energy vibration signals generated by the gearbox completely mask the signal of interest—a low-energy bearing vibration signal.

Kurtosis analysis of the raw vibration signals does not deliver any diagnostic information. The kurtosis values of the raw vibration signals (respectively 3.44 and 3.10) are similar and their low level does not indicate any bearing fault.

Amplitude spectra and amplitude spectra of Hilbert-transform-based envelopes of acquired vibration signals (mean values were removed from the envelopes) are presented in Fig. 3. It can be observed that the spectral analysis of raw vibration signals also does not provide useful diagnostic information about the technical condition of the pulley bearings.

3.2 Decomposing of Vibration Signals

Figure 4 presents the waveforms of the vibration signals and the waveforms of the high-frequency signal components determined by the EMSD and MSD method.

3.3 Fault-Related Analysis of High-Frequency Signal Components

The kurtosis values of the high-frequency signal components are significantly different in the case of the undamaged and the damaged bearing (respectively, 16.16 and 34.70 for the EMSD method, 9.05 and 70.21 for the MSD method). High kurtosis value of the high-frequency signal component indicates that in this case

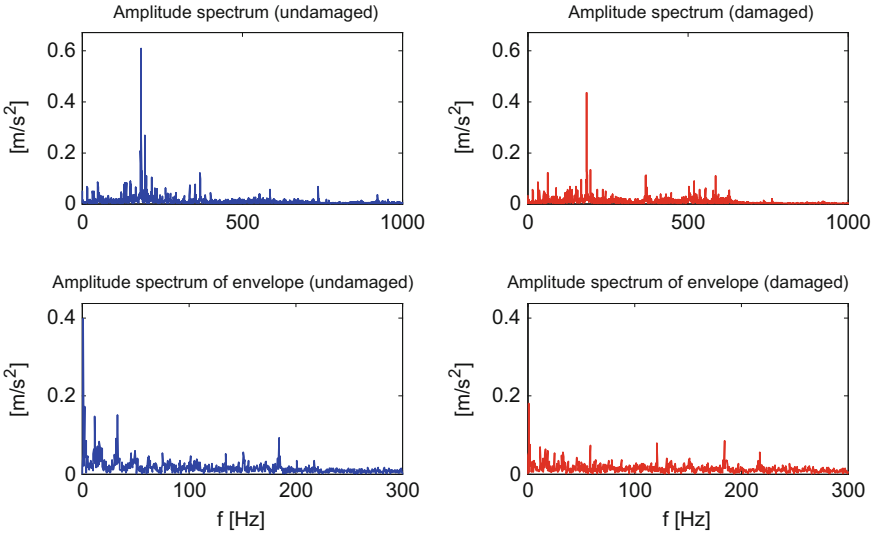

Fig. 3 Amplitude spectra (*top left*—undamaged bearing, *top right*—damaged bearing) and amplitude spectra of envelopes (*bottom left*—undamaged bearing, *bottom right*—damaged bearing) of vibration signals

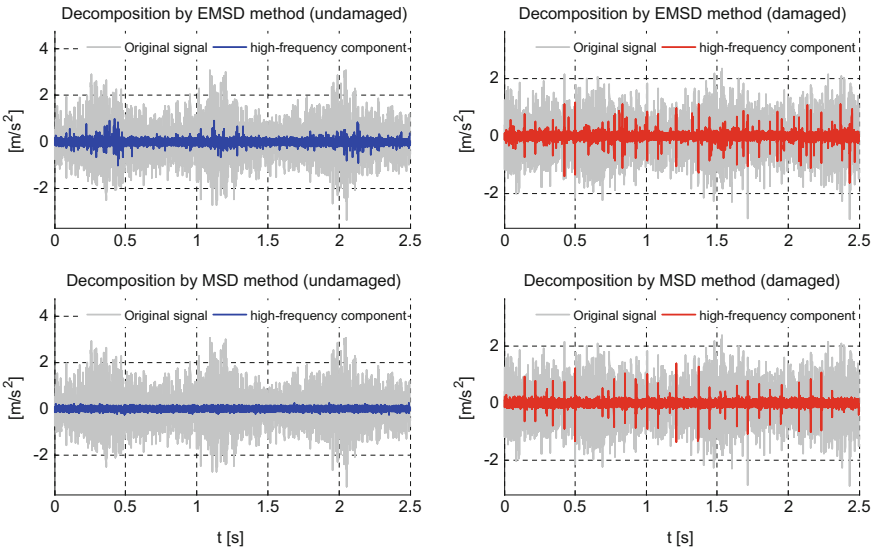

Fig. 4 Results of signal decomposition by the EMSD method (*top left*—undamaged bearing, *top right*—damaged bearing) and by the MSD method (*bottom left*—undamaged bearing, *bottom right*—damaged bearing)

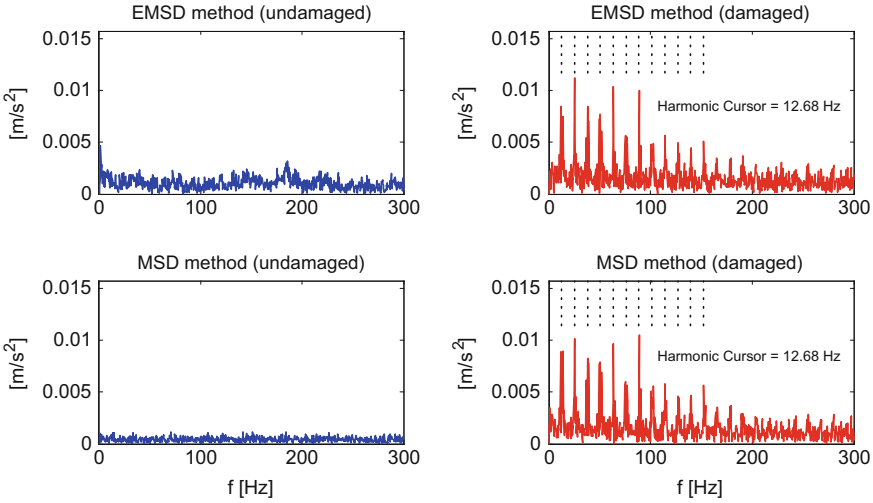

Fig. 5 Amplitude spectra of the empirically determined local amplitudes of the high-frequency signal components determined by the EMSD method (*top left*—undamaged bearing, *top right*—damaged bearing) and by the MSD method (*bottom left*—undamaged bearing, *bottom right*—damaged bearing)

some bearing fault occurs. Unfortunately, the precise nature of the fault cannot be defined by the kurtosis analysis and it is necessary to use more sophisticated diagnostic methods.

In order to perform a fault-related analysis, the spectral analysis of the empirically determined local amplitude of a signal is used. The empirically determined local amplitude of the signal is defined as:

$$a(t) = 0.5 \cdot (E_U(t) - E_L(t)) \tag{2}$$

where $E_U(t)$ is the empirically determined upper envelope of the signal and $E_L(t)$ is the empirically determined lower envelope of the signal. In order to conduct the spectral analysis, mean value was removed from the empirically determined local amplitude. Amplitude spectra of the empirically determined local amplitudes of the high-frequency signal components are presented in Fig. 5.

The detection of high-amplitude spectral components of the empirically determined local amplitude indicates that some bearing fault occurs. The basic frequency of those spectral components equals 12.68 Hz and corresponds (with 3% tolerance) to Ball Pass Frequency Outer Race (f_{BPFO}). The meaningful coincidence between these frequencies enables, with high probability, the identification of this defect as the bearing outer race defect.

4 Conclusion

This paper presents two approaches for rolling bearing diagnostics based on two robust and fast empirical signal decomposition methods. It has been shown that the developed methods enable extraction of that part of a signal from a raw vibration signal of a complex machine, which is generated by the rolling bearing. The analysis of the extracted low-energy bearing vibration signals is a two-stage process that involves the kurtosis analysis and the spectral analysis of the empirically determined local amplitude of this signal's part. The bearing fault was detected through kurtosis analysis of the extracted signal's part even when the bearing vibration signal was completely masked by machine noise. The exact nature of the bearing fault was determined by the spectral analysis of the empirically defined local amplitude of the extracted bearing vibration signal. Discovering high-amplitude spectral components of the empirically determined local amplitude allowed for identification of the defect, because the basic frequency of those spectral components was typical for the defined bearing fault.

The conducted experiment showed that the proposed methods of the bearing vibration signal extraction are very useful and important from the diagnostic point of view. They make it possible to detect damage at early stages of its development, when the signal generated by the faulty component is not an energy-significant part of a recorded and analyzed vibration. The methods have also great practical importance, as much of the rotating machinery is composed of a few shafts coupled by gears, and shafts are mounted on rolling bearings. In such a case, a bearing vibration signal can be completely masked by a gear vibration signal and vibro-diagnostics of bearings becomes problematic.

Further research will concern the attempts to implement developed methods in commercial machine condition monitoring systems. In addition, work will be undertaken on the development of adaptive median filtering, which enables, among others, adaptive determination of the filter window size.

References

1. Jasiński, M., & Radkowski, S. (2001). Bispectrum as a symptom of damages in a rolling bearing diagnostics. *Machine Dynamics Problems, 25*(1), 93–107.
2. Nadabaică, D. C., Nedeff, V., Radkowski, S., & Mączak, J. (2013). The importance of FFT and BCS spectrums analysis for diagnosis and prediction of rolling bearing failure. *Diagnostyka, 14*(4), 3–12.
3. Randall, R. B., & Antoni, J. (2011). Rolling element bearing diagnostics—A tutorial. *Mechanical Systems and Signal Processing, 25*(2), 485–520. doi:10.1016/j.ymssp.2010.07.017.
4. Ho, D., & Randall, R. B. (2000). Optimization of bearing diagnostic techniques using simulated and actual bearing fault signal. *Mechanical Systems and Signal Processing, 14*(5), 763–788. doi:10.1006/mssp.2000.1304.

5. McFadden, P. D., & Smith, J. D. (1984). Vibration monitoring of rolling element bearings by the high-frequency resonance technique—a review. *Tribology International, 17*(1), 3–10. doi:10.1016/0301-679X(84)90076-8.
6. Antoni, J., & Randall, R. B. (2004). Unsupervised noise cancellation for vibration signals. Part I—evaluation of adaptive algorithms. *Mechanical Systems and Signal Processing*, *18*(1), 89–101. doi:10.1016/S0888-3270(03)00012-8.
7. Barszcz, T. (2009). Decomposition of vibration signals into deterministic and nondeterministic components and its capabilities of fault detection and identification. *International Journal of Applied Mathematics and Computer Science, 19*(2), 327–335. doi:10.2478/v10006-009-0028-0.
8. Chaturvedi, G. K., & Thomas, D. W. (1981). Adaptive noise cancelling and condition monitoring. *Journal of Sound and Vibration, 76*(3), 391–405. doi:10.1016/0022-460X(81)90519-8.
9. Khemili, I., & Chuchane, M. (2005). Detection of rolling element bearing defects by adaptive filtering. *European Journal of Mechanics—A/Solids, 24*(2), 293–303. doi:10.1016/j.euromechsol.2004.10.003.
10. Lee, S. K., & White, P. R. (1998). The enhancement of impulsive noise and vibration signals for fault detection in rotating and reciprocating machinery. *Journal of Sound and Vibration, 217*(3), 485–505. doi:10.1006/jsvi.1998.1767.
11. Shao, Y., & Nezu, K. (2005). Design of mixture de-noising for detecting faulty bearing signals. *Journal of Sound and Vibration, 282*(3–5), 899–917. doi:10.1016/j.jsv.2004.03.051.
12. Tse, P. W., Gontarz, S., & Wang, X. J. (2007). Enhanced eigenvector algorithm for recovering multiple sources of vibration signals in machine fault diagnosis. *Mechanical Systems and Signal Processing, 21*(7), 2794–2813. doi:10.1016/j.ymssp.2007.02.010.
13. Zimroz, R., & Bartelmus, W. (2011). Application of adaptive filtering for weak impulsive signal recovery for bearings local damage detection in complex mining mechanical systems working under condition of varying load. *Solid State Phenomena, 180,* 250–257. doi:10.4028/www.scientific.net/SSP.180.250.
14. Dong, H., Qi, K., Chen, X., Zi, Y., He, Z., & Li, B. (2009). Sifting process of EMD and its application in rolling element bearing fault diagnosis. *Journal of Mechanical Science and Technology, 23*(8), 2000–2007. doi:10.1007/s12206-009-0438-9.
15. Dybała, J., & Zimroz, R. (2012). Application of empirical mode decomposition for impulsive signal extraction to detect bearing damage—industrial case study. In T. Fakhfakh et al. (Eds.), *Condition Monitoring of Machinery in Non-Stationary Operations. Proceedings of the Second International Conference "Condition Monitoring of Machinery in Non-Stationary Operations" CMMNO2012* (pp. 257–266). Berlin Heidelberg: Springer. http://dx.doi.org/10.1007/978-3-642-28768-8_27.
16. Dybała, J., & Zimroz, R. (2014). Rolling bearing diagnosing method based on empirical mode decomposition of machine vibration signal. *Applied Acoustics, 77,* 195–203. doi:10.1016/j.apacoust.2013.09.001.
17. Yu, D., Cheng, J., & Yang, Y. (2005). Application of EMD method and Hilbert spectrum to the fault diagnosis of roller bearings. *Mechanical Systems and Signal Processing, 19*(2), 259–270. doi:10.1016/S0888-3270(03)00099-2.
18. Huang, N. E., Shen, Z., Long, S. R., Wu, M. C., Shih, H. H., Zheng, Q., Yen, N. C., Tung, C. C., & Liu, H. H. (1998). The empirical mode decomposition and the Hilbert spectrum for nonlinear and non-stationary time series analysis. *Proceedings of the Royal Society of London, Series A—Mathematical, Physical and Engineering Sciences, 454*(1971), 903–995. http://dx.doi.org/10.1098/rspa.1998.0193.
19. Astola, J., & Kuosmanen, P. (1997). *Fundamentals of Nonlinear Digital Filtering, Electronic Engineering Systems Series*. CRC Press. ISBN 0-8493-2570-6.

20. Huang, T., Yang, G., & Tang, G. (1979). Fast two-dimensional median filtering algorithm. *IEEE Transactions on Acoustics, Speed and Signal Processing, 27*(1), 13–18.
21. Pitas, I., & Venetsanopoulos, A. (1990). *Nonlinear Digital Filters. Principles and Applications* (Vol. 84). The Springer International Series in Engineering and Computer Science, ISBN 978-1-4419-5120-5.

Using Vibroacoustic Signals in Evaluation of Knocking Combustion in a Dual Fuel Engine

Krzysztof Szczurowski, Stanisław Radkowski, Łukasz Zieliński and Damian Walczak

Abstract Current development of automotive domain heading towards the ever decreasing pollution emission as well as using the alternative fuels resulted in analysis of the possibilities to power the combustion engines with combinations of several fuels. The multi-fuel engines designed in such a way can use the advantages of specific fuel. The most popular trend uses self-ignition engines to operate on the fluid fuels such as the diesel oil or its mixtures, and on the gaseous fuel such as CNG or LPG. In Poland, because of the extensive network of LPG stations, the interest in adapting vehicles to this type of fuelling increases. This is particularly vital for heavy and large goods vehicles, in the case of which the fuel saving possibility of a few to a dozen or so percent is very interesting. Using gaseous fuels in engines with the self-ignition results in the occurrence of the previously unknown phenomena. Such a phenomenon is, among others, the knocking combustion, the cause for which is the premature ignition of the air-fuel mixture most frequently occurring in the area of the top dead centre. The knocking combustion is characterized by a faster increase in pressure as compared to normal combustion, and it is a detrimental phenomenon to the engine operation, especially before the top dead centre. The growth speed of the combustion pressure can be correlated with the manner of combustion, which is also evident in the vibroacoustic signal, whose characteristics will undergo changes alongside the combustion speed. The analysis of the remaining work parameters influencing the vibroacoustic signal will enable

K. Szczurowski (✉) · S. Radkowski · Ł. Zieliński · D. Walczak
Warsaw University of Technology, Institute of Vehicles,
Narbutta 84, 02-524 Warsaw, Poland
e-mail: kszczur@simr.pw.edu.pl

S. Radkowski
e-mail: ras@simr.pw.edu.pl

Ł. Zieliński
e-mail: lzielinski@mechatronika.net.pl

D. Walczak
e-mail: d.walczak@mechatronika.net.pl

A. Timofiejczuk et al. (eds.), *Advances in Condition Monitoring of Machinery in Non-Stationary Operations*, Applied Condition Monitoring 9,
https://doi.org/10.1007/978-3-319-61927-9_15

determining the moments of the knocking combustion occurrence and will thus allow for optimization of the gaseous fuel dose, which directly influences the pollution emission as well as the economical aspect.

Keywords Knocking · CI · Model · Dual fuel

1 Introduction

In relation to the increasingly popular use of alternative fuels employed to power combustion engines [1] and tightened requirements connected with exhaust emissions of engines with compression-ignition, the works are being carried out on making use of engines with compression-ignition as engines with multi-fuel powering and using the diesel oil dose as an impulse igniting the other fuel supplied in a gaseous form to the intake manifold. The most frequently used fuels are LPG [2, 3] and CNG [4]. These fuels are characterized with considerable resistance to self-ignition, defined by the octane number, and hence, for example LPG has the octane number dependent upon the composition and amounting to over 100 and CNG- to over 110 [5].

Using two fuels to power a combustion engine allows for utilizing the advantages of both fuels and obtaining a higher engine efficiency than in the case of one fuel [6]. An important factor motivating to more intensive search for unconventional fuels is an ecological aspect. In Poland, LPG (Liquified Petroleum Gas) i.e. the liquid gas, a mixture of propane and butane, is most popular because of the of cost reduction of consuming fuel. Vehicle use is the operational cost that consists of maintenance costs as well. LPG is produced as a by-product of petroleum refining or from natural deposits.

Commercially used control of the dual-fuel supply, diesel + LPG, is an emulation of a signal from the accelerator pedal (APP—Accelerator Pedal Position) [7], and adding a share of LPG in place of the reduced diesel oil dose. In the common rail system engines, emulation influences the pressure in the common rail. The maps of the gas injection size are created, depending on the engine rotational speed and position of the accelerator pedal. This was the simplest way of adjusting the LPG dose to the diesel oil dose, so as to obtain the proper engine operation and the LPG addition size of about 20%, relative to the whole diesel oil dose.

Such a share size was determined on the basis of tests conducted by many subjects dealing with this area of interest [8, 9]. It would be advisable to increase this share, unfortunately, feeding gaseous fuel through the intake valve results in creation of the fuel-air mixture in the cylinder during compression, instead of just air present there so far. During compression of the mixture, the phenomena take place which have been known so far only from engines with spark ignition, for example knocking combustion [10].

Addition of a gaseous LPG fuel in place of a 20% dose of diesel oil, with similar calorific value of both fuels kept, allows to observe a greater increase in pressure values resulting from a different character of the LPG fuel combustion process, increasing torque and power relative to the 100% dose of diesel oil without addition of LPG. The increase rates are big enough to influence significantly the speed of the pressure growth, therefore they need to be controlled in order to avoid engine damage.

However, this method of dose adjustment is not sufficient to maximize the LPG dose and achieving the most optimized composition of diesel oil + LPG. The best way to control the dose in a dual-fuel engine is developing the system creating the dual-fuel dose adjusted to current conditions of engine work (load, rotational speed, temperature in the intake and exhaust systems, and in many others). Such an approach will enable also the indirect consideration of a difference in composition of a summer and winter LPG fuel.

In the case of vibroacoustic tests of the engines powered with the diesel oil + LPG mixture, rapid pressure changes caused by knocking combustion play an important role. To make it possible to take them into consideration in the created models, a description of the phenomenon occurring during knocking combustion should be developed. Because of the significantly random character of the thermodynamic phenomena taking place during knocking combustion, developing the models satisfying the expectations thermodynamic-wise has not been possible yet.

In the presented scheme, the effects of knocking combustion in the form of rapid pressure changes spreading in the combustion chamber came into focus. At the moment of ignition a wave is created, which propagates the air/fuel mixture causing local pressure changes that could be responsible for generation of subsequent self-ignition outbreaks. The proper compilation of created pressure impulses generating the fast-extinguished waves can enable the description of the phenomenon, complying with the model requirements with vibroacoustic tests.

2 Model

During the compression stroke, a fast pressure and temperature increase takes place, which can result in ignition of the fuel-air mixture, that will cause a rapid increase in pressure and will cause the occurrence of the acoustic wave propagating in the cylinder. From the perspective of developing mathematical models for the occurring phenomena, such an impulse can be developed using the Dirac's delta function. The theoretical description of this phenomenon (1) as well as its graphic representation (Fig. 1a) are commonly known.

$$\delta(x)\begin{cases} +\infty, & x=0 \\ 0, & x\neq 0 \end{cases} \tag{1}$$

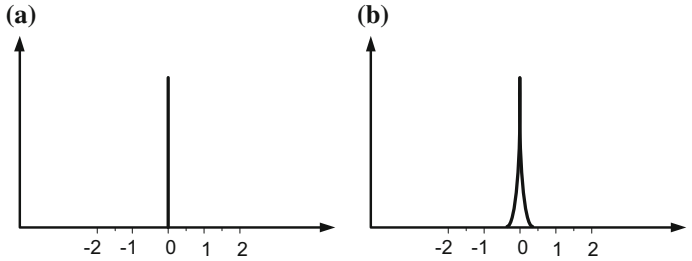

Fig. 1 The dirac delta function: **a** theoretical plot, **b** curve used as a curve of the pressure growth

As is a well-known fact, a property of the Dirac delta function is the normalized area under the curve, which is shown in relationship 2.

$$\int_{-\infty}^{+\infty} \delta(x)dx = 1 \tag{2}$$

To fulfil the condition of relationship 1, the amplitude tending to infinity, the time tending to 0 must be ensured, unfortunately, in the case of combusting the mixture, and hence the pressure increase, the time, even though very short, does not tend to 0. Because of this, using the property illustrated by relationship 2, the decision was taken to describe the excitation as a Gaussian function, which also meets the requirements from relationship 2, and is described by relationship 3.

$$\sigma_a(x) = \frac{1}{a\sqrt{\pi}} e^{-x^2/a^2}; gdzie \quad a \to 0 \tag{3}$$

It is shown in Fig. 1b.

Observation of a propagating wave and of the other pressure changes takes place at one point with the use of a pressure sensor, so-called engine indicating. With such an approach, the wave created by the knocking ignition will be visible as a fast-fading response to the impulse excitation described by relationship 4 and is shown in Fig. 2a.

$$y(t) = Ae^{-at} sin(\omega_1 * t). \tag{4}$$

where:

a, ω1 Model parameters.

Analyzing the curve of pressure changes in the combustion chamber requires taking into consideration a few additional variables, such as: a change in volume caused by the moving piston or a propagating wave in the chamber which will cause a local pressure growth higher than the compression pressure, which can result in subsequent knocking ignition instances. In such a case, a model consisting

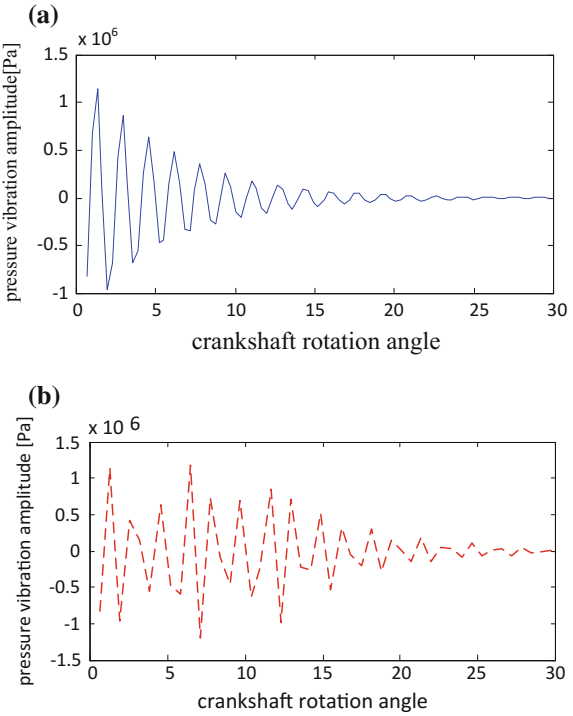

Fig. 2 **a** Pressure changes caused by an impulse described by the Gaussian function. **b** Pressure changes caused by an N impulse described by the Gaussian function

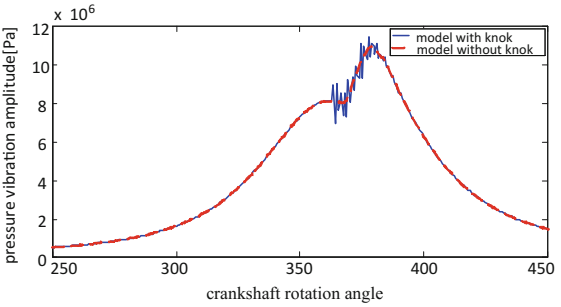

Fig. 3 Curve of combustion pressure changes by the models

of several impulses occurring with a delay caused by a propagating pressure wave should be considered. Figure 2b shows the curve of the response to such an excitation. Figure 3 presents combustion pressure changes compared with the model.

The curve illustrating the pressure inside the combustion chamber of an engine with compression ignition with dual-fuel supply is shown in Fig. 4 with the phenomenon of knocking combustion taken into account. The figure shows the pressure curves for the 30% LPG share (this level of an LPG participation ensures the occurrence of knocking combustion) and various engine loads.

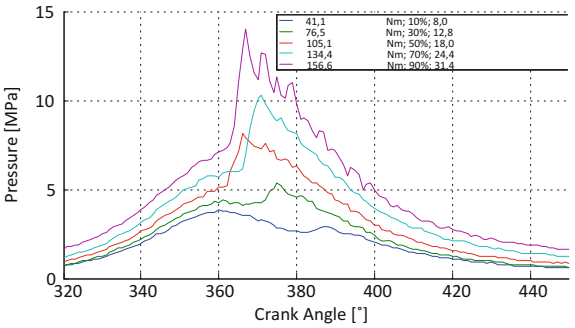

Fig. 4 Curve of combustion pressure changes by the measurements

3 Measurements

In order to verify the suggested approach, the measurement results were used. The investigation was conducted in a series of tests: acceleration, during operation with the constant load and constant rotational velocity. They were carried out on the chassis dynamometer at the Automotive Industry Institute. During the tests, the head vibrations (the B&K and knock sensors), the excess oxygen ratio (λ), the air temperatures in the intake and exhaust manifolds, fuel doses, amount of air, pressure in the intake manifold, pressure inside the combustion chamber (PSG), rotational velocity, engine load, torque, were registered among other parameters.

During the tests, the LabVIEW software was used to register all measured signals. For the registration of vibrations, the knock sensor was used (Bosch 0 261 231 004), whereas for the registration of accelerations—a three-axis vibration sensor (B&K, 4504 type). The signals were sampled with the frequency of 51.2 kHz, and every measurement lasted 5 s. The NI 9234 measurement cards were used for the measurements. The whole vehicle located on the chassis dynamometer is shown in the last picture of this chapter. The tests were performed for different LPG shares and for various rotational velocities.

The engine of the tested vehicle was adapted to the dual-fuel operation by means of mounting an additional LPG installation with injectors located in the intake manifold tubes. The gas is injected sequentially, supplying all cylinders one by one.

As a result of the conducted experiment, the curves of pressure changes in the combustion chamber were obtained. The signals were processed to enable levelling out the influence of disturbances, and next, they were compared while maintaining certain parameters unchanged. Below, (Fig. 4) the pressure curves are shown for the 30% LPG share; this participation value was selected because, as ensued from the data presented earlier, it would ensure the occurrence of the knocking combustion phenomenon during combustion of the fuel-air mixture.

In order to determine the occurrence of the knocking combustion phenomenon, a notion of intensity of knocking combustion was used, defined in the works of [11, 12]. To check the speed of the combustion pressure increase, the curves of pressure increase for diesel oil only (Fig. 5) and with the share of 30% LPG (Fig. 6).

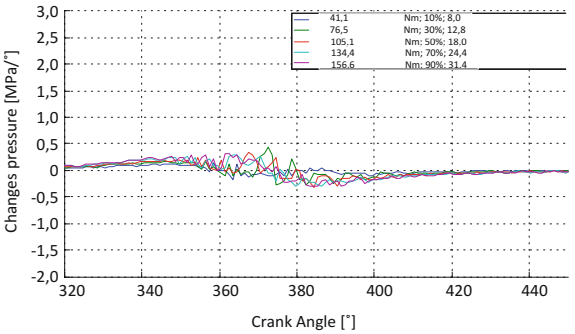

Fig. 5 Curve of changes in the speed of combustion pressure increase for diesel oil only

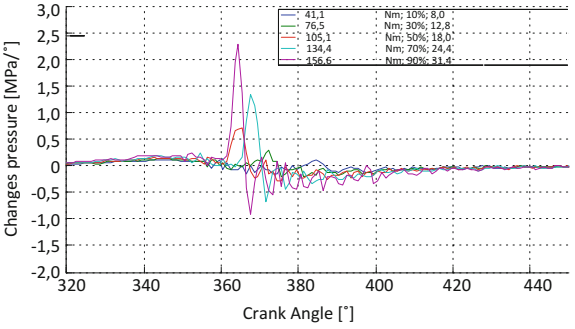

Fig. 6 Curve of changes in the speed of combustion pressure increase for diesel oil with 30% LPG share

As can be seen in Fig. 7, after the parameters were selected, the model precisely reflects the pressure changes taking place during the occurrence of knocking combustion. The greatest importance, deciding about the occurrence of knocking combustion and its maximal amplitude of the pressure changes during the mixture combustion, has not the LPG fuel share in the dose but physically its absolute quantity located in the combustion chamber during the compression stroke. Among visible discrepancies, other dynamic phenomena taking place during operation of the piston-crankshaft assembly and therefore in the space over the piston during its motion in the work-stroke, also should be taken into consideration.

It should be kept in mind that with the use of the piston-crankshaft assembly, the measured cylinder is coupled with other cylinders, where similar phenomena take place, only shifted in time, and the shift depends on the engine's rotational velocity.

Comparison of the pressure change signals with the measured vibration signals (Figs. 7 and 8) allows for an observation that the proportion of changes is maintained, i.e. the pressure changes occurring during knocking combustion are transferred proportionally on the excited amplitude of vibration accelerations. This should allow for determination of the intensity of the pressure increase on the basis of the measured amplitude of vibration accelerations.

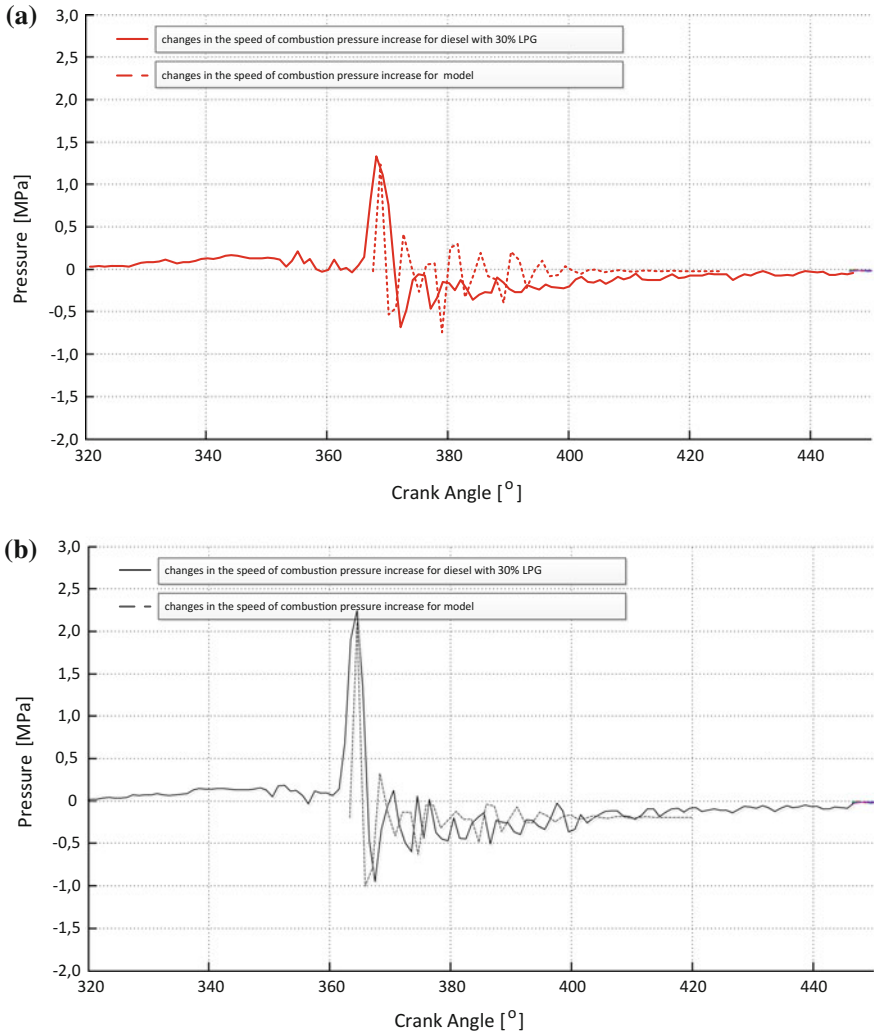

Fig. 7 Curve of changes in the speed of combustion pressure increase for the measurement and model: **a** for 70% load, **b** for 90% load of the maximal moment generated at the investigated engine's rotational velocity

4 Conclusion

Using the description of the phenomenon of wave propagation, induced by the uncontrolled ignition inside the engine's combustion chamber, makes it possible to prepare the description of the knocking combustion phenomenon, illustrating the dynamic pressure changes influencing the system's dynamic behavior. Such a description of the knocking combustion phenomenon can be used to build models

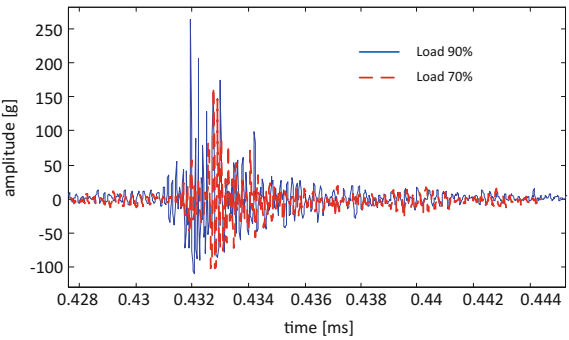

Fig. 8 Curve of changes in vibration amplitude, perpendicular to cylinder axis, for 70 and 90% load of the maximal moment for investigated rotational velocity with 30% LPG share

describing the system's dynamics, particularly in vibration-noise tests of dual-fuel engines with compression-ignition. This kind of description will enable taking into consideration this phenomenon while creating the limits determining the operation conditions for the tested engine, as well as allowing for mineralization of its influence on the environment through vibrations and noise.

References

1. Lasocki, J., Kołodziejczyk, K., & Matuszewska, A. (2015). Laboratory-scale investigation of biogas treatment by removal of hydrogen sulfide and carbon dioxide. *Polish Journal of Environmental Studies, 24*(3), 1427–1434.
2. Luft, S. (2007). Analysis of combustion process in dual fuel compression ignition engine fuelled with LPG in the liquid phase. *Journal of Kones, Powertrain and Transport, 14*(3), 355–362.
3. Wierzbicki, S. (2011). Effect of the parameters of pilot dose injection in a dual fuel diesel engine on the combustion process. *Journal of KONES Powertrain and Transport, 18*(3), 499–506.
4. Zulkifli, F. H., Fawzi, M., & Osman, S. A. (2015). A review on knock phenomena in CNG-diesel dual fuel system. *Applied Mechanics and Materials, 773–774,* 550–554.
5. CNG na świecie. PGNiG SA. [dostęp 2011-02-10].
6. Szczurowski, K., Radkowski, S., Walczak, D., & Zieliński, Ł. (2014). The effect of addition of LPG and camelina oil esters on noise and vibration in a dual fuel CI engine. *Diagnostyka, 15*(4). e-ISSN 2449-5220.
7. Walczak, D., Zieliński, Ł., Szczurowski, K., & Radkowski, S. (2015). Proposed methods of controlling dual fuel CI engine using CAN-BUS information. *Dynamical Systems, Mechatronics and Life Sciences*, 543–554. ISBN 978-83-7283-707-3.
8. Wierzbicki, S., Śmieja, M., & Piętak, A. (2013). Preliminary tests on an integrated laboratory control system for the feeding system of a dual-fuel diesel engine and its load. *Journal of KONES Powertrain and Transport, 20*(2).
9. Stelmasiak, Z. (2014). Limitations of enrichment of gaseous mixture in dual fuel engines. *Eksploatacja i Niezawodnosc—Maintenance and Reliability, 16*(4), 537–544.
10. Witwit, A. R., et al. (2013). Modern methods in engine knock signal detection. *Procedia Technology, 11,* 40–50.

11. Różycki, A. (2009). Wskaźnik intensywności spalaniastukowego w dwupaliwowym silniku spalinowymo zapłonie samoczynnym. *Silniki Spalinowe,* (S.C2).
12. Różycki, A. (2011). Stuk i zadymienie spalin jako kryteria doboru parametrów wtrysku oleju napędowego. *Transcomp—XV International Conference Computer Systems Aided Science, Industry and Transport, Logistyka, 6*, 2563–2570.

Hybrid Scheme for Wind Turbine Condition Monitoring Based on Instantaneous Angular Speed and Pattern Recognition

Ilyes Khelf, Jose L. Gomez, Adeline Bourdon, Hugo Andre and Didier Remond

Abstract Wind turbines are designed to operate under varying conditions of speed and load. These rough operational conditions undermine conventional monitoring techniques and lead to unexpected failures of mechanical components. This work comes within the framework of wind turbine on-line condition monitoring. For this purpose, a particular attention was given to Instantaneous Angular Speed (IAS) emerging as a viable alternative to vibration analysis, especially in non stationary conditions. In this work, IAS signals were recorded from extensive measurement campaigns on different operating wind turbines. Suitable processing techniques have been specifically developed and allowed to analyze signals in healthy condition and in the presence of different bearing faults. Based on the latter, a huge number of expected relevant indicators was extracted. Different configurations of features transformation, selection and classification tools were tested. An optimized hybrid scheme has been designed. This approach allowed an optimal exploitation of IAS information and the construction of an effective tool for wind turbine condition monitoring.

Keywords Condition monitoring · Instantaneous angular speed · Wind turbine · Feature selection · Pattern recognition

1 Introduction

Nowadays, wind is considered as one of the most attractive alternative energy solutions. Wind turbine energy production market is getting bigger and optimal use of available resources becomes important. To get the most of wind energy sources, intensive attention of turbine component operation condition should be taken [1].

I. Khelf (✉) · J.L. Gomez · A. Bourdon · D. Remond
CNRS UMR5259, INSA-Lyon, LaMCoS, Univ Lyon, 69621 Lyon, France
e-mail: ilyes.khelf@insa-lyon.fr

I. Khelf · J.L. Gomez · H. Andre
MAIA EOLIS, Tour de Lille, Boulevard de Turin, 59000 Lille, France

A. Timofiejczuk et al. (eds.), *Advances in Condition Monitoring of Machinery in Non-Stationary Operations*, Applied Condition Monitoring 9,
https://doi.org/10.1007/978-3-319-61927-9_16

Wind turbines belong to a specific category of rotating machines. They operate in non-stationary conditions undermining conventional monitoring techniques [2].

In recent years, Instantaneous Angular Speed (IAS) emerged as an alternative condition monitoring tool, tailored to machines operation monitoring in non-stationary conditions. This technique has proven effective where promising results and developments were seen and discussed in previously published papers [3–7].

The extraction of relevant information from IAS Signal is a critical aspect of an efficient condition monitoring. This information may be represented in a set of indicators extracted from the signals [8]. Mainly, two approaches are seen in literature to optimize the construction of indicator sets. The former, based on the selection of a number of indicators from the entire set [9]. The second is about the transformation of indicators from one space to another [10, 11].

For the evaluation of indicators sets relevance, pattern recognition tools could be used as objective assessors. In fact, the classifier accuracy depends greatly on the quality of indicators composing their input vector, and their ability to distinguish the different operating conditions.

In this paper, a hybrid scheme for condition monitoring of operating wind turbines is introduced. Firstly, descriptions of the performed experiments and the exploited data sources are presented. Then, an attention was taken on indicators construction and processing techniques, within these techniques, standardization and Principal Component Analysis (PCA) were used for the indicator transformation, while Genetic Algorithms (GA) and selection filters have been tested for the indicator selection. Radial Basis Function neural networks (RBF) were subsequently built and the classification results used to assess the relevance of the constructed indicators sets.

2 Materials and Methods

2.1 Experimental Procedure

A judicious instrumentation allowed MAIA EOLIS to collect information on their wind turbine condition over long periods. In this paper data collected on two different machines is used. Both machines have the same transmission kinematic shaft line. The wind turbine set up is presented in Fig. 1. Two encoders were installed on the wind turbine drive train (three stages gear box), mounted on the High Speed Shaft (HSS) and on the Low Speed Shaft (LSS). In this paper only the HSS signals are studied.

Mainly, two different bearing defects were observed (Bearing A: Spalling in the inner and the outer rings and Bearing B: Spalling in the outer ring, Fig. 1), one on each machine. The two defective bearings are both installed on the HSS, on different locations.

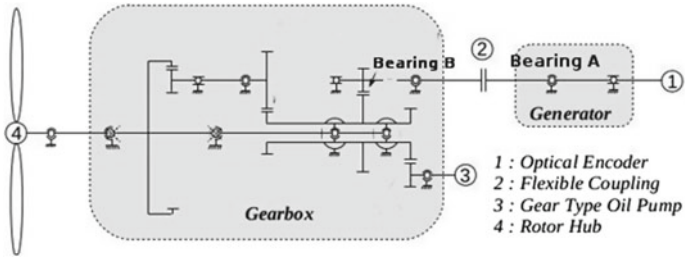

Fig. 1 Wind Turbine Set-up

In this work, we seek for the construction of specific monitoring tools for each element of the machine. Therefore, for monitoring bearing (A), we have considered: signals from the faulted bearing (A), signals from a healthy machine, and, to enhance the robustness of the tool, a set of signals presenting other defects affecting the machine.

2.2 IAS Signal

The Elapse time method is used in this work for the processing of encoder signals and the construction of IAS [2]. The rotating speed ω_i is estimated for each rising edge of the encoder signal i by counting the pulses delivered by a high frequency clock, respecting Eq. 1

$$\omega_i = \frac{60}{R} \cdot \frac{f_c}{N + \epsilon} \tag{1}$$

where R denotes the resolution of the encoder; fc the counter frequency; N is the entire number of pulses delivered by the High frequency clock between two rising edges of the encoder; ϵ an uncertainty term that globally includes the geometrical, electrical and quantification measurement errors.

An apodization window is then applied to the IAS signal to prevent from the broadband effect induced by the macroscopic trend of the angular speed [6]. An adapted Fourier Transform can also be applied to the construction of an Angular Frequency Spectrum in order to emphasize cyclic periodicities. Figure 2 shows in (a) an extracted IAS signal, and in (b) two Angular Frequency Spectra, one with (red) and one without (blue) the presence of bearing defects, focused around the characteristic frequency (Bearing BPFO: Ball Pass Frequency Outer (Outer ring)).

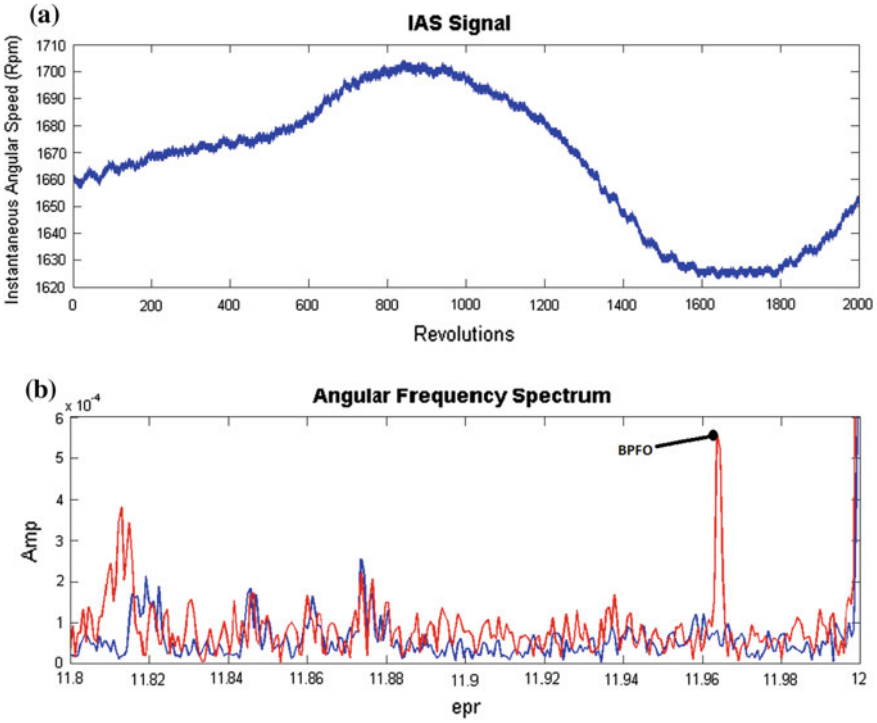

Fig. 2 **a** IAS Signal **b** IAS Spectra

3 Construction of the Databases

In this work, the monitoring process is only focused on the bearing A (see Fig. 1) installed on the first Wind Turbine (WT1), the bearing B defect condition is considered as the third condition.

3.1 Indicators Extraction

As the monitoring process presented in this work focuses only on a bearing (A) defect, specific indicators were extracted from IAS signals and order spectra at characteristic angular frequencies. Globally four kinds of indicators were extracted:

- **Defect Frequencies Amplitude level**: The amplitude level at the characteristic frequencies.
- **Band RMS**: the Root Mean Square of energetic frequency bands.
- **Ratio**: Different ratios(amplitude/amplitude and amplitude/band).
- **Scalar**: Scalar indicators extracted from the raw signal.

Besides raw indicators extraction, two indicator transformation procedures were done:

- Standardization procedure according to rotational speed, which allows moderating the effects of speed and load variation on indicators amplitudes [5].
- Principal Components Analysis creates uncorrelated indicators in a low dimensional representation [10].

3.2 Indicator Selection

Indicator selection allows finding from a complete set of indicators those that are most relevant and that can separate the best operating conditions.

Indicator selection can be undertaken in two approaches (Filter and Wrapper), according to their dependence or independence on the desired application. In the filter approach, we seek an individual evaluation of indicators based on some relevance measures. By contrast Wrapper approach seek a global evaluation of indicator sets based on classifier accuracy [9, 12].

3.2.1 ReliefF Filter

ReliefF seeks an estimation of indicator quality based on the distance between nearest neighbors. For this purpose, given a randomly selected example A from a data set S with k indicators, ReliefF searches the data set to its nearest neighbors: one of the same class, called the nearest hit H, and others from different classes, called the nearest miss M. It updates the quality estimation $W[IN_I]$ for all indicators IN based on the values of difference function $Diff()$ to X, H and M, on m iterations.

$$Diff\left(A, I_1, I_2\right) = \frac{\left|value\left(A, I_1\right) - value\left(A, I_2\right)\right|}{min\left(A\right) - max\left(A\right)} \tag{2}$$

and for $P(c)$ the prior probability of the class and $1 - P(class(r))$ represents the sum of probabilities for the misses classes we have: $W[IN_I] = W[IN_I] - \sum_{j=1}^{k} Diff(A, R_i, H_j)/(m.k)$

$$+ \sum_{C \neq cl(R_i)} \left[\frac{P(C))}{1 - P(class(R_i))} \sum_{j=1}^{k} Diff(A, R_i, M_j(C))\right]/(m.k) \tag{3}$$

3.2.2 Information Gain

The information gain criterion measures the difference between two probability distributions. It was intensively adopted for feature selection in decision tree construction [9]. After selection, we keep only indicators with maximal information gain.

3.2.3 Chi-2

The Chi-2 statistic quantifies the dependence between an indicator IN and a class cl by measuring their chi-squared statistics with respect to the classes. For the case of numeric indicators, it proceeds by a discretization of each indicator on a number of iterations. On each one, the discretized intervals are merged according to the values of the obtained χ^2 (Eq. 4). Indicators with the greatest number of intervals have the highest rank.

$$\chi^2 = \sum_{i=1}^{2} \sum_{j=1}^{k} \frac{\left(A_{ij} - E_{ij}\right)^2}{E_{ij}} \tag{4}$$

where k is the number of classes, A_{ij} the number of examples in the ith interval, jth class; and E_{ij} the expected frequency of A_{ij}.

3.2.4 Genetic Algorithm

Belonging to the evolutionary algorithms class, Genetic algorithms (GA) are derived from genetics and natural evolutionary mechanisms. These algorithms are particularly suitable for the combinatorial problems optimization "NP-Hard problems". Those latters require a computing time growing exponentially with the problem complexity [12].

GA are based on the natural evolution and selection, and survival of the fittest ideas. The genetic algorithm represents a solution to the problem as a chromosome. It then creates a population of possible solutions and applies genetic operators such as mutation and crossover to find the fittest solution. In this work the GA seeks the selection of input vector (composed of relevant indicators) allowing the best classification performances and pursues the following steps:

First population generation In this step is proposed a generation of the first chromosome population. In each chromosome, a set of indicators is constructed randomly. The population is composed of 100 chromosomes

Evaluation The performance of each input vector is based on RBF classification accuracy on a fixed validation set.

Selection The steady-state selection is used. In every generation, few chromosomes are selected (the 50 fittest ones) to create children. Subsequently, the worst chromosomes are removed and replaced randomly with newly created ones.

Evolution Operators: *Crossover* it applies on two different chromosomes. As a result, it produces new chromosomes formed from genes of both parents for the next generation. In this work, a cross at a random point strategy was applied.
Mutation it applies to an individual by modifying one or more genes, chosen randomly from the population. The percentage of mutation is set to 1%.
Stopping Criterion The algorithm stops at one of the following criteria:

- Maximum number of iterations = 200.
- 50% of the population of chromosomes is similar to the first gene.

3.3 Radial Basis Function Neural Network

In this work Radial Basis Function Network (RBF) is utilized as a classification tool. RBF network is a feed forward neural network type with three layers: one input layer, one hidden layer "RBF layer" and one output layer. Each layer is fully connected to the next. Each neuron in the hidden layer is described by a Gaussian law centered on a point of the input space. For a given input x, the output of the neuron in the hidden layer is the amplitude of the Gaussian at that point.

The output of the network is a linear combination of the outputs of neurons in the hidden layer adjusted by the weight of their respective connections. The response depends on the distance function between the input vector x, the vector prototype (center) and the size of the influence field [10].

4 Results and Discussion

In this work, we seek the optimal use of IAS information for wind turbine condition monitoring. In this way, a hybrid scheme (Fig. 3) was designed combining indicators transformation, selection and classification tools.

- Firstly, a stratified extraction of signals was done in order to get the same ratio of signals (100) in each class (Healthy condition; Bearing A defect and other defects).
- Then, an indicator extraction was performed on IAS signal and spectra, where 76 raw indicators (RI) were extracted from each signal.
- A Parametric Standardization Process was applied, then on the raw indicators, creating a new set composed of 76 standardized indicators (SI).
- Principal Component Analysis was applied and 30 Principal Components (PC) were added to the database.
- All extracted and transformed indicators were then mixed in one database (MI).
- Classification experiment was done based on MI in order to asses indicator transformation procedures
- Indicator selection procedure was applied on MI, where different approaches were tested in order to pull out only relevant indicators from the whole set.

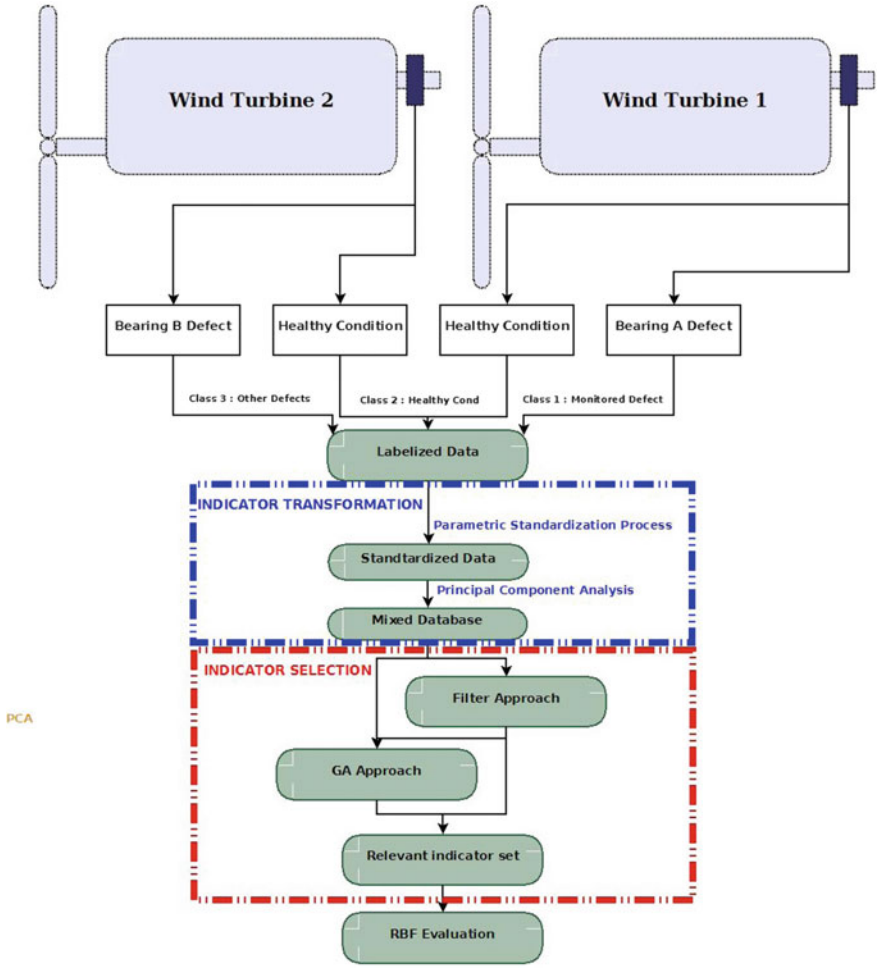

Fig. 3 Hybrid Scheme for wind turbine condition monitoring

  - Firstly, one stage selection based on each of Genetic Algorithms and selection filters (Chi2; GI and ReliefF) approaches.
  - Then, a two stages approach was constructed, where the first stage is based on filter approach in order to get a reduced set of relevant indicators followed by a GA seeking the best combination.

- The effectiveness of each scheme was evaluated based on RBF classification accuracy (66% of the data used for training and 33% for test). The obtained results are resumed in the Table 1.

Table 1 Performances evaluation

		Indicators number	Accuracy (%)
Raw indicators		76	83
Indicator transformation		182	93
One stage	GA	91	94
Indicator selection	Chi-2	17	94
	GI	17	94
	ReliefF	32	94
Multi stage	Chi-2	11	95
Indicator selection	GI	12	95
	ReliefF	**14**	**97**

Indicator transformation improved the classifier accuracy from 83% on Raw Indicators Dataset to 93% on the mixed database. However, the dimension of input vector became huge (183 Indicators).

One stage Indicator selection improved slightly the latter accuracy, where GA and Filter based approaches gave the same results (94%). Nevertheless, GI and CHI2 used only 17 indicators to reach it where ReliefF used 32 indicators and GA based used 91 indicators.

The main problem using the GA approach is the high risk to quickly converge on a local optimum (which seems to be the case in this application). On the other hand, filter approaches don't consider redundancy between indicators, which is considered as a disturbing phenomenon on classifier performances.

The Multi-Stage Scheme improved more significantly performances in terms of Accuracy and indicators number. The best results were obtained using the combination ReliefF filter-GA, where 97% accuracy was reached using only 14 indicators. GA approach was more effective dealing with reduced datasets, where the risk of falling on local optimum is lower. Also, the use of a filter approach as prepossessing technique guarantee to have only relevant indicators on the reduced set.

The projection of three indicators among the selected ones can be seen in Fig. 4 and demonstrate their effectiveness to separate the different classes.

A closer look at the input vector composition can be seen in Fig. 5, where a repartition of the indicators composing it is drawn according to their originating databases. Half of the indicators are Standardized ones (proving the effectiveness of the standardization giving more relevant indicators). Only one Principal Component was pulled out on the selected input vector. The construction of each Principal Component requires the computation of the whole set of indicators which seems incompatible with such an industrial application. The low number of retained PCs does not encourage to proceed in this way.

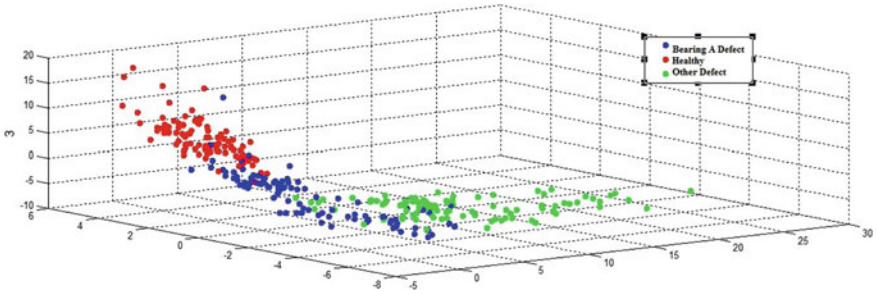

Fig. 4 Selected indicators representation

Fig. 5 Selected input vector composition

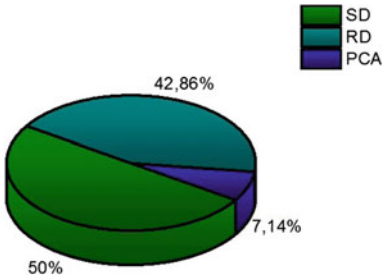

5 Conclusion

In this work, wind turbine condition monitoring issue was tackled, where IAS signals were proposed as an alternative information source to conventional analysis. Specifically developed processing techniques were applied to IAS raw signal and allowed the monitoring of two industrial wind turbines during healthy and defective periods. From each measured IAS signal, a huge number of representative indicators can be extracted. To get the most from the available information, numerous indicator transformation and selection approaches were experimented, and hybrid Scheme based on a multi stage indicator selection designed.

The proposed scheme based on the combination ReliefF selection Filter and Genetic algorithm avoids falling into local optimum and indicator redundancy problems and allow us to get the most relevant indicators and the highest classification accuracy. Furthermore, the proposed approach gave an objective assessment of transformation procedures where standardization process demonstrated its effectiveness. In this paper, only IAS information was used. In future works, a closer look to other information sources will be taken, where indicator selection presents an attractive solution to information fusion.

References

1. Machado de Azevedo, H. D., Maurício Araújo, A., & Bouchonneau, N. (2016). A review of wind turbine bearing condition monitoring: State of the art and challenges. *Renewable and Sustainable Energy Reviews*, *56*, 368–379.
2. Andre, H., Bourdon, A., & Remond, D. (2012). Instantaneous angular speed monitoring of a 2MW wind turbine using a parametrization process. In *Condition Monitoring of Machinery in Non-Stationary Operations: Proceedings of the Second International Conference Condition Monitoring of Machinery in Non-Stationnary Operations*. Berlin: Springer.
3. Remond, D., Antoni, J., & Randall, R. B. (2014). Editorial for the special issue on Instantaneous Angular Speed (IAS) processing and angular applications. In *Mechanical Systems and Signal Processing* (vol. 44, Issue 1–2, pp. 1–4).
4. Renaudin, L., Bonnardot, F., Musy, O., Doray, J. B., & Remond, D. (2010). Natural roller bearing fault detection by angular measurement of true instantaneous angular speed. *Mechanical Systems and Signal Processing*, *24*(7), 1998–2011.
5. Andre, H., Girardin, F., Bourdon, A., Antoni, J., & Remond, D. (2014). Precision of the IAS monitoring system based on the elapsed time method in the spectral domain. In *Mechanical Systems and Signal Processing* (vol. 44, Issues 1–2, pp. 14–30).
6. Andre, H., Remond, D., & Bourdon, A. (2011). On the use of the instantaneous angular speed measurement in non stationary mechanism monitoring. In *ASME 2011 International Design Engineering Technical Conferences and Computers and Information in Engineering Conference Volume 1: 23rd Biennial Conference on Mechanical Vibration and Noise, Parts A and B Washington, DC, USA, Aug 28–31, 2011*. ASME Collection.
7. Bourdon, A., Andre, H., & Remond, D. (2014). Introducing angularly periodic disturbances in dynamic models of rotating systems under non-stationary conditions. *Mechanical Systems and Signal Processing*, *44*(1–2), 60–71.
8. Gomez, J. L., Bahmani, A., Andre, H., Remond, D., & Bourdon, A. (2014). Non-stationary statistical fault indicators estimation applied on IAS machine surveillance. In *Proceedings of the Biennial ISMA Conference on Noise and Vibration Engineering, ISMA 2014, Leuven (Belgium), 15–17 Sept 2014*.
9. Khelf, I., Laouar, L., Bouchelaghem, A. M., Remond, D., & Saad, S. (2013). Adaptive fault diagnosis in rotating machines using indicators selection. *Mechanical Systems and Signal Processing*, *40*(2), 452–468.
10. Khelf, I., Laouar, L., Bendjama, H., & Bouchelaghem, A. M. (2012). Combining RBF-PCA-ReliefF filter for a better diagnosis performance in rotating machines. In *Condition Monitoring of Machinery in Non-Stationary Operations: Proceedings of the Second International Conference Condition Monitoring of Machinery in Non-Stationnary Operations*. Berlin: Springer.
11. Zimroz, R., & Bartkowiak, A. (2013). Two simple multivariate procedures for monitoring planetary gearboxes in non-stationary operating conditions. *Mechanical Systems and Signal Processing*, *38*(1), 237–247.
12. Karabadji, N. E. I., Seridi, H., Khelf, I., Azizi, N., & Boulkroune, R. (2014). Improved decision tree construction based on attribute selection and data sampling for fault diagnosis in rotating machines. *Engineering Applications of Artificial Intelligence*, *35*, Oct 2014.
13. Karabadji, N. E. I., Khelf, I., Seridi, H., & Laouar, L. (2012). Genetic optimization of decision tree choice for fault diagnosis in an industrial ventilator. In *Condition Monitoring of Machinery in Non-Stationary Operations: Proceedings of the Second International Conference "Condition Monitoring of Machinery in Non-Stationnary Operations*. Berlin: Springer.

Fault Diagnostic of Machines Under Variable Speed Operating Conditions Using Order Tracking and Novelty Detection

O. Cardona-Morales and G. Castellanos-Dominguez

Abstract Condition-Based Monitoring (CBM) of rotating machinery is becoming increasingly important because it allows improving the machine performance. Nevertheless, most of the real-world machinery operate unique pieces, which are not suitable for inducing faults, and thus making unfeasible to collect useful data from undamaged machine conditions. To this end, novelty detection (ND) had been developed, modeling the normal state to detect machine faults. Therefore, the extraction of a representative feature set must be carried out accurately to represent the target class under different machine states. However, there can be several operating conditions that reflect the dynamic behavior of the machinery, often resulting in non-stationary signals. To improve the stochastic description of non-stationary operating conditions, we propose a CBM methodology that relies on a set of the time-varying narrow-band features that are extracted from the order tracking approach, aiming to encode the time-varying behavior of the acquired vibration signals. With the goal of modeling the target machine condition, the key point here is conceiving the order components like dynamic features, and then, estimating several statistical and similarity parameters for those features to characterize each narrow-band component. Afterward, the multi-dimensional outlier detection problem is solved using both distance- and distribution-based data description classifiers. The ND scheme is tested on test-rig databases holding different types of machine faults when the machine operates under variable speed. As a result, the proposed methodology improves the classification rates compared with the state-of-the-art features and allows characterizing the machine state under its actual operating conditions.

Keywords Non-stationary vibration signals · Order tracking · Novelty detection

O. Cardona-Morales (✉)
Research Group of Technological and Environmental Advances,
Universidad Catolica de Manizales, Manizales, Colombia
e-mail: ocardonam@ucm.edu.co

G. Castellanos-Dominguez
Signal Processing and Recognition Group, Universidad Nacional de Colombia,
Manizales, Colombia
e-mail: cgcastellanosd@unal.edu.co

A. Timofiejczuk et al. (eds.), *Advances in Condition Monitoring of Machinery in Non-Stationary Operations*, Applied Condition Monitoring 9,
https://doi.org/10.1007/978-3-319-61927-9_17

1 Introduction

Nowadays, condition monitoring of rotating machinery is becoming increasingly important for the industry because it allows reducing accidental damages and improving the machine performance at the same time. Nevertheless, most of the real-world machinery operate unique pieces, which are not suitable for inducing faults, making unfeasible to collect useful data from damaged machine conditions. Therefore, training datasets are unbalanced, presenting enough information just about normal class. Regarding this matter, the *novelty detection* techniques had been developed that aim at inferring or modeling the undiscovered or missing data.

According to the extensive review in [7], the novelty detection methods (also termed one-class classifiers OCC) can be constructed using generative or discriminative models. Nonetheless, extraction of a representative feature set must be carried out accurately to provide robust performance on test data. To this end, feature extraction achieves a trade-off that maximizes the exclusion of novel samples while minimizes the exclusion of known samples.

For training of Condition-based Monitoring (CBM) systems, the vibration analysis is more frequently used because of its low cost and high performance usually provided [8]. Furthermore, a set of statistical features has been already proposed for extracting a set of discriminating features from vibration signals [4, 5, 11]. Nonetheless, several machine operations often lead to non-stationary signals due to the dynamic behavior of the machinery excitations, resulting in time-varying operating conditions. Therefore, the development of signal analysis methods suited to extracting the time-varying features from non-stationary signals has become increasingly relevant for machinery fault diagnosis [2]. To obtain valuable information from non-stationary signals, several principles of feature extraction have been suggested for diagnosis of machinery health conditions [13]. Where it is possible to highlight linear time-varying decompositions (harmonic analysis [1, 3], time-frequency analysis [12], non-linear time-varying decompositions) empirical mode analysis [6], among others.

In this work is introduced a CBM methodology for non-stationary operating conditions that relies on a set of the time-varying narrow-band features extracted from order tracking approach so-called Square Root Cubature Kalman Filter (SRCKF_OT) [1], aiming to encode the non-stationary behavior of the acquired vibration signals. The key point here is conceiving the order components like dynamic features, and then, estimating several statistical parameters over those features to carry out the dimension reduction of the input training set as discussed in [6]. Another approach to adequately characterize each narrow-band component is employing similarity measures as is presented in [9]. Mainly, the multi-dimensional outlier detection problem is solved using two different data description classifiers, including the *Support Vector Data Description* (SVDD) and *Gaussian Distribution One-Class Classifier* (GDOCC) [10], as OCC methods that assume a spherical boundary and a Gaussian model of the boundary, respectively. To validate the proposed methodology, two datasets obtained on a test-rig are used, where the first one includes undam-

aged, unbalanced and misaligned instances under speed-varying machine conditions (coast-down), and the second one comprises bearing faults under coast-down operating machine condition. The obtained results show the advantage of using order components as features because it provides an interesting interpretation of the machine condition.

2 Order/Spectal Components as Features

With the purpose of separating the information of spectral sub-bands, the filter bank methods (FBM) decompose bandwidth-limited signals into a set of narrow-band components. Thus, a given signal $y(t) \in \mathbb{R}(T)$ that has a finite bandwidth ΔF (with $F = [0, f_s/2]$, being f_s the sampling frequency) is decomposed into $K \in \mathbb{R}^+$ narrow-band components $x = \{x_k(t) : k \in K\}$ so that each one has a bandwidth ΔF_k such that $F \subseteq \bigcup_k F$.

In that sense, the order tracking model (OT) proposed in [1] decomposes the signal $y(t)$ in a set of order components $x_k(t) \in \mathbb{R}(T)$ such that:

$$y(t) = \sum_{k=1}^{K} x_k(t), \forall t \in T \tag{1}$$

where each order component is $x_k(t) = a_k(t)\cos(k\omega(t) + \varphi_k(t))$, being $a_k(t)$ the order amplitude, $k\omega(t)$ the k-th harmonic of the fundamental rotational frequency $\omega(t)$ and $\varphi_k(t)$ the order phase. It is worth noting that depending on the amount of K order components extracted, it is feasible that $x_k(t)$ could be associated with a mono-component signal, i.e. the spectral information is contained in a singular frequency $k\omega(t)$, but considering that in the most of cases K is lower than the actual harmonics in $y(t)$, each $x_k(t)$ has a limited-bandwidth ΔF_k.

Due to the narrow-band components comprises much information about the machine condition, it is necessary to estimate a set of features that may be fed into the classification scheme. In that sense, two different type of features is computed from each order component including the statistical and similarity characteristics. The former case it is related to well-known statistical features as root-mean-square (RMS), Standard Deviation (STD), and Kurtosis (KURT).

Regarding with the last type of features, it is computed a similarity measure between the input signal $y(t)$ and each extracted k-the narrow-band component, $x_k(t) \in \mathbb{R}(T)$, quantifying their mutual statistical dependence. To this end, it is measured the statistical dependence through the *cross-correlation spectral density (CCSD)* between $\{y(t), x_k(t)\}$ that depicts the distribution of signal content over the frequency domain, defined as below:

$$S_{yx_k}(\omega) = \left| \int_T \int_T y(\tau) x_k(t+\tau) d\tau \exp(-j\omega t) dt \right|^2 \tag{2}$$

where $\omega = 2\pi f$. Derived from the spectral measure in (2), it could be consider the following generalizing values of mutual statistical dependence:

- *Pearson's correlation coefficient (PCC)*, $\rho_{y,x_k} \in \mathbb{R}[-1,1]$, that is a straightforward way to quantify the linear relationship of dependence as below:

$$\rho_{y,x_k} = \boldsymbol{\mathcal{E}} \left\{ S_{yx_k}(\omega) : \forall \omega \in F_k \right\} / \sigma_y \sigma_{x_k} \tag{3}$$

  where $\sigma_\xi^2 = (2\pi)^{-1} \int_{F_k} |S_\xi(\omega)|^2 d\omega$ is the variance. Note that both $y(t)$ and $x_k(t)$ are assumed zero-mean values.
- *Cumulative spectral density index (CSDI)* introduced as follows:

$$\varrho_{y,x_k} = \boldsymbol{\mathcal{E}} \left\{ \int_{-\infty}^{\omega} S_{yx_k}(\widetilde{\omega}) d\widetilde{\omega} : \forall \omega \in F_k \right\}, \ \varrho_{y,x_k} \in \mathbb{R}^+ \tag{4}$$

It is worth noting that the higher the values of ρ_{y,x_k} and ϱ_{y,x_k}, the higher statistical association between variables. More details about the similarity measures could be found in [9].

3 Experimental Setup

The proposed methodology is based on a traditional pattern recognition process, where OCC algorithms are trained with a feature set $Z \in \mathbb{R}^{N \times p}$, such that the goal is detecting if any fault exists or not. Here, three distinct ways to build the feature sets are considered: (*i*) $p = 24$ statistic features from the raw signal $y(t)$ (discussed in [4, 11]); (*ii*) a singular statistical features ($p = K$) from each order component $x_k(t)$ such as standard deviation (OT-STD), root mean square (OT-RMS) and kurtosis (OT-KURT), due to those statistics provided basic information about the physical nature of each narrow-band component; and (*iii*) the similarity measures (OT-CCSD, OT-CSDI and OT-PCC) computed between $x_k(t)$ and $y(t)$ (i.e. $p = K$), aiming to encode the relevant spectral information that each dynamic feature enclosed. In consequence, 8 feature sets are individually tested and fed into the OCC algorithms. It is worth noting that order decomposition could obtain a different amount of orders, and hence, to accomplish a square feature matrix Z, it is needed to fix the p features according to the minimum number of decomposed components K.

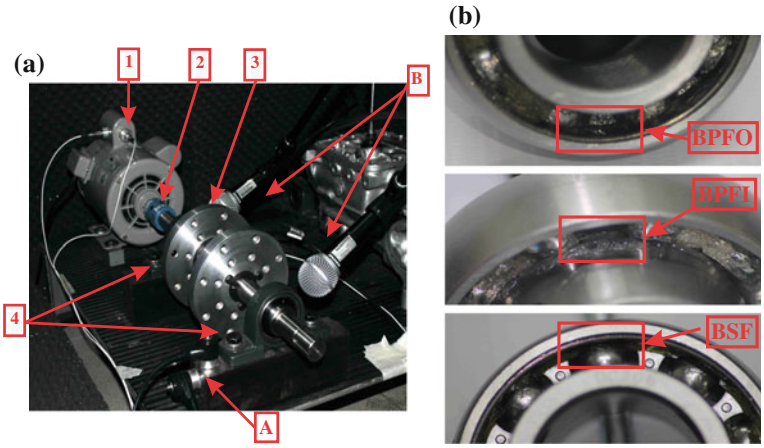

Fig. 1 Experimental test rig (*left*): (1) Motor driven, (2) Rigid coupling, (3) Drilling wheels, (4) Bearing housing. Sensors location: (**a**) Accelerometers and (**b**) Microphones. The simulated BPFO, BPFI and BSF defects (*right*)

For the classification stage, a 20-fold cross-validation and 75% of target objects to training the algorithms aiming to reduce the overtraining, inasmuch the number of observations is very low. The tuning of free parameters both SVDD and GDOCC are founded by grid search, in particular, the former case is $\sigma \in [1, 100000]$ using a logarithmic scale, and the last case uses the regularization of Σ given by $\tilde{\Sigma} = (1 - \beta)\Sigma + \beta I_p$, being $\beta \in [0.05, 1]$ and I_p the identity matrix of dimension p.

The methodology is tested using two different experiments obtained in a test rig from Universidad Nacional de Colombia (shown in Fig. 2): (*i*) a dataset that comprises unbalance and misalignment damages under coast-down operating conditions. And, (*ii*) a dataset including bearing faults such as inner race (BPFI), outer race (BPFO) and ball bearing (BSF) defects, under coast-down operating condition. The mechanical system is displayed in Fig. 1a, and consists of a shaft driven by a 1.5 HP DC electric motor able to reach 1720 rpm through the equipped rigid coupling. Drilling wells are designed to create either static or dynamic unbalance problems. The test rig has two bearings `"HTH-UC206"` where the different faults are simulated, and the damages are introduced on the bearing located at shaft end by a crack on the surface of interest with a motor tool (Fig. 1b).

3.1 Identification of Shaft Faults

In this experiment, just the `"ACC102"` accelerometer placed near the machine is employed, which has a measurement range of 0 − 10 kHz and 100 mV/g of sensitivity. The `"National Instruments USB-6009"` data acquisition card acquires vibration recordings at 20 kHz sampling frequency.

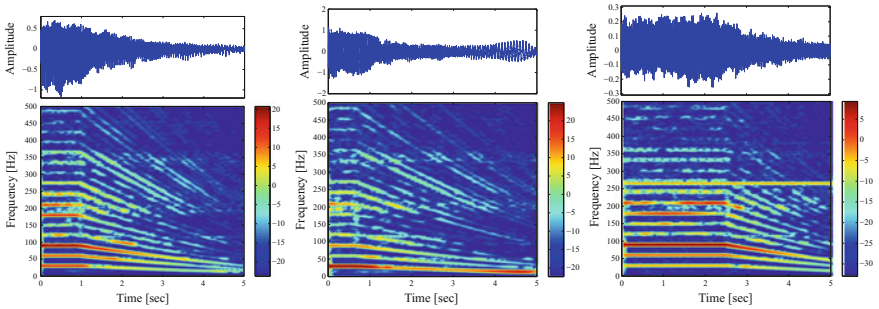

(a) Undamaged (b) Unbalance (c) Misalignment

Fig. 2 An exemplary of signals under coast-down operating conditions. Each type of signal is presented in time domain (*top*) and its time-frequency representation (*bottom*)

The data set holds the following types of acquired outliers regarding the considered machine states: (*i*) a static unbalance generated by a mass of 0.5 gr located on the drilled wheel closer to the rigid coupling. And (*ii*) an angular misalignment caused by a horizontal and vertical displacements of 0.3 and 0.7 μm, respectively. The data collection also includes an undamaged condition that is assumed as the target class. The recordings are measured under coast-down operating conditions, where each signal contains three phases: (*i*) maximum speed (1800 rpm), (*ii*) turning motor off, and (*iii*) steady–state regime (see Fig. 2). The working phases are not synchronized, that is, the decreasing may begin at different times within each recording. As a result, 20 recordings were acquired for undamaged and unbalance classes, whereas for misalignment were 8. Taking into account that the maximum spectral information is around 1.2 kHz each recording is downsampled to 4 kHz to reduce the computational cost, yielding a recording length of $L = 20000$ samples in 5 s.

To extract the order components, the number of harmonics showed in Fig. 3 are computed using a local maxima estimation algorithm (discussed in [1]), and then, are introduced to the SRCKF_OT algorithm to estimate the OT features. For the sake of estimate the order components, the amount of harmonics of each observation is around $K = 11$, $K = 8$ and $K = 11$ for undamaged, unbalance and misalignment, respectively. Since the number of harmonics depends on the spectral information of the signal. Besides, the covariances of the OT algorithm are heuristically fixed to

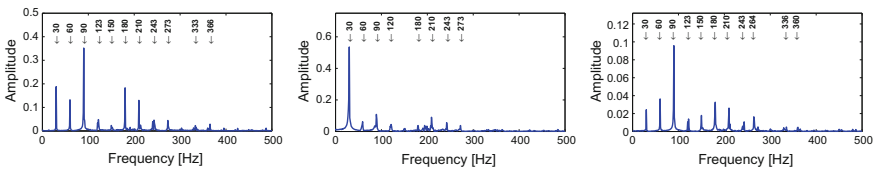

(a) Undamaged (b) Unbalance (c) Misalignment

Fig. 3 Orders estimated from coast-down regime using maximum harmonics algorithm

Table 1 Performance results in (%) of faults associated to shaft under coast-down regime

Feature set	GDOCC			SVDD		
	prec	*rec*	f_1	*prec*	*rec*	f_1
SFS	86 ± 5,6	92 ± 11	89 ± 6.6	**100 ± 0**	**86 ± 22**	**91 ± 16**
OT-STD	**100 ± 0**	**96 ± 8.2**	**98 ± 4.6**	**100 ± 0**	**93 ± 9.8**	**96 ± 5.4**
OT-RMS	**100 ± 0**	**96 ± 8.2**	**98 ± 4.6**	**100 ± 0**	**89 ± 15**	**93 ± 9.3**
OT-KURT	14 ± 2.6	88 ± 12	24 ± 2.9	33 ± 4.9	79 ± 19	47 ± 8.2
OT-CSDI	83 ± 29	95 ± 14	84 ± 22	**100 ± 0**	**88 ± 14**	**93 ± 8.2**
OT-CCSD	88 ± 26	96 ± 14	88 ± 22	**100 ± 0**	**88 ± 15**	**93 ± 9.2**
OT-PCC	100 ± 0	81 ± 17	89 ± 10	99 ± 5.6	67 ± 25	77 ± 19

$q_i^a = 10^{-4}$, $q^f = 10^{-8}$ and $r = 10^{-8}$, which may present changes of $10^{\pm 1}$, avoiding performing the complete searching.

When the classification scheme is applied, the OT-STD and OT-RMS achieve the best performance again, both using the GDOCC (with $\beta = \{0.45, 0.8\}$) and SVDD (with $\sigma = \{9000, 8500\}$) classifiers. In Table 1, it is observed that GDOCC overcomes to SVDD, but the last increases the performance (over 90%) when the similarity measures are employed. This fact implies that SVDD has a better generalization capability than GDOCC and offers more feature set options to characterize the considered faults. The possibility of working with a major set of distinct features allows assessing relevant information that provides different physical interpretations.

3.2 Identification of Bearing Faults

The goal of this experiment is validating the proposed methodology to detect bearing faults. The database holds 20 vibration recordings lasting 5 s at 25.6 kHz sampling rate, and it is just used the signals collected in the horizontal plane. Here, the coast-down operating condition implies that the machine works at maximum speed (around ∼30 Hz) at the beginning of each signal, and then, the electromotor is turned off decreasing the speed to zero. An exemplary of each machine condition is displayed in the top part of the Fig. 4.

A visual inspection from the raw signals allows determining that the signal harmonics decrease proportionally to the speed change, which may be clearly observed in the undamaged case Fig. 4c. Nonetheless, when the bearing faults are introduced a cyclo-non-stationary behavior emerges, causing AM-FM modulations that depend on the variable speed. That particular condition has been studied when the analyzed signal is mono-component, but in this type of vibration signals the spectral content is multi-component. In that sense, the signal is treated as angle cyclostationary, and the SRCKF_OT approach could be employed. Therefore, a signal pre-conditioning is carried out to alleviate the variable speed effects on the signal, applying the following

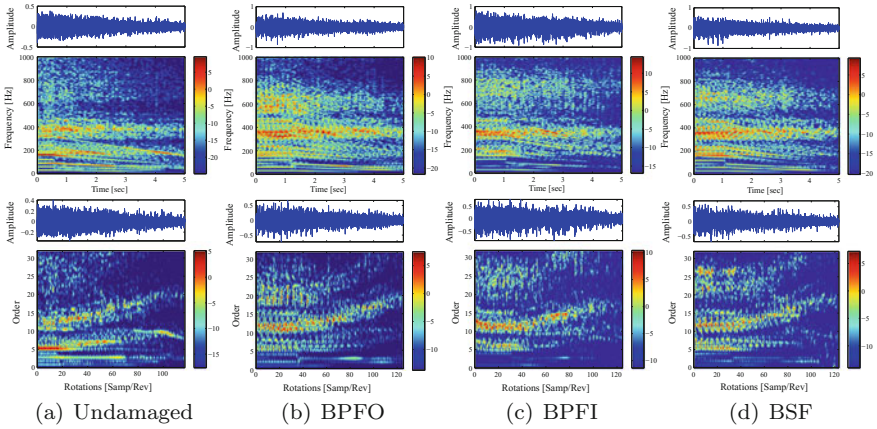

Fig. 4 Exemplary of bearing fault signals from the machine under coast-down operating condition, both raw signal (*top*) and its resampled version (*bottom*)

two-steps approach: (*i*) Instantaneous speed estimation using the SRCKF_OT over the first 5th order components, because in the most of the cases, those components are stationary. And (*ii*) an angle-order domain transformation by Computed Order Tracking (COT), using the estimated IF. In the concrete case of the bearing fault signals used in this experiment, the resampling method is performed with 64 samples per revolution, obtaining the angle-order map displayed on the bottom part of the Fig. 4. As a result of the signal pre-conditioning, the obtained order-normalized signals $\hat{y}_i(t)$ are shown in Fig. 4-(right), where it is possible to observe that both time and angle domain signals are similar, but several differences are found from the visual inspection of the time-frequency representations. Firstly, the coast-down behavior was removed causing that the order components appear closer to a limited spectral band, and obtaining more separability among them. Secondly, the amplitude of the order components close to shaft speed (low orders) decreases and apparently they are not constant through the angle axis, yet the STFT scaling generates this visual effect. So lastly, the cyclic order components at the interval of $[300, 450]$ Hz (i.e., [10, 15]th orders) preserve its structure but under constant speed. Nonetheless, those components give a false sensation that the speed is increased, because of the spectral information at the time interval of $[2, 3]$ s is of a higher order than between $[0, 2]$ s.

Afterwards, the set of harmonics Γ is calculated from the Fourier transform of each observation $\mathfrak{F}\{\hat{y}(\theta)\}$, obtaining the narrow-band components $\hat{x}_{i,k}(\theta)$. Figure 5 displays the order spectra of the considered faults and the order components to be tracked, where it is possible to see that there exist order components with significant amplitude above at 10th order for the faulty instances. As a result, $K = \{21, 19, 21, 18\}$ are the number of harmonics that are included into the SRCKF_OT algorithm for undamaged, BPFO, BPFI and BSF, respectively. In this case, the covariance parameters are heuristically fixed as $q_i^a = 10^{-4}$, $q^f = 10^{-5}$ and $r = 10^{-9}$ for all machine states, having deviations of 10^1 and 10^{-1} for q_i^a and q_i^f, respectively.

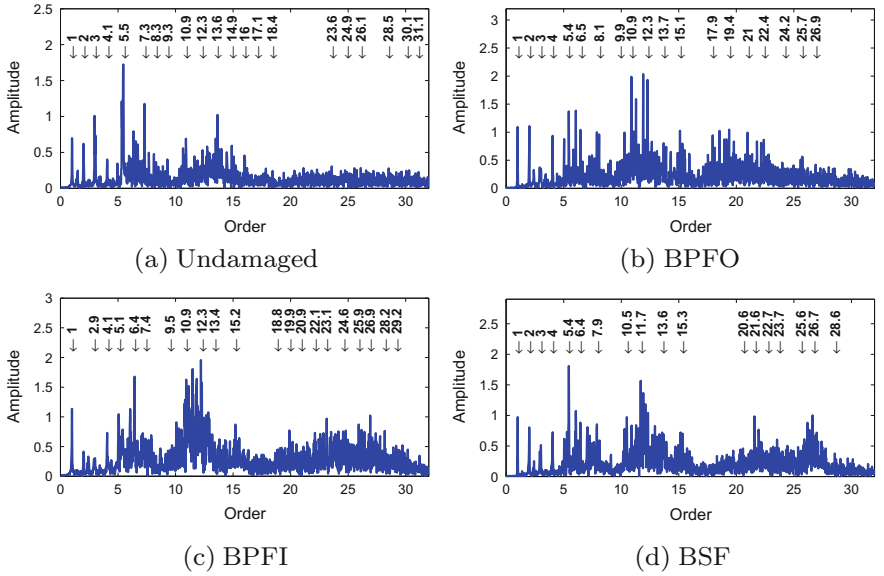

Fig. 5 Orders estimated from bearing fault signals after COT is applied, when the machine operates under a dynamic regime, and its respective spectrum

Table 2 Performance results in (%) of bearing faults under non-stationary regime

Feature set	GDOCC			SVDD		
	prec	*rec*	f_1	*prec*	*rec*	f_1
SFS	**100 ± 0**	**83 ± 23**	**89 ± 16**	75 ± 6.4	85 ± 18	79 ± 13
OT-STD	**100 ± 0**	**87 ± 17**	**92 ± 10**	**100 ± 0**	**72 ± 22**	**82 ± 16**
OT-RMS	**100 ± 0**	**92 ± 15**	**95 ± 8.9**	**100 ± 0**	**75 ± 21**	**84 ± 15**
OT-KURT	23 ± 6.9	87 ± 25	35 ± 8.8	20 ± 4.4	75 ± 21	32 ± 7.3
OT-CSDI	78 ± 16	73 ± 26	73 ± 17	71 ± 10	78 ± 25	73 ± 16
OT-CCSD	92 ± 13	75 ± 26	79 ± 17	67 ± 15	80 ± 25	71 ± 17
OT-PCC	54 ± 22	73 ± 26	56 ± 12	38 ± 8.8	70 ± 21	47 ± 9.4

As regards traditional OCC scheme, the 7 feature sets computed from the $\hat{x}_{i,k}(\theta)$ and the SFS set are each one fed into both classifier algorithms, obtaining the outcomes exposed in Table 2. Consequently, it is observed that OT-RMS and OT-STD achieve a performance rate above 90 and 80%, overcoming the other feature sets using both GDOCC and SVDD, respectively. Nonetheless, when the GDOCC is employed, the classical features reaches a relevant performance due to that the precision is 100% and all false positives are rejected.

4 Conclusion

The presented methodology in this work provides an alternative way to characterize non-stationary vibration signals using an order tracking algorithm and novelty detection. In general, the signal must be enhanced and analyzed by frequency bands due to the narrow-spectral response that describes each considered fault. In that sense, the proposed dynamic features based on OT decomposition performs a satisfactory signal characterization, because it preserves the signal properties comprised in a band-limited frequency. Different methods to comprise the order component information allow inferring that the similarity measures overcome the statistic features because it takes into account the spectral information of each band compared with the complete signal. In consequence, the CBM system provides better interpretability about the identified outliers.

Acknowledgements The authors acknowledge to the Universidad Catolica de Manizales, Universidad Nacional de Colombia at Manizales, and Colciencias by the financial support through the research project entitled "Desarrollo de un sistema de monitoreo de condición y diagnóstico de fallas en línea de sistemas de generación de energía hidroeléctrica empleando una red de sensores inalámbricos de datos de alta resolución".

References

1. Cardona-Morales, O., Avendano, L., & Castellanos-Dominguez, G. (2014). Nonlinear model for condition monitoring of non-stationary vibration signals in ship driveline application. *Mechanical Systems and Signal Processing*, *44*(1–2), 134–148. Special Issue on Instantaneous Angular Speed (IAS) Processing and Angular Applications.
2. Feng, Z., Liang, M., & Chu, F. (2013). Recent advances in time-frequency analysis methods for machinery fault diagnosis: A review with application examples. *Mechanical Systems and Signal Processing*, *38*(1), 165–205.
3. Heo, Y., & Kim, K.-J. (2015). Definitions of non-stationary vibration power for time-frequency analysis and computational algorithms based upon harmonic wavelet transform. *Journal of Sound and Vibration*, *336*, 275–292.
4. Lei, Y., Kong, D., Lin, J., & Zuo, M. J. (2012). Fault detection of planetary gearboxes using new diagnostic parameters. *Measurement Science and Technology*, *23*(5), 055605.
5. Lei, Y., Zuo, M., He, Z., & Zi, Y. (2010). A multidimensional hybrid intelligent method for gear fault diagnosis. *Expert Systems with Applications*, *37*(2), 1419–1430.
6. Lu, L., Yan, J., & de Silva, C. W. (2015). Dominant feature selection for the fault diagnosis of rotary machines using modified genetic algorithm and empirical mode decomposition. *Journal of Sound and Vibration*, *344*, 464–483.
7. Pimentel, M. A., Clifton, D. A., Clifton, L., & Tarassenko, L. (2014). A review of novelty detection. *Signal Processing*, *99*, 215–249.
8. Randall, R. B. (2011). *Vibration-based condition monitoring: Industrial, aerospace and automotive applications*. Wiley.
9. Sierra-Alonso, E. F., Cardona-Morales, O., Acosta-Medina, C. D., & Castellanos-Dominguez, G. (2014). In *Spectral Correlation Measure for Selecting Intrinsic Mode Functions, Progress in Pattern Recognition, Image Analysis, Computer Vision, and Applications: 19th Iberoamerican Congress, CIARP 2014, Puerto Vallarta, Mexico, Nov 2–5* (pp. 231–238). Cham: Springer International Publishing.

10. Tax, D. M. J., & Duin, R. P. W. (2004). Support vector data description. *Machine Learning*, *54*(1), 45–66.
11. Wang, D. (2016). K-nearest neighbors based methods for identification of different gear crack levels under different motor speeds and loads: Revisited. *Mechanical Systems and Signal Processing*, *70–71*, 201–208.
12. Wang, Y., Xiang, J., Mo, Q., & He, S. (2015). Compressed sparse time-frequency feature representation via compressive sensing and its applications in fault diagnosis. *Measurement*, *68*, 70–81.
13. Worden, K., Staszewski, W. J., & Hensman, J. J. (2011). Natural computing for mechanical systems research: A tutorial overview. *Mechanical Systems and Signal Processing*, *25*(1), 4–111.

Bearing Fault Identification Based on Blind Extraction of Cyclostationary Signals Using Order Tracking

O. Cardona-Morales, E.F. Sierra-Alonso and G. Castellanos-Dominguez

Abstract Mostly, a vibration signal from rotating machines comprises stationary and non-stationary components, whose description should be as accurate as possible to infer the internal and external forces that affect the system behavior. Moreover, either component can provide diverse but relevant information about the machine health. Thus, bearing faults foster the non-stationary component that is characterized by time-varying statistical moments, periodically changing through the time (or cyclostationary signals). Therefore, the problem to detect a bearing fault signal is usually addressed to separate the deterministic and the stochastic components of the vibration signal to make clear the damage characteristics. To this end, we present the novel order tracking (OT) method that decomposes the non-stationary vibration signal into narrow-band spectral components, aiming to enhance the cyclostationary characteristics. Moreover, a similarity measure is computed between the envelopes of the raw signal and each component, allowing to quantify the cyclic behavior of signal components. Since the proposed method acts as a narrow-band filter, a comparison with the spectral kurtosis (SK) is performed using a rolling element bearing dataset that includes an inner race, outer race, and rolling element defects. Specifically, the Case Western Reserve University data is carried out aiming to improve the diagnosis of bearing failures that are categorized in a recent work using the benchmark methods. As a result, the proposed blind extraction method allows capturing the cyclostationary behavior hidden in the signal and improves the identification of the bearing faults when the signal is noisy.

Keywords Cyclostationary vibration signals · Order tracking · Blind signal extraction

O. Cardona-Morales (✉)
Research Group of Technological and Environmental Advances,
Universidad Catolica de Manizales, Manizales, Colombia
e-mail: ocardonam@ucm.edu.co

E.F. Sierra-Alonso · G. Castellanos-Dominguez
Signal Processing and Recognition Group, Universidad Nacional de Colombia,
Manizales, Colombia
e-mail: cgcastellanosd@unal.edu.co

A. Timofiejczuk et al. (eds.), *Advances in Condition Monitoring of Machinery in Non-Stationary Operations*, Applied Condition Monitoring 9,
https://doi.org/10.1007/978-3-319-61927-9_18

1 Introduction

The vibration signal from rotating machines, in most of the cases, comprises stationary and non-stationary components that describe the different processes occurring inside the machine. In the concrete case of the stationary components, these appear if the machine is running at steady-state regime where the speed and load are not time-varying. Nonetheless, when bearing faults arise, non-stationary processes also appears, whose statistical characteristics vary periodically with time depending on some period and are called *cyclostationary processes* [3, 8]. The bearing failure frequency governs the cyclic behavior, which may be generated by defects of the inner race, outer race, rolling elements and the cage (holding rolling elements together). Those frequencies are commonly known as *cyclic frequencies* generating AM modulations of the shaft speed [4, 10].

In practice, one of the most used methods is the classical envelope spectrum of the raw signal because of its simplicity is preferred in the industry. Other methods consist of analyzing the time-frequency response of the signal to identify and characterize the frequency band where the fault occurs, being employed techniques like the Short-Time Fourier Transform [9, 10]. Nonetheless, the problem to detect a bearing fault signal had been addressed to separate the deterministic and the stochastic parts of the signal, extracting a signal of interest that exhibits the damage characteristics [5]. On this matter, the synchronous averaging explained in [3] is validated in real-world signals and modified versions presented in [1] allow introducing speed fluctuations by a resampling into the angle domain. In spite of the multiple methods that could be applied to detect bearing faults, one of the most popular is based on the spectral kurtosis, which was formalized by [2], and provides an accurate frequency band where the modulation exist. On the other hand, there are the approaches based on the cyclic spectrum [4] where the representation of the data in a cycle frequency-frequency domain allows observing precisely the effect of the different modulations that are present in the signal.

In this work, the order tracking (OT) model proposed in [6] is used as a decomposition approach where each order component is defined as a particular case of the cyclic autocorrelation and cyclic power spectrum. Since the proposed method acts as a narrow-band filter, a comparison with the spectral kurtosis is performed using bearing faults under steady-state. The experiment is based on the recent benchmark study presented in [12], where the recordings of the Case Western Reserve University are labeled as diagnosable, partially diagnosable, and not diagnosable, providing the conditions to use that dataset.

2 Order Tracking Model as Cyclostationary Process

A signal is cyclostationary (CS) of order p (in the wide sense) if and only if it is possible finding some pth-order nonlinear transformation of the signal that will generate finite-strength additive sine-wave components [7]. In that sense, a CS process

is a stochastic process that exhibits some hidden periodicities in its statistical structure and encompasses a subclass of non-stationary signals with an inherent cyclic behavior [2].

In consequence, the essence of the difference between stationary and cyclostationary or almost cyclostationary processes is that the latter exhibit spectral correlation. Furthermore, this spectral correlation is completely and conveniently characterized by the cyclic power spectrum $\{S_y^\alpha\}$ or equivalently by the cyclic autocorrelations $\{R_y^\alpha\}$.

From the OT model discussed in [6], the vibration signal $y(t) = x_{1,k}(t) = a_k(t)\cos(2\pi k f_r t + \phi(t))$ could be expressed in the *quadrature-amplitude-modulation* (QAM) form [7]:

$$x_{1,k}(t) = u(t)\cos(2\pi k f_r t) + v(t)\sin(2\pi k f_r t), \tag{1}$$

for any value of f_r and $k = 1$, provided $u(t)$ and $v(t)$ can be calculated by using the standard trigonometric identity as follows:

$$\begin{aligned} u(t) &= x_1(t)\cos(2\pi f_r t) + x_2(t)\sin(2\pi f_r t) \\ v(t) &= x_2(t)\cos(2\pi f_r t) - x_1(t)\sin(2\pi f_r t), \end{aligned} \tag{2}$$

being $x_2(t)$ the Hilbert transform of $x_1(t)$. In this case, if $x_1(t)$ is bandlimited to $f \in (f_r - B, f_r + B)$, then $u(t)$ and $v(t)$ are bandlimited to $f \in (-B, B)$, and hence, if $B < f_r$, $u(t)$ and $v(t)$ are uniquely determined by $x_1(t)$ and $x_2(t)$. Besides, it can be shown that for any process $x_1(t)$, (1) and (2) yield a unique definition of envelope magnitude, for which

$$\begin{aligned} a(t) &= [u^2(t) + v^2(t)]^{1/2} \\ \phi(t) &= \tan^{-1}\left[\frac{v(t)}{u(t)}\right]. \end{aligned} \tag{3}$$

This QAM representation, called *Rice's representation*, is valid regardless of the probabilistic model for $x_1(t)$. That is, $x_1(t)$ can be stationary, cyclostationary, almost cyclostationary, or more generally non-stationary. To this end, in [7] a complete study of the correlation and spectral properties is presented, including the cyclic correlations and cyclic spectra, for $x_1(t)$ and its in-phase and quadrature components $u(t)$ and $v(t)$.

Specifically, let consider the process $u(t)$ as a *Linear Periodically Time-Variant* (LPTV) transformation of the two-dimensional vector of processes $\{x_1(t), x_2(t)\}$, for which the vector of impulse-response functions, that specify the LPTV transformation, $h(t+\tau, t) = \sum_{n=-\infty}^{\infty} g_n(\tau) e^{i2\pi n t/T}$ is periodic in t for each τ, where $\{g_n(\tau)\}$ are a set of Fourier coefficients. The representation of the impulse-response functions both in-phase and quadrature components is as follows:

$$h(t, z) = \{\cos(2\pi f_r t)\delta(t - z), \sin(2\pi f_r t)\delta(t - z)\}, \tag{4}$$

Therefore, the LPTV transformation, $u(t)$, in terms of cyclic autocorrelation, is as follows

$$\begin{aligned} R_u^{\alpha}(\tau) = & \frac{1}{2}\left[R_{x_1}^{\alpha}(\tau) + R_{x_2}^{\alpha}(\tau)\right]\cos(2\pi f_r \tau) + \frac{1}{2}\left[R_{x_2x_1}^{\alpha}(\tau) - R_{x_1x_2}^{\alpha}(\tau)\right]\sin(2\pi f_r \tau) \\ & + \frac{1}{4}\sum_{n=-1,1}\left\{\left[R_{x_1}^{\alpha+2nf_r}(\tau) - R_{x_2}^{\alpha+2nf_r}(\tau)\right] + ni\left[R_{x_2x_1}^{\alpha+2nf_r}(\tau) + R_{x_1x_2}^{\alpha+2nf_r}(\tau)\right]\right\} \end{aligned} \tag{5}$$

and the Fourier transformation of $R_u^{\alpha}(\tau)$ allows to obtain the cyclic power spectrum as

$$\begin{aligned} S_u^{\alpha}(f) = & \frac{1}{4}\sum_{n=-1,1}\left\{\left[S_{x_2}^{\alpha}(f+nf_r) + S_{x_1}^{\alpha}(f+nf_r)\right] + ni\left[S_{x_2x_1}^{\alpha}(f+nf_r) - S_{x_1x_2}^{\alpha}(f+nf_r)\right]\right\} \\ & + \frac{1}{4}\sum_{n=-1,1}\left\{\left[S_{x_1}^{\alpha+2nf_r}(f) - S_{x_2}^{\alpha+2nf_r}(f)\right] + ni\left[S_{x_2x_1}^{\alpha+2nf_r}(f) + S_{x_1x_2}^{\alpha+2nf_r}(f)\right]\right\}. \end{aligned} \tag{6}$$

Equations (5) and (6) reveal that the set of cyclic autocorrelations and the set of cyclic spectra are each self-determinant characteristics under an LPTV transformation. Since the only features of the excitation that determine the cyclic autocorrelations (cyclic spectra) of the response are cyclic autocorrelations (cyclic spectra) of the excitation [7]. As a consequence, it is possible to infer that the order components obtained using the oscillatory model from [6] could include cyclostationary information.

3 Experimental Setup

To demonstrate the capability of the SRCKF_OT model as a blind cyclostationary signal extraction method, a set of rolling element bearing signals is used. In the concrete case of localized bearing faults, its modeling may be carried out as a cyclostationary process taking into account that the possible defects are governed by a cyclic frequency [11]. In particular, each cyclic frequency may be approximated by the geometrical properties of the rolling element bearings and the shaft rotational speed f_r of the machine. A graphical description of the experimental setup is shown in Fig. 1, where both methodologies discussed in this work are displayed: the proposed SRCKF_OT model and the spectral kurtosis. The selection of the most representative component obtained with the OT algorithm, it is carried out by the correlation index between the envelope signal of $y(t)$ and the envelope signal provided by each order $x_k(t)$. The obtained measure could be understood as a cyclic correlation that measures the similarity between each narrow-band decomposition and the raw signal.

The experiment is performed using selected recordings from the public dataset provided by Case Western Reserve University (CWRU). Considering the labels defined in [12], the challenge in this experiment is centered in validating the capability of the proposed approach in data not diagnosable for each particular bearing fault. The signals employed correspond with drive-end (DE) at 12 kHz of a sampling

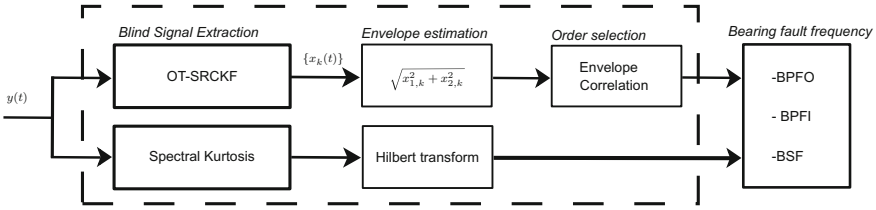

Fig. 1 Experimental diagram for BSE using the proposed SRCKF_OT model

frequency, and the labels could be Y1, Y2, P1, P2, N1, and N2. The capital letter indicates if the bearing fault is clearly (Y), partial (P) or not (N) diagnosable, and the number provides a grade of difficulty. Regarding with the bearing faults, the theoretical bearing fault frequencies are $BPFI = 5.415f_r$, $BPFO = 3.585f_r$, $BSF = 2.357f_r$, and $FTF = 2.357f_r$ which were calculated based on the kinematic information provided by the bearing manufacturer. Therefore, a set of cursors is located into the envelope spectrum to inspect the spectral components that match with the bearing fault frequencies. In that sense, each bearing failure is analyzed using both the proposed scheme and the SK as a filter.

3.1 Inner Race Fault—BPFI

From the set of bearing faults on inner race, there was chosen the recording DE171, which was labeled in [12] as P1. Analyzed bearing fault signal is shown in Fig. 2, where the time domain representation (a) displays a one-second signal segment, and it is observed the record DE171 presents an impulsive pattern that is not constant

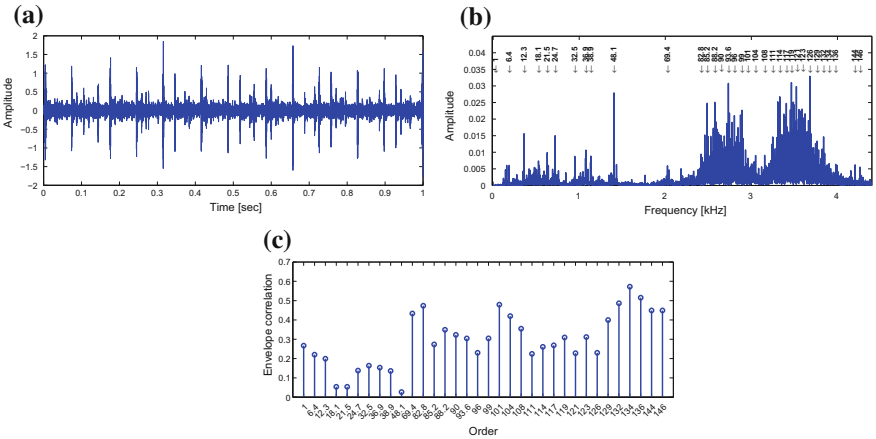

Fig. 2 Recording DE171 in time domain (**a**), frequency domain (**b**), and the envelope correlation indexes (**c**)

through time. When the frequency domain is inspected (b), it is possible to see that the spectrum of DE171 presents harmonics entirely different amongst themselves, and it just exhibits a pattern similar to wide-banded noise, hiding any characteristic of the inner race defect.

Afterward, a set of harmonics is used to compute the proposed OT decomposition. The harmonics are disposed of regarding orders normalizing each one concerning the shaft speed, in Fig. 2b. As a result, a total of 34 order components are obtained, noting that the 1 st order is added to set a reference associated to the shaft speed, and the harmonics displayed are the most representatives from the author's point of view.

In Fig. 2c, the envelope correlation indexes between the obtained $x_k(t)$ order components and the raw signal $y(t)$ for both recordings are shown. The covariance parameters used to carry out the SRCKF_OT algorithm were $q_i^a = 10^{-4}$, $q^f = 10^{-11}$, and $r = 10^{-12}$, for the vibration signal analyzed in this experiment. It is observed that, assuming a threshold of 0.5, if the envelope correlation works as an indicator of cyclostationary processes, the highest order component correlated with the signal may exhibit the fault condition.

From a visual inspection in Fig. 3, it is clearly diagnosable the inner race defect because the *BPFI* frequency is perceptible with high amplitude, and there are multiple sidebands spaced at $BPFI \pm f_r$. As a result, both approaches changes the category from P1 to Y2, taking into account the groups defined in [12], because the *BPFI* frequency is differentiable in amplitude from its sidebands and the shaft speed harmonics. Furthermore, the signal in the time domain does not exhibit a periodic impulsive behavior.

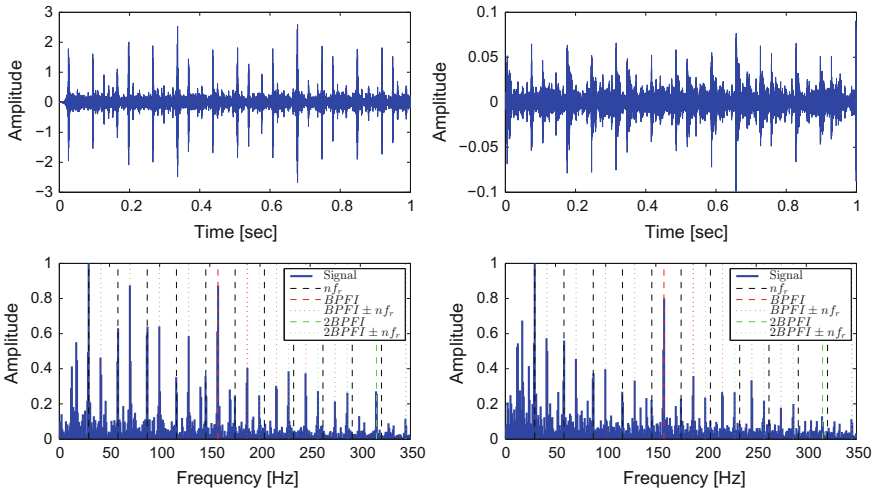

Fig. 3 Identification of the BPFI frequencies on the envelope spectrum from DE171 using both SK (*left*) and proposed SRCKF_OT (*right*) approaches

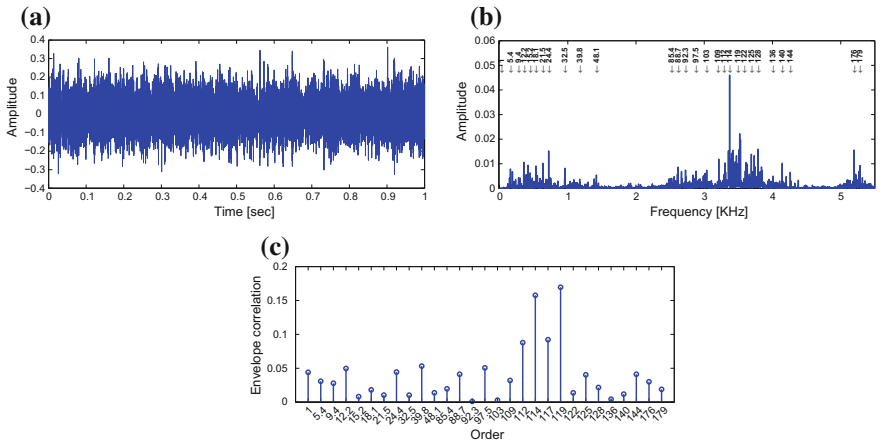

Fig. 4 Recording DE198 in time domain (**a**), frequency domain (**b**), and the envelope correlation indexes (**c**)

3.2 Outer Race Fault— BPFO

In this experiment, the DE198 was the bearing fault signal chosen which present an outer race defect. That signal is analyzed because it is not diagnosable (N2) in accordance with [12]. In fact, the signal in time domain shows appreciable differences, since, from a visual inspection, the record DE198 is indistinguishable from noise (Fig. 4a).

The displayed signal spectra (Fig. 4b) presents low amplitude spectral components where the harmonic 114 th of 29.5 Hz stands out, and there is no evidence of the cyclic fault frequency. Nonetheless, in spite that the envelopes of the order components obtained from the record DE198 are not highly correlated with the envelope of the raw vibration signal, the components with higher correlation (119 and 114th) describe a modulation processes that may be associated with the bearing fault (see Fig. 4c). For the sake of obtaining the order components, the SRCKF_OT free parameters were heuristically fixed as $q_i^a = 10^{-4}$, $q^f = 10^{-11}$, and $r = 10^{-12}$, and as a result, 25 order components were extracted.

As regards the SK comparison, the filtered signal with SK (left side) and the most relevant order component (right side) by the highest envelope correlation are displayed in Fig. 5. The blind signals extracted from the record DE198 using both approaches exhibit notable differences. In the case of SRCKF_OT, the 119th order component gives the best signs of the outer race defect, which is characterized by a low frequency modulation associated to low sidebands of the frequencies *BPFO* and $2BPFO$ (i.e. the frequencies $BPFO - f_r, BPFO - 2f_r, BPFO - 3f_r, 2BPFO - 6f_r$, and $BPFO - 7f_r$). Besides, there is a spectral component that matches with *BPFO*, yet its amplitude is small. In contrast, the filtered signal with SK in the time domain is similar to wide-band noise, but the envelope spectrum shows that the third harmonic

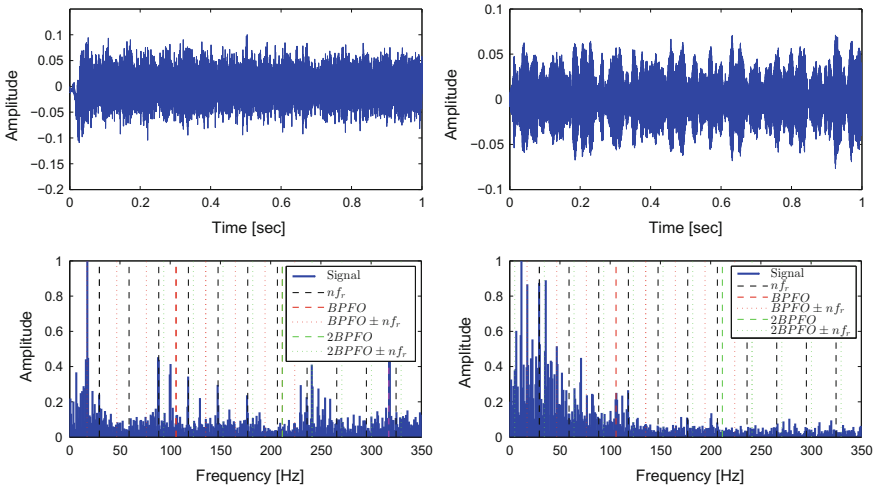

Fig. 5 Identification of the BPFO frequencies on the envelope spectrum from DE198 using both SK (*left*) and proposed SRCKF_OT (*right*) approaches

of $BPFO$ appears as well as some sidebands like $BPFO - 3f_r$ and $2BPFO + f_r$. In conclusion, both methods exhibit some characteristics of the outer race fault, being potentially diagnosable (P2) according to with the categories provided in [12].

3.3 Rolling Element Fault—BSF

In the case of rolling element defects, the BSE approaches are validated using the recording DE225 (N1). In particular, when the failure becomes large enough to allow movement of the shaft speed, the rolling element signal becomes modulated with the machine speed, generating a sideband to BSF at $\pm FTF$. Figure 6 shows the analyzed record both in the time and frequency domains, where it is possible to see that the impulsive behavior caused by the damage is a random process. This process in the case of record DE225 is virtually indistinguishable from noise, yet its spectrum shows a singular pattern of bearing faults at the frequency interval $[3.1 - 3.5]$ kHz, and a modulation process at 48.1th order with the sidebands spaced at $\pm f_r = 28.82$ Hz.

In Fig. 6c, the envelope correlation indexes computed between the order components and the raw signal are displayed. For the sake of estimating the order components, the covariances of SRCKF_OT were heuristically fixed as $q_i^a = 10^{-4}$, $q^f = 10^{-11}$, and $r = 10^{-12}$, and as a result, 30 order components were extracted from DE225. Afterwards, from the comparison between filtered signals by using both SK and SRCKF_OT (Fig. 7), it is possible to infer that the extracted signal using SK (left part) is not diagnosable (N1) as rolling element fault because there are no frequen-

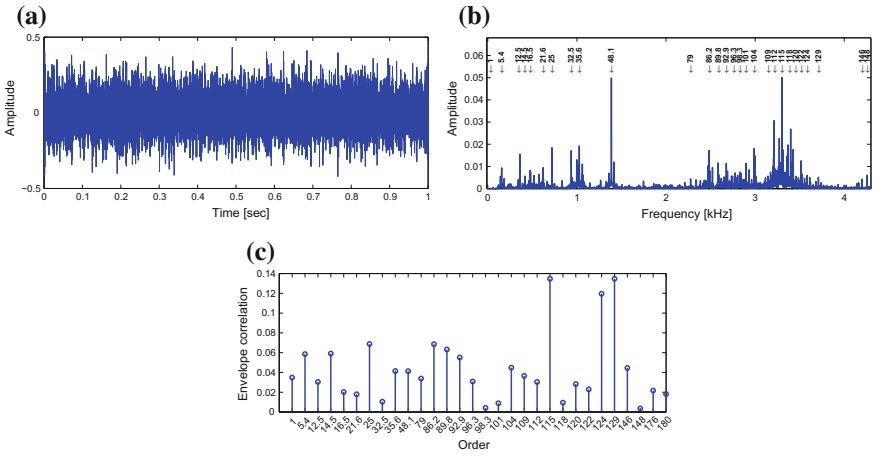

Fig. 6 Recording DE225 in time domain (**a**), frequency domain (**b**), and the envelope correlation indexes (**c**)

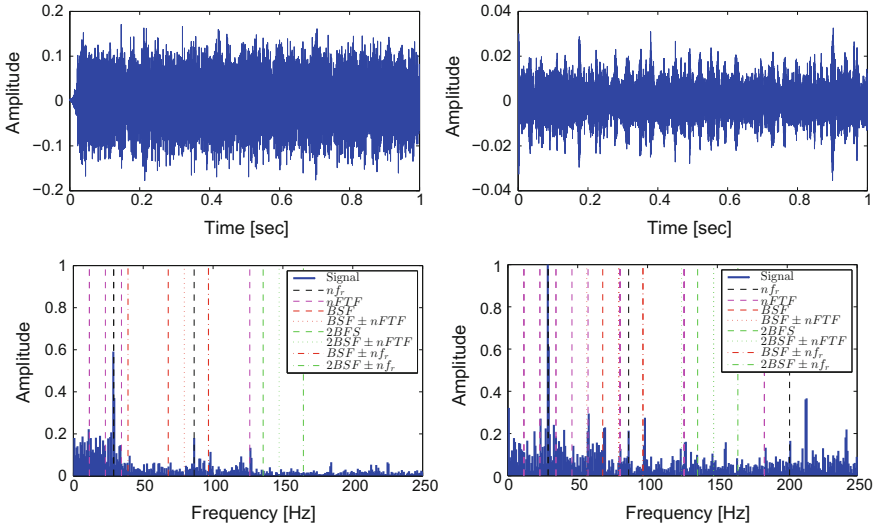

Fig. 7 Identification of the BSF frequencies on the envelope spectrum from DE225 using both SK (*left*) and proposed SRCKF_OT (*right*) approaches

cies that match with *BSF* neither *FTF* in the envelope spectrum. On the contrary, the obtained component by SRCKF_OT scheme presents some characteristics of this type of fault like the *BSF* frequency, its sidebands spaced $\pm FTF$, and some low amplitude harmonics of the *FTF*. Moreover, sidebands of the *BSF* spaced at $\pm f_r$, and a dominant component associated with the shaft speed indicating that the outer race fault is masked by that frequency. In consequence, the record DE225 is probably

diagnosable (P1) using the proposed approach since the envelope spectrum shows discrete components at the expected fault frequency but they are not dominant in the spectrum.

4 Conclusion

In this work, an alternative method for performing blind cyclostationary signal extraction is introduced by the SRCKF_OT approach. In that sense, the obtained order components comprise relevant information about the bearing faults and the modulation processes that occur in the vibration signal, which is very useful as a vibration analysis tool when the process is cyclostationary. The comparison against the SK allows showing that, in some cases, the proposed method can improve the diagnostic of bearing faults. As a future work, it is considered an analysis of the complete information provided by SRCKF_OT as well as the optimization of its parameters, and the validation of the method in real-world applications.

Acknowledgements The authors acknowledge to the Universidad Catolica de Manizales, Universidad Nacional de Colombia at Manizales, and Colciencias by the financial support through the research project entitled “Desarrollo de un sistema de monitoreo de condición y diagnóstico de fallas en línea de sistemas de generación de energía hidroeléctrica empleando una red de sensores inalámbricos de datos de alta resolución”.

References

1. Abboud, D., Antoni, J., Sieg-Zieba, S., & Eltabach, M. (2016). Deterministic-random separation in nonstationary regime. *Journal of Sound and Vibration*, *362*, 305–326.
2. Antoni, J. (2006). The spectral kurtosis: a useful tool for characterising non-stationary signals. *Mechanical Systems and Signal Processing*, *20*(2), 282–307.
3. Antoni, J. (2009). Cyclostationarity by examples. *Mechanical Systems and Signal Processing*, *23*(4), 987–1036.
4. Borghesani, P. (2015). The envelope-based cyclic periodogram. *Mechanical Systems and Signal Processing*, *58–59*, 245–270.
5. Borghesani, P., Pennacchi, P., Randall, R., & Ricci, R. (2012). Order tracking for discrete-random separation in variable speed conditions. *Mechanical Systems and Signal Processing*, *30*, 1–22.
6. Cardona-Morales, O., Avendano, L., Castellanos-Dominguez, G. (2014). Nonlinear model for condition monitoring of non-stationary vibration signals in ship driveline application. *Mechanical Systems and Signal Processing*, *44*(1–2), 134–148. Special Issue on Instantaneous Angular Speed (IAS) Processing and Angular Applications.
7. Gardner, W. A., (1990). *Introduction to random processes with applications to signals & systems* (2nd edn.). McGraw-Hill International.
8. Gardner, W. A., Napolitano, A., & Paura, L. (2006). Cyclostationarity: Half a century of research. *Signal Processing*, *86*(4), 639–697.
9. Obuchowski, J., Wyłomańska, A., & Zimroz, R. (2014). The local maxima method for enhancement of time-frequency map and its application to local damage detection in rotating machines. *Mechanical Systems and Signal Processing*, *46*(2), 389–405.

10. Obuchowski, J., Wyłomańska, A., & Zimroz, R. (2014). Selection of informative frequency band in local damage detection in rotating machinery. *Mechanical Systems and Signal Processing*, *48*(1–2), 138–152.
11. Randall, R., Antoni, J., & Chobsaard, S. (2001). The relationship between spectral correlation and envelope analysis in the diagnostics of bearing faults and other cyclostationary machine signals. *Mechanical Systems and Signal Processing*, *15*(5), 945–962.
12. Smith, W. A., & Randall, R. B. (2015). Rolling element bearing diagnostics using the case western reserve university data: A benchmark study. *Mechanical Systems and Signal Processing*, *64–65*, 100–131.

Rotating Machinery Diagnostics Based on Fusion of Infrared and Vibration Measurements

Sebastian Budzan, Dariusz Buchczik, Marek Pawełczyk and Roman Wyżgolik

Abstract Systems for on-line vibration diagnostics of rotary machines requires the installation of vibration sensors on practically each bearing. For a typical machine there are at least a couple of bearings to be monitored and for many machines to be monitored it generates considerable costs arising from the price of sensors, diagnostic modules, software and wiring. In this paper we discuss the possibility of reduction in the number of vibration measurement points, with occasional inspection with IR (Infra-Red) camera, which globally could reduce the system costs without compromising the quality of the machine diagnostic. A measurement stand modeling operation of a simple machine driven by an electric motor and a typical industrial vibration diagnostics system together with a thermal imaging camera were used for this purpose. It allows controlled induction of various defects that result in vibrations. Vibrations was measured with properly parameterized system for on-line vibration diagnostic, separately for each bearing. The research involved performing a few experiments, which modeled a typical defect in rotating machines: quasi static unbalance of the shaft, outer race defect of the bearing and cage defect of the bearing. The fusion of obtained IR and vibration information was discussed.

Keywords Vibration measurements · Machine diagnostics · Infrared thermography

S. Budzan · D. Buchczik · M. Pawełczyk · R. Wyżgolik (✉)
Measurement and Control Systems Group, Institute of Automatic Control, Silesian University of Technology, ul. Akademicka 16, 44-100 Gliwice, Poland
e-mail: roman.wyzgolik@polsl.pl

S. Budzan
e-mail: sebastian.budzan@polsl.pl

D. Buchczik
e-mail: dariusz.buchczik@polsl.pl

M. Pawełczyk
e-mail: marek.pawelczyk@polsl.pl

A. Timofiejczuk et al. (eds.), *Advances in Condition Monitoring of Machinery in Non-Stationary Operations*, Applied Condition Monitoring 9,
https://doi.org/10.1007/978-3-319-61927-9_19

1 Introduction

Rotating machinery plays very important role in industry, therefore the machine conditioning and fault diagnostic is crucial to prevent unplanned breakdowns due to the machine failure. The most popular technique for machine health conditioning is vibration analysis, where signals are acquired from accelerometers mounted on bearings [1]. In number of articles one can find modern approach to machine vibration analysis, especially for bearing, e.g. with utilization of wavelets [2, 3].

Systems for on-line vibration diagnostics of machines requires the installation of vibration sensors on practically each bearing mounted in the machine. For a typical machine there are at least a couple of bearings to be monitored. It generates considerable costs arising from the price of sensors, diagnostic modules, software and wiring. Reduction in the number of vibration measurement points, with occasional inspection of thermal imaging could reduce those costs without compromising the quality of the machine diagnostic. The research conducted by the authors aimed to verify this approach. A measurement stand modeling operation of a simple machine driven by an electric motor and a typical industrial vibration diagnostics system together with a thermal imaging camera were used for this purpose.

2 Experimental Setup

The measurement stand used during the tests is shown in Fig. 1. It allows controlled induction of various defects that result in vibrations. The main types of defects that may be generated include various types of unbalance of the shaft, the different types of misalignment of the shaft and the rotor of the electric motor, damage to rolling bearings of different nature.

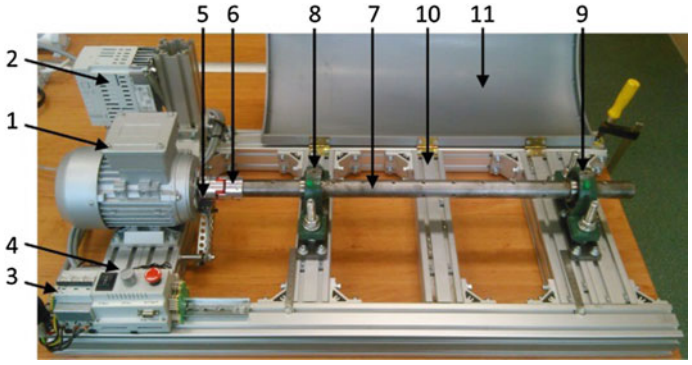

Fig. 1 View of the measurement stand: *1* electric engine, *2* frequency inverter, *3* fuse, *4* control panel, *5* encoder, *6* claw clutch, *7* main shaft, *8* left bearing, *9* right bearing, *10* stand frame, *11* safety cover

The shaft is driven by an asynchronous electric engine of 0.37 kW and a nominal rpm 2755. A frequency inverter type SV004iG5A-4 is used to control the speed and direction of rotation. The main shaft is made of a steel rod of a diameter of 30 mm and a length of 680 mm. Over its entire length at intervals 50 mm there are arranged sets of four orthogonal M6 threaded holes for mounting weights inducing unbalance. The connection of the motor to the main shaft is made by the claw clutch. An elastic element placed between the teeth, allows compensation for minor inaccuracies in the alignment of the shaft and an engine rotor.

The shaft is mounted on two single row self-aligning ball bearings type UCP206 which are embedded in cast iron housings. The upper surfaces of the housings are aligned and equipped with a threaded hole UNF 10–32 for mounting vibration sensors. The housings are screwed to the stand frame using threaded connections, allowing them to move in the vertical and horizontal plane to adjust the misalignment of the shaft. Screws M6x50, each weighing of 0.025 kg with mounted on the end additional nut M10, serve as elements responsible for adjusting the unbalance of the shaft. Prepared set of bolts is screwed into the main shaft into a suitable aperture. The steel safety cover prevents accidental contact with rotating parts.

Industrial system for on-line vibration diagnostics of machines used during the research was constructed using components manufactured by IFM Electronic. The most important element of the system is a diagnostic module VSE100, whose function is to measure and process signals from up to four vibration sensors. The module allows to diagnose up to 20 diagnosis objects on the basis of the vibration analysis in the frequency domain of up to 80 characteristic frequencies. Furthermore, it is possible to monitor in the time domain maximum acceleration and effective velocity values according to the ISO 10816 standard. Built-in Ethernet TCP/IP is used for communication with a PC or the OPC server. Analogue and digital outputs allow the direct communication with e.g. PLC controller. The memory of the history of events and trends in device includes up to 30,850 values with time real stamp.

In the course of the research two capacitive MEMS accelerometers type VSA004 were used to measure the vibrations. Their output signal was sampled at 50 kS/s. The sensors were mounted on the respective bearing housings using dedicated mounting magnets. Measurement characteristics and methods of MEMS based vibration sensors are presented in [4].

Parameterization of the system and reading of determined diagnostic values performed using software Efector Octavis VES003 2.5. Parameterization was accomplished on the basis of analysis of measurement stand construction, according to the manufacturer's instructions delivered by IFM Electronic [5] and without interfering with the advanced settings for the respective functions.

Vibration diagnostics of measurement stand performed separately for the left and right bearing using the following diagnosis values:

- For a diagnostic object of type unbalance there were determined acceleration value based on FFT for the characteristic frequency equal to the frequency of shaft rotation.

- An diagnostic object of type rolling bearing there were determined acceleration values on the basis of the analysis of the envelope of the acceleration data e-FFT separately for the three characteristic frequencies associated with defects of the outer race, inner race and rolling elements of the bearing. The characteristic frequencies were selected on the basis of the bearing database which is part of the Efector Octavis software.
- Furthermore determined the maximum acceleration a_peak and the effective value of vibration velocity v_eff in the frequency range from 10 Hz up to 1 kHz according to the ISO 10816.

In total, for each measuring point determined 6 diagnostic variables, which yields 12 variables for the two bearings [5].

3 Measurement Results and Discussion

The research involved performing a few experiments, which modeled a typical defect in rotating machines. The course of study included the following configurations:

- Experiment 1. No artificially induced defects, the rotational speed of 900 rpm
- Experiment 2. No artificially induced defects, the rotational speed of 1500 rpm
- Experiment 3. Quazi-static unbalance of the shaft, two extra weights of 0.025 kg on both sides of the right bearing, the rotational speed of 900 rpm
- Experiment 4. Quazi-static unbalance of the shaft, two extra weights of 0.025 kg on both sides of the right bearing, the rotational speed of 1500 rpm
- Experiment 5. Outer race defect of the right bearing, a crosscut of width 1 mm on the outer race, the rotational speed of 1500 rpm
- Experiment 6. Cage defect of the right bearing, fracture and deformation of the cage, the rotational speed of 900 rpm

The results for the vibration diagnostics are presented in Table 1.

Infrared thermography as a non-contact and generally non-intrusive technique of object temperature measurement can monitor all components of the machine by observing temperature variations between different parts or one part in a time [6].

In course of the experiments there were investigated different parameters which should provide some information about possible damage of the machine, e.g. average and maximal temperature in the Region Of Interest (ROI), distribution of temperature in the ROIs, including segmentation of the ROIs. Eventually all of the results evaluated with thermal camera have been connected with the vibration signals.

Thermal images used in this work have been captured using Wuhan-Guide TP8 IR camera. The camera is equipped with a 384 × 288 pixel uncooled FPA microbolometer, spectral range is 8–14 μm and thermal sensitivity 0.08 °C. The time required for stable response of the camera is more than 75 min, other case temperature error about 2 °C may occur [7].

Table 1 Diagnostic values determined in course of experiments

	Sensor	Unbalance (mg)	Bearing inner (mg)	Bearing outer (mg)	Bearing balls (mg)	a_peak (mg)	v_eff (mm/s)
Experiment 1	Left	0.595	21.7	17.3	19.5	2240	0.86
900 rpm	Right	0.034	13.2	11.8	10.6	1590	0.55
Experiment 2	Left	2.38	23.1	45.7	32.7	3790	2.53
1500 rpm	Right	0.721	16.6	17.7	20.8	3570	1.56
Experiment 3	Left	1.37	15.4	15.7	9.54	2140	1.46
900 rpm	Right	2.67	11.2	10.7	12.7	2040	2.67
Experiment 4	Left	10.5	27.8	37.9	27.9	4590	10.4
1500 rpm	Right	2.31	22.3	21.5	18.6	3980	2.74
Experiment 5	Left	3.97	29	69.8	50.9	4920	4.01
1500 rpm	Right	1.37	10.6	311	7.12	22300	4.99
Experiment 6	Left	0.261	15.3	21.6	15.2	1990	0.58
900 rpm	Right	0.071	14.7	16.1	14.6	4720	0.51

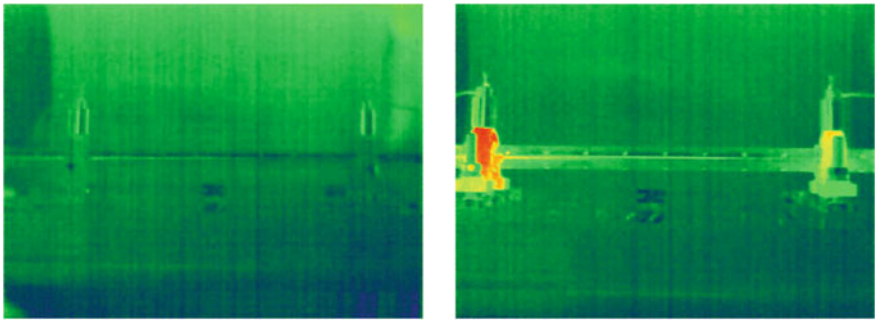

Fig. 2 Thermal image of the machine taken in front view in 1 m distance at time 0 min (*left*), at 35 min from motor start (*right*)

Each experiment performed during the research present different type of the damage. Duration of each experiment has been set up to 35 min with 2 min step.

In Fig. 1 the visual image of the tested machine has been presented. Thermal image in the stable state with two bearings in good condition (Experiment 1 and 2) before start the motor (0 min) and after 35 min of continuous motor work have been presented in the Fig. 2. As it can be seen the temperature on the left and right bearings generally doesn't differ from background, only the contours of the vibration sensors mountings have been showed, but this is a result of the different emissivity coefficient value, not the temperature change. On the right image the

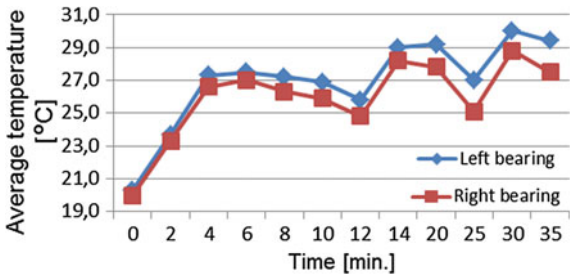

Fig. 3 Changes of the bearings temperature in time for 900 rpm motor speed

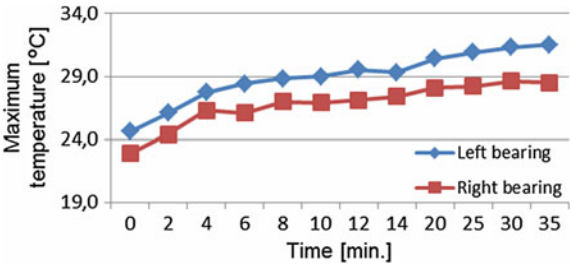

Fig. 4 Changes of the bearings temperature in time for 900 rpm motor speed

temperature of the left bearing increases dramatically to 30.9 °C from the starting 20.3 °C. That is a consequence of motor and shaft impact like in case of right bearing, where the temperature changes also from about 20.1 °C to about 29 °C. However there can be seen one problem regarding to the many typical situations in industry, e.g. right bearing is visible only in a part of them, because in front of the bearing we can see one of the screws which are used to mount the bearing case to the stand.

Thus, usage only of the average temperature without knowledge about other objects in the scene, which can impact the temperature of the examined object, may be the cause of incorrect diagnostic result (Fig. 3). In similar situations the usage of the maximum temperature values and distribution of the temperature in some interesting regions of the thermal image can solve the problem.

The unbalance near to the right bearing was a first type of investigated damage (Experiment 3 and 4). Based only on the temperature values presented in Fig. 4 we can determine that the left and right bearing temperature increases at constant speed. Obviously the temperature of the left bearing is still higher than the right bearing, what is the consequence of motor and clutch impact.

On the other hand, when the distribution of the temperature is taken into account, there can be found one difference to the normal state in which the temperature are higher around the bearings. When the unbalance was investigated, the temperature on the shaft surface near to the right bearing increased especially in first 2 min (Fig. 5 left) in contrast to situation in normal state (Fig. 5 right). In our opinion this is the result of unbalance produced near the right bearing.

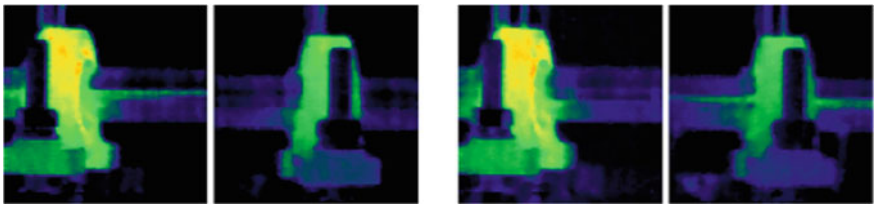

Fig. 5 Changes of the bearings temperature (left bearing−right bearing) in normal state (*left*), unbalance (*right*) for 2 min after motor starts

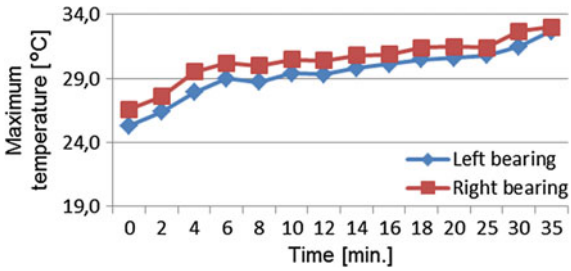

Fig. 6 Changes of the bearings temperature for outer race damage of the right bearing

In the case of unbalance near the right bearing the vibration diagnostic system registered a significant increase in the diagnosis values of unbalance and v_eff on both bearings for the speed of 900 and 1500 rpm. Regardless of the rotational speed the diagnosis value of unbalance or v_eff with a use of one sensor on any bearing is sufficient for the detection of shaft unbalance. Thermal imaging analysis of the bearing temperature leads to the false conclusion that the damage was near the left bearing. Only a comparison of the temperature distribution on the shaft relative to the good condition may indicate that unbalance arises near the right bearing.

The second investigated typical damage of bearings (Experiment 5) is the outer race fault. This type of the damage can be recognized using thermal images without any problems, even when the temperature values are taken in long period of time (Fig. 6). In comparison to the normal state there is higher value of the right bearing temperature immediate after the motor was started. The difference to the temperature of left bearing decreases with a time, but in a first 35 min it has higher value. The outer race fault impact only right bearing. The same result has been evaluated after analyzing the thermal images and the distribution of temperature (Fig. 7). Thermal images of this fault show that the comparison between temperatures of the different parts of machine enable correct fault recognition.

In case of the outer race defect there was a significant increase in the diagnosis values of unbalance, outer race, a_peak and v_eff. When the sensor is mounted on the faulty bearing, there was 20-fold increase in the value of outer race and more than sixfold increase in peak.

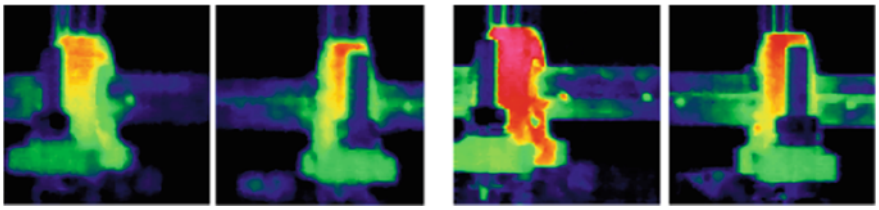

Fig. 7 Thermal images (left bearing–right bearing) of outer race fault (*left*) and normal state (*right*) for 30 min

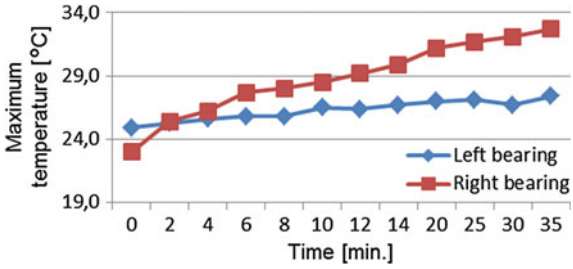

Fig. 8 Changes of the bearings temperature for cage damage of the right bearing

The rise in the same diagnosis values is approximately 1.5 and 1.3 times for the second bearing. Using only one vibration sensor may result in the lack of failure detection. As a result, there is no cause for the use of the IR camera to detect the location of the defect. There is no conclusion even if the camera is applied.

Third type of the fault (Experiment 6) is connected with the bearing cage damage. Based only on the temperature values this type of fault can be recognize with high probability. Generally, the temperature of the right bearing is higher than for left bearing, similarly for the outer race damage, but in this case the right bearing temperature increases in time dramatically in comparison to the left bearing, even if we take into account that the left bearing is influenced by the motor (Fig. 8).

In Fig. 9 four segmented thermal images have been presented. For all of them the distribution of temperature will slowly increase on the left bearing, opposite to the right bearing where the temperature changes rapidly.

In case of the bearing cage defect the vibration diagnostics showed increase in value of peak in the signal measured exclusively on the faulty bearing. Consequently, the use of only one vibration sensor can result in not detecting the defect.

A custom parameterization of the diagnostic enables detection of the failure with the use of a sensor mounted on a good bearing. In such a case the measurement based on e-FFT data for the characteristic frequency 0.4 of shaft rotation frequency may be used. The difference between the e-FFT spectra for the good and faulty bearing for this case is shown in Fig. 10.

Images recorded by the IR camera clearly shows an increase in temperature of the defected bearing, enabling the correct location of the fault.

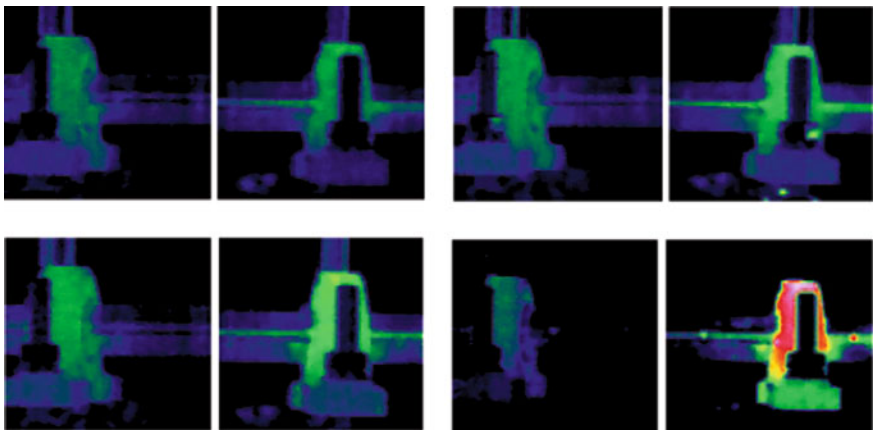

Fig. 9 Thermal images (left bearing−right bearing) for 2 and 4 (*top*), 20 and 30 (*bottom*) min of the bearings temperature for bearing cage damage

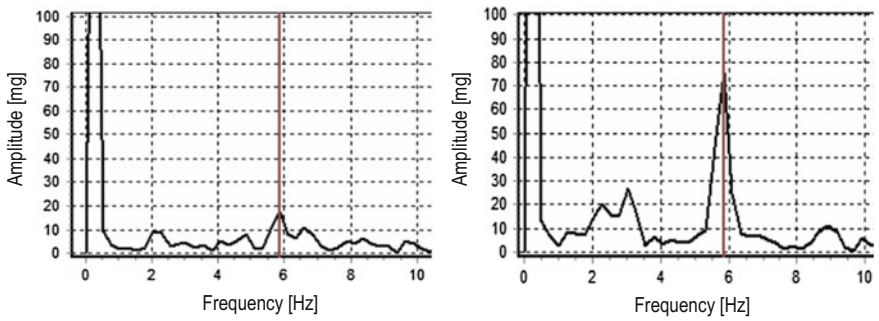

Fig. 10 Comparison of e-FFT spectra for good bearing (*left*) and bearing with cage defect (*right*)

4 Conclusion

The studies conducted on the described measurement stand does not give a clear resolve as to whether it is possible to reduce the number of vibration sensors with the additional use of thermal camera to the correct location of the fault.

In case of defects of type unbalance and outer race it is possible to reduce the number of sensors, however, the picture obtained from the thermal camera does not indicate the fault.

While in the case of the bearing cage defects, the standard parameterized vibration diagnostic system using one sensor mounted on the good bearing does not detect failure, while the thermal image indicates the fault and its location. But in case when the IR is used for temperature measurement, the operator has to take under consideration that the time required for stable response of the camera can be longer than 1 h from power. In other case the error can exceed 2 °C.

Acknowledgements The work has been partially supported by Institute of Automatic Control of Silesian University of Technology, BK funds No. BK/213/RAU1/2016/7.

References

1. Tandon, N., & Choudhury, A. (1999). A review of vibration and acoustic measurement methods for the detection of defects in rolling element bearings. *Tribology International, 32,* 469–480.
2. Kumar, R., & Singh, M. (2013). Outer race defect width measurement in taper roller bearing using discrete wavelet transform of vibration signal. *Measurement, 46,* 537–545.
3. Lau, E. C. C., & Ngan, H. W. (2010). Detection of motor bearing outer raceway defect by wavelet packet transformed motor current signature analysis. *IEEE Transactions on Instrumentation and Measurement, 59,* 2683–2690.
4. Buchczik, D., Wyżgolik, R., & Pietraszek, S. (2006). Comparative study of acceleration transducers for biomedical applications. In *Proceedings of SPIE 6348:63480U-1-63480U-10*.
5. IFM. (2013). Programming manual Software for efector octavis. Retrieved July 1, 2016, from http://www.ifm.com/mounting/704316UK.pdf.
6. Bagavathiappan, S., Lahiri, B. B., Saravanan, T., et al. (2013). Infrared thermography for condition monitoring—A review. *Infrared Physics & Technology, 60,* 35–55.
7. Budzan, S., & Wyżgolik, R. (2012). Face and eyes localization algorithm in thermal images for temperature measurement of the inner canthus of the eyes. *Infrared Physics & Technology, 60,* 225–234.

Calibration of Accelerometers Using Multisinusoidal Excitation

Dariusz Buchczik and Marek Pawełczyk

Abstract Vibrational diagnostics of machines is usually based on use of accelerometers. Their calibration is required in order to obtain reliable results. This paper presents method for calibration of accelerometers using a multisinusoidal excitation. There is also proposed a procedure for estimating uncertainty of the obtained characteristics. The routine is based on an analysis of signals in the frequency domain using evaluation of cross power spectral density between the signals from the calibrated and standard accelerometer and evaluation of power spectral density of the signal from the standard accelerometer. The procedure allows to determine the nominal sensitivity, amplitude-frequency characteristics and estimate their uncertainties. The experiments were performed using a piezoelectric sensor PCB 338B35, and a sensor based on ADXL 202 capacitive accelerometer constructed at Silesian University of Technology. Results of this study show that the proposed method can be successfully used. The main advantage of the routine is a very short duration of the measurement experiment. Values of estimated relative uncertainties reach several percent. The procedure can be applied when it is necessary to quickly check the sensor characteristics, for example in the field for periodical maintenance of sensors mounted on the machine.

Keywords Calibration · Uncertainty · Accelerometers

D. Buchczik (✉) · M. Pawełczyk
Measurement and Control Systems Group, Institute of Automatic Control, Silesian University of Technology, ul. Akademicka 16, 44-100 Gliwice, Poland
e-mail: dariusz.buchczik@polsl.pl

M. Pawełczyk
e-mail: marek.pawelczyk@polsl.pl

A. Timofiejczuk et al. (eds.), *Advances in Condition Monitoring of Machinery in Non-Stationary Operations*, Applied Condition Monitoring 9,
https://doi.org/10.1007/978-3-319-61927-9_20

1 Introduction

The method of calibration of accelerometers using uncommon excitation waveforms is not described in detail in the standards. In contrast to the method of comparison with the standard, which uses the effective values of the signals, the proposed method is based on an analysis of output signals of a standard accelerometer and a calibrated accelerometer in the frequency domain [1]. Frequency characteristics of the accelerometers are determined using evaluation of cross power spectral density between the signals from the calibrated and standard accelerometer and evaluation of power spectral density of the signal from the standard accelerometer. Although, the calibration based on periodic, random and impulsive excitation is also presented in [2, 3], the uncertainty estimation of calibration results exclusively for random excitation is proposed in [4].

2 Procedure of Calibration

Latest ISO 16063-21 [5] standard describes the method of comparison with the standard but does not describe exactly procedure for calibration using waveforms other than sine wave. The possibility of a calibration based on random and multisinusiodal excitation is merely mentioned without a detailed description of this procedure.

According to the ISO 16063-21 standard suggested value of the relative expanded uncertainty of calibration shall not be larger than 2% in the frequency range from 0.4 Hz up to 1000 Hz, 4% for the range from 1 kHz up to 2 kHz or 6% in the range of 2–10 kHz.

Calibration based on comparison with the standard involves the use of the signal from the reference accelerometer $u(i)$ and the accelerometer under test $y(i)$. The signals are sampled with a period T_p and have a length of N samples. Next, the signals are split into L segments, each with a length of N_p samples in order to perform an averaging operation in the course of further calculations. The amplitude-frequency characteristic and the phase-frequency characteristic for each of the L segments are calculated from formulas:

$$H_n\left(\Omega' m'\right) = \left| \frac{\hat{S}_{uy}^{Np}\left(j\Omega' m'\right)}{\hat{S}_{uu}^{Np}\left(j\Omega' m'\right)} Q_r \right|, \tag{1}$$

$$\varphi_n\left(\Omega' m'\right) = \arg\left[\frac{\hat{S}_{uy}^{Np}\left(j\Omega' m'\right)}{\hat{S}_{uu}^{Np}\left(j\Omega' m'\right)} Q_r \right] + \varphi_r, \tag{2}$$

where: $\hat{S}_{uy}^{Np}(j\Omega' m')$ is cross-power spectral density estimate between signals from reference and calibrated accelerometers, $\hat{S}_{uu}^{Np}(j\Omega' m')$ is power spectral density estimate of signals from reference accelerometer, Q_r is nominal sensitivity of reference accelerometer, φ_r is phase shift of reference accelerometer.

Eventually, there are determined the averaged amplitude-frequency and phase-frequency characteristic according to:

$$\overline{H(\Omega' m')} = \frac{1}{L}\sum_{n=1}^{L} H_n(j\Omega' m'), \tag{3}$$

$$\overline{\varphi(\Omega' m')} = \frac{1}{L}\sum_{n=1}^{L} \varphi_n(j\Omega' m'). \tag{4}$$

The multisinusoidal signal used for calibration is a sum of k sinusoidal signals that are periodic in time window of length N samples:

$$x(i) = \sum_{k=1}^{K} A_k \sin(\omega_k T_p i + \phi_k), \tag{5}$$

where: $\omega_k T_p \in \left\{\frac{2\pi m}{N}; m = 1, 2, \ldots, \frac{N}{2}\right\}$.

An example of the multisinusoidal waveform signal and its power spectral density is shown in Fig. 1. The power spectral density estimate of the multisinusoidal signal is expressed by the relation:

$$S_{xx}^{N}(\omega m) = \begin{cases} \frac{T_p N}{4} A_k^2 & \text{for } \Omega m \in \{\omega_k T_p,\ 2\pi - \omega_k T_p\} \\ 0 & \text{for } \Omega m \notin \{\omega_k T_p,\ 2\pi - \omega_k T_p\} \end{cases}, \tag{6}$$

for $m = 0, 1, \ldots, N - 1$.

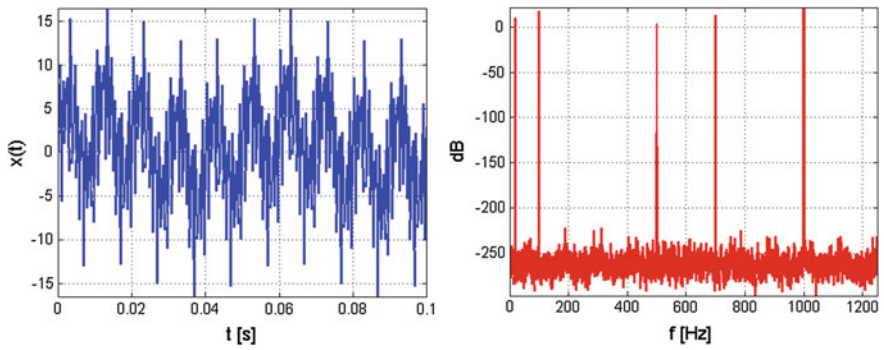

Fig. 1 Time waveform (*left*) and power spectral density (*right*) of exemplary multisinusoidal signal

3 Estimation of Uncertainty

Estimation of the uncertainty type A is based on a statistical analysis of series of measurements. The best estimate of the expected (true) value of the measured quantity is the arithmetic mean of a series of measurements.

Estimation for the amplitude-frequency characteristic is possible due to the averaging of the characteristic on the basis of L values (number of segments). Uncertainty type A can be estimated only for particular relative frequency $\Omega' m'$ of the characteristic [4]. The true value of the characteristic is calculated according to (3) and (4).

Corrected sample standard deviation for the relative frequency $\Omega' m'$ equals:

$$\sigma_{H(\Omega' m')} = \sqrt{\frac{1}{L-1} \sum_{n=1}^{L} \left[H_n(\Omega' m') - \overline{H_n(\Omega' m')} \right]^2}. \tag{7}$$

Standard uncertainty type A for the relative frequency $\Omega' m'$ is computed as:

$$u_A = \sigma_{\overline{H(\Omega' m')}} = \frac{\sigma_{H(\Omega' m')}}{\sqrt{L}}. \tag{8}$$

Consequently, relative standard uncertainty type A is given by:

$$u_A^o = \frac{\sigma_{\overline{H(\Omega' m')}}}{\overline{H(\Omega' m')}}. \tag{9}$$

The final result of the estimation is a set of uncertainties type A consisting of the uncertainties of averaged values, calculated according to (8) and (9), for all relative frequencies $\Omega' m'$.

Estimation of the uncertainty type B refers to the calculation of uncertainty by means other than the statistical analysis of series of measurements. The standard uncertainty type B is determined by analysis based on all available information (accuracy specification of measurement instruments, results of previous calibration, etc.). Taking into account maximum permissible errors Δ_{gi} of all instruments on the test stand, the uncertainty type B of the test stand is calculated from the formula:

$$u_B = \frac{\sqrt{\sum_i \Delta_{gi}^2}}{\sqrt{3}}. \tag{10}$$

Relative standard uncertainty type B equals:

$$u_B^o = \frac{\sqrt{\sum_i \delta_{gi}^2}}{\sqrt{3}}. \tag{11}$$

Combined standard uncertainty taking into account the uncertainty of type A and B is determined from the equation:

$$u_C = \sqrt{u_A^2 + u_B^2}. \tag{12}$$

Eventually, expanded uncertainty is the product of coverage factor k_α and the combined standard uncertainty:

$$U = k_\alpha u_C. \tag{13}$$

The value of the coverage factor k_α is determined by the dominant uncertainty. For a small series of measurements, where the number segments $L < 10$, the coverage factor is determined from the t-distribution for a confidence level of 95% and a degree of freedom $v = L - 1$.

In the case of a larger number of segments $L \geq 10$ coverage factor is determined based on the normal distribution. Usually the confidence level of 95% is assumed, that results in $k_\alpha = 2$.

4 Test Stand

The test stand applied in the research is very similar to the typical measurement system dedicated to calibration of accelerometers using the method of comparison with the standard [5, 6]. The system is based on electromagnetic vibration exciter whose parameters limits frequency and amplitude range of the calibration. Instead of the voltmeter which measures the effective voltage of output signals from the accelerometers a DAQ board is used, which allows measurement of the waveform at a certain sampling rate for further data processing in the frequency domain.

The equipment includes also a reference piezoelectric accelerometer type BK 8305S, a measuring amplifier type BK 2525 and a vibration exciter type BK 4809. The PXI platform from National Instruments equipped with a M-series DAQ board type PXI 6251 is used for waveform generation, measurement and data processing. The PXI system runs on Windows XP and Microsoft Office allows preparation of the reports. Access to the network facilitates the data transfer. A scheme of the system is shown in Fig. 2.

The total standard uncertainty type B of the test stand is $u_B^o = 4.2\%$. The dominant source of uncertainty type B is the error of multisinusoidal signal amplitude. Appropriate value of the amplitude is difficult to adjust due to non-linearity of the vibration exciter and power amplifier.

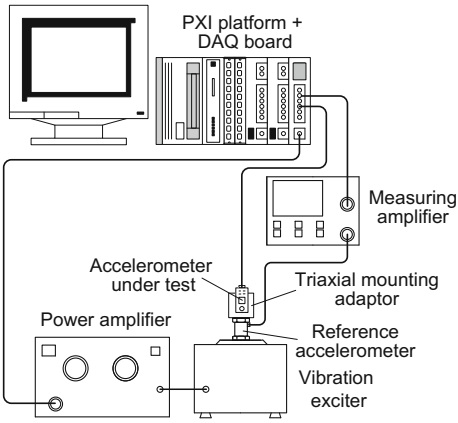

Fig. 2 Diagram of the measurement system for calibration of accelerometers

The complex processing of the measurement data required to develop appropriate applications. Dedicated software written in LabView environment handle measurement and recording of measurement data, execute calculations and display resulting graphs, waveforms and parameters. The program has been written according to the producer-consumer design pattern. The main application consists of several subroutines (subVIs) performing designated tasks.

5 Experimental Results

Studies on the calibration procedure were performed using two types of accelerometers. The first one is a single-axis piezoelectric sensor type PCB 338B35 and the second sensor, constructed in the Institute of Electronics of Silesian University of Technology, is based on a dual-axis capacitive accelerometer type ADXL 202.

The construction of the ADXL 202 based sensor is optimized for measurement of relatively small acceleration in the low frequency range. It is equipped with a simple low pass filter, which narrows the frequency band to 200 Hz. The construction of sensors and their use for biomedical measurements are described in [6, 7].

5.1 Calibration of Piezoelectric Accelerometer

The multisinusoidal signal, used during the calibration is composed of frequencies of 10, 12.5, 16, 20, 25, 31.5, 40, 50, 63, 80, 100, 125, 160, 200, 250, 315, 400, 500, 630, 800, 1000, 1250, 1600, 2000, 2500 Hz (according to ISO 266) and accelerations of 3, 4, 5, 6, 7 m/s^2. The sampling frequency of acceleration signals was 6 kHz, and the number of segments used to average characteristics was $L = 10$.

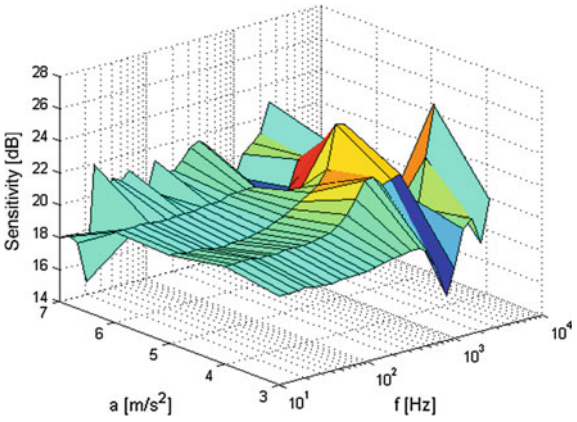

Fig. 3 Sensitivity characteristic of the PCB 338B35 piezoelectric accelerometer determined in course of the research

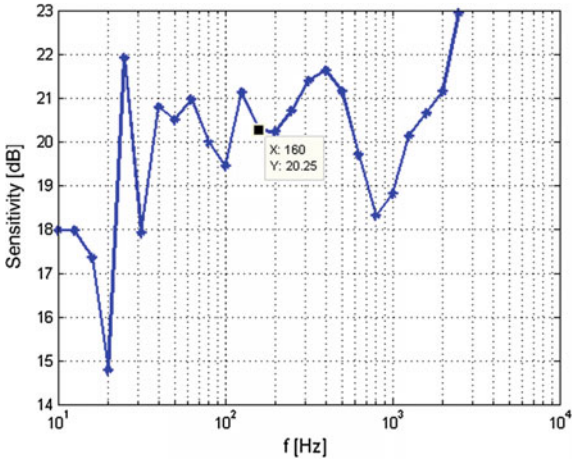

Fig. 4 Resulting amplitude-frequency characteristic of the PCB 338B35 piezoelectric accelerometer

The resulting sensitivity characteristic of the piezoelectric accelerometer is shown in Fig. 3. Its amplitude-frequency characteristic for the acceleration of 7 m/s^2 is shown in Fig. 4. The reference sensitivity of the accelerometer for frequency 160 Hz is 10.29 mV/(m/s^2) (20.25 dB) with the expanded uncertainty of 1.34 mV/(m/s^2). The largest deviation from the nominal sensitivity in the frequency range of the sensor is 47% at a frequency of 20 Hz (5.18 mV/(m/s^2)).

The curve of the sensitivity characteristic is very irregular, there are visible large deviations from the nominal value. The reason for this phenomenon is the previously mentioned error of amplitude setting for a particular frequency component of the multisinusoidal signal.

5.2 Calibration of Capacitive Accelerometer

The calibration of the capacitive accelerometer was accomplished using frequency component of 10, 12.5, 16, 20, 25, 31.5, 40, 50, 63, 80, 100, 125, 160, 200, 250, 315, 400, 500, 630, 800, 1000, 1250, 1600, 2000, 2500, 3150, 4000 Hz (according to ISO 266) and accelerations of 4, 5, 6, 7, 8 m/s^2. Sampling frequency was 12 kHz and number of segments was $L = 10$.

The sensitivity characteristic and amplitude-frequency characteristic for the acceleration of 7 m/s^2 are shown in Fig. 5 and Fig. 6, respectively. The capacitive accelerometer has higher reference sensitivity (for frequency 160 Hz) with comparison to the piezoelectric one which is 27.64 mV/(m/s^2) (27.64 dB) with the expanded uncertainty of 3.12 mV/(m/s^2). The maximum deviation from the nominal sensitivity in the frequency range limited by low-pass filter to 200 Hz is 14% at a frequency of 31.5 Hz.

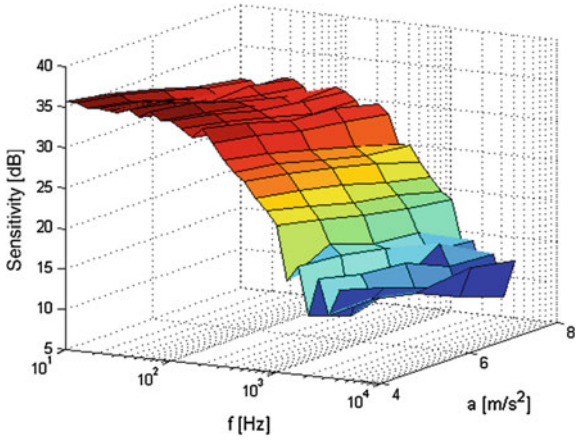

Fig. 5 Sensitivity characteristic of the sensor based on ADXL 202 capacitive accelerometer determined in course of the research

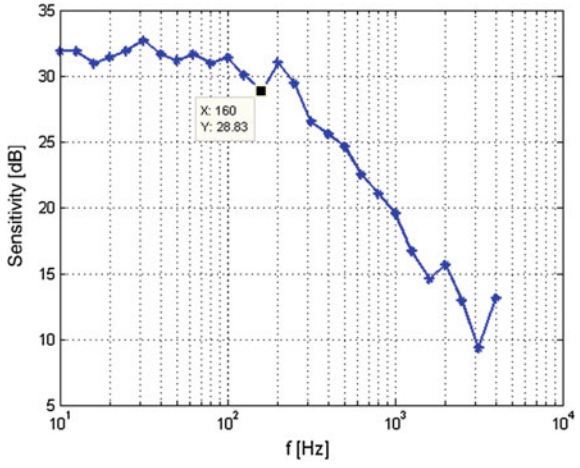

Fig. 6 Resulting Amplitude-frequency characteristic of the sensor based on ADXL 202 capacitive accelerometer

Table 1 Parameters of the calibrated accelerometers determined in course of experiments

	Nominal sensitivity ($mV/(m/s^2)$)	Maximum deviation in frequency range (%)
Piezoelectric accelerometer PCB 338B35	10.29 ± 1.34	47
Capacitive accelerometer based on ADXL 202	27.64 ± 3.12	14

The sensitivity characteristic is approximately flat up to the frequency of 200 Hz. Further sensitivity rapidly decreases as a result of the low pass filter operation.

The results obtained for the examined accelerometers in the course of the experimentation are summarized in Table 1.

6 Conclusions

Results of this study show that the method of calibration using multisinusoidal excitation can be successfully used to calibrate both piezoelectric and capacitive accelerometers, however, the uncertainty of the results is relatively large. The procedure allows to determine the nominal sensitivity for the reference frequency, amplitude-frequency and phase-frequency characteristics as well as estimation of the uncertainty of the results.

The most important advantage of the method based on multisinusoidal excitation with comparison to the classic method based on the sinusoidal excitation is very short duration of the measurement experiment. Usually it does not exceed a few seconds.

Values of uncertainty estimated during the calibration procedure for frequency reference are far larger than the ISO 16063-21 standard describes and they reach several percent. The method can be successfully applied when it is necessary to quickly check the accelerometer characteristics and large uncertainty of the results is acceptable, for example, in the field for the periodic maintenance of the sensors mounted on the object.

An important factor influencing the outcomes of the calibration are a number of sections used in averaging of the characteristics and the number of recorded samples. Further work on the optimal selection of these parameters can lead to a reduction in the uncertainty of the parameters and improving the designated characteristics.

Acknowledgements The research reported in this paper was co-financed by the National Centre for Research and Development, Poland, under Applied Research Programme, project no. PBS3/B3/28/2015.

References

1. Wang, F. Q., Guo, Y. Z., & Xu, X. Z. (1995). Influence of different excitation methods on vibration calibration. *ISA Transactions, 34,* 87–92. doi:10.1016/0019-0578(95)00002-H.
2. Albarbar, A., Badri, A., Sinha, J. K., & Starr, A. (2009). Performance evaluation of MEMS accelerometers. *Measurement, 42,* 645–804. doi:10.1016/j.measurement.2008.12.002.
3. Sinha, J. K. (2005). On standardisation of calibration procedure for accelerometer. *Journal of Sound and Vibration, 286,* 417–427. doi:10.1016/j.jsv.2004.12.004.
4. Buchczik, D., & Ryba, A. (2014). Calibration of accelerometers using random excitation. *PAK, 8,* 544–548.
5. ISO 16063-21. (2003). Methods for the calibration of vibration and shock transducers—Vibration calibration by comparison to a reference transducer.
6. Buchczik, D., Wyżgolik, R., & Pietraszek, S. (2006). Comparative study of acceleration transduc-ers for biomedical applications. In *Proceedings of SPIE 6348:63480U-1-63480U-10*. doi:10.1117/12.721118.
7. Wyżgolik, R., Buchczik, D., & Pietraszek, S. (2008). Low-frequency acceleration transducers for biomedical applications—the construction and the calibration. In *XXII Eurosensors, Dresden, Conference Proceedings*, pp. 417–420.

Operational Condition Monitoring of Wind Turbines Using Cointegration Method

Phong B. Dao, Wieslaw J. Staszewski and Tadeusz Uhl

Abstract This paper presents a cointegration-based method for condition monitoring and fault detection of wind turbines. The proposed method is based on the residual-based control chart approach. The main idea is that cointegration is a property of some sets of nonstationary time series where a linear combination of the nonstationary series can produce a stationary residual. Then the stationarity of cointegration residuals can be used in a control chart as a potentially effective damage feature. The method is validated using the experimental data acquired from a wind turbine drivetrain with a nominal power of 2 MW under varying environmental and operational conditions. Two known abnormal problems of the wind turbine are used to illustrate the fault detection ability of the method. A cointegration-based procedure is performed on six process parameters of the wind turbine where data trends have nonlinear characteristics. Analysis of cointegration residuals —obtained from cointegration process of wind turbine data—is used for operational condition monitoring and fault/abnormal detection. The results show that the proposed method can effectively monitor the wind turbine and reliably detect abnormal problems.

Keywords Wind turbine · Condition monitoring · Cointegration · SCADA

P.B. Dao (✉) · W.J. Staszewski · T. Uhl
AGH University of Science and Technology, Al. Mickiewicza 30,
30-059 Kraków, Poland
e-mail: phongdao@agh.edu.pl

W.J. Staszewski
e-mail: w.j.staszewski@agh.edu.pl

T. Uhl
e-mail: tuhl@agh.edu.pl

A. Timofiejczuk et al. (eds.), *Advances in Condition Monitoring of Machinery in Non-Stationary Operations*, Applied Condition Monitoring 9,
https://doi.org/10.1007/978-3-319-61927-9_21

1 Introduction

It is well known that unexpected failures of turbine components—such as gearboxes, generators, rotors—can lead to costly repair and often months of machine unavailability, thereby increasing operation costs and subsequently cost of energy. Therefore condition monitoring (CM) and fault diagnosis of wind turbines (WTs), in particular at the early stage of fault occurrence, is an important problem in wind turbine engineering [1].

Many CM techniques were developed to diagnose abnormalities of WTs, as reviewed in [2, 3]. These include: vibration analysis, oil monitoring, acoustic emission, ultrasonic testing, strain measurement, radiographic inspection, and thermography. Another solution—based on the analysis of Supervisory Control And Data Acquisition (SCADA) data—has been employed in [1, 4–8]. This technique is cost-efficient, readily available, and is beneficial for identifying abnormal components since only key operational parameters need to be tracked [1, 6]. Monitoring of trends and removal of undesired trends from these parameters is one of the most important problems when SCADA approaches are used. Various methods have been developed for data trend analysis. Recent years have attracted numerous applications based on the cointegration approach, which was originally developed in the field of Econometrics in the late 1980s [9, 10]. The major idea used in these investigations is based on the concept of stationarity. In a simplified description, nonstationary processes are cointegrated if a linear combination of these processes leads to a stationary process. When cointegration is used for damage detection, monitored variables are cointegrated to create a stationary residual whose stationarity represents normal condition. Then any departure from stationarity can indicate that monitored processes or structures are no longer operating under normal condition. The cointegration approach has been successfully employed as a reliable tool for dealing with the problem of operational and/or environmental variability in Process Engineering [11] and Structural Health Monitoring [12–16, 18, 19].

The current paper builds upon previous investigations on the cointegration method for data trend analysis, process monitoring and structural damage detection. The main goal is to present a new SCADA data analysis approach—based on cointegration method—for condition monitoring of WTs. SCADA data from a WT drivetrain with a nominal power of 2 MW were used to validate the method. The results show that the proposed method can effectively monitor the wind turbine and reliably detect abnormal problems.

2 Condition Monitoring of Wind Turbines Using SCADA Data

Previous research on the use of SCADA data for condition monitoring and fault diagnosis of WTs has established considerable achievements, as reported in [1, 4–8]. However, there exists two major problems with respect to SCADA-based approaches, as discussed in the literature.

1. Wind turbine SCADA data are generally collected, averaged and stored at 10-min intervals (i.e. low-sampling rate), as illustrated in [4–8]. Although SCADA signals are acquired at low-sampling rate, a variety of process parameters from different components of a WT are usually recorded continuously in a period of months under varying operating conditions; and when it comes to a wind farm with hundreds of WTs then the SCADA database obtained is diversified and intensive.
2. SCADA data not only depend on the health condition of a WT, but also vary over wide ranges under varying operating conditions [4–8]. In other words, a serious fault can lead to the change of SCADA data, however the change of SCADA data does not necessarily mean a fault [6]. Besides effects of variable operational conditions, changes in ambient environment conditions (e.g. wind speed, ambient temperature and humidity) also influence on WT SCADA data. Therefore it is hard to detect exactly and reliably an incipient fault from raw SCADA data if without an appropriate data analysis tool [6].

Recent studies on condition monitoring and fault diagnosis of WTs have been focusing on solving these two problems. Concerning the first problem, due to the great number of WTs to be monitored and the large amount of low-sampling rate SCADA signals to be analysed, human intervention in data interpretation and analysis should be avoided [7]. Consequently, most solutions—taking advantage of Artificial Intelligence techniques—have been proposed and used to analyse SCADA data. The most advanced systems using this approach are Neural Network (NN) algorithms and Adaptive Neuro-Fuzzy Interference Systems (ANFIS). However, it is well known that NN-based and ANFIS-based algorithms are complicated and require long training period and excessive computation time. With respect to the second problem, each WT requires intelligent CM techniques that can be fully adapted to varying operating conditions. Unfortunately such technique has not been fully achieved today [6]. Therefore the main objective of the work presented in this paper is to develop a proper SCADA data analysis/processing method—based on cointegration technique—that can automatically interpret and analyse a large amount of low-sampling rate SCADA data, and additionally, is able to deal with undesired effects of environmental and operational variability in data used for condition monitoring and fault detection of wind turbines.

3 Cointegration Analysis—Theoretical Background

In mathematics the concept of stationarity can be introduced using time series analysis. A given time series y_t can be presented in the form of the first-order Auto-Regressive $AR(1)$ process [20], which is defined as

$$y_t = \phi y_{t-1} + \varepsilon_t \tag{1}$$

where ε_t is an independent Gaussian white noise process with zero mean, i.e. $\varepsilon_t \sim IWN(0, \sigma^2)$. Then three different time series can be distinguished for different values of coefficient ϕ [20]. These are: (1) stationary time series $(|\phi| < 1)$; (2) nonstationary time series $(\phi > 1)$; and (3) random walk $(\phi = 1)$.

Any time series y_t that exhibits the form of random walk without a trend is considered as an integrated series of order 1, denoted $I(1)$ [21]. For such a series Eq. (1) yields

$$\Delta y_t = y_t - y_{t-1} = \varepsilon_t \tag{2}$$

Equation (2) shows that, the first difference of y_t, i.e. $y_t - y_{t-1}$, is just a stationary white noise process ε_t. In other words, a nonstationary $I(1)$ time series becomes a stationary $I(0)$ time series after the first difference. By analogy, a nonstationary $I(2)$ time series would require differencing twice to induce a stationary $I(0)$ time series.

Next, the concept of cointegration can be introduced using a vector Y_t of $I(1)$ time series defined as $\mathrm{Y}_t = (y_{1t}, y_{2t}, \ldots, y_{nt})^T$. This vector is linearly cointegrated if there exists a vector $\beta = (\beta_1, \beta_2, \ldots, \beta_n)^T$ such that

$$\beta^T \mathrm{Y}_t = \beta_1 y_{1t} + \beta_2 y_{2t} + \cdots + \beta_n y_{nt} \sim I(0) \tag{3}$$

In other words, the nonstationary $I(1)$ time series in Y_t are linearly cointegrated if there exists (at least) a linear combination of them that is stationary, i.e. having the $I(0)$ status. This linear combination, denoted as $\beta^T \mathrm{Y}_t$, is referred to as a cointegration residual or a long-run equilibrium relationship between time series [21]. The vector β is called a cointegrating vector. The action of creating the cointegration residual $\left(u_t = \beta^T \mathrm{Y}_t\right)$ is considered as the action of projecting the vector Y_t on the cointegrating vector β.

In essence, testing for cointegration is testing for the existence of long-run equilibriums (or stationary linear combinations) among all elements of Y_t. Such tests have two important requirements [21]. Firstly, any analysed time series must exhibit at least a common trend. Secondly, the analysed time series must have the same degree of nonstationarity.

In general, the cointegration test consists of two steps:

1. The first step is to determine the existence of cointegration relationships and the number of linearly independent cointegrating vectors among multivariate (nonstationary) time series and to form the cointegration residuals.
2. The second step is to perform unit root tests on the cointegration residuals found to determine if they are stationary series (i.e. testing for stationarity).

For the first step, the Johansen's cointegration method [10] has been widely used. It is a sequential procedure based on maximum likelihood techniques, which basically is a combination of cointegration and error correction models in a Vector Error Correction Model. For the second step, the augmented Dickey-Fuller (ADF) test [22] is the most popular unit root test. The ADF test checks the null hypothesis that a time series is nonstationary against the alternative hypothesis that it is stationary, assuming that the dynamics in the data have an Auto-Regressive Moving Average (ARMA) structure.

4 Cointegration-Based Approach to Condition Monitoring of Wind Turbines Using SCADA Data

Cointegration technique has been successfully applied to compensate for environmental and/or operational variability in various damage detection and condition monitoring applications when data are linearly or nonlinearly related and environmental-operational variability trends are linear or nonlinear, as presented in [11–16, 18, 19]. In the current work, the cointegration approach is employed for on-line condition monitoring of wind turbines using SCADA data and analysing nonlinear relations (or trends) between process/operational parameters of wind turbines.

The cointegration-based procedure involves two stages:

1. Off-line stage: calculate (or estimate) cointegrating vectors using SCADA data that are acquired from the monitored wind turbine under normal operating conditions or modes (usually at the beginning of the WT's lifetime when its components are considered "healthy");
2. On-line stage: calculate cointegration residuals used for continuous (on-line) condition monitoring using the cointegrating vectors found and SCADA data acquired from the monitored wind turbine under regular operating or working phase (i.e. during electricity production phase).

The computation algorithm—performed in the off-line stage—can be considered as an unsupervised learning process because it uses only SCADA data under normal operating conditions to calculate cointegrating vectors. More specifically, this off-line stage performs the maximum eigenvalue statistic method [10] for

calculating cointegrating vectors using process parameters of the wind turbine under a normal operating condition. The stationarity-based approach [17] is used in this off-line stage to determine the optimal lag length(s) to be included in cointegration analysis to calculate optimal cointegrating vectors. Next, the resulting optimal cointegrating vectors are applied to SCADA data acquired from the monitored wind turbine during the electricity production phase to create the cointegration residuals used for condition monitoring.

In comparison with commonly used data-mining algorithms (e.g. neural network, support vector machines) the cointegration-based algorithm is very simple and requires much less computational resources. The calculation of cointegrating vectors in the off-line stage takes only few seconds on a normal computer. For the second stage, the calculation algorithm is basically performed through projecting the SCADA data—acquired from the monitored WT under regular working phase for producing electricity—on the resulting optimal cointegrating vectors. This is done simply by multiplying a vector of time series variables by a cointegrating vector to form a cointegration residual (described by Eq. (3)). This computation process can be promptly executed in real-time manner on a computer-based condition monitoring system, thereby providing a simple on-line condition monitoring solution for wind turbines using SCADA data.

5 Experimental Wind Turbine Data

The wind turbine data used in this paper originate from a series of experimental measurements for a WT drivetrain with a nominal power of 2 MW. SCADA data collection and condition monitoring for the WT was performed at 10-min intervals during thirty days in November 2012. The collected data were influenced by environmental conditions (e.g. wind speed, ambient temperature variations between day and night, and air humidity). In addition, twelve process parameters were monitored and recorded under varying operating conditions. As a result, 4320 data samples were acquired for each process parameter under the effect of both environmental and operational variability. Because wind speed is a key parameter in wind energy systems [1, 6], the nonlinear relations between this parameter and other ones were identified. It is observed that there is a common trend presenting in these nonlinear relations—i.e. amplitudes of all four investigated process parameters increase nonlinearly together with the increase of wind speed.

The work presented in this paper assumed that under the normal operating condition the investigated wind turbine operated at wind speeds varying between 5 mps (or 11 mph) and 11 mps (or 25 mph). To illustrate the cointegration-based approach presented in Sect. 4. Besides the task of continuous condition monitoring for the WT, it is expected that the method can accurately and reliably detect two known abnormal problems (denoted as “F1” and “F2”) and described below.

1. F1 represents an abnormal operating state that occurred during a time interval (80 min) between the data samples 410 and 418. This abnormal operation happened when the wind speed was varying within the range [3.25–4.75] mps (in other words, it varied below the lower limit 5 mps). Consequently, the generator speed rapidly dropped off from 800 rpm to almost stationary state (standstill), then suddenly increased up to more than 600 rpm and afterward decreased to 0 rpm, and finally boosted up to the speed nearly 800 rpm. At the same time, the generated power was quickly dropped down from 20 to 0 kW. It is clear that this abnormal state of the WT should be continuously and accurately monitored to guarantee its proper operating condition and avoid more serious problems.
2. F2 represents a specific fault that occurred at the data sample 1230. This fault happened when the generator speed and generated power as well as the generator voltage and generator current were suddenly dropped down to the zero value, whereas at the same time, the wind speed was relatively stable around [5, 6] mps (i.e. it was varying within the normal operating condition). It was assumed that this fault might be caused by a bearing failure or journal damage in the gearbox. Therefore it is important to accurately detect this fault at the early stage of its occurrence.

6 Experimental Results

SCADA data of the wind turbine—described in Sect. 5—were used to validate the cointegration-based method presented in Sect. 4. Six process parameters of the wind turbine were selected for this purpose. These are: wind speed, generator speed, generated power, generator temperature (front part), generator current, and gearbox temperature. This forms *a six-variable cointegrated system*.

Selected results of condition monitoring process and fault diagnosis (F1 and F2) for the wind turbine using the 1st and 5th cointegration residuals are presented in Fig. 1. The results are shown only for the first 1400 data samples. The pairs of dotted horizontal lines indicate the upper and lower limits of the parameters under the assumed normal operating condition. In order to make the results more clear and readable, the 99.7% statistical confidence levels—with respect to the average of each cointegration residual—were calculated as $\nu \pm 3\sigma$, where ν and σ are the mean and standard deviation, respectively. Two pairs of red dotted horizontal lines indicate these confidence intervals. The values of cointegration residuals between these two confidence levels fall into the area representing that the wind turbine is still operating in the normal condition. In contrast, abnormal problems or faults would occur whenever the cointegration residual goes beyond the confidence levels. The results in Fig. 1 show that the 1st cointegration residual successfully detected both F1 and F2 while the 5th cointegration residual only detected the fault F2.

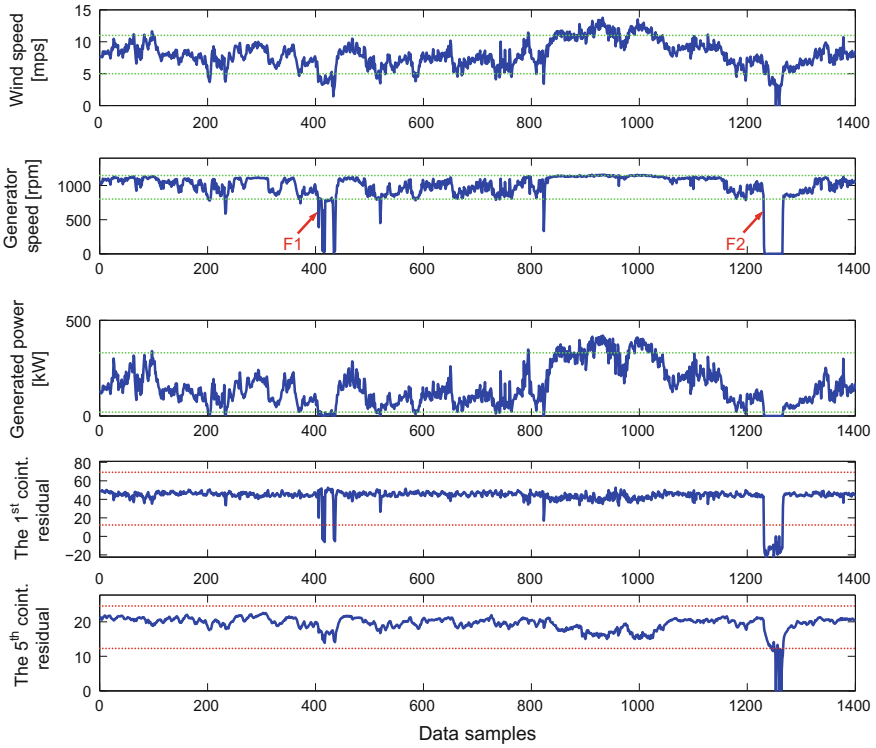

Fig. 1 Monitoring process of the abnormal operation F1 and the fault F2

In order to illustrate more specifically how cointegration residuals can be used for condition monitoring and fault detection of the wind turbine, monitoring processes of the fault F2 are enlarged and presented in Fig. 2. One can observe that both cointegration residuals successfully detected the fault F2. However, it is easy to notice that the first residual responded to the fault occurrence much faster than the fifth one. By observing the plot results, the fault F2 was detected by the first residual in the middle of the data samples 1230 and 1231 when the residual goes beyond the confidence level indicated by the dotted horizontal line; while the fifth residual identified the fault F2 at the data sample 1240 (not shown in Fig. 2). Moreover, Fig. 2 shows that this fault really came to effect at the data sample 1232 after the generator speed and generated power as well as the generator voltage and generator current were dropped down to the zero value, while the wind speed was still equal to 5.7 mps (i.e. within the normal operating condition). A conclusion can be drawn from these results is that the 1st cointegration residual predicted in advance the occurrence of the fault F2.

It is necessary to note that the entire SCADA data (4320 data samples for each process parameter) were used in the present work. However only a part of the dataset —corresponding to the first 10 days of condition monitoring process (or in other

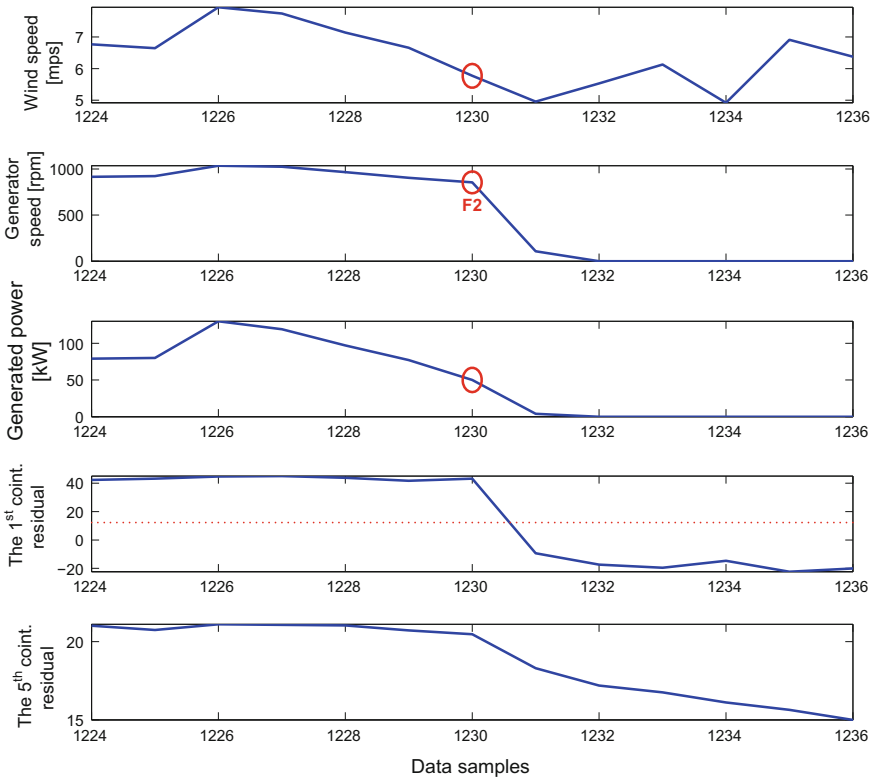

Fig. 2 Zoom in the monitoring process of the fault F2

words, the first 1400 data samples)—has been selected to present and discuss the results in this paper. This is because of the fact that the selected period of time contains interesting events of condition monitoring and fault diagnosis. In addition, due to the maximum page limit so that only selected results are presented in the paper.

7 Conclusions

Condition monitoring and fault diagnosis of wind turbines—based on cointegration analysis of SCADA data—has been addressed in this paper. An two-stage cointegration-based procedure has been proposed to deal with this problem. The method was tested in two case studies with known faults. Analysis of cointegration residuals—obtained from cointegration process of wind turbine data—is used for operational condition monitoring and automated fault/abnormal detection. The results show that the proposed method can effectively monitor the wind turbine and reliably detect abnormal problems.

The method can automatically interpret and analyse a large amount of low-sampling rate SCADA data and enables a transition from a singular process parameter analysis to automatic interpretation and analysis of a large number of process parameters. The proposed method has been motivated by the fact of its simplicity and low computational cost in comparison to other commonly used data-mining techniques such as Neural Network algorithms.

The work presented is a feasibility study. Therefore, further research work is required to test the method to other wind turbine SCADA database. In addition, the proposed methodology should be investigated for a large number of wind turbines with different types of fault/abnormal components.

Acknowledgements The work presented in this paper was supported by funding from the WELCOME research project no. 2010-3/2 sponsored by the Foundation for Polish Science (Innovative Economy, National Cohesion Programme, EU). The authors are grateful to the financial support from the Department of Robotics and Mechatronics at the AGH University of Science and Technology.

References

1. Kusiak, A., & Li, W. (2011). The prediction and diagnosis of wind turbine faults. *Renewable Energy, 36*(1), 16–23.
2. Hameed, Z., Hong, Y. S., Cho, Y. M., Ahn, S. H., & Song, C. K. (2009). Condition monitoring and fault detection of wind turbines and related algorithms: A review. *Renewable and Sustainable Energy Reviews, 13*(1), 1–39.
3. Garcia Marquez, F. P., Tobias, A. M., Pinar Perez, J. M., & Papaelias, M. (2012). Condition monitoring of wind turbines: Techniques and methods. *Renewable Energy, 46,* 169–178.
4. Zaher, A., McArthur, S. D. J., Infield, D. G., & Patel, Y. (2009). Online wind turbine fault detection through automated SCADA data analysis. *Wind Energy, 12*(6), 574–593.
5. Qiu, Y., Feng, Y., Tavner, P., Richardson, P., Erdos, G., & Chen, B. (2012). Wind turbine SCADA alarm analysis for improving reliability. *Wind Energy, 15*(8), 951–966.
6. Yang, W., Court, R., & Jiang, J. (2013). Wind turbine condition monitoring by the approach of SCADA data analysis. *Renewable Energy, 53,* 365–376.
7. Schlechtingen, M., Santos, I. F., & Achiche, S. (2013). Wind turbine condition monitoring based on SCADA data using normal behavior models. Part 1: System description. *Applied Soft Computing, 13*(1), 259–270.
8. Feng, Y., Qiu, Y., Crabtree, C. J., Long, H., & Tavner, P. J. (2013). Monitoring wind turbine gearboxes. *Wind Energy, 16*(5), 728–740.
9. Engle, R. F., & Granger, C. W. J. (1987). Cointegration and error-correction: Representation, estimation and testing. *Econometrica, 55,* 251–276.
10. Johansen, S. (1988). Statistical analysis of cointegration vectors. *Journal of Economic Dynamics and Control, 12,* 231–254.
11. Chen, Q., Kruger, U., & Leung, A. Y. T. (2009). Cointegration testing method for monitoring non-stationary processes. *Industrial and Engineering Chemistry Research, 48,* 3533–3543.
12. Cross, E. J., Worden, K., & Chen, Q. (2011). Cointegration: A novel approach for the removal of environmental trends in structural health monitoring data. *Proceedings of the Royal Society A, 467,* 2712–2732.

13. Dao, P. B., & Staszewski, W. J. (2013). Cointegration approach for temperature effect compensation in Lamb wave based damage detection. *Smart Materials and Structures, 22*(9), 095002.
14. Dao, P. B. (2013). Cointegration method for temperature effect removal in damage detection based on Lamb waves. *Diagnostyka, 14*(3), 61–67.
15. Dao, P. B., & Staszewski, W. J. (2014). Data normalisation for Lamb wave-based damage detection using cointegration: A case study with single- and multiple-temperature trends. *Journal of Intelligent Material Systems and Structures, 25*(7), 845–857.
16. Dao, P. B., & Staszewski, W. J. (2014). Lamb wave based structural damage detection using cointegration and fractal signal processing. *Mechanical Systems and Signal Processing, 49,* 285–301.
17. Dao, P. B., Staszewski, W. J., & Klepka, A. (2015). Stationarity-based approach for the selection of lag length in cointegration analysis used for structural damage detection. *Computer-Aided Civil and Infrastructure Engineering, 32*(2), 138–153.
18. Zolna, K., Dao, P. B., Staszewski, W. J., & Barszcz, T. (2016). Towards homoscedastic nonlinear cointegration for structural health monitoring. *Mechanical Systems and Signal Processing, 75,* 94–108.
19. Zolna, K., Dao, P. B., Staszewski, W. J., & Barszcz, T. (2015). Nonlinear cointegration approach for condition monitoring of wind turbines. *Mathematical Problems in Engineering,* Article ID 978156, 11.
20. Tsay, R. S. (2005). *Analysis of financial time series* (Vol. Wiley Series in Probability and statistics, 2nd ed., 576 pp.). New York: Wiley Interscience.
21. Zivot, E., & Wang, J. (2006). *Modeling financial time series with S-PLUS* (2nd ed.) Springer.
22. Dickey, D., & Fuller, W. (1981). Likelihood ratio statistics for autoregressive time series with a unit root. *Econometrica, 49,* 1057–1072.

Knocking Sounds in the Wind Turbine Gearbox During Slowing Down—Case Study

Tomasz Barszcz, Rafał Gawarkiewicz, Adam Jabłoński, Michał Sękal and Michał Wasilczuk

Abstract In the gearbox of a wind turbine under investigation, a knocking sound was noticed during coasting down of the machine. The noise was present in one of several gearboxes of the same type and the search for the source of the sound was undertaken. Gearbox manufacturer specialists after an inspection were pointing out sources outside the gearbox—runner unbalance or generator, but the machine owner ordered an additional research comprising vibration measurement and further analyses. The analysis of the vibration signal was carried out with the use of advanced signal analysis tools and the knocking vibration frequency was found to be the same as the frequency of the intermediate shaft. A machine inspection which was carried out pointed at a few potential sources of the sound, but did not specifically determined its source.

Keywords Wind turbine gearbox · Vibration analysis · Machine inspection

T. Barszcz · A. Jabłoński
Faculty of Mechanical Engineering and Robotics, AGH University of Science and Technology, Al. Mickiewicza 30, 30-059 Kraków, Poland
e-mail: tbarszcz@agh.edu.pl

A. Jabłoński
e-mail: ajab@agh.edu.pl

R. Gawarkiewicz · M. Wasilczuk (✉)
Faculty of Mechanical Engineering, Gdansk University of Technology, Narutowicza St. 11/12, 80-233 Gdańsk, Poland
e-mail: mwasilcz@pg.gda.pl

R. Gawarkiewicz
e-mail: gawar@pg.gda.pl

M. Sękal
ENERGA Wytwarzanie S.A., al. Grunwaldzka 472, 80-309 Gdańsk, Poland
e-mail: Michal.Sekal@energa.pl

A. Timofiejczuk et al. (eds.), *Advances in Condition Monitoring of Machinery in Non-Stationary Operations*, Applied Condition Monitoring 9,
https://doi.org/10.1007/978-3-319-61927-9_22

1 Introduction

In the gearbox of a wind turbine of 1.5 MW, a strong knocking sounds were noticed during coasting of the machine. The noise was only present in one of several gearboxes of the same type and since the gearbox was relatively new, a search for the source of the sound was undertaken. Gearbox manufacturer specialists after a thorough visual inspection were pointing out sources outside the gearbox—runner unbalance or generator. That was the reason why the machine owner ordered an additional research comprising vibration measurement and further signal processing analyses.

The analyzed wind turbine FUHRLAENDER MD77 equipped with a multiplicating gearbox, of a standard configuration, consisting of one planetary stage and two parallel stages with helical gears—Fig. 1 [1].

2 Vibrodiagnostic Measurements and Data Analysis

2.1 Measurement Setup

The difficulty of the problem lied in the fact that the knocking sound could only be noticed during a short time while the machine was slowing down, and acquiring data at decreasing speed was one of the problems. The tests were carried out with

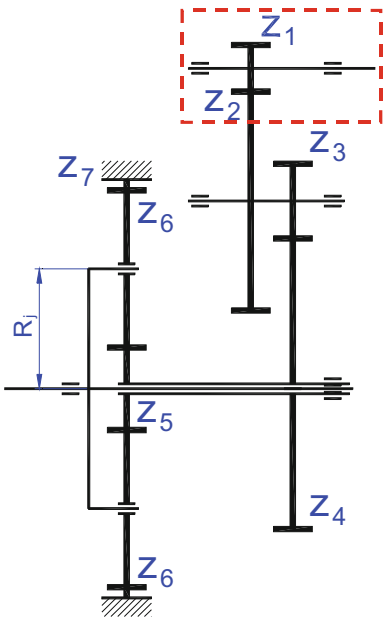

Fig. 1 Fuhrlaender wind turbine gearbox [1]

Table 1 Parameters of the data acquisition

Parameters	Value
Frequency	25 kHz
Resolution	24 bit
Time of acquisition	>120 s

the composite shaft connecting the gearbox and generator dismantled, so that there was no vibration of the generator.

The measurements were performed with the VIBstudio system with the VIBmonitor front-end with recording configuration. The system featured fully simultaneous data acquisition of signals from all the inputs.

The measurement system was equipped in 7 vibration sensors of the type VIS-B of 100 mV/g sensitivity and the phase marker. The vibration sensors were mounted in radial and axial direction on the gearbox, according to section 5.4 of ISO 10816 norm (ISO [2]. The phase marker was installed on the high speed shaft (HSS), i.e. at the output of the gearbox to the generator (Fig. 1 and Table 1).

2.2 Measurement Results and Data Analysis

The analysis of the vibration signal was carried out with the use of advanced signal processing tools including high resolution speed tracking algorithm. The recovered speed was next applied for accurate resampling of the vibration signal [3]. The repetition frequency of the knocking phenomenon was found to be the same as the frequency of the intermediate shaft (IMS) and not the sub-synchronous frequency of the high speed shaft or the hypersynchronous frequency of the low speed shaft (LSS), although these three frequencies were very close due to ratios of the gear. The signal was best visible in the axial direction so there are hypotheses that it can be attributed to the axial clearance in the tapered roller bearing system [4]. During slowing down the power is transmitted in the opposite direction than during the normal operation, and the directions of forces acting in the gearbox, including axial force between the helical gears, change. After having defined the source of the knocking sounds a visual inspection was planned.

After initial analysis of stored signal, the signal from the sensor mounted in the axial direction in vicinity of the IMS was selected for further analysis. This signal had the clearest impulses, which represented the knocking sound. The waveform of the signal is presented in the Fig. 2.

Using the rotational speed of the high speed shaft the vibration signal was resampled to the angle domain and then recalculated to the rotational speed of intermediate speed shaft. Result of one coast down resampling is shown in the Fig. 3.

Final verification was performed to check whether the investigated impacts are tied to the IMS or maybe to 4th harmonic of the LSS or 1/4th harmonic of the HSS.

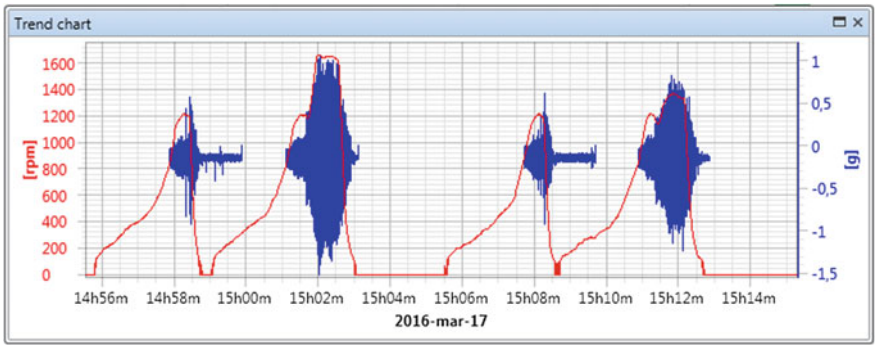

Fig. 2 Raw vibration signal waveform form the axial IMS sensor together with the rotational speed signal. Four coast downs can be seen

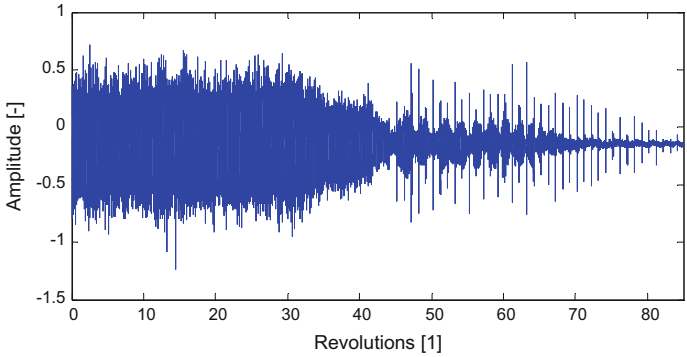

Fig. 3 One coast down signal resampled to the angle domain. The *horizontal axis* was scaled to represent revolutions of the IMS

The Fig. 4 presents consecutive revolutions of the IMS. The Fig. 5 presents on the single plot zoomed part of the signal from the Fig. 4 with lines marking periods of:

- 1/4th of HSS, which rotational speed was 4.12 times faster than IMS (green),
- IMS (red),
- 4th harmonic of LSS, which rotational speed was 4.095 times slower than IMS (black).

Visual analysis of several dozen revolutions is shown in Fig. 5—it is clear with no doubt that the impacts, responsible for the knocking phenomenon are directly related to the period of the intermediate shaft.

On the zoomed fragment (Fig. 5) it can be clearly seen that the vertical red lines (IMS) ideally mark the consecutive impacts, while the other ones are out of phase. It can be seen around the revolution no 47, when all three lines overlap and then around the revolution 59, when the red line is still in phase, the black one is half a revolution in advance and the green one is lagging half a revolution.

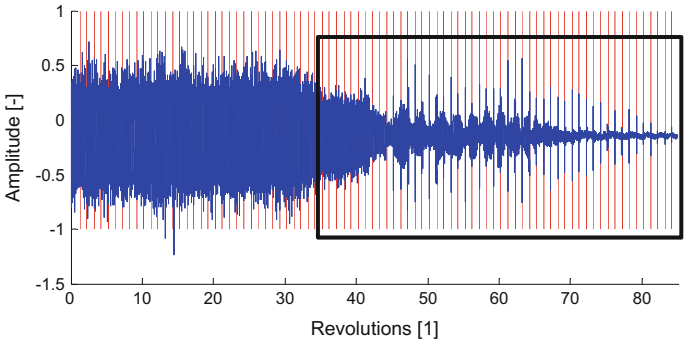

Fig. 4 Vibration signal resampled to the angle domain with IMS revolutions marked as vertical lines

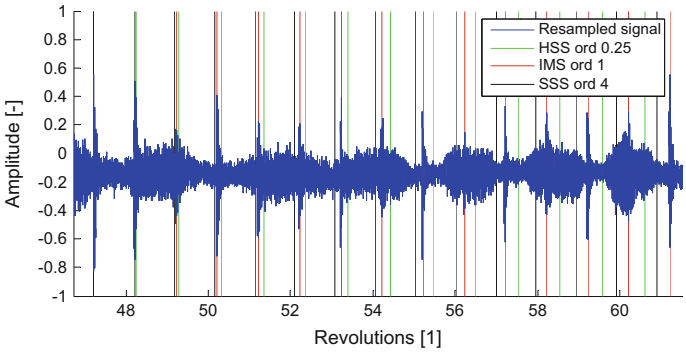

Fig. 5 Zoomed fragment of the vibration signal from the Fig. 5 resampled to the angle domain with three cycle families marked: 4th harmonic of LSS (*black*), IMS (*red*) and 1/4th of HSS (*green*)

Another interesting aspect is the energy of the vibration signal generated by different shafts. Figure 6 presents order spectrum from a selected stationary part of considered signal.

More precise analysis of all the drivetrain components allows to closer identify the malfunction by means of novel methods [5, 6] or classical methods.

A classical order spectrum shows dominating harmonics of gear meshing at the high speed shaft (HSS), namely 25th, 50th, and 75th orders. However, in case of gear meshing at the intermediate stage (IMS), two symptoms are detected:

(a) the IMS meshing component is relatively high in reference to a typical wind turbine spectral data,
(b) the odd harmonic of IMS are dominating.

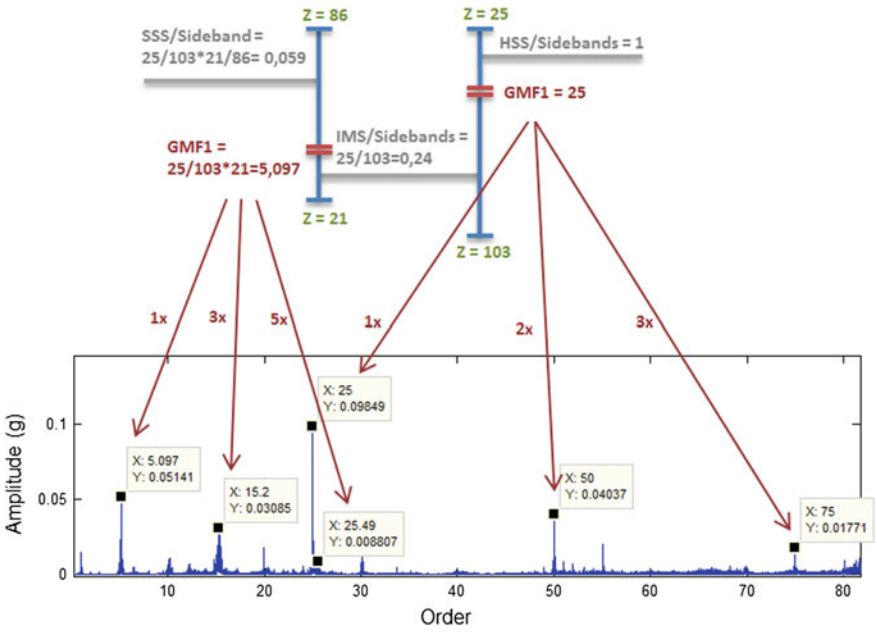

Fig. 6 Order spectrum in the 0–85 order range in stationary operating conditions at about 1350 rpm

Typically, the IMS meshing might be order of magnitude less than HSS meshing. In Fig. 6, it is only two times smaller. Furthermore, the presence of dominating odd harmonics might be caused by additional non-linearity of an object due to improper technical condition.

3 Machine Inspection

The most important findings form the vibrodiagnostic analysis were occurrence of the dominating noises with the frequency of IMS rotation, only during coast down of the machine, and dominating vibrations with the frequency of HSS during the steady state operation. That is why the IMS was analyzed with greater care.

As shown in Fig. 7, the bearing system of the IMS consists of a couple of taper roller bearings of different contact angles located at the generator side (RH side in the drawing) acting as a locating support and a cylindrical roller bearing, as a non-locating bearing on the rotor side (LH side at Fig. 7). The use of locating support is necessary in helical teeth gearboxes to accommodate axial loads generated at the teeth mesh. In all gears the direction of tooth forces changes when the direction of power transmission changes, i.e. when the gear which was a driving gear becomes a driven gear, or vice versa, then at first the circumferential clearance

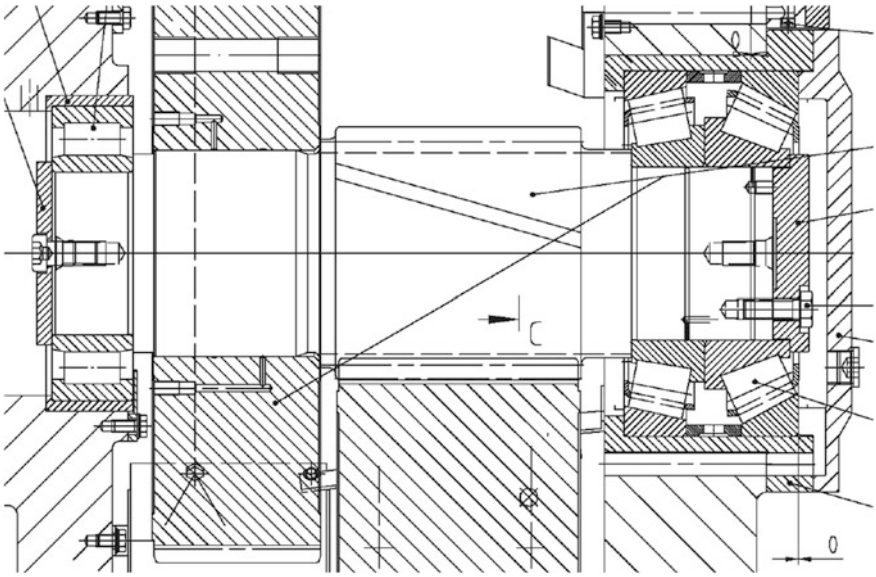

Fig. 7 Details of the design of IMS of the analyzed gearbox [10]

is zeroed at one tooth flank and appears at the other side of the tooth. Such a situation can happen during slowing down, or when the wind force suddenly decreases. In such a case, the power is no more transmitted from the turbine rotor to the generator, but the rotating inertia forces of the generator start to drive the whole system for a shorter or longer period of time. Such condition is known in unloaded car transmission and referred to as gear rattle phenomena [7]. Additionally, in a helical gear there exists the axial component of the tooth force, which also changes the direction in this time. Thus, the following possible sources of the noise can be pointed out:

- Repeated circumferential backlash on both sides of the tooth;
- Repeated reciprocating axial movements of the shaft—possible within the range of axial clearance in the pair of taper roller bearing;
- Failure of the bearing separator (cage) in either of the three IMS bearings.

An attempt was made to determine the reasons of the knocking sounds by the inspection of the machine. During the inspection a visual assessment of the gears was done revealing some faults of the teeth caused, either by overload or poor teeth alignment (Fig. 8) and other traces of metal to metal contact between the teeth.

During the inspection axial and circumferential backlash was measured—the circumferential was found to be equal to 0.4 mm, which can be considered normal. The axial backlash was measured to be approximately 0.08 mm, which is over the manufacturers recommendation of the zero backlash (see Fig. 7). During slow rotation of the gears it was also noticed that in the unloaded zone the rolling

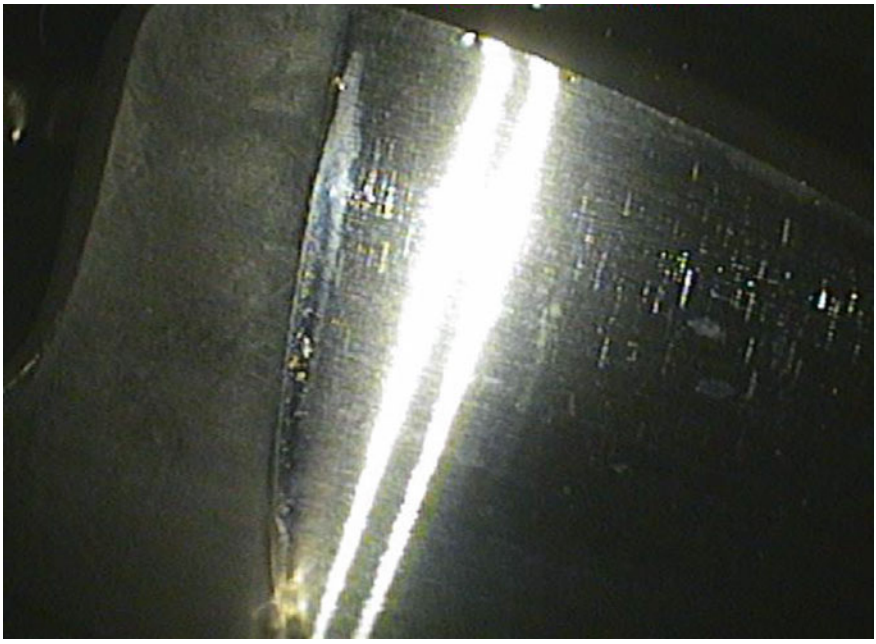

Fig. 8 Marks of contact between teeth on the IMS pinion [11]

elements are sliding instead of rolling, due to the clearances between them and the races, which is another proof of insufficient preload of the pair of taper bearings. Such sliding is considered as an important reason of premature failures of the bearings [8]. With the change of the direction of the tooth forces causing repeated deleting of the clearances knocking sound can be generated as circumferential backlash is deleted on one side of the tooth and appears on the other side. Gear rattle phenomena is known to occur in unloaded transmission systems of the cars at a certain proportion of the stiffness and inertia of the system components [7]. It seems worth pointing out that a very similar sound was generated when direction of rotation of the shaft was changed manually.

For the acquired vibration signal sidebands have the frequency of approximately 2.0 Hz. These can be the frequencies generated by the bearing cage, but it was impossible to find the data concerning characteristic frequencies of the bearings used in this gearbox. As described in various case studies [9], cage failures frequently generate unique effects, e.g. the FTF (fundamental train frequency) may not be observed, but can modulate other frequencies, in some cases even depending on the instantaneous axial load. Additionally a broken cage can change its shape only at some operating or load conditions generating vibrations only at specific conditions. Unfortunately, because of the need to keep machine in operational readiness it was not possible to dismantle the bearings cover and make a visual inspection of the taper bearing cages. The cylindrical roller bearing, at the upwind side is also

inaccessible for a direct visual inspection. Finally, the integrity of the bearing cages was not checked.

4 Conclusion

The main conclusions of this research are:

- The knocking sound has a repetition rate of the IMS rotation period;
- Due to the advanced angle domain analysis of the vibration signal it was possible to prove that this frequency was different from very similar frequencies of 4th harmonic of the LSS and 1/4th of the HSS frequency;
- Further data analysis show sidebands, which are a sign of deteriorated state of the tooth mesh in the IMS stage;
- Knocking sound was not noticed at steady state operations and energy of of the IMS is lower than that of HSS vibrations of the IMS is lower than that of HSS vibration;
- The fact that the knocking sound can only be noticed during coasting may be attributed to the change of tooth force direction occurring in the time when the power is transmitted in the opposite direction. Then, circumferential backlash is deleted on one side of the tooth and appears on the other side and axial backlash is deleted and the shaft moves with reciprocating movements axially. With any irregularity of the rotational speed these effects can cause repeating knocking sound. A similar sound was generated when direction of rotation of the shaft was changed manually.
- Further visual analysis of the IMS bearings, both at downwind and upwind side was recommended; for a cylindrical roller bearing at upwind side it is only possible by endoscopy.

Acknowledgements This work is partially supported by Energa Wytwarzanie. The authors also gratefully acknowledge the helpful comments and suggestions of the reviewers, which have improved the presentation.

References

1. Wasilczuk, M., et al. (2015). Łożyskowanie wałów przekładni turbin wiatrowych – problemy eksploatacyjne (Bearing systems of wind turbines—Maintenance problems). *Tribologia, 4–2015,* 187–198.
2. ISO 10816. (2015). Mechanical vibration—Evaluation of machine vibration by measurements on non-rotating parts—Part 21: Horizontal axis wind turbines with gearbox.
3. Urbanek, et al. (2013). A two-step procedure for estimation of instantaneous rotational speed with large fluctuations. *Mechanical Systems and Signal Processing, 38*(1).
4. Adamczyk, et al. (2016). Research methods and testing stand developed to examine vibrations generated by rolling bearing. *Diagnostyka, 17*(1).

5. Katunin. (2016). Application of time-frequency distributions in diagnostic signal processing problems: A case study. *Diagnostyka, 17*(2).
6. Kotowski. (2016). The method of frequency determination of impulse response components based on cross-correlation vs. Fast Fourier Transform. *Diagnostyka, 17*(1).
7. Miyasato, H. H., et al. (2011). Study of the gear rattle phenomena in automotive powertrain systems. In *Proceedings of COBEM 2011*.
8. Gary, L., & Doll, L. G. (2011). Tribological Challenges in Wind Turbine Technology, Wind Turbine Tribology Seminar, Broomfield, Colorado.
9. Discussion Forum. (2016). http://www.vtab.se/PHP-NBoard/html/images/materiali/Forum2/HTML/003987.html. Accessed May 2016.
10. Eickhoff Fuhrlaender FL MD 70/77. Helical Planetary Gearboxes EBN 932, EBN 831—Operating Manual Rev. No.: 02.
11. FWT. (2015). Inspection report of the TW-07 wind turbine 16.07.2015, by FWT for Energa.

Multifractals in Technical Diagnostics General Concept

Damian Skupnik

Abstract In general there are three basic tasks of technical diagnostics, i.e. we want to know in what technical state a considered object was in the past (1st), we want to find out what is the state of the object right now (2nd), and finally what it will be in the future, especially a far one (3rd). The paper presents general concept of using multifractals theory to solving the third task mention earlier. The idea of multifractals was introduced by Benoit Mandelbrot who claimed that multifractal model was more reliable type of financial theory than conventional financial models. According to Mandelbrot and other researchers the advantage of multifractal theory consists in better prediction of occurrence of low predictability and large impact phenomenons. And to know beforehand about rising possibility of occurrence of these phenomenons is crucial just because of their large impact to the whole system. Nowadays we can make pretty accurate diagnosis of the technical state of the considered object. However it is based on the assumption that variation of features of diagnostics signals can be modelled by random processes that follow rather "mild" or "slow" pattern of randomness and to be fair this is almost always true. But such approach completely neglects the presence of "wild" randomness and this can lead to the serious failures. In Author's opinion the idea of a fractal or a multifractal view of risk, ruin and reward in financial theory can be used successfully in the context of technical diagnostics. Perhaps thanks to it will be possible to prevent or to prepare for unknown unknowns, i.e. for occurrence of low predictability and simultaneously very serious failures.

Keywords Technical diagnostics · Rare events · Multifractals

1 Introduction

For the so-called critical technical objects (e.g. of an airplane) it is necessary to do something in order to avoid or to prepare for occurrence of rare events which have a large impact (e.g. crash of an airplane). Dealing with rare events demands

D. Skupnik (✉)
Institute of Fundamentals of Machinery Design, Silesian University of Technology, Konarskiego 18a, 44-100 Gliwice, Poland
e-mail: damian.skupnik@polsl.pl; dskupnik@tutamail.com

A. Timofiejczuk et al. (eds.), *Advances in Condition Monitoring of Machinery in Non-Stationary Operations*, Applied Condition Monitoring 9,
https://doi.org/10.1007/978-3-319-61927-9_23

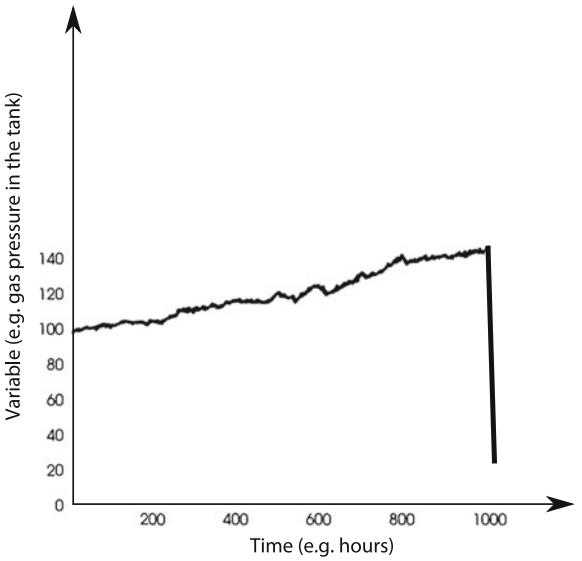

Fig. 1 Occurrence of a rare event

analysis in a relatively longer time scale. In classical data analysis the extremes, i.e. phenomenons of low probability and large impact, are often just ignored. This means that the forecasting model created without such data may be usefull but only in case of events that happen relatively often. For the rare events, usage such a model may lead to a serious failure what has been shown in the Fig. 1. As one can see, the history of a process over a 1000 h does not tell anything about what is going to happen next.

Modern and complicated objects (e.g. an airplane) combine the interactions of many elements (e.g. Boeing 747-400 has approximately 6 million parts [1]). Technical diagnostics of such complicated systems can be very difficult especially, if we wanted to predict a technical state in the long time perspective. This difficulty is caused mainly by the relation between limited description precision of dynamics processes occuring in the considered object, and an error size of a forecast. The smaller description precision and/or longer time perspective, the bigger error of a forecast. Thus in practice we are not able to prepare of longterm forecasts.

Fortunately we do not have to predict values of the given variable. It should be enough to foresee a risk of the rare event occurence and some tools to deal with this problem were developed.

One of them is *Extreme Value Theory* (EVT) [2, 3]. EVT provides a confirmed theoretical basis on which one can build statistical models describing extreme events (predicting the size of the rare event), i.e. events that do not happen very often. Research concerning EVT has shown possible ways of combining different risk factors.

The second interesting tool is undoubtly application of the multifractals idea introduced by Mandelbrot [4]. Mandelbrot claimed that multifractal model was more

reliable than conventional financial models. According to Mandelbrot and other researchers (e.g. [5–9]) the advantage of multifractal theory in comparison to the traditional approach, is better prediction of occurence of phenomenons low predictability and large impact.

As far as the author know, usage of multifractals theory in the context of technical diagnostics is not enough researched. There are some papers that deal with this topic (e.g. [10]) but the number of them is very small. It seems strange because the multifractals measures are successfully applied in many others domains, e.g.: agronomy, astronomy, ecology, geology, geochemistry, genetics, hydrology, meteorology, biology, medicine, network traffic modelling, seismology, soil science, turbulence, finance, etc.

This paper presents a general concept of using the multifractals theory to prediction of rising risk of serious failure occurrence of the considered object especially in a further future. It should be clearly stated that the author's aim is not to prove mathematically that diagnostics signals are fractals or multifractals. The aim is to perceive a different, maybe fruitful, approach to the technical diagnostics.

2 Theory of Fractals and Multifractals in a Nutshell

2.1 What is a Fractal?

Formal definition of a fractal is not established. According to Falconer [11] a fractal is a set that has all or the most of the following properties:

- its fractal dimension (defined in some way, e.g. (1)) is usually greater than its topological dimension;
- it has some form of self-similarity either exact or approximate or statistical;
- it is defined in a very simple way, very often recursively;
- it is too irregular in order to be described in traditional geometrical language, both locally and globally (fractal is often called as the geometry of roughness);
- its structure is detailed on arbitrarily small scales.

Figure 2 shows the process of generating of a fractal, called the Koch curve. Fractal dimension D_s of the Koch curve equals in approximation 1.2619. The result can be obtained by using formula (1)

$$D_s = -\frac{\log Q}{\log c}, \tag{1}$$

where Q is the number of subsets (here $Q = 4$) of the initial set and c is the scalling factor (here $c = \frac{1}{3}$).

Another example of a fractal is presented in the Fig. 3. It is the Weierstrass function known since 1872 (of course, the function was not called a fractal then). As one

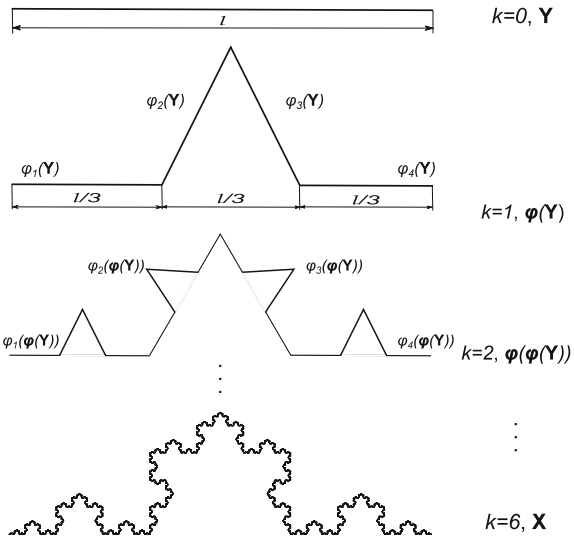

Fig. 2 Generating a fractal—the Koch curve

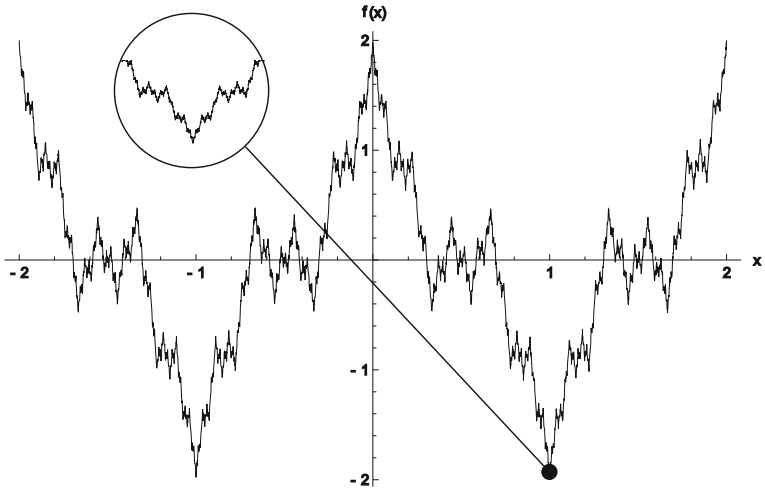

Fig. 3 The Weierstrass function considered as a fractal

can see, the function exhibits self-similarity: every zoom (black circle) is similar to the global plot.

It should be emphasized that self-similar object is not only invariant under dilations, but also rotations. It means that the rescaling operators are the same in each direction. If the rescaling operators are not the same in each direction then the object is called self-affine.

2.2 Fractal and Multifractal Processes

In fractals context the scaling factor c does not have to relate only to the geometric objects and measures. It can also be applied to the processes changeable in time because in the fractal analysis, time is flexible.

A random process $X(t)$ that satisfies

$$X(ct) \stackrel{d}{=} c^H X(t) \tag{2}$$

for some scalling exponent $0 < H < 1$ and $c \geq 0$, is called fractal (self-similar or self-affine) process [8].

The exponent H, known as the Hurst exponent, measures the long-term dependency of time series and their tendency to be cyclical. If [9]:

- $0 < H < 0.5$ then the increments of the process are negatively correlated, so it is an anti-persistent, i.e. the change will probably continue in the reverse direction;
- $H = 0.5$ then the process is in standard Brownian motion, so the observations are not correlated;
- $0.5 < H < 1$ then the increments of the process are positively correlated so the process exhibits long-range dependence, i.e. the change will probably continue in the same direction.

In some processes there are periods alternation of large changes with periods of smaller changes. It is typically described as the fluctuation of "volatility" over time. The theory of multifractals facilitates modelling of temporal heterogeneity in time series by establishing more general scalling rule, i.e.

$$X(ct) \stackrel{d}{=} M(c)X(t) \tag{3}$$

where X and M are independent random functions and $c \geq 0$. The scaling factor $M(c)$ is a random variable and, as one can see, its distribution does not depend on the time. Process that satisfies (3) is called multifractal.

For the self-similar process (2) $M(c) = c^H$, thus one can define the generalized index $H(c)$ as

$$H(c) = \log_c M(c). \tag{4}$$

In consequence one can rewrite the relation (3) to the following form:

$$X(ct) \stackrel{d}{=} c^{H(c)} X(t). \tag{5}$$

2.3 Example of a Multifractal Process

A multifractal process $X(t)$ on a bounded interval $[0, T]$ can be obtained by compounding Brownian motion $B(t)$ with a stochastic time deformation process $\Theta(t)$ [6], i.e.

$$X(t) \equiv B[\Theta(t)], \tag{6}$$

wherein $B(t)$ and $\Theta(t)$ are independent.

Standard Brownian motion is one of the best known Levy processes and its mathematical model is called the Wiener process. A single realization of a one-dimensional Wiener process is presented in the Fig. 4.

The time deformation $\Theta(t)$ (bending of time) is the cumulative distribution function of a multifractal measure μ defined on a bounded interval $[0, T]$.

Multifractal measures are built by iterating a simple tranformation (a mathematical process called a multiplicative cascade). A simple example of such a measure is the binomial measure called also the Bernoulli or Besicovitch measure [8]. The idea of the binomial measure on the compact interval $[0, 1]$ is presented below (on the basis [6]; more pictorial description one can find, e.g. in [13]).

Let t_0 and t_1 are the two positive numbers, which here represent the amount of time, and their sum is equal to 1. At stage $k = 0$, we start the construction with the uniform probability measure μ_0 on $[0, 1]$. In the step $k = 1$, the measure μ_1 uniformly spreads the value equal to t_0 on the subinterval $\left[0, \frac{1}{2}\right]$ and the value equal to t_1 on

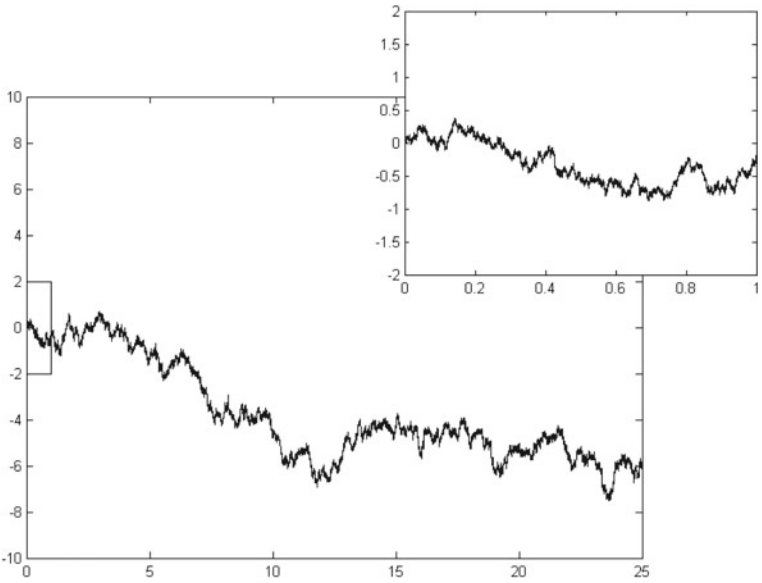

Fig. 4 A one-dimensional Wiener process [12]

$\left[\frac{1}{2}, 1\right]$. In step $k = 2$, the set $\left[0, \frac{1}{2}\right]$ is split into two subintervals, $\left[0, \frac{1}{4}\right]$ and $\left[\frac{1}{4}, \frac{1}{2}\right]$, which respectively receive a fraction t_0 and t_1 of the total meassure $\mu_1 \left[0, \frac{1}{2}\right]$. We apply the same procedure to the dyadic set $\left[\frac{1}{2}, 1\right]$ and obtain:

$$\mu_2 \left[0, \frac{1}{4}\right] = t_0 t_0,\ \mu_2 \left[\frac{1}{4}, \frac{1}{2}\right] = t_0 t_1,\ \mu_2 \left[\frac{1}{2}, \frac{3}{4}\right] = t_1 t_0,\ \mu_2 \left[\frac{3}{4}, 1\right] = t_1 t_1.$$

Repeating of this procedure generates an infinite sequence of measures μ_k that weakly converges to the binomial measure μ.

One should notice that the binomial construction may be easily generalized by:

- splitting of the intervals into an arbitrary number $b \geq 2$ of cells at each stage of the cascade,
- randomizing the allocation of the value between subintervals.

Figure 5 ilustrates the density of the measure μ obtained after $k = 1, 4$ and 10 steps of the recursion (Fig. 5c shows the random density). As one can see the original area is partitioned irregularly, with tall peaks (high concentration of time) and low valleys (low concentration of time).

An example of the simulated multifractal process, obtained by means of the formula (6), is presented in the Fig. 6 [6]. The example shows simulated price changes (Fig. 6a) and the first differences of the prices (Fig. 6b). Analyzing the figure, one

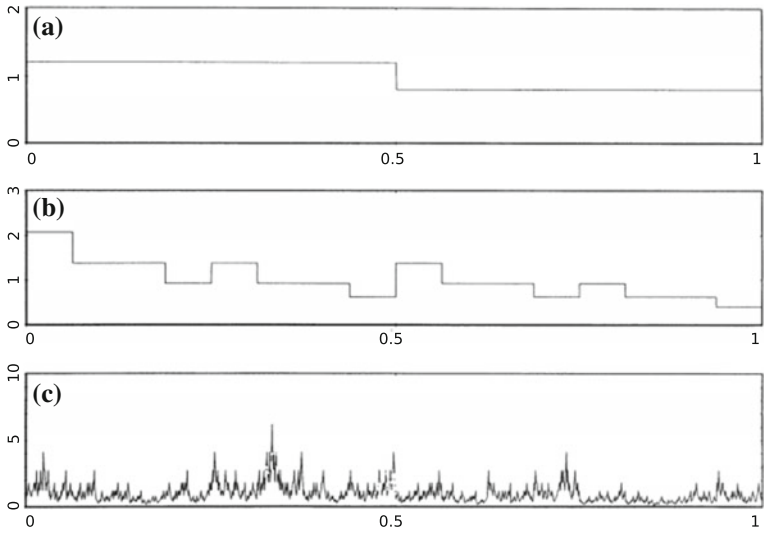

Fig. 5 Binomial meassure (density function): **a** iteration $k = 1$ and $t_0 = 0.6$, **b** iteration $k = 4$, **c** iteration $k = 10$ with parameters $b = 2$, $p = 0.5$ and $t_0 = 0.6$ (on the basis of [6])

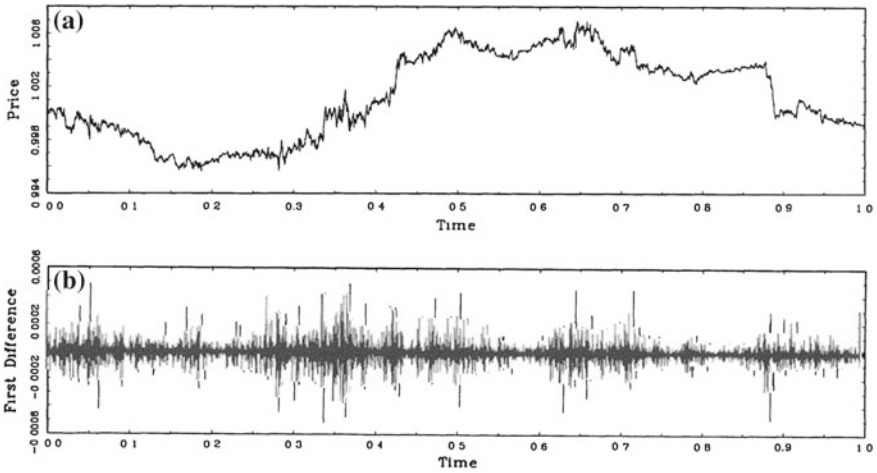

Fig. 6 Simulated multifractal process: **a** simulated price changes, **b** simulated the first differences of the prices (on the basis of [6])

can notice that volatility is clustering at all time scales (temporal heterogenity) and it is intermittent by large fluctuations (simulation of occurence of a rare event with large impact to the system).

3 Concept of the Multifractals Application in Technical Diagnostics

Taking into account theory of fractals and multifractals presented in a nutshell in the Sect. 2, one can establish some necessary attributes which have to characterize a technical process or diagnostic signal in order to consider them as a multifractal. The basic features are listed below.

1. Increments in the examined process (signal) should be stationary and independent, i.e. they should be statistically identical over different time intervals of the same length (Levy process).
2. There are possible jumps with arbitrarily large value (i.e. variance is not finite; again Levy process).
3. During progress of the examined process it should be noticeable the alternation of periods of large changes with periods of smaller changes (significant changes should have inclination to cluster and follow one another, although their directions not necessarily have to be the same).
4. Process (signal) is characterized by a long but finite memory (in such a case the autoregressive model does not work well because it usually gives good results for the short and the medium term).

5. Process (signal) contains repeating patterns which may reveal as limited nonperiodic cycles, generated by nonlinear, delayed effects.

If analyzed technical process or diagnostic signal has all or most of the attributes listed above, then we ought to realize, that the process (signal) allows on occurence of phenomenons low predictability and large impact. In consequence the process (signal) should be considered as multifractal.

Application of ordinary methods for such cases is not the best idea because it completely neglects the presence of "wild" randomness and it can lead to the serious failures. Instead one should try to create a multifractal model of considered process in order to simulate the possibility of occurence of rare and very serious events.

If analyzed technical process or diagnostic signal is considered as multifractal, then one ought to think in terms of affordable risks instead of trying to make a long term forecast, i.e. searching for the value of probability (belief) that an event will occur.

In order to avoid risk we can prepare a list of the events with large impact to the system and think about how to prepare for them and what early indicators one should track. The advantage of such approach is that it simulates potential extreme events and allows to determine the outcomes, if such extreme scenarios will occur. Thanks to it one can establish not only what may happen but also what to do when it will happen. Such knowledge may even turn some risks into opportunities.

4 Summary

In the author's opinion usage of models built on the basis of the multifractal theory may be fruitful in technical diagnostics domain. It should be emphasized that multifractals measures are not only limited to specific fractal tools—for instance the Hurst exponent which was presented in the Sect. 2.2. In fact there are many different methods and techniques based on the multifractals measures, e.g. in image processing for the needs of medicine. These tools can be applied in some subdomains of technical diagnostics without any special preparations.

References

1. Benson, T. (2016). *Boeing 747 History*. https://www.grc.nasa.gov/WWW/K-12/////aerosim/LessonHS97/Boeing747.html. Last Accessed July 2016.
2. Chavez-Demoulin, V., & Roehrl, A. (2004, January). *Extreme value theory can save your neck*. http://www.risknet.de/fileadmin/eLibrary/EVT-Paper-Roehrl-Chavez-Demoulin.pdf. Last Accessed July 2016.
3. Schaumburg, J. (2010). Predicting extreme value at risk: Nonparametric quantile regression with refinements from extreme value theory. *Computational Statistics & Data Analysis, 56*(12), 4081–4096.

4. Mandelbrot, B. (1972). Possible refinement of the lognormal hypothesis concerning the distribution of energy dissipation in intermittent turbulence. Statistical models and turbulence. In M. Rosenblatt & C. Van Atta (Eds.). Lecture Notes in Physics 12 (pp. 333–351). New York: Springer.
5. Mandelbrot, B. (1997). *Fractals and scaling in finance: Discontinuity, concentration, risk*. New York: Springer.
6. Mandelbrot, B., Fisher, A., & Calvet, L. (1997). A multifractal model of asset returns. Cowles Foundation Discussion Yale University Paper 1164. http://users.math.yale.edu/~bbm3/web_pdfs/Cowles1164.pdf. Last Accessed July 2016.
7. Calvet, L., & Fisher, A. (2002). Multifractality in asset returns: Theory and evidence. *Review of Economics and Statistics*, *84*(3), 381–406.
8. Calvet, L., & Fisher, A. (2008). *Multifractal volatility. Theory, forecasting and pricing*. New York: Elsevier.
9. Kobeissi, Y. (2013). *Multifractal financial markets. An alternative approach to asset and risk management*. New York: Springer.
10. Milan Pavlovic, M., & Ristic, D. (2011). Applications of multifractals in the analysis of room impulse response—Initial research. *Telfor Journal, 3*(2), 116–120.
11. Falconer, K. (2003). *Fractal geometry. Mathematical foundations and applications* (3rd ed.). Wiley.
12. Wiener process. https://en.wikipedia.org/wiki/Wiener_process. Last Accessed July 2016.
13. Mandelbrot, B., & Hudson, R. (2004). *The (Mis) behaviour of markets*. Basic Books.

Complementary View on Multivariate Data Structure Based on Kohonen's SOM, Parallel Coordinates and t-SNE Methods

Anna M. Bartkowiak and Radosław Zimroz

Abstract Nowadays, it is often required in modern condition monitoring applications, to describe acquired signal by set of parameters. It directly leads to mD diagnostic data. Before starting the proper analysis of the recorded data, it is advisable to look at the data globally to get an idea what really they are representing. Visualization of mD data is a challenging problem and probably it is not possible to find an ideal method that could take into account all aspects in case of high dimensional, nonlinear, redundant, etc., data. We propose to use for that goal jointly the triplet multivariate visualization methods: Self-organizing maps, Parallel coordinate plots and t-distributed Stochastic neighbor embedding. The methods use concepts of Machine Learning, simple Geometry and Probabilistic Modeling for finding indices of distances or similarities between the data vectors represented in the multivariate data space as data points. The methods permit to visualize the data points in a plane with possibly preserving their mutual between-point distances in the multidimensional data space. The three proposed methods are complementary, and they are supplementing each other. The considerations are illustrated using a data matrix X of size (1000×15) containing gearbox diagnostic data structured into 4 (sub)groups. Indeed, the three applied (unsupervised) methods permit to get an insight into the 15-dimensional data space and to state that data points belonging to different subgroups of X have different geometrical location. However, the employed methods do not yield indications for reducing the dimensionality (number of variables) of the considered data.

Keywords Vibration signal · Gearbox diagnostics · Visualization of multivariate data

A.M. Bartkowiak
Institute of Computer Science, University of Wroclaw, Wrocław, Poland
e-mail: aba@cs.uni.wroc.pl

R. Zimroz (✉)
Diagnostics and Vibro-Acoustic Science Laboratory, Wroclaw University of Science and Technology, Wrocław, Poland
e-mail: radoslaw.zimroz@pwr.edu.pl

A. Timofiejczuk et al. (eds.), *Advances in Condition Monitoring of Machinery in Non-Stationary Operations*, Applied Condition Monitoring 9,
https://doi.org/10.1007/978-3-319-61927-9_24

1 Introduction

Data Science is today one of the hottest topics around. Data are collected everywhere. It is preferred to have the data given as the real valued multivariate matrix X of size $(n \times d)$, comprising in its rows sample vectors of measurements of d parameters relevant in the given context. Each row of the matrix may be imagined also as a data point in R^d, the d-dimensional data space. The entire set of data points appears in R^d as a multivariate data cloud.

Such approach is also often used in condition monitoring of machines. Using Data Acquisition Systems one might get many diagnostic signals (multichannel system). Obviously, when analyzing all data together we directly obtain mD (multidimensional, alias multivariate) data. Another frequent case is when one considers one complex signal, but due to its complexity, it is advised to use advanced parametrization of time series. Such description of raw time series leads to 1D vector or even 2D matrix. In this work we will play with vibrational data described by 15 features (for each signal) obtained using spectral representation—by employing 3 methods visualizing multivariate data.

In this paper we will consider gearbox diagnostics data used in [1, 2, 4]. For the two investigated gearboxes we obtain two data matrices of size $n1 \times d$ and $n2 \times d$ appropriately, where $n1$ and $n2$ denote the number of the data vectors obtained from the two sets of recorded vibration signals. Putting the data for the two gearboxes together we will obtain one common data matrix X of size $n \times d$, where $n = n1 + n2$.

Our question is: Could we get insight into the d-dimensional data space R^d and see there the recorded data vectors as data-points in proper locations of that space? Could we also learn visually, if the data clouds coming from the two monitored gearboxes are geometrically separated or mixed together? In principle, humans are not capable to perceive data clouds in high-dimensional ($d > 3$) data space. However, on the basis of mathematical reasoning, some principles of geometry were formalized. Then, by applying specialistic multivariate (mD) visualization tools, humans may learn about the shape of such multivariate data cloud, also about the homogeneity or aberrancy of its elements and ways they cluster together. This is done usually by performing projections of the data cloud into a 2-dimensional subspace, which can seen by humans. Depending on the criterion used in the projection we may obtain a diversified information on the shape and content of the data cloud.

We propose to apply for that purpose the following multivariate graphical visualization algorithms:

- Self-Organizing Maps, proposed by Teuvo Kohonen [7, 10];
- Parallel Coordinate plots, launched by Alfred Inselberg [5, 6];
- t-SNE proposed and elaborated by van der Maaten and Hinton [9].

We advise to use these 3 visualization algorithms jointly, accordingly to the paradigm expressed by Arun K. Majumdar and John Sowa (2009):
Two paradigms are better than one, and multiple paradigms are even better.

The jointly usage of the 3 visualizing algorithms will elucidate various geometrical aspects of the analyzed data vectors, not obtainable when using only one of the methods. The 3 methods taken jointly complement each other and permit us to get a holistic imagination of our data when looking at them as data points residing in R^d.

Description of the data. We will use in our demonstrations data containing information about the condition state of two gearboxes, one in the healthy, the other in the faulty state. The data were gathered by Bartelmus and Zimroz and are described in our earlier works [1, 2, 12]. Generally, there are $d = 15$ parameters obtained from a spectral analysis of the observed vibration segments. Additionally, each segment has attached an external variable called *zwe*, which denotes external load of the gearbox during measurement. The principle is: $zwe <= 990 \rightarrow$ *heavy load*, $zwe > 990 \rightarrow$ *small/no load*.

We have sampled for our analysis from the data mentioned above 500 data vectors characterizing the healthy gearbox, and 500 data vectors characterizing the faulty gearbox. In such a way we obtained the sets B500 and A500 corresponding to the healthy and the faulty gearbox appropriately. Taking into account the status of the *zwe* variable, each of the sets B500 and A500 was further subdivided into two subgroups. It happened, that B500 contained 61 and A500 contained 66 data vectors with small/no load.

Finally, the $(n \times d) = (1000 \times 15)$ data matrix X was established for further analysis. The matrix is structured into four groups:

group 1: healthy gearbox (B), heavy load, $n_1 = 439$;
group 2: healthy gearbox (B), no/light load, $n_2 = 61$;
group 3: faulty gearbox (A), no/light load, $n_3 = 66$;
group 4: faulty gearbox (A), heavy load, $n_4 = 434$.

In the following, we perform the visualization of the data matrix X using Kohonen's self-organizing maps (Sect. 2), Parallel coordinate plots (Sect. 3) and t-SNE (Sect. 4). Finally, Sect. 5 contains discussion of the results and final remarks.

2 Kohonen's Self-Organizing Maps (SOMs)

Kohonen's SOM partitions the data space R^d into M disjoints regions (so called Voronoi regions, VRs) and maps them to a regular (usually 2D) *map* (the SOM) with possibly preserving the topology (neighborhoods) of the VRs. A typical SOM is constructed as a regular net composed from adjacent squares or hexagons(see Fig. 1 depicting various maps with hexagonal structure). The SOM uses a neural network model with M neurons [7, 10] which have a dual representation: in the (2D) map space and in the data space R^d. The network uses unsupervised learning with a simple computational form.

Say, the map is composed from $M = m_1 \times m_2$ hexagons. Each hexagon contains one neuron localized in the hexagon's center (neuron's reference address). The same

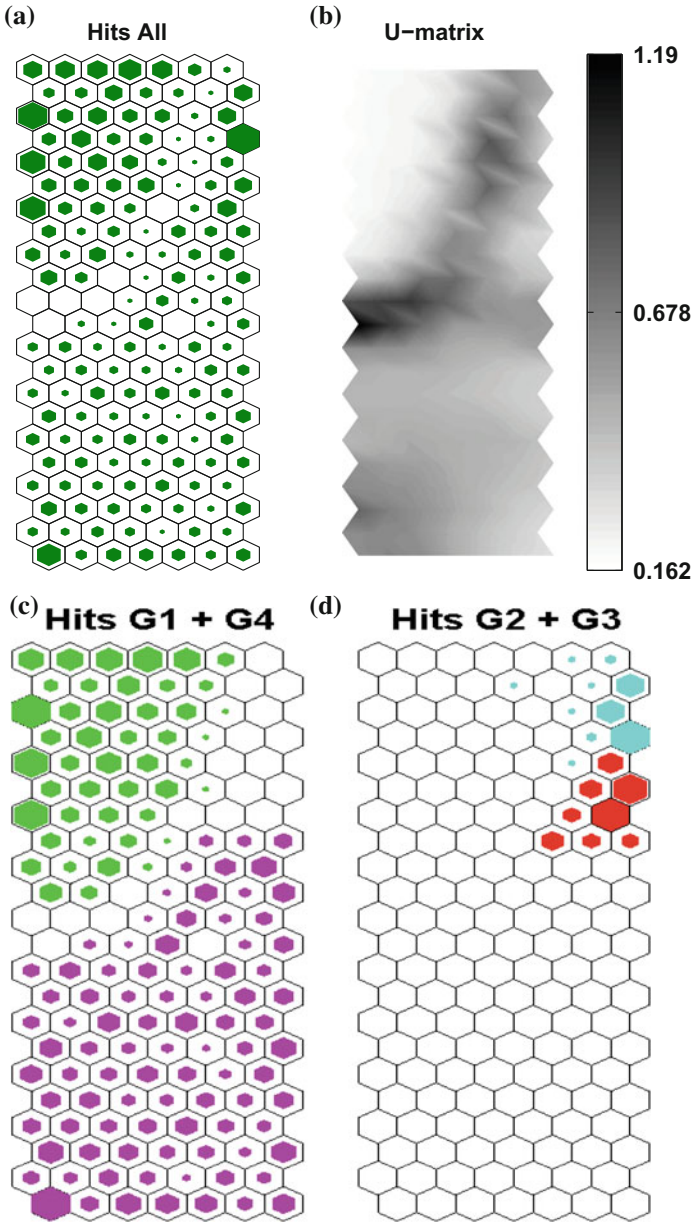

Fig. 1 Kohonen's hexagonal SOMs of size 22×7. **a** All data. Colored interior hexagons are proportional to the number of data vectors residing in the corresponding R^d Voronoi regions. **b** Graph U-matrix showing the distances between codebook vectors located in the data space R^d. **c** Only frequency counts from groups no. 1 (*green*) and no. 4 (*magenta*) are shown. **d** Only frequency counts from groups no. 2 (*cyan*) and no. 3 (*red*) are shown

neuron no. (*no. i*, $i = 1, \ldots, M$) has its representation $\mathbf{w}_i = [w_{i1}, \ldots, w_{id}]$ residing in the data space R^d and called *vector of weights* or *codebook vector* [7]. This fact creates a one-to-one link between the given hexagon in the map and corresponding VR in R^d.

The structure of the map and its neural network is determined by the user. We have chosen a hexagonal structure composed as a 22×7 lattice, which implies a neural network with $M = 154$ neurons. The quality of the representation of the $n = 1000$ multidimensional data points by the neuronal vectors $\{\mathbf{w}_i\}$ is measured by two indices: the quantization error and the topological error. *The quantization error* shows (in R^d, for each VR) an averaged Euclidean distance of the data points to their representative code-book vector. The *topological error* is defined as the percentage of data points, for which the first and second best matching code-book vectors are not adjacent neighbors in the map. For the maps exhibited in Fig. 1 the quality indices amount: *quant_err = 15.976, topol_err = 0.*

The values of the weights $\{\mathbf{w}_i\}$ are obtained in the iterative way. They are initialized at random or as a regular grid in the PC (principal component) plane [10]. In subsequent iterations (k) a randomly chosen data vector $\mathbf{x}_k$ is presented to the network. Say, it happened that neuron *no. c* was the nearest to the presented data point ('was the winner'). The neuronal weights $\mathbf{w}_i$, $i = 1, \ldots, M$, are then updated according to the rule:

$$\mathbf{w}_i(k+1) = \mathbf{w}_i(k) + \eta(k) \cdot h_{i(c)}(k) \cdot [\mathbf{x}_k - \mathbf{w}_i(k)], \tag{1}$$

where $\eta(k)$ denotes a learning constant, and $h_{i(c)}(k)$ is a constant proportional to the distance of the i-th to the c-th neuron. The distance is evaluated from a gaussian-like neighbor membership function $\varphi(i; c)$ defined in the map and centered at the c-th neuron ($h_{i(c)}(k)$ attains largest value for $i = c$).

As a result of this training, the entire data set in R^d is subdivided into M parts (the VRs), with frequency counts $n_1, n_2, \ldots n_M$ appropriately. Of course, $\sum_i n_i = 1000$. The obtained map is depicted in Fig. 1 as exhibit (a). The frequency counts n_i of the VRs are visualized as smaller sub-hexagons painted in olive color, with radiuses proportional to $\sqrt{n_i}$. For example, the frequency counts of the VRs linked with the first row and last row of hexagons in exhibit (a) are: [14, 15, 16, 20, 16, 7, 2] and [22, 5, 9, 8, 7, 4, 8] appropriately.

Exhibit (c) show the same map, however only for data from group 1 and group 4 (interior hexagons painted in green and magenta). Exhibit (d) shows the same for group 2 (color cyan) and group 3 (color red). One may see that the groups are practically disjoint.

Could it be seen in the map, how large are the true code-book distances in R^d? This problem can be solved by calculating the U-matrix [8, 10], that is shown in exhibit (b) of Fig. 1. The corresponding distances in R^d are shown (proportionally) by color. We used gray colormap. Pure white color means small distances (min = 0.162) and pure black color means very big distances (max = 1.19). Looking at that graph one may state, that there is a black valley, which separates the data points into two parts which are far apart. The upper part, covered by group 1, is more condensed.

3 Parallel Coordinate Plots

The parallel coordinate plots [6] are constructed in a simple way: For a $n \times d$ data matrix X one draws vertically in parallel d short line segments of equal length. They correspond to the d observed variables. The j-th line segment is scaled by having its minimum and maximum equal to the minimum and maximum of the j-th ($j = 1, \ldots, d$) observed variable. Next each data vector $\mathbf{x}_i$ ($i = 1, \ldots, n$) is marked as horizontal line segment with its values $x_{i1}, x_{i2}, \ldots, x_{id}$ marked in subsequent vertical line segments. In such a way the global representation (profile) of $\mathbf{x}_i$ is obtained (see Figs. 2 and 3).

By drawing in one plot such horizontal representations for a number of data vectors, one obtains not only their individual profiles, but also a holistic representation of all of them depicted in the same place. This may easily serve for their comparison

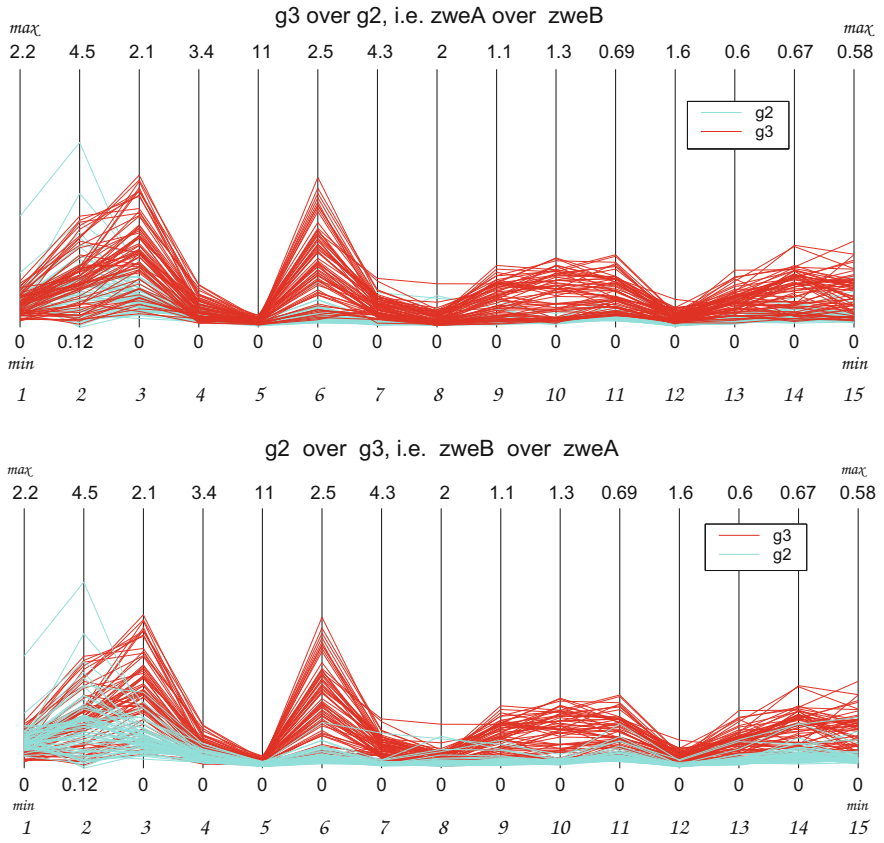

Fig. 2 Parallel. Comparison of zweB (group 2, color *cyan*) and zweA (group 3, *red*). The groups are overlapping. To see them more distinctly, they are depicted twice. *Top* zweA over zweB. *Bottom* zweB over zweA

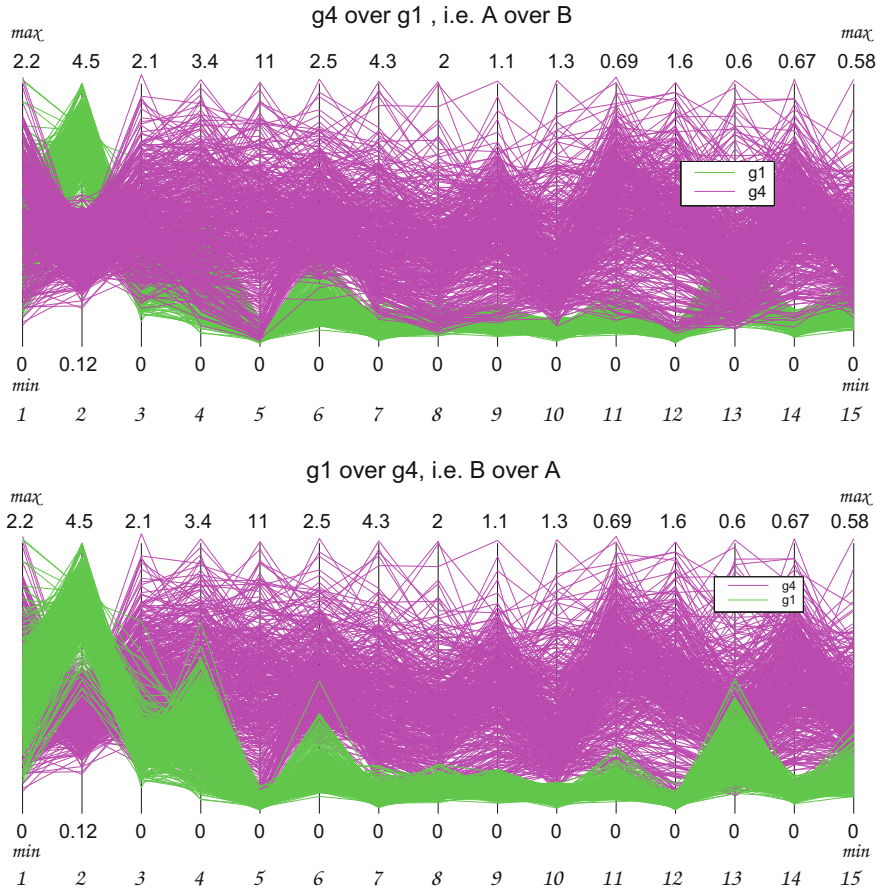

Fig. 3 Parallel coordinate plots. Comparison of group 1 (B-zwe, color *green*) and group 4 (A-zwe, color *red*). The groups are overlapping. To see them more distinctly, they are depicted twice: g4 over over g1 (*top*) and g1 over g4 (*bottom*)

'en bloc'. With a flexible software at hand, the method may serve for a variety of diverse applications, as shown in [5, 11]. The method is limited by the number of variables (d) and the number of compared data vectors (n): with increasing values of d or n an overcrowding may occur, and the subsequently plotted line segments may cover the previous ones.

Figure 2 depicts the smaller groups no. 2 ($n_2 = 61$) and no. 3 ($n_3 = 64$) obtained from the two gearboxes when being without load or very small load. The upper exhibit shows the case, when group 2 was plotted first, and group 3 was added last (g3 over g2), and has overshadowed previous plotting. The lower exhibit shows the reverse case: g2 over g3.

Comparing the two exhibits it becomes obvious that group 3 has systematically (except variable no. 2) larger values as group 2. One may also notice that group 2 has two or three data vectors with atypically large values in variables 1 and 2.

Figure 3 depicts the larger groups 1 ($n_1 = 439$) and 4 ($n_4 = 434$) obtained from the two gearboxes being fully loaded. Figure 3 shows clearly that—except variable no. 2—all other variables of group 4 dominate the respective values of group 1 (are significantly larger).

4 t-SNE, t-Distributed Stochastic Neighbor Embedding

The t-SNE method [4, 9] projects the original data points $\mathbf{x}_i$, $i = 1, \ldots, n$, (located in R^d) to a two-dimensional plane by constructing the correspondent projections $\mathbf{y}_i$, $i = 1, \ldots, \mathbf{y}_n$, located in that plane. The projection plane is called 'the map'. The aim is to retain between the pairs $\mathbf{y}_i, \mathbf{y}_j$ in the map the respective distances (similarities) between the original data points $\mathbf{x}_i, \mathbf{x}_j$. The method can deal with high-dimensional data located located in several low-dimensional manifolds, when seen from multiple viewpoints.

The method works using a stochastic methodology. The Euclidean distances between pairs of the respective data points are converted into conditional probabilities that represent similarities between pairs. It is assumed [4, 9] that the high-dimensional data points $\{\mathbf{x}_i\}$ are generated by a probability function with Gaussian kernel centered at $\mathbf{x}_i$. For each j, $(j \neq i)$, the distance/neighborhood of $\mathbf{x}_j$ to the point $\mathbf{x}_i$ is computed as the conditional probability $p_{j|i}$. Applying a symmetrization technique, the overall symmetric distribution $P = \{p_{ij}\}$ modelling the affinities between all the pairs of points $\mathbf{x}_i$ and $\mathbf{x}_j$ residing in R^d is established.

An analogous distribution $Q = \{q_{ij}\}$, modelling the affinities between projection points $\mathbf{y}_i$ and $\mathbf{y}_j$ in the map, is established too. However now, for reasons explained in [9], the symmetrized conditional probabilities $\{q_{ij}\}$ are assumed to follow the Student-t distribution with one degree of freedom, which for this case is identic with a Cauchy distribution:

$$q_{ij} = \frac{(1 + ||\mathbf{y}_i - \mathbf{y}_j||^2)^{-1}}{\sum_{k \neq i} (1 + ||\mathbf{y}_i - \mathbf{y}_k||^2)^{-1}} \tag{2}$$

The probability distributions P and Q should be possibly similar. This can be stated using the Kullback-Leibler divergence:

$$C = \sum_i KL(P||Q) = \sum_i \sum_j p_{ij} log \frac{p_{ij}}{q_{ij}}. \tag{3}$$

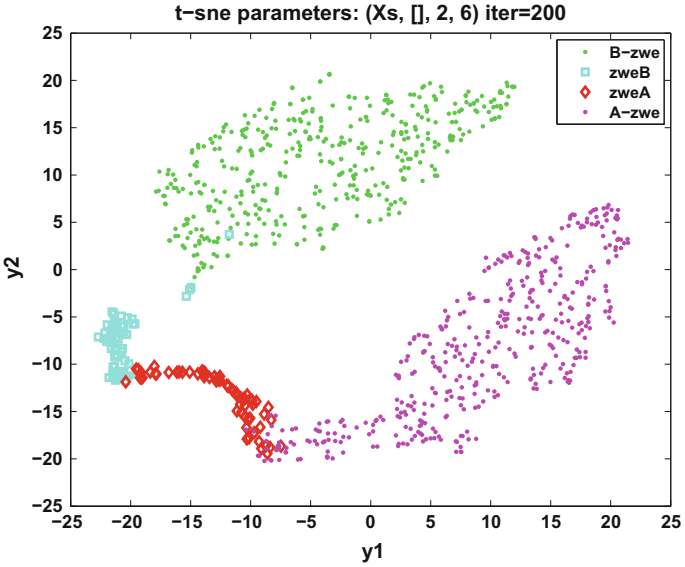

Fig. 4 Depicting the four group gearbox data using t-SNE. Group 1 is separated from remaining groups, in particular, is far away from group 4. Groups 2 and 3 (small load) are differentiated with few data points in common

Minimizing the criterion C with respect to the sought values $\mathbf{y}_j$'s (accessible via Eq. 2) we obtained the projections shown in Fig. 4. One may notice that the obtained projection points reflect nearly perfectly the true data structure. Data points belonging to different groups are practically separated.

5 Discussion of the Results and Conclusions

The three multivariate data visualization algorithms yielded interesting results about the geometry and structure of the recorded data points (rows of the gearbox diagnostics data X, obtained from the respective vibration signal) and their location in the multivariate data space R^{15}. This was shown in different ways.

The SOM and t-SNE algorithms were able to recognize (and visualize) the geometrical localization of the data points in the multivariate data space. It appeared, that groups 1 and 4 are far apart separated by empty regions. Both methods show a strong separation of group 1 from remaining groups. What concerns groups 2 and 3: they are more close each other as groups 1 and 4; yet they reside in separate areas with an interface of perhaps three points. One may really say, that SOM and t-SNE—working with quite different principles—are complementary. The results yielded by

them are topologically equivalent. Taken together they strengthen and consolidate our imagination on the geometrical location of the analyzed data.

The second applied method (Parallel Coordinate plot) provided the details about the contents of the groups. It shows directly values of variables characterizing the data values. For example: the variables in group 4 have predominantly higher values as variables in group 1, and this is the reason for their big separation in the data space.

The calculations of SOM and t-SNE were performed using the free `Matlab SOM Toolbox` [10] and the free Matlab function `tsne` ([9]). Both methods work in an iterative way. The calculations of SOM were straightforward and repeatable, due to starts from points in the PC plane. The calculations in `tsne` start from purely random normal values of the map projections $\mathbf{y}_i$'s, they need also fine-tuning of several parameters. This takes several (perhaps four) times more time as the SOM needs. The obtained results are in majority topologically equivalent, yet we got several simulations with weird content. Summarizing, we like the t-SNE method for giving more details on the geometry of the data points in R^d, as for example the SOM does. Other methods, like Principal Components and Non-negative Matrix Factorization, have given—for the same data—results more squeezed and clumped together [2].

For Parallel Coordinate plots we have used own Matlab function `para`. It is safe and quick, however only for moderate values of d (number of variables) and n (number of displayed data vectors).

Concerning the diagnostic issues, we come to the conclusions:

1. The data coming from the two gearboxes working under load differ significantly by their geometrical location in the multivariate date space.
2. The data coming from the two gearboxes working without load reside in different areas with a very small joint interface.
3. The results are based on 3 independent analyzes, which strengthens their faithfulness. They also confirm suggestions provided in [1] that it is better to diagnose gearboxes under loaded than unloaded condition.

All the three elaborated methods look at the data globally as points in the d-dimensional data space. A problem: Is it possible to get similar displays when working with a smaller number r ($r < d$) of the variables? In [3] it is shown that it is possible to obtain an effective comparable diagnostics when working with a reduced set of variables. It would be interesting to find out if this is true also when depicting the reduced data using the proposed methods.

References

1. Bartelmus, W., & Zimroz, R. (2009). A new feature for monitoring the condition of gearboxes in non-stationary operating systems. *Mechanical Systems and Signal Processing*, *23*(5), 1528–1534.

2. Bartkowiak, A. M., & Zimroz, R. (2015). NMF and PCA as applied to gearbox data. In K. Jackowski, et al. (Eds.), *Intelligent data engineering and automated learning– IDEAL 2015* (pp. 199–206). LNCS 9375, Springer.
3. Bartkowiak, A., & Zimroz, R. (2014). Dimensionality reduction via variables selection—Linear and nonlinear approaches with application to vibration-based condition monitoring of planetary gearbox. *Applied Acoustics*, *77*, 169–177.
4. Hinton, G. E., & Roweiss, S. T. (2002). Stochastic neighbor embedding. In *Advances in neural information processing systems* (pp. 833–840), Vol. 15. USA.
5. Inselberg, A. (2009). *Parallel coordinates: Visual multidimensional geometry and its applications* (Textbook 554 pages). New York: Springer.
6. Inselberg, A. (1985). The plane with parallel coordinates (invited paper). *The Visual Computer*, *1*, 69–91.
7. Kohonen, T. (2001). *Self-organizing maps* (3rd ed.). Heidelberg: Springer.
8. Ultsch, A., & Siemion, H. P. (1990). Kohonen's self organizing feature maps for Explorative Data Analysis. In *Proceedings of International Neural Network Conferences (INNC'90)* (pp. 305–308). Dordrecht, NL: Kluwer.
9. van der Maaten, L., & Hinton, G. (2008). Visualizing data using t-SNE. *Journal of Machine Learning Research*, *1*, 1–48.
10. Vesanto, J., et al. (2000). *SOM toolbox for Matlab 5* (pp. 1–54). HUT, Libella Oy, Espoo, Finland: Som Toolbox Team. http://www.cis.hut.fi/projects/somtoolbox/.
11. Wegman, E. (1990). Hyperdimensional data analysis using parallel coordinates. *Journal of the American Statistical Association*, *85*(411), 664–675.
12. Zimroz, R., & Bartkowiak, A. (2013). Two simple multivariate procedures for monitoring planetary gearboxes in non-stationary operating conditions. *Mechanical Systems and Signal Processing*, *38*(1), 237–247.

Engine Diagnosis Based on Vibration Analysis Using Different Fuel Blends

Jairo A. Grajales, Héctor F. Quintero, Carlos A. Romero and Edison Henao

Abstract Fault diagnosis of an internal combustion engine is proposed herein by means of vibration analysis; in order to show the reliability of it, this paper presents a comparative study of normal and faulty scenarios. An engine test bench was used to acquire the vibration signals. For this study, the fault considered on the bench was misfire, which was induced by removing the spark plug wire of a cylinder. Fast Fourier Transform was used to obtain the frequency domain of the signal as a preliminary step to the subsequent identification process based on statistical characteristics extraction. In order to validate previous works on misfire with pure gasoline, measurements included tests performed with ethanol-gasoline fuel blends, namely E30, E20 and commercially available E8 at three different speeds. A simpler classification process was obtained with the extraction of several statistical characteristics from several frequency bands, based on the excited frequency components. The presence of three peaks (at 0.75, 1.25, and 1.5 of the combustion frequency) in the vibration signal of the engine block in the transversal direction for the induced misfire condition, provided differentiation between normal and faulty conditions with all tested fuel blends. According to results, changes in the fuel mix seem to have little impact on the performance and behavior of the engine vibration signals.

Keywords Engine diagnosis · Vibration analysis · Frequency analysis

1 Introduction

Given the importance of internal combustion engines within the modern industry, many manufacturing plants depend on predictive maintenance for these machines. Due to its relevance, approaches like condition monitoring have gained growing interest. The main measurement used for this purpose is cylinder pressure [1], since

J.A. Grajales · H.F. Quintero (✉) · C.A. Romero · E. Henao
Universidad Tecnológica de Pereira, Pereira, Colombia
e-mail: Pereira.hquinte@utp.edu.co

A. Timofiejczuk et al. (eds.), *Advances in Condition Monitoring of Machinery in Non-Stationary Operations*, Applied Condition Monitoring 9,
https://doi.org/10.1007/978-3-319-61927-9_25

it shows a great deal of information concerning the internal combustion process. However, it is an invasive and expensive procedure due to additional costs of sensors and engine modifications.

In an attempt of finding more affordable options, the use of less specific type of sensors has reported good performance in techniques such as angular speed measurement [2], oil analysis [3], surface temperature and exhaust emissions. But, great interest has been placed on the study of acceleration measurement using sensors, such as accelerometers [4], acoustic sensors [5] and knock sensors [6], with satisfactory results and widespread deployments in condition monitoring of rotating machinery [7]. However, they have been found to present problems when using conventional analysis methods for assessment in the particular conditions of internal combustion engines, since the measured signals are non-stationary.

The identification of diverse causes to engine block vibration from single point measuring in [6] was achieved based on short time Fourier transform on the signal, collected with a commercial knock sensor. A determination of combustion parameters by means of neural networks reported in [2] was supported on angular velocity measuring. Both indicated and load torques were estimated in [8] using the variations in motor speed. An assessment of the influence of the shape variations of the piston bowl on the combustion process was given in [9], for this purpose vibration data from the engine block was analyzed. According to [10], results from studies with only gasoline in faulty operations, such as a misfire, reported changes in the spectral composition of the vibratory signal of an engine and the presence of peaks different from the combustion frequency.

Nevertheless, these researches did not take into account the influence of alcohol-gasoline fuel blends on the vibration features. [11] used a chassis dynamometer to report on engine performance at different speeds and loads of a vehicle driven by fuel blends consisting of gasoline and alcohol derivatives like ethanol and methanol (E5, E10, M5 and M10). Their results showed that alcohol-gasoline blends increased brake specific fuel consumption and delayed cylinder gas pressure.

The present study was conducted to assess the effects of using different blends of gasoline and ethanol as fuel on the spectral composition of the vibration signal of the engine, in the presence of a fault, in this case a simulated misfire on cylinder 4. Additional sensors were used during the experiments to consolidate a robust database. This work showed that the same characteristic frequencies and peaks reported on pure gasoline are present on gasoline-ethanol blends of commercial fuel (E8), E20 and E30, when testing under misfire conditions. And that some statistical characteristics can be extracted from the frequency domain signals, on certain frequency bands, to simplify the identification process. This article describes in detail the experimental setup, test procedure and a comparative analysis of measurements under normal conditions and induced misfire.

2 Experimental Setup

The experimental test bench for this study consisted of a four cylinder, four stroke spark ignited internal combustion engine from a truck with a capacity of 2 l, and mounted on a movable structure that allowed access to the components of the motor as well as better control of temperatures and leaks which in turn simplified condition monitoring.

Vibrations analyzed herein correspond to three different measured accelerations. These accelerometers were installed on three different areas (the first one vertically positioned at the top of the engine, the second one longitudinally positioned in respect to the crankshaft axis and mounted close to cylinder one, and the last one mounted in the middle of cylinders two and three with a normal direction to the crankshaft axis). Respective data acquisition resorted to two equipments mounted on a NI cDAQ 9174 four-slot chassis (NI 9232, 3 channel ±30 V analogue input module and a NI 9234, 4 channel ±5 V analogue input module).

In order to determinate stable speeds of the engine for measurement and reliable conditions for the running periods of testing, a preliminary test was run.

Since the test bench allowed easy access to the engine components, it was possible to test two different operational conditions with no load. (1) Normal: with four cylinders running and (2) Misfiring Piston: Induced misfire of a piston by disconnecting the spark plug from cylinder four. The comparative analysis between normal and faulty operations of the engine was based on an experimental testing that focused on different variables of speed and fuel blend. Three fuels were used during the tests:

(i) E8: Blend of gasoline with 8% ethanol.
(ii) E20: Blend of gasoline with 20% ethanol.
(iii) E30: Blend of gasoline with 30% ethanol.

Data was collected at three different speeds: 1500, 1700 and 2000 rpm, for each condition, running on each fuel previously presented, and recording the data from the eight instruments at the same time. Three sets of data were collected for each condition on each constant speed. Making use of the available data acquisition setup the sampling frequency was set to 51.2 kHz/channel, and measurements were recorded for 2 s, for each set of data.

The process of differentiation between normal and faulty conditions was based on data obtained from signals in time domain and frequency domain transformation of the signal, namely full spectrum of acceleration vibrations and subsequent focus on areas/zones of special interest due to the presence of excited frequencies. This study also resorted to the extraction of the following eight statistical features applied to all the data obtained from the aforementioned signals: Root mean square (RMS), Arithmetical mean, Kurtosis, Standard deviation, Skewness, Energy, Maximum value, Minimum value.

3 Results

Measuring started after installing the pressure sensor on the engine, which was previously heated and set up to maintain a stable operation. Firstly, the normal condition was tested for the E8 fuel blend; three different measurements were taken for each one of the speeds selected. Afterwards, misfire is induced by disconnecting the spark plug of the fourth cylinder, and the measuring process is repeated for each speed. After completing the tests for E8, remaining fuel was removed from the tank before introducing the next fuel blend. The same measuring procedure described above was repeated until obtaining complete data from the remaining fuel blends (E20 and E30). Figure 1 depicts the measurements with the vertical accelerometer.

To analyze the signals in the frequency domain, the fast Fourier transform was applied. With all these new signals, a comparison was performed to identify differences in the frequency components of the signal in the different operating conditions, and see if the differences are still present when the different fuels are used. Frequency domain signals for the three fuel blends under both normal and faulty conditions at 1500 rpm can be seen in Fig. 2. In the graphic, two tendencies are recurrent in both conditions for all the fuel blends. Firstly, from 400 to 700 Hz,

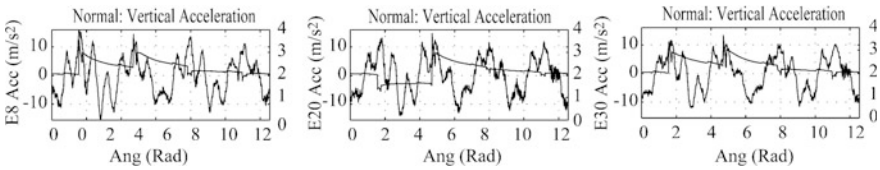

Fig. 1 Vertical acceleration, normal operating conditions on three fuels, second axis, spark detection

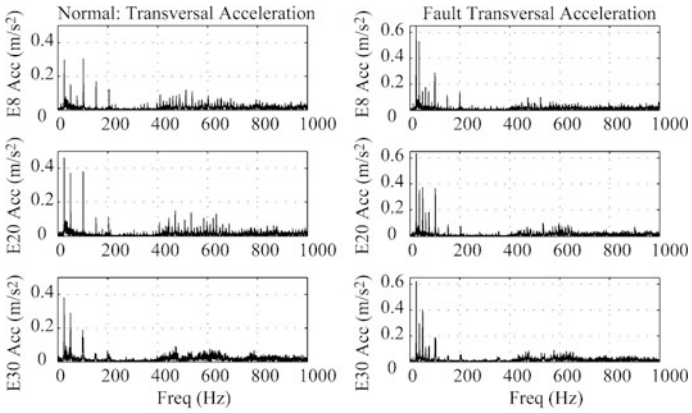

Fig. 2 Transversal acceleration, normal and fault operating conditions on three fuels, 1500 rpm

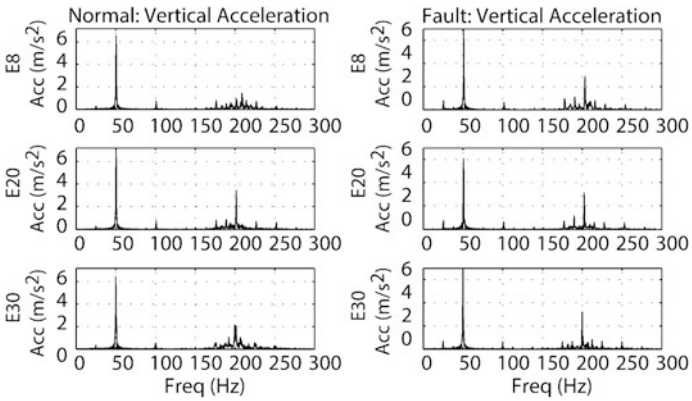

Fig. 3 Vertical acceleration, normal and fault operating conditions on three fuels, 1500 rpm

several smaller peaks can be seen, which may be resonant responses from the supporting structure due to their repetitive presence in almost every measurement. And secondly, the prominence of three particular peaks is recurrent: namely at 25, 50, and 100 Hz. As expected for the engine used, under normal conditions at 1500 rpm combustion frequency (CF) was reported at 50 Hz but oddly the peak at 25 Hz corresponding to revolution or speed frequency (RF) also appeared in CF peak is the only one expected to appear and the peak at 100 Hz may be considered its harmonic, hence the presence of RF peak should have stemmed from some unbalance and differences in the support of the mounting.

From faulty conditions, the two tendencies described above kept taking place, however a couple of new facts provided enough distinction between faulty and normal conditions. Firstly, RF peak at 25 Hz is reported to be the highest. And secondly, under faulty conditions there was a constant presence of another three peaks at 37.5, 62.5 and 75 Hz. Such frequencies may also be considered as 0.5 CF, 0.75 CF, 1.25 CF and 1.5 CF respectively. It is worth of noting that these distinctive and discrepant tendencies of normal and faulty conditions took place with all fuel blends. Results with similar behaviors were obtained for tests run at 1700 and 2000 rpm.

Neither the longitudinal nor the vertical acceleration measurements reveal any significant discrepancy between faulty and normal conditions. The results obtained with vertical accelerometers reported in Fig. 3 are in accordance with [10]: On both operational modes, CF peaks took place very clearly and the only differentiating elements are minor increases of the small RF peaks for the instances of induced misfire. Just like in the previous measurements, all the tested fuel blends repeatedly shared tendencies.

Since the first comparisons based on frequency domain transformations revealed that distinguishing elements between operating modes exhibited greater salience at frequencies below each one of the CF peaks, the analysis of statistical characteristics focused on such lower frequencies. The first frequency band selected for statistical

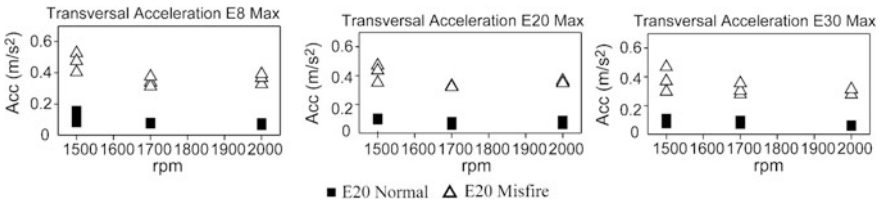

Fig. 4 Transversal acceleration, normal and fault operating conditions on three fuels, maximum value, 0.6–0.9 CF

characteristics extraction corresponded to the zone 0.6–0.9 CF. Analyzing this frequency from transversal measurements, only one (minimum value) out of the eight statistical properties did not report discrepancies that allowed to differentiate between normal and faulty conditions. The constant tendency of the seven differentiating properties was higher values under faulty conditions. Maximum values and Standard Deviations were the ones that provided a better distinction, i.e. a greater gap between values of the two conditions tested. Maximum values (Fig. 4) serve as an example to illustrate the satisfactory distinction obtained by means of statistical characteristics extraction from transversal acceleration measurements at the aforementioned frequency band for all the speed and fuel blends variables of this study.

Further analysis on transversal acceleration at the wider frequency band 0–0.9 CF reported that five statistical characteristics (maximum value, RMS, mean value, standard deviation and energy) allowed clear distinction between conditions for the three fuel blends at 1500 and 1700 rpm, however differentiation didn't took place at all from measurements at 2000 rpm. The remaining three characteristics (Kurtosis, Skewness, and Minimum value) exhibited inconsistency in their results, whether they didn't report differences whatsoever or only for isolated conditions.

Despite full spectrum readings of vertical vibrations reported an overall similarity unpromising for signs of differentiating elements between operational modes, the corresponding statistical characteristics surprisingly allowed some distinctions. Maximum value was the only statistical characteristic capable of differentiating normal and faulty conditions at the 0–0.9 CF frequency band from vertical vibrations. Such a distinction was present for all the speed and fuel blends variables of the study as shown on Fig. 5. It is plain to see that considerably lower maximum

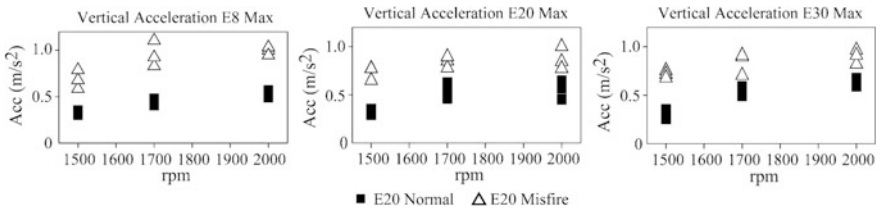

Fig. 5 Vertical acceleration, normal and fault operating conditions on three fuels, maximum value, 0–0.9 CF

values took place in normal conditions in comparison to those for conditions with induced misfire. None of the other statistical characteristics provided results as reliable as those from maximum values to assist in the differentiation process between operation conditions. Yet again, longitudinal vibrations signal didn't yield any statistical characteristic capable of providing constant and reliable distinction between the operation modes tested herein.

Frequency domain analysis reported some excited frequencies during normal operation, most of them correspond to the combustion frequency (CF) and its harmonics, a foreseen fact due to typical characteristics of a spark ignited internal combustion engine. The equipment used herein was a four-cylinder engine, whose CF is known to be two times the revolution frequency (RF). The latter also appeared in the analysis. As opposed to literature reporting the largest magnitudes for CF peaks on normal conditions, normal conditions tested at 1500 rpm (Fig. 3) revealed RF peaks to be the highest, which in turn can be explained with a test bench problem stemmed from unbalance of the pieces. Specially, the inertia added to the system by the dynamometer attached to the engine.

In parallel with the above analysis, the non-harmonic nature of readings from faulty conditions was confirmed with the presence of 0.75, 1.25 and 1.5 CF peaks for all the speed and fuel blend variables of the study, such peaks never appeared on normal conditions measurements. That anharmonicity was also a foreseen fact due to one idle cylinder leading to three combustions in a two cycle period.

This work extends the scope of previous studies by including different fuel blends and thus more scenarios for assessment. Extra amount of oxygen provided by the addition of ethanol changes the characteristics of the combustion process particularly in respect to speed and power of the combustion. However, the same excited frequencies reported in literature with only gasoline operations were also found in the three ethanol-gasoline blends tested herein, despite that the carburetor used was not the appropriate for the new conditions of the combustion.

4 Conclusions

A time frequency transformation was applied on three vibration signals (vertical, transversal and longitudinal accelerations) from an internal-combustion, spark-ignited engine; focusing on finding frequency components able to differentiate normal from induced misfired condition. Induced misfire was achieved by taking off spark plug number four. Besides the measurements at three different speeds, the study also expands the research scope by including three gasoline-ethanol fuel blends (E8, E20 and E30). Additional sensors were used for future investigations.

The results herein coincided with the literature. The expected presence of three peaks (referred to as 0.75, 1.25, and 1.5 CF) in the transversal vibration signal for the induced misfire condition, provided differentiation between the two operation conditions examined, in all tested fuel blends.

A subsequent extraction of eight statistical characteristics was performed on the signal in the time domain and on several frequency domain bands, aiming to simplify the differentiation process. Seven of the eight statistical characteristics extracted from transversal vibrations exploring the frequency band 0.6–0.9 CF, provided a clear distinction between operational conditions for all the variables tested.

In the case of vertical vibrations signals, the only statistical property capable of distinguishing operational conditions for all the variables tested was the maximum value in the frequency band 0–0.9 CF. Data from longitudinal vibrations only were able to provide isolated distinctions between conditions since inconsistency was reported throughout the variables of fuel blends and speed during the analysis.

References

1. Chandroth, G. O., Sharkey, A. J. C., & Sharkey, N. E. (1999). Cylinder pressures and vibration in internal combustion engine condition monitoring. In *Proceedings of Comadem, 99*.
2. Taglialatela, F., Lavorgna, M., Mancaruso, E., & Vaglieco, B. M. (2013). Determination of combustion parameters using engine crankshaft speed. *Mechanical Systems and Signal Processing, 38*(2), 628–633. doi:10.1016/j.ymssp.2012.12.009.
3. Jiang, R., & Yan, X. (2008). Condition monitoring of diesel engines. In *Complex System Maintenance Handbook [Electronic resource]*. Springer.
4. Gravalos, I., Loutridis, S., Moshou, D., Gialamas, T., Kateris, D., Tsiropoulos, Z., & Xyradakis, P. (2013). Detection of fuel type on a spark ignition engine from engine vibration behavior. *Applied Thermal Engineering, 54*, 171–175. doi:10.1016/j.applthermaleng.2013.02.003.
5. Arroyo, J., Muñoz, M., Moreno, F., Bernal, N., & Monné, C. (2013). Diagnostic method based on the analysis of the vibration and acoustic emission energy for emergency diesel generators in nuclear plants. *Applied Acoustics, 74*(4), 502–508. doi:10.1016//j.apacoust.2012.09.010.
6. Vulli, S., Dunne, J. F., Potenza, R., Richardson, D., & King, P. (2009). Time-frequency analysis of single-point engine-block vibration measurements for multiple excitation-event identification. *Journal of Sound and Vibration, 321*(3–5), 1129–1143. doi:10.1016/j.jsv.2008.10.011.
7. Li, Y., Tse, P. W., Yang, X., & Yang, J. (2010). EMD-based fault diagnosis for abnormal clearance between contacting components in a diesel engine. *Mechanical Systems and Signal Processing, 24*(1), 193–210. doi:10.1016/j.ymssp.2009.06.012.
8. Bengtsson, F. (2006). Estimation of indicated- and Load-torque from engine speed variations. *Master's Thesis*. Linkoping University.
9. Torregrosa, A., Broatch, A., Marant, V., & Beauge, Y. (2004). Analysis of combustion chamber resonance in DI automotive diesel engine. In *Thermo and Fluid Dynamic Processes in Diesel Engines 2*. Berlin Heidelberg: Springer.
10. Ben-Ari, J., de Botton, G., Itzhaki, R., & Sher, E. (1999). Fault detection in internal combustion engines by the vibration analysis method. SAE Technical Paper 1999-01-1223. doi:10.4271/1999-01-1223.
11. Eyidogan, M., Necati, A., Canakci, M., & Turkcan, A. (2010). Impact of alcohol–gasoline fuel blends on the performance and combustion characteristics of an SI engine. *Fuel, 89*(10), 2713–2720. doi:10.1016/j.fuel.2010.01.032.

Application of Cepstrum Prewhitening on Non-stationary Signals

L. Barbini, M. Eltabach and J.L. du Bois

Abstract In the field of vibration based condition monitoring a trusted symptom of a defective bearing is the observation of peaks, at characteristic frequencies, in the squared envelope spectrum (SES). If a machine is operating in a varying speed regime the SES is computed on the order tracked signal, i.e. the signal resampled at constant angular increments, and the SES can still be used for diagnostic. Despite its versatility a common problem with the SES is that peaks from other sources of vibrations, as for instance gears, can prevent the diagnosis of a defective bearing. Therefore pre-processing techniques are applied to the vibrational signal before the computation of the SES to enhance the signal from the bearings. Among these techniques cepstral pre-whitening (CPW) has gained much attention offering a remarkable capability of eliminating, in a blind way, both harmonics and modulation sidebands of the unwanted components. In the case of a varying speed regime the usual procedure consists of three steps: order track the signal, calculate the CPW, evaluate the SES. In this paper on the contrary the CPW is applied before the step of order tracking; therefore the proposed approach is: CPW the raw time signal, order tracking, evaluation of the SES. The remarkable observation is that for this approach the cepstrum does not present peaks at characteristic quefrencies, being the raw signal acquired in a varying speed regime. However this paper shows by means of numerical simulations and analysis of experimental data, that with the proposed methodology the masking components coming from the gears are suppressed and the signal from the defective bearing is enhanced.

Keywords Bearing diagnosis · Non stationary conditions · Cepstrum pre-whitening · Order tracking

L. Barbini (✉) · J.L. du Bois
Department of Mechanical Engineering, University of Bath,
Claverton Down, Bath BA2 7AY, UK
e-mail: l.barbini@bath.ac.uk

M. Eltabach
CETIM, Avenue Félix-Louât, 60300 Senlis, France

A. Timofiejczuk et al. (eds.), *Advances in Condition Monitoring of Machinery in Non-Stationary Operations*, Applied Condition Monitoring 9,
https://doi.org/10.1007/978-3-319-61927-9_26

1 Introduction

In a faulty bearing an impact occurs every time a rolling element hits a defect in the raceway or a defective rolling element hits the raceway. The detection of the shock generating from each impact is often a challenge due to the presence of other sources of vibrations, in particular gears, masking the presence of the defect. Therefore signal pre-processing methods have to be implemented before the evaluation of the widely established diagnostic technique of the squared envelope spectrum (SES). Cepstrum editing (CE) has been proposed as an efficient method for the suppression of gear components from a vibrational signal [1] and it performs well when compared with other techniques [2]. The working principle uses the fact that vibrations from gears result in a series of peaks at constant distances in the frequency spectrum. Therefore all these peaks can be eliminated suppressing, by means of a lifter, the corresponding peak in the cepstrum. Sawalhi et al. [3] introduce the cepstral pre-whitening (CPW) as a further application of the cepstrum for the removal of all the discrete components from the spectrum, both vibrations from the gears and resonance effects.

When machines are operating at varying speed peaks corresponding to the vibrations from gears are smeared in the frequency domain and the cepstrum does not present significant peaks. In such cases the CPW is implemented in the order domain, after the operation of order tracking (OT) [4, 5]. However changing to a rotation angle basis smears the resonance frequencies excited by the impacts from the faulty bearing. Recently [6, 7] has been suggested to enhance the signal from the bearing directly in the time domain and to implement the OT only after this operation. Borghesani et al. [6] propose to band-pass filter the non stationary signal and Randall et al. [7] compare the performances of the application of three common techniques:spectral kurtosis for band selection, minimum entropy deconvolution and an exponential lifter.

The paper follows these methodologies and shows that CPW can be applied directly on time vibrational signals from machinery operating at varying speed conditions, before the operation of OT. The paper is organised as follows: Sect. 3 presents the proposed method, Sect. 2 evaluates its performance on a numerical simulation and Sect. 3 on experimental data sets. Conclusions are presented in the final section.

2 Methods

In this paper two techniques will be used to pre-process, before the computation of the squared envelope spectrum (SES), vibrational signals from machines operating at varying speed. The two techniques are cepstral pre-whitening (CPW) and order tracking (OT). CPW can be implemented without the computation of the cepstrum [4], using only the Fourier transform:

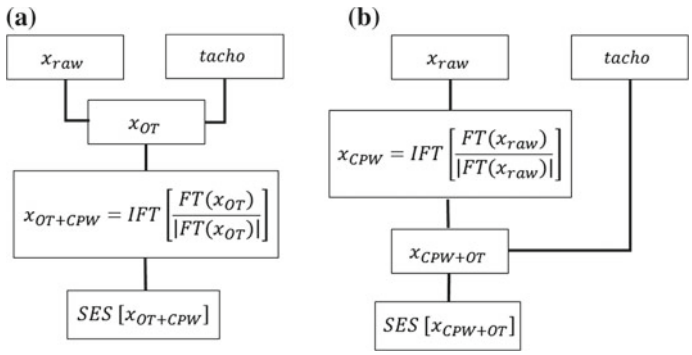

Fig. 1 Schemes of the two processing methods

$$x_{cpw} = IFT\left[\frac{FT\,(x)}{|FT\,(x)|}\right] \tag{1}$$

This operation is equivalent to setting to zero the real cepstrum and recombine it, in the frequency domain, with the phase of the original signal. The result is a white signal with a flat spectrum of amplitude one. OT is applied in the time domain implementing a digital re-sampling of the signal synchronously with the shaft rotation speed. In this paper the shaft rotation speed is considered to be provided by a tachometer. The envelope for the computation of the SES is calculated as the absolute value of the analytical representation of the full band signal. The SES is normalised by means of the ratio: $\tilde{SES}[l] = SES[l]/SES[0]$. In the following the ˜ will be omitted. The common procedure using such techniques consists of a first step of OT and afterwards CPW the x_{OT} signal [4, 5], as it is shown in Fig. 1a. However the resonant frequencies excited by the impacts from a faulty bearing are constant or vary more slowly than the operational speed of the machine. OT effectively produces a sequence of impacts equally spaced in the time domain, but the resonant frequencies excited by the impacts will be smeared [6] by the re-sampling. Therefore after OT the dynamic information is lost and the application of CPW may result in unwanted amplification of low signal to noise ratio bands [5].

To address this issue in this paper the CPW is applied directly on the non stationary signal and afterwards the OT is performed. The proposed approach is shown in Fig. 1b. The central assumption is that the restriction of applying CPW only to signals showing periodic components in a spectrum can be relaxed. Equation 1 is more generally effective and able for instance to enhance impacts masked by a strong non stationary signal, as shown by a numerical simulation in the next section. This follows from the observation that Eq. 1 is equivalent to what has been called the phase only signal [8] and used in [9] for detection of defects on surfaces.

3 Numerical Investigation

The numerical simulation consists on the application of CPW to a signal constructed as the superposition of a deterministic non stationary component and a sequence of random impacts. Such signal does not show peaks in the cepstrum, nevertheless it will be shown that CPW is still capable of enhancing the sequence of impacts. A chirp signal with the frequency increasing linearly from 10 to 200 Hz and amplitude 1 [a.u.], is used for the deterministic non stationary component. The impacts have mean occurrence frequency of 48.7 Hz plus a random jitter of 2%, in order to resemble a random component coming from a defective bearing. The resonance frequency is simulated in the band 2200–3000 Hz and the amplitude of the impacts is 0.1 [a.u.]. The signal is shown in Fig. 2a in black, the total length is 2 s and the sampling frequency is 12.8 kHz, zoomed sections at different times are shown on the left and right sides, in yellow is superimposed only the sequence of impulses. As expected the real cepstrum of the simulated signal has no clear peaks, as shown in Fig. 3a. The real cepstrum is calculated as the inverse Fourier transform of the logarithm of the magnitude of the Fourier transform of the signal. The SES, shown in Fig. 3b, does not present indications of the presence of impulses, being masked by the high energy chirp. The signal after the operation of CPW is shown in blue in Fig. 2b, the chirp is completely removed and the presence of the impacts is highly enhanced, for comparison in yellow it is shown the original sequence of impacts. The SES of the CPW signal is shown in Fig. 3c where peaks are present at the expected mean occurrence frequency of the impacts and the first harmonic.

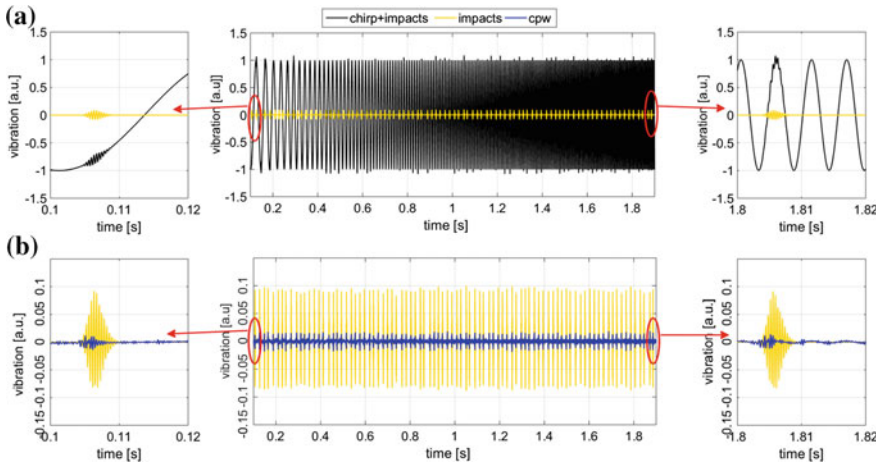

Fig. 2 **a** Simulated non stationary signal. **b** Simulated non stationary signal after CPW. See legend for description of signals

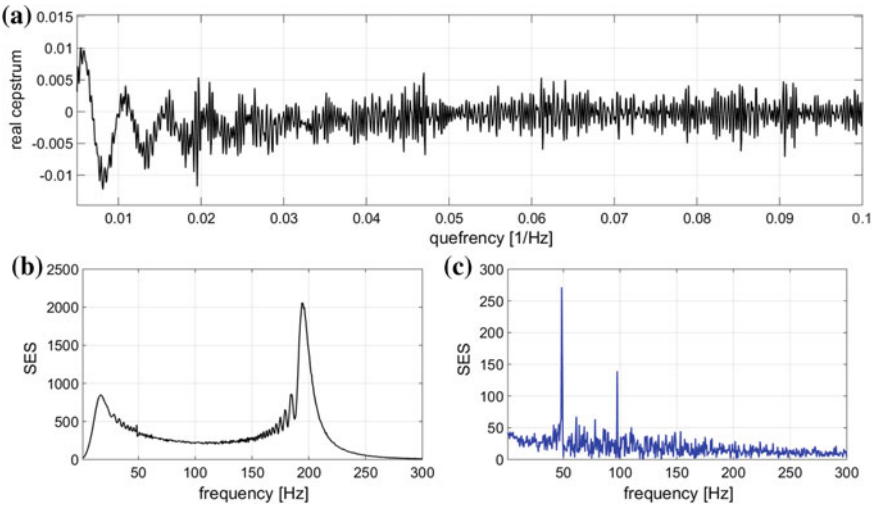

Fig. 3 **a** Real cepstrum of the simulated non stationary signal comprising the two components, **b** corresponding SES. **c** The SES of the CPW signal

4 Experimental Investigation

This section shows a benchmark comparison between the SES obtained using the proposed approach of Fig. 1b and the SES obtained from the usual procedure of applying CPW in the order domain Fig. 1a. The data sets used in this section were provided by the Centre Technique des Industries Mécaniques (CETIM).

4.1 Test Rig and Data Sets

Figure 4a shows the photograph of the test rig. A variable speed asynchronous electric motor drives the input shaft of a parallel spur-gear of ratio one and 18 teeth, and an alternator applies a constant load. The output shaft is supported by two rolling elements bearings of which the one close to the gearbox is in healthy conditions while the other one has an outer race defect with expected repetition of 3.04 orders (BPOO). An accelerometer mounted on the casing of the healthy bearing is used as a vibration transducer.

Two signals are analysed in this paper: a run-up profile and a randomly varying speed, the lengths of the signals are of 15 and 20 s respectively, both are sampled at Fs = 12.8 kHz. Figure 4b and c show the two speed profiles as a function of time: in the run-up the speed is varying approximately of 10 Hz increasing constantly from 25 to 35 Hz, while in the case of random variations the speed changes more drastically for example of approximately 30 Hz in 2.5 s. The SES of the run up signal is shown in Fig. 5a and for the random speed signal in Fig. 5b. The speed variations

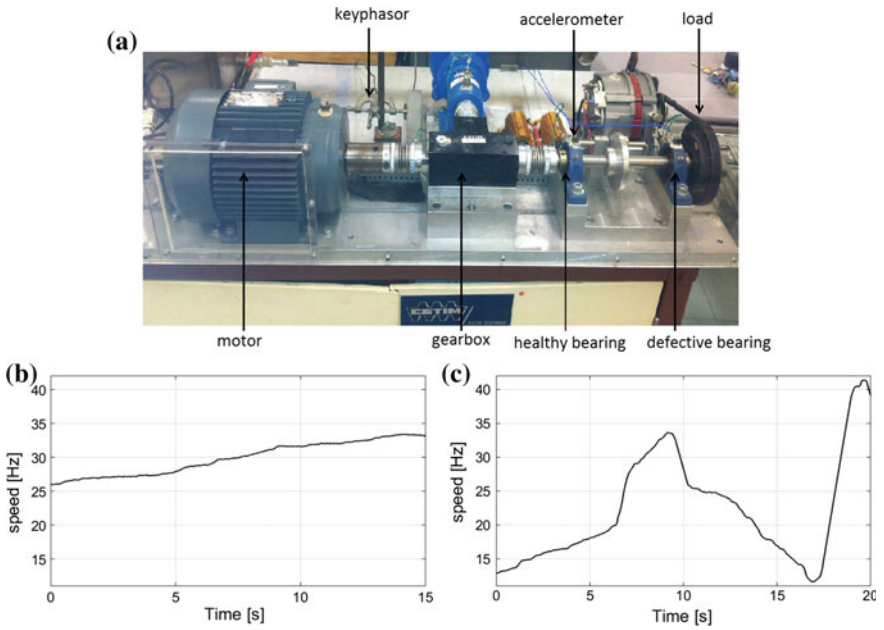

Fig. 4 **a** The photograph of the test rig. **b** The run up speed profile. **c** The randomly varying speed profile

are large in both cases therefore the SES are smeared and no clear peaks are present at the theoretical bearing fault order. The SES after OT the signals are shown in Fig. 5c and d and the presence of the defective bearing is revealed, however can be noticed disturbing components among which 1X has the highest energy and 2BPOO is almost masked. The real cepstra of the signals before and after OT are shown in Fig. 5e for the run up case and Fig. 5f for the random speed profile. In both cases after the operation of OT, in black, the gear components contribute a periodic spectrum resulting in a cepstrum with peaks separated by 1/X. On the other hand the cepstra for the raw non stationary signals, in blue, do not present peaks.

4.2 Results

The aim of the CPW step in the common procedure of Fig. 1a, is that of removing the disturbing components from the SES of Fig. 5c and d. After the operation of OT the spectrum shows periodicity contributing the peaks in the cepstra, as shown in Fig. 5e and f in black, therefore this is the typical application of cepstral pre-whitening on a non stationary signal [4].

In the method proposed in this paper, as shown in Fig. 1b, the CPW is applied directly on the time non stationary signals for which the cepstra does not presents peaks at characteristic frequencies, Fig. 5e and f in blue, and the SES Fig. 5a and b

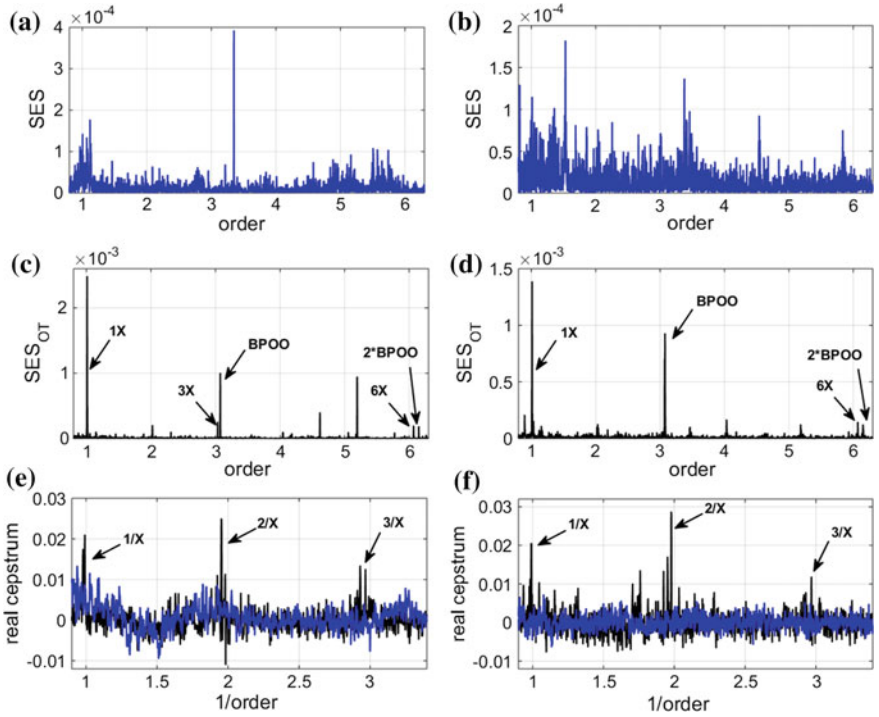

Fig. 5 **a** SES of raw signal for the run-up speed and **b** randomly varying speed. **c**, **d** Corresponding SES after OT. **e**, **f** Real cepstra: in *blue* of the original signals and in *black* of the OT signals

has smeared peaks. The SES resulting from the two methods are shown in Fig. 6 for the run up case and randomly varying speed respectively, top raw is the OT followed by CPW and bottom raw is CPW followed by OT. The vertical scales are defined, for a comparison, according to the SES of Fig. 5c and d. The proposed method performs well when compared to the common procedure: the masking components are more suppressed and the peaks at characteristic fault frequencies have higher relative amplitude for both the analysed speed profiles.

5 Conclusion

The paper shows the effectiveness of cepstrum pre-whitening to enhance the presence of impacts from a faulty bearing when applied directly on acceleration signals from machinery operating at varying speed. The paper also shows that in variable speed situations it is beneficial to apply cepstrum pre-whitening directly to the time non-stationary signals instead of the order-tracked signals, because the resonant frequencies appear to change with speed in the order domain. The method proposed

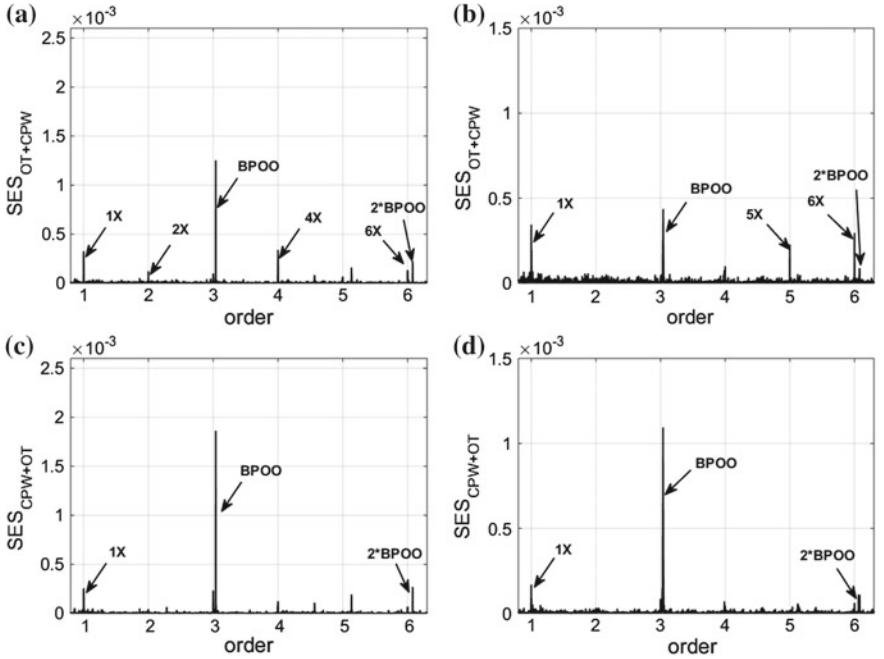

Fig. 6 SES after processing the signals. OT followed by CPW for **a** run up speed, **b** randomly varying speed. CPW followed by OT for **c** run up speed, **d** randomly varying speed

here consists of order tracking the signal only after the operation of whitening the time non-stationary signal, and finally calculating the squared envelope spectrum for diagnostics.

Both numerical simulations and analysis of experimental data have been carried out. The proposed method has been compared with the common procedure of order tracking the signal as a first step and afterwards use the cepstrum pre-whitening in the order domain. The evaluation of the squared envelope spectra obtained by the two methods shows that, as proposed in this paper, the cepstrum pre-whitening performs well on the time non-stationary signal and that it is advisable to apply it before order tracking.

References

1. Randall, R. B., & Sawalhi, N. (2011). A new method for separating discrete components from a signal. *Sound and Vibration*.
2. Randall, R. B., Sawalhi, N., & Coats, M. (2011). A comparison of methods for separation of deterministic and random signals. *The International Journal of Condition Monitoring*, *1*(1), 11–19, June.

3. Sawalhi, N., & Randall, R. B. (2011). Signal pre-whitening for fault detection enhancement and surveillance in rolling element bearings. In *Eighth International Conference on Condition Monitoring and Machinery Failure Prevention Technologies*. Cardiff, UK.
4. Borghesani, P., Pennacchi, P., Randall, R., Sawalhi, N., & Ricci, R. (2013). Application of cepstrum pre-whitening for the diagnosis of bearing faults under variable speed conditions. *Mechanical Systems and Signal Processing*, *36*(2), 370–384.
5. Abboud, D., Eltabach, M., Antoni, J., & Sieg-Zieba, S. (2015). Envelope preprocessing techniques for rolling element bearing diagnosis in variable speed conditions. In *The twelfth International Conference on Condition Monitoring (CM) and Machinery Failure Prevention Technologies (MFPT)*. Oxford, UK: The Oxford Hotel.
6. Borghesani, P., Ricci, R., Chatterton, S., & Pennacchi, P. (2013). A new procedure for using envelope analysis for rolling element bearing diagnostics in variable operating conditions. *Mechanical Systems and Signal Processing*, *38*(1), 23–35, July.
7. Randall, R., Smith, W., & Coats, M. (2014). Bearing diagnostics under widely varying speed conditions. In *Proceedings of the 4th Conference in Condition Monitoring of Machinery in Non-stationary Operations*. Lyon, France, 14–16, December.
8. Oppenheim, A., & Lim, J. (1981). The importance of phase in signals. *Proceedings of the IEEE*, *69*(5), 529–541.
9. Aiger, D., & Talbot, H. (2010). The phase only transform for unsupervised surface defect detection. In *2010 IEEE Conference on Computer Vision and Pattern Recognition (CVPR)* (pp. 295–302). San Francisco, CA.

Using of Entropy Method in Failure Diagnostics

Stanisław Radkowski, Marcin Jasiński, Robert Gumiński and Adam Gałęzia

Abstract Occurring of failure is accompanied by changing of energy distribution of vibroacoustic signal generated by a dynamic system. Hence, comparing the energy distributions of signals observed for technical conditions without failure and for failure states of dynamic model one has access to information about the formation and development of damaging process. The tool to estimate the probability distribution changes corresponding to changes in the distribution of signal energy can be failure oriented measure of information. The paper discusses the problem of proper selection of entropy methods, for detecting and the identification of the failures, both for the signals generated by the actual dynamic systems and simulated one. Particular attention was paid to the possibility of using bispectral entropy and singular entropy change for example signals generated during the formation and propagation of the gear tooth crack. The next interesting resultants of analyzing changes was in the entropy energy of vibration signal recorded during the tests on the back to back test-bed. It was given the observation the chosen harmonic and its modulated bands. During analysis we determined energy change as a function of time in the bands of different widths around the successive harmonics engagement. On the basis of such a limited energy of signal, the technical state of entropy was calculated.

Keywords Entropy method · Bispectrum · Failure diagnostics

S. Radkowski (✉) · M. Jasiński · R. Gumiński · A. Gałęzia
Institute of Vehicles, Warsaw University of Technology,
Narbutta 84, 02-524 Warsaw, Poland
e-mail: ras@simr.pw.edu.pl

M. Jasiński
e-mail: jachuu@simr.pw.edu.pl

R. Gumiński
e-mail: rgumin@simr.pw.edu.pl

A. Gałęzia
e-mail: agalezia@simr.pw.edu.pl

A. Timofiejczuk et al. (eds.), *Advances in Condition Monitoring of Machinery in Non-Stationary Operations*, Applied Condition Monitoring 9,
https://doi.org/10.1007/978-3-319-61927-9_27

1 Introduction

The subject applications vibroacoustics in technical systems, including the question of vibroacoustic diagnostics assemblies and components machines are the contents of numerous publications [4, 6]. Note that the underlying vibroacoustic methods and associated methodology of diagnosis and prediction, the assumption of proportional increase energy in vibration and noise. The presented approach is proposed to detect and analyze diagnostic information about the stages of development of failure taking into account the impact of nonlinear effects and nonstationary phenomena based on the analysis of changes in the energy distribution of the signal analyzing changes in entropy. Because the actual measured signal will contain both the part generated by a diagnosed kinematic pair as components transmitted through the structure to the measuring point, other an additional problem to be solved is the problem of the separation of diagnostically useful signal part.

The problem is to develop an algorithm which takes into account the impact of small low-energy phases of failure to the changes in the amplitude values and the fact that important diagnostic information is transmitted by a modulated phase angle. Hence, the proposed algorithm on the one side give the possibility of a choice of modulated frequency bands on the basis of properly constructed models the establishment of the analytical signal and conducting demodulation amplitude and phase using Hilbert transform. On the other side it gives possibilities of study changes in the distribution of energy in a wide frequency band which take into account a lot of harmonics. Additional studies the impact of nonlinear effects require linkage analysis between the individual harmonics as a function of the development of failure.

Next step issue is the selection of the right model, because formulated diagnostic tasks. The main problem with this approach is the problem of modelling the impact of disturbances on the signal generated by the diagnosed object and then use the results obtained for further analysis diagnostic and prognostic: reference evaluation of the remaining useful life. The simplest solution is to directly incorporate the results into the diagnostic inference. In fact, the results should be regarded as uncertainty information. The concept of uncertainty is related to the degree of compliance information with reality. Despite the existence of other approaches [2] are still fundamental probabilistic methods, using entropy as a measure of uncertainty. At the same time it was taking into consideration the relationship between diagnostic information and changes in the distribution of signal energy. In the paper was used the concept of entropy change, using the energy distribution in vibration signal.

2 Analysis Information of Signal

According to the theory of Shannon [3, 11, 13, 14], entropy is a measure of the uncertainty, while the amount of mutual information contained in the random η of the random process is described by the relation:

$$I(\zeta/\eta) = H(\zeta) - H(\zeta/\eta) \tag{1}$$

where:

$I(\zeta/\eta)$ mutual information;
$H(\zeta)$ the marginal entropies;
$H(\zeta/\eta)$ the conditional entropies;

and determines a reduction in uncertainty from the experiment and measurements. Using the measurement [2] allows to determine the dependence of random size of the input and the output of the line and detect the presence in them of random disturbances. Greater possibilities involve the use of Kullback'a information that can be used to determine changes in the probability distribution as a measure of distance [10]:

$$D(\alpha/\kappa) = H(\alpha/\kappa) + H(\kappa/\alpha) \tag{2}$$

$$H(\alpha/\kappa) = \sum_{i=1}^{n} q_i ln \frac{q_i}{p_i} \tag{3}$$

where:

α $(p_1, p_2, \ldots, p_n), \kappa = (q_1, q_2, \ldots, q_n)$
κ a priori probability distribution,
α a posterior probability distribution

and allows you to assess the impact parameter change the shape parameter on the hazard function of the function failure rate. Equation (3) was the basis for the development of an algorithm to detect damage to the immediate impact on the form of the probability distribution depends on changes in parameters describing the distribution of the test.

In this case, assuming a Waybill's distribution entropy will be described in equation [12]:

$$H(\alpha, \beta) = -ln\alpha + 1 + \frac{\alpha - 1}{\alpha}\gamma + ln\beta \tag{4}$$

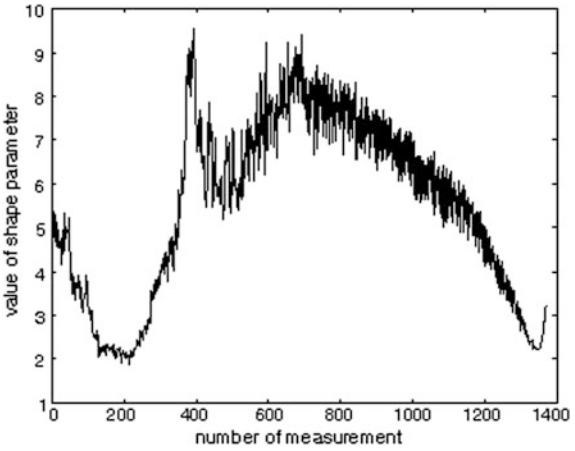

Fig. 1 The parameter of shape in function of measurement number of wheel no

where:

α the shape parameter,
β scale parameter,
γ Euler's constant

Note that changing the scale parameter can be thought of as a disorder independent of changes in the shape parameter, which changes have a major impact on the reliability of the system. Provided this study by the authors regarding the process a tooth crack in the gear confirm the high sensitivity of the analyzing parameter of probability distribute to the process of damaging and clearly show the successive phases of the process (Fig. 1).

3 The Characteristics of Entropy

Bearing in mind that different types of damage and their diverse impact directly affect the value of the entropy of the signal at this angle analyzed NVH signal generated by the kinematic node, which is a couple of gears. One such characteristic is the entropy bispectral specified in bispectrum [8]. Cumulants of the second order ($k = 2$) and third order ($k = 3$) are described by equations:

$$C_{2x}(k) = E\{x^*(n)x(n+k)\} \tag{5}$$

$$C_{3x}(k,l) = E\{x^*(n)x(n+k)x(n+l)\} \tag{6}$$

where E [$x^*(n)$] is expected value from $x^*(n)$, x^* its conjugate.

The k-order spectra are defined as Fourier's transformants of the cumulants. So:

$$S_{2r}(f) = \sum_{k=-\infty}^{\infty} C_{2x}(k) e^{-j2\pi fk} \tag{7}$$

$$S_{3r}(f_1, f_2) = \sum_{k=-\infty}^{\infty} \sum_{l=-\infty}^{\infty} C_{2x}(k) e^{-j2\pi f_1 k} e^{-j2\pi f_2 l} \tag{8}$$

where f is frequency. They are called respectively spectrum of power and bispectrum

Detailed characterization of the measurement are shown in bispectral operation [5]. Referring to the energy distribution of signal on bispectral plane we determine the entropy of the classical Shannon's way:

$$H(\zeta) = \sum_{i=1}^{N} p_{si} ln p_{si} \tag{9}$$

where:

$$p_{si} = \frac{\sum_{si} E(\zeta_i)}{\sum_s E(\zeta_i)}$$

For similar analysis capabilities of the energy distribution throughout the experiment tooth crack, a further measure of entropy to create time-frequency plane using the Hilbert transform (4). First, the whole plane is divided into smaller elements, which calculate energy E_i ($i = 1 \ldots N$). Then we can calculate the normalized energy values for each item:

$$p_i = \frac{E_i}{E} \tag{10}$$

hence:

$$H[E] = -\sum_{i=1}^{N} p_i ln p_i \tag{11}$$

From the point of view of identification of the type of damage, in particular the detection capabilities and its stage of development and location specific possibilities does a signal analysis of information of the plane E-E ¨. At the outset created a matrix whose elements are the energy values for each segment of plane E-E. Note that studying the autonomics system in which the damping function is described by the equation:

$$\ddot{x} + f(x) = 0 \tag{12}$$

Equation (12) we will write in the form of equations:

$$\begin{cases} \dot{x} = y \\ \dot{y} = -f(x) \end{cases} \tag{13}$$

Taking proposed by [1] plane, whose coordinates are expressed using parentheses Lie:

$$\psi(x, y) = -y^2 - xf(x) \tag{14}$$

and Φ (*x*, y) as the derivative of this function ψ (x, y)

$$\Phi(x, y) = xf'(x) - yf(x) \tag{15}$$

Note that in this way coordinate defined function (14) has a dimension of energy: ψ (*x*, *y*) = *E*, and Φ (*x*, *y*) = *e*-dimension derivative energy.

Assuming the opportunity of presentation of signal spectral structure by means of a Fourier series, it suggested examination of the characteristics of an information signal using the Singular entropy [15]. For this purpose the individual segments of the plane *E*-*E* ˙ established observation matrix A [5]. Using the procedure of decomposition Singular (singular value decomposition)

$$\mathrm{A} = \mathrm{USV}' \tag{16}$$

where:

U is a m × m, unitary matrix,
S is a diagonal m × n matrix with non-negative real numbers on the diagonal, and
V′ is a n × n, unitary matrix over plane *E*, V′ is the conjugate transpose of the n × n unitary matrix, V

We obtain diagnostic matrix S of the elements $s_i \ldots s_k$.
Hence:

$$p_i = \frac{s_i}{\sum_{j=1}^{k} s_j} \tag{17}$$

Determines the distribution of power between the specific elements of the matrix singular. A measure of the distribution is singular entropy signal:

$$H_s = \sum_{i=1}^{k} p_i ln p_i \tag{18}$$

Analysis of entropy characteristics of vibroacoustic signal generated when accelerated attempts to the tooth crack is presented later in this work.

4 Results of Laboratory Experiments

The experiment was conducted at the FZG back to back test-bed. The particular description of test best is in [7].

They were subjected to accelerated fatigue test. Figure 2 present the changes of subsequent mesh harmonics of a vibroacoustic signal registered on the toothed gear's casing during the whole experiment.

The changes which accompany the subsequent phases of development of fatigue-related defects are observable in a bispectrum [9]. Next step was to create a new measure which is able to predict the moment of fatigue tooth crack. Integral of bispectral noise from bispectral maximum diagrams and integral of bispectral noise from bispectral residual maximum diagrams (Fig. 3) were calculated with maximum level 0.5E8 (everything higher than maximum level was equalize to this maximum level) for full life time of this wheel. At Fig. 3 we can see that calculated derivative of this diagrams (applying a smoothed curve) we can build effective and sensitive diagnostic parameter of quality changes of fatigue process of toothed wheel damage.

Based the bispectrum entropy model mentioned, bispectrum entropy of the test signal are calculated.

This illustrates the problem of effectiveness of diagnostic observations results in the task of diagnosis of early stages of defect development. Figure 4 present the

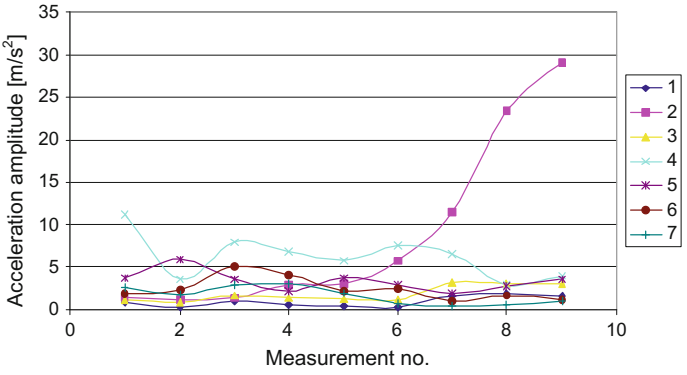

Fig. 2 The changes of subsequent mesh harmonics (no. 1–7)

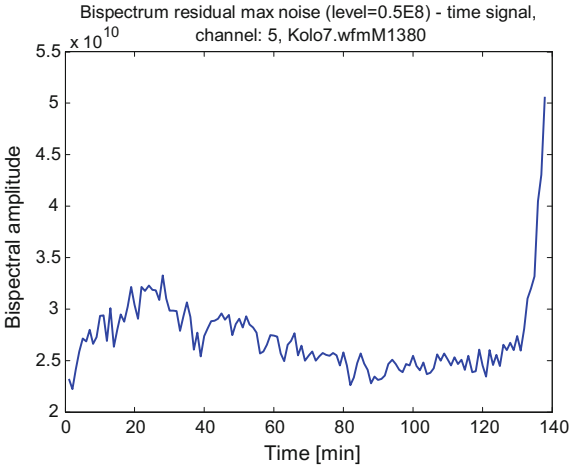

Fig. 3 Integral of bispectral noise from bispectral residual maximum diagrams, full investigation of wheel no. 7

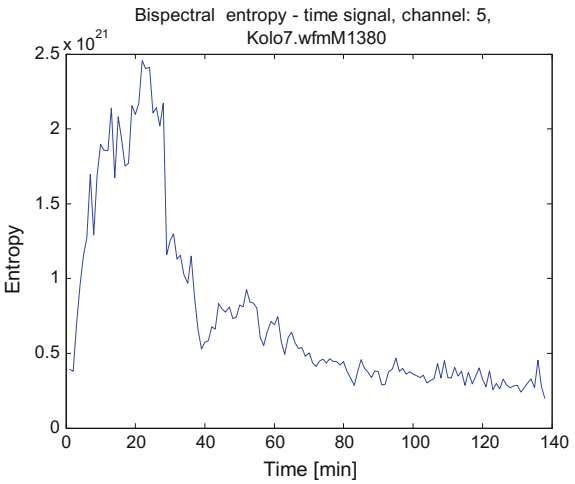

Fig. 4 Bispectrum entropy, full investigation of wheel no. 7

values of bispectral entropy corresponding to these changes. Let us note that this measure, similar to shape parameter of probability distribution depend on defect development while the value of shape factor in particular, does not change monotonously. In order to achieve higher efficiency in application of the results of vibroacoustic diagnosis, we should take seriously into account, the individual vibroacoustic characteristics which were defined during preliminary measurements and analysis.

The next interesting resultants of analyzing changes in the entropy energy of vibration signal recorded during the tests on the back to back test-bed. Give the observation the chosen harmonic and its modulated bands. During analysis we determined energy change as a function of time in the bands of different widths

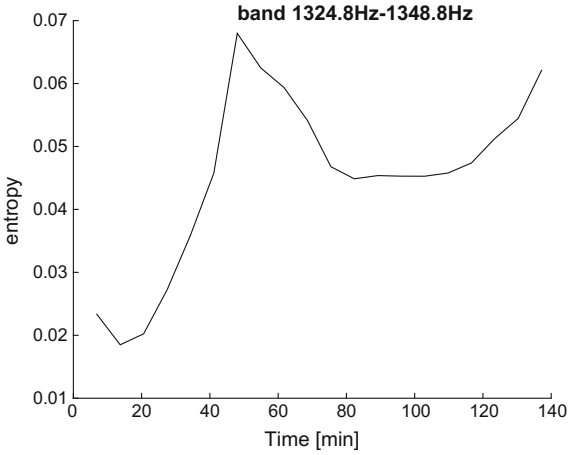

Fig. 5 Shows the change of entropy energy as a function of the duration of the experiment

around the successive harmonics engagement. On the basis of such a limited energy of signal, the technical state of entropy calculated in accordance with Eq. (11). Particular attention was paid to the results obtained on the basis of energy designated in bands around the second harmonic meshing (Fig. 5). In the discovery of determining the entropy assumed that it varies as a function of time along with the change gear, so long the experiment was divided into a plurality (twenty) of equal length intervals and each of these intervals determined entropy.

In addition, energy and entropy then determined in bands of different width symmetrical around the second harmonic. The above waveforms relate to the narrowest bandwidth (+12 Hz). It should be noted that the results in wider bands differ slightly, which is due to the fact that the power of the harmonic engagement considered bands around the second harmonic is dominant.

There next approach is based singular entropy (18) estimated on *E-E* plane (14–15). Analysis of the impact of changes in model parameters on the value of entropy basic parameters: $f_{mesh} = 540$; $f = 10$ Hz; $f_{AM} = 25$ Hz; $f_{FM} = 25$ Hz.

Division of space into a small number of cells is not useful. The most useful seems to be entropy calculated from the formula of division 100/100. For regular borders the space (and consequently the division and cell boundaries) with the increase of the parameter value of the modulation is an increase in entropy (Table 1). However, for the permanent borders of entropy it is sensitive to the distinction between AM and FM modulations but not to distinguish between AM and AMFM (similar range of variation values). In addition, entropy in this case is not sensitive to the occurrence of the disorder. For depending on type of failure space (and consequently the dynamic division borders and cells) with increasing modulation parameter takes no clear change in the entropy (FM AMFM). However, for dynamic boundaries, entropy is allows you to distinguish between AM and FM

Table 1 Expanding borders

Modulation	Parameter variable	Entropy H_s 10/10	Entropy H_s 100/100	Entropy Shannon's
AM	M = 0.1	0.8236	2.6445	0.4227
AM	M = 0.2	0.8046	2.7748	0.3969
AM	M = 0.3	0.7924	2.8644	0.3786
FM	m = 0.5	0.7914	3.3112	0.3064
FM	m = 1	0.7934	3.2892	0.3099
FM	m = 2	0.8004	3.2939	0.3098
AMFM	M = 0.1; m = 0.5	0.8039	2.6714	0.4263
AMFM	M = 0.2; m = 1	0.8132	2.6323	0.4327
AMFM	M = 0.3; m = 2	0.9176	2.7801	0.4092
AMFMz	M = 0.2; m = 1; z = 5%	0.7836	2.2029	0.4957
AMFMz	M = 0.2; m = 1; z = 10%	0.6580	1.9487	0.5444
AMFMz	M = 0.2; m = 1; z = 20%	0.0379	1.5989	0.5943

modulations but no longer distinguish AM from AMFM (similar range of variation values). In addition, entropy in this case allows to detect the occurrence of disturbances (other than the cases of the modulation without disruption).

5 Conclusion

The work shows that it is possible to diagnose the changes of the condition of the objects by means of vibroacoustic techniques with an assumption of significantly small energy dissipation. The presented approach not only correctly explains and defines the phenomena from the qualitative point of view but also enables their quantitative evaluation, while maintaining, for defined conditions, a satisfactory consistence.

A significant practical advantage of an approach such as that presented in this paper is that it allows to start diagnose the changes of the condition of the objects without having to develop detailed deterioration models of objects. One can start managing their facilities with a set of entropy measure bispectral measures, which are not only very sensitive on changes of frequency structure of vibroacoustic signal but also are sensitive on changes of kind of nonlinearity and phase coupling connected with analyzing phenomena. The analyze of bispectral noise changes could be effective and sensitive diagnostic parameter of quality changes of the engines technical state.

References

1. Bogusz, W. (1966). *Stability of nonlinear systems*. Warszawa: RWN (in Polish).
2. Bolc, L., Boradziewicz, W., & Wójcik, M. (1991). *The basis of information processing uncertain and incomplete.* Warszawa: PWN (in Polish).
3. Dejie, Y., Yu, Y., & Junsheng, Ch. (2007). Application of time-frequency entropy method based on Hilbert-Huang transform to gear fault diagnosis. *Measurement* (Elsevier), *40*(2007), 823–830.
4. Dybała, J. (2013). Vibrodiagnostics of gearboxes using NBV-based classifier: A pattern recognition approach. *Mechanical Systems and Signal Processing (in Polish), 38*(1), 5–22.
5. Dybała, J., Mączak, J., & Radkowski, S. (2006). *Using of vibroacoustic signal at risk analysis*. Warszawa-Radom: Wyd. ITE-PIB (in Polish).
6. Gałęzia, A., Gumiński, R., Jasiński, M., & Mączak, J. (2015). Use of energy operators in condition monitoring of gearboxes. In J. Awrejcewicz, M. Kaźmierczak, J. Mrozowski, & P. Olejnik (Eds.), *Dynamical systems mathematical and numerical approaches* (s.177–188). ISBN 978-83-7383-706-6 (in Polish).
7. Gumiński, R. (2010). Doctor's thesis: Using of diagnostics information of analysis of technical risk, OWPW 2010 (in Polish).
8. Huang, J. (2010). Bispectrum entropy feature extraction and its application for fault diagnosis of gearbox.
9. Jasiński, M., & Radkowski, S. (2010). Use of bispectral-based fault detection method in the vibroacoustic diagnosis of the gearbox. *Engineering Asset Lifecycle Management*, *19*, 651–660. doi:10.1007/978-0-85729-320-6_76 (in Polish).
10. Kulback, S. (1959). *Information theory and statistics*. New York: Willey.
11. Mingming, L., Yindong, J., Longlong, Ch., Wei, D., & Xinya, S. (2015). Application of information entropy in fault diagnosis of high speed train wheel set. In *3rd International Conference on Mechatronics and Industrial Informatics (ICMII 2015)*.
12. Radkowski, S. (2002). *Vibroacoustic diagnostics of low-energy failure*. Warszawa-Radom: Wyd. ITE (in Polish).
13. Shunfang, W., & Ping, L. (2015). A new feature extraction method based on the information fusion of entropy Matrix and covariance Matrix and its application in face recognition. *Entropy*, *17*, 4664–4683. doi:10.3390/e17074664.
14. Stratowicz, R. L. (1975). *Information theory radio.* Moscow.
15. Wang, L., & He, Y. (2011). Singular spectrum and singular entropy used in signal processing of NC table. In *Seventh International Symposium on Precision Engineering Measurements and Instrumentation, Proceedings of SPIE* (Vol. 8321 83211H-1).

Use of Bispectral Measures in Machines Faults Diagnostics—Examples

Marcin Jasiński

Abstract It is common knows that the power spectrum based methods cannot detect the phase relationship between different frequency components and additionally suppresses the phase information. It is therefore necessary to explore spectral measures of higher order, like the bispectral measures, to detect various forms of phase coupling between frequency components. In the paper was analyzed the impact of nonlinearity of the sub-section on the behaviour of the whole system by using of bispectral measures: diagonal bispectrum, maximum bispectrum and residual bispectrum. The results pointed to high sensitivity of bispectral measures to changes of the signal's frequency structure and to the possibility of using these relations while constructing models of development of degradation-and-fatigue-related processes. In the paper was build effective and sensitive diagnostic measure of quality changes of fatigue crack growth at low-amplitude fatigue testing, fatigue process of toothed wheel damage or electric motors bearings faults. To do this, It was create a new measure (nobody else didn't that way) which is able to extract the relevant diagnostic information. Integral of bispectral noise from bispectral maximum diagrams and integral of bispectral noise from bispectral residual diagrams were calculated with maximum given level (everything higher than maximum level was equalized to this maximum level) for every measurements.

Keywords Bispectral measures · Technical diagnostics · Residual bispectrum

1 Introduction

Development of mechatronic systems, especially the development of measurements and analysis of dynamic quantities, resulted in a situation in which a constructor is able to account for a product's evolution, caused by wear and tear processes during

M. Jasiński (✉)
Institute of Vehicles, Warsaw University of Technology, Narbutta 84, 02-524 Warsaw, Poland
e-mail: jachuu@simr.pw.edu.pl

A. Timofiejczuk et al. (eds.), *Advances in Condition Monitoring of Machinery in Non-Stationary Operations*, Applied Condition Monitoring 9,
https://doi.org/10.1007/978-3-319-61927-9_28

a product's operations, already during the design phase. Effective use of this knowledge will in many cases decide about the adopted operational strategy [11], the level and the extent of diagnostic resources involved, the method of achieving the desired safety level during each phase of a product's life, especially during the maintenance [12] and repair phases.

The value of diagnostic information can be expressed in the form of a measure which accounts for change of the decision-makers' efficiency. In other words, the ability to provide information of relevant quality resulted in lower uncertainty as regards the right action to be taken and hence it enabled the right decisions to be made.

Let us note that while assessing the utility value of the information provided at a product's design phase, we deal not so much with the volume of information but with the impact it has on change of a decision maker's efficiency in respect of maintenance activity [1–3].

Increasing operational requirements set for de-vices and machines because of safety reasons and due to need for operating cost minimization result in the need for searching for new methods of defect detection in diagnosed objects, e.g. based on the analysis of vibroacoustic signals [1, 4]. The natural feature of vibroacoustic diagnosis is the possibility of easy and fast registration of a big number of heavily redundant vibroacoustic signals and the associated surplus of information. This leads to the necessity of reducing the utilized information down to the level enabling building of an adequate diagnostic model [5].

In next sections it was described how to build new effective and sensitive diagnostic parameters (maximum bispectrum and residual bispectrum) of quality changes of: fatigue crack growth at low-amplitude fatigue testing, fatigue process of toothed wheel damage or electric motors bearings faults.

2 Bispectral Measures

The central issue is how to extract the relevant diagnostic information and use it in the fore-casting process. Let us note that the measured vibroacoustic signal is a real signal which fulfils the requirement of causality. Thus, by using the measured signal $z(t)$ and a defined formalism, we are able, by means of addition of an imaginary part of $v(t)$, to form an analytical signal:

$$a(t) = z(t) + jv(t) \tag{1}$$

In accordance with the theory of analytical functions the real and the imaginary components are functions with two variables x and y.

Let us assume that the analysis of analytical signal is conducted on the basis of observation of the changes of the length of vector A and the phase angle of φ:

$$z(x,y)+jv(x,y)=A(\cos\varphi+j\ \sin\varphi) \tag{2}$$

Thus,

$$z=A\ \cos\varphi,\ \ v=A\ \sin\varphi \tag{3}$$

which means that the measured signal is an orthogonal projection of the vector A on the real axis. Basing on Cauchy-Riemann condition, finally we get:

$$\frac{\mathrm{d}z}{\mathrm{d}\tau}=\frac{\mathrm{d}A}{\mathrm{d}\tau}\cos\varphi-A\ \sin\varphi\frac{\mathrm{d}\varphi}{\mathrm{d}\tau} \tag{4}$$

The obtained relationship, in accordance with our expectations, presents an equation which enables the analysis of the measured signal on the basis of observation of A and φ. What simultaneously captures our attention is the fact that for the low-energy processes, when we can disregard the changes of vector length and assume that $A\cong\mathrm{const}$, the whole information about the changes in the measured signal is contained in the phase angle:

$$\frac{\mathrm{d}z}{\mathrm{d}\tau}=-A\ \sin\varphi\frac{\mathrm{d}\varphi}{\mathrm{d}\tau} \tag{5}$$

It is common knows that the power spectrum based methods cannot detect the phase relationship between different frequency components and additionally suppresses the phase information. It is therefore necessary to explore spectral measures of higher order, like the bispectral measures, to detect various forms of phase coupling between frequency components. Investigating this possibility we try to write, the bispectrum in form [6, 9]:

$$B(f_x,f_y)=E\left[S(f_x)S(f_y)S^*(f_x+f_y)\right]. \tag{6}$$

where

$E[.]$ denotes the expectation operator,
$S(f)$ it's a power spectrum

It is easy to see the bispectrum is complex and that the bispectral values depend on two frequencies f_x and f_y. Writing the Eq. (6) in terms of amplitude and phase quantities one becomes:

$$B(f_x,f_y)=|S(f_x)||S(f_y)||S(f_x+f_y)|e^{j\Theta_\beta(f_x,f_y)} \tag{7}$$

where $\Theta_\beta(f_x,f_y)=\Theta(f_x)+\Theta(f_y)-\Theta(f_x+f_y)$ and is called the biphase.

Using the fast Fourier transform (FFT) algorithm it is possible to calculate the raw bispectrum:

$$B_i(f_x,f_y) = S_i(f_x)S_i(f_y)S_i^*(f_x+f_y) \tag{8}$$

The raw bispectrum can be estimate over the inner triangular region $0 \le f_y \le f_x,\ f_x+f_y=f_\mu/2$. This is sufficient for a complete description of the bispectrum, since, due to symmetry in the $f_x - f_y$ plane of the bispectrum, all of the significant information is contained in the principal domain that consists of the inner and outer triangles [9].

In addition to the basic bispectrum, the bispectrum diagonal slice is defined as:

$$B_s(f,f) = E\left[S(f)S(f)S^*(2f)\right] \tag{9}$$

with $f_x = f_y = f$.

The bispectrum diagonal slice is especially useful in detection of nonlinear effect [5, 6, 9]:

The changes which accompany the subsequent phases of development of fatigue-related defects are observable in a bispectrum [6]. Particularly interesting results have been obtained for a diagonal bispectral measure, for a maximum bispectral measure:

$$B_{max}(f,f) = \max(B_i(f,f)) \tag{10}$$

and for measure created from vector of maximum values of triangular matrix separated from bispectrum matrix by removing main diagonal of this matrix [5]—residual bispectrum:

$$B_{res}(f,f) = B_{\max}(f,f) - B_s(f,f) \tag{11}$$

Values that remain are "residuals".

As a result, the phase reactions defined by the dominant non-linear effect become blurred. The results point to high sensitivity of bispectral measures to changes of the signal's frequency structure and to the possibility of using these relations while constructing models of development of degradation- and-fatigue-related processes which are required while creating the procedures of proactive maintenance strategies.

It was create a new measure (nobody else didn't that way) which is able to extract the relevant diagnostic information. Integral of bispectral noise from bispectral maximum diagrams:

$$BI_{max} = \int B_{max}(f,f)\mathrm{d}f \tag{12}$$

and integral of bispectral noise from bispectral residual diagrams:

$$BI_{res} = \int B_{res}(f,f)\mathrm{d}f \tag{13}$$

were calculated with maximum given level (everything higher than maximum level was equalize to this maximum level) for every measurements.

3 Machine Diagnosis Examples

3.1 The Fatigue Crack Growth at the Low-Amplitude Fatigue Testing

It was developed [5] and built a test bed for low-amplitude tests of fatigue processes. For the preset maximum deformation from 5 to 40 μm range as well as the generated frequency of 10 kHz, we selected a piezoelectric actuator—type PPA80L, that can be powered with 150 V current, which inter works with LA75C amplifier. The typical low-amplitude test beds rely on the frames of machines used for testing the fatigue durability and are usually of big dimensions and weight. The authors proposed a small-dimension test bed for diagnosing the low-amplitude fatigue processes, with dimensions of usually 0.2 × 0.2 × 0.2 m and its weight does not exceed 2 kg, with a titan head mounted directly on the piezoelectric generator. To do away with play, the beam in the head is mounted by means of an eccentric cam. The authors also analysed the resonant frequencies of individual elements of the test-bed so as to avoid resonance of the test-bed when applying the beam's resonance frequency.

After analysing the assumptions of the test-bed that it is a big problem to select a relevant kinematic node which could enable mating of the head with a sleeve in the upper plate of the test-bed and had durability of 10^8–10^9 cycles. The authors designed solution: mating of two very hard surfaces; was proposed covering the two mating surfaces, the head's pin and the sleeve in the test-bed's casing, with a coat of titanium nitrate (it is practically a pioneer solution in Poland and around the world). A recording-control program has been developed in the LabView 7.1 environment which has the task of tracking the resonant frequency of a beam based on the spectral analysis of a vibration signal registered by a use of the non-contact measurement system and the piezoelectric accelerometer. The frequency value estimated in this way is in the next step sent to the generator in order to correct the frequency of the signal stimulating the piezoelectric converter. Thus it is possible to track the changes of frequency (at the resonant curve) of a beam's proper vibration connected with the developing fatigue-related crack. This investigation enables not only detection of surface failures, but also detection of failures appearing in the specimen core. Investigations done up to now in Integrated Laboratory of the Mechatronics System of Vehicles and Construction Machinery in Warsaw

University of Technology [5] confirming possibility of elaborating measurements of fatigue failure development.

Lab tests were intended to verify the impact that various types of notches had on fatigue strength of materials in the case of low-amplitude fatigue tests where the amplitudes were in the range of several hundred micrometers.

The size of the sample (height × width × length) was 10 mm × 5 mm 40 mm. The small notches were added on both sides of the mounting point, for load stress increase.

Bispectrum from channel no. 2 (laser vibration meter), which measured the amplitude at the free end of the beam, was calculated during the measurements. Modulating frequencies appeared at 2×10^6 cycles, just before the sample broke. Thus bispectral analysis can be a useful tool for detecting fatigue-related tracks. A similar effect was observed while building the bispectral measures in the function of change of the loads, including the maximum bispectrum and the diagonal bispectrum. The next step was to calculate bispectral measures (maximum and residual bispectrum) which would be able to foresee the moment of emergence of a fatigue-related crack in a much better way. Integrals for the entire lifecycle of a sample were calculated based on the graphs of the maximum bispectrum and the maximum bispectrum (12) and calculated on the basis of a triangular matrix—the residual bispectrum (13) (Fig. 1), which emerged as a result of cutting out the main diagonal which described the impact of modulation phenomena and non-linear effects. In addition the cut-off level for maximum amplitudes was applied at 0.25E8 m/s^2 (everything which had a higher value than this level was reduced to this level).

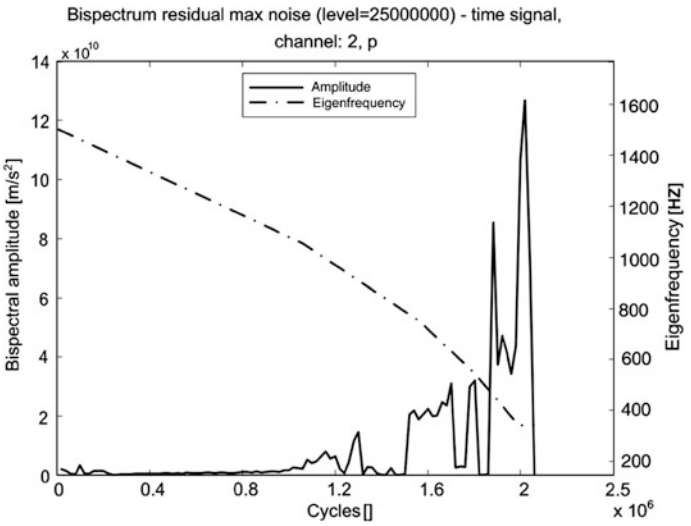

Fig. 1 Integrals from residual bispectrum graphs (level of 0.25E8)—full line and eigen frequency of a beam (*dot-* and *dash-line*)

We can observe an upward trend of the amplitude which accompanies the presumed development of a fatigue-related crack. While by analysing Fig. 1 it could be concluded that the fatigue-related crack most probably started developing from 1.2 million cycles and reached the critical (pre-failure) level at 1.9 million cycles. Thus, based on these findings it is possible to build a very sensitive and reliable diagnostic parameter which describes the development of a fatigue-related crack. Of course, at this point we cannot talk about defining the quantitative relationships, and even more so the statistical ones. The essence of the surveys was to exploit the resonant amplification of the sample's vibration amplitude in the high frequency band and to check whether this type of a test could prove useful while examining the impact of a notch's shape as well as whether vibroacoustic signals could be used for detecting early stages of defects. The above findings call for confirmation during further research aimed at verifying them.

3.2 The Fatigue Process of Toothed Wheel Damage

The experiment was conducted at the FZG back to back test-bed [7, 8]. The test-bed consists of two toothed gears operating in a revolving power setup and it enables examination of both toothed wheels as well as gear lubricants.

The shaft connecting the pinions is divided, which enables rotating one of its sections versus the other and thus introducing relevant meshing forces. Strain gauges are affixed to the shaft and they enable measuring the torque. Wheels with straight teeth are installed in the examined gear, while wheels with helical teeth are installed in the closing gear. Thanks to such a set up it was the examined toothed gear that was subject to defect-development during the experiment. Parameters of the test-bed:

- Maximum tensioning torque 1200 Nm (or 1500 Nm for shafts with bigger torsional rigidity):
- Motor speed: 1460 rpm;
- Gear ratio in both toothed gears: 1.296;
- Module of test specimen wheels and counter-test specimen wheels 4 mm;
- Number of teeth in test specimen wheels: 27;
- Number of teeth in counter-test specimen wheels: 35;
- Axle base for wheels: 125 mm.

Toothed wheels made of 20H2N4A carburized steel, hardened to 60 HRC hardness were used for the research. They were subjected to accelerated fatigue test.

The changes which accompany the subsequent phases of development of fatigue-related defects are observable in a bispectrum. Particularly interesting results have been obtained for a diagonal bispectral measure, for a maximum bispectral measure [6]. We use maximum bispectrum and residual bispectrum to predict the moment of fatigue tooth crack. Integral of bispectral noise from

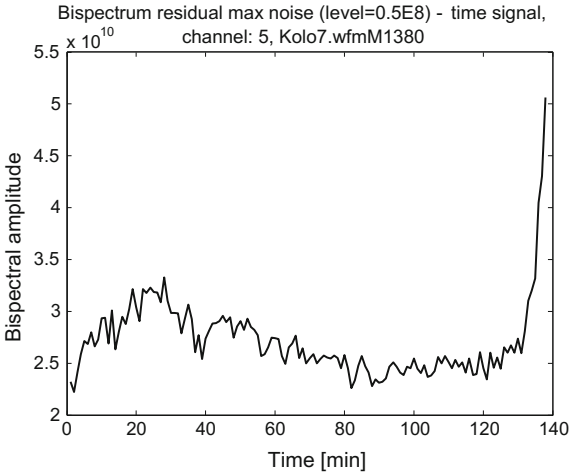

Fig. 2 Integral of bispectral noise from bispectral residual maximum diagrams, full investigation of wheel no. 7

bispectral maximum diagrams (12) and integral of bispectral noise from bispectral residual maximum diagrams (Fig. 2) (13) were calculated with maximum level 0.5E8 (everything higher than maximum level was equalize to this maximum level) for full life time of this wheel. At Fig. 2 we can see that calculated derivative of this diagrams (applying a smoothed curve) we can build effective and sensitive diagnostic parameter of quality changes of fatigue process of toothed wheel damage.

3.3 Electric Motors Bearings Faults

Rolling element bearings are one of the most widely used elements in machines and their failure one of the most frequent reasons for machine breakdown.

It was analysed current supply signal from electric motors with rolling elements bearings model-fault [10]. An interesting effect was observed when compared the engine without the bearings faults and engine with damaged bearings (external and internal race heavily faults) using the maximum bispectrum, diagonal bispectrum and the maximum bispectrum calculated on the basis of a triangular matrix—residual bispectrum, formed by cut-outs of the main diagonal of the bispectral matrix [5], which describes the influence of modulation phenomena and nonlinear effects.

The most promising measure, when it comes to distinguishing rolling element bearings state is residual bispectrum.

The next step was to use bispectral measures (residual bispectrum), which are much better detect bearing failure. It is created by calculating the integral of residual bispectrum charts for different engine loads (13). In addition, the best results were obtained for channel 1, using a cut-off level of the maximum amplitude equal to 30,000—all of which had a value higher than this level was equal to it. The biggest

difference values for undamaged and damaged bearings (about 2 ×) occurs at a load of 1.1 kW.

The next goal was to qualify the state of bearings for the above measure. Re-calculated integrals of the charts residual bispectrum, this time for different engines (different bearing faults or no fault—Table 1), with the same load of 1.1 kW, channel 1, using the cut-off equal to the maximum amplitude of 70,000—all of which had a value of higher than this level was equal to it (Fig. 3).

We are able to distinguish between engines with good bearings (measuring 4 and 8, 6 doubtful) from engines with damaged bearings (1.5 − 2 × higher level), you can even distinguish between the type of bearing fault (inner race, outer), unfortunately only for the engine 15 (measurement # 1 and 3). This is partly the fault of the lack of measurements made on the same engines, bearing a good and bad (different types of faults).

Table 1 Classification of bearing failures

Measurement #	Bearing state	Engine #
1	The outer race severe fault	15
2	The inner race severe fault	13
3	The inner race average fault	15
4	No fault	82,255
5	The inner race weak fault	13
6	No fault (the inner race slightly fault!)	11
7	The internal race average fault—doubtful	12
8	No fault	1
9	The inner race severe fault	309,923
10	The inner and outer race severe faults	14
11	The inner race severe fault	4

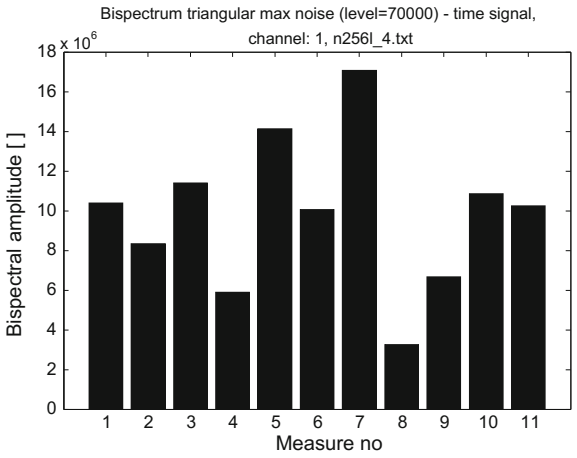

Fig. 3 Integrals of the residual bispectrum, the cut-off level of 70,000, various bearings faults for various engines—Table 1, 1.1 kW load, channel 1

Based on the bispectral analysis, in particular the use of the integral of residual bispectrum, we are able to carry out the initial classification of rolling element bearings: good/bad, set-up the level of classification.

The correct diagnosis types of bearing's faults not only requires further analysis, but mostly perform additional measurements made on the same engines, a good and also bad bearings.

4 Conclusion

The work shows that it is possible to diagnose the changes of the condition of the objects by means of vibroacoustic techniques with an assumption of significantly small energy dissipation. The presented approach not only correctly explains and defines the phenomena from the qualitative point of view but also enables their quantitative evaluation, while maintaining, for defined conditions, a satisfactory consistence.

We can build effective and sensitive diagnostic parameters (bispectral maximum and bispectrum residual) of quality changes of fatigue crack growth at low-amplitude fatigue testing, fatigue process of toothed wheel damage or electric motors bearings faults.

References

1. Eykhoff, P. (1980). *Identification in dynamic systems*. Warsaw: PWN (in polish).
2. Gontarz, S., & Radkowski, S. (2015). Diagnostic model of hysteresis for condition monitoring of large construction structures. In: P. W. Tse, J. Mathew, K. Wong, et al. (Eds.), *Engineering asset management—systems, professional practices and certification. Lecture notes in mechanical engineering* (pp. 611–623).
3. Gontarz, S., Szulim, P., Seńko, J., & Dybała, J. (2015). Use of magnetic monitoring of vehicles for proactive strategy development. *Transportation Research Part C: Emerging Technologies, 52,* 102–115.
4. Han, T., & Yank, B. S. (2006). Development of an e-maintenance system integrating advanced techniques. *Computers in Industry, 53,* 569–580.
5. Jasinski, M., & Radkowski, S. (2011). Use of the higher spectra in the low-amplitude fatigue testing. *Mechanical Systems and Signal Processing, 25*(2),704–716. doi:10.1016/ymssp.2010.06.001.
6. Jasinski, M., & Radkowski, S. (2010). Use of bispectral-based fault detection method in the vibroacoustic diagnosis of the gearbox. *Engineering Asset Lifecycle Management, 19,* 651–660. doi:10.1007/978-0-85729-320-6_76.
7. Maczak, J. (2013). Local meshing plane analysis as a source of information about the gear quality. *Mechanical Systems and Signal Processing, 38,* 154–164. doi:10.1016/j.ymssp.2012.09.012.
8. Maczak, J., & Radkowski, S. (2001). Use of factorial simulation experiment in gearbox vibroacoustic diagnostics. In *Proceedings of the 14th International Congress of Condition Monitoring and Diagnostic Engineering Management, Manchester, UK*.

9. Radkowski, S., & Jasinski, M. (2015). Use of condition monitoring in the proactive maintenance strategy. In P. W. Tse, J. Mathew, K. Wong, et al. (Eds.), *Engineering asset management—Systems, professional practices and certification. Lecture notes in mechanical engineering* (pp. 601–610).
10. Swędrowski, L. (2010). Current measurement and analysis for induction motor diagnostics. *Metrology and Measurement Systems*, (1), 87–94.
11. Szczepaniak, J., Pawlowski, T., Grzechowiak, R., et al. (2015). Experimental tests and computer simulations of a combination tractor/potato planter: the identification and optimization of parameters. *Applied Engineering in Agriculture, 31*(5), 709–716.
12. Szczepaniak, J., Tanas, W., & Kromulski, J. (2014). Vibration energy absorption in the whole-body system of a tractor operator. *Annals of Agricultural and Environmental Medicine, 21*(2), 399–402.

Hybrid Method for Researching Pulsating Flows in Pipes Exemplified with Orifice Application

Tomasz Pałczyński and Wojciech Rydlewicz

Abstract This paper presents a measurement process based on a test rig for investigating pulsating flow in pipes, with the possibility of changing several key parameters: temperature, closed end nozzle diameter, mass flow rate and pulsation frequencies or orifice plate rate. The main flow parameters needed to evaluate temperature, pressure and mass flow were measured at three control sections along the tested pipe. The measurement process was based on the LabView environment. The transient parameters were processed using Matlab scripts supported with a Graphic User Interface to make the proposed procedure more legible. FFT procedures were used to estimate transient flow parameters. The research potential of the presented method is exemplified in a study of the influence of orifice plate dimensions on the dynamic parameters of the tested pipe. The influence of the estimated parameters on amplitude-frequency characteristics is shown using 3D maps. The research process was significantly improved due to the synergy effects of using a hybrid of Labview and Matlab software together.

Keywords Pulsating flows in pipes · Amplitude-frequency characteristics · Matlab simulink · Orifice

1 Introduction

A hybrid method can be broadly defined as the synthesis of a variety of available methodologies into a composite technique, which, taken as a whole, is more useful than any of the individual methods [1, 2]. As reciprocating compressors deliver

T. Pałczyński (✉)
Institute of Turbomachinery, Lodz University of Technology, 219/223 Wólczańska street, 90-924 Łódź, Poland
e-mail: tomasz.palczynski@p.lodz.pl

W. Rydlewicz
Centrum Systemów Softdesk, ul. Beli Bartoka 24/93, 92-547 Łódź, Poland
e-mail: wojciech.rydlewicz@softdesk.pl

A. Timofiejczuk et al. (eds.), *Advances in Condition Monitoring of Machinery in Non-Stationary Operations*, Applied Condition Monitoring 9,
https://doi.org/10.1007/978-3-319-61927-9_29

pulsating flow, for safe and reliable operation it is essential to keep the amplitudes and frequencies of the pressure pulsations within close limits [3–5]. The measurement settings in LabView and math calculations based on matrix calculus in Matlab are well known. The presented methodology uses the best features of each, in an easy to use and intuitive research system for investigating pipes supplied with pulsating flow, especially with orifice application. A second order system model was used for approximation and modelling the elaborated characteristics [6, 7].

1.1 Research Goals

A test rig was prepared to investigate the transitional states in pulsating flows in pipes with orifice application. The application of the orifice at the pipeline caused by decreasing flow resonances is very popular. The location of the orifice enables the influence of the chocking effect to be investigated at the opening of the pipeline. The frequency bandwidth was determined using the available test rig frequency.

In what follows, the results of a series of measurements taken for various frequencies and orifice diameters are presented. The main flow parameters evaluated were pressure, temperature and mass flow, measured at three control sections. The measurement procedure was automated in the LabView environment to ensure rapid and reliable processing. Amplitude frequency and phase frequency characteristics were estimated using Matlab software. A script was authored to process the data acquired from each probe with an automatically repeated loop for the entire results database. A very painstaking and tedious process was thereby automated, accelerating the research process (faster processing of large databases, elimination of random errors caused by human participation, possibility of repeated probes). Hybridization based on software synthesis achieved synergy and improved the overall methodology. LabView measurement settings and math calculations based on matrix calculus in Matlab were used. Estimates were based on second-order inertial elements, and provide quite a good representation of the acquired data. Three-dimensional matrixes were elaborated to provide three dimensional (3D) maps of the estimated characteristics for frequency and the orifice diameter coefficient.

2 Hybrid Measurement Method

The proposed hybrid measurement method is presented schematically in Fig. 1. The National Instrument NI USB-6259 measurement card is designed to operate in the LabView environment and is not supported by Matlab. Therefore, the experimental part of this project was based on LabView software. The second part, focusing on analog data processing, FFT (Fast Fourier Transform) analysis and Fourier series

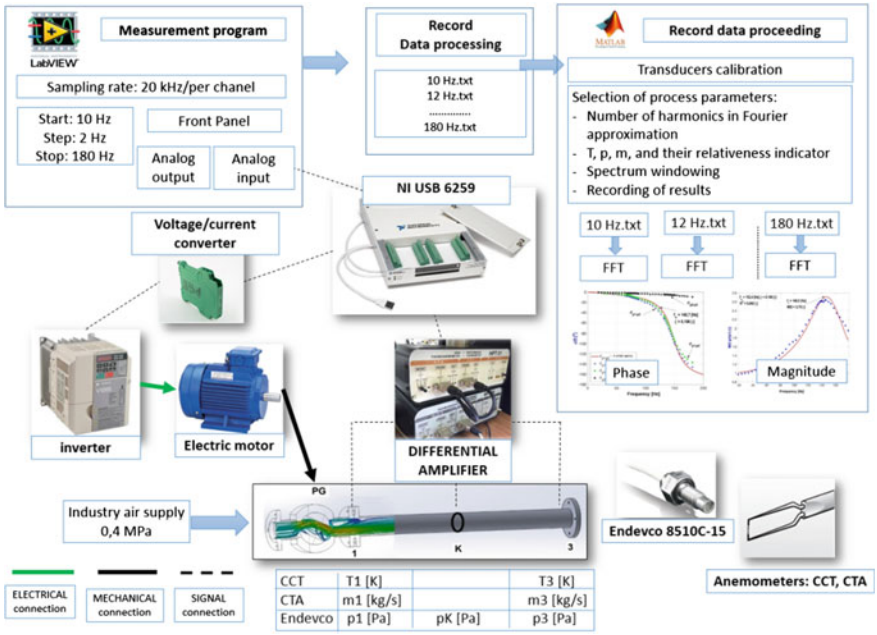

Fig. 1 Structure of the hybrid system for researching pulsating flows

approximation, was conducted in Matlab. This clear division of process requirements demanded hybridization of the measurement process.

Automated testing and recording was performed with LabView 2013 software. Calibration was performed using reference transmitters. Pressure transducers (Endevco 8510C-15 and 8510C-50) were calibrated using the glass tube water level gauge and Vaisala PTB 330 reference barometer. Steady-state characteristics and performance were estimated using this procedure. Constant current thermometers (CCTs) were calibrated using a Type E reference thermoelectric element. Constant temperature anemometers (CTAs)—mass flow rate transducers—were calibrated using an Annubar-type flow meter.

A calibration process was carried out before each measurement series to ensure the required accuracy. The outputs of this process are the parameters of the assumed steady-state characteristics. The same method for curve approximation was used in all the experiments.

The following default parameters were defined: starting frequency 20 Hz, frequency step 2 Hz, final frequency 180 Hz, time delay 500 ms, sampling rate 20 kHz/per channel and number of samples 20,000 (–). Frequency step defines the degree of frequency increase between particular probes. Time delay describes the time needed to stabilize flow parameters and the pulse generator at each new pulsation frequency. Decreasing the frequency enables the time delay to be reduced.

A simplified front panel is assumed, which enables the definition of particular testing parameters. The test program (described above) can then be chosen.

An electric motor was connected with the pulse generator frequency set as an analog output using NI USB-6259. This analog output voltage signal is converted into a standard current signal which is at the same time an input signal for the electric motor inverter.

The real pulse generator frequency is measured using a photoelectric sensor, which is mounted on the electric motor shaft. One peak is generated per revolution. A pulse generator (PG) is used to produce variable reliable and repeatable flow pulsations, as presented in Fig. 2. The pulse generator was designed to have as little friction loss as possible and is driven by an electric motor.

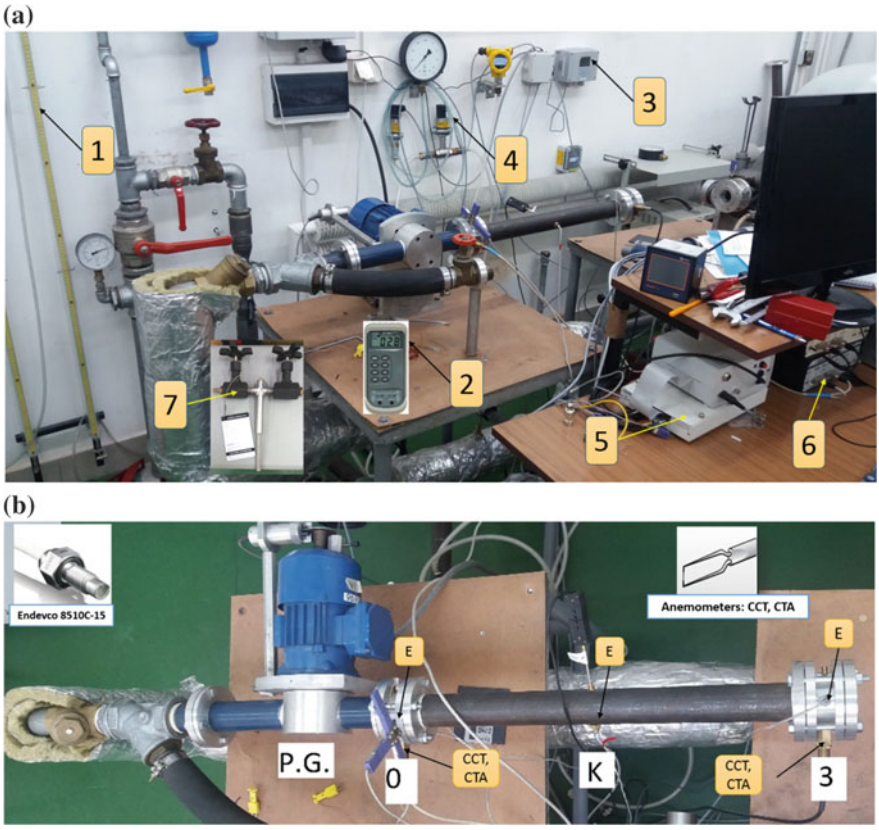

Fig. 2 **a** Main elements of the test rig. *1* water manometer, *2* thermocouple type E, *3* Vaisala PTB 330—reference barometer, *4* reference manometers—annubar mass flow rate, *5* NI USB 6259—measurement card, *6* differential amplifier, *7* Annubar probe—mass flow rate. **b** Main elements of the tested pipe. *P.G.* pulse generator, *O, K, 3* tested cross sections, *E* endevco pressure transducers, *CCT* constant temperature thermometers, *CTA* constant temperature anemometer

The real position of the pulse generator is shown via a photoelectric sensor. It is thereby possible to indicate the phase of the measured waves. This peak signal is a reference point for Fourier series analysis. It enables Fourier windowing (cutting a finite number of whole periods from an estimated wave).

The second part of the method (realized in the Matlab environment) performs the following tasks:

(a) Implementation of steady-state characteristics parameters. These parameters are processed during the calibration process.
(b) Selection of the appropriate data folder to be automatically transformed into appropriate physical values for pressure, temperature and mass flow rate;
(c) Selection of a finite number of particular full waves to be analyzed. This is based on the acquired peak signal from the photoelectric sensor;
(d) Approximation of coefficients identified using the Fourier series function. The following approximation of the Fourier series was assumed:

$$p(t) \text{ or } m(t) \text{ or } T(t) = a_0 + \sum_{k=1}^{\infty} c_k \sin(k2\pi f_1 t + \phi_k) \tag{1}$$

where:

a_0 The constant part of reconstructed variation
a_k, b_k Coefficient of the k harmonics
c_k Amplitude of the k harmonics calculated from a_k and b_k
f_1 Value of the I harmonics pulsation frequency (Hz)
ϕ_k Phase displacement of the k harmonics (rad)

This approximation must be performed for each parameter with several probes (three at cross sections 1 and 3, one at cross section K) and repeated for each frequency. The results are also recorded in the Matlab workspace.

(e) Collection of results in the domain of frequency and the orifice diameter coefficient. The selected parameters must be compared to each other and collected in a separate matrix to enable frequency domain analysis.
(f) Second order oscillating element approximation. Amplitude frequency characteristics were estimated using Eq. 2 following [8]. Phase delay characteristics in the frequency domain were approximated using Eq. 3.

$$M(f) = \left\{ \left[1 - \left(\frac{f}{f_n} \right)^2 \right]^2 + \left[\frac{2\zeta f}{f_n} \right]^2 \right\}^{-1/2} \tag{2}$$

Table 1 Main parameters of orifice influence on pulsating flows in pipes [10]

Orifice β (–)	$M(f)$ (–)	f_r (Hz)	ζ (–)	f_n (Hz)
1 (w/o orifice)	9.02	147.3	0.083	148.4
0.93	8.82	146.4	0.086	147.5
0.81	7.82	145.2	0.109	147.0
0.69	4.82	142.5	0.166	146.6
0.6	2.81	134.2	0.188	147.0

$$\phi = -arctg\left[\frac{\frac{2\zeta f}{f_n}}{1-\left(\frac{f}{f_n}\right)^2}\right] \tag{3}$$

where:

$M(f)$ magnitude of oscillations (–)
f_n natural frequency (Hz)
ζ relative damping coefficient (–)
f input frequency (Hz)
ϕ phase displacement (^{o})

The approximated amplitude frequency characteristics reach the maximum value at resonant frequency, defined as follows:

$$f_r = f_n\sqrt{1-2\zeta^2} \tag{4}$$

where:

f_r Resonance frequency (Hz)

The main parameters of the test rig are as follows [9]:

(a) Range of desired values for pulse generator frequency $f = (20 \div 180)$ Hz.
(b) Pipe diameter $D_p = 42 \times 10^{-3}$ m.
(c) Pipe length $L_p = 0.544$ m, determined with resonance at 70 and 140 Hz.
(d) Nozzle diameter $D_n = 10 * 10^{-3}$ m. The nozzle is mounted on one end of the pipe, at cross section (3).
(e) Desired flow temperature $T = 313.15$ K.
(f) Mean Flow speed $u = 20$ m/s (mean value).
(g) Mean Pressure p = 115,000 Pa.

$$\beta = \frac{D_{orifice}}{D_{pipe}}\ (-) \tag{5}$$

(h) Orifices: β = 0.93; 0.81; 0.69; 0.6. The tested orifices were defined dimensionless as the quotient of orifice $D_{orifice}$ and pipe D_{pipe} diameter (m) coefficient defined below, Eq. 5:

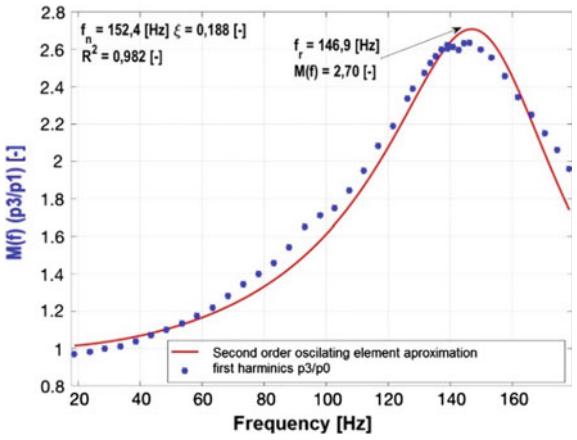

Fig. 3 Amplitude frequency characteristics—orifice $\beta = 0.60$

3 Experimental Results

An experiment was constructed based on the assumptions defined above to investigate the influence of orifice diameter on the dynamics of pulsating flows in pipes. The main parameters estimated following the proposed hybrid procedure are summarized in Table 1.

The conclusions from the experiment are as follows:

(a) The proposed method significantly improves the research process. The human factor was eliminated to the minimum necessary. The length of the experiment was reduced tenfold—from 60 to 6 min;
(b) The hybridization of existing research methods was justified, especially by the development of specialized scientific software.
(c) The orifice coefficient was clearly shown to have a significant influence on the dynamics of the tested pipe, especially for values lower than $\beta = 0.7$. Values of $\beta = 0.9$ and above do not influence the dynamics of the tested pipe;
(d) Decreasing resonant frequency is observed as the relative damping coefficient increases;
(e) The example characteristics presented in Fig. 3 (amplitude frequency characteristics) and Fig. 4 (phase-frequency characteristics) confirm the assumed form of the dynamics (as a second order oscillating element). Quite high coefficients of determination, no less than 0.98, were obtained.
(f) The phase delay reaches 90° at resonant frequencies.
(g) Example three-dimensional pressure amplitude characteristics were elaborated in the domain of frequency and the orifice coefficient. This 3D map (presented in Fig. 5) greatly facilitates analysis of pulsating flows in pipes.

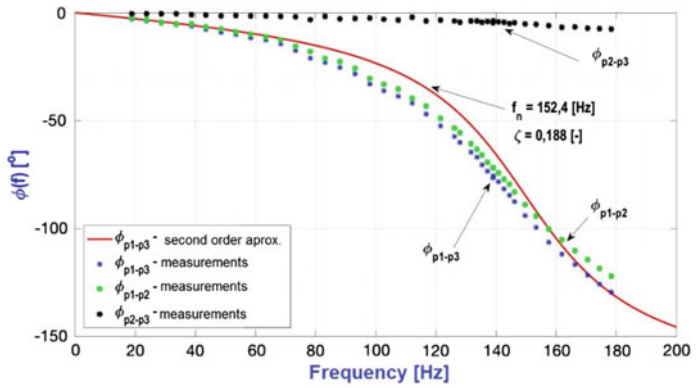

Fig. 4 Phase frequency characteristics—orifice $\beta = 0.60$

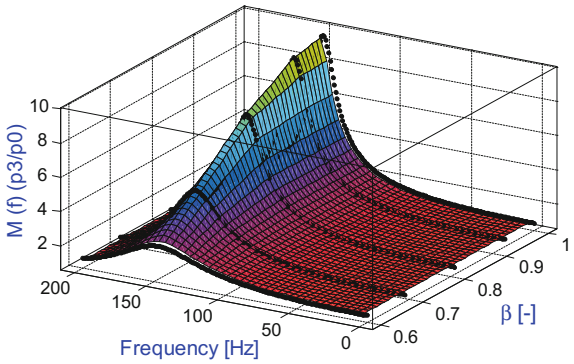

Fig. 5 3D Pressure magnitude in the frequency and orifice coefficient domain

4 Conclusion

In this paper, a hybrid method of researching pulsating flows in pipes was presented and its validity confirmed. The proposed method has two main advantages: decreasing the human factor in the experimental process, and significantly reducing the time required for the research process. The exemplified test case can thereby be processed almost just in time. This enables new uses of the presented test rig for training and teaching purposes.

The relatively complex influence of orifice diameter on pipes supplied with pulsating flow was analyzed as follows:

(a) The orifice was mounted at the inlet of a pipe supplied with pulsating flow. The orifice diameter, especially below $\beta = 0.7$, changed the properties of the pipe dynamics significantly. This type of orifice can be used to decrease the amplitude of pulsation.

(b) The second order oscillating element transfer function is suitable for modeling the examined case. The resonant frequency and damping coefficient include the influence of orifice diameter on pulsating flow.

In previous work, the author has elaborated a 1D model for researching pulsating flows in pipes using Matlab/Simulink software based on the method of characteristics [11, 12]. This software enables analysis and estimation of transient states between defined cross-sections. The experimental results presented in the current study will be subsequently investigated according to this method for instantaneous approximation of cross section parameters. In the opinion of the author, this combination of technologies provides a quite nuanced research tool for investigating pipes supplied with pulsating flow.

Acknowledgements The author gratefully acknowledges the helpful comments and suggestions of the reviewers, which have improved the manuscript.

References

1. Turner, J. L., et al. (1988). Hybrid methods in experimental mechanics. In *Computational Mechanics' 88* (pp. 1391–1394). Berlin, Heidelberg; Springer.
2. Abe, T., et al. (1997). Hybrid control of response of pressure pulsation of gas in piping excited by compressor. *Transactions of the Japan Society of Mechanical Engineers, Part C, 63*(607), 929–936.
3. Vetter, G., & Seidl, B. (1993). Pressure pulsation dampening methods for reciprocating pumps. In *Proceedings of the 10th International Pump Users Symposium, Houston, Texas* (Vol. 19).
4. Metwally, M. (2009). Review of compressible pulsating flow effects on system performance. In: *13th International Conference on Aerospace Sciences & Aviation Technology, ASAT-13, 26–28 May 2009*.
5. Kozanecka, D., Kozanecki, Z., & Łagodziński, J. (2011). Active magnetic damper in a power transmission system. *Communications in Nonlinear Science and Numerical Simulation, 16* (5), 2273–2278.
6. Samuelson, R. D. (1969). A second order system model for pneumatic instrumentation lines. *IEEE Transactions on Nuclear Science*, *16*(1), 271–276.
7. Olczyk, A. (2009). Investigation of the specific mass flow rate distribution in pipes supplied with a pulsating flow. *International Journal of Heat and Fluid Flow, 30*(4), 637–646.
8. Olczyk, A. (2006). Measurements of unsteady flow parameters in pipe-receiver and pipe-turbocharger systems. *Metrology and Measurement Systems, 13*(1), 67–78.
9. Olczyk, A. (2009). Identification of dynamic phenomena in pipes supplied with a pulsating flow of gas. *Proceedings of the Institution of Mechanical Engineers, Part C: Journal of Mechanical Engineering Science, 223*(8), 1851–1867.
10. Rydlewicz, W. (2016). Experimental analysis of influence of chosen pipeline parameters in transient phenomena in fluid flow. Master thesis, Ph.D. T. Pałczyński—promoter.
11. Pałczyński, T. (2012). A boundary conditions at modeling 1-D pulsating flows in pipes according to the method of characteristics. *Journal of KONES, 19*, 395–402.
12. Pałczyński, T. (2016). A hybrid method of estimating pulsating flow parameters in the space-time domain. *Mechanical Systems and Signal Processing*. http://dx.doi.org/10.1016/j.ymssp.2016.09.021.

Dynamic Behavior of Spur Gearbox with an Elastic Coupling Under Acyclism Regime

Atef Hmida, Ahmed Hammami, Mohamed Taoufik Khabou, Fakher Chaari and Mohamed Haddar

Abstract For many researchers and industrials the dynamic behavior of gearbox remains a paramount concern. In fact the diagnosis as well as the improvement of efficiency of gearbox is an ultimate goal for users such as machine builders, aeronautic and automotive manufacturers or energy producers. We should remind that the dynamic behavior of a gearbox depends on its design parameters and is also influenced by the engine operating conditions as well as the type of driving unit. A single stage spur gearbox is considered in this paper to investigate its dynamic behavior under acyclism regime. In fact the studied spur gear is powered by a four strokes four cylinders diesel engine using an elastic coupling modeled by Nelson and Crandell approach [7]. A numerical model is proposed taking into account the excitations induced by the motor torque fluctuation as well as the load variation and the fluctuation of meshing stiffness cased by acyclism regime. The implicit Newmark algorithm is used to investigate dynamic response of the studied system and the obtained results show the significant influence of both acyclism effect and elastic coupling on it.

Keywords Acyclism · Dynamic behavior · Elastic coupling · Spur gearbox

A. Hmida (✉) · A. Hammami · M.T. Khabou · F. Chaari · M. Haddar
Laboratory of Mechanics, Modeling and Production (LA2MP),
National School of Engineers of Sfax, BP1173, 3038 Sfax, Tunisia
e-mail: abdallahatef@yahoo.fr

A. Hammami
e-mail: ahmed.hammami2109@gmail.com

M.T. Khabou
e-mail: mtkhabou@hotmail.com

F. Chaari
e-mail: fakher.chaari@gmail.com

M. Haddar
e-mail: mohamed.haddar@enis.rnu.tn

A. Timofiejczuk et al. (eds.), *Advances in Condition Monitoring of Machinery in Non-Stationary Operations*, Applied Condition Monitoring 9,
https://doi.org/10.1007/978-3-319-61927-9_30

1 Introduction

The acyclism is a transient regime that can be observed for combustion engines. It is characterized by the fluctuation of the torque which is a significant external source of excitation on mechanical transmissions such as gearboxes espicially. Actually the effect of acyclism regime on gears dynamic behavior is investigated by few authors such as Barthod et al. [1] who studied the effect of acyclism on the rattle threshold inside different gearbox configurations: unloaded gear with different inertia and backlash. Rattle phenomenon is at the origin of impulses that occurs on gears which does not transmit any power. The input speed is a sinusoidal function in the initial inertia. When the inertia decreased, the input speed will be composed of several harmonics with relative amplitudes and phases. The same authors [2] proved that threshold kinetic energy and threshold are linked together and behave in the same way.

The effect of meshing stiffness and engine speed fluctuations on a tortional gear model is investigated by Sika and Velex [8] who considered the engine speed fluctuations as a sinusoidal and multi-harmonic function and they introduced modulations in the meshing stiffness function. The authors observed the existance of unstable areas which expand due to the mesh stiffness variation increase. Mono-harmonic engine speed fluctuations generate additional secondary instabilities side-bands located around the main area. For the multi-harmonic speed fluctuations, more instability side-bands are obtained

A spur gear transmission coupled to a diesel engine is investigated by Khabou et al. [4] who considered the engine applied torque as a multi-harmonic function with a period of acyclism. The period of transmission error and its fluctuation is proportional to the loading conditions.

Elastic coupling is used to join rotating parts and it is able to reduce transmitted vibration induced by acyclism phenomenon between them providing that the dynamic characterization of the coupling is well determined. Tadeo and Cavalca [9] studied the effects of flexible coupling on the dynamic behavior of rotating mechanical system, especially on the natural frequencies. They used a system composed of two flexible shafts supported by four hydrodynamic bearings connected through a flexible coupling and divided into beam elements of continuous mass and constant cross section. They introduced the flexible coupling using five different models. The first model of coupling was introduced as a rigid disk; the second model was developed according to the first approach of Kramer [5] where the coupling is modeled by two nodes with mass and inertia effects in each node. The second approach of Kramer [5] which included the rotational stiffness and damping was adopted in the third case. The first model of Nelson and Crandall [7] is adopted and the inertia of the coupling as well as the translational and rotational stiffness are considered for the fourth case. The translational and rotational dampings of the flexible coupling are added to the second model of Nelson and Crandall [7] and is adopted in the fifth case.

Tadeo et al. [10] compared the numerical results of the last four cases presented previously to an experimental investigation and found that the second model of Nelson and Crandall is the best one to describe the dynamics of an elastic coupling. They found also that the second model of Kramer including the rotational stiffness and damping is the best in controlling the dynamic response for the experimental setup.

In this paper the effect of acyclism on the dynamic behavior of a mechanical system is investigated. The studied system is composed by one stage spur gearbox and an elastic coupling powered by four strokes four cylinders diesel engine. The elastic coupling is mounted between the driving motor and the gearbox in order to reduce the transmitted vibrations. Nelson and Crandall approach [7] is adopted to model this coupling. Excitations due to the motor torque, load variation, the input engine speed fluctuations and the fluctuation of meshing stiffness due to this regime are introduced to the numerical model.

2 Dynamic Model

The studied system is composed of a motor driving a load through a spur gearbox. An elastic coupling is introduced between the motor and the pinion. Each transmission shaft is supported by a bearing.

The corresponding lumped parameter model of a faultless system is shown in Fig. 1 and can be divided into three blocks.

The first block includes the motor and the first part of the elastic coupling. They are connected through a transmission shaft (1). The second block is composed by the second part of the coupling and the pinion gear (21) connected through the shaft (2). The third block is composed by the wheel (22) and the loading machine (32) connected to each other by a transmission shaft (3).

Pinion and wheel are assumed as rigid bodies. Shafts are assumed to be massless and have torsional stiffness $K_{\theta i}$ with torsional damping $C_{\theta i}$ (i = 1, 2, 3). They are supported by bearings which are modeled with parallel springs (K_{xi}, K_{yi}) and damping (C_{xi}, C_{yi}).

The second model proposed by Nelson and Crandall is adopted for the elastic coupling with a translation stiffness (K_{xc}, K_{yc}), torsional stiffness ($K_{\theta c}$), translation damping (C_{xc}, C_{yc}) and torsional damping ($C_{\theta c}$). Inertial effects are included in the model as two rigid disks in the first block (I_{12}) and the second block (I_{21}).

The equation of motion is obtained using Lagrange formalism:

$$M\ddot{q} + (C_m + C_s)\dot{q} + (K(t)) + K_s)q = F(t) \tag{1}$$

q is the degree of freedom vector and it is expressed as following

$$\mathrm{q} = (\theta_{11}, \theta_{12}, \theta_{21}, \theta_{22}, \theta_{31}, \theta_{32}, \mathrm{x}_1, \mathrm{y}_1, \mathrm{x}_2, \mathrm{y}_2, \mathrm{x}_3, \mathrm{y}_3) \tag{2}$$

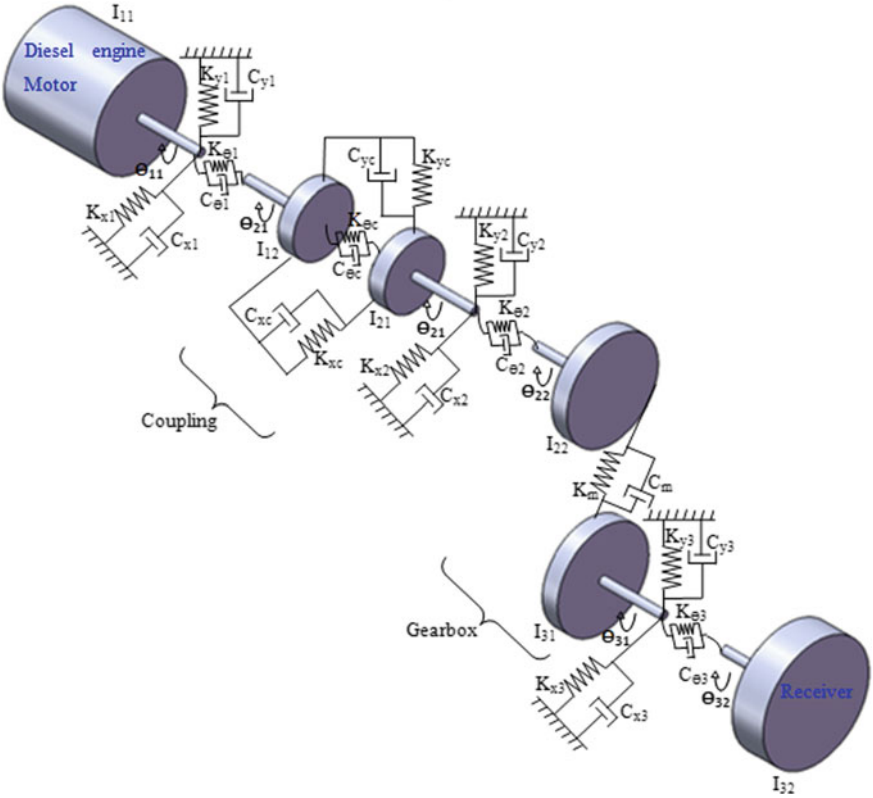

Fig. 1 Dynamic model of spur gearbox with an elastic coupling

[M] is the global mass matrix. [Ks] and [K(t)] are respectively the structural stiffness matrix of the system and the time varying mesh stiffness matrix. [Cs] and [Cm] are respectively the structural damping matrix and the mesh damping matrix. These entire matrixes are defined by Hmida et al. [3].

3 Numerical Results

The lumped-parameter values of the dynamic model are shown in Table 1.

The engine generates a variable load and speed during the power stroke.

The rotational speed of the engine $\Omega(t)$ is written by Sika and Velex [8] as

$$\Omega(t) = \Omega_{10}(1 + \sum_n \rho_n(\Omega_{10}) \sin(n\Omega_{10}t + \varphi_n)) \quad (3)$$

Table 1 Values of the model parameters

Gear box parameters	
Teeth number	$Z_{12} = 20$; $Z_{21} = 30$
Mass (kg)	$m_{12} = 1.77$; $m_{21} = 2.5$
Pressure angle	$\alpha = 20°$
Teeth module (m)	$m_n = 2 \times 10^{-3}$
Contact ratio	$\varepsilon_\alpha = 1.6$
Average mesh stiffness (N/m)	$K_{moy} = 2.11 \times 10^8$
Coupling characteristics	
Inertia (kg m^2)	4×10^{-3}
Mass (kg)	4.5
Torsional stiffness (Nm/rad)	352
Translation stiffness (N/m)	462×10^2
Engine characteristics	
Inertia (kg m^2)	4×10^{-3}
Maximum pressure inside cylinders P_{max} (Bar)	49
Average of engine torque $\overline{C_m}$ (N m)	17.5
Cylinders capacity V_{cyl} (cm^3)	2000
Receiver characteristics	
Inertia (kg m^2)	6×10^{-3}
Shafts and bearings characteristics	
Torsional shaft stiffness (Nm/rad)	5×10^5
Bearing stiffness (N/m)	5×10^8

where Ω_{10} is the average velocity, n is the harmonic of the generated speed function, ρ_n and φ_n are respectively the corresponding amplitude and phase. According to the last equation limited on the 2nd harmonic, the evolution of the rotational speed generated by the combustion engine motor is shown in Fig. 2.

The evolution of the rotational speed of the Diesel engine is quasi sinusoidal. This shape generates a periodic fluctuation of the gear meshing function as shown in Fig. 3.

Combustion engine develops torque C_m which can be written according to Ligier and Baron [6] as

$$C_m \approx \overline{C_m} + \frac{P_{max}}{192} V_{cyl}(0.46 \sin 2\alpha_c + 0.24 \sin 4\alpha_c + 0.03 \sin 6\alpha_c)$$

where α_c is the angular position of the crankshaft, P_{max} is the maximum pressure inside cylinders $\overline{C_m}$, is the average of engine torque and V_{cyl} is the cylinders capacity. Hence the applied torque is also periodic as shown in Fig. 4.

After taking into account the previous parameters, numerical results are computed using Newmark algorithm.

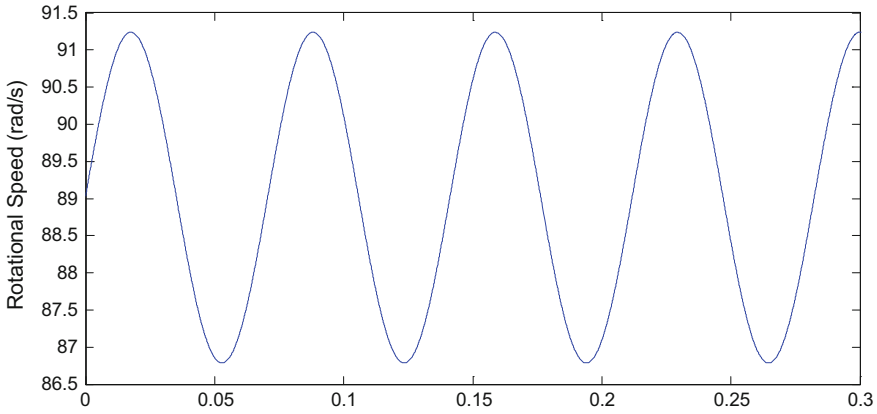

Fig. 2 Time evolution of the engine rotational speed

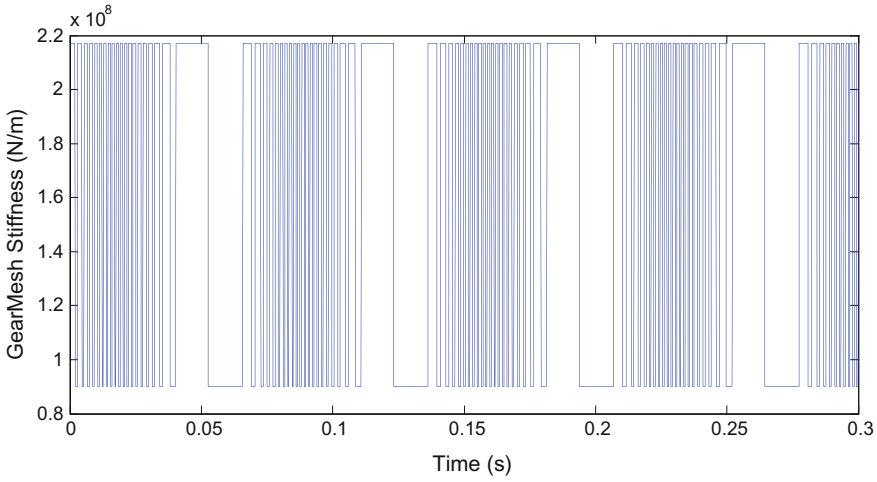

Fig. 3 Time evolution of the gear mesh stiffness

Time displacement signal of the second bloc in the X direction is shown in Fig. 5. The displacement is periodic with acyclism period. Fluctuations are also observed, they correspond to the influence of the meshing phenomena on the dynamic response.

The amplitude of displacement is reduced in the bearing of this bloc compared to the amplitude of displacement obtained by Khabou et al. [4]. In fact, the amplitude without elastic coupling was 5×10^{-5} m and it is reduced to 1.5×10^{-5} m using the elastic coupling. It is then obvious that the vibration produced by the diesel engine can be damped thanks to the vibration reduction capabilities of the elastic coupling.

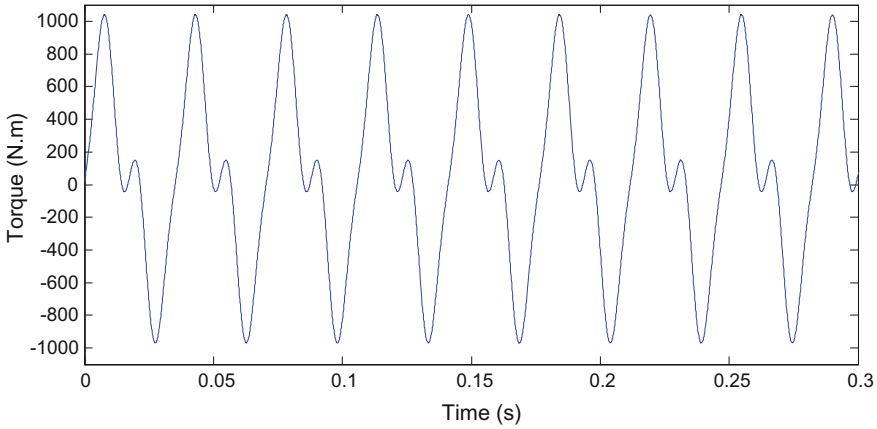

Fig. 4 Time evolution of the engine torque

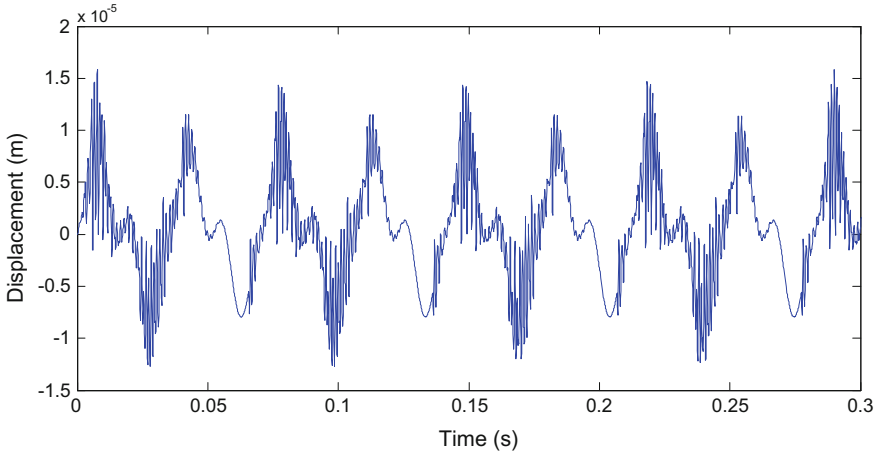

Fig. 5 Time displacement signal of the second bloc in the X direction

Time–frequency map is used to analyze the cyclo-stationary behavior of the signal and Fig. 5 represents the Wigner–Ville distribution of the acceleration of the second bloc.

In fact, the meshing frequency and its harmonics which excites the system are variable in time. Inclined lines confirm the variation of the meshing frequency and its harmonics and higher amplitudes corresponds to high applied torque conditions. This will result in simultaneous amplitude and frequency modulations as shown in Fig. 6.

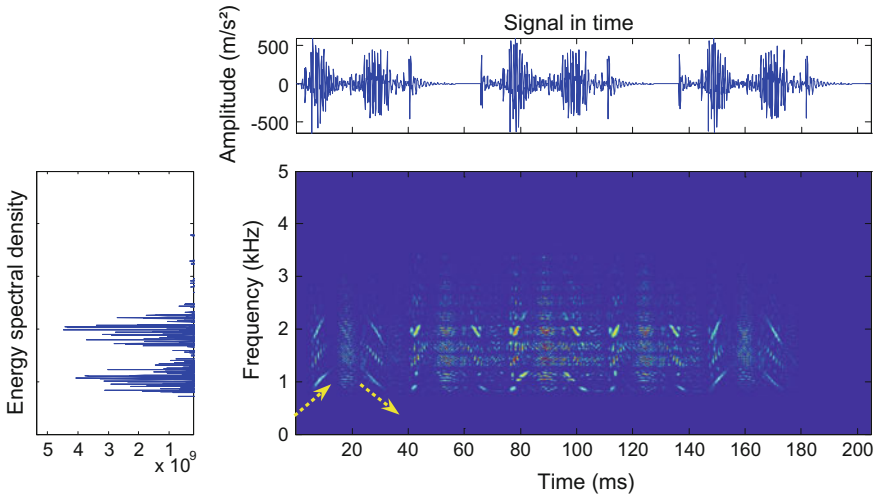

Fig. 6 Wigner–Ville distribution of the acceleration of the second bloc

4 Conclusion

In this paper, the dynamic behavior of one stage spur gearbox connected to a four stroke four cylinders engine by an elastic coupling is studied in cyclo-stationary regime which is acyclism. The dynamic model is based on lumped parameter model in order to study the effect of a modulated engine speed on the dynamic behavior of this gearbox. The variations of the diesel engine speed and the torque generated by combustion engine are modeled and included in simulations. In addition, the gear mesh stiffness was modeled as square function with varying period to take into account the speed variation.

This regime affects the dynamic behavior of the gearbox as the applied torque and rotational speed varies periodically. Time–frequency map was used to analyze its behavior.

It was highlighted the effects of coupling in reducing the transmitted vibration between the engine and mechanical transmissions.

Future investigation will be focused mainly on the dynamic behavior of the studied system with defects under acyclism regime.

References

1. Barthod, M., Hayne, B., Tebec, J.-L., & Pin, J.-C. (2007). Experimental study of dynamic and noise produced by a gearing excited by a multi-harmonic excitation. *Applied Acoustics, 68,* 982–1002.
2. Barthod, M., Hayne, B., Tebec, J.-L., & Pin, J.-C. (2007). Experimental study of gear rattle excited by a multi-harmonic excitation. *Applied Acoustics, 68,* 1003–1025.

3. Hmida, A., Hammami, A., Khabou, M. T., Chaari, F., & Haddar, M. (2016). Modal analysis of spur gearbox with an elastic coupling. In *International Conference of Acoustics and Vibrations, Hammemet, Tunisia.*
4. Khabou, M. T., Bouchaala, N., Chaari, F., Fakhfakh, T., & Haddar, M. (2011). Study of a spur gear dynamic behavior in transient regime. *Mechanical Systems and Signal Processing, 25,* 3089–3101.
5. Kramer, E. (1993). *Dynamics of rotors and foundations*. New York: Springer.
6. Ligier, J. L., & Baron, E. (2002). Acyclisme et vibrations. In: *Applications Aux Moteurs Thermiques et Aux Transmissions* (vol. 1, Editions TECHNIP). Paris.
7. Nelson, H. D., & Crandall, S. H. (1992). Analytic prediction of rotordynamic response. In F.E. Ehrich (Ed.), *Handbook of rotordynamics.* New York: McGraw-Hill Inc.
8. Sika, G., & Velex, Ph. (2008). Instability analysis in oscillators with velocity-modulated time-varying stiffness—Applications to gears submitted to engine speed fluctuations. *Journal of Sound and Vibration, 318,* 166–175.
9. Tadeo, A. T., & Cavalca, K. L. (2003). A comparison of flexible coupling models for updating in rotating machinery response. *Journal of the Brazilian Society of Mechanical Sciences and Engineering, XXV*(3), 235–246.
10. Tadeo, A. T., Cavalca, K. L., & Brennan, M. J. (2011). Dynamic characterization of a mechanical coupling for a rotating shaft. *Proceedings of the Institution of Mechanical Engineers, Part C: Journal of Mechanical Engineering Science, 225,* 604–616.

Possibilities of Faults Detection of Rolling Bearings Using Energetic Descriptors of Vibrations Signals

Adam Gałęzia, Roman Barczewski and Bartosz Jakubek

Abstract The need for fast and reliable evaluation of technical state of rotating machines forces constant development and research for condition monitoring techniques. The paper presents energetic characteristics of vibration signals as a promising new approach in condition monitoring of rolling bearings. The presented approach is based on application of the differential Teager-Kaiser energy operator. The operator makes possible to the detection of short-time disturbances in the signal which are caused by developing faults. Authors assumed that the energetic characteristics and measures would be good tool for detection of faults and defects in rolling bearings, especially when vibration signals are non-stationary in the amplitude and/or the frequency sense. The paper presents the energetic characteristics of the bearing vibration signal in the form of the time history, the energetic trajectories and measures parameterizing them. The obtained results give ability to determine the basic features of characteristics and measures,. The presentation of qualitative changes in the form of characteristics caused by different kinds of faults of rolling bearings was one of the main aims of the research. From practical point of view the assessment of the sensitivity of the above-mentioned energetic measures on changes in technical condition of bearings was also crucial. The presented results have been obtained by testing the set of tapered roller bearings of the same type and size. New bearings, defective ones and bearings with artificially introduced faults were tested.

Keywords Rolling bearings · Condition monitoring · Teager-Kaiser operator

A. Gałęzia
Warsaw University of Technology, Narbutta St. 84, 02-524 Warsaw, Poland
e-mail: agalezia@simr.pw.edu.pl

R. Barczewski · B. Jakubek (✉)
Poznan University of Technology, Jana Pawla II St. 24, 60-965 Poznan, Poland
e-mail: bartosz.jakubek@put.poznan.pl

R. Barczewski
e-mail: laboratoria@tlen.pl

A. Timofiejczuk et al. (eds.), *Advances in Condition Monitoring of Machinery in Non-Stationary Operations*, Applied Condition Monitoring 9,
https://doi.org/10.1007/978-3-319-61927-9_31

1 Introduction

The rolling bearings are common components of many machines. Their failure can cause machine breakdown, resulting in high economic and environmental costs. Vibration signals generated by bearings have been widely studied over the past years. Despite that, new condition monitoring techniques are still developed in order to increase trustworthiness of diagnostic and prognostic inference.

There are many publications discussing various techniques of condition monitoring of the rolling bearings. In general there can be distinguished two most common groups of techniques, i.e. techniques based on the time-domain approach and those based on the frequency-domain approach.

The most basic condition monitoring tool, advised by many standards, utilizes the wideband root-mean-square value of vibrations [1]. However, due to low sensitivity of this tool, often other parameters are used, such as kurtosis, crest factor [2] or XSK [3]. The fore mentioned parameters are usually calculated from the raw vibration signal or its envelope [4]. Evaluation of technical condition is often based on diagnostic matrixes taking into account a number of parameters [5]. The simplest frequency-domain technique methods uses detection of the so-called characteristic fault frequencies. Their appearance in the signal spectrum is a symptom of advanced development of a fault. In bearing condition monitoring it is important to be able to determine whether changes in the diagnostic signal were caused by the evolution of a fault or by the change of a propagation path. This can be emphasised by the use of cepstrum. The cepstrum [6] allows us to detect separated harmonics of the characteristic fault frequencies of a rolling bearing over a wide range of other frequencies. Attempts to use bispectral analysis in fault detection have also been reported [5, 7].

Precise estimation of technical condition requires using a method that allows early detection and identification of signal components associated with an emerging fault. To increase the low sensitivity of energetic symptoms different approaches are used. To extract diagnostically useful information researchers use the following methods empirical mode decomposition [8], wavelet analysis and neural networks [9]. The shock pulse method (SPM) has been widely used in industry since the 1970s and is successful in the determination of rolling bearings condition [10–12] This method uses band filtration of the vibration signal recorded in the acceleration sensor resonance band. Next, using demodulation techniques, the envelope is calculated in order to obtain SPM measures and the SPM spectrum [5]. An attempt to use acoustic signals and acoustic emission response was also reported as a method for bearing fault detection [12]. Early detection of rolling element bearing failure can also be provided using REBAM-Rolling Element Bearing Activity Monitor [13, 14].

In many publications [1, 5, 6] authors state that the best methods of rolling bearing condition monitoring are based on detection and enhancing impulsiveness of the signal from bearing. An important requirement which a diagnostic technique

must fulfil is the ability to identify transient disturbances in the signal. Such a technique can be based on the Teager-Kaiser energy operator.

2 Energetic Descriptors

The Teager-Kaiser energy operator (TKEO) is a non-linear differential operator. As a result of application of the TKEO on a time signal a waveform of an energetic measure is obtained (Teager-Kaiser energy—E_{TK}) It can be interpreted as a waveform of energy of this signal [15]. The operator was described and its properties were analyzed in many publications [16–19]. For a continuous signal the Teager-Kaiser operator is defined as follows:

$$\Psi(x(t)) = \dot{x}^2(t) - x(t)\ddot{x}(t) \tag{1}$$

An interesting property of the energy operator (1) is its sensitivity to sudden changes in analyzed signals, such as transient disturbances of the signal waveform. It is reported that the Teager-Kaiser energy operator was successfully applied in condition monitoring of gearboxes [20–23]. Thanks to its properties, TKEO was also used for condition monitoring of bearings [24–27]. It is worth noticing that a Teager-Huang transform was also used for bearing condition monitoring [28].

In this paper the authors discuss the possibility of the fault detection of rolling bearings using energetic descriptors of vibrations signals. The considered energetic descriptor of a diagnostic signal is the energetic trajectory of the vibration signal. The Teager-Kaiser energetic trajectory represents a signal on the Teager-Kaiser energetic plane. This tool was first introduced for models of signals with disturbance or modulation [29]. It was noticed that it detects disturbances related to the diagnostic symptoms in the energetic structure of the signal.

The creation of the Teager-Kaiser energetic plane was based on the assumption that the emergence and development of a fault disturb the energetic structure of the vibration signal. This disturbance is characterized by high values of the Teager-Kaiser energy and high velocity of change of Teager-Kaiser energy. Taking into account both measures, i.e. the energy and the velocity of change of energy, it is possible to detect transient events in the signal and to specify the significance of observed phenomena.

The Teager-Kaiser energetic plane is defined by canonical coordinates: $E_{TK}(x(t))$—the energy descriptor of the signal $x(t)$ and $\dot{E}_{TK}(x(t))$—the velocity of change of energy descriptor of the signal $x(t)$. Both components of the analytical signal are obtained with the use of the Teager-Kaiser energy operator $\Psi(x(t))$. For a given vibration signal $x(t)$, $E_{TK}(x(t))$ and $\dot{E}_{TK}(x(t))$ create a representation on the energetic plane $E_{TK} - \dot{E}_{TK}$ in the form of the Teager-Kaiser energetic trajectory or shortly the energetic trajectory.

3 Experiment

Potential possibilities of rolling bearing faults detection based on E_{TK} have been determined experimentally. Roller tapered bearing type CBK-171 was chosen as a test object. The tested bearings set included an undamaged bearing and bearings with artificially introduced faults of various types. Intentionally introduced bearing defects (Fig. 1) and their codes are detailed in Table 1.

During experiments the following parameters have been applied: axial bearing load (spring washer) $F_A = 55$ N, radial load (vertical)—gravitational load by a mass m equal to 1545 g, $F_V = 15.16$ N; lubricant—silicone oil (1/8 ml); rotating speed 1450 rpm; recorded signal—vibration accelerations; transducer localization—at the bearing housing; analyzed signal interval 60 s, recorded 90 s after test start (after stabilization of the bearing operating conditions).

All energetic characteristic and their parameters mentioned in the introduction were obtained by application of a digital signal processing system elaborated in the DASyLab® environment. Acceleration of vibrations was recorded up to 50 kHz (linear) but the determination of E_{TK} was carried out in the narrow frequency band (18.5–20.0 kHz), covering the local resonance of the bearing-housing system (the highest available in the frequency sense). It should be remembered that faulty bearings generate short-time impact excitations besides the background noise.

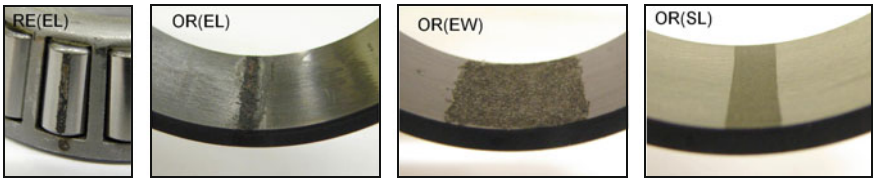

Fig. 1 Examples of artificially introduced bearing defects (sandblasting and electroerosion)

Table 1 The set of tested rolling bearings

Defect code	Bearing code	Faulty element	Damage type	Defect size	Defect width (mm)	Defect depth (μm)
UD	N02	Undamaged	–	–	–	–
IR(EL)	N00	Inner race	Electroerosion	Local	0.5	NA
RE(EL)	N19	Rolling element	Electroerosion	Local	1	NA
OR(EL)	N14	Outer race	Electroerosion	Local	2	approx. 85
OR(EW)	N17	Outer race	Electroerosion	Wide	11	approx. 50
OR(EF)	N03	Outer race	Electroerosion	Extensive	Whole race	approx. 50
OR(SL)	N12	Outer race	Sandblasting	Local	3	approx. 12
OR(SW)	N01	Outer race	Sandblasting	Wide	11	approx. 12
OR(SF)	N16	Outer race	Sandblasting	Extensive	Whole race	approx. 13

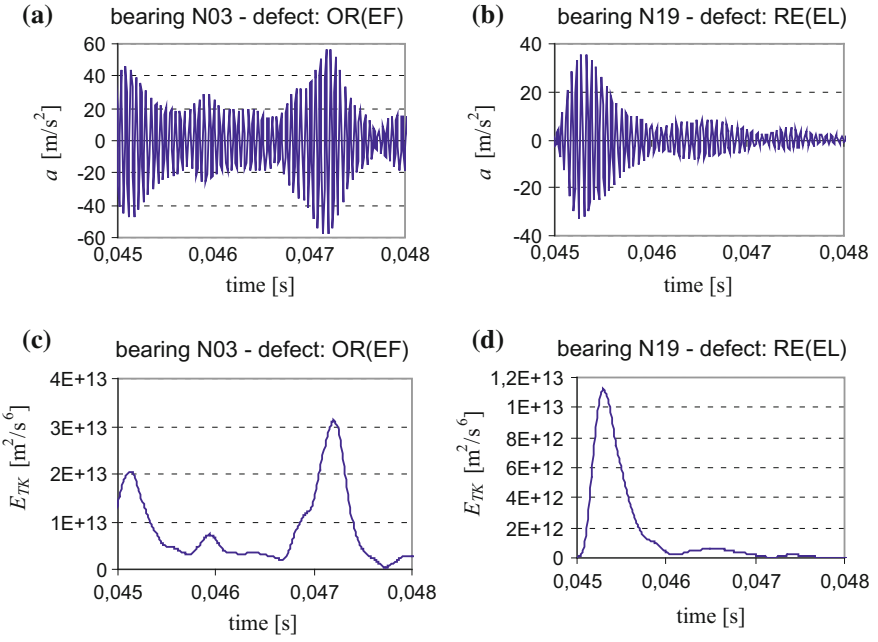

Fig. 2 Short signals sequences: vibration acceleration of bearings (**a**, **b**) and corresponding energetic characteristics E_{TK} (**c**, **d**)

Taking the above into consideration, we can assume that this approach leads to processing the quasi-harmonic signal with amplitude modulation. Some features of E_{TK} described in ([30], p. 25) particularly that changes of E_{TK} reflect changes occurring in analysed signal, allows us to create an energetic envelope of the signal of vibration accelerations. This feature of the energy descriptor is visible in Fig. 2. It can be assumed that the obtained energetic characteristics will be a good tool for detection of the short-term signal disturbances which are typical for local defects of rolling bearings.

A comparison of acceleration signals recorded on bearing housing (with extensive defects Fig. 2a and local defects Fig. 2b of the bearing elements) and energetic characteristics corresponding to these signals are shown in Fig. 2.

Table 2 contains basic parameters of E_{TK} determined for the tested bearings set. One of the possible methods of the technical degradation degree assessment of bearings and type of damage detection is presented in Fig. 3.

Diagnostic inference can be based on the size as well as on the shape of energetic trajectories, which are shown in Fig. 4.

The trajectory fitting a circular shape (Fig. 4b) evidences the occurrence of extensive damage, which continuously stimulates the bearing housing system to vibrate resonantly. The asymmetry of the trajectory (Fig. 4c) and predomination of positive values of $\dot{E}_{TK}$ are typical for a transient decaying vibration signal (e.g. an

Table 2 Basic parameters of the energetic characteristics E_{TK} of the testing bearings set

Defect code	Bearing code	Faulty element	E_{TK} [m^2/s^6]		
			Max	Average	RMS
UD	N02	Undamaged	9.87E+12	8.01E+10	2.03E+11
IR(EL)	N00	Inner race	3.55E+13	2.95E+11	6.00E+11
RE(EL)	N19	Rolling element	2.53E+14	4.66E+11	2.80E+12
OR(EL)	N14	Outer race	2.53E+14	4.66E+11	2.80E+12
OR(EW)	N17	Outer race	8.48E+13	5.50E+11	1.19E+12
OR(EF)	N03	Outer race	1.38E+14	4.67E+12	7.20E+12
OR(SL)	N12	Outer race	1.07E+13	1.47E+11	3.16E+11
OR(SW)	N01	Outer race	3.32E+13	4.78E+11	9.77E+11
OR(SF)	N16	Outer race	8.26E+13	1.06E+12	2.00E+12

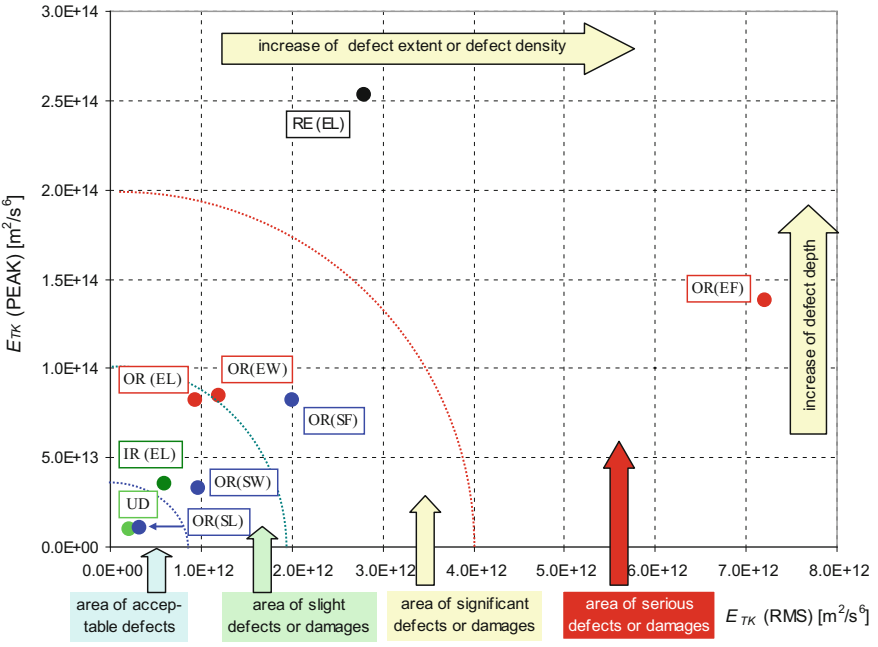

Fig. 3 An example of one of the possible methods of bearings defects detection and assessment of faults size based on E_{TK} parameters (for description of bearing faults see Table 1)

answer of a mechanical structure after the periodic impact excitation). That trajectory shape can be evidence of local defects of race or rolling element.

The next method of fault detection is based on analysis and parameterization of the probability density function of E_{TK}. Figure 5 shows comparisons of these functions determined for undamaged bearing and bearings with various types of artificially introduced defects. For extensive damage, a significantly larger share of components with higher E_{TK} values can be seen.

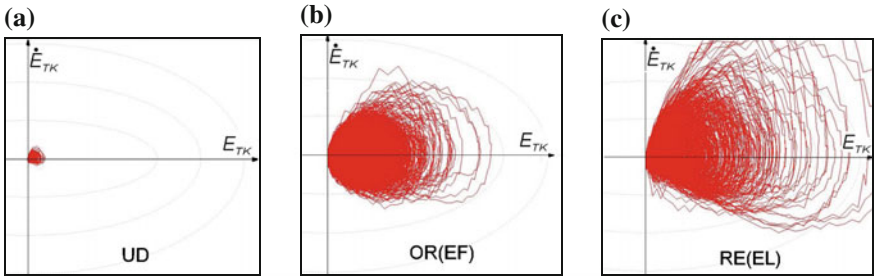

Fig. 4 Qualitative changes in energetic trajectories of bearing vibration signals (pictures have the same scale); **a** bearing without defects, **b** extensive defect of outer race—electro erosion, **c** local defect of rolling element

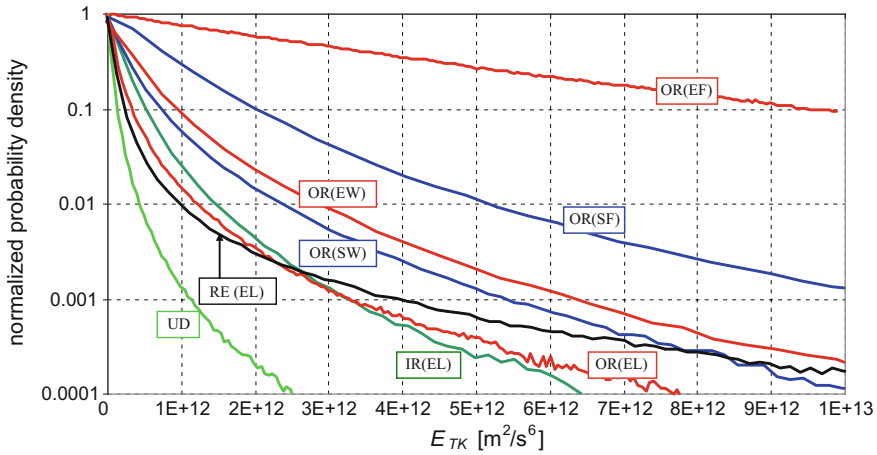

Fig. 5 The comparison of probability density functions of E_{TK} for various types of faults of rolling bearings (for description of faults see Table 1)

4 Conclusions

The results of experiments allow us to conclude that energetic descriptors of vibrations signals, e.g. E_{TK}, $\dot{E}_{TK}$ and their measures may be a base of new methods of the rolling bearing diagnosing. Estimates obtained as a result of parametrization of E_{TK} allow evaluation of the technical condition of bearings and assessment of form/extensity of defects of bearings. The analysis of the shape of the energetic trajectory can be useful in determining the defects forms (local or extensive). The trajectory size is significantly related to defect intensity and can be applied for quantitative evaluation of the degradation process.

The probability density function of E_{TK} can be applied to evaluate the condition of bearings. In this case passing of the probability alarm/limit value can be used as a diagnostic symptom. The decision threshold (e.g. good/faulty) should be determined experimentally.

Acknowledgements The research covered in this paper was partially financially supported in the year 2016 by research projects 02/21/DSMK/3482 and 02/21/DSPB/3478.

Authors thank Michał Jakubowicz Ph.D. for the initial selection of bearings.

References

1. Żółtowski, B., & Cempel, C. (Eds.). (2004). *Inżynieria Diagnostyki Maszyn*. Radom: ITS.
2. Williams, T., Ribadeneira, X., Billington, S., & Kurfess, T. (2001). Rolling element bearing diagnostics in run-to-failure lifetime testing. *Mechanical Systems and Signal Processing, 15,* 979–993. doi:10.1006/mssp.2001.141.
3. Xi, F., Qiao Sun, Q., & Krishnappa, G. (2000). Bearing diagnostics based on pattern recognition of statistical parameters. *Journal of Vibration and Control, 6,* 375–392. doi:10.1177/107754630000600303.
4. Randall, R. B., & Antoni, J. (2010). Rolling element bearing diagnostics—A tutorial. *Mechanical Systems and Signal Processing, 25,* 485–520. doi:10.1016/j.ymssp.2010.07.017.
5. Radkowski, S. (2002). *Wibroakustyczna diagnostyka uszkodzeń niskoenergetycznych*. Radom: ITE.
6. Randal, R. B. (2011). *Vibration-based condition monitoring: Industrial, aerospace and automotive applications*. New Delhi: Wiley.
7. Li, H. (2010). Bi-spectrum analysis based bearing fault diagnosis. *Fuzzy Systems and Knowledge Discovery (FSKD), 6,* 2599–2603. doi:10.1109/FSKD.2010.5569850.
8. Dybała, J., & Zimroz, R. (2014). Rolling bearing diagnosing method based on Empirical Mode Decomposition of machine vibration signal. *Applied Acoustics, 77,* 195–203. doi:10.1016/j.apacoust.2013.09.001.
9. Bin, G. F., Gao, J. J., Li, X. J., & Dhillon, B. S. (2012). Early fault diagnosis of rotating machinery based on wavelet packets—Empirical mode decomposition feature extraction and neural network. *Mechanical Systems and Signal Processing, 27,* 696–711. doi:10.1016/j.ymssp.2011.08.002.
10. Butler, D. E. (1973). The shock-pulse method for the detection of damaged rolling bearings. *Non-Destructive Testing, 6*(2), 92–95. doi:10.1016/0029-1021(73)90116-3.
11. Allenby, G. (1990). Condition based maintenance. In R. Rao (Ed.), *Condition monitoring and diagnostic engineering management.* (pp. 155–161). Padstow: Chapman and Hall. doi:10.1007/978-94-009-0431-6.
12. Tandon, N., & Choudhury, A. (1999). A review of vibration and acoustic measurement methods for the detection of defects in rolling element bearings. *Tribology International, 32,* 469–480. doi:10.1016/S0301-679X(99)00077-8.
13. Harker, R. G., & Hansen, J. S. (1985). Rolling element bearing monitoring using high gain eddy current transducers. *Journal of Engineering for Gas Turbines and Power, 107,* 160–164. doi:10.1115/1.3239677.
14. Bently, D. E., Goldman, P., & Yu, J. J. (2001). Rolling element bearing defect detection and diagnostics using REBAM probes. *Orbit*, 12–25.
15. Kaiser, J. F. (1990). On a simple algorithm to calculate the 'energy' of a signal. In *Proceedings of the IEEE ICASSP-90*, Albuquerque.

16. Kaiser, J. F. (1990). On Teager's Energy Algorithm and its generalization to continuous signals a simple algorithm to calculate the 'energy' of a signal. In *Proceedings of the IEEE Digital Signal Processing Workshop*, New Paltz.
17. Kvedalen, E. (2003). Signal processing using the Teager Energy Operator and other nonlinear operators. Master of science thesis, University of Oslo.
18. Maragos, P., Kaiser, J. F., & Quatieri, T. F. (1995). On amplitude and frequency demodulation using energy operators. *IEEE Transactions on Signal Processing, 41,* 1532–1550.
19. Maragos, P., & Potamianos, A. (1995). Higher order differential energy operators. *IEEE Signal Processing Letters, 2,* 152–154.
20. Li, H., Zheng, H., & Tang, L. (2010). Gear fault detection based on Teager-Huang transform. *International Journal of Rotating Machinery*, Article ID 502064. doi:10.1155/2010/502064.
21. Antoniadou, I., Manson, G., Dervilis, N., Barszcz, T., Staszewski, W. J., & Worden, K. (2012). Use of the Teager-Kaiser energy operator for condition. Monitoring of a wind turbine gearbox. In *International Conference on Noise and Vibration Engineering 2012, ISMA 2012, including USD 2012: International Conference on Uncertainty in Structure Dynamics* (Vol. 6, pp. 4255–4268).
22. Zhong, X., Zeng, L., Zhao, C., Liu, X., & Chen, S. (2013). Fault diagnosis for wind turbine gearboxes based on EMD and the energy operator. *Applied Mechanics and Materials, 281*, 10–13. doi:10.4028/www.scientific.net/AMM.281.10.
23. Gałęzia, A. (2014). Averaged signal measures of TKEO energy waveform in detection of tooth break in gearbox. *Measurement Automation and Monitoring, 60,* 31–34.
24. Liang, M., & Soltani, B. I. (2010). An energy operator approach to joint application of amplitude and frequency-demodulation for bearing fault detection. *Mechanical Systems and Signal Processing, 24,* 1473–1494.
25. Feng, Z., Wang, T., Zuo, M.J., Chu, F., & Yan, S. (2011). Teager energy spectrum for fault diagnosis of rolling element bearings. In *Journal of Physics: Conference Series 305, 9th International Conference on Damage Assessment of Structures (DAMAS)*.
26. Henríquez, R. P., Alonso, J. B., Ferrer, M. A., & Travieso, C. M. (2013). Application of the Teager-Kaiser energy operator in bearing fault diagnosis. *ISA Transactions, 52,* 278–284. doi:10.1016/j.isatra.2012.12.006.
27. Antoniadou, I., Howard, T. P., Dwyer-Joyce, R. S., Marshall, M. B., Naumann, J., Dervilis, N., et al. (2014). Envelope analysis using the Teager-Kaiser energy operator for condition monitoring of a wind turbine bearing. *Applied Mechanics and Materials, 564,* 170–175.
28. Li, H., Zhang, Y., & Zheng, H. (2010). Bearing fault detection and diagnosis based on order tracking and Teager-Huang transform. *Journal of Mechanical Science and Technology, 24,* 811–822. doi:10.1007/s12206-009-1211-9.
29. Gałęzia, A., & Radkowski, S. (2014). Signals representation on energetic plane based on Teager-Kaiser energy operator. *Vibrations in Physical Systems, 26,* 235–245.
30. Gałęzia, A. (2015). Utilization of non-stationary signals in detection of early phases of failures in vehicle power transmission systems. Dissertation, Warsaw University of Technology.

Bearing Fault Feature Extraction Using Autoregressive Coefficients, Linear Discriminant Analysis and Support Vector Machine Under Variable Operating Conditions

Mourad Kedadouche, Zhaoheng Liu and Marc Thomas

Abstract Advanced monitoring requires automatic diagnosis of machines operating under variable conditions. In this paper, an intelligent method is introduced in order to enhance the classification and achieves a higher precision for the diagnosis of degradation of rolling bearings operating under condition variations. The method uses the coefficients of autoregressive modeling (AR) of the bearing vibration signal as the features of a classifier. A Linear Discriminant Analysis (LDA) of the matrix feature obtained from AR analysis is applied in order to extract the components that discriminate the different fault modes since it is insensitive to the working conditions. Finally, the results obtained from LDA are used as the input of a support Vector Machine (SVM) classifier to automatically identify the bearing state. The experimental results show that the performance of the proposed method is effective and achieve a good accuracy.

Keywords Bearing fault · Autoregressive modeling (AR) · Linear discriminant analysis (LDA) · Support vector machine (SVM)

M. Kedadouche · Z. Liu · M. Thomas (✉)
Department of Mechanical Engineering, École de technologie supérieure, Montreal, QC H3C 1K3, Canada
e-mail: marc.thomas@etsmtl.ca

M. Kedadouche
e-mail: mourad.kedadouche@hotmail.fr

Z. Liu
e-mail: zhaoheng.liu@etsmtl.ca

A. Timofiejczuk et al. (eds.), *Advances in Condition Monitoring of Machinery in Non-Stationary Operations*, Applied Condition Monitoring 9,
https://doi.org/10.1007/978-3-319-61927-9_32

1 Introduction

Rolling bearing fault diagnosis has been the subject of numerous researches about machine monitoring. Many techniques were developed and enhanced in order to detect a possible fault. Generally, the fault diagnosis methodology is realised following the following steps: signal acquisition, feature extraction and finally fault identification and classification. The feature extraction is a key of a good diagnosis. Selecting sensitive features which present a good discrimination between different classes of the fault modes enhance the performance of the classifier. In case of rolling bearing operating under variable conditions, many features present a variation and are non-stable. This makes the fault-diagnosis methods less effective. So, it is important to develop a rolling bearing diagnostic method that is relevant to different working conditions.

Recently, some research works have been conducted to correlate the features extracted from different sensors and the working conditions [1, 2]. For example, Shao et al. [3] used an intelligent bearing equipped with several sensors to track the time-varying parameters. Ruiz-Cárcel et al. [4] propose a method to analyse a combination of process, electric and vibration measurements. These methodologies need more sensors devices to be integrated into the system. Other researches have focused on the use of time-frequency analysis such as Wavelet Transform (WT) [5], Empirical Mode Decomposition (EMD) [6, 7], and Hilbert Huang Transform (HHT) [8]. The features extracted from time-frequency analysis are complex and need a good expertise to explore and use them efficiently for pattern recognition. Consequently, a reduction of the matrix dimension is required by searching a new representation of the features in the low dimension in order to select only the components with a good discrimination between the classes to enhance the classification accuracy. In order to reduce the matrix of the features extracted, Hongmei et al. [8] employed Singular Value Decomposition (SVD) extracted from HHT and demonstrated that the SVD presents a good stability. Ye et al. [9] used the Local Mean Decomposition (LMD) for bearing faults. However, the techniques based on EMD and LMD suffer from amode mixing which limits the accurate estimation of the instantaneous frequencies. To overcome this drawback, EEMD [10] and ELMD [11] are proposed which are noise-assisted data analysis methods. These noise-assisted data analysis methods determine the true component as the mean of a set of trials. It was demonstrated that introduce artificial noise helps data analysis and attenuates the mode mixing. Unfortunately, guidance is lacking on how to choose the appropriate parameters of the EEMD and ELMD methods [7].

Autoregressive (AR) model is one of the methods that have been efficiently used to extract the information of system conditions that reflect the characteristic dynamics of the system [12, 13]. The basic idea is to use the coefficients of the model as the feature inputs of the classifier for pattern recognition. However, the parameters of the autoregressive model are sensitive to the working conditions and are not efficient if the machine works under variable conditions. To overcome this drawback, combined methods have been proposed. Junsheng et al. [14] used the autoregressive parameters

of all IMF obtained from the decomposition of the vibration bearing signal by using EMD. These features are used as input classifiers. The same authors [14] have used the same methodology in order to diagnosis gears fault [15]. Liye Zhao et al. [16] used the Complementary Ensemble Empirical Mode Decomposition (CEEMD) to decompose the signal into multiple components and the autoregressive model parameters are established for the IMF selected from correlation coefficients.

In this paper, the authors used the autoregressive model parameters for bearing fault diagnosis under variable conditions. For one fault mode (one class) taken under different velocity variations, it is obvious that the parameters extracted present a certain dispersion. The deal is to minimize the dispersion within class and maximize the dispersion between others classes. Linear Discriminant Analysis (LDA) [17] is proposed in this study to achieve this purpose. The particularity of the LDA is its ability to find a new representation of the data in a low dimension space that minimize the dispersion within class and in the same time maximize the dispersion between classes. Therefore, integrating this technique can help to minimise the dispersion of the features extracted within the classes caused by the working condition variation. The adopted methodology is to establish the autoregressive parameters of the vibration signal and then to use LDA to reduce the matrix dimension and found a new representation with a low dimension. At this stage, we select only the pertinent information and use it as the feature input of the SVM classifier. The analysis results of experimental data demonstrate that the proposed methodology is effective.

This paper is organized as follows: Sect. 2 gives a theoretical background of LDA; Sect. 3 introduces the proposed methodology; Sect. 4 describes a history case performed to validate the method, and Sect. 5 presents the conclusions and related future works.

2 Theoretical Background of LDA

Linear Discriminant Analysis (LDA) is dedicated for dimensionality reduction and classification [17]. LDA gives an optimal transformation of the data in a low dimension by minimizing the within-class distance and maximizing the between-classes distance simultaneously.

Given a data set with c classes where N_i represents the number of samples in the ith class and x_j^i is the jth sample from the ith class. The between-classes scatter matrix S_B and the total scatter matrix S_W are defined as:

$$S_B = \frac{1}{N}\sum_{i=1}^{c}(\mu_i - \mu)\cdot(\mu_i - \mu)^T \tag{1}$$

$$S_W = \frac{1}{N}\sum_{i=1}^{c}\sum_{j=1}^{N_i}(x_j^i - \mu_i)(x_j^i - \mu_i)^T \tag{2}$$

where $N = \sum_{i=1}^{c} N_i$ is the total number of the samples, μ_i is the centroid of the ith class and μ is the centroid of the data set.

LDA aims on finding a linear transformation $W = [W_1, W_2 \ldots W_d]$ such that between-classes scatter matrix is large whereas the within class covariance is small. The vector W is obtained by maximizing the following equation:

$$J(W) = \arg\max_{W} \frac{|W^T S_B W|}{|W^T S_W W|} \tag{3}$$

The W is obtained by finding the eigenvectors corresponding to the d largest generalized eigenvalues of $S_W^{-1} S_B W = \lambda W$.

The samples x are transformed in the new d-dimension space by the following equation:

$$y = W^T x \tag{4}$$

3 Feature Extraction Method Based on AR-LDA

The extracted features are used as input of the classifier in order to identify the mode fault. Thus, the feature extraction is a primordial step for automatic diagnosis and the performance of the classifier depends on the quality of the extracted features. The chart of the proposed fault diagnosis method for rolling bearings is shown in Fig. 1.

For each signal, the AR model [12, 13] is established using the following equation:

$$x(t) - \sum_{k=1}^{m} a_k x(t-k) = e(t) \tag{5}$$

where: $a_k (k = 1, 2, \ldots, m)$ are the model parameters; m is the order of the model of the AR model and $e(t)$ is the error term of the model.

The parameters $a_k (k = 1, 2, \ldots, m)$ may reflect the characteristics of a roller bearing vibrating system. Then, the LDA is used to reduce the matrix size of the feature and extract only the components which have a good discrimination and less sensitivity to the working conditions. Finally the selected features are used as input to the SVM classifier. According to the extracted feature vectors, the fault mode is identified.

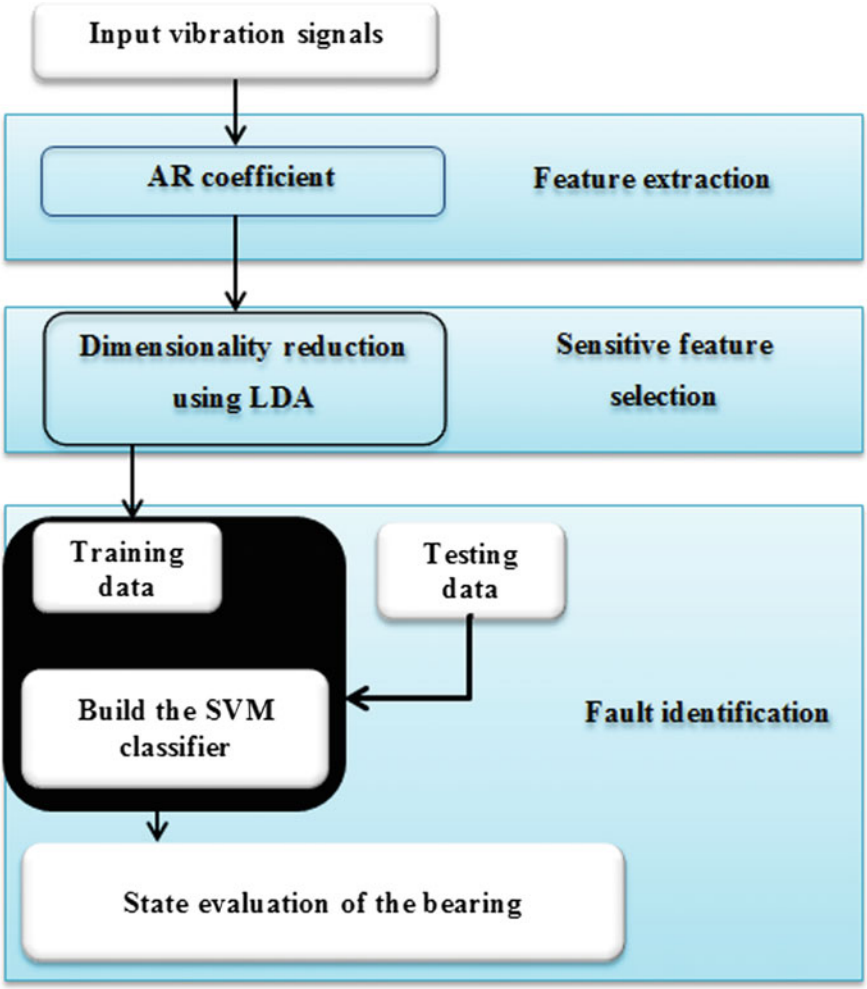

Fig. 1 The follow chart of the proposed method

4 Experimental Results and Discussion

4.1 Experimental Data Sources

This study uses experimental data from the bearing data center of Case Western Reserve University (CWRU) [18]. Experiments were conducted using induction motor (left), a torque sensor (middle) and a dynamometer (right) connected by a self-aligning coupling (middle), as shown in Fig. 2. The dynamometer is controlled so that desired torque load levels can be achieved. The test bearing (SKF 6205-2RS JEM) supports the motor shaft at the drive end. Single point faults were introduced

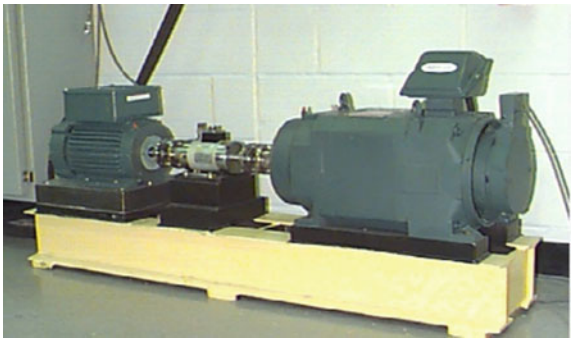

Fig. 2 The test rig

Table 1 The geometric characteristic of the bearing (mm)

Inside diameter	Outside diameter	Thickness	Ball diameter	Pith diameter
25	52	15	7.94	39

Table 2 The dataset used in this study

Label	Status	Working conditions				
		0 hp (1797 RPM)	1 hp (1772 RPM)	2 hp (1750 RPM)	3 hp (1720 RPM)	Total dataset
1	Healthy	20	20	20	20	80
2	Outer race fault	20	20	20	20	80
3	Inner race fault	20	20	20	20	80
4	Rolling element fault	20	20	20	20	80
Total						320

into the test bearing using electro-discharge machining. Bearing faults under consideration cover outer race fault, inner race fault and rolling element fault. The considered fault size is very small: 178 μ in diameter and 279 μ in depth. The fault position relative to the load zone is: 'centred' (fault in the 6.00 o'clock position).

The geometric characteristics of the bearing are listed in Table 1. Acceleration was measured in the vertical direction on the housing of the drive-end bearing. Besides, the sampling frequency is 12,000 Hz and 120,000 data samples are used (10 s acquisition).

For each fault condition, the data were collected under different speeds operating at 1730, 1750, 1772, and 1797 rpm (motor loads of 0, 1, 2 and 3 horsepower (hp)). As shown in Table 2, four datasets sampled under normal state, inner-ring fault, outer ring fault and rolling element fault were recorded. In the following

experiments, the vibration signals are divided into several non-overlapping segments with the length N = 6000. Each condition has 20 samples, and there are total 80 samples each dataset. Consequently, the full four datasets contain 360 samples.

4.2 Fault Feature Extraction

The features are the coefficients a_k of the AR model of the vibration signal. These coefficients reflect the characteristics related to the bearing fault. The AR model order is determined according to the Final Prediction Error (*FPE*) method given as:

$$FPE = V\left(1 + \frac{2m}{N-m}\right) \tag{6}$$

where V is the residual sum of squares, m is the order of the model and N is the number of the data points.

For different fault modes under variable working conditions, the AR model is established. Figure 3 shows the variation of FPE values as a function of model order for different fault modes working in different conditions (0, 1, 2 and 3) hp. It can be seen that for the healthy bearing, outer race fault and rolling element fault, the FPE observe a minimum value which stay stable for $m \geq 10$, except for the inner race fault where the order is about 20. So, to have the same dimension of the

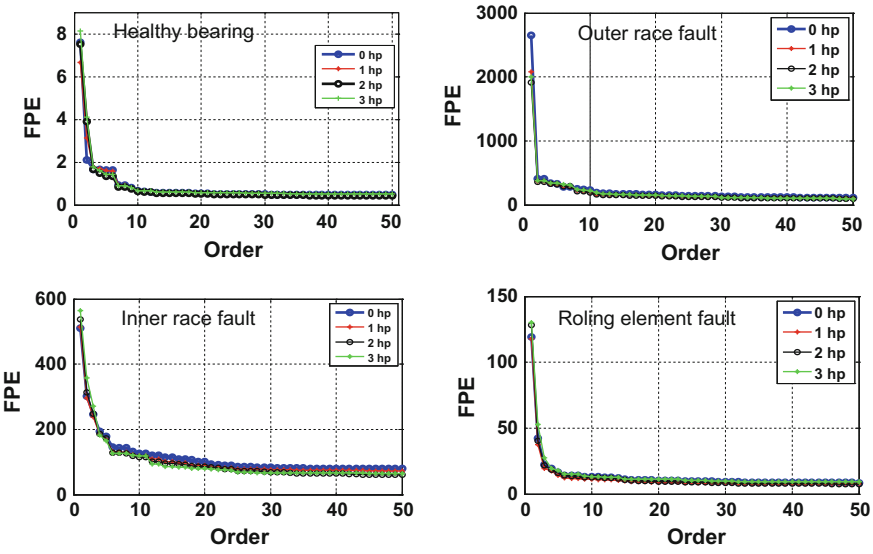

Fig. 3 Variation of FPE values with AR model order

feature, a vector $m = 20$ is selected in this study. It means that each signal may be characterised by 20 coefficients $[a_1, a_2, \ldots, a_{20}]$.

As mentioned in Table 2, the operating states of rolling bearings contain normal, inner ring fault, outer ring fault, and rolling element fault. The effectiveness of the extracted features is evaluated from their capability to distinguish between different types of the degradations in different working conditions (0, 1, 2 and 3) hp. It means that these features allows a good discrimination between the classes (healthy, outer ring fault, inner ring fault and rolling element fault).

The AR coefficients $a_k(k = 1, 2, \ldots, 20)$ are computed for all dataset given in Table 2. To verify their discrimination capability, the mean and standard deviation of the coefficients are displayed in Fig. 4. This representation is an easy way to summarize the distribution of all features extracted for different fault modes under variable conditions. It is clear that these features are overlapped, except for a_1 in which the gaps between the healthy case and other mode is satisfactory. This is due to the fact that AR model is applied directly to the nonstationary signals (for one fault mode, the working condition is variable) and the analysis results are unsatisfactory. The AR model is more suitable for stationary signal processing (same working conditions). As a first conclusion, it is not interesting to use directly these coefficients as input to the classifier because the discrimination between the fault modes is not satisfactory and this affects the decision of the classifier to distinguish between the classes. Thus, a pre-treatment is needed in order to improve the discrimination capability of the features. For this reason, the authors propose to use the

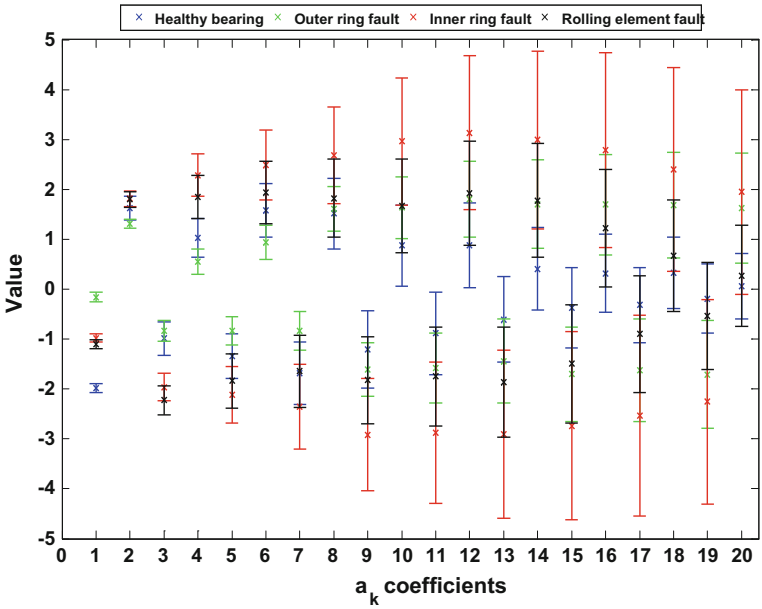

Fig. 4 Distribution of the coefficient $a_k(k = 1, 2, \ldots, 20)$ for different fault modes

LDA to transform the features on another dimension in order to reduce the dispersion of the features for one fault mode and increase the distance classes.

4.3 Fault Feature Selection

Originally, the data feature parameters (the AR coefficients $a_k(k = 1, 2, \ldots, 20)$) are completely overlapping and cannot be clustered well for each condition of faults. To avoid this drawback, we should extract the useful features and reduce the dimension of original data features. In this part, dimensionality reduction is used to select the optimal features for classification. The LDA gives an optimal transformation of the data (the AR coefficient $a_k(k = 1, 2, \ldots, 20)$) in a low dimension by minimizing the within-class distance and maximizing the between-class distance simultaneously. A comparison between LDA and PCA (principal component analysis) is conducted. Based on the eigenvalues, we select the largest eigenvalue to reduce the matrix dimension. The eigenvalues of LDA and PCA result are plotted in Fig. 5. It can be seen that, in both cases, the three first components present high eigenvalues. Consequently, these three components are selected. The first three LDA and PCA components are plotted in Figs. 6 and 7, respectively.

In case of LDA, It can be seen that the clusters for the four fault modes under different working conditions are well separated without overlapping (Fig. 6). However, The PCA can only separate the healthy case from the other fault modes (Fig. 7). The feature extraction using PCA observe an overlapping between outer ring fault, inner ring fault and the rolling element fault. It is then obvious that LDA is better than PCA. Unlike LDA, PCA deals to find the features with the highest variation without considering the class structure.

For the rolling bearing feature extraction under variable operating conditions, the proposed method based on AR-LDA performs better than PCA. The features can well separate the different classes. Therefore, it is easy for classifiers to identify the bearing state.

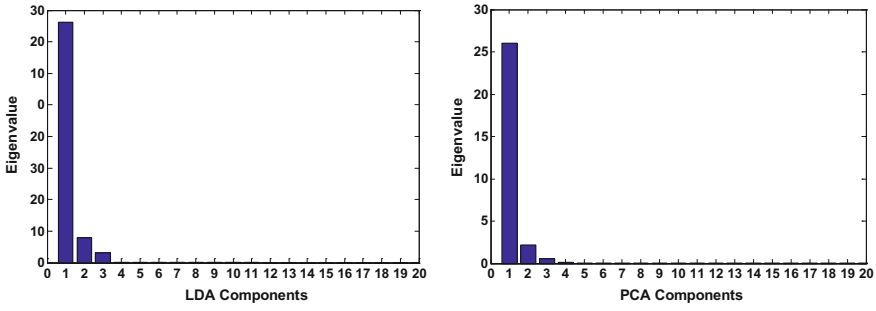

Fig. 5 Representation of the 20 eigenvalues for LDA and PCA

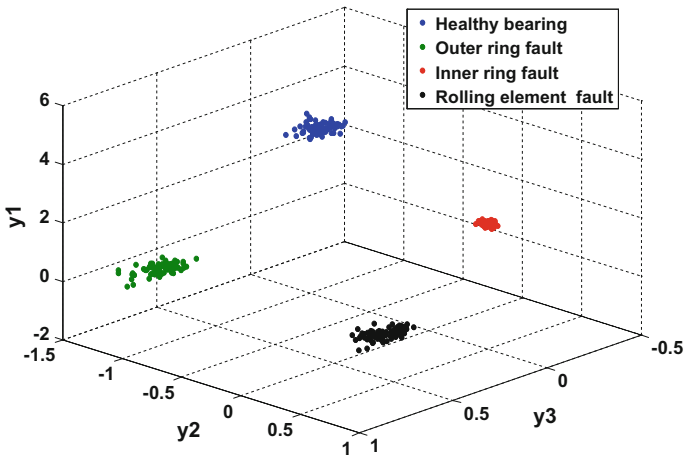

Fig. 6 The feature selected using LDA

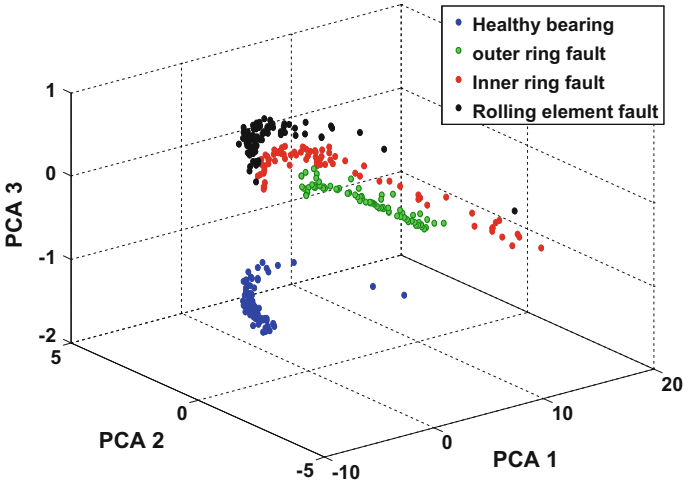

Fig. 7 The feature selected using PCA

4.4 Classification Performance Based on SVM

State classification of rolling bearings is based on the selected feature vectors extracted using AR-LDA method. The data is divided into two groups, training and test data, with 160 samples for each group.

The SVM classifier is based on supervised learning [19, 20]. A multiclass SVM is adopted to perform the classification using one-vs-all methods. In this study, the

Table 3 Classification accuracy for the training data with the best parameters (C, γ and d)

Kernel	Feature extraction	Parameters	Classification rate (%)
Polynomial	AR-LDA	$d = 1$	100
RBF	AR-LDA	$c = \{2^0\}$ $\gamma = \{2^{-3}\}$	100

polynomial and RBF kernel are used as the basic kernel function. Their mathematical formulas are given respectively as:

$$K(x_i, x) = \exp\left(\frac{-\|x_i - x\|^2}{2\gamma^2}\right) \tag{7}$$

$$K(x_i, x) = (x_i \cdot x + 1)^d \tag{8}$$

The kernel function is characterised by two parameters (C and γ) for the RBF and d for the polynomial function) which must be selected to get a good performance for the classifier. To evaluate the performance of the classifier built with the training data, the cross-validation method is used [19]. The grid search approach is an effective way to find the best C and γ [20]. Principally, all the pairs of (C, γ) for the RBF kernel and (d) for the polynomial are tested and the parameters with the high cross-validation accuracy are chosen. In this work, several combinations have been tested to choose the optimal parameters of the RBF function ($C \in \{2^0, 2^1 \ldots 2^7\}$, $\gamma \in \{2^{-3}, 2^{-2}, \ldots 2^3\}$ and $d \in \{1, 2, \ldots, 7\}$) The best combination is the one with the lowest C value and the smallest γ value. For the polynomial function, the simplest model is selected. Table 3 summarize the selected parameters. The performance of the classifiers built, regardless of the feature extraction method or kernel function, is 100% accuracy.

With the designed classifier using the parameters listed in Table 3, the 160 samples of test data are classified. The classification results are displayed in Figs. 8 and 9. Both figures show the SVM outputs and the desired outputs. From Fig. 8, it may be noticed that there is just one sample misclassified. The classification accuracy when using RBF function is 99.38%. For the polynomial function, all samples are well classified (100% of accuracy). In the both cases, the proposed method performs very well which is important and what is needed for automatic diagnosis operation.

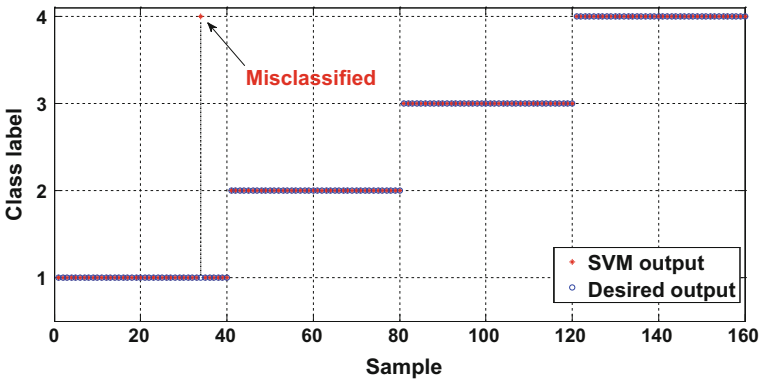

Fig. 8 Classification results for test data using RBF function ($c = 2^0, \gamma = 2^{-3}$)

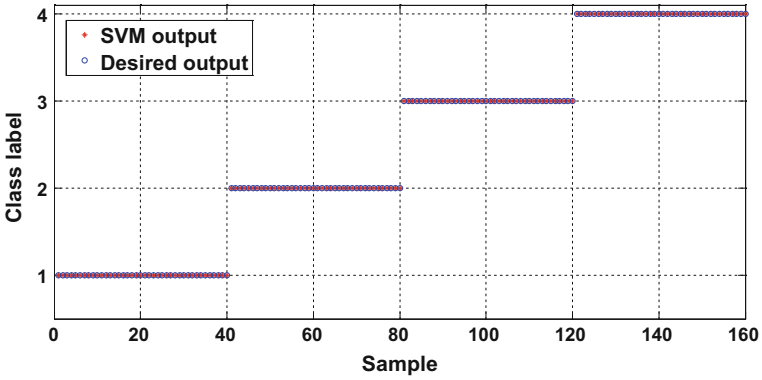

Fig. 9 Classification results for test data using polynomial function with $d = 1$

5 Conclusions

In this paper, a new methodology for feature extraction and selection is proposed. The method is based on the autoregressive modelling, linear discriminant analysis and support vector machine methods. It is found that the features extracted using AR-LDA are insensitive to working condition variations and the features have a good discrimination under the variable states of degradation which is useful to enhance the classification accuracy. The features selected are used as input of the SVM classifier in order to automatically classify the data. SVMs-based multi-class classification based on one-against-all strategy is applied. The results show that SVMs achieves high accuracy. So, the proposed method is effective for rolling fault diagnosis under variable working condition.

Further works will be done in order to introduce other dimensionality reduction techniques to verify their efficacy for bearing fault under variable conditions and extend the method to other rotating machinery with more data.

Acknowledgements The financial support of NSERC (Natural Sciences and Engineering Research Council of Canada) is gratefully acknowledged. The authors thanks Case Western Reserve University Bearing Data Center for having allowed the use of their data via the website.

References

1. Bartelmus, W., & Zimroz, R. (2009). A new feature for monitoring the condition of gearboxes in non-stationary operating condition. *Mechanical Systems and Signal Processing, 23*(5), 1528–1534.
2. Zimroz, R., Bartelmus, W., Barszcz, T., & Urbanek, J. (2014). Diagnostics of bearings in presence of strong operating conditions non-stationarity-a procedure of load-dependent features processing with application to wind turbine bearings. *Mechanical Systems and Signal Processing, 46*(1), 16–27.
3. Shao, Y., Ge, L., & Fang, J. (2008). Fault diagnosis system based on smart bearing. In *Proceedings of the International Conference on Control, Automation and Systems (ICCAS '08)* (pp. 1084–1089).
4. Ruiz-Cárcel, C., Jaramillo, V. H., Mba, D., Ottewill, J. R., & Cao, Y. (2016). Combination of process and vibration data for improved condition monitoring of industrial systems working under variable operating conditions. *Mechanical Systems and Signal Processing, 66–67,* 699–714.
5. Mallat, S. (1999). *A wavelet tour of signal processing*. Academic press.
6. Lei, Y., Lin, J., He, Z., & Zuo, M. J. (2013). A review on empirical mode decomposition in fault diagnosis of rotating machinery. *Mechanical Systems and Signal Processing, 35*(1–2), 108–126.
7. Kedadouche, M., Thomas, M., & Tahan, A. (2016). A comparative study between empirical wavelet transforms and empirical mode decomposition methods: application to bearing defect diagnosis. *Mechanical Systems and Signal Processing, 81,* 88–107.
8. Liu, H., Wang, X., & Lu, C. (2014). Rolling bearing fault diagnosis under variable conditions using Hilbert-Huang transform and singular value decomposition. *Mathematical Problems in Engineering, 2014,* Article ID 765621, 10 pages.
9. Tian, Y., Ma, J., Chen, L., & Wang, Z. (2015). Rolling bearing fault diagnosis under variable conditions using LMD-SVD and extreme learning machine. *Mechanism and Machine Theory, 90,* 175–186.
10. Wu, Z. H., & Huang, N. E. (2009). Ensemble empirical mode decomposition: a noise assisted data analysis method. *Advances in Adaptive Data Analysis, 1,* 1–41.
11. Yang, Y., Cheng, J., & Zhang, K. (2012). An ensemble local means decomposition method and its application to local rub-impact fault diagnosis of the rotor systems. *Measurement, 45*(3), 561–570.
12. Baillie, D. C., & Mathew, J. (1996). A comparison of autoregressive modeling techniques for fault diagnosis of rolling element bearings. *Mechanical Systems and Signal Processing, 10*(1), 1–17.
13. Vu, V. H., Thomas, M., Lakis, A. A., & Marcouiller, L. (2011). Operational modal analysis by updating autoregressive model. *Mechanical Systems and Signal Processing, 25,* 1028–1044.
14. Junsheng, C., Dejie, Y., & Yu, Y. (2006). A fault diagnosis approach for roller bearings based on EMD method and AR model. *Mechanical Systems and Signal Processing, 20,* 350–362.

15. Junsheng, C., Dejie, Y., & Yu, Y. (2008). A fault diagnosis approach for gears based on IMF AR model and SVM. *EURASIP Journal on Advances in Signal Processing*. doi:10.1155/2008/647135.
16. Zhao, L., Yu, W., & Yan, R. (2014). Rolling Bearing Fault Diagnosis Based on CEEMD and Time Series Modeling. *Mathematical Problems in Engineering, 2014,* Article ID 101867, 13 pages.
17. Martinez, A. M., & Kak, A. C. (2001). PCA versus LDA. *IEEE Transactions on Pattern Analysis and Machine Intelligence, 23,* 228–233.
18. Case Western Reserve University Bearing Data Center website. Retrieved from http://csegroups.case.edu/bearingdatacenter/pages/download-data-file.
19. Weston, J., & Watkins, C. (1998). Multi-class support vector machines. *Technical Report CSD-TR-98-04.* Department of Computer Science, Royal Holloway, University of London.
20. Huang, C., Lee, Y., Lin, D., & Huang, S. (2007). Model selection for support vector machines via uniform design. *Computational Statistics and Data Analysis, 52,* 335–346.

Multidimensional Data Segmentation Based on Blind Source Separation and Statistical Analysis

Jacek Wodecki, Pawel Stefaniak, Pawel Śliwiński and Radosław Zimroz

Abstract Horizontal transport in underground copper ore mines mainly consists of LHD machines (loaders, haulers) and belt conveyors. One of the most crucial mining issues for assessment of efficiency of production is identification of operation cycles of haulage machines. In the literature one can find procedure based on analyzing of pressure signal variability developed for loader (Polak et al Identification of loading process based on hydraulic pressure signal pp 459–466, 2016, Stefaniak et al An effectiveness indicator for a mining loader based on the pressure signal measured at a bucket's hydraulic cylinder 15, pp 797–805 [6, 7]). The algorithm allows to identify partial operations of loader cycles like: loading, haulage and return to mining face. For haulers this task can seem to be very easy to solve—machines are driving from point A to point B. Nevertheless, when we take into account harsh and specific conditions of underground mine, the problem remains very hard to solve using classical methods based on single variable and *if-then-else* rules. In most cases, those methods are not robust enough due many random factors (logistical, human factors, work organisation with loaders etc.). In this paper, we propose some kind of data fusion approach to recognition of partial hauler operations. Our method is based on blind source separation approach with particular focus on independent component analysis technique that uses JADE algorithm based on joint approximate diagonalization of eigenmatrices. Obtained components allow for easy segmentation of the signals.

Keywords Haulers · Segmentation · Blind source separation · Multivariate analysis

1 Introduction

Dump trucks are designed for the haulage of ore from mining faces to local transfer points with rock-breaker to break oversize material on the screen. The single cycle of a hauler consists of four basic steps:

J. Wodecki (✉) · P. Stefaniak · R. Zimroz
KGHM CUPRUM Ltd, R&D, Sikorskiego 2-8, 53-659 Wrocław, Poland
e-mail: jwodecki@cuprum.wroc.pl

P. Śliwiński
KGHM Polska Miedź SA, Lubin, Poland

A. Timofiejczuk et al. (eds.), *Advances in Condition Monitoring of Machinery in Non-Stationary Operations*, Applied Condition Monitoring 9,
https://doi.org/10.1007/978-3-319-61927-9_33

- loading of cargo box at the mining face,
- driving to the dumping point,
- unloading process,
- return to loading zone at mining face.

During loading, the ore is directly passed from loader bucket to the cargo box. Generally, capacity of hauler determines what type of loader can work together with it. It is usually assumed that loading of cargo box requires three full cycles of a loader. Haulage machines travel up to 1500 m-long distances along separate dedicated access roads. The machines' driving speed is up to 12 km/h. Unloading process usually is short and takes not more than one minute.

Considering the aforementioned description of partial operations of these machines, identification of cycles of hauler operation can be achieved by analysis of its basic operational parameters like: speed, engine rotational speed or fuel consumption. It is obvious that loading process will be characterized by a few minutes idling in mining faces. Driving along access road is easy to recognize using the machine speed, engine rotational speed and fuel consumption. Of course, driving of haulage machine to dumping point with full cargo box will be different compared to its return to mining face when engine load is lower. Short time break between these cycles of driving is related to unloading process.

There are also some difficulties for this kind of analysis. Partial operations are not always comparable due to constantly varying operational conditions. For example, driving time depends on the conditions along the access road, and the degree of dumping point occupation; time of bucket loading depends on the skill and performance of the loader operator, and this on the other hand depends on other things like amount and fragmentation degree of blasted ore etc. All the aspects are interconnected, and it does not make the analysis any easier.

2 Monitoring System and Industrial Data

Self-propelled machines as basic machines in exploitation area are one of the most expensive assets using in production process. For this reason, nowadays, the increasing tendency to use monitoring system for estimation of reliability and performance assessment is observed. An underground mine is a specific case where monitoring system is restricted by many factors, such as the size of the mine, the number of machines and their technological diversity and, above all, complicated environmental conditions characterized by high temperature and humidity, and high levels of dust and salt in the air. The development of a system for the operation monitoring of hundreds of self-propelled machines working over one kilometer underground requires to provide relevant robustness regarding the infrastructure. The crucial challenges are related to supply of equipment for data acquisition integrated with these machines, the design and maintenance of the data transmission network in the underground mine, data management, analysis and software operating system on the ground surface.

According to the type, these machines are playing completely different role in exploitation process. Therefore, in many cases information needs in terms of machine operations of haulers concern another parameters than for other type of self-propelled machine. In haulers case, basic requirements for the monitoring system are related to engine, drive transmission system, hydraulics of cargo box and tyres. From view point of investigated assessment of the efficiency of haulers performance and work organization the key variables are:

- engine rotational speed,
- driving speed,
- fuel consumption,
- driving direction and current gear,
- total distance travelled.

Exemplary data set of above listed variables from ten hauler cycles has been presented in Fig. 1.

As mentioned early haulers operation is not complex—machines are driving from point A to point B. As one can see in Fig. 1 time series are characterised by cyclic variability, very similar in following haulage cycles. Assessment of their performance requires development of algorithm to identify each operation regime of haulage (loading, haulage, unloading, return to mining face) by appropriate signals segmentation [5–9]. For haulers this task can seem to be very easy to solve. However, taking into account harsh and specific conditions in mining corridors, recognition of these regimes is hard to achieve using classical methods based on single variable and *if-then-else* rules. Currently development of signals separation techniques leads to obtain components with a variable content regard to signal segmentation.

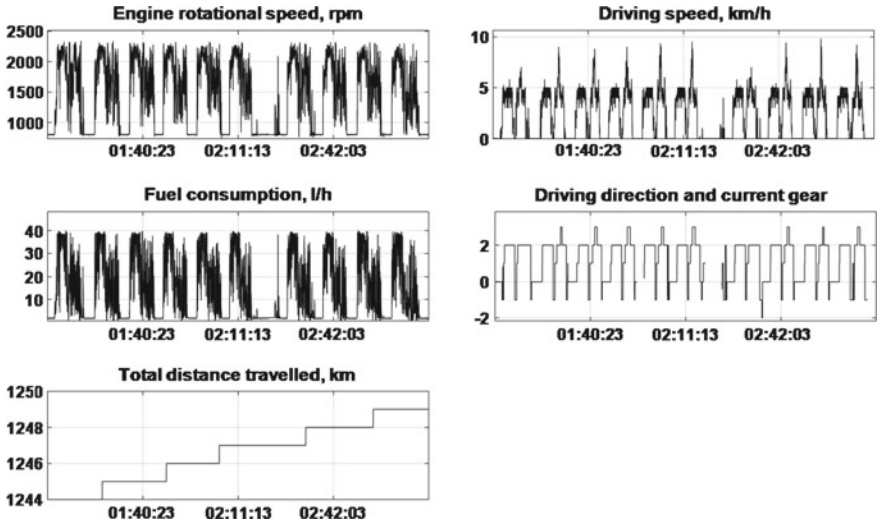

Fig. 1 Key variables for efficiency assesment of haulars operation

3 Methodology for Identification of Haulage Process

3.1 JADE-ICA Algorithm

Joint Approximation Diagonalization of Eigenmatrices (JADE) is one of several blind source separation (BSS) techniques from the family of Independent Component Analysis (ICA) algorithms [1–4]. It exploits the fourth order moments in order to extract the source signals from mixed signals. Principle of operation of JADE is given as follows:

- Set of input data $\mathbf{X}$ is provided in the form of M-by-N matrix of M input vectors of the length N.
- The whitening matrix $\mathbf{P}$ and the set of prewhitened data $\boldsymbol{Z} = \boldsymbol{PX}$ are estimated.
- The fourth cumulants of the whitened mixtures $\hat{\boldsymbol{Q}}_i^Z$ are computed. Their m most significant eigenvalues λ_i and their corresponding matrices V_i are determined. An estimate of the unitary matrix $\boldsymbol{R}$ is obtained by maximizing the criteria $\lambda_i\ V_i$ by means of joint diagonalization. If $\lambda_i\ V_i$ cannot be exactly jointly diagonalized, the maximization of the criteria defines a joint approximate diagonalization.
- An orthogonal contrast is optimized by finding the rotation matrix $\boldsymbol{R}$ such that the cumulant matrices are as diagonal as possible, according to the equation:

$$\mathbf{R} = arg \min_R \sum_i Off\left(\mathbf{R}^T \hat{\mathbf{Q}}_i^Z \mathbf{R}\right)$$

- The mixing matrix $\boldsymbol{A}$ is estimated as $\hat{\boldsymbol{A}} = \boldsymbol{RP^{-1}}$ and the output components are estimated as matrix $\hat{\boldsymbol{S}} = \hat{\boldsymbol{A}}^{-1}\boldsymbol{X}$ of the same size as $\mathbf{X}$.

4 Application to the Real Data

Based on visual inspection and physical meaning three variables were selected for the analysis as the most promising: engine rotational speed, fuel consumption and vehicle speed. Vectors were merged into 3-by-N matrix and provided to JADE algorithm, that returned 3-by-N matrix of output components. First output feature includes sufficient information about haulage process and its variability. It ensures easy segmentation in the context of regime recognition. Hence, it has been selected for further analysis. Selection can be done automatically, because JADE in contrast to some other ICA algorithms (e.g. FastICA) always outputs resulting component vectors in the same order (see Fig. 2).

Features were then slightly smoothed using moving average with window length equal to 20. It allowed to obtain clearer signal with more visible trend of behavior (see Fig. 3).

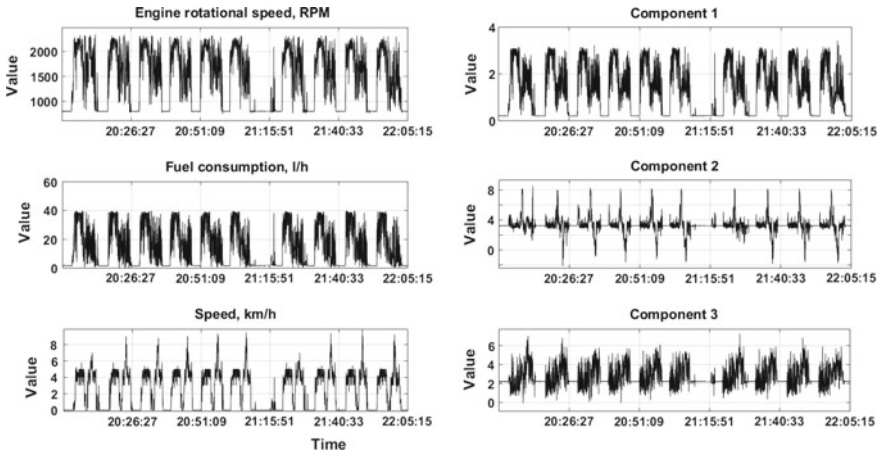

Fig. 2 Input data (*left panels*) and smoothed independent components (*right panels*). Charts zoomed in time domain for better visibility

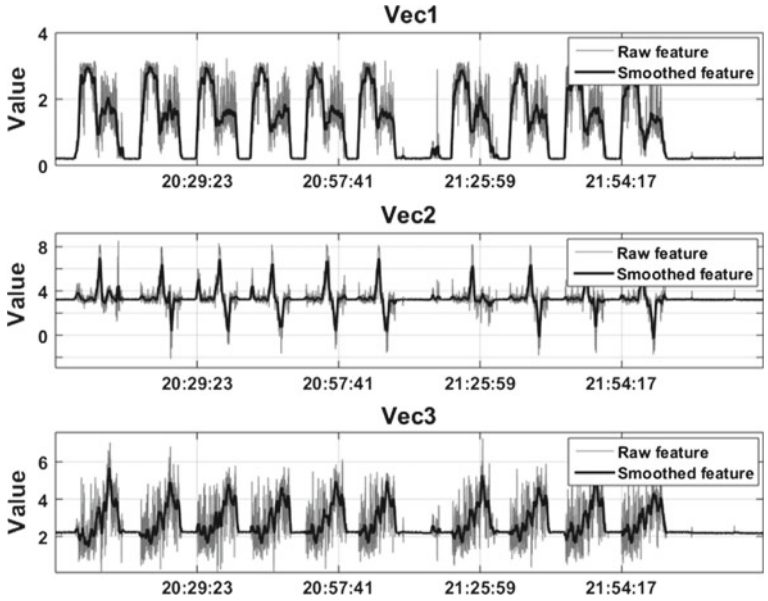

Fig. 3 Raw and smoothed output features

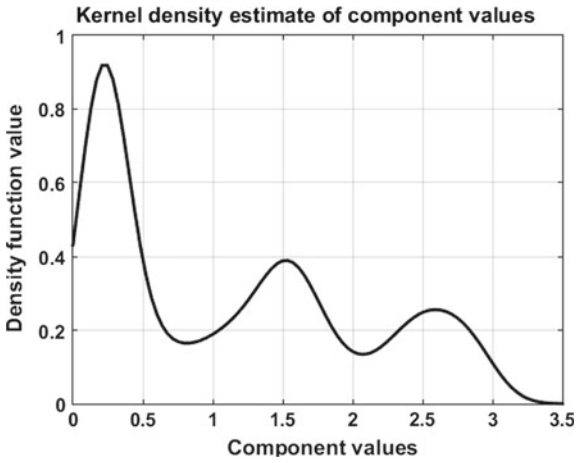

Fig. 4 Smoothed kernel density estimate of the selected component no. 1

In the next step we investigated expected subsets of values in the extracted feature. Smoothed kernel density estimate for selected component has been calculated (see Fig. 4), and its local minima define two thresholds that divide component values into three main regimes that are identified as:

- loading of a cargo box,
- driving to dumping point,
- return from dumping point with empty cargo box.

We can make an assumption here, based on visual inspection of input data and output components, that first component selected for further analysis is connected to vaguely stated "machine operational load", since it is structurally mostly similar to engine speed and fuel consumption. We can then easily identify mentioned regimes:

- **Loading of a cargo box** will take the lowest values. Machine is standing still and its cargo box is being loaded, engine load is the lowest.
- **Driving to dumping screen** will take the highest values. Cargo bucket is full and machine is driving under load.
- **Returning from the screen** will take medium values. Machine is driving, but with empty cargo bucket, which results in moderate load.

Signal of this component is then segmented according to obtained regimes of values (see Fig. 5). At the end of segmentation, data is post-processed just to eliminate very short improperly detected regimes originating from unexpected spikes in the signal, that were present because of the way that decomposition into independent components occurred.

As Fig. 5 shows, regimes are identified in very clear and correct way, that can allow for further statistical analysis related to process optimisation see Fig. 6.

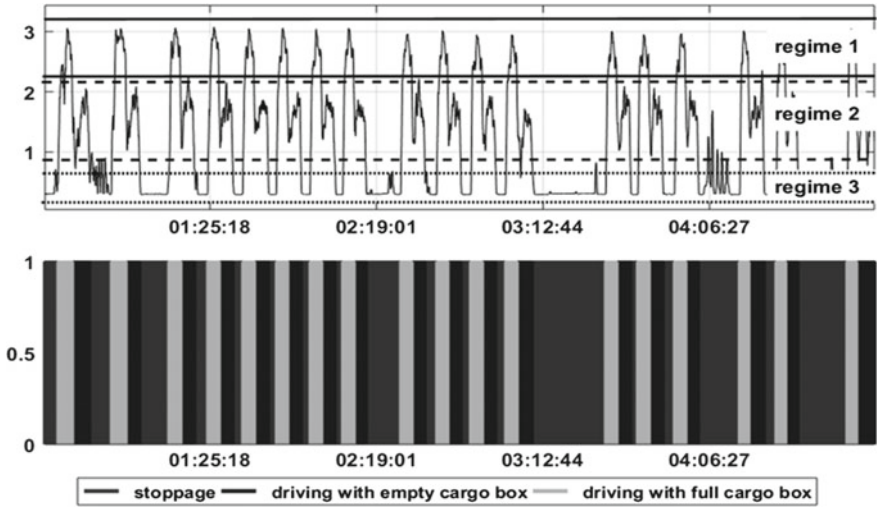

Fig. 5 Segmented component signal

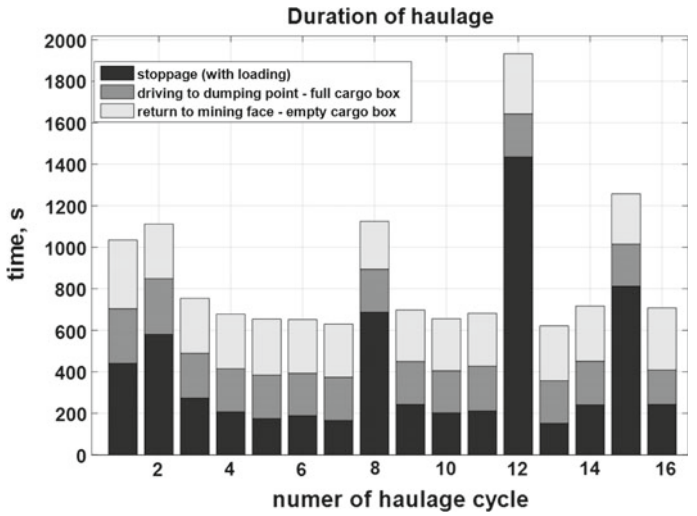

Fig. 6 Duration of particular partial operations of haulage cycles from single shift

5 Summary

Segmentation of operational data is just a pre-processing stage for further analysis. Extraction of cycles with its partial operations might allow to analyse performance of machines. In haulers case, identification of operational regimes and working cycles leads to constructing the algorithms like e.g. counting cycles in relation to time, analysis of regimes and cycles duration, detection of unexpected stoppages in the workflow etc. (see Fig. 6). Such indicators might give many information about realization of production in mining face and allow to support mining staff in context of better work organization. In this paper we present signal segmentation method based on independent component decomposition of hauler operational data. Results show that feature extraction methods can create good foundation for parameterization before applying segmentation procedures.

References

1. Cardoso, J. F. (1999). *High-order contrasts for independent component analysis*. *Neural Computation, 11*(1), 157–192.
2. Cardoso, J. F., Bose, S., & Friedlander, B. (1996). On optimal source separation based on second and fourth order cumulants. In *8th IEEE signal processing workshop in Corfu, statistical signal and array processing* (pp. 198–201).
3. Comon, P., & Jutten, Ch. (2010). *Handbook of blind source separation: Independent component analysis and applications*, Elsevier, ISBN: 978-0-12-374726-6.
4. Krishnaveni, V., Jayaraman, S., Manoj Kumar, P. M., Shivakumar, K., & Ramadoss, K. (2005). *Measurement Science Review*, *5*(2), 67–78.
5. Lopatka, M., Laplanche, C., Adam, O., Motsch, J.-F., & Zarzycki, J. (2005). Non-stationary time-series segmentation based on the Schur prediction error analysis. In *13th Workshop on statistical signal processing* (pp. 251–256). doi:10.1109/SSP.2005.1628601.
6. Polak, M., Stefaniak, P. K., Zimroz, R., Wylomanska, A., Sliwinski, P., & Andrzejewski, M. (2016). Identification of loading process based on hydraulic pressure signal. In *The conference proceedings of 16th International multidisciplinary scientific geoconference SGEM 2016* (pp. 459–466).
7. Stefaniak, P. K., Zimroz, R., Obuchowski, J., Sliwinski, P., & Andrzejewski, M. (2015). An effectiveness indicator for a mining loader based on the pressure signal measured at a bucket's hydraulic cylinder. In *Procedia Earth and Planetary Science* (Vol. 15, pp. 797–805).
8. Stefaniak, P. K., Zimroz, R., Sliwinski, P., Andrzejewski, M., & Wylomanska, A. (2016). Multidimensional signal analysis for technical condition, operation and performance understanding of heavy duty mining machines. In *Advances in Condition Monitoring of Machinery in Non-Stationary Operations*. *Applied Condition Monitoring*, *4*, 197–210.
9. Wylomanska, A., & Zimroz, R. (2014). Signal segmentation for operational regimes detection of heavy duty mining mobile machines—A statistical approach. *Diagnostyka*, *15*(2), 33–42.

Unsupervised Anomaly Detection for Conveyor Temperature SCADA Data

Jacek Wodecki, Paweł Stefaniak, Marta Polak and Radosław Zimroz

Abstract Belt conveyor system is a crucial element of ore transport process in underground copper ore mine. Damage of single belt conveyor might cause stopping of huge part of underground transport network, especially when failure concerns the main haulage conveyor line. For that reason it is important to use SCADA monitoring system. The symptom of damage can be found in increasing temperature measured within the system. Unfortunately, operating belt conveyors can be considered as time-varying system and direct decision making using temperature value is difficult. Long-term analysis of time series enables to learn how to recognize alarming moment. Thus the removal of failure can be scheduled so as to minimize the losses in production. In this paper the clustering method was applied to the long-term observations of the temperature in order to gearbox fault detection. Moreover, the breaks in the activity of belt conveyors (no operation) caused by holidays will be determined. The clustering algorithm identifies also the specific character of the work at the beginning and end of week.

Keywords Clustering algorithms · Scada system · Belt conveyor system · Temperature measurements

1 Introduction

Today extraction of deposit is reaching into increasingly deeper parts of rock mass what is closely related to much higher deterioration of mining conditions in context of environment, safety and reliability of machinery park. Currently underground mining industry demands in terms of assumed efficiency relate to ensure high reliability and availability of the machines. Conscious planning of repair works allows to achieve full integration of machine system in good condition during the operation. Such approach is closely connected with predictive maintenance (PdM) based

J. Wodecki (✉) · P. Stefaniak · M. Polak · R. Zimroz
KGHM CUPRUM Ltd, R&D, Sikorskiego 2-8, 53-659 Wrocław, Poland
e-mail: jwodecki@cuprum.wroc.pl

A. Timofiejczuk et al. (eds.), *Advances in Condition Monitoring of Machinery in Non-Stationary Operations*, Applied Condition Monitoring 9,
https://doi.org/10.1007/978-3-319-61927-9_34

on condition monitoring that should crowd out currently machine maintenance procedures in use in mining industry [1–3]. In copper ore mine case, this is especially important for belt conveyor network where damage of one belt conveyor might cause stopping of huge part of underground transportation system as well as LHD machinery operation [3].

In the literature the topic of the optimal control and efficiency of the belt conveyors system is widely investigated [4–6]. In the process of belt conveyors exploitation, SCADA systems record a lot of data represented as physical variables to monitor technological processes, especially degree of utilization, operational load and technical condition of the machines during their operation. Long term analysis of this data is very important in terms of understanding nature of the degradation process [7–9]. It can allow to identify any anomalies occurring in the context of well established general case of behavior. In practical application in industry, especially in mining, acquired data are difficult to interpret due to external disturbances (noise, missing values, etc.) and the complexity of monitored processes/systems. Temperature time series are varying in time and difficult to estimate in wider time window. It depends on many factors like:

- Conveyor technical condition,
- Conveyor design features,
- External load of conveyor,
- Location and role in transportation system,
- Engine operation mode,
- Environment parameters [10, 11].

Definition of set of statistical parameters and selection of appropriate analytical model for further classification is expected to lead to extraction of diagnostic information which is undoubtedly necessary to support maintenance staff [12, 13]. Early detection of damage might establish opportunities to determine repair moment in optimal time during planned standstill of given conveyor systems.

In this paper, a procedure for processing and analysis of temperature data from gearbox has been presented. The paper is organized as follows. Firstly, description of industrial acquisition process data and its pre-processing procedure will be shown. Next, we will move on to the proposed algorithm for clustering of multivariate data. At the end of the article, the context analysis of temperature data and identification of anomalies in operation process will be discussed.

2 Real Data Acquisition and Pre-processing Procedures

SCADA systems used in copper ore mine allow to collect the data concerning information about operational parameters of underground machines. Measurement of the specific physical variables helps in monitoring of condition of the machines and preventing damages. In this paper we analyze temperature data acquired by commercial,

multichannel low frequency data logger installed on the belt conveyor gearbox in copper ore mine.

Before starting any data analysis one should be sure that the data were acquired properly and were cleaned from the incorrect values, what allow to avoid the false conclusions of analysis. The pre-processing procedures are obligatory in case of temperature data from belt conveyor gearbox, where we applied two-step procedure: cleaning data and resampling [14].

First step of data pre-processing was to remove the outliers observations. In the recorded data there were clearly visible incorrect values, for example negative temperatures. Such observations are not possible in the underground mine reality, where temperature varies between 20 and 90 °C. Therefore the all outliers observations should be erase from the recording.

Another problem is the not-equally sampling of examined data. For memory saving, temperature data begin record while the difference between two consecutive observations is large enough, that means it is higher than predefined threshold. Although that algorithm minimizes the size of data, the observations are not equally sampled, what hinders the analysis. Due to that, we should focus on adequate resampling procedure. In [14] authors proposed the linear interpolation procedure to fill the missing observations. In view of the relatively small changes in the temperature during the short period of time, the mentioned method is appropriate to this kind of data. For each missing data time point, two neighboring recorded temperatures were taken and next the first order polynomial were fitted to them. The missing observation is replaced by value of fitted curve in specific time point. The data after application of pre-processing procedures are shown in Fig. 1. As one can see on the time series in Fig. 1, there are visible cyclic drops of the temperature. They are connected to breaks at work in underground mine. In that time the gearbox is cooled to the ambient temperature. That specific behavior allows to easily split the data into fragments corresponding to each week of the belt conveyor operation. Moreover one can notice that at 33rd day of collected data the sudden increase of the temperature occurs. Higher values of temperature remains for long time. The increase of temperature might be a symptom of damage. Therefore the aim of the article is to propose anomaly detection procedure, which automatically indicates the alarming time point. Such tool can help in preventing damages and in advance planning the repair. Using the time-date information, pre-processed data was split into sub-signals relating to one day of belt conveyor operation. In Fig. 2 one can see a difference between behavior of examined data depending on the day of the week. It should be mentioned that in copper ore mine there is a four shift work system. Moreover, on Saturday the work finishes at 6 p.m. and then begins at 6 a.m. on Monday. Therefore, during the 36 h break in operation, the belt conveyor is cooled to the ambient temperature. This time is used for planned maintenance tasks. In other days the cyclic breaks in working are caused by blasting procedures, which in copper ore mine are performed twice during the day. It is reflected in the time series as two temperature local minima about 9 a.m. and 21 p.m. Such different behavior of time series can be the indicator in the clustering process, which is used to recognized working days when the overheating has placed.

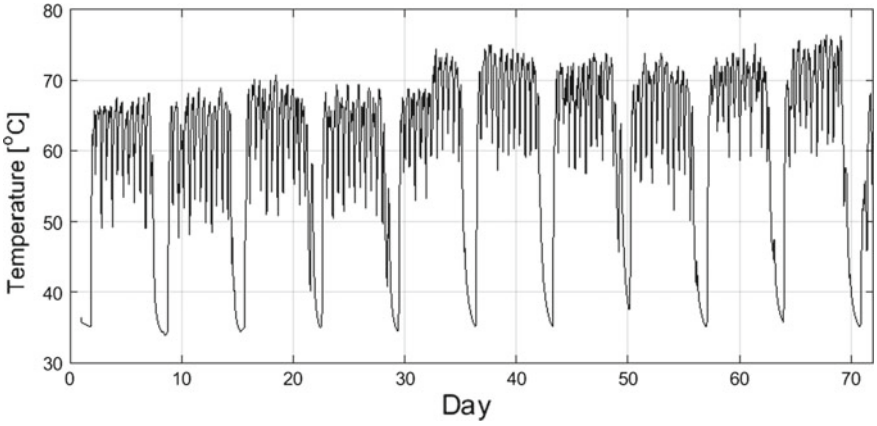

Fig. 1 Real temperature data from belt conveyor gearbox after pre-processing

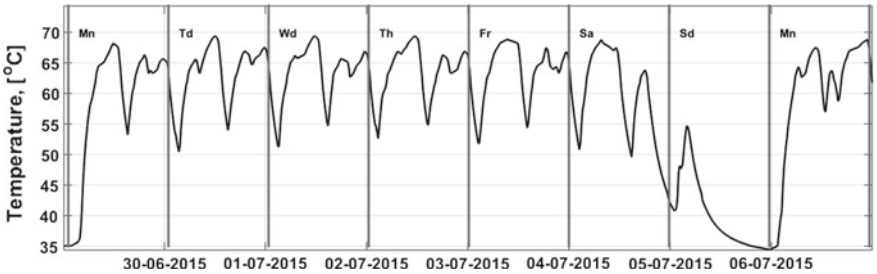

Fig. 2 Behavior of the temperature time series depending on day of the week

3 Description of Clustering Method

The clustering procedure used for unsupervised anomaly detection is the Expectation —Maximization algorithm. It is an iterative optimization method for estimation of unknown parameters, given measured data and latent variables representing missing data. EM is particularly useful for separating mixtures of Gaussian distributions over the considered feature space. It consists of two main steps: Expectation (E-step) and Maximization (M-step), which are iterated until convergence [15–18].

In the first iteration algorithm has to be provided with some initial values of parameters. It can be done by picking random means, covariances and distribution weights, but it is a good practice to pre-estimate means $\overrightarrow{\mu_l}$ using some simpler algorithm like k-means or hierarchical clustering, then compute covariance matrices Σ_l basing on results of this pre-clustering, and set weights α_l to normalized amount of points in each pre-cluster.

It is important to remember about limitations of EM methodology. EM only *tries to find* the maximum likelihood estimate, and not *finds* it with 100% confidence,

because EM estimate only guarantees *not to get worse* in the process. If the likelihood function has multiple peaks (non-concavity case) EM will not necessarily find the global optimum of the likelihood. In practice, one can never trust one single run. It is very common to start EM multiple times with multiple random initial guesses, and choose the one with the largest likelihood as the final estimate for parameters.

EM is widely used for data clustering in machine learning and computer vision techniques. In natural language processing, two prominent instances of the algorithm are the Baum-Welch algorithm and the inside-outside algorithm for unsupervised induction of probabilistic context-free grammars. In our method we also propose to estimate optimal amount of clusters with Silhouette criterion [12, 19] for limited range of number of clusters k (in our application k = 2:6) with Euclidean measure of distance.

In our application we use Expectation—Maximization algorithm under the assumption that point clouds in feature space will form clusters distributed normally.

Statistics used to feed the clustering algorithm were simple, yet informative. We chose:

- Maximum value of the day,
- Dispersion of values of the day,
- Value at the end of the day.

Time plot of statistics is presented in Fig. 3.

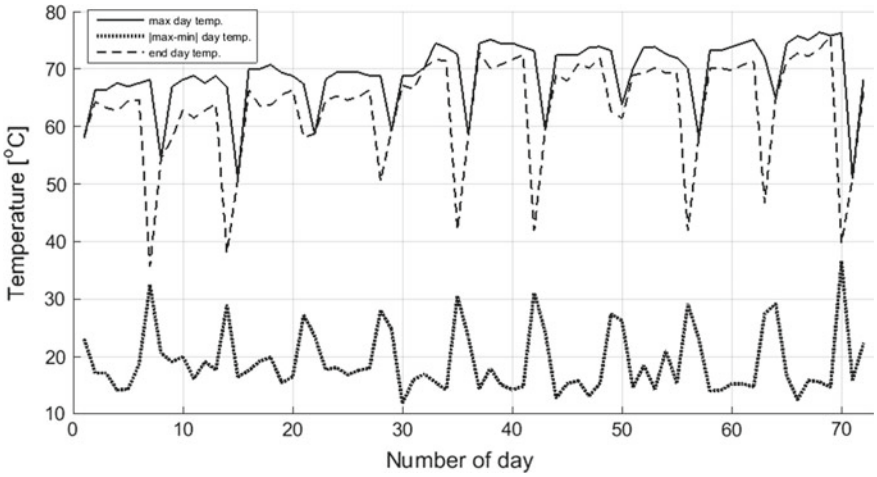

Fig. 3 Statistics used in clustering process

4 Clustering Results

Obtained feature data points constructed from described statistics distributed themselves in the 3D feature space as shown in Fig. 4. It is clearly visible that there are four or even five clusters possible to be distinguished. For this dataset Silhouette criterion returned optimal amount of clusters equal to 5. As a result of presented procedure we obtained information about individual days belonging to certain clusters (see Fig. 5). Each cluster defines in correct and accurate way one of five possible outcomes:

- Mondays,
- Saturdays,
- Sundays,
- Other days of the week in good condition,
- Other days of the week in bad condition.

All of those classes are important to be detected and identified. Mondays, Saturdays and Sundays reveal very outlying behavior, hence they are not informative and are detected only to be eliminated from further analysis. On the other hand, theoretically all days of the week could be divided into classes of good and bad conditions, but it would require more data. Greater amount of data might cause points in feature space to fill empty spaces within the clusters. Because of that, point clouds would be denser and more consistent. It would allow the Silhouette criterion to estimate larger optimal cluster amount, which then could possibly lead to distinction between good and bad condition on Mondays, Saturdays and Sundays. This outcome is impossible to obtain with the currently possessed amount of data, even if we force larger amount of clusters, because classification algorithm cannot properly construct clusters with this little amount of points in feature space. Figure 6 presents the results in time domain. Algorithm assigned particular days to correct classes.

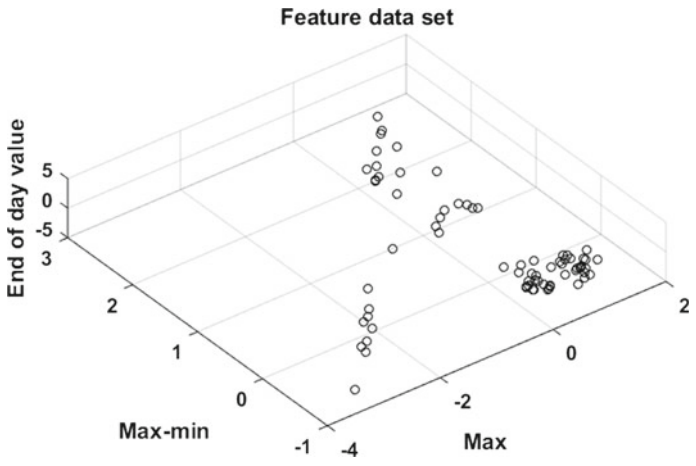

Fig. 4 Distribution of points in 3D feature space

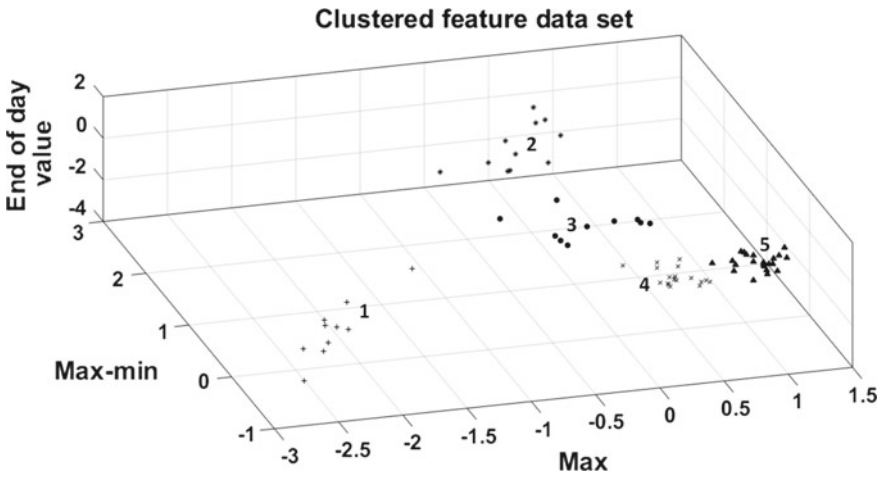

Fig. 5 Clustering results in feature space (values normalized). Clusters represent Sundays (*1*), Mondays (*2*), Saturdays (*3*), other days in good condition (*4*), and other days in bad condition (*5*)

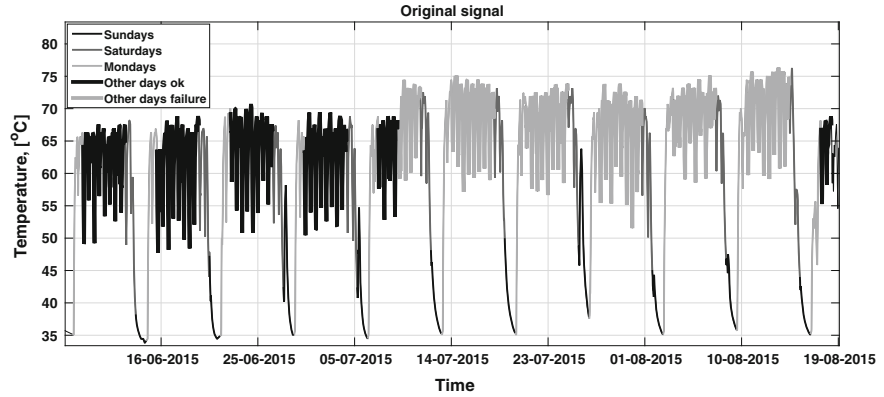

Fig. 6 Clustering results in time domain

5 Conclusions

In this paper we have presented the application of unsupervised learning method used for data classification in order to detect anomalies in diagnostic temperature signal from heavy duty gearbox used in underground mining industry. The methodology is based on Expectation—Maximization algorithm for Gaussian mixture model estimation, and parameterization with simple statistics. Introduced technique applied to real data gives much better and more reliable results than direct one-dimensional time series analysis. Obtained results allow to detect unusual behavior of the gearbox.

Acknowledgements This work is supported by the Framework Programme for Research and Innovation Horizon 2020 under grant agreement no. 636834 (DISIRE—Integrated Process Control based on Distributed In-Situ Sensors into Raw Material and Energy Feedstock).

References

1. Blazej, R., Sawicki, M., Kirjanow, A., Kozlowski, T., & Konieczna, M. (2016). Automatic analysis of themrograms as a means for estimating technical of a gear system. *Diagnostyka*, *17*(2), 43–48.
2. Jonak, J., & Gajewski, J. (2006). Operating diagnostics and monitoring issues of selected mining belt conveyers. *Maintenance and Reliability*, *4*(32), 74–78.
3. Stefaniak, P., Zimroz, R., Krol, R., Gorniak-Zimroz, J., Bartelmus, W., & Hardygora, M. (2012). Some remarks on using condition monitoring for spatially distributed mechanical system belt conveyor network in underground mine—A case study. In *Condition monitoring of machinery in non-stationary operations* (pp. 497–507). Springer. doi:10.1007/978-3-642-28768-8_51.
4. Bartelmus, W. (2014). Object and operation supported maintenance for mining equipment. *Mining Science, 21*, 7–21.
5. Krol, R., Kisielewski, W., Kaszuba, D., & Gladysiewicz, L. (2016). Testing belt conveyor resistance to motion in underground mine conditions. *International Journal of Mining*. Reclamation and Environment. doi:10.1080/17480930.2016.1187967.
6. Zhang, S., & Xia, X. (2010). Optimal control of operation efficiency of belt conveyor systems. *Applied Energy, 87*(6), 1929–1937.
7. Astolfi, D., Castellani, F., & Terzi, L. (2014). Fault prevention and diagnosis through SCADA temperature data analysis of an onshore wind farm. *Diagnostyka, 15*(2)71–78.
8. Bongers, D. R., & Gurgenci, H. (2008). Fault detection and identification for longwall machinery using SCADA data. In *Complex system maintenance handbook*, Springer Series in Reliability Engineering (pp. 611–641).
9. Zimroz, R., Bartelmus, W., Barszcz, T., & Urbanek, J. (2014). Diagnostics of bearings in presence of strong operating conditions non-stationarity-a procedure of load-dependent features processing with application to wind turbine bearings. *Mechanical Systems and Signal Processing*, *46*(1), 16–27.
10. Kruczek, P., Obuchowski, J., Zimroz, R., & Wyłomańska, A. (2016). Belt conveyor diagnostics—Damage detection based on multivariate data analysis. In *Proceedings of 16th SGEM International Multidisciplinary Scientific GeoConferences* (pp. 99–106). doi:10.5593/sgem2016B12.
11. Sawicki, M., Wyłomańska, Obuchowski, J., Stefaniak, P., Żak G. & Zimroz, R. (2015). An automatic procedure for multidimensional temperature signal analysis of a SCADA system with application to belt conveyor components. *Procedia Earth and Planetary Science*, *15*, 781–790.
12. Kaufman, L., & Rouseeuw, P. J. (1990). *Finding groups in data: An introduction to cluster analysis*. NJ: Wiley.
13. Stefaniak, P., Wylomanska, A., Obuchowski, J., & Zimroz, R. (2015). Procedures for decision thresholds finding in maintenance management of belt conveyor system—statistical modeling of diagnostic data. In *Proceedings of the 12th International Symposium Continuous Surface Mining—Aachen 2014* (pp. 391–402). Springer.
14. Wodecki, J., Stefaniak, P., Sawicki, M., & Zimroz, R. (2016). Application of independent component analysis in temperature data analysis for gearbox fault detection, submitted to Applied Condition Monitoring, Springer.
15. Dempster, A. P., Laird, N. M., & Rubin, D. B. (1977). Maximum likelihood from incomplete data via the EM algorithm. *Journal of the Royal Statistical Society, Series B, 39*(1), 1–38. JSTOR 2984875. MR 0501537.

16. Hastie, T., Tibshirani, R., & Friedman, J. (2001). The EM algorithm. *The elements of statistical learning* (pp. 236–243). New York: Springer. ISBN 0-387-95284-5.
17. Neal, R., Hinton, G., & Jordan, M. I. (1999). A view of the EM algorithm that justifies incremental, sparse, and other variants. In *Learning in graphical models* (pp. 355–368). Cambridge, MA: MIT Press. ISBN 0-262-60032-3. Retrieved 2009-03-22.
18. Sundberg, R. (1974). Maximum likelihood theory for incomplete data from an exponential family. *Scandinavian Journal of Statistics, 1*(2), 49–58. JSTOR 4615553. MR 381110.
19. Rouseeuw, P. J. (1987). Silhouettes: A graphical aid to the interpretation and validation of cluster analysis. *Journal of Computational and Applied Mathematics, 20*(1), 53–65.

Index

A

Acceleration of vibrations, 332
Acyclism, 319–321, 324, 326
Alpha-Stable Distribution (ASD), 92, 93, 96, 98, 99
Amplitude, 333
Amplitude-frequency characteristics, 309
Analysis, 91–93, 96, 97, 99
Autoregressive modeling (AR), 339, 340, 342, 345, 346, 350

B

Bearing, 34, 35, 37–42
Bearing default modelling, 33–35, 37, 39–41
Bearing diagnostics, 148, 154
Bearing fault, 332, 334, 340, 341, 344, 345, 351
Belt conveyor system, 361, 362
Binomial measure, 250, 251
Blind signal extraction, 191, 195, 197, 200
Blind source separation, 353, 356

C

Calibration of accelerometers, 214
Capacitive accelerometer, 220
Cepstral pre-whitening, 276

Cepstrum pre-whitening, 275, 281, 282
CI, 158, 165
Classification, 97, 99, 134, 135, 138–144
CI Model
Clustering algorithm, 361, 365
Clustering analysis, 87
Cointegration, 224–231
Complex systems, 92–94, 99
Conclusion, 176
Condition monitoring, 147, 148, 154, 167–169, 225, 227–231, 329–331
Construction of the databases, 170
Covariance matrix, 12, 13, 15–17, 19
Covariance matrix estimation, 12, 13, 15, 19
Cross-power spectral density, 215
Cyclostationary vibration signals, 191–194, 196, 200

D

Damping, 71, 72, 74, 76–79
Data acquisition, 111, 112, 114, 115, 118
Data classification, 133, 134, 143, 144
Data-driven, 91, 92, 99
Deceleration, 71–73
Detection of faults, 330–332, 334
Detrended Fluctuation Analyses (DFA), 92
Diagnostics, 92, 93, 96, 97, 99
Diagnostic signal, 330, 331
Diagnostic technique, 276
Dual fuel, 158, 159, 161, 162, 165
Dynamic behavior, 319–321, 326

E

Elastic coupling, 319–322, 324, 326

Energetic characteristics, 332–334
Energetic descriptors, 331, 335
Energetic envelope, 333
Energetic plane, 331
Energetic trajectories, 329, 331
Environmental conditions, 228
Estimation, 12, 15, 17–19
Experimental results, 229

F

False alarms, 55, 64, 68, 69

A. Timofiejczuk et al. (eds.), *Advances in Condition Monitoring of Machinery in Non-Stationary Operations*, Applied Condition Monitoring 9,
https://doi.org/10.1007/978-3-319-61927-9

Fault, 330
Fault detection, 330, 331
Fault diagnosis, 229
Feature selection, 172
FFT, 309, 310
Filtered Signals, 67–69
Fluctuation, 92–95, 99
Fractal dimension, 92, 94
Fractals, 247, 249, 252
Frequency, 330, 332
Frequency-domain, 330

G

Gaussian, 91, 93
Gear, 34, 36, 37, 39, 41
Gearbox, 235–237, 240–242
Gearbox diagnostics data, 256, 263

H
Haulers, 353, 355, 360
Hurst exponent, 249, 253

I
Impulse-like nature, 93

Index, 93, 94, 96, 97
Infrared thermography, 203, 206
Inspection, 235–237, 240–243
Instantaneous Angular Speed (IAS), 33–35, 40–42, 167, 168

K
Kalman estimator, 11–16, 19
K-means clustering, 87
Knife diagnostics, 82
Knocking, 157–164

L
Levy process, 250, 252
Linear Discriminant Analysis (LDA), 339, 341, 350
Linear discriminant analysis, 350

M

Maintenance state, 96–99
Materials and methods, 168
Matlab, 310, 311, 313, 317
mD (multidimensional, alias multivariate), 256
MEMS, 111, 114, 115, 118–120
MF-DFA, 92, 94
Model, 91, 92, 95, 96, 99, 158–161, 163
Modelling, 34–37, 92–94
Monitoring techniques, 330
Multifractality, 92, 95, 97
Multifractal measures, 250
Multifractal process, 250–252
Multifractals, 245–247, 249, 252, 253
Multiplicative cascade, 250
Multisinusiodal excitation, 214
Multivariate data visualization, 263

N

Natural frequency, 314
Non-linear, 92, 99
Non-stationary signal, 11, 18, 329
Non-stationary vibration signals, 188
Novelty detection, 180, 188

O
Operating at varying speed, 276
Optimisation, 123, 125
Order tracking, 11, 12, 180, 181, 186, 188, 191, 192, 276, 282
Orifice, 309, 310, 313–317

P

Pattern recognition, 168
Phase frequency characteristics, 310, 315, 316
Piezoelectric accelerometer, 218
Power spectral density, 215
Powertrain, 93, 96, 97, 99
Probability density function, 92, 96
Pulsating flows in pipes, 310, 314–317
Pulse generator, 311–314

R
Rare events, 245, 246
Residual Signals, 63, 64, 66, 67, 69

Resonance, 72, 74–76, 79
Resonant frequency, 314, 315, 317
Results and discussion, 173
Rolling bearings, 329–333, 335
Rolling element bearing, 133, 134, 148
Root-mean-square, 330

S
SCADA, 224, 225, 227–232
SCADA data, 228
SCADA systems, 362

Scale parameter, 93, 97

Segmentation, 353, 355, 356, 358, 360
Self-affinity, 248, 249
Self-similarity, 247, 248
Self-similar process, 249
Signal, 92–99
Signal decomposition, 147–150, 152, 154
Signal processing, 148
Signal spectrum, 330
Signal waveform, 331
Singularity, 93, 95–98
Specialistic multivariate (mD), 256
Spectrum, 92, 96
Speed recovery, 103, 109
Spur gearbox, 319, 321, 322, 326
Stable distributions, 92–94, 97
Stochastic Resonance, 56, 63, 67
Supervised classification, 134, 135
Support Vector Machine (SVM), 88, 339, 342, 348–350

T

Tapered bearing, 332
Teager-Kaiser energy operator, 329, 331
Technical condition, 330
Technical diagnostics, 245–247, 253
Technical state, 329
Temperature measurements, 361–363
Temporal heterogenity, 252
Thermocouple, 312
Time-domain, 330
Time history, 329
Time series, 91–96, 99
Transient disturbances, 331

U

Uncertainty of calibration, 214

V

Varying operating conditions, 228
Vibration, 235–240, 242, 243
Vibration diagnostics, 203–206, 210
Vibration exciter, 217
Vibration measurement, 203, 204
Vibration signals, 92, 96–99, 330, 331, 333, 335
Vibrodiagnostics, 91, 92
Visualizing multivariate data, 256

W

Wind turbines, 167–170, 173, 174, 176, 224, 225, 227–232